Journal of Engineering for Gas Turbines and Power

Published Monthly by ASME

VOLUME 132 • NUMBER 6 • JUNE 2010

RESEARCH PAPERS

Gas Turbines: Coal, Biomass, and Alternative Fuels

Gas Turbines: Combustion, Fuels, and Emissions

Gas Turbines: Cycle Innovations

(Contents continued on inside back cover)

This journal is printed on acid-free paper, which exceeds the ANSI Z39.48-1992 specification for permanence of paper and library materials. ♾™
♻ 85% recycled content, including 10% post-consumer fibers.

Editor
D. R. BALLAL (2011)

Assistant to the Editor
S. D. BALLAL

Associate Editors
Gas Turbine (Review Chairs)
T. SATTELMAYER (2010)
K. THOLE (2010)

Coal, Biomass & Alternative Fuels
K. ANNAMALAI (2013)

Combustion & Fuels
N. K. RIZK (2012)
T. SATTELMAYER (2012)

Controls, Diagnostics, & Instrumentation
A. VOLPONI (2013)

Cycle Innovation
W. SANZ (2013)

Electric Power
P. CHIESA (2011)

Structures and Dynamics
P. S. KEOGH (2010)
J. SZWEDOWICZ (2012)

Advanced Energy Systems
J. KAPAT (2010)

Internal Combustion Engines
C. RUTLAND (2012)
J. WALLACE (2011)
M. WOOLDRIDGE (2011)

Nuclear Engineering
J. KUNZE (2011)
I. PIORO (2011)

PUBLICATIONS COMMITTEE
Chair, **B. RAVANI**

OFFICERS OF THE ASME
President, **A. E. HOLT**

Executive Director,
T. G. LOUGHLIN

Treasurer,
W. MARNER

PUBLISHING STAFF

Managing Director, Publishing
P. DI VIETRO

Manager, Journals
C. MCATEER

Production Coordinator
J. SIERANT

Transactions of the ASME, Journal of Engineering for Gas Turbines and Power (ISSN 0742-4795) is published monthly by The American Society of Mechanical Engineers, Three Park Avenue, New York, NY 10016. Periodicals postage paid at New York, NY and additional mailing offices.
POSTMASTER: Send address changes to Transactions of the ASME, Journal of Engineering for Gas Turbines and Power, c/o THE AMERICAN SOCIETY OF MECHANICAL ENGINEERS, 22 Law Drive, Box 2300, Fairfield, NJ 07007-2300.
CHANGES OF ADDRESS must be received at Society headquarters seven weeks before they are to be effective. Please send old label and new address.
STATEMENT from By-Laws. The Society shall not be responsible for statements or opinions advanced in papers or ... printed in its publications (B7.1, par. 3).
COPYRIGHT © 2010 by the American Society of Mechanical Engineers. For authorization to photocopy material for internal or personal use under circumstances not falling within the fair use provisions of the Copyright Act, contact the Copyright Clearance Center (CCC), 222 Rosewood Drive, Danvers, MA 01923, Tel: 978-750-8400, www.copyright.com.
Canadian Goods & Services Tax Registration #126148048

Downloaded 03 Jun 2010 to 171.66.16.160. Redistribution subject to ASME license or copyright; see http://www.asme.org/terms/Terms_Use.cfm

Journal of Engineering for Gas Turbines and Power JUNE 2010

Volume 132, Number 6

Gas Turbines: Industrial & Cogeneration

Gas Turbines: Manufacturing, Materials, and Metallurgy

Gas Turbines: Microturbines and Small Turbomachinery

Gas Turbines: Oil and Gas Applications

Gas Turbines: Structures and Dynamics

TECHNICAL BRIEFS

The ASME Journal of Engineering for Gas Turbines and Power is abstracted and indexed in the following:

AESIS (Australia's Geoscience, Minerals, & Petroleum Database), Applied Science & Technology Index, Aquatic Sciences and Fisheries Abstracts, Civil Engineering Abstracts, Compendex (The electronic equivalent of Engineering Index), Computer & Information Systems Abstracts, Corrosion Abstracts, Current Contents, Engineered Materials Abstracts, Engineering Index, Enviroline (The electronic equivalent of Environment Abstracts), Environment Abstracts, Environmental Science and Pollution Management, Fluidex, INSPEC, Mechanical & Transportation Engineering Abstracts, Mechanical Engineering Abstracts, METADEX (The electronic equivalent of Metals Abstracts and Alloys Index), Pollution Abstracts, Referativnyi Zhurnal, Science Citation Index, SciSearch (The electronic equivalent of Science Citation Index), Shock and Vibration Digest

Downloaded 03 Jun 2010 to 171.66.16.160. Redistribution subject to ASME license or copyright; see http://www.asme.org/terms/Terms_Use.cfm

Simone Colantoni
e-mail: simone.colantoni@ge.com

Stefania Della Gatta

Roberto De Prosperis

Alessandro Russo

GE Oil & Gas,
Via F. Matteucci 2,
50127 Florence, Italy

Francesco Fantozzi

Umberto Desideri

Department of Industrial Engineering,
University of Perugia,
Via G. Duranti 1A/4,
06125 Perugia, Italy

Gas Turbines Fired With Biomass Pyrolysis Syngas: Analysis of the Overheating of Hot Gas Path Components

Alternative resources, such as biomass, and municipal and industrial waste are being considered as a source for the production of syngas to replace natural gas as a power turbine fuel. Pyrolysis of biomass produces a syngas composed primarily of CO, CO_2, CH_4, and H_2 with a medium-low lower heating value that is strongly dependent on the process boundary conditions such as the pyrolysis temperature and product residence time in the reactor. The issues associated with conventional gas turbines also apply to syngas turbines with the added complexity of the fuel and impurities. At present, syngas turbines are operated at firing temperatures similar to those of turbines fired on natural gas by increasing the fuel mass flow through the turbine. While this produces a higher turbine power output, the heat transferred to the hot flow-path vanes and blades is also greater. The aim of this paper is to report on the use of numerical modeling to analyze the fundamental impact of firing gas turbines with biomass pyrolysis syngas. To complete the analysis, the results have been compared with data from the literature on gas turbines fired with coal gasification syngas. The test engine used to perform this analysis is a General Electric GE10-2 gas turbine. The performance, aerodynamics and secondary flows were computed using proprietary software, while a commercial finite element software was used to perform the thermal and local creep analyses.

[DOI: 10.1115/1.4000134]

1 Introduction

Biomass is a renewable energy source with low or zero life-cycle CO_2 emissions, since the carbon produced in the combustion is balanced by the formation of new biomass. Moreover biomass-derived syngas has the potential to achieve a negative carbon balance if the CO_2 produced from combustion is sequestered. For this reason, in the future world energy scenario, biomass will play an important role for greenhouse effect mitigation. In addition, it represents an alternative to traditional fossil fuels. According to International Energy Agency (IEA) [1], in 2006 combustible renewables and waste (i.e., solid biomass, liquid biomass, biogas, industrial waste, and municipal waste) contributed 10.1% of the world's energy supply, which totaled 11,741 Mtoe.

For power generation, biomass and waste are generally used directly as solid fuel in conventional "grate-type" boilers for a steam cycle. This type of plant is generally characterized by a mid-to-high scale output range (10–40 MW) and medium to low efficiency (20–30%). Alternatively, the pyrolysis and gasification of biomass and waste allow an efficiency higher than 30% to be reached since the gas produced can be used in a very efficient energy conversion system, such as a gas turbine combined cycle [2–4]. Studies have indicated that a suitable thermal pyrolysis method can be used to both resolve municipal solid waste (MSW) disposal problems and to generate energy effectively [5,6]. As biomass does not contain sulfur, pyrolysis products (syngas and bio-oil) produce virtually no SO_x emissions and, therefore, would not be subject to SO_x taxes. Moreover, emissions of NO_x and heavy metals from the combustion of pyrolysis products [7] are much lower than those produced by direct combustion [8], and emission control is easier for pyrolysis than for incineration due to the reduced oxygen content, lower temperature, and greatly reduced air flow rate, which minimizes the need for expensive post-process gas scrubbing [9]. Based on these factors an integrated pyrolysis regenerated plant (IPRP, Fig. 1) was designed and optimized for biomass and waste conversion on a medium to small scale [3]. Experimental and numerical inputs [10–12] provided reliable data, and an 80 $\mathrm{kW_{el}}$ demonstration IPRP unit was built and is currently running with a regenerative microturbine in Central Italy [13]. However, compared with "clean" burning natural gas, gas turbines fired on syngas present issues associated with gas contaminants not successfully removed in the upstream cleaning stages, such as alkalis, trace metals, tars, and particulates. The development of reliable and economical cooling and cleaning systems, the application of suitable corrosion resistant coatings, and the understanding of related degradation mechanisms are priority research and development (R&D) topics.

1.1 Objective. This paper investigates the fundamental impacts of firing biomass pyrolysis syngas in gas turbines in terms of performance, aerodynamics, and secondary flows. The final objective is to determine the creep life reduction of turbine flow-path components due to expected overheating caused by the combustion of low lower heating value (LHV) fuel.

Analyses were performed on the General Electric GE10-2 engine (Fig. 1), and results will be compared with the same results for natural gas. Both analyses were performed at the same firing temperature. The stage one bucket (S1B) was selected as the component for evaluation of the reduction in life.

2 Pyrolysis Model: Fuel Composition

Pyrolysis is the thermal decomposition of biomass without oxygen (or in the presence of a low concentration of oxygen). The products of pyrolysis are the following:

Contributed by the International Gas Turbine Institute (IGTI) of ASME for publication in the Journal of Engineering for Gas Turbines and Power. Manuscript received April 15, 2009; final manuscript received July 14, 2009; published online March 19, 2010. Review conducted by Dilip R. Ballal.

Copyright © 2010 by ASME

Downloaded 02 Jun 2010 to 171.66.16.96. Redistribution subject to ASME license or copyright; see http://www.asme.org/terms/Terms_Use.cfm

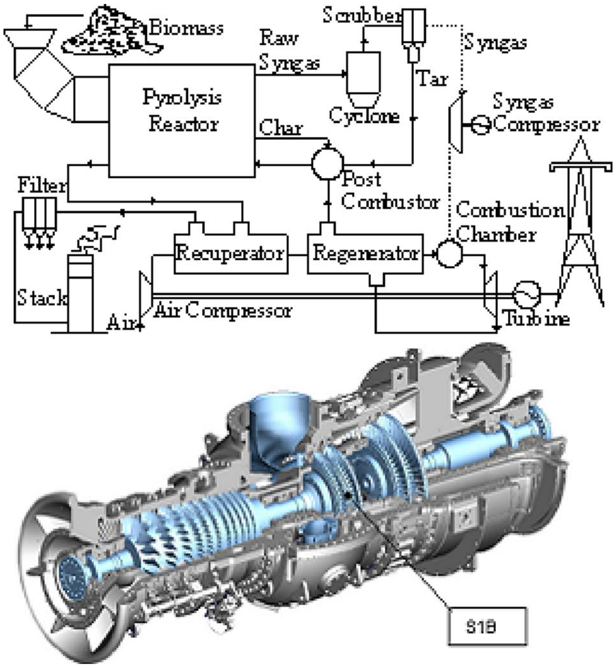

Fig. 1 IPRP plant layout [3] and gas turbine engine (GE10-2)

- solid: char composed of carbon and inerts
- liquid: tar, an organic product also referred to as bio-oil
- gas: syngas composed primarily of CO, CO_2, CH_4, and H_2

According to Browne [14], the pyrolysis process is divided into four zones, or temperature ranges, all of which can be present simultaneously in samples of wood of appreciable thickness.

> Zone A, below 200°C, in which only noncombustible gases, primarily water vapor, are produced. Dehydration of sorbed water is complete.
>
> Zone B, from 200°C to 280°C, in which the reactions are endothermic, and the products are almost entirely nonflammable.
>
> Zone C, from 280°C to 500°C, in which active pyrolysis takes place under exothermic conditions, leading to secondary reactions among the products. The products are largely combustible (carbon monoxide, methane, etc.) and include highly flammable tars in the vapor state.
>
> Zone D, above 500°C, in which the residue consists primarily of charcoal, which provides an extremely active site for further secondary reactions and therefore acts as a catalyst.

Temperature is therefore a very important parameter in the pyrolysis reaction because it influences both the quantity and quality of the products obtained.

Apart from temperature, many other factors determine the yield of pyrolysis products and the syngas composition. The most important are the pyrolysis process (slow, fast, and flash) [15], the type of reactor (fluid bed, circulating fluid bed, transported bed, ablative, rotating cone, entrained flow, vacuum moving bed, and rotary kiln) [16], the heating rate [17], the residence time [18], the biomass particle size [19], the biomass moisture content [20], and the biomass composition [21].

Fagbemi et al. [21] showed the effect on syngas composition (Table 2) using three different types of biomass: wood, coconut shell, and straw (Table 1).

As shown in Table 2 the composition of the gas fraction versus temperature between 500°C and 900°C does not vary significantly with the type of biomaterial tested.

Table 1 Elemental composition of solid fractions [21]

	C	H	O	N	Ash	HHV (kJ/kg)
Wood	45.68	6.30	47.42	0.30	0.3	18,988
Coconut shell	45.97	5.88	45.57	0.30	0.5	19,450
Straw	42.69	6.04	47.11	0.46	3.7	17,534

In this paper, the pyrolysis model is based on the pyrolysis of wood biomass, and the syngas composition was simulated as a function of pyrolysis temperature in accordance with the results found by Fagbemi et al. [21]. Table 3 summarizes the syngas composition and lower heating value at different pyrolysis temperatures for the reference wood.

The concentrations of CH_4 and C_2H_x (considered as C_2H_6 in the following analysis) reach a maximum value between 600°C and 700°C. A regular decrease in CO_2 concentration with temperature occurs with a simultaneous increase in CO and H_2 concentration. High temperatures are known to favor the production of H_2 to the detriment of higher hydrocarbons, which are dehydrogenated by thermal cracking. The lower heating value ranges from 6 MJ/kg to 18 MJ/kg and increases with process temperature.

3 Numerical Modeling

3.1 Baseline Case and Assumptions. The General Electric GE10-2 two-shaft gas turbine was used as the expander, and natural gas (methane) was used as a baseline fuel. The GE10-2 package is designed for optimum performance in pipeline, re-injection, and other oil and gas field applications (on- and off-shore), as a pump drive, and also for power generation applications. The com-

Table 2 Pyrolysis syngas composition for wood, coconut shell, and straw at different reaction temperatures [21]

Temperature (°C)		400 % vol	500 % vol	600 % vol	700 % vol	800 % vol	900 % vol
H_2	Wood	1.3	7.6	10.8	15.5	20.8	25.3
	Coconut s.	1.0	5.4	12.4	18.5	23.5	-
	Straw	-	7.4	12.8	19.2	23.4	24.6
CH_4	Wood	9.3	12.8	16.5	16.1	14.2	12.1
	Coconut s.	10.2	13.2	16.8	17.2	15.8	-
	Straw	-	11.8	13.0	15.3	13.7	12.1
CO	Wood	34.2	39.7	42.5	44.3	50.1	53.5
	Coconut s.	31.0	35.0	38.1	40.1	44.2	-
	Straw	-	35.0	37.7	41.0	48.1	53.3
CO_2	Wood	51.9	36.6	23.0	16.7	9.1	5.0
	Coconut s.	53.1	42.2	28.7	17.9	9.8	-
	Straw	-	40.7	30.0	15.8	8.4	4.5
C_2H_x	Wood	3.3	3.3	7.2	7.4	5.8	4.1
	Coconut s.	4.7	4.2	4.0	6.3	5.3	-
	Straw	-	5.1	5.5	8.7	6.5	5.5

Table 3 Wood pyrolysis syngas versus reaction temperature [21]

Temperature (°C)	400	500	600	700	800	900
Fuel identification code	A % vol	B % vol	C % vol	D % vol	E % vol	F % vol
H_2	1.3	7.6	10.8	15.5	20.8	25.3
CH_4	9.3	12.8	16.5	16.1	14.2	12.1
CO	34.2	39.7	42.5	44.3	50.1	53.5
CO_2	51.9	36.6	23.0	16.7	9.1	5.0
C_2H_x	3.3	3.3	7.2	7.4	5.8	4.1
LHV (MJ/kg)	6.3	9.2	14.1	15.9	17.3	17.6

Downloaded 02 Jun 2010 to 171.66.16.96. Redistribution subject to ASME license or copyright; see http://www.asme.org/terms/Terms_Use.cfm

Table 4 GE10-2 baseline case data

GE10-2 (ISO conditions for standard combustor)		
Electrical output	kW	11,982
Electrical efficiency	%	33.3
Exhaust flow	kg/s	47.0
Exhaust temperature	°C	480

bustion chamber (CC) and the fuel feed system can accommodate different gas/liquid fuel compositions and NO_x emission requirements. The key parameters are shown in Table 4. Both the low pressure turbine (LPT) and high pressure turbine (HPT) consist of two air-cooled stages. To optimize the behavior at partial speed/load, a variable nozzle guide vane is installed between the high pressure (HP) and low pressure (LP) sections.

This study aims to compare in detail the differences between natural gas and pyrolysis syngas from a double perspective: performance and engine life. The next few paragraphs present the impact on cycle efficiency and highlight the most promising syngas compositions of those presented. Then, the new thermal conditions of the gas path are assessed through aerodynamic analysis, which includes the secondary air system. Finally, the results of the mechanical analysis are presented. The analysis of the firing with biomass pyrolysis syngas was performed assuming the same firing temperature as for natural gas and assuming the syngas to be dry and free from tar and impurities.

3.2 Performance. The GE10-2 "cycle deck" was employed for the evaluation of the engine performance with the fuels shown in Table 3 (CH_4 and Fuels A–F). The cycle deck is the aerothermal model of the gas turbine, which includes the characteristics (maps) of the individual components (compressor, HPT, and LPT) and the control schedules and logic. By solving the equations of flow continuity and the energy balance, the thermodynamic cycle and the engine performance can be evaluated at any operating condition. The GE10-2 cycle deck model was validated on the basis of the data collected during a precision engine test, with special instrumentation installed both in the flow path and in the secondary air system. This model can therefore be considered an accurate representation of the engine behavior and thermodynamics. A comparison of the main engine performance parameters calculated with the cycle deck for different fuels at the same firing temperature is reported in Table 5. The firing temperature is an input to the simulations, and the necessary fuel flow is calculated by the cycle deck as a consequence. The value of the firing temperature used in this application is the design firing temperature. The conditions of the different fuels at the combustor inlet are assumed to be equal with respect to temperature and pressure, so that the results are fully comparable.

Table 5 shows that the shaft power increased by 3% to 21% compared with that for natural gas firing. This increment is mainly driven by the additional fuel gas flow that is necessary to reach the target firing temperature. Fuel A (the leanest of the test fuels) required the highest flow rate at the considered firing temperature, and this also resulted in the highest power increment.

Table 5 Main engine performance parameters for Fuels A–F $\Delta[\%]=\%$ variation in changing from natural gas to syngas

Fuel name	A Δ%	B Δ%	C Δ%	D Δ%	E Δ%	F Δ%
Pressure ratio	9.45	5.57	2.96	2.41	2.06	1.97
Compressor discharge *T*	3.85	2.23	1.19	0.97	0.85	0.80
HPT discharge *T*	3.93	2.34	1.15	0.88	0.69	0.60
Shaft power	20.94	12.20	6.02	4.7	3.75	3.45
Thermal efficiency	5.06	3.29	1.68	1.32	1.08	1.02

Table 6 HTC preliminary assessment for Fuels A–F $\Delta[\%]=\%$ variation in changing from natural gas to syngas

Fuel name	A Δ%	B Δ%	C Δ%	D Δ%	E Δ%	F Δ%
Prandtl number	−6.54	−3.77	−1.70	−1.26	−0.91	−0.81
Reynolds number	12.43	7.35	3.98	3.22	2.77	2.62
Nusselt number	7.40	4.50	2.59	2.14	1.90	1.82
HTC	14.11	7.89	3.70	2.81	2.14	1.92

Some other effects are also associated with higher fuel flow rate. The principle factor is the increase in the compressor pressure ratio, which derives from the assumption of choked flow at the turbine and constant firing temperature. Assuming constant turbine corrected flow W_t, an increase in fuel mass flow requires an increase in the turbine inlet pressure P_{HPT}.

$$W_t = \frac{m_{\mathrm{HPT}} \cdot \sqrt{T_{\mathrm{HPT}}}}{P_{\mathrm{HPT}}} \approx \frac{(m_C + m_F) \cdot \sqrt{T_{\mathrm{firing}}}}{P_{\mathrm{HPT}}} = \text{constant}$$

$$\text{therefore} \quad \frac{(m_C + m_F)}{P_{\mathrm{HPT}}} = \text{constant} \tag{1}$$

A secondary effect of the increased pressure ratio is the increase in compressor discharge temperature (from 0.8% to 3.9%), which results in a lower cooling capacity for the components cooled with this air. Furthermore, despite the equal firing temperature, syngas shows a higher HPT discharge temperature, which results in higher blade temperatures. The level and variation in temperature within the component material (which causes thermal stresses) must be limited to achieve reasonable durability goals. The creep life of metal components in the hot section of a gas turbine is extremely sensitive to metal temperature. In addition, a preliminary assessment of the heat transfer coefficient (HTC) can be done starting from nondimensional analysis. In fact, the Nusselt number (Nu) can be correlated with the Reynolds (Re) and Prandtl (Pr) numbers, as elaborated on the next paragraph (see Eqs. (2)–(5)). First, the Prandtl and Reynolds numbers were estimated starting from the characteristics of the gas and the data produced by the cycle deck. The results as a percentage of the natural gas case are reported in Table 6.

Due to the concentrations of hydrogen-containing species in Fuels A–F of Table 3, the concentration of H_2O in the combustion products increases from Fuel A to Fuel F. This results in an increase in the Prandtl number, since it depends on the gas composition. On the contrary, the Reynolds number decreases due to a lower mass flow rate (and hence velocity) from Fuel A to F. Table 6 shows that the effect of the Reynolds number is dominant in evaluating the Nusselt number, which means a decrease in HTC from Fuel A to F.

The higher HTC and the higher cooling gas temperature point to Fuel A as the worst case for creep life reduction. Consequently, Fuel A was selected for the analyses that follow.

3.3 Aero- and Secondary Flows. The operating point identified in the previous paragraph gives the boundary conditions to explore the new gas path conditions. The scope of the aerodynamic analysis is to provide the thermal boundary conditions for the mechanical analysis. A GE proprietary through-flow code was employed for the main flow. Three-dimensional (3D) effects, such as hot streak migration or full development of vortices, are not addressed by this approach. However, considering that the analysis is conduced on a delta-basis, in the authors' experience a two-dimensional model provides sufficient detail.

The analysis of component life was focused on S1B, the most severely affected component based on the following.

Downloaded 02 Jun 2010 to 171.66.16.96. Redistribution subject to ASME license or copyright; see http://www.asme.org/terms/Terms_Use.cfm

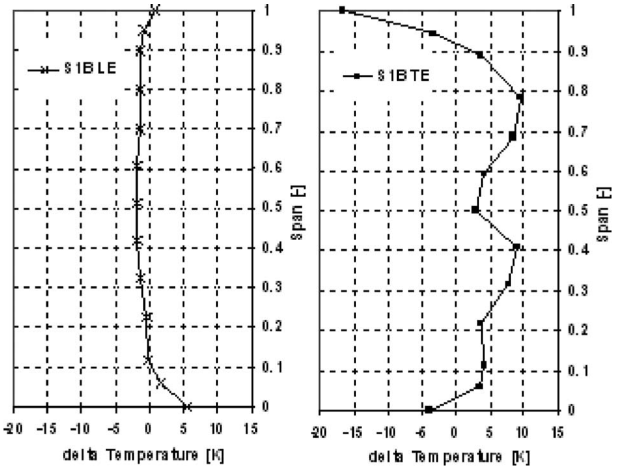

Fig. 2 Differences in total temperature between Fuel A and CH_4, respectively, at the inlet and exit of the first stage blade

Table 7 HTC and *T* hot gas path calculation: % variation in changing from natural gas to syngas for average values on the PS and SS

	Pressure side		Suction side	
Span	Delta HTC (%)	Delta *T* (°C)	Delta HTC (%)	Delta *T* (°C)
0.96	12	−4	13	−4
0.88	13	1	10	1
0.81	12	3	8	3
0.73	11	3	7	4
0.65	9	2	8	2
0.58	9	2	8	2
0.50	9	2	8	2
0.42	8	2	8	3
0.35	8	3	7	4
0.27	10	3	8	3
0.19	8	6	6	6
0.12	10	4	8	4
0.04	13	5	11	5

- The maximum cooling air temperature increase occurs at S1B because the air is extracted from the compressor discharge.
- The S1B temperature, which is higher than that of the other downstream components, is a fundamental parameter in terms of creep life.
- S1B, like other nozzles and buckets, is affected by overheating in the flow-path.

The results reported in Fig. 2 refer to the differences in total temperature at the inlet and exit of the first stage bucket between operation with Fuel A versus methane. The differences at the inlet are lower and are mainly due to differences in cooling. At the trailing edge (TE), this difference spans from −18 K to 10 K. This is due both to a change in the work extracted by the first stage and to different coolant conditions. In fact, the increase in the compressor discharge temperature corresponds to an increase in the coolant temperature of the first stage.

The finite element modeling (FEM) analysis required the thermal boundary conditions at both the hot gas path side and the shank/dovetail side of the blade. The heat transfer conditions in the hot gas path were calculated leveraging the results of the aerodynamic calculations. To simplify the calculation, a through-flow approach was adopted using a cylinder in cross-flow for the leading edge (LE) area (2) and a flat plate for the suction and pressure sides of the airfoil far from the leading edge (3) [22]

$$\mathrm{Nu} = a \cdot \left(1.14 \cdot \mathrm{Re}_D^{1/2} \cdot \mathrm{Pr}^{0.4} \cdot \left(1 - \left|\frac{\Phi}{90}\right|^3\right)\right) \tag{2}$$

$$-80 \ \mathrm{deg} < \Phi < 80 \ \mathrm{deg}$$

$$\mathrm{Nu} = 0.0296 \cdot \mathrm{Re}_x^{0.8} \cdot \mathrm{Pr}^{1/3} \tag{3}$$

where Nu is the Nusselt number, a is the augmentation factor for highly turbulent mainstream, D is the LE diameter, Re_D is the Reynolds number based on LE diameter, Pr is the Prandtl number, Φ is the angular distance from LE stagnation point, x is the distance from LE, and Re_x is the Reynolds number based on distance x.

No flow 3D structures were taken into account. Further improvement should include 3D computational fluid dynamics (CFD) analysis of the hot gas path. Since the firing temperature was set at the same nominal value for both fuel cases, the major impact in the hot gas path was expected to be a significant HTC delta. The calculation results are summarized in Table 7.

The analysis of the secondary air system was performed to assess the heat transfer boundary conditions impacting the first stage blade in the shank, cooling system, and dovetail areas. Proprietary correlations were employed for the shank area, while duct flow correlations (4) and (5) for laminar and turbulent convection [23,24] were adopted for the dovetail region and blade cooling radial holes

$$\mathrm{Nu} = 1.86 \cdot (DH/X)^{1/3} \cdot (\mathrm{Re} \cdot \mathrm{Pr})^{1/3} \cdot (\mu_b/\mu_w)^{0.14} \tag{4}$$

$$\mathrm{Nu} = 0.023 \cdot (1 + 1.2 \cdot (DH/X)) \cdot \mathrm{Re}^{4/5} \cdot \mathrm{Pr}^{1/3} \tag{5}$$

where Nu is the Nusselt number, Re is the Reynolds number, Pr is the Prandtl number, DH is the hydraulic diameter, X is the length, μ_b is the viscosity at the fluid bulk temperature, and μ_w is the viscosity at the wall temperature.

The calculated heat transfer coefficients were found to be about 3% higher in the radial cooling holes, 0.5% higher in the dovetail region, and 5% higher in the shank region when feeding the turbine with syngas. Moreover, the increased pressure ratio provided by the axial compressor leads to a higher compressor discharge temperature (+14°C), thus, impacting the effectiveness of the blade cooling system fed by the compressor discharge itself. Figure 3 shows the variation on changing from natural gas to Fuel A of bulk temperature (Tb) both on the pressure and suction sides (PS) and (SS).

4 Part Life Analysis

The durability of hot flow-path components, such as nozzles and buckets, represents a key factor for the designer of gas turbines because a high percentage of the maintenance costs of the unit can be associated with the repair and replacement of these high value parts. Hence, one of the most important design goals is extending the lives of these components and increasing the interval between inspections and replacements.

As previously discussed, the results of the aerodynamic and secondary flow analyses indicated that the hot flow-path component most affected by the overheating is the stage one bucket. Analyses of S1B (thermal and local creep) were performed using commercial finite element software, ANSYS®, and the thermal boundary conditions were mapped on a FEM model of the blade as HTC and Tbulk. The results of the thermal analysis showing the difference in metal temperatures for the Fuel A and natural gas cases for both the pressure and suction sides are shown in Fig. 4.

To evaluate the influence of increased metal temperature on the creep life of S1B, a local creep analysis was performed under the application of constant mechanical and thermal loads. The analysis was performed both for natural gas and Fuel A to determine the

Downloaded 02 Jun 2010 to 171.66.16.96. Redistribution subject to ASME license or copyright; see http://www.asme.org/terms/Terms_Use.cfm

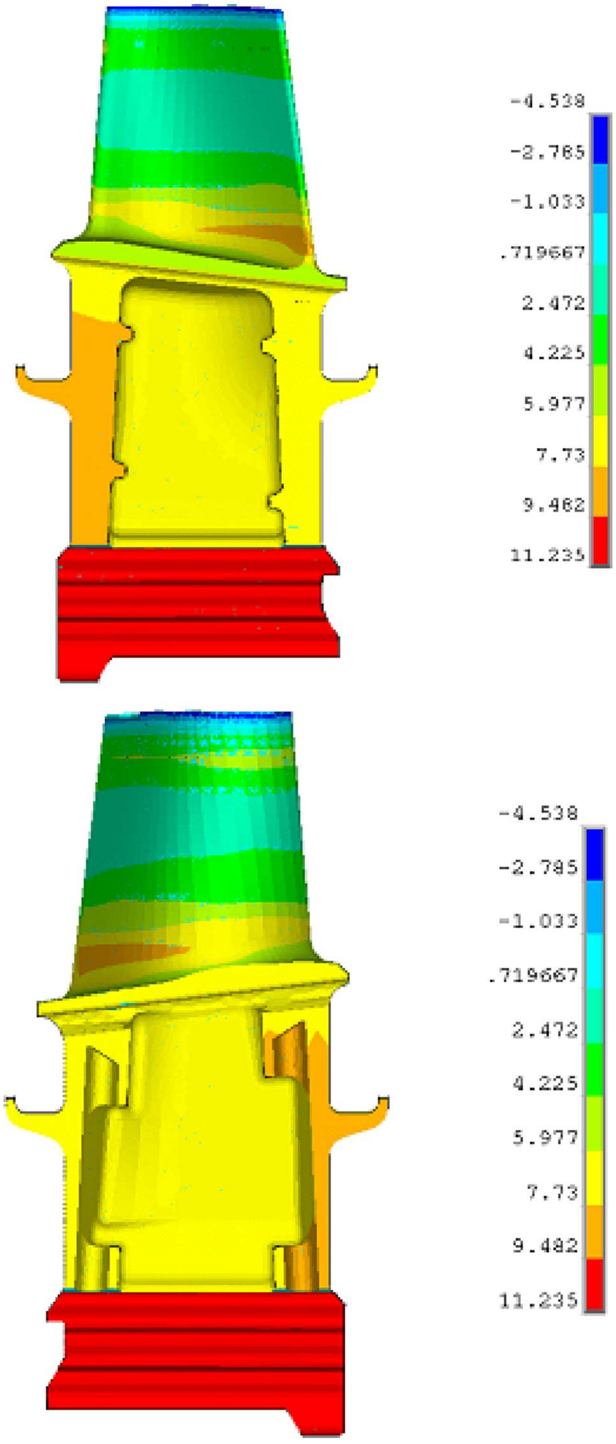

Fig. 3 GE10-2 S1B thermal boundary conditions PS and SS; ΔTb(°C)=(Tb Fuel A(°C))−(Tb natural gas(°C))

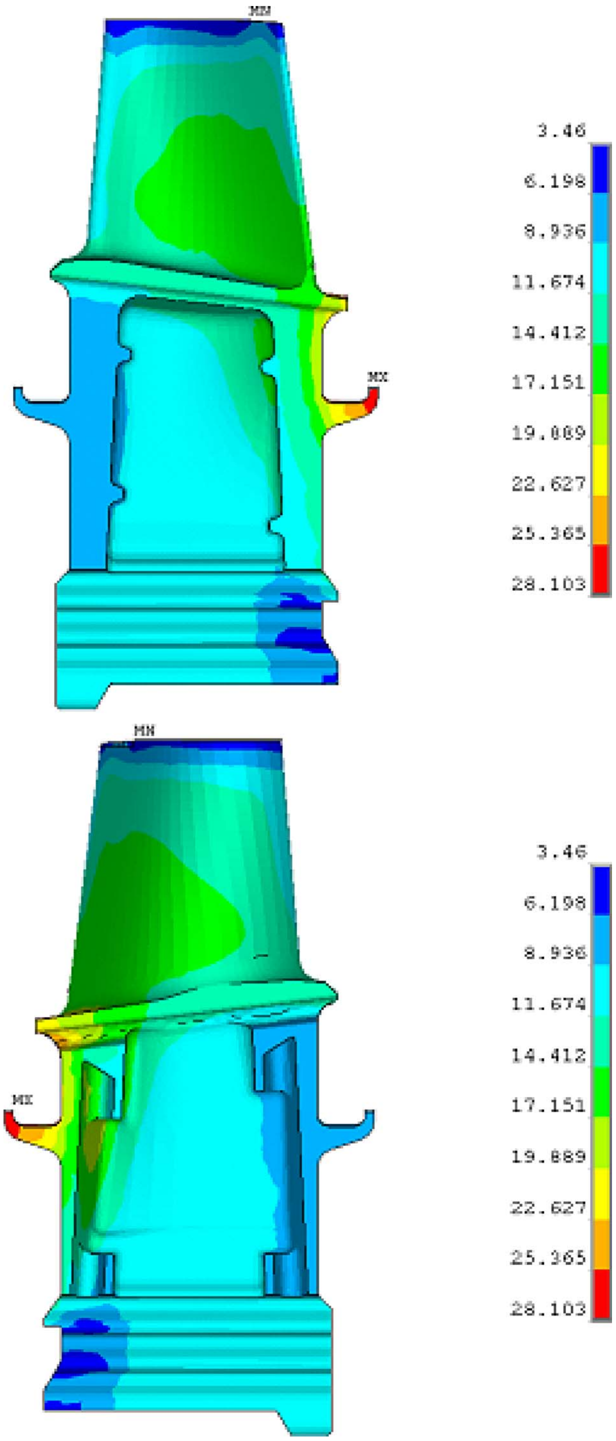

Fig. 4 GE10-2 S1B thermal analysis PS and SS; Δ*T*(°C) =(*T* Fuel A(°C))−(*T* natural gas(°C))

strain ε after a time interval (h). Figure 5 shows the difference in strain for Fuel A and natural gas after 500,000 h for both the pressure and suction sides of the bucket.

The results show the following differences in strain after 500,000 h for Fuel A and natural gas.

- On the trailing edge, the strain for the natural gas case is about 0.02% higher than that for Fuel A.
- On the tip, the strain for the natural gas case is about 0.01% higher than that for Fuel A.
- On the suction side, the strain for the Fuel A case is about 0.13% higher than that for natural gas.
- On the pressure side, the strain for the Fuel A case is about 0.18% higher than that for natural gas.

Figure 6 shows the time history of the parameter $\Delta\varepsilon$ for the four points that present higher strain values on the trailing edge, the pressure side (PS), the tip (TIP), and the suction side.

The increased strain on the suction and pressure sides with Fuel A is more critical than the small decrease for the trailing edge and tip zones. Moreover, from Fig. 6 it is easy to understand the trend

Downloaded 02 Jun 2010 to 171.66.16.96. Redistribution subject to ASME license or copyright; see http://www.asme.org/terms/Terms_Use.cfm

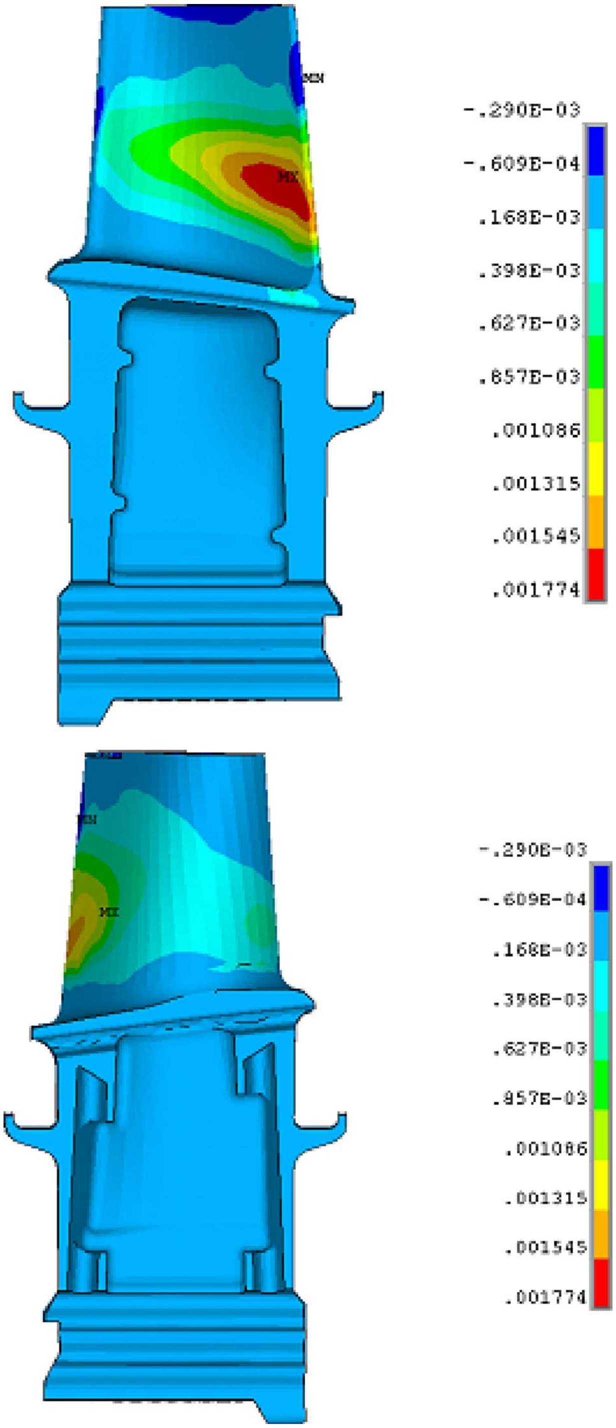

Fig. 5 GE10-2 S1B local creep analysis PS and SS at 500,000 h; $\Delta\varepsilon = (\varepsilon \text{ Fuel A}) - (\varepsilon \text{ natural gas})$

of these curves and, therefore, how the increments in strain resulting from Fuel A have a higher slope with respect to time.

5 Results and Discussions

The final objective of this analysis is assessing the reduction in S1B creep life due to the overheating of the flow path. According to GE bucket design practice, the creep life is determined when the local creep strain exceeds a fixed value $\varepsilon_{\text{limit}}$

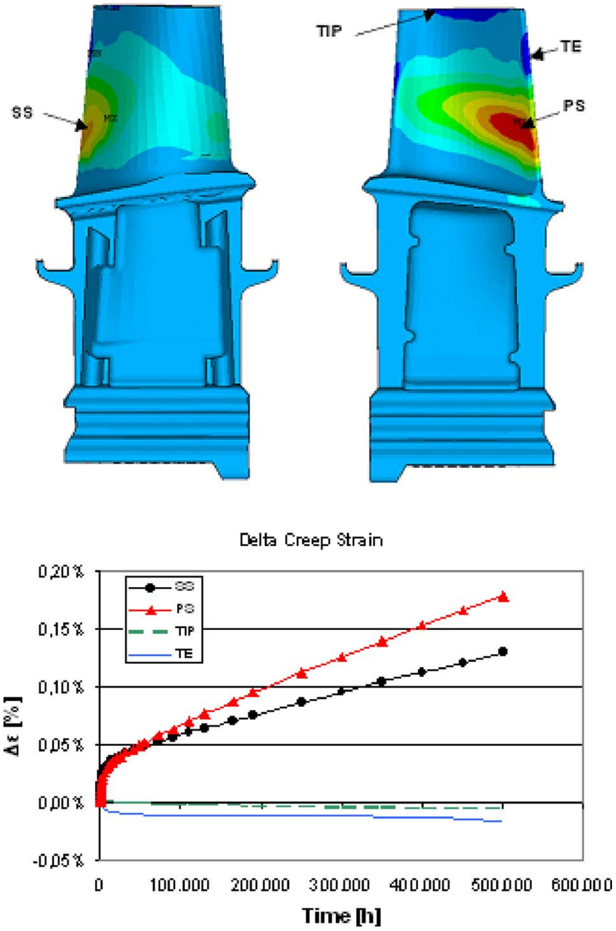

Fig. 6 $\Delta\varepsilon(\%) = (\varepsilon \text{ Fuel A}(\%)) - (\varepsilon \text{ natural gas}(\%))$ versus time (h)

$$\text{creep life} = \text{life}(\varepsilon = \varepsilon_{\text{limit}}) \cdot K \qquad (6)$$

K is a factor (<1) that takes into account the variability of the temperature and material properties, and it is obtained for a defined quality specification level. A comparison of the results of local creep analyses has shown how the combustion of Fuel A provides an increase in strain. Applying the strain limit ($\varepsilon_{\text{limit}}$) suggested by GE design practice, through Eq. (6) it is possible to determine the S1B creep life both for methane and pyrolysis syngas. The result is

$$\text{S1B}_{\text{creep life syngas}} = 0.57 * \text{S1B}_{\text{creep life CH4}}$$

which is a creep life reduction of about 43%.

A qualitative comparison of this result can be made with data from the literature on an integrated gasification combined cycle (IGCC) in which a gas turbine was fired with a gas synthesized by coal gasification [25]. Gasification processes may use either air or oxygen as the oxidant in the gasifier vessel, and such gasifiers are referred to as either air-blown or oxygen-blown gasifiers. Syngas is primarily composed of carbon monoxide and hydrogen (up to 61%), but also contains a significant fraction (up to 50%) of noncombustibles such as steam, carbon dioxide, and nitrogen; the LHV is about 1/3 the lower heating value of natural gas. The dilution of the fuel with nitrogen and water (syngas saturation) is usually employed to reduce NO_x emissions by reducing the peak flame temperatures. This results in a further reduction in the LHV and in an increase in water in both the diluted syngas and the combustion products.

The coal syngas (referred to as "Fuel C" in Ref. [25]) selected for the comparison has an LHV of the same magnitude as that of

Downloaded 02 Jun 2010 to 171.66.16.96. Redistribution subject to ASME license or copyright; see http://www.asme.org/terms/Terms_Use.cfm

Table 8 Diluted coal syngas composition [25]

Fuel name	C (% vol)
H_2	39.28
CH_4	0.14
CO	0.92
CO_2	2.92
N_2	47.44
Ar	0.60
H_2O	8.00

the Fuel A biomass syngas, i.e., ~6 MJ/kg. The equivalence of the LHV will be the basis of the comparison. The diluted coal gasification syngas composition is shown in Table 8.

In this case, the creep life was evaluated using the relationship developed by Larson and Miller [26] that introduced the very useful concept of a time-temperature parameter in the form of $T(C+\log t)$. This parameter is known as the Larson–Miller parameter (LMP). The value of C (usually 20) depends on the characteristics of the material, while the temperature (T) is taken in absolute units, and time t is in hours. In general, the following equation is used: stress (σ)=function of LMP where

$$\mathrm{LMP} = (T)(20 + \log_{10} t)^{*}10^{-3} \tag{7}$$

The results show that the creep life of a gas turbine fired with Fuel C (at the same firing temperature as for natural gas) is reduced by about 60% when compared with natural gas at 15°C ambient temperature. Oluyede and Phillips [25] showed how the percentage by volume of the hydrogen content in the syngas fuels significantly impacts the life of the hot section components as a consequence of a higher flame temperature for hydrogen-rich fuels and also the moisture content of combustion products. Thus, comparing fuels with similar values of LHV and, therefore, similar fuel flows, the higher the hydrogen content, the higher the water content of the products of combustion and the hotter the metal temperature will become, thereby reducing the relative life fraction of the turbine hot section.

Hence, it is possible to say that the life reduction (−43%) found when a gas turbine is fired with biomass syngas is comparable to the results obtained with a coal gasification syngas with a comparable LHV. However it is necessary to point out the qualitative nature of this comparison due to the fact that many other variables including those identified below, which for now have been neglected, must be taken into account:

- different type of engine (different power range and efficiency)
- different evaluation of creep life

(a) In this paper the flow-path component most affected by the overheating effect (S1B) was first evaluated and was followed by the evaluation of its life reduction through a local creep analysis and a comparison of the results with a "limit" suggested by GE design practice.

(b) In the reference paper [25], life reduction was evaluated through the LMP using as input data the design metal temperature and estimated creep life of the first stage nozzle and rotor blades.

It is probable that the lower creep life reduction found when burning biomass syngas (−43% versus −60% for watered down coal syngas) is due to the fact that the biomass syngas was dry, so the effect of the moisture in the products that leads to a further increase in overheating (the higher the quantity of vapor carried by the mixture, the more heat will be transferred to the blades) was not present in this case.

6 Conclusions

The present study has documented the fundamental phenomena associated with firing biomass pyrolysis syngas in combustion turbines in order to evaluate the reduction in creep life due to the overheating of the flow path, when the firing temperature is maintained at a level typical of natural gas firing. The increase in the fuel mass flow significantly impacts the life of the cooled flow-path components as a result of higher cooling flow temperature and higher HPT discharge temperature, which results in a higher gas flow-path temperature.

This analysis is a first step toward achieving greater "fuel flexibility" for gas turbines in the future. The reduction in creep life must be evaluated in a wider context that takes into account the degradation of turbine hot sections, including a detailed analysis of the number of start-ups and shut-downs, full load and full speed trips, material stress and strain properties, mechanical requirements, and life criteria.

Acknowledgment

The authors gratefully acknowledge the contribution of Nicola Pieroni and Tommaso Delpero.

Nomenclature

C = material coefficient in Larson–Miller relation
DH = hydraulic diameter
HHV = higher heating value
K = creep life factor
Nu = Nusselt number
P = pressure
Pr = Prandtl number
Re = Reynolds number
T = temperature
W = corrected flow
X = length
a = augmentation factor for highly turbulent mainstream
m = mass flow
t = time
ε = strain
σ = stress
Φ = angular distance from the LE stagnation point
μ = viscosity

Subscripts

b = bulk
C = compressor
D = diameter of the LE
F = fuel
t = turbine
w = wall
x = distance from the LE

References

[1] International Energy Agency (IEA), 2008, "Key World Energy Statistics."
[2] Solantausta, Y., Bridgwater, A. V., and Beckman, D., 1995, "Feasibility of Power Production With Pyrolysis and Gasification Systems," Biomass Bioenergy, **9**(1), pp. 257–269.
[3] Fantozzi, F., D'Alessandro, B., and Desideri, U., 2005, "Integrated Pyrolysis Recuperated Plant (IPRP): An Efficient and Scalable Concept for Gas Turbine Based Energy Conversion From Biomass and Waste," ASME J. Eng. Gas Turbines Power, **127**(2), pp. 348–357.
[4] Fantozzi, F., Di Maria, F., and Desideri, U., 2002, "Integrated Micro-Turbine and Rotary Kiln Pyrolysis System as a Waste to Energy Solution for a Small Town in Central Italy—Cost Positioning and Global Warming Assessment," ASME Paper No. GT-2002-30652.
[5] Levie, B., Diebold, J. P., and West, R., 1988, *Research on Thermochemical Biomass Conversion*, A. V. Bridgwater and J. L. Kuester, eds., Elsevier, London, p. 312.
[6] Diebold, J., Evans, R., and Scahill, J., 1990, Energy From Biomass and Wastes, Vol. 13, p. 851.
[7] Whitty, K. J., Zhang, H. R., and Eddings, E. G., 2008, "Emissions From

Downloaded 02 Jun 2010 to 171.66.16.96. Redistribution subject to ASME license or copyright; see http://www.asme.org/terms/Terms_Use.cfm

Syngas Combustion," Combust. Sci. Technol., **180**(6), pp. 1117–1136.
[8] Avenell, C. S., Griffiths, A. J., and Syred, N., 1993, *IEEE Clean Power 2000 Conference Proceedings*, London.
[9] Li, A. M., Li, X. D., Li, S. Q., Ren, Y., Shang, N., Chi, Y., Yan, J. H., and Cen, K. F., 1999, "Experimental Studies on Municipal Solid Waste Pyrolysis in a Laboratory—Scale Rotary Kiln," Energy, **24**, pp. 209–218.
[10] Fantozzi, F., Colantoni, S., Bartocci, P., and Desideri, U., 2007, "Rotary Kiln Slow Pyrolysis for Syngas and Char Production From Biomass and Waste—Part 1: Working Envelope of the Reactor," ASME J. Eng. Gas Turbines Power, **129**(4), pp. 901–907.
[11] Fantozzi, F., Colantoni, S., Bartocci, P., and Desideri, U., 2007, "Rotary Kiln Slow Pyrolysis for Syngas and Char Production From Biomass and Waste—Part 2: Introducing Product Yields in the Energy Balance," ASME J. Eng. Gas Turbines Power, **129**(4), pp. 908–913.
[12] Fantozzi, F., and Desideri, U., 2004, "Micro Scale Rotary Kiln Slow-Pyrolysis for Syngas and Char Production From Biomass and Waste. Reactor and Test Bench Realization," ASME Paper No. GT 2004-54186.
[13] Fantozzi, F., D'Alessandro, B., and Desideri, U., 2007, "An IPRP (Integrated Pyrolysis Regenerated Plant) Microscale Demonstrative Unit in Central Italy," ASME Paper No. GT 2007-28000.
[14] Browne, F. L., 1958, "Theories on the Combustion of Wood and Its Control," U.S. Forest Products Laboratory, Madison, WI, Report No. 2136.
[15] Onay, O., and Mete Kockar, O., 2003, "Slow, Fast and Flash Pyrolysis of Rapeseed," Renewable Energy, **28**, pp. 2417–2433.
[16] Bridgwater, A. V., and Peacocke, G. V. C., 2000, "Fast Pyrolysis Processes for Biomass," Renewable Sustainable Energy Rev., **4**, pp. 1–73.
[17] Sensoz, S., Demiral, I., and Gercel, H. F., 2006, "Olive Bagasse Pyrolysis," Bioresour. Technol., **97**(3), pp. 429–436.
[18] Shen, L., and Zhang, D. K., 2003, "An Experimental Study of Oil Recovery From Sewage Sludge by Low Temperature Pyrolysis in a Fluidised-Bed," Fuel, **82**(4), pp. 465–472.
[19] Li, S., Xu, S., Liu, S., Yang, C., and Lu, O., 2004, "Fast Pyrolysis in Free-Fall Reactor for Hydrogen-Rich Gas," Fuel Process. Technol., **85**, pp. 1201–1211.
[20] Demirbas, A., 2004, "Effect of Initial Moisture Content on the Yields of Oily Products From Pyrolysis of Biomass," J. Anal. Appl. Pyrolysis, **71**(2), pp. 803–815.
[21] Fagbemi, L., Khezami, L., and Capart, R., 2001, "Pyrolysis Products From Different Biomasses: Application to the Thermal Cracking of Tar," Appl. Energy, **69**, pp. 293–306.
[22] Colladay, R. S., 1994, "*Turbine Cooling*," Turbine Design and Application, Vol. III, NASA Report No. SP-290.
[23] Holman, J. P., 1968, *Heat Transfer*, 2nd ed., McGraw-Hill, New York.
[24] Kreith, F., and Bohn, M. S., 1986, *Principles of Heat Transfer*, 4th ed., Harper & Row, New York.
[25] Oluyede, E. O., and Phillips, J. N., 2007, "Fundamental Impact of Firing Syngas in Gas Turbines," ASME Paper No. GT2007-27385.
[26] Larson, F. R., and Miller, J., 1952, "A Time-Temperature Relationship for Rupture and Creep Stress," Trans. ASME, **74**, pp. 765–775.

Downloaded 02 Jun 2010 to 171.66.16.96. Redistribution subject to ASME license or copyright; see http://www.asme.org/terms/Terms_Use.cfm

Interaction Between the Acoustic Pressure Fluctuations and the Unsteady Flow Field Through Circular Holes

Jochen Rupp[1]

Jon Carrotte

Adrian Spencer

Department of Aeronautical and Automotive Engineering,
Loughborough University,
Leicestershire LE11 3TU, UK

Gas turbine combustion systems are prone to thermo-acoustic instabilities, and this is particularly the case for new low emission lean burn type systems. The presence of such instabilities is basically a function of the unsteady heat release within the system (i.e., both magnitude and phase) and the amount of damping. This paper is concerned with this latter process and the potential damping provided by perforated liners and other circular apertures found within gas turbine combustion systems. In particular, the paper outlines experimental measurements that characterize the flow field within the near field region of circular apertures when being subjected to incident acoustic pressure fluctuations. In this way the fundamental process by which acoustic energy is converted into kinetic energy of the velocity field can be investigated. Experimental results are presented for a single orifice located in an isothermal duct at ambient test conditions. Attached to the duct are two loudspeakers that provide pressure fluctuations incident onto the orifice. Unsteady pressure measurements enable the acoustic power absorbed by the orifice to be determined. This was undertaken for a range of excitation amplitudes and mean flows through the orifice. In this way regimes where both linear and nonlinear absorption occur along with the transition between these regimes can be investigated. The key to designing efficient passive dampers is to understand the interaction between the unsteady velocity field, generated at the orifice and the acoustic pressure fluctuations. Hence experimental techniques are also presented that enable such detailed measurements of the flow field to be made using particle image velocimetry. These measurements were obtained for conditions at which linear and nonlinear absorption was observed. Furthermore, proper orthogonal decomposition was used as a novel analysis technique for investigating the unsteady coherent structures responsible for the absorption of energy from the acoustic field. [DOI: 10.1115/1.4000114]

1 Introduction

Gas turbine combustion systems are susceptible to thermo-acoustic instabilities because of the potential for unsteady heat release. This causes fluctuations in fluid properties (e.g., velocity and pressure), which results in the propagation of acoustic waves away from the heat release region. Subsequently these waves can be reflected back by the combustion chamber geometry and its associated boundary conditions. As a consequence further increases in the unsteady heat release can occur as these waves interact with the fuel injector flow field. This feedback mechanism can potentially lead to self excitation if the heat release is in phase with the acoustic pressure oscillations. Furthermore modern, low emission systems are more prone to these thermo-acoustic instabilities since the heat release process is more sensitive to fluctuations when operating at the lean conditions typical of these systems. To avoid such instabilities several strategies can be adopted. For example, the magnitude of the unsteady heat release process and its sensitivity to acoustic pressure waves can be reduced by changes to the fuel injector geometry. Alternatively increasing the absorption (i.e., damping) of the acoustic waves by the combustion chamber geometry can reduce the magnitude of the feedback and hence the likelihood of self excitation. In this case various devices can be potentially used to dissipate acoustic energy.

Helmholtz resonators have been successfully used to suppress acoustic pressure fluctuations [1]. However, such devices provide absorption over a narrow frequency range, which often conflict with the requirement to ensure adequate absorption throughout the operability range of a gas turbine engine. Alternatively the dissipation of acoustic energy can be achieved through the use of perforated liners, which can provide a level of acoustic dissipation over a wide frequency bandwidth [2,3]. Furthermore, it has been found that incorporation of a net mean flow through the liner holes can lead to enhanced absorption [4,5]. Absorption is achieved via the unsteady flow that is generated through the liner holes by the acoustic pressure oscillations. This fluctuating flow results in the generation of unsteady vorticity, which is shed from around the rim of the hole [4]. In this way acoustic energy is transferred into kinetic energy of the velocity field, which is then dissipated into heat by turbulent dissipation processes in the shear layer surrounding the aperture. Many authors have considered the energy dissipation through holes or liners [2,6–8] using linear absorption based models. In this case the amount of energy absorbed relative to the incident acoustic energy is constant. However, when the fluctuating velocity introduced by the acoustic pressure oscillations is comparable with, or greater than, the mean velocity of the flow through the holes, then nonlinear absorption is observed [8–10]. In this case the amount of energy absorbed relative to the incident energy is no longer constant but is a function of the amplitude of the incident acoustic wave. It is worth noting that a gas turbine combustion system contains a range of apertures with hole length to diameter ratios (L/D) from 0.5 and below to greater than 10. These holes may be in the form of, for example,

---

[1] On secondment from Rolls-Royce plc.

Contributed by the International Gas Turbine Institute of ASME for publication in the JOURNAL OF ENGINEERING FOR GAS TURBINES AND POWER. Manuscript received March 31, 2009; final manuscript revised May 16, 2009; published online March 17, 2010. Review conducted by Dilip R. Ballal.

Copyright © 2010 by Rolls-Royce plc

Downloaded 02 Jun 2010 to 171.66.16.96. Redistribution subject to ASME license or copyright; see http://www.asme.org/terms/Terms_Use.cfm

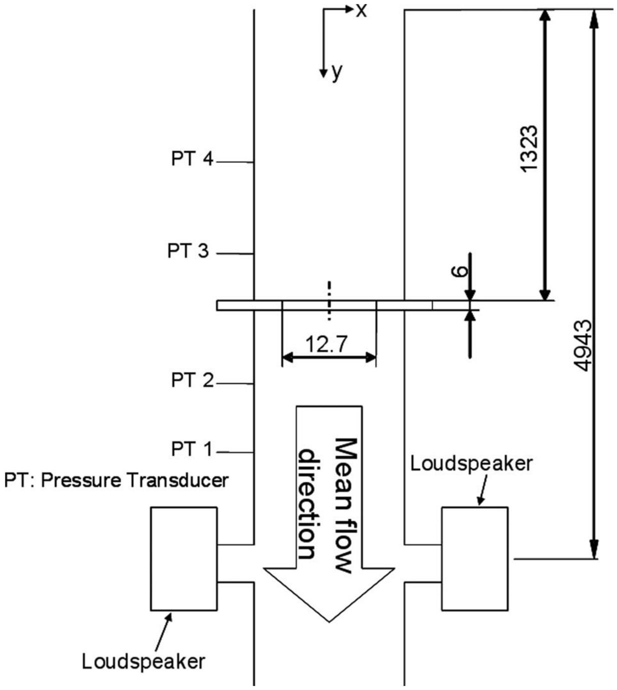

Fig. 1 Schematic of the experimental test rig, dimensions in millimeters not to scale

cooling rings, combustor ports, or perforated liners, and the mean flow velocity through their holes can vary significantly. More recent work by, for example, Tran et al. [11] utilized perforated screens to change the inlet acoustic boundary condition to a fuel injector. In addition, the nature of thermo-acoustic instabilities means that high amplitude growth rates can occur within the combustion system under certain conditions. Thus over the range of operating conditions there is the potential for both linear and nonlinear absorption.

The work described in this paper is part of a long term program aimed at characterizing the absorption or damping properties for a range of apertures operated over a range of conditions. However, particular emphasis is placed on the mechanisms by which acoustic energy is transferred into the kinetic energy of the flow field and the unsteady flow field generated in the near field region of the aperture. Hence the paper presents results from a single aperture and describes the experimental methodologies that have been developed to characterize both the acoustic absorption characteristics and the unsteady flow field that is generated. The single orifice experiments represent an isolated orifice in a multi-aperture liner as this was conducted analytically in Ref. [4]. This is valid if the distance between neighboring apertures is assumed to be sufficiently large that interactions between the apertures can be neglected. A study of the influence of aperture spacing on the absorption characteristic of multi-aperture liners will be conducted in future work. The single orifice experiments have been undertaken over a range of operating conditions in which both linear and nonlinear absorption occurs. In the long term it is hoped this work will enable the total acoustic absorption offered by a particular combustor geometry to be determined but also how this absorption can be optimized.

2 Experimental Facility

2.1 Acoustic Absorption Measurements. The experiments have been conducted on an isothermal test facility at ambient conditions. A schematic of the test rig used in this investigation is shown in Fig. 1, which consisted of a $120 \times 120\ \text{mm}^2$ rectangular duct, which contained a 6 mm thick orifice plate in which an aperture of 12.7 mm was centrally located $(L/D \sim 0.47)$. At both ends of the rectangular duct large plenums were located $(\sim 50\ \text{m}^3)$ effectively providing open end terminations. For the tests with mean flow air was drawn from the upstream plenum through the test section in the indicated flow direction and exhausted into the lower plenum. Two JBL AL6115 600W loudspeakers attached to the duct were used to generate plane waves. For the results reported in this paper a constant excitation frequency of 125Hz was maintained, and the orifice plate was located 1323 mm downstream of the duct inlet. Allowing for the end correction this corresponds to a half wavelength so that on the upstream side of the orifice a pressure node was located (i.e., zero pressure fluctuations). This was verified via experimental measurements. A range of operating conditions was achieved by varying both the amplitude of the incident acoustic pressure waves (115–143 dB) and the mean pressure drop (i.e., mean flow velocity) through the aperture $(\Delta p = 0 - 2900\ \text{Pa})$. To measure the acoustic absorption, two pairs of Kulite dynamic pressure transducers were located upstream and downstream of the test section.(PT1–PT4 in Fig. 1). The waves (Fig. 2) upstream (u) and downstream (d) of the orifice consisted of those waves incident onto (+) and those reflected away from $(-)$ the orifice.

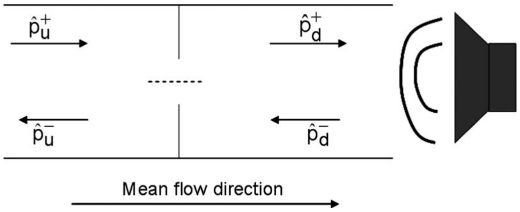

Fig. 2 Upstream and downstream traveling wave components

These waves were calculated from the fluctuating pressure measurements using the two microphone method [12] with allowances being made for the mean flow direction relative to the acoustic waves.

The absorption coefficient was calculated using the stagnation enthalpy $(B' = p'/\bar{\rho} \cdot (1 \pm M))$ and is defined as the difference between the incident and reflected enthalpy relative to the incident enthalpy, i.e., [2]

$$\Delta = \frac{\hat{B}_d^- + \hat{B}_u^+ - \hat{B}_d^+ - \hat{B}_u^-}{\hat{B}_d^- + \hat{B}_u^+} = 1 - \frac{\hat{B}_d^+ + \hat{B}_u^-}{\hat{B}_d^- + \hat{B}_u^+} \tag{1}$$

Both past and current works undertaken on this rig indicate the power absorption coefficient is repeatable to within 1% of its value.

2.2 Velocity Field Measurement. To measure the unsteady velocity field during linear and nonlinear acoustic absorption particle image velocimetry (PIV) was used. The PIV system consists of a Quantronix Darwin-Duo double headed neodymium:yttrium lithium fluoride (Nd:YLF) laser generating two pulses of laser light of 527 nm wavelength with a pulse energy of 30 mJ and a repetition rate of 1000 Hz. A −10 mm focal length diverging lens was used at the end of a LaVision laser guiding arm to generate the light sheet in the test section across the centerline of the orifice. Furthermore a LaVision High Speed Star 5 camera was used containing a charged-coupled device (CCD) array of 1024×1024 pixels with a frame rate of 1000 Hz. At an acoustic excitation frequency of 125 Hz this corresponds to eight captured images per acoustic cycle. One data set consisted of 3072 double images equivalent to a recording time of 3.072 s per test point. A Sigma 105 mm focal length lens was used to image a $30 \times 30\ \text{mm}^2$ field of view (FOV) in the test section. The detailed view of the test section is shown in Fig. 3.

Downloaded 02 Jun 2010 to 171.66.16.96. Redistribution subject to ASME license or copyright; see http://www.asme.org/terms/Terms_Use.cfm

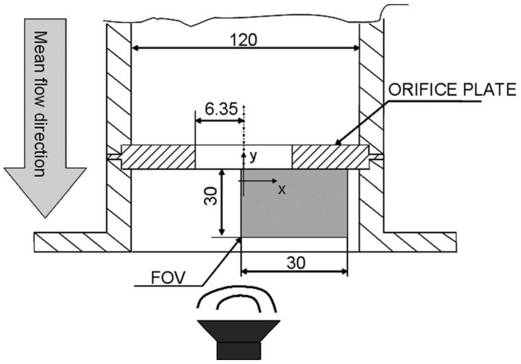

Fig. 3 Schematic of PIV measurement section, dimensions in millimeters not to scale

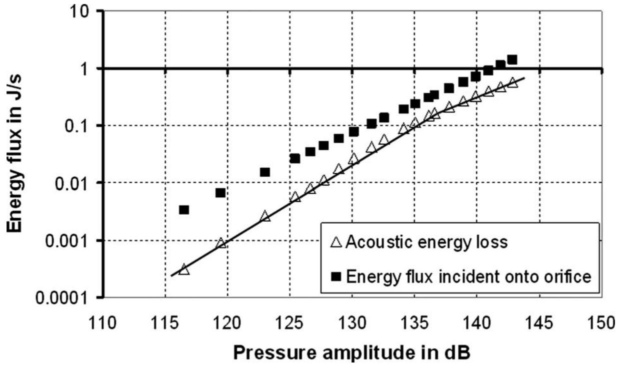

Fig. 5 Acoustic energy loss

The coordinate system is aligned with the center of the orifice at $x=0$ mm. The origin of the y-axis is 8.1 mm downstream of the orifice and is positive in the upstream direction.

To seed the flow field a SAFEX fog generator was used to create particles with a Sauter-mean-diameter of 3.7 μm. Using the particle diameter for the particle slip calculation [13], as well as the guidelines defined for PIV applied to an acoustic flow field [14], the velocity error due to the particle slip velocity was estimated to be 1%.

The DAVIS 7.2 software was used to calculate the vector fields from the captured image pairs with multipass adaptive gridding starting at interrogation cells of 64×64 pixels and reducing the interrogation window to 32×32 pixels with 50% overlap. This generates a velocity vector field of 64×64 vectors for the 3072 double frame images. The optimization of the optical parameters of the PIV setup has been conducted based on best practices [15]. This has led to 98% first choice vectors during the vector field calculation in DAVIS for the shown test case at nonlinear absorption. The first choice vector percentage was lower in the linear regime as the increased mean jet velocity results in an increased dynamic range in measured velocity between the jet velocity and the acoustic velocity in the surrounding duct. Therefore only 95% of first choice vectors were indicated in DAVIS.

3 Acoustic Absorption Measurements

3.1 No Mean Flow Through Aperture. The result of the acoustic absorption measurement for the test case without mean flow is shown in Fig. 4. The absorption is plotted over the excitation pressure amplitude in decibels. This represents the magnitude of the complex peak pressure amplitude of the mode shape traveling from the loudspeakers toward the orifice.

The results indicate that the absorption coefficient is a function of the incident acoustic energy and hence that absorption is nonlinear. It can be seen that the absorption coefficient increases between 117dB and 137dB where the absorption coefficient reaches a value of 0.49. However, further increases in the incident energy results in a decrease in absorption. It could be argued that in excess of 137 dB the absolute amount of energy that can be absorbed by the flow field is fixed, and so the absorption coefficient decreases due to the increasing incident energy.

However, as Fig. 5 shows, a saturation of energy loss is observed. At excitation amplitudes higher than 137 dB the acoustic energy absorbed increases less than the acoustic energy flux onto the orifice. It is the decreasing rate at which the energy is lost with increasing pressure amplitude that is responsible for reducing the absorption coefficient value (Fig. 4). The acoustic energy loss was estimated from the difference of incidental and reflected acoustic energy flux in the duct.

3.2 Mean Flow Through Aperture. Some of the results with mean flow can be seen in Fig. 6. In addition, for reference purposes the results with no mean flow (Fig. 4) have also been included. It is evident that the absorption levels for the test cases with a mean pressure drop across the orifice of 1000–2900 Pa (solid symbols) are independent of the excitation amplitude. Hence this result indicates linear absorption as, for a given mean pressure drop, the absorption coefficient is constant with pressure amplitude over the range of values tested.

It can also be seen that a decrease in the pressure drop and, hence, the mean flow passing through the orifice, results in an increase in absorption coefficient. Comparing the linear absorption coefficients with the nonlinear absorption coefficients (curve indicated with no mean flow in Fig. 6) for excitation amplitudes up to 125 dB is showing similar levels of absorption in both cases. In fact it can be seen that the mean bias flow case with 500 Pa pressure drop generates higher absorption coefficients in this area than the nonlinear absorption (less than 125 dB). An interesting test point indicated in Fig. 6 is the absorption curve for a mean

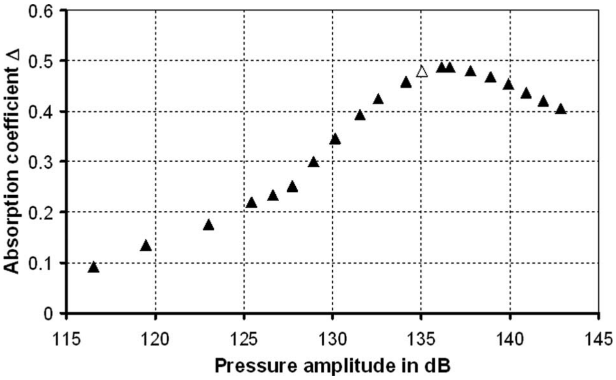

Fig. 4 Acoustic absorption without mean flow

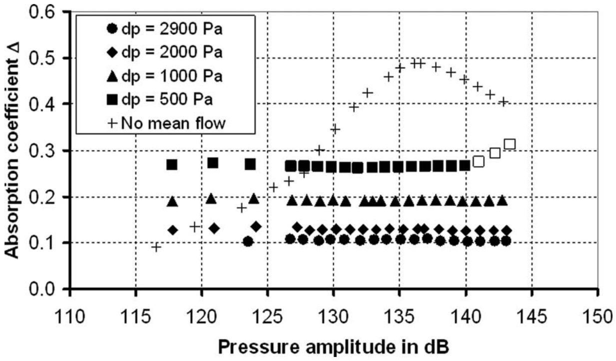

Fig. 6 Acoustic absorption with mean flow

Downloaded 02 Jun 2010 to 171.66.16.96. Redistribution subject to ASME license or copyright; see http://www.asme.org/terms/Terms_Use.cfm

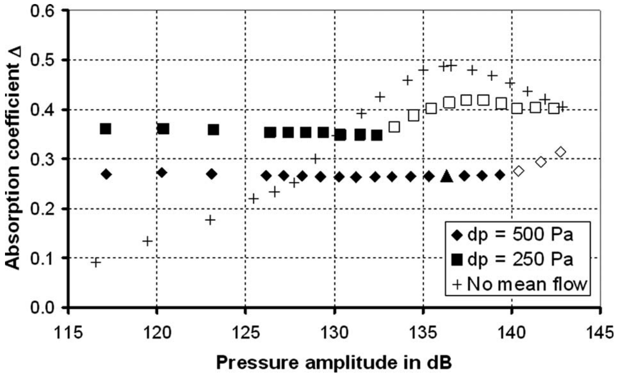

Fig. 7 Transition from linear to nonlinear absorption

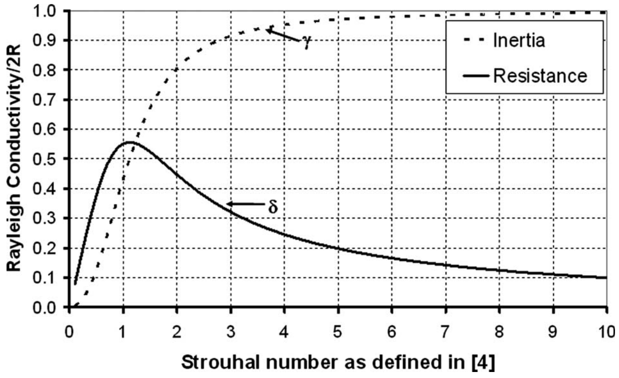

Fig. 9 Rayleigh conductivity of a thin aperture [4]

pressure drop of 500 Pa. It can be seen that between 117 dB and 140 dB excitation amplitude the absorption coefficient is constant (solid squares) indicating linear absorption. However, above 140 dB an increase in absorption is observed suggesting the transition to nonlinear type absorption (hollow squares). Reducing the mean pressure drop further to 250 Pa results in a similar characteristic with, in this case, the point of transition being indicated at 133 dB, as shown in Fig. 7. Furthermore, in this case a peak is observed at 137 dB with the characteristic being similar to that observed for the case with no mean flow through the orifice.

One would assume that the absorption curves in the presence of mean flow would more and more converge toward the characteristic in Fig. 4 for decreasing mean pressure differences. However, this is not entirely the case, as the absorption results in Fig. 8 show. It can be seen that all curves converge to the nonlinear absorption characteristic in the pressure excitation range of 137–143 dB.

However the test results for 75 Pa and 140 Pa mean pressure drop show a sudden increase (at 126 dB for $dp=140$ Pa and 122 dB for $dp=75$ Pa) but decreasing with further increases in excitation amplitude.

3.3 Comparison With Theoretical Models. The acoustic dissipation in the vicinity of circular holes is governed by the interaction of unsteady fluid dynamics with the acoustic excitation of the velocity field. Howe [4] initially developed a model to predict the linear absorption associated with flow passing through circular apertures based on the Rayleigh conductivity

$$K_{\mathrm{R}} = \frac{-i\omega\hat{Q}}{p_u - p_d} \tag{2}$$

This describes the ratio of unsteady volume flux of fluid passing through the orifice relative to the unsteady pressure fluctuations across the orifice. A model was developed for the Rayleigh conductivity [4] such that

$$K_{\mathrm{R}} = 2R(\gamma + i\delta) \tag{3}$$

where γ represents the inertia of the aperture and δ denotes the resistance of the flow, which determines the acoustic losses. These quantities are a function of the Strouhal number associated with the steady flow (Fig. 9)

$$\mathrm{St} = \frac{2\pi f \cdot R}{U} \tag{4}$$

It should be noted that the velocity (U) is in the plane of the hole, whereas the velocity ($\bar{v}$) derived from the mean pressure drop and the incompressible Bernoulli equation occurs downstream at the vena contracta (Fig. 10). The difference between these velocities is a function of the relative areas at these locations (i.e., the hole discharge coefficient) so the velocity (U) can be estimated if a hole discharge coefficient value is assumed. Using this model a normalized energy loss (i.e., the energy absorbed relative to the square of the unsteady pressure fluctuation across the orifice) can be defined as

$$\frac{\Pi}{|p_u - p_d|^2} = R\frac{\delta}{\omega\bar{\rho}} \tag{5}$$

This model, and variations in this model, has been used in many investigations relating to perforated liners (e.g., Refs. [2,4,6,8,16]).

The normalized energy loss from the model in Ref. [16] is presented graphically in Fig. 11. This model assumes the orifice is located within a thin wall and utilizes a discharge coefficient (C_D) of 0.5. Variations in this model have also been developed to include, for example, the effect of wall thickness for which examples are also included. In addition, the experimental data for the regimes where linear absorption was observed are presented for comparison with these models (using assumed C_D values of 0.5 and 0.75).

Although differences are apparent between the experimental measurements and model predictions it can be seen that there is

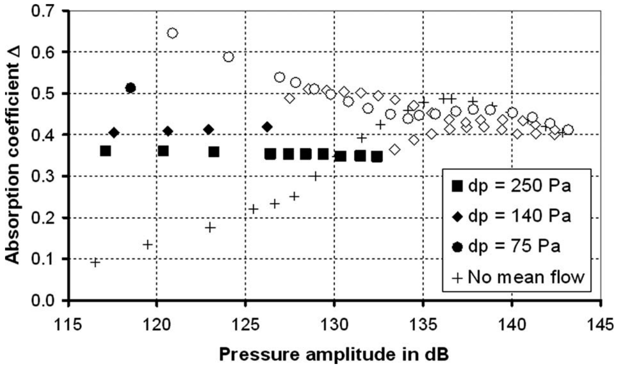

Fig. 8 Linear versus nonlinear absorption

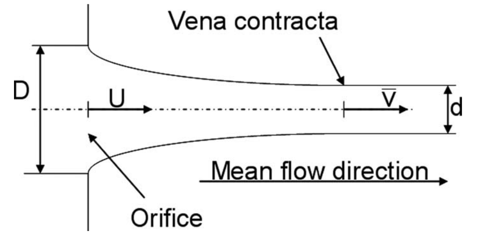

Fig. 10 Schematic of aperture velocities and vena contracta

Downloaded 02 Jun 2010 to 171.66.16.96. Redistribution subject to ASME license or copyright; see http://www.asme.org/terms/Terms_Use.cfm

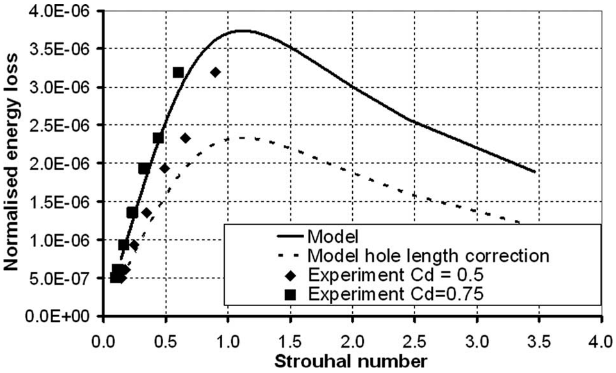

Fig. 11 Linear model comparison with experiment

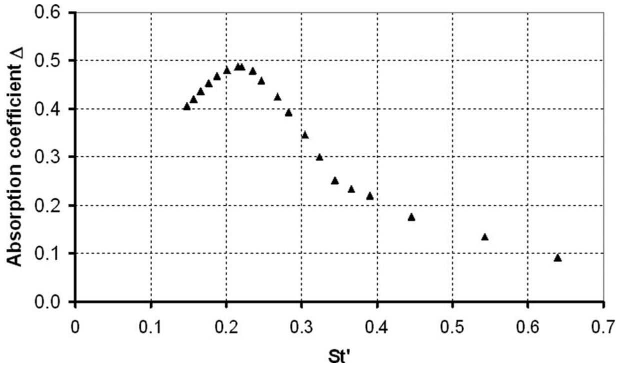

Fig. 12 Nonlinear acoustic absorption dependent on the Strouhal number

broad agreement in terms of the observed trends. For example, at the Strouhal numbers for which experimental data was acquired the observed absorption increase with decreasing mean pressure drop is also consistent with the predictions. As described by Howe [4], the variation in the resistance (δ), and hence absorption, with the Strouhal number is due to the length scales associated with the vorticity produced by the incident acoustic waves around the rim of the aperture. At large Strouhal numbers the shed vorticity will have a small influence on the fluctuating orifice flow. This is because small length scales mean the induced velocities from individual vortex rings cancel. However, at low Strouhal numbers the large length scales mean the vorticity of one sign can stretch far downstream and will impact on the flow through the orifice and tend toward a quasisteady response.

In addition to the linear regime, where the absorption was independent of excitation amplitude, regions of nonlinear absorption were also observed. For example, the transition point into nonlinear absorption occurred at excitation amplitudes of 133 dB and 140 dB for mean pressure drops of 250 Pa and 500 Pa (Fig. 7). This corresponds to the velocity (U) in the plane of the orifice approaching zero for parts of the unsteady cycle.

For acoustic applications the nonlinear regime without mean flow was investigated by several authors (e.g., Ref. [9,10,17]). In both cases it is mentioned that the flow visualization has shown large vortex ring structures, with the energy associated with these structures being obtained from the acoustic field and the nonlinear loss of acoustic energy. With this in mind it is interesting to note the observations of several authors whose investigations were not directly linked to that of acoustic absorption. Several authors [18,19] have studied the formation of vortex rings and the optimum conditions, whereby the vorticity in the vortex core obtains a maximum value. It was not possible to increase the maximum circulation of the vortex ring, and hence the kinetic energy associated with the vortex ring, despite increasing the fluctuating velocity in the orifice used to form the rings. Instead secondary flow features, e.g., wakes, start to absorb the energy and become visible in the flow field. With this in mind recent work on the vortex rings formed by synthetic jets [20] has defined a Strouhal number based on the unsteady flow through an aperture

$$\mathrm{St}' = \frac{f \cdot D}{\hat{v}} \quad \text{with} \quad \hat{v} = \frac{1}{T}\int_0^{T/2} v'(t)dt \qquad (6)$$

where the fluctuating jet velocity $v'(t)$ was estimated assuming quasisteady conditions and applying the Bernoulli equation for incompressible flow.

The solution was then averaged over half of the oscillation cycle. Based on this Strouhal number optimal vortex ring formation, where the vorticity in the vortex core reaches its maximum, occurs at $\mathrm{St}'=0.25$. With this in mind Fig. 12 shows the nonlinear absorption behavior from Fig. 4 plotted against this Strouhal number based on the unsteady flow velocity. As indicated the measured absorption reaches an optimum at a $\mathrm{St}'=0.22$, which is close to the Strouhal number quoted in Ref. [20]. As the nonlinear absorption is dominated by large structures being shed off the orifice rim the scenario described by Gharib et al. [18], Linden and Turner [19], and Jabbal et al. [20] could be a possible explanation for the occurrence of an optimum in the nonlinear absorption distribution.

4 Velocity Field Characterization

The unsteady flow field in the vicinity of the orifice is directly linked to the amount of energy absorbed from the acoustic field. Hence interrogation of the unsteady flow field in the vicinity of the orifice will provide a greater understanding of these flow processes. Experimental techniques have therefore been developed to enable interrogation of this region using particle image velocimetry (PIV) so as to provide spatial and temporal velocity field information. However, even in the absence of an acoustic field, the mean pressure drop across the orifice will generate a mean flow field, and the viscous nature of the flow will generate turbulence. Thus processing techniques have to be developed and applied that identify the turbulent velocity fluctuations caused by the flow through the orifice from the fluctuations and turbulence caused by the incident acoustic pressure waves. One potential method by which this can be achieved is through the application of proper orthogonal decomposition (POD).

4.1 Proper Orthogonal Decomposition. The proper orthogonal decomposition, which is also known as Karhunen–Loeve-decomposition [21], is a method to calculate time averaged instantaneous velocity field data. Before the proper orthogonal decomposition is applied, the time averaged flow field

$$\bar{u}(x) = \langle \boldsymbol{u}(x,t)\rangle = \frac{1}{T}\sum_{i=1}^{N} \boldsymbol{u}(x,t) \qquad (7)$$

is subtracted from the data set. The symbol $\langle\ \rangle$ represents an ensemble average and N denotes the amount of samples. The resulting data set investigated in the proper orthogonal decomposition is then defined by the instantaneous fluctuating velocity vectors, where the time average is

$$\bar{u}''(x) = \langle u''(x,t_i)\rangle = \frac{1}{N}\sum_{i=1}^{N} u''(x,t_i) = 0 \qquad (8)$$

where the time index is defined as $i=1,\ldots,N$.

The aim is to extract time-independent orthonormal basis functions (structural modes) $\varphi_k(x)$ and time dependent orthonormal coefficients (temporal coefficients) $a_k(t_i)$ such that their reconstruction of the instantaneous velocity field

Downloaded 02 Jun 2010 to 171.66.16.96. Redistribution subject to ASME license or copyright; see http://www.asme.org/terms/Terms_Use.cfm

$$u''(x,t_i) = \sum_{k=1}^{N} a_k(t_i) \cdot \varphi_k(x) \tag{9}$$

is optimal. Parameter k defines the mode number. The reconstruction is optimal in that the original data can be constructed most accurately from the first $m(<N)$ sequential modes if only m modes are available. The definition of the mathematical optimality and the derivation of the resulting eigenvalue problem are well documented in Refs. [21,22]. Furthermore the Snapshot-POD method [23] was used in this work to reduce the computational time and effort.

An important characteristic of the POD analysis is that the eigenvalue associated with a particular POD mode divided by the sum of all eigenvalues of all POD modes is representative of the kinetic energy contained in each mode relative to the total fluctuating kinetic energy. Therefore the POD modes are ordered in terms of kinetic energy. The first POD mode contains the most energy averaged over the field of view.

The maximum amount of samples per test point specified by the high speed camera was 3072. At a sampling frequency of 1000 Hz this results in eight data points (i.e., velocity fields) per cycle for the excitation frequency of 125 Hz. The POD analysis was conducted on all 3072 data points. The reconstruction of the flow field from the specified POD modes was then phase averaged giving 384 independent samples per phase angle of the cycle.

4.2 Methodology to Define the Coherent Velocity Field. The instantaneous velocity at a given location can be decomposed into mean and fluctuating components. In addition, the unsteady fluctuations can be further divided into fluctuations that

(i) contain coherent structures that demonstrate some form of correlation with the acoustic field and the incident waves and
(ii) fluctuations that are more random and exhibit no correlation with the acoustic field, i.e.,

$$\boldsymbol{u}(x,t) = \underbrace{\bar{u}(x)}_{\text{mean flow field}} + \underbrace{\tilde{u}(x,t)}_{\text{coherent structures generated by the periodic velocity field}} + \underbrace{u'(x,t)}_{\text{random turbulent fluctuations}} \tag{10}$$

4.2.1 Results of the POD Analysis in the Nonlinear Regime. A test point at an excitation amplitude of 135 dB was chosen in the nonlinear regime for the flow field investigation using the POD analysis (Fig. 4—hollow triangle). Note that a small mean pressure difference ($\Delta P \sim 4$ Pa) was applied to convect sufficient seeding particles into the field of view for the PIV measurement. However, this mean pressure difference had no impact on the measured absorption.

As already mentioned the POD modes are ordered in terms of their fluctuating energy. Figure 13 shows the cumulative energy distribution averaged over the field of view. It can be seen that a relatively large percentage of the kinetic energy is stored in the first five modes (84%). The kinetic energy distribution for the linear absorption will be discussed in Sec. 4.2.2. Hence reconstructing the nonlinear field with the first five POD modes would be representative of 84% of the fluctuating energy stored in the total flow field. After five modes the energy increase from mode to mode is in the order of 1%. However the shown cumulative energy content does not indicate if the energy content of a given mode is caused by the acoustic fluctuation. Therefore the spectra of the temporal coefficients have to be investigated.

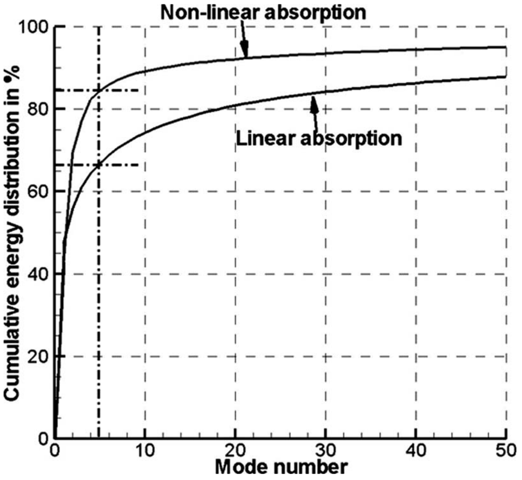

Fig. 13 Cumulative energy distribution for each POD mode

Figure 14 shows the spectra for POD mode 2, which carries 26% of the average fluctuating energy, with POD mode 10, which is carries 0.6% of the fluctuating energy. Evident in the spectra of the temporal coefficients are frequencies up to the third order (500 Hz) harmonic, with the sampling frequency of 1000 Hz, meaning it is not possible to determine higher frequency components. The measured acoustic pressure spectrum showed that there is only a small pressure signal at 250 Hz measured by the pressure transducers. In other words the harmonics in the flow field is being generated as a response to the incident acoustic waves at the fundamental excitation frequency (125 Hz) and not due to any harmonics associated with the incident acoustic waves. The amplitude at the fundamental frequency of 125 Hz in mode 2 is larger than for mode 10. It is also visible that random turbulent noise levels are increased for POD mode 10 compared with POD mode 2.

The characteristics shown in the temporal coefficients are also visible in the structural POD modes shown in Fig. 15. Evidence of large and more vortexlike structures can be observed in mode 2, whereas smaller (and higher frequency) structures are evident in mode 10.

To assess the amount of energy stored in the relevant spectral frequency component the maximum magnitude of each structural mode was calculated and multiplied with the relevant temporal coefficient. The resulting velocity spectra for the first six POD modes are shown in Fig. 16. It can be seen that the highest velocity amplitudes are contained in POD mode 1, with the velocity amplitudes in POD mode 6 an order of magnitude less. This leads to the conclusion that the first five POD modes are probably sufficient to reconstruct the periodic velocity field for the purpose of this work. In other words it is assumed that the energy content and structures contained within these five modes are associated with the periodic unsteady flow field being generated by the incident acoustic waves.

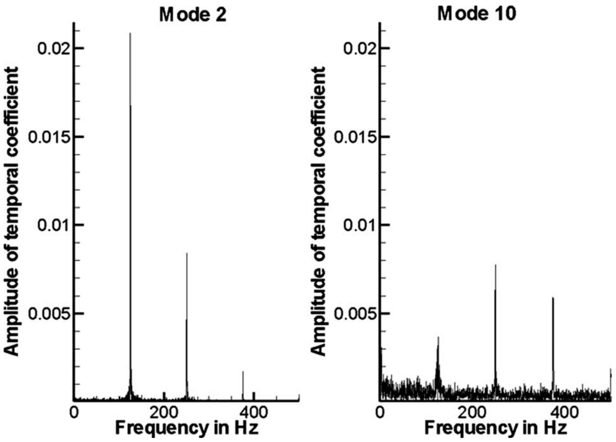

Fig. 14 Example of temporal coefficients

Downloaded 02 Jun 2010 to 171.66.16.96. Redistribution subject to ASME license or copyright; see http://www.asme.org/terms/Terms_Use.cfm

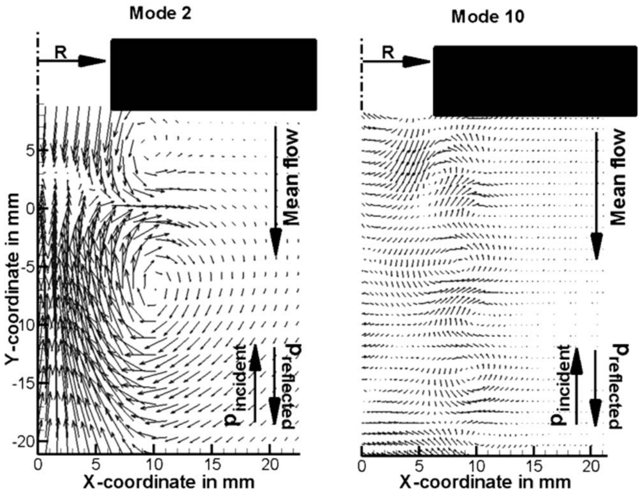

Fig. 15 Comparison of POD modes 2 and 10

Figure 17 shows the power spectral density (PSD) of the fluctuating velocity at two locations in the flow field. These locations correspond to the orifice centerline or the shear layer region around the orifice periphery (Fig. 18—points indicated by a cross). The spectra are calculated from modes 1 to 5 (i.e., the coherent fluctuation) or the sixth mode and upwards (i.e., the turbulent fluctuations).

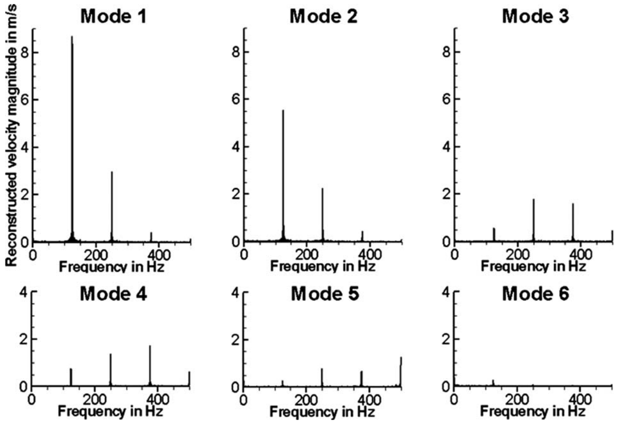

Fig. 16 Velocity spectra for POD modes 1–6

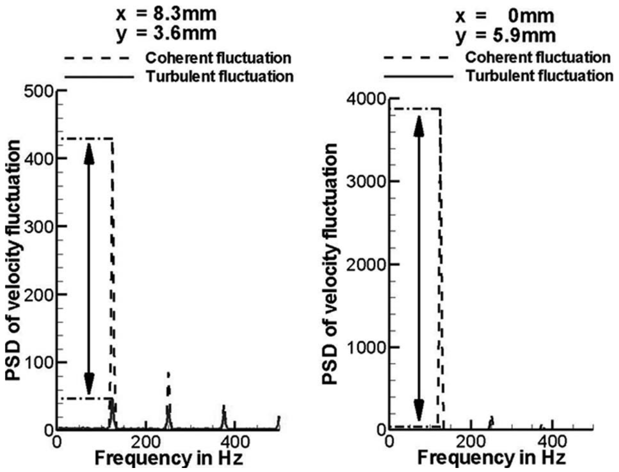

Fig. 17 Power spectral density (PSD) comparison

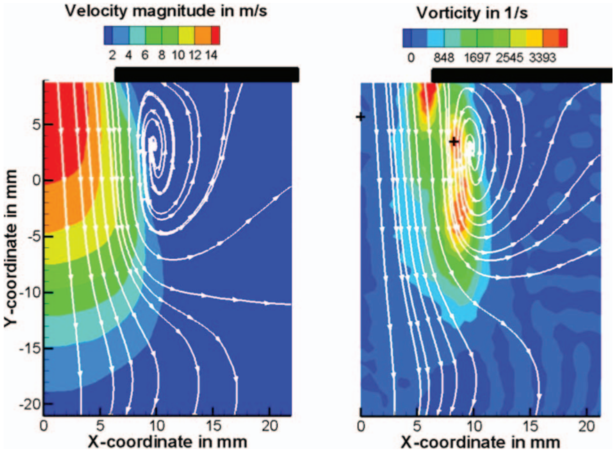

Fig. 18 Phase averaged reconstructed velocity field including the mean flow field (45 deg phase angle)

For the worst case in the shear layer ($x=8.3$ mm and $y=3.6$ mm) it can be seen that there is some periodic energy content in the turbulent spectrum at the excitation frequency. This is of order 10% of the coherent fluctuation. In other words reconstructing the flow field with the first five modes leads to a 10% loss of fluctuating energy in this region of the flow. However, on the centerline of the unsteady jet this error is reduced to 0.3%. Furthermore in this region the power spectral density at 125 Hz for the coherent structures is an order of magnitude higher than in the shear layer region. Hence this confirms that most of the fluctuating energy is captured within modes 1–5.

The reconstruction of the unsteady velocity field was undertaken using the mean flow field and the first 5 POD modes. This reconstructed flow field was then phase averaged for which the first two phases of the cycle (45 deg and 90 deg) are shown in Figs. 18 and 19.

Contours of velocity magnitude are presented while stream traces are used to highlight the flow structures. Furthermore contours of vorticity are shown in the right hand side of the figures. It can be seen that in the initial part of the cycle (45 deg) a vortex ring is generated close to the orifice exit plane, and the associated induced velocities then cause this vortex ring to be convected away from the orifice, as shown by the next (90 deg) and subsequent phases (not shown here). The vorticity field shows two regions of maximum vorticity in Fig. 18: one directly at the exit of the orifice and a region, which travels with the vortex structure.

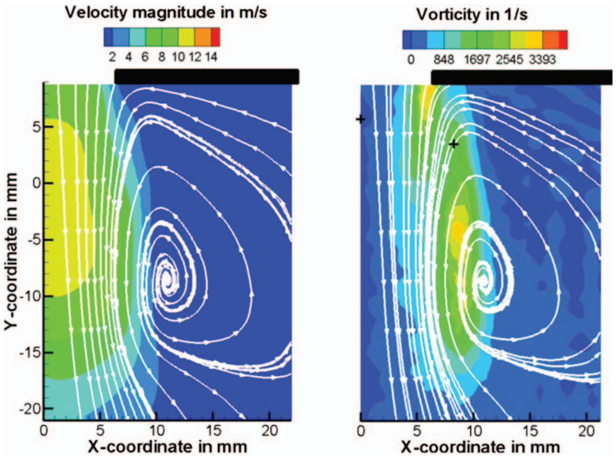

Fig. 19 Phase averaged reconstructed velocity field including the mean flow field (90 deg phase angle)

Downloaded 02 Jun 2010 to 171.66.16.96. Redistribution subject to ASME license or copyright; see http://www.asme.org/terms/Terms_Use.cfm

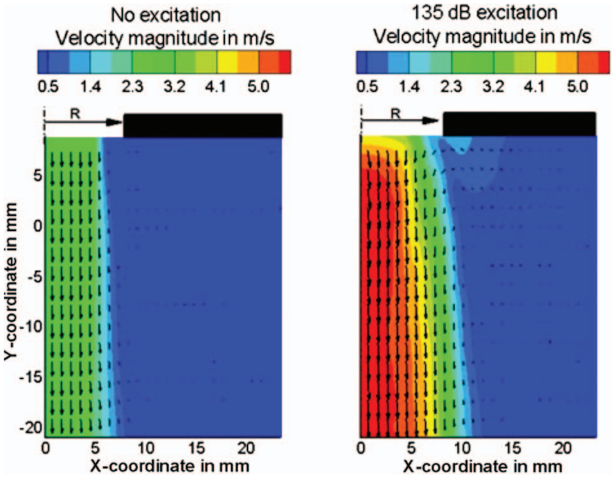

Fig. 20 Mean flow field comparison with and without excitation

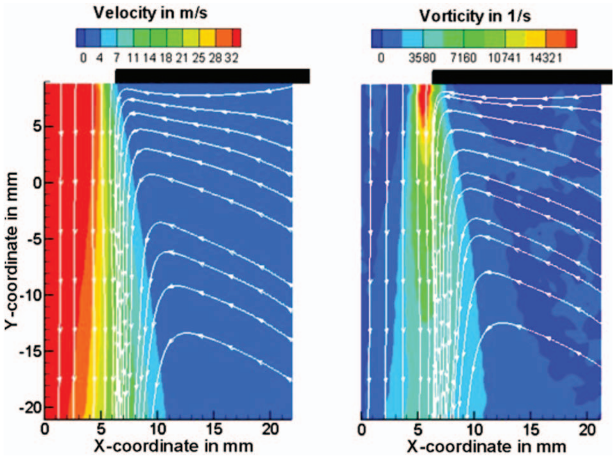

Fig. 21 Phase averaged reconstructed velocity field including the mean flow field (45 deg phase angle)

This vorticity decays with the distance traveled downstream, as Fig. 19 indicates. Interestingly the maximum vorticity in the vortex flow field is not aligned with the core of the vortex. However the ring vortex shows a significant influence on the vorticity field surrounding the circular aperture. With this in mind a further important consideration is the potential impact of the acoustically generated ring vortices on the mean flow field, and this is clearly evident in Fig. 20.

The mean flow fields obtained with and without excitation can be compared, and the velocity contours for the excited case show approximately double the magnitude along the centerline (Fig. 20). This is due to the mean velocity field induced by the ring vortex generated by the incident acoustic waves. Hence this additional energy in the mean flow field must also be included when considering the amount of energy that has been absorbed from the acoustic field. The flow field observed during nonlinear acoustic absorption contains large scale features such as ring vortices that have been captured using the experimental methods and the data analysis outlined. The kinetic energy associated with such features represents the energy that is being absorbed from the incident acoustic waves. This is now being investigated in further work but initial results indicate a good balance between the measured power absorption and the kinetic energy of the mean and periodic unsteady flow field features using this analysis technique.

4.2.2 Results of the POD Analysis in the Linear Absorption Regime. A test point corresponding to a mean pressure difference across the orifice of 500 Pa and an excitation amplitude of 136 dB was chosen to illustrate the flow field associated with the linear absorption regime (Fig. 7—solid triangle). In this case significant amounts of energy that are correlated with the 125 Hz and its harmonics are visible up the fourth POD mode. Higher modes show a drop in amplitude by an order of magnitude and these can therefore be neglected for the purpose of this study. As seen for the nonlinear absorption the spectrum of the linear absorption shows frequencies components up to the second harmonic of the excitation frequency.

Figures 21 and 22 show the velocity magnitude and the vorticity distribution of the reconstructed flow field using four POD modes, including the mean flow field, with data being presented at 45 deg and 180 deg of the acoustic cycle. The maximum vorticity indicated with the red contours is reached at a phase angle of 45 deg. The maximum vorticity is located close to the orifice rim between $x=4-8$ mm. At half an oscillation period later (180 deg—Fig. 22), the vorticity is reduced by nearly an order of magnitude. This vorticity field and the fact that there are no vortex structures in the flow field carrying vorticity in the vicinity of the vortex cores confirms that the linear absorption is characterized by a cylindrical vorticity layer surrounding the aperture [2–8]. Furthermore, in this case the mean velocity field for the excited case was identical to that of the unexcited case. Hence in this case no large vortex ring structures are present strong enough to have an influence on the time averaged velocity field (as it was the case during nonlinear absorption).

5 Conclusions

Experimental measurements have been undertaken on an orifice to investigate its acoustic absorption characteristics and the associated transfer of energy into the velocity field. Measurements were conducted over a range of operating conditions and included both linear and nonlinear absorption regimes.

From pressure measurements of the acoustic field regions of linear absorption were observed in which, for a given mean pressure drop across the orifice, the amount of absorption was invariant with excitation amplitude. However, the level of absorption could be varied by changing the mean pressure drop across the orifice. Data were also presented, which demonstrated the transition from linear to nonlinear absorption in which absorption becomes a function of the magnitude of the incident acoustic waves. In this regime the amount of absorption generally increases with excitation amplitude. However, a peak in the absorption coeffi-

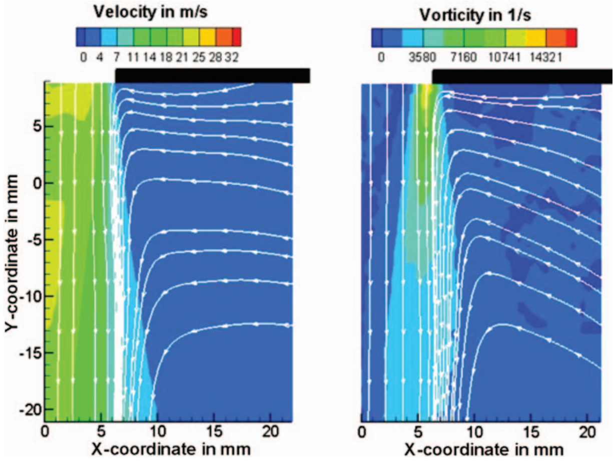

Fig. 22 Phase averaged reconstructed velocity field including the mean flow field (180 deg phase angle)

Downloaded 02 Jun 2010 to 171.66.16.96. Redistribution subject to ASME license or copyright; see http://www.asme.org/terms/Terms_Use.cfm

cient was observed after which further increases in excitation amplitude resulted in a reduction in the absorption coefficient.

The energy absorbed from the incident acoustic waves is transferred into the kinetic energy of the velocity field. Example measurements have therefore been presented of the velocity field in the near field region of the orifice. A methodology was outlined based on a POD analysis, which enabled the unsteady flow field structures associated with the incident acoustic waves to be identified from the random turbulence also present. Examples were shown for both the linear and nonlinear regimes and enabled the identification of various features, such as vortex layers and ring vortices, into which the acoustic energy has been transferred. The type and size of these flow field structures influences the flow through the orifice and the amount of energy that can be absorbed from the acoustic field.

The presented data in the linear and nonlinear regimes are broadly consistent with the ideas and theories put forward in the literature to explain linear and nonlinear absorption. Further work will include the calculation of the energy contained in the structures responsible for the acoustic dissipation and the comparison with the acoustic absorption measurement. The method will then be applied onto flow field studies investigating a range of representative L/D ratios for gas turbine combustors.

Acknowledgment

This research work is supported by Rolls-Royce plc, which is gratefully acknowledged by the authors.

Nomenclature

$a_k(t_i)$ = temporal coefficient
B = stagnation enthalpy
D = orifice diameter
dp, Δp = mean pressure difference across orifice
f = frequency
k_0 = wave number
K_R = Rayleigh conductivity
L = length of orifice
M = Mach number
N = number of samples
p = pressure
Q = volume flux
R = orifice radius
T = time period of oscillation
t = time
St = Strouhal number
U = mean velocity in orifice plane
$\boldsymbol{u}$ = velocity vector from PIV data
v = jet velocity from incompressible Bernoulli
x, y = Cartesian coordinates
Δ = absorption coefficient
Π = acoustic energy loss
$\varphi_k(x)$ = structural POD mode

Superscripts

$+, -$ = upstream and downstream traveling
$\wedge$ = complex amplitude
$'$ = fluctuating quantity
$-$ = time averaged quantity
$\hat{}$ = time averaged over half the cycle
$\sim$ = coherent fluctuation
$''$ = sum of coherent and turbulent fluctuation

Subscripts

u and d = upstream and downstream of orifice

References

[1] Dupère, I. D. J., and Dowling, A. P., 2005, "The Use of Helmholtz Resonators in a Practical Combustor," ASME J. Eng. Gas Turbines Power, **127**, pp. 268–275.
[2] Eldredge, J. D., and Dowling, A. P., 2003, "The Absorption of Axial Acoustic Waves by a Perforated Liner With Bias Flow," J. Fluid Mech., **485**, pp. 307–335.
[3] Heuwinkel, C., Enghardt, L., and Röhle, I., 2007, "Experimental Investigation of the Acoustic Damping of Perforated Liners With Bias Flow," AIAA Paper No. AIAA 2007-3525.
[4] Howe, M. S., 1979, "On the Theory of Unsteady High Reynolds Number Flow Through a Circular Aperture," Proc. R. Soc. London, Ser. A, **366**, pp. 205–223.
[5] Bechert, D. W., 1980, "Sound Absorption Caused by Vorticity Shedding Demonstrated With a Jet Flow," J. Sound Vib., **70**, pp. 389–405.
[6] Hughes, I. J., and Dowling, A. P., 1990, "The Absorption of Sound by Perforated Linings," J. Fluid Mech., **218**, pp. 299–335.
[7] Macquisten, M. A., Holt, A., Whiteman, M., Moran, A. J., and Rupp, J., 2006, "Passive Damper LP Tests for Controlling Combustion Instability," ASME Paper No. GT2006-90874.
[8] Bellucci, V., Flohr, P., and Paschereit, C. O., 2004, "Numerical and Experimental Study of Acoustic Damping Generated by Perforated Screens," AIAA J., **42**(8), pp. 1543–1549.
[9] Ingard, U., and Labate, S., 1950, "Acoustic Circulation Effects and the Nonlinear Impedance of Orifices," J. Acoust. Soc. Am., **22**, pp. 211–218.
[10] Cummings, A., 1983, "Acoustic Nonlinearities and Power Losses at Orifices," AIAA Paper No. AIAA 83-0739.
[11] Tran, N., Ducruix, S., and Schuller, T., 2008, "Passive Control of the Inlet Acoustic Boundary of a Swirled Turbulent Burner," ASME Paper No. GT2008-50425.
[12] Seybert, A. F., and Ross, D. F., 1977, "Experimental Determination of Acoustic Properties Using a Two-Microphone Random-Excitation Technique," J. Acoust. Soc. Am., **61**, pp. 1362–1370.
[13] Adrian, R. J., 1991, "Particle-Imaging Techniques for Experimental Fluid Dynamics," Annu. Rev. Fluid Mech., **23**, pp. 261–304.
[14] Tondast-Navæi, A., 2005, "Acoustic Particle-Image Velocimetry—Development and Applications," Ph.D. thesis, University of Edinburgh, Edinburgh.
[15] Raffel, M., Willert, C., and Kompenhans, J., 1998, *Particle Image Velocimetry*, Springer-Verlag, Berlin.
[16] Luong, T., Howe, M. S., and McGowan, R. S., 2005, "On the Rayleigh Conductivity of a Bias Flow Aperture," J. Fluids Struct., **21**, pp. 769–778.
[17] Tam, C. K. W., and Kurbatskii, K. A., 2000, "Microfluid Dynamics and Acoustics of Resonant Liners," AIAA J., **38**(8), pp. 1331–1339.
[18] Gharib, M., Rambod, E., and Shariff, K., 1998, "A Universal Time Scale for Vortex Ring Formation," J. Fluid Mech., **360**, pp. 121–140.
[19] Linden, P. F., and Turner, J. S., 2001, "The Formation of 'Optimal' Vortex Rings and the Efficiency of Propulsion Devices," J. Fluid Mech., **427**, pp. 61–72.
[20] Jabbal, M., Wu, J., and Zhong, S., 2006, "The Performance of Round Synthetic Jets in Quiescent Flow," Aeronaut. J., **110**, pp. 385–393.
[21] Holmes, P., Lumley, J. L., and Berkooz, G., 1996, *Turbulence, Coherent Structures, Dynamical Systems and Symmetry*, Cambridge University Press, Cambridge, England.
[22] Berkooz, G., Holmes, P., and Lumley, J. L., 1993, "The Proper Orthogonal Decomposition in the Analysis of Turbulent Flows," Annu. Rev. Fluid Mech., **25**, pp. 539–575.
[23] Sirovich, L., 1987, "Turbulence and the Dynamics of Coherent Structures, Part I: Coherent Structures," Q. Appl. Math., **45**, pp. 561–571.

Downloaded 02 Jun 2010 to 171.66.16.96. Redistribution subject to ASME license or copyright; see http://www.asme.org/terms/Terms_Use.cfm

On the Adequacy of Chemiluminescence as a Measure for Heat Release in Turbulent Flames With Mixture Gradients

Martin Lauer
e-mail: lauer@td.mw.tum.de

Thomas Sattelmayer

Lehrstuhl für Thermodynamik,
Technische Universität München,
Boltzmannstraße 15,
85748 Garching, Germany

The determination of the heat release in technical flames is commonly done via bandpass filtered chemiluminescence measurements in the wavelength range of OH^* *or* CH^* *radicals, which are supposed to be a measure for the heat release rate. However, these indirect heat release measurements are problematic because the measured intensities are the superposition of the desired radical emissions and contributions from the broadband emissions of* CO_2^**. Furthermore, the chemiluminescence intensities are strongly affected by the local air excess ratio of the flame and the turbulence intensity in the reaction zone. To investigate the influence of these effects on the applicability of chemiluminescence as a measure for the heat release rate in turbulent flames with mixture gradients, a reference method is used, which is based on the first law of thermodynamics. It is shown that although the integral heat release can be correlated with the integral chemiluminescence intensities, the heat release distribution is not properly represented by any signal from* OH^* *or* CH^**. No reliable information about the spatially resolved heat release can be obtained from chemiluminescence measurements in flames with mixture gradients.*

[DOI: 10.1115/1.4000126]

1 Introduction

The heat release distribution of the flame is the most important parameter for the understanding and prediction of unstable combustion states, such as thermoacoustic instabilities [1–3], pulsed combustion, and flame propagation due to combustion induced vortex breakdown [4]. Also in other research fields such as combustion noise the knowledge of the heat release rate distribution is very important [5–8].

1.1 Basics. The direct measurement of the spatially resolved heat release rate of flames is difficult because existing time resolved and spatially resolved measurement techniques are too complex to be applied to the above mentioned research fields [9]. As a consequence, traditionally the light emission of the flame, the so-called chemiluminescence, is used as an indirect measure for the heat release rate. The chemiluminescence spectrum of a hydrocarbon flame consists of the emissions from the radicals OH^*, CH^*, and C_2^*, and of CO_2^* emissions. The radicals emit light in narrow spectral bands. These emissions are superimposed by the broadband emissions from CO_2^*, as shown in Fig. 1. In most studies narrow bandpass filters in the wavelength range of OH^*, CH^*, or C_2^* are used because these radicals are supposed to correlate with the heat release rate.

For laminar premixed flames the applicability of chemiluminescence as an indirect measure for heat release has been shown in many experimental and theoretical studies. Most authors consistently report a linear increase in the integral chemiluminescence intensity with increasing fuel-flow rate, and a decreasing intensity with increasing air excess ratio [10–14]. But for turbulent flames the correlation between chemiluminescence and heat release is more complicated and not fully understood, yet. A positive monotonic dependency of the chemiluminescence intensity on fuel-flow rate has been reported, similar to laminar flames [10,13,15], as well as contrary observations have been made [11,12,16].

1.2 Motivation. For confined and adiabatic turbulent flames the integral chemiluminescence intensity has successfully been used to monitor the integral heat release of the flame in many studies (e.g., Refs. [1,3,17]). The correlation between heat release and chemiluminescence has been determined empirically in these studies. This led to the unconfirmed conclusion that also the spatially resolved heat release can be obtained via chemiluminescence, and that the chemiluminescence distribution of a flame can be used as a measure for flame length. This conclusion is questionable because flame parameters such as turbulence intensity, strain rate, and curvature, which influence the chemiluminescence intensity strongly [12,15,16,18], may vary substantially in turbulent flames. Additionally, in applications such as aircraft engines or gas turbines, cooling air enters the flame and dilutes the mixture. This causes mixture gradients, which also influence chemiluminescence intensities.

Another basic problem when measuring chemiluminescence is the use of bandpass filters. The measured signals are the superposition of the desired radical intensities and contributions from the broadband emission of CO_2^*. In turbulent flames the signal from CO_2^* contributions can be of the same order as the radical chemiluminescence or even exceed the radical intensity (Fig. 1).

In this study, the applicability of indirect, spatially resolved heat release measurements via chemiluminescence in turbulent swirl flames is investigated. The effect of mixture gradients and the effect of CO_2^* contributions in bandpass filtered signals are investigated. Additionally the influence of turbulence intensity on the chemiluminescent emissions is shown. The heat release distribution, measured with a reliable reference method, is compared with the distributions obtained from bandpass filtered and CO_2^*

Contributed by the International Gas Turbine Institute (IGTI) of ASME for publication in the Journal of Engineering for Gas Turbines and Power. Manuscript received April 9, 2009; final manuscript revised April 14, 2009; published online March 18, 2010. Editor: Dilip R. Ballal.

Copyright © 2010 by ASME

Downloaded 02 Jun 2010 to 171.66.16.96. Redistribution subject to ASME license or copyright; see http://www.asme.org/terms/Terms_Use.cfm

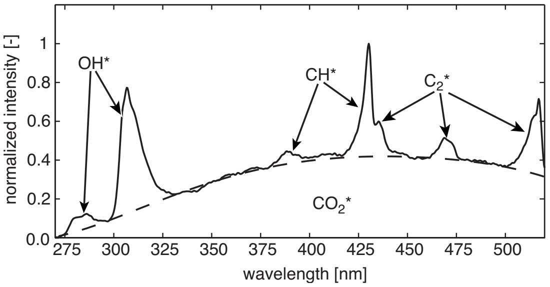

Fig. 1 Chemiluminescence spectrum of a stoichiometric premixed methane-air flame. The narrowband radical emissions from OH*, CH*, and C_2^* are superimposed by the broadband emission from CO_2^*.

contribution corrected chemiluminescence measurements.

In Sec. 2, a short literature review of heat release measurements via chemiluminescence is given and the experimental setup and the flame under investigation are described. Then the reference technique for the calculation of the spatially resolved heat release is briefly described and discussed. After that the measurement techniques used in this study are presented, and the procedure to obtain the radical intensities from bandpass filtered measurements is explained. Finally, the comparison of the heat release determined from chemiluminescence and the reference method is presented.

2 Literature Review

The first experimental investigations on the correlation of chemiluminescent light emissions with the integral heat release of a flame date back to the 1950s. Clark and Bittker [10] investigated the integral chemiluminescence of laminar and weakly turbulent propane-air flames. They found a linear dependency of the chemiluminescence intensity on fuel-flow rate at constant air excess ratios, and a decrease in the intensity with increasing air excess ratio for Reynolds numbers up to 6000.

John and Summerfield [11] investigated the light emissions from CO_2^*, C_2^*, and CH* in laminar and turbulent flames with Reynolds numbers up to 100,000. For all investigated chemiluminescent species the turbulence was found to reduce the specific intensity of the chemiluminescence. The intensity reduction was found to be stronger for CO_2^* than for C_2^* or CH*.

Hurle et al. [12] investigated the emissions from C_2^* and CH* in laminar and moderately turbulent ethylene-air flames. For Reynolds numbers up to 10,000 a linear dependency of chemiluminescence intensity on fuel-flow rate and heat release rate, respectively, has been observed. The slope of the correlation has been found to be a function of the air excess ratio. For Reynolds numbers in the range from 10,000 to 13,000 lower intensities have been observed than expected from linear extrapolation from lower Reynolds numbers. For Reynolds numbers higher than 17,000 decreasing intensities with increasing fuel-flow rate have been observed.

In 1995 Samaniego et al. [13] studied the emissions from CO_2^* in laminar and turbulent premixed methane-air and propane-air flames numerically. They found CO_2^* chemiluminescence to be a good indicator for fuel consumption in flames with varying dilution, strain rate, and air excess ratio. However, in the investigation of Najm et al. [16] a complicated dependency of CO_2^* chemiluminescence on curvature and flow history is reported, which leads to an ambiguous correlation of the chemiluminescence with burning rate and heat release. Furthermore, Najm et al. [16] showed a detailed analysis of the reaction mechanism of the methane oxidation. The relative amounts of carbon in the different possible reaction paths have been quantified. In this analysis Najm et al. [16] concluded that only a small portion of the carbon follows side reaction paths, which lead to the chemiluminescent radicals OH*, CH*, and C_2^*. Most of the carbon follows the main reaction path, which may yield some CO_2^* (Fig. 2).

Moreover, it was shown that for stoichiometric to lean flames there is the tendency to transfer carbon from side paths to the main reaction path, which reduces the chemiluminescence intensity from the radicals. Finally Najm et al. [16] concluded that OH*, CH*, and C_2^* are not reliable markers for the turbulent flame front, burning rate, or heat release rate because their appearance in the flame is not an indicator for the pathway of carbon oxidation for the main portion of carbon.

Lee and Santavicca [15] investigated the integral visible chemiluminescent emission from a turbulent swirled flame. They reported a linear dependency of the chemiluminescence signal on fuel-flow rate and an exponentially decreasing signal with increas-

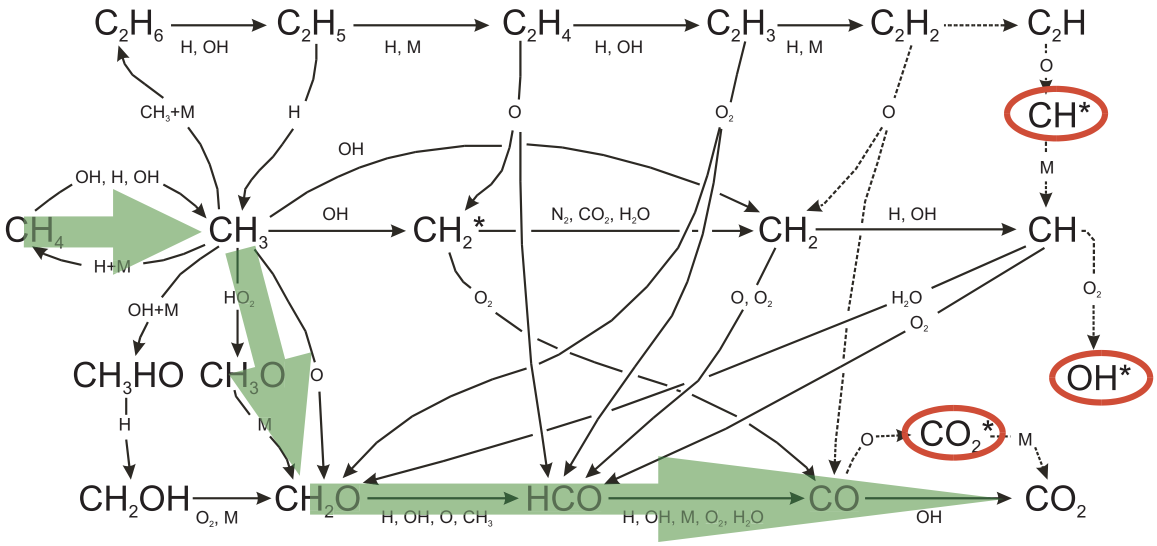

Fig. 2 The simplified methane oxidation mechanism [16]. The main portion of the carbon follows the marked reaction path. Only a small portion follows the side paths, which yield OH*, CH*, and C_2^*. From this, Najm et al. [16] concluded that OH*, CH*, and C_2^* are not reliable markers for reaction rate or heat release rate in the flame.

Downloaded 02 Jun 2010 to 171.66.16.96. Redistribution subject to ASME license or copyright; see http://www.asme.org/terms/Terms_Use.cfm

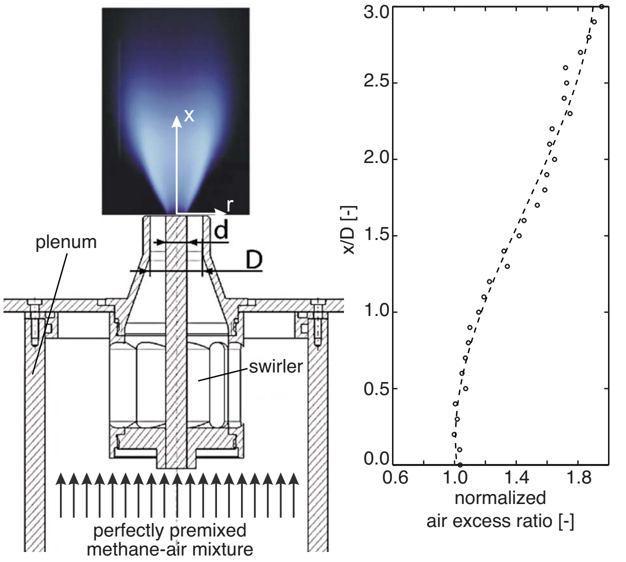

Fig. 3 Sketch of the test rig and exemplary axial air excess ratio distribution due to ambient air entrainment

ing air excess ratio. Moreover, they reported a strong influence of premix level, curvature, and stretch on the chemiluminescence signal.

Ayoola et al. [18] used heat release rate imaging to characterize OH^* chemiluminescence as a measure for the spatially resolved heat release rate. Heat release rate imaging is the pixel-by-pixel product of OH and CH_2O planar laser induced fluorescence (PLIF) signals, which correlates very well with the local heat release rate. Several turbulent, premixed, ethylene-fueled flames with Reynolds numbers in the range of 19,000–29,000 were under investigation. OH^* was found to be very sensitive to strain and turbulence. It was observed that strong OH^* chemiluminescence signals emerged from regions within the flame with a relatively low heat release rate. It was also observed that in bluff-body stabilized flames the air excess ratio dependency of the OH^* chemiluminescence was different for different positions in the flame brush. Ayoola et al. [18] concluded that OH^* chemiluminescence is not a reliable indicator for heat release.

In summary, the studies, especially of Hurle et al. [12], Najm et al. [16], Lee and Santavicca [15], and Ayoola et al. [18], showed the problems of heat release measurements via chemiluminescence in turbulent flames. The chemiluminescence signal of all emitting species are strongly affected by turbulence intensity, strain rate, curvature, fuel-flow rate, degree of premixing, and air excess ratio. But these quantities are not necessarily spatially or temporally constant in turbulent flames. Nevertheless, the integral chemiluminescence intensity is often used successfully as a measure for the integral heat release in turbulent flames. This can be explained with the fact that the change in a chemiluminescence relevant quantity, e.g., fuel-flow rate, influences the chemiluminescent emissions in all parts of the flame volume. Thus, a monotonic dependency of the integral light emission and the integral heat release is found and can be evaluated with an empirically determined calibration. This led to the conclusion that also the local heat release can be measured by the local chemiluminescence intensity. The limits of applicability of this conclusion are the main subject of this study.

3 Experimental Setup

The experimental study is carried out with a modular, swirl stabilized burner with center body. The swirl number was held constant at 0.55 in this study. The inner diameter of the nozzle is $D=40$ mm, the diameter of the center body is $d=16$ mm (Fig. 3). Fuel is natural gas with a methane content of 98%. The air-fuel mixture is externally premixed to avoid any mixture fraction fluctuations in plenum and burner. The thermal power can be adjusted in the range from 10 kW to 120 kW, the air excess ratio λ inside the plenum can be varied between 0.8 and 2.0. The test rig is operated with a nonpreheated air-fuel mixture in this study.

3.1 Ambient Air Entrainment. Since the flame is operated unconfined without a combustion chamber, the air excess ratio of the flame is not constant. As Wäsle et al. [19] showed, a linear increase in the axial mass flow downstream of the burner exit occurs due to turbulent mixing in the shear layer between the swirled flow and the quiescent ambient air. As a consequence, the mixture becomes leaner with increasing axial distance from the burner nozzle (Fig. 3, right hand side) [6,20]. This property of unconfined flames was used in the study to explore the influence of radial fuel concentration profiles in partially premixed burners or to mimic air admixing into turbulent confined gas turbine flames leading to mixture gradients, respectively.

3.2 Operating Points. The fuel-flow rate is equivalent to 60 kW of thermal power for all experiments in this study. Eight operating points with air excess ratios ranging from slightly rich mixtures ($\lambda=0.9$) to lean mixtures ($\lambda=1.6$) close to the lean blow-off limit of the burner are investigated. The Reynolds number in the burner nozzle ranges from 25,600 ($\lambda=0.9$) to 43,600 ($\lambda=1.6$).

4 Reference Technique

In this section a brief review of the reference technique is given. This technique is based on the first law of thermodynamics and, thus, is capable to provide the spatially resolved heat release rate of the flame with high accuracy and reliability. The detailed description of the reference technique can be found in Ref. [21]. Because the results derived from the reference technique are very important for the later comparison with chemiluminescence measurements the obtained heat release rate distributions are explicitly discussed for plausibility.

4.1 Basic Approach. The type of flame under investigation in this study can be described as an open, stationary system with constant pressure and chemical reaction. The following equation is derived from the first law of thermodynamics:

$$\dot{q}_{\text{net}} = \rho(\lambda,c)\cdot c_p(\lambda,c)\cdot(\vec{v}\circ\nabla T(\lambda,c)) \tag{1}$$

This equation balances the volumetric net heat release of the flame with the increasing sensible enthalpy due to the combustion. It is valid for flames with equal temperatures of the mixture and the entrained air, e.g., the case without preheat of the air-fuel mixture.

The volumetric net heat release rate of the flame $\dot{q}_{\text{net}}$ is a function of the density ρ of the fluid, the isobaric heat capacity c_p, the fluid velocity $\vec{v}$, and the temperature gradient ∇T. Density, heat capacity, and temperature are functions of the fluid composition, which can be described by the local air excess ratio of the mixture λ and progress variable of combustion c.

In this study all measured experimental variables are time averaged. This gives the time averaged heat release rate of the flame.

4.2 Required Input Parameters. The desired measures for the calculation of the heat release rate from Eq. (1) are the flow velocity $\vec{v}$, the progress variable of combustion c, and the air excess ratio λ. The underlying measurement techniques are described in detail in Sec. 5.

- The flow velocity of the reacting flow is measured via particle image velocimetry (PIV).
- The progress variable of combustion is calculated from OH-PLIF.
- The air excess ratio is measured via the OH^*/CH^* chemilu-

Downloaded 02 Jun 2010 to 171.66.16.96. Redistribution subject to ASME license or copyright; see http://www.asme.org/terms/Terms_Use.cfm

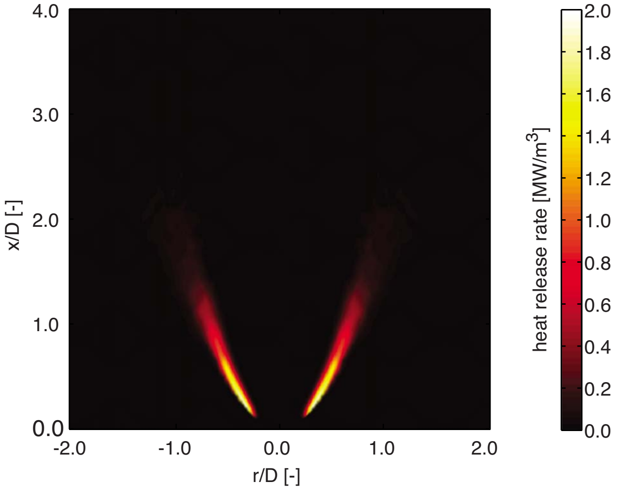

Fig. 4 Heat release rate in the flame midplane of the λ=1.2 operation point

minescence ratio. Despite the shortcomings in determining the heat release rate from the chemiluminescence of a single radical, pointed out in the literature review, it has been shown in a number of studies that the OH^*/CH^* chemiluminescence ratio unambiguously characterizes the air excess ratio of laminar and turbulent flames [20–25].

All measures are taken in the midplane of the flame, which is regarded as the reference plane for the time averaged flame.

4.3 Plausibility Discussion. The result of the determined heat release rate in the flame midplane for the $\lambda=1.2$ operating point is shown in Fig. 4.

To check the results of the reference technique, the determined integral heat release of the flames is compared with the heat release expected for the measured fuel-flow rate (Fig. 5). The integral heat release of the $\lambda=0.9$ operation point matches the expected value of 60 kW. However, with increasing air excess ratio a linearly decreasing integral heat release can be observed.

This observation can be explained with the ambient air entrainment in the flame. As previous studies have shown, the dilution of the mixture starts about 0.5*D* downstream of the burner nozzle. From there the air excess ratio increases linearly about 0.3 per burner diameter [20,21]. As a consequence, the ignition condition of the mixture degrades increasingly with increasing distance from the burner exit. In the shear layer between the swirled flow and the ambient air an increasing amount of mixture is not burned because of the intense dilution with ambient air. This effect has also been shown by Hoffmann [26] by measuring the composition of the products of turbulent, swirl stabilized, unconfined flames.

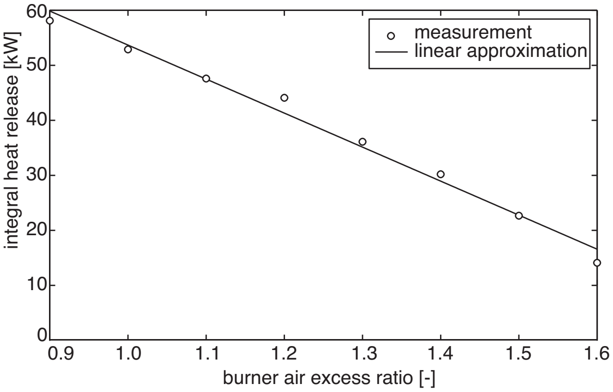

Fig. 5 Integral heat release of the flame determined with the reference technique

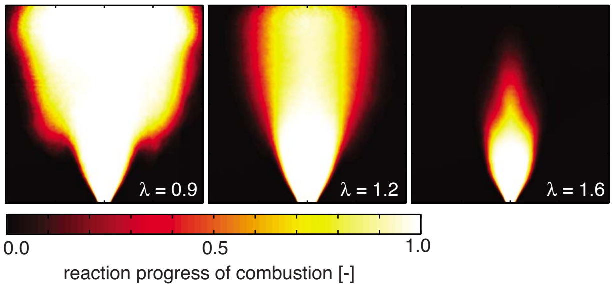

Fig. 6 Time averaged reaction progress of combustion for burner air excess ratios of 0.9, 1.2, and 1.6. With increasing burner air excess ratio an increasing portion of the mixture in the shear layer between the swirled flow and the ambient air is not burnt.

The quenching of combustion in the shear layers can also be seen in the spatial distribution of the time averaged reaction progress of combustion (Fig. 6). Close to the burner exit the flame is not influenced by the air entrainment. Further downstream the reaction is increasingly quenched in the shear layers with increasing burner air excess ratio. This can be seen in the smaller flame surface of the leaner flames.

Figure 7 shows the axial heat release distributions of the eight investigated operation points. In this figure three different regimes can be observed.

- For the rich flame ($\lambda=0.9$) the heat release distribution is shifted downstream compared with the stoichiometric and lean flames. Because of the rich mixture, additional air has to be transported into the flame to reach favorable ignition conditions. This results in a lower heat release near the burner exit [26].
- For $\lambda=1.0-1.4$ the flames show an identical heat release rate up to an axial distance of 0.5*D* downstream of the burner nozzle. Further downstream the heat release distribution is lower for higher air excess ratios due to the increased portion of the fuel flow that is not burned in the leaner flames.
- The $\lambda=1.5-1.6$ flames, which are close to the lean blow-off limit of the burner, show lower heat release rates near the burner exit. This might be an indicator for these flames that are not being properly stabilized anymore.

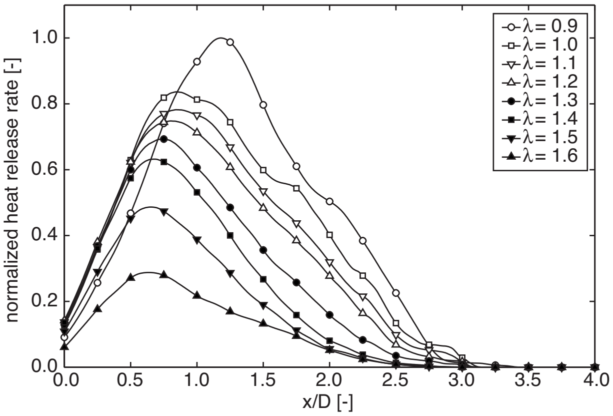

Fig. 7 Axial heat release distribution determined with the reference technique

Downloaded 02 Jun 2010 to 171.66.16.96. Redistribution subject to ASME license or copyright; see http://www.asme.org/terms/Terms_Use.cfm

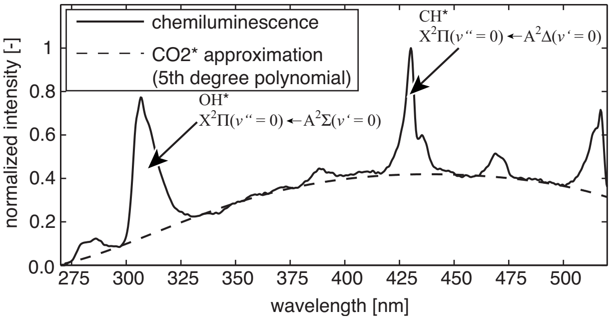

Fig. 8 Chemiluminescence spectrum with the fifth-degree polynomial fit for the CO_2^* emission

Especially the determined heat release rates close to the burner exit for the properly stabilized $\lambda = 1.0-1.4$ flames are in very good agreement with theoretical expectations: The heat release rate is proportional to the volumetric fuel mass flow, which has been kept constant and, therefore, is no function of the burner air excess ratio for the flames under investigation in this study. The determination of identical heat release rates for axial distances up to $0.5D$, which is the region of steepest gradients in the flame volume, shows the potential of the reference technique.

It can be concluded that the results from the reference technique are reasonable and in good agreement with theoretical expectations and former studies.

5 Measurement Techniques and Data Processing

The strongest chemiluminescent emissions emerge from the $X^2\Pi_i(v''=0) \leftarrow A^2\Sigma^+(v'=0)$ transition of OH^* around 306.4 nm and from the $X^2\Pi(v''=0) \leftarrow A^2\Delta(v'=0)$ transition of CH^* around 431.5 nm (Fig. 8). The chemiluminescence from these two transitions is under investigation in this study and is compared with the heat release rate obtained with the reference technique. C_2^* is not considered because C_2^* can only be seen in rich to slightly lean flames. For air excess ratios larger than 1.3 the C_2^* intensity is close to zero.

5.1 Bandpass Filtered Chemiluminescence. The bandpass filtered chemiluminescence signals are detected with a high speed camera with a fiber optically coupled image intensifier and a silica glass camera lens. The lens has a focal length of 45 mm and a maximum aperture of 1:1.8. The spatial resolution of the CMOS (complementary metal oxide semiconductor) sensor of the camera is 1024 × 1024 pixels. For each measurement 2048 images are captured and averaged. The averaged images are deconvoluted to obtain the spatially resolved chemiluminescence intensities in the flame midplane [27]. Three bandpass filters are used in this study.

- The chemiluminescence of the OH^* transition with superimposed CO_2^* background is measured with an interference filter with a maximum transmission of 16.57% at 309.65 nm and a half-power bandwidth of 5.1 nm.
- The chemiluminescence of the CH^* transition with superimposed CO_2^* background is measured with an interference filter with a maximum transmission of 48.63% at 431.39 nm and a half-power bandwidth of 5.3 nm
- A third interference filter with a maximum transmission of 68.18% at 456.42 nm and a half-power bandwidth of 1.2 nm is used. The measurement signal from this filter gives a characteristic value for the CO_2^* chemiluminescence, which is used to obtain the CO_2^* contribution corrected integral values of the radical transitions from the bandpass filtered OH^* and CH^* signals (see Sec. 5.5).

5.2 Spectrally Resolved Chemiluminescence. The used spectrometer is an Acton Research Corporation SpectraPro-275. The attached camera is identical to the camera used for the bandpass filtered measurements. The optical system of the spectrometer is a Czerny-Turner type with an inline optical path. The focal length is 275 mm with an aperture ratio of 1:3.8. The used grating in this study has 150 g/mm, allowing the observation of approximately 300 nm of the flame spectrum with the attached camera. The slit width of the spectrometer is set to 10 μm in this study. 2048 spectra are averaged for each operation point.

5.3 Velocity and Turbulence Intensity. The mean velocity field for the reference technique and the spatially resolved turbulence intensity, respectively, are measured via PIV. A high speed double cavity Nd:YLF (neodymium-doped yttrium lithium fluoride) laser (527 nm, 10 mJ/pulse) is used. The light sheet has a height of four burner exit diameters. The width is about 2 mm. In this study the double pulses are separated by 20 μs. The detection camera is a high speed CMOS camera with a 1024 × 1024 pixel sensor. The camera uses an 85 mm focal length lens with a maximum aperture of 1:1.4. However, the aperture was closed to 1:5.6 during the experiments to increase the depth of focus. Additionally, a 532 nm bandpass filter was used for the suppression of disturbing signals from the flame. The maximum transmission of the filter is 90%, the half-power bandwidth 10 nm. TiO_2 particles are used as tracer, due to their high temperature resistance.

The double frames were analyzed with a commercial software. The interrogation area measured 16 × 16 pixels. A three-step adaptive cross-correlation with 8 pixel separation was used. For each operation point 1024 image pairs are recorded and evaluated. From these data the time averaged velocity field of the flame and the spatially resolved turbulence intensity are calculated.

5.4 Reaction Zone. To characterize the reaction zone of the flame OH-PLIF measurements are used. From the sudden increase in the hydroxyl radical concentration, the boundary between the burned gas and the unburned gases can be detected [28]. A Rhodamine 6 G operated, frequency doubled dye laser, pumped with a Nd:YAG (neodymium-doped yttrium aluminum garnet) laser, is used for excitation of the $Q_1(6)$ line in the $A^2\Sigma^+(v'=1) \leftarrow X^2\Pi(v''=0)$ transition of the hydroxyl radical at 282.925 nm. The resulting fluorescence signal of the excited radicals is frequency shifted due to collisional energy transfer processes. The laser system is operated with 1 kHz repetition rate and 80 μJ pulse energy. The illuminated height of the flame is four burner exit diameters. The fluorescence signal around 306.4 nm is bandpass filtered for the suppression of scattered laser light. The detection camera and lens are identical to the bandpass filtered measurements.

5.5 Subtraction of the CO_2^* Contribution. In spectrally resolved chemiluminescence measurements the broadband emission from CO_2^* can be identified easily and the desired emissions from the radicals can be isolated. This is not possible in a single bandpass filtered measurement. However, spectrometer measurements only provide one-dimensional spatial resolution, whereas bandpass filtered measurements provide a two-dimensional spatial resolution.

A new measurement and data processing procedure is used to separate radical and CO_2^* chemiluminescence in bandpass filtered measurements. In the first step of this procedure chemiluminescence spectra of all operating points have been measured. From this data it was found that the broadband CO_2^* signal can be approximated with a polynomial of fifth degree with high accuracy (Fig. 8). The polynomial fit has been found to be self-similar for all investigated operating points. Moreover, it has been found that the shape of the $X^2\Pi_i(v''=0) \leftarrow A^2\Sigma^+(v'=0)$ transition of OH^* and of the $X^2\Pi(v''=0) \leftarrow A^2\Delta(v'=0)$ transition of CH^* are self-similar, too. However, the shapes of the radical transitions are too complex to be approximated by polynomial fits. Thus, they are defined

Downloaded 02 Jun 2010 to 171.66.16.96. Redistribution subject to ASME license or copyright; see http://www.asme.org/terms/Terms_Use.cfm

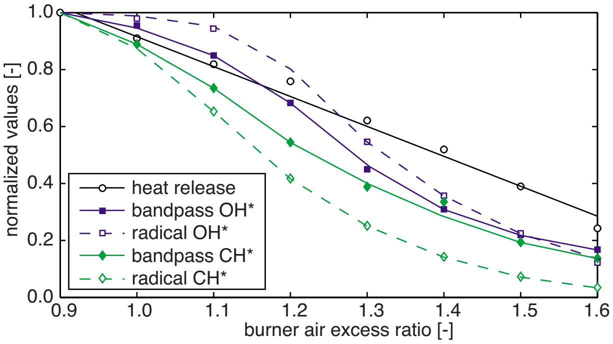

Fig. 9 Comparison of the integral chemiluminescence intensities and the heat release of the flame. All variables are normalized to their maximum value.

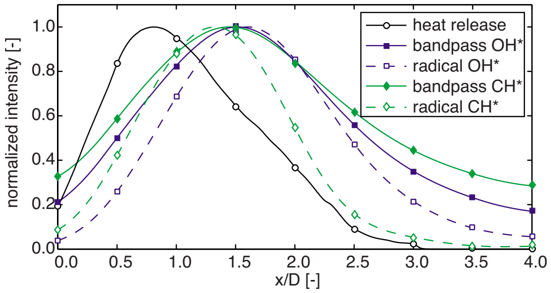

Fig. 10 Comparison of the axial chemiluminescence distribution of bandpass filtered and CO_2^* contributions corrected OH^* and CH^* with the axial heat release distribution

pointwise. The chemiluminescence of CO_2^* and the radicals, respectively, can be written as the product of the self-similar function and a specific proportionality constant.

With this information the bandpass filtered chemiluminescence signal in the wavelength range of OH^* can be approximated mathematically

$$S_{\mathrm{BP,310\ nm}} = \int_0^\infty ((C_{\mathrm{OH}^*} \cdot F_{\mathrm{OH}^*}(\lambda_\nu) + C_{\mathrm{CO}_2^*} \cdot F_{\mathrm{CO}_2^*}(\lambda_\nu)) \cdot T_{\nu,\mathrm{OH}^*}(\lambda_\nu))d\lambda_\nu \tag{2}$$

In this equation S_{BP} denotes the bandpass filtered measurement signal, F denotes the self-similar descriptions of the radical and CO_2^* chemiluminescence, C denotes the corresponding proportionality constants, and T_ν denotes the wavelength dependent transmission of the used bandpass filter. λ_ν is the wavelength.

The self-similar descriptions $F(\lambda_\nu)$ are known from the spectrometer measurements described above, the filter transmission $T(\lambda_\nu)$ is known from the manufacturer. The proportionality constants have to be calculated. $C_{\mathrm{CO}_2^*}$ can be derived from a bandpass filtered measurement in a wavelength range where only CO_2^* is emitting light. Such a wavelength range can be found between the $a^3\Pi_h(v'=0) \leftarrow d^3\Pi_g(v''=2)$ and the $a^3\Pi_h(v'=2) \leftarrow d^3\Pi_g(v''=3)$ transitions of C_2^* at 438 nm and 476 nm, respectively. For this purpose the third bandpass filter described above, centered at 456 nm, is used. Here the measurement signal can be written as follows:

$$S_{\mathrm{BP,456\ nm}} = \int_0^\infty ((C_{\mathrm{CO}_2^*} \cdot F_{\mathrm{CO}_2^*}(\lambda_\nu)) \cdot T_{\nu,\mathrm{CO}_2^*}(\lambda_\nu))d\lambda_\nu \tag{3}$$

The proportionality constant $C_{\mathrm{CO}_2^*}$ can be obtained by solving Eq. (3) numerically. The proportionality constant C_{OH^*} can then be calculated from Eq. (2). The desired intensity of the radical chemiluminescence is

$$I_{\mathrm{OH}^*} = \int_0^\infty (C_{\mathrm{OH}^*} \cdot F_{\mathrm{OH}^*}(\lambda_\nu))d\lambda_\nu \tag{4}$$

The integral intensity of the CH^* transition can be calculated accordingly.

6 Results and Discussion

Below, the comparison between chemiluminescence and heat release rate from the reference technique is presented for traditionally bandpass filtered chemiluminescence data and for the CO_2^* contribution corrected chemiluminescence intensities from the radical transitions.

6.1 Integral Values. In Fig. 9 the normalized integral values of heat release and chemiluminescence intensities are shown.

It can be seen that all investigated chemiluminescence signals are monotonically decreasing with increasing burner air excess ratio. But all chemiluminescence signals show a more complicate characteristic than the linearly decreasing heat release of the flame. This can be explained with the fact that for the flames investigated in this study a change in the burner air excess ratio also changes the integral heat release of the flame. Thus, the effect from the change in air excess ratio and the effect from the simultaneously changing integral heat release interfere with each other. As a consequence, no direct proportionality between any chemiluminescence signal and the heat release can be observed. It can also be seen that for the comparison of the integral heat release and the integral chemiluminescence intensities the CO_2^* contributions in bandpass filtered measurements have little influence.

6.2 Axial Distributions. Figure 10 shows the axial distribution of the chemiluminescence intensities and the heat release rate for the $\lambda = 1.2$ operation point. The characteristics of the distributions and the conclusions drawn for this operation point are the same for all operation points investigated in this study.

The influence of the CO_2^* contribution in the bandpass filtered signals can be seen clearly from the normalized chemiluminescence distributions: Close to the burner exit $(x/D < 0.5)$ and at axial distances $x/D > 3.0$ the CO_2^* contribution strongly distorts the shape of the radical intensities in the bandpass filtered measurements. The relative CO_2^* contribution in the bandpass filtered signals at axial distances $x/D < 0.5$ and $x/D > 3.0$ is higher than at axial distances between $0.5 < x/D < 3.0$. Close to the burner exit and at high axial distances almost the complete bandpass filtered signals consists of CO_2^* chemiluminescence. As a consequence, substantial errors are done when bandpass filtered chemiluminescence signals are interpreted as radical intensities. The CO_2^* contribution corrected CH^* signal is the best approximation of the heat release distribution, even though a significant downstream shift remains.

This obvious downstream shift of the chemiluminescence signals compared with the heat release is the second observation in Fig. 10. Since the air excess ratio is almost constant near the burner exit (Fig. 3) this effect is not caused by the ambient air entrainment. The shift can be explained with the local turbulence intensities in the flame. For the flames under investigation in this study the turbulence intensity in the reaction zone is high near the burner exit $(x/D < 1)$. With increasing axial distance from the burner exit the turbulence intensity in the reaction zone decreases. Figure 11 shows on the left hand side the reaction progress of combustion as an indicator for the reaction zone, and on the right hand side the local turbulence intensity. The contours indicate a reaction progress of 0.1, 0.5, and 0.9, and represent the time averaged reaction zone of the flame. For $x/D < 1$, the three contours are close together in a region of high turbulence intensity. Further downstream the reaction zone becomes wider with a lower turbu-

Downloaded 02 Jun 2010 to 171.66.16.96. Redistribution subject to ASME license or copyright; see http://www.asme.org/terms/Terms_Use.cfm

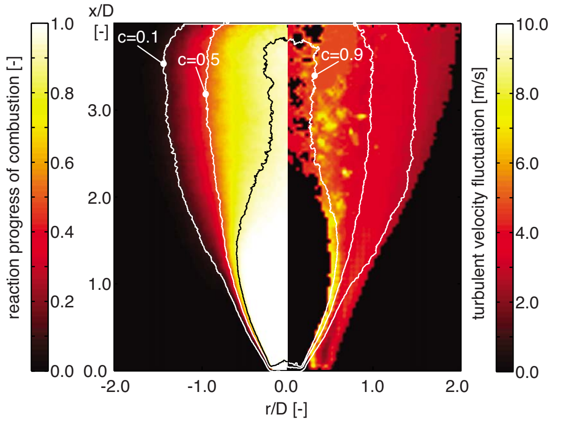

Fig. 11 Comparison of reaction progress of combustion (left hand side) and turbulence intensity (right hand side). The contours indicate the time averaged reaction zone with a reaction progress of 0.1, 0.5, and 0.9.

lence intensity. The observed downstream shift is due to quenching of the chemiluminescence in the region close to the burner exit and is similar to the effect reported by John and Summerfield [11], Hurle et al. [12], and Ayoola et al. [18].

The findings in this section are identical for all investigated operating points in this study. Thus, it can be concluded that the observed shift between heat release distribution and chemiluminescence distribution is independent of the air excess ratio and the integral heat release rate of the flame, respectively. This indicates that a similar shift is also to be expected in confined, adiabatic flames without mixture gradients.

6.3 Flame Length. In many applications a characteristic value of the chemiluminescence distribution is used as the measure for flame length. One characteristic value, which is commonly used, is the location of the maximum emission $x_{\max}$. Figure 12 shows the burner air excess ratio dependency of $x_{\max}$ for the heat release rate and chemiluminescent emissions. Because of the quenched chemiluminescence near the burner exit the flame appears to be longer than indicated by the maximum heat release rate. It can be observed that the CO_2^* contributions in the bandpass filtered measurements have little effect on locations of maximum emission.

Similar results were observed for other definitions for the flame length, such as the balance point of the axial distributions. As pointed out before, similar discrepancies between a chemiluminescence based flame length and the actual flame length are also to be expected for confined, adiabatic flames without mixture gradients. This means that for turbulent swirl stabilized flames no reliable information about flame length can be obtained from chemiluminescence measurements.

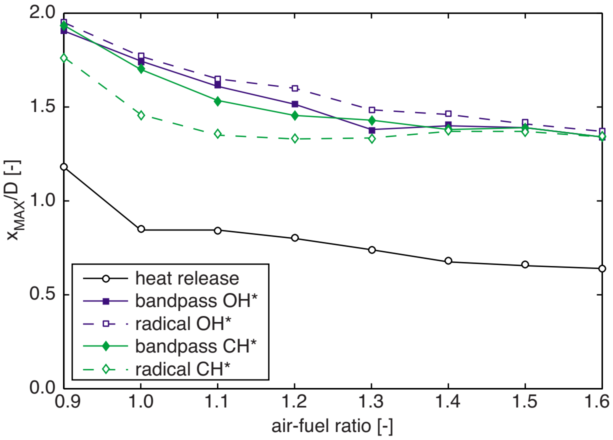

Fig. 12 Comparison of the location of maximum emission

7 Conclusions

In this experimental study the applicability of chemiluminescence as the measure for heat release rate in turbulent, swirl stabilized flames with mixture gradients has been investigated. For reference, a heat release rate measurement technique has been used, which is based on the first law of thermodynamics. The results of this technique have been discussed and have been found to be in good agreement with theoretical expectations and former publications.

The determined heat release rate has been compared with traditionally bandpass filtered chemiluminescence in the wavelength range of OH^* and CH^*, and with the integral chemiluminescence from the CO_2^* contribution corrected radical emissions. It has been found that the integral heat release of the flame and the integral chemiluminescence emission of any of the investigated species show an identical monotonic behavior. However, the axial heat release distribution is not properly represented by any signal either from OH^* or CH^*. The reason for this has been found in the high turbulence intensity in the reaction zone close to the burner exit. In this region of the flame the chemiluminescence is quenched, which results in a downstream shift of the chemiluminescence distribution compared with the actual heat release rate distribution. As a consequence, the flame appears to be longer than it is in reality. This observation is not limited to the flames investigated in this study. Similar effects have to be expected for all turbulent, swirl stabilized flames.

It can be concluded that chemiluminescence can be used to monitor the integral heat release of turbulent flames, if an empiric correlation between chemiluminescence and heat release can be obtained, which implies a known integral heat release of the flame. This is especially important for the use of chemiluminescence for the investigation of dynamic phenomena, such as the measurement of flame transfer functions. But no reliable information about the spatially resolved heat release rate distribution can be obtained from chemiluminescence data for turbulent, swirl stabilized flame.

Acknowledgment

The authors gratefully acknowledge the financial support provided by the DFG through the research unit “Chemilumineszenz und Wärmefreisetzung.”

Nomenclature

Re = Reynolds number
$\dot{q}$ = volumetric heat release (W/m^3)
T = temperature (K)
c_p = isobaric heat capacity (kJ/kg K)
ρ = density (kg/m^3)
c = time averaged reaction progress of combustion
λ = air excess ratio
$\vec{v}$ = velocity (m/s)
C = proportionality constant
F = self-similarity function
T_ν = transmission
I = intensity
S = measurement signal
D = burner nozzle diameter (mm)
d = burner center body diameter (mm)
λ_ν = wavelength (nm)
x = axial coordinate
r = radial coordinate
* = chemiluminescent
BP = bandpass

Downloaded 02 Jun 2010 to 171.66.16.96. Redistribution subject to ASME license or copyright; see http://www.asme.org/terms/Terms_Use.cfm

References

[1] Auer, M., Gebauer, C., Mösl, K., Hirsch, C., and Sattelmayer, T., 2005, "Active Instability Control: Feedback of Combustion Instabilities on the Injection of Gaseous Fuel," ASME J. Eng. Gas Turbines Power, **127**, pp. 748–754.

[2] Auer, M., Hirsch, C., and Sattelmayer, T., 2005, "Influence of the Interaction of Equivalence Ratio and Mass Flow Fluctuations on Flame Dynamics," *Proceedings of the ASME Turbo Expo*, Reno-Tahoe, NV.

[3] Freitag, E., Konle, H., Lauer, M., Hirsch, C., and Sattelmayer, T., 2006, "Pressure Influence on the Flame Transfer Function of a Premixed Swirling Flame," *Proceedings of the ASME Turbo Expo*, Barcelona, Spain.

[4] Konle, M., Kiesewetter, F., and Sattelmayer, T., 2008, "Simultaneous High Repetition Rate PIV-LIF-Measurements of CIVB Driven Flashback," Exp. Fluids, **44**, pp. 529–538.

[5] Wäsle, J., Winkler, A., and Sattelmayer, T., 2005, "Spatial Coherence of the Heat Release Fluctuations in Turbulent Jet and Swirl Flames," Flow, Turbul. Combust., **75**, pp. 29–50.

[6] Wäsle, J., Winkler, A., Lauer, M., and Sattelmayer, T., 2007, "Combustion Noise Modeling on Experimental Data Using Chemiluminescence as an Indicator for Heat Release Distribution," *Proceedings of the European Combustion Meeting*.

[7] Wäsle, J., 2007, "Vorhersage der Lärmemission turbulenter Vormischflammen," Ph.D. thesis, TU München, Germany.

[8] Winkler, A., 2007, "Validierung eines Modells zur Vorhersage turbulenten Verbrenungslärms," Ph.D. thesis, TU München, Germany.

[9] Balachandran, R., Ayoola, B. O., Kaminski, C. F., Dowling, A. P., and Mastorakos, E., 2005, "Experimental Investigation of the Nonlinear Response of Turbulent Premixed Flames to Imposed Inlet Velocity Oscillations," Combust. Flame, **143**, pp. 37–55.

[10] Clark, T., and Bittker, D., 1954, "A Study of the Radiation From Laminar and Turbulent Open Propane-Air Flames as a Function of Flame Area, Equivalence Ratio, and Fuel Flow Rate," NACA Report No. RM E54F29.

[11] John, R., and Summerfield, M., 1957, "Effect of Turbulence on Radiation Intensity From Propane-Air Flames," Jet Propul., **27**, pp. 169–179.

[12] Hurle, I. R., Price, R. B., Sugden, T. M., and Thomas, A., 1968, "Sound Emission From Open Turbulent Premixed Flames," Proc. R. Soc. London, Ser. A, **303**, pp. 409–427.

[13] Samaniego, J.-M., Egolfopoulos, F., and Bowman, C., 1995, "CO_2^* Chemiluminescence in Premixed Flames," Combust. Sci. Technol., **109**, pp. 183–203.

[14] Haber, L., Vandsburger, U., Saunders, W., and Khanna, V., 2000, "An Experimental Examination of the Relationship Between Chemiluminescent Light Emissions and Heat-Release Rate Under Non-Adiabatic Conditions," *RTO AVT Symposium on Active Control Technology for Enhanced Performance Operational Capabilities of Military Aircraft, Land Vehicles and Sea Vehichles*, Braunschweig, Germany, 8–11 May, published in RTO MP-051.

[15] Lee, J., and Santavicca, D., 2003, "Experimental Diagnostics for the Study of Combustion Instabilities in Lean Premixed Combustors," J. Propul. Power, **19**(5), pp. 735–750.

[16] Najm, H., Paul, P., Mueller, C., and Wyckoff, P., 1998, "On the Adequacy of Certain Experimental Observables as Measurements of Flame Burning Rate," Combust. Flame, **113**, pp. 312–332.

[17] Fanaca, D., Alemela, P., Ettner, F., Hirsch, C., Sattelmayer, T., and Schuermans, B., 2008, "Determination and Comparison of the Dynamic Characteristics of a Perfectly Premixed Flame in Both Single and Annular Combustion Chambers," *Proceedings of the ASME Turbo Expo*, Berlin, Germany.

[18] Ayoola, B., Balachandran, R., Frank, J., Mastorakos, E., and Kaminski, C., 2006, "Spatially Resolved Heat Release Rate Measurements in Turbulent Premixed Flames," Combust. Flame, **144**, pp. 1–16.

[19] Wäsle, J., Winkler, A., Rössle, E., and Sattelmayer, T., 2006, "Development of an Annular Porous Burner for the Investigation of Adiabatic Unconfined Flames," *Proceedings of the 13th International Symposium on the Application of Laser Techniques to Fluid Mechanics*.

[20] Lauer, M., and Sattelmayer, T., 2007, "Luftzahlmessung in einer turbulenten Drallflamme auf Basis spektral aufgelöster Chemilumineszenz," VDI-Ber., **1988**, pp. 735–741.

[21] Lauer, M., and Sattelmayer, T., 2008, "Heat Release Calculation in a Turbulent Swirl Flame From Laser and Chemiluminescence Measurements," *Proceedings of the 14th International Symposium on Applications of Laser Techniques to Fluid Mechanics*.

[22] Haber, L., 2000, "An Investigation Into the Origin, Measurement and Application of Chemiluminescent Light Emissions From Premixed Flames," MS thesis, Virginia Polytechnic Institute and State University, Blacksburg, VA.

[23] Hardalupas, Y., and Orain, M., 2004, "Local Measurements of the Time-Dependent Heat Release Rate and Equivalence Ratio Using Chemiluminescent Emission From a Flame," Combust. Flame, **139**, pp. 188–207.

[24] Ikeda, Y., Nishiyama, A., Kim, S. M., Kawahara, N., and Tomita, E., 2006, "Anchor Point Structure Measurements for Laminar Propane/Air and Methane/Air Premixed Flames Using Local Chemiluminescence Spectra," *Proceedings of the 31st International Symposium on Combustion*.

[25] Nori, V., and Seitzman, J., 2007, "Chemiluminescence Measurements and Modeling in Syngas, Methane and Jet-A Fueled Combustors," *Proceedings of the AIAA*.

[26] Hoffmann, A., 2004, "Modellierung turbulenter Vormischverbrennung," Ph.D. thesis, Universität Karlsruhe (TH), Germany.

[27] Dribinski, V., Ossadtchi, A., Mandelshtam, V. A., and Reisler, H., 2002, "Reconstruction of Abel-Transformable Images: The Gaussian Basis-Set Expansion Abel Transform Method," Rev. Sci. Instrum., **73**, pp. 2634–2642.

[28] Eckbreth, A. C., 1996, *Laser Diagnostics for Combustion Temperature and Species*, 2nd ed., W. A. Sirignano, ed., Gordon and Breach, The Netherlands.

Downloaded 02 Jun 2010 to 171.66.16.96. Redistribution subject to ASME license or copyright; see http://www.asme.org/terms/Terms_Use.cfm

Impact of Swirl Fluctuations on the Flame Response of a Perfectly Premixed Swirl Burner

Thomas Komarek
e-mail: komarek@td.mw.tum.de

Wolfgang Polifke[1]
e-mail: polifke@td.mw.tum.de

Lehrstuhl für Thermodynamik,
Technische Universität München,
D-85747 Garching, Germany

Combustion instabilities represent a long known problem in combustion technology. The complex interactions between acoustics and turbulent swirling flames are not fully understood yet, making it very difficult to reliably predict the stability of new combustion systems. For example, the effects of fluctuations of swirl number on the heat release of the flame have to be investigated in more detail. In this paper a perfectly premixed swirl stabilized burner with variable axial position of the swirl generator is investigated. In experiments, the position of the swirl generator has a strong impact on the dynamic flame response, although it does not influence the time-averaged distribution of the heat release significantly. This phenomenon is further investigated using computational fluid dynamics combined with system identification. The generation of fluctuations of swirl number, their propagation to the flame, and their effect on the dynamic flame response are examined. A simple model based on convective time lags is developed, showing good agreement with experiments. [DOI: 10.1115/1.4000127]

1 Introduction

In order to meet stringent pollution regulations, lean combustion technology has been introduced in stationary gas turbines. Unfortunately this resulted in an increased susceptibility to thermo-acoustic instabilities, a phenomenon frequently observed in various types of combustion systems ranging from small household burners to rocket engines. High amplitude pressure oscillations can result in reduced combustion efficiency, increased emissions, and increased thermal, as well as mechanical, stress, which can strongly reduce the lifetime of components or even cause immediate structural damage.

Thermo-acoustic instabilities arise from a complex interaction between acoustic waves in the combustor and fluctuations of heat release in the flame. The acoustic impedance at the flame may be influenced by boundary conditions far away from the flame. For example, small changes in a fuel supply line can alter the acoustic characteristics such that a stable configuration becomes unstable. It is therefore very difficult to predict stability boundaries. The present state of the art is such that the thermo-acoustic stability of a new combustor cannot be predicted dependably in the early design process. However, combustion instabilities occurring during commissioning result in high costs and represent an unacceptable high level of uncertainty.

Network models are frequently used to assess the stability of new systems. These tools have predicted the stability of many configurations successfully but have also failed for other configurations [1]. This is because an accurate description of the acoustic properties of all elements of the network is required. For simple acoustic elements, such as ducts, exact analytical models have been developed.

The description of the flame response is more difficult. Various models were proposed, which take into account a variety of thermo-acoustic coupling mechanisms. A number of authors investigated and successfully modeled effects of equivalence ratio fluctuations or flame front kinematics [2–7]. Swirl number fluctuations are also mentioned as a thermo-acoustic coupling mechanism (see Ref. [8]), but the effect itself has not yet been studied in detail. Straub and Richards [9] investigated a burner with different positions of a vane swirl generator and found a strong influence on the magnitude of combustion oscillations. This proved the effect of swirl fluctuations on the flame response. Straub and Richards suggested a time lag approach to capture this effect but did not explain the impact on the heat release of the flame. Garca-Villalba et al. [10] investigated the effect of swirl fluctuations in nonreacting flows using large eddy simulations (LES) by excitation of different velocity components at the inlet of a combustion chamber. They especially studied the impact on the flow field in the combustion chamber and the development of vortex structures, but did not analyze the impact on the flame response. Hirsch et al. [11] investigated the effect of different swirler designs and developed a model for the impact of swirl number fluctuations. The fluctuation that is being transported through the flame induces an axial velocity fluctuation, which causes a modulation of the heat release as do other models. It was argued that this additional time lag caused the differences in the acoustic behavior of the burners investigated.

In this paper the impact of fluctuations of the swirl number on the heat release rate of a premix flame is investigated with an experimental setup, which was especially designed for a detailed analysis of this effect. The burner features an axial swirl generator with variable axial position. Thus it is possible to change the relative phase of the swirl fluctuations and to study the impact on the dynamic flame response. The experimental work is supplemented with numerical studies, where computational fluid dynamics (CFD) is combined with system identification (SI).The generation, the propagation of swirl number fluctuations, and finally the impact on the flame are investigated by means of a transient CFD simulation, which is capable of modeling the complex interaction of acoustics, fluid dynamics, and combustion. System identification methods are then employed to analyze the effect on both time and frequency domain, resulting in a detailed insight into the relevant interaction mechanisms that lead to the changes in the flame response. Furthermore, a time lag model of the swirl number fluctuations is developed and validated against experimental data.

2 Experimental Setup

2.1 Test Rig. The BRS burner is a swirl stabilized burner with an axial swirl generator mounted on a central bluff body (see Fig. 1).

---

[1] Corresponding author.

Contributed by the International Gas Turbine Institute of ASME for publication in the JOURNAL OF ENGINEERING FOR GAS TURBINES AND POWER. Manuscript received April 9, 2009; final manuscript received July 19, 2009; published online March 18, 2010. Review conducted by Dilip R. Ballal.

Copyright © 2010 by ASME

Downloaded 02 Jun 2010 to 171.66.16.96. Redistribution subject to ASME license or copyright; see http://www.asme.org/terms/Terms_Use.cfm

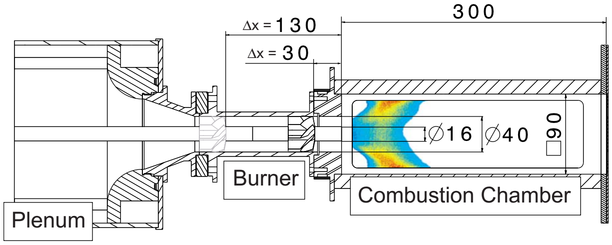

Fig. 1 Sketch of the BRS burner

The modular design allows the possibility to change the axial position of the swirl generator. By increasing the distance to the flame, the time required for convective transport of a fluctuation in swirl number to the flame is also increased. The burner is operated in "perfectly premixed" mode with a completely homogeneous mixture of natural gas and air to eliminate any equivalence ratio fluctuations. Figure 1 shows the plenum, the swirl generator in the front axial position ($\Delta x = 30$ mm) and in the rear axial position ($\Delta x = 130$ mm) and the combustion chamber. The Δx of the swirl generator corresponds to the distance between the swirl generator and the burner exit plane. The end of the combustion chamber is equipped with a perforated plate in order to create a low reflective acoustic boundary condition. The position of the flame is indicated by the heat release distribution obtained through OH^* chemiluminescence measurements. The heat release distribution was measured in order to investigate the impact of different positions of the swirl generator on the flame length. The acoustic properties of the burner were determined by measurements of the flame transfer function.

2.2 Measurements of the Heat Release Distribution. The OH^* chemiluminescence emissions were recorded as an indicator of the instantaneous heat release of the perfectly premixed flame. In order to separate the signal from other emissions, an interference filter centered on a wavelength of $307.1 + 3/-0$ nm with a half power bandwidth of 10 ± 2 nm and a transmission of 15% was used. The signal was recorded with an intensified CMOS camera. Two hundred pictures with a recording time of about 4 s were averaged in order to determine the steady state average of the OH^* emissions. From the data obtained the spatial distribution of the heat release and the flame length were determined.

For a power rating of 70 kW and an equivalence ratio of $\phi = 0.77$, the axial heat release distribution with the swirl generator in the front and rear positions, respectively, are compared against each other in Fig. 2. It can be seen that the distribution of heat release—the "shape of the flame"—is quite insensitive to changes in the position of the swirl generator. This conclusion is corroborated by flame images (not shown). This behavior was expected because for the given burner design, a change in the swirler position does not change significantly the average flow field nor the overall swirl number at the burner exit.

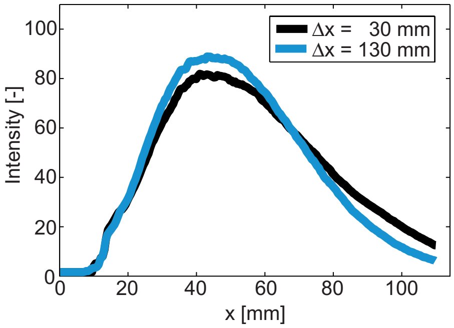

Fig. 2 Axial heat release distribution with swirler in front ($\Delta x = 30$ mm) and rear position ($\Delta x = 130$ mm)

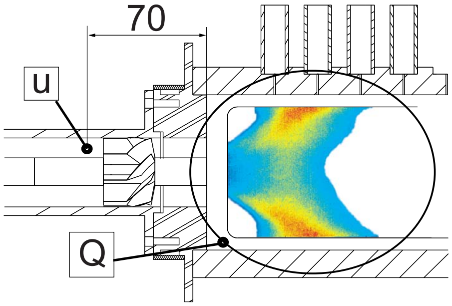

Fig. 3 Experimental setup for FTF measurements

2.3 Flame Transfer Function Measurements. The flame transfer function (*FTF*) of the burner was measured as acoustic characterization of the flame dynamics. The *FTF* relates the flame response in terms of heat release fluctuations Q' to an excitation by acoustic velocity fluctuations u'. The fluctuations are normalized with their mean values $\bar{Q}$ and $\bar{u}$. The *FTF* is a complex function in the frequency domain

$$FTF = \frac{Q'/\bar{Q}}{u'/\bar{u}} \tag{1}$$

The velocity signal was obtained by CTA measurements. The position of the CTA probe is illustrated in Fig. 3.

It was placed 10 mm upstream of the swirl generator in the front position, which corresponds to a distance of 70 mm to the burner exit. The heat release signal was obtained with a photomultiplier in combination with the interference filter that was also used for the measurements of the time-average spatial distribution of heat release. The excitation was realized by a siren that modulated the flow rate of the incoming mixture to the plenum. The excitation amplitude can be varied by a bypass valve separating a modulated and an unmodulated stream.

When measuring the *FTF* for different positions of the swirl generator, a strong impact on the dynamic response of the flame was observed. With increasing time lag, the prominent local minimum of the "gain" (the amplitude of the *FTF*) moves to lower frequencies, while the modulation of the phase is increased. *FTF*s for three axial positions are displayed in Fig. 4 versus frequency f and Strouhal number Sr

$$\mathrm{Sr} = \frac{fd}{\bar{u}} \tag{2}$$

where d and $\bar{u}$ are the burner exit diameter ($d = 40$ mm) and the mean velocity at the burner exit ($\bar{u} = 26.1$ m/s). The burner exit diameter was chosen as characteristic length instead of the flame length (≈ 45 mm) because it stays constant for all cases.

3 CFD and System Identification

The combined use of CFD simulations and system identification to determine (thermo-) acoustic transfer functions or transfer matrices (TFMs) was originally proposed by Polifke et al. [12–14], inspired by work of Bohn and Deucker [15], Krüger et al. [16], and Sklyarov and Furletov [17]. A transient CFD simulation is performed to model the complex interactions between acoustics, flow field, and combustion in burner and combustor. System identification methods are then used to extract the acoustically relevant data like FTFs or TFMs from the CFD simulation data [18].

Downloaded 02 Jun 2010 to 171.66.16.96. Redistribution subject to ASME license or copyright; see http://www.asme.org/terms/Terms_Use.cfm

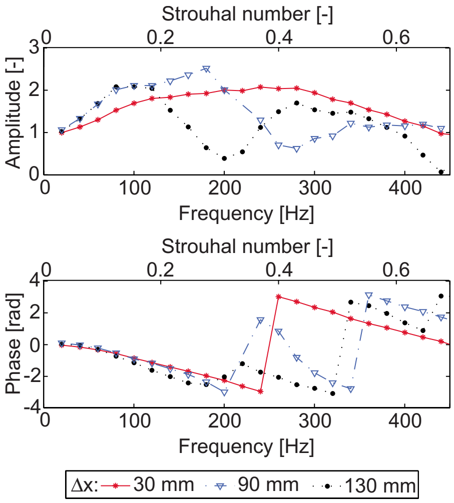

Fig. 4 FTFs for *P*=70 kW, *ϕ*=0.77, and three different positions of the axial swirl generator

A transient CFD simulation of the system is performed with an excitation of the system applied over the boundary condition. In this paper an excitation signal was imposed at the inlet boundary condition. During the simulation, time series of relevant signals are exported. In general, it is of advantage not to use the excitation signal that is applied at the boundary condition but rather a signal that is being monitored from within the computational domain.

For moderate excitation levels, it should be justified to regard the flame's response to upstream flow perturbations as a linear, time-invariant system. Such a system can be characterized completely by its unit impulse response (UIR) in the time domain or by its equivalent description in the frequency domain, the frequency response (e.g., the FTF). The Wiener–Hopf equation, an optimal linear least square estimator, is used to calculate the UIR of the system

$$\Gamma h = C \tag{3}$$

where h, Γ, and C are the unit impulse response, the auto, and the cross-correlation, respectively. In a further step the frequency response $F(\omega)$ is calculated from the UIR by a z-transformation

$$F(\omega) = \sum_{k=0}^{M} h_k e^{-i\omega k \Delta t} \tag{4}$$

A great advantage of this method is that it uses signals with broadband frequency content. With a properly designed excitation signal the complete frequency range of interest can be investigated with a single transient CFD run. A frequency limited pseudorandom binary signal (PRBS) was utilized as excitation signal. This signal type provides a very effective excitation for a given amplitude (in this paper the amplitude of the fluctuations was 4% of the mean values).

4 Numerical Setup

The CFD software package ANSYS-CFX 11.0 was used to model the burner numerically. Unsteady Reynolds-averaged Navier-Stokes (RANS) simulations were performed with a time step of 5.0×10^{-5} s. A RANS CFD approach instead of a LES approach was chosen because it was not expected that the temporal resolution of large scale turbulent structures significantly influences the thermo-acoustic response. Two numerical domains were investigated, which are displayed in Figs. 5 and 6. For the generation and propagation of swirl number fluctuations, domain A (Fig. 5) was simulated with a compressible formulation.

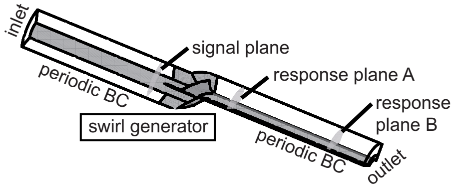

Fig. 5 Domain A: burner and swirl generator with export planes

The axial velocity was averaged over the signal plane upstream of the swirl generator, serving as input signal for the postprocessing, and the output signals were determined at the response planes downstream of the swirl generator. For identifying the flame transfer function, domain B (Fig. 6) was investigated. As input signal the velocity was averaged at the signal plane upstream of the burner exit (5 mm before the burner exit) and as output signal the heat release (weighted reaction progress source term) was integrated over the domain. For each domain, a quarter of the geometry was extended to the full geometry by the use of periodic boundary conditions. Domain A has ≈120,000 cells and domain B has ≈190,000 cells.

A second order backward Euler scheme time resolution was used in combination with the high resolution space discretization. The standard k-ϵ turbulence model was utilized. The inlet temperature was 293 K, and the wall boundary conditions were defined as adiabatic. The flame response for this kind of combustion system is caused predominantly by velocity fluctuations but is nearly unaffected by acoustic pressure oscillations. Taking advantage of this fact, an incompressible flow formulation was chosen for the combustion simulations in domain B. This increased the quality of the excitation in the computational domain and also improved the convergence speed of the simulations. The densities of the different materials were defined in dependency of temperature with a constant pressure. The "burning velocity model" (BVM) was used to model turbulent combustion, where a transport equation for the total enthalpy (sensible and chemical enthalpy) and a transport equation for the weighted reaction progress are solved [9,19].

The calculation of the reaction source term $\dot{\omega}$ is based on the turbulent flame speed closure (TFC) model by Zimont and Lipatnikov [20]

$$\dot{\omega} = \rho_u S_t |\nabla c| \tag{5}$$

$$S_t = 0.52 G u''^{3/4} S_l^{01/2} \chi_u^{-1/4} l_t^{1/4} \tag{6}$$

where ρ_u, c, S_t, S_l, G, u'', χ_u, and l_t are the density of the unburnt mixture, the reaction progress, the turbulent and laminar burning velocity, the stretch factor, the turbulent velocity fluctuation, the thermal diffusivity (evaluated at the unburnt conditions), and the integral length scale, respectively.

5 Generation and Propagation of Swirl Number Fluctuations

The development of swirl number fluctuations was investigated by a detailed analysis of the swirl generator (domain A, Fig. 5). A broadband pseudorandom binary signal excitation was applied at

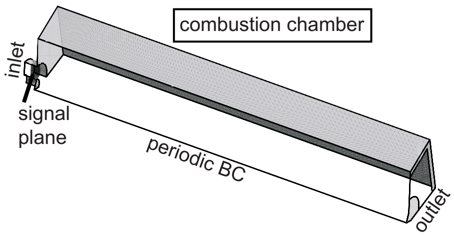

Fig. 6 Domain B: combustion chamber with signal plane

Downloaded 02 Jun 2010 to 171.66.16.96. Redistribution subject to ASME license or copyright; see http://www.asme.org/terms/Terms_Use.cfm

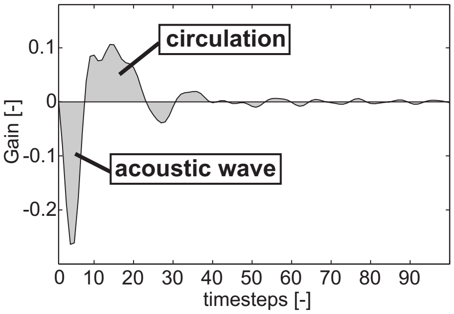

Fig. 7 Unit impulse responses of the swirl number in response plane 1: the contributions of the acoustic wave and circulation are highlighted

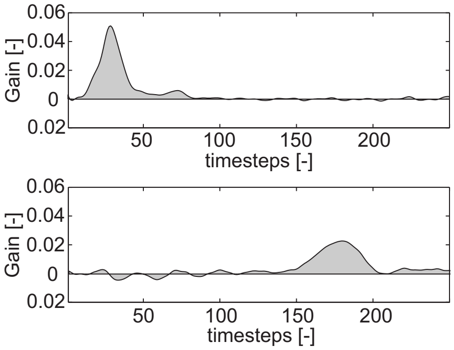

Fig. 8 Unit impulse responses of the circulation at upstream (top) and downstream (bottom) response planes

the velocity inlet boundary condition, and an acoustically low reflective boundary condition was used at the outlet. The axial velocity was exported from the signal plane (Fig. 5) upstream of the swirl generator and the swirl number from response plane 1 downstream. The UIR of the identification (Fig. 7) shows that the swirl number first is decreased and then increased by the acoustic perturbation.

This observation is explained as follows: at the swirl generator, the swirl angle of the flow is independent of the bulk velocity, unless massive flow separation occurs. The latter is not expected in the present case due to the large number of vanes, the moderate swirl angle, and the low excitation amplitudes. In other words, the local swirl number at the swirl generator is constant even in the presence of acoustic perturbations.

However, fluctuations in the swirl number will develop downstream of the swirl generator due to the different transport mechanisms for axial and tangential components of the velocity perturbations. The fluctuation in axial velocity associated with the acoustic wave travels with speed of sound, while the fluctuation in tangential velocity is transported convectively by the flow field. The resulting spatial-temporal separation of perturbation signals can already be observed in response plane A (Fig. 5). The acoustic wave passes the response plane first and increases the axial velocity, therefore, reducing the swirl number. The fluctuation in the tangential velocity that was created by the acoustic wave when passing the swirl generator reaches the response plane later. Now, only the tangential velocity is increased, resulting in a corresponding increase in the swirl number. With increasing distance from the swirl generator the temporal separation of both effects increases further.

The first reduction in the swirl number is only a secondary effect of the acoustic wave, while the acoustic wave also creates a fluctuation in the swirl number, which is then convectively transported to the flame. In order to separate the effects, the circulation Γ_F was used subsequently as output signal of the swirl generator and as input signal to the flame. It was determined according to Eq. (7)

$$\Gamma_F = \oint \vec{v} d\vec{r} \tag{7}$$

$\vec{v}$ is the velocity vector and $\vec{r}$ is the radius. The effect of the different propagation speeds has also been observed by Wang and Yang [21], who studied the flow field in swirl burners. Figure 8 now shows the UIRs with the circulation as output signal for both response planes. While being transported through the burner the time lag distribution is stretched over a longer period of time.

6 Flame Response

The response of the flame to the disturbance was investigated with the numerical domain of the combustion chamber (domain B, Fig. 5) using a velocity inlet and a pressure outlet boundary condition. Two different setups were studied. First only the axial velocity component of the inlet velocity was modulated with a pseudorandom binary signal in order to evaluate the effect of the plane acoustic wave passing the burner exit. Then, in the second setup, only the tangential velocity component was modulated in order to evaluate the effect of the fluctuation in circulation that was created at the swirl generator. The input signals used for the system identification were exported at the signal plane located 5 mm after the inlet and 5 mm before the burner exit. The heat release of the flame was monitored as the flame response or as the output signal of the system.

In Fig. 9 the UIRs of the flame are displayed for the two cases. The response to a unit impulse perturbation in axial velocity (top) shows a typical distribution. The disturbance is being transported through the flame and the heat release is being modulated while the flame is disturbed. The shape of the distribution is similar to the axial distribution of heat release (see Fig. 2) and shows almost a Gaussian profile. A unit impulse of the axial velocity results in additional mixture that is supplied to the flame, which is burned while being transported through the flame. This results in an overall increase in heat release, directly proportional to the increase of mixture flow rate. This implies—as Polifke and Lawn [22] showed—a low frequency limit of unity for the flame transfer function amplitude (see Fig. 4).

The response to the unit impulse perturbation of circulation (Fig. 9, bottom) shows a different characteristic. The disturbance

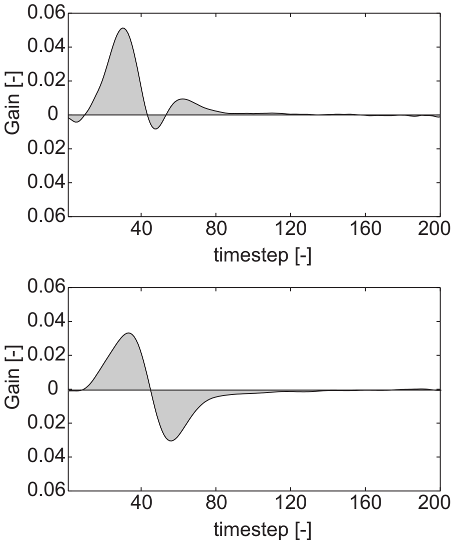

Fig. 9 Unit impulse responses: upper plot: response to an axial excitation and lower plot: response to a tangential excitation

Downloaded 02 Jun 2010 to 171.66.16.96. Redistribution subject to ASME license or copyright; see http://www.asme.org/terms/Terms_Use.cfm

is also transported through the flame but in distinction to the axial perturbation, the increase in heat release is followed by a decrease in heat release of comparable magnitude. A closer analysis of the simulation results shows that the fluctuation in circulation causes a radial and an axial velocity fluctuation downstream of the burner exit. This creates an increase in both the flame surface area and overall heat release rate. However, as the fluctuation in circulation is not supplying more mixture to the flame, this temporary increase in heat release has to be followed by a later decrease in heat release, such that the integral response, expressed as the sum over the coefficients h_k of the unit impulse response vanishes. Because

$$\lim_{\omega \to 0} F(\omega) = \sum_{k=0}^{M} h_k \tag{8}$$

according to Eq. (4), this implies that the corresponding FTF vanishes for small frequencies.

The combination of both effects will have an integral response of unity. The existence of both positive and negative contributions (coefficients h_k of the UIR vector) makes it possible to obtain a flame frequency response $F(\omega)$ with a gain exceeding unity for frequencies ω greater than zero.

7 Dynamic Flame Response Model

To model the impact of swirl number fluctuations besides the impact of the axial velocity fluctuations a time lag distribution model was developed. The model is similar to the approach used by Lawn and Polifke [5] or Schuermans et al. [7] to model equivalence ratio fluctuations. The UIR displayed in Fig. 9 (top) showed that the response to an axial excitation is similar to a Gaussian time lag distribution. For the fluctuation in circulation, the generation and propagation of the fluctuation can also be modeled with Gaussian profiles with a standard deviation σ increasing with axial distance (see Fig. 8). The impact on the flame was modeled with a Gaussian distribution, followed by another Gaussian distribution with negative amplitude. The combination of the generation, propagation, and impact on the flame was approximated with a time lag distribution of two Gaussian profiles with positive and negative amplitudes, with increased standard deviation (due to the stretching effect observed in Fig. 8 and due to the combination of both unit impulse responses).

All effects on the unit impulse response h can be modeled by four parameters: two main time lags τ_1 and τ_2, a constant standard deviation σ_1 for the first time lag (acoustic wave), and a standard deviation, increasing with Δx, for the second and third time lag τ_2 and τ_3 (fluctuation in circulation). The difference between the second and the third time lag was optimized to fit the unit impulse response in Fig. 9 and subsequently kept constant (see Eq. (10)). Therefore, the third time lag can be calculated from the second time lag, and the standard deviation of the third time lag σ_3 equals the second standard deviation σ_2. Finally, Eq. (9) was obtained. The first part models the impact of theacoustic wave on the flame, and the second and third parts model the impact of the fluctuation in circulation

$$h_k = \overbrace{\frac{1}{\sigma_1\sqrt{2\pi}} e^{-1/2((k\Delta t - \tau_1)/\sigma_1)^2}}^{\text{acoustic wave}} + \underbrace{\frac{1}{\sigma_2\sqrt{2\pi}} e^{-1/2((k\Delta t - \tau_2)/\sigma_2)^2} - \frac{1}{\sigma_3\sqrt{2\pi}} e^{-1/2((k\Delta t - \tau_3)/\sigma_3)^2}}_{\text{fluctuations in circulation}} \tag{9}$$

with

$$\tau_3 = \tau_2 + 3.2\sigma_1 \tag{10}$$

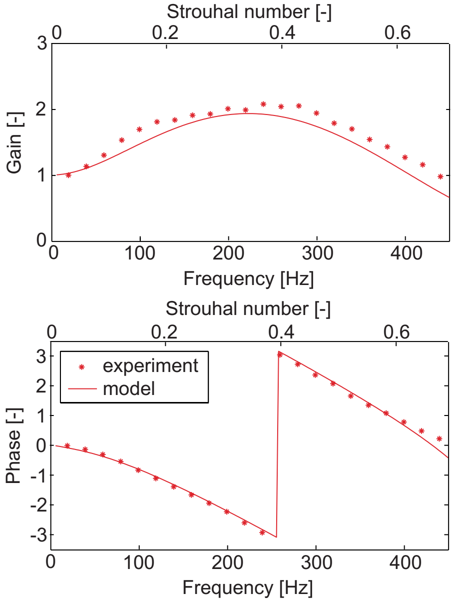

Fig. 10 FTF experiment and model Δx=30 mm

7.1 Flame Transfer Function Fit. In order to model the FTFs, Eq. (9) was used to fit the UIRs of the measured FTFs. The UIRs of the system were calculated, and the FTFs were finally obtained by the z-transformation into the frequency domain. The parameters were manually optimized to reduce the error between the modeled FTFs and the measurements. The FTFs are displayed in Figs. 10–12.

It can be seen that the main effects in the dynamic flame response are captured well by the model.

The optimized parameters that were used for the fit of the FTFs are displayed in Table 1. The time lag τ_1 of the response to the axial velocity fluctuation was kept constant for all three measurements. This is consistent with the fact that the flame shape is quite insensitive to changes in swirler position. The impact of the axial velocity fluctuation is initiated at the root of the flame front and convectively transported through the flame.

The time lag τ_2 of the fluctuation in circulation exceeds τ_1

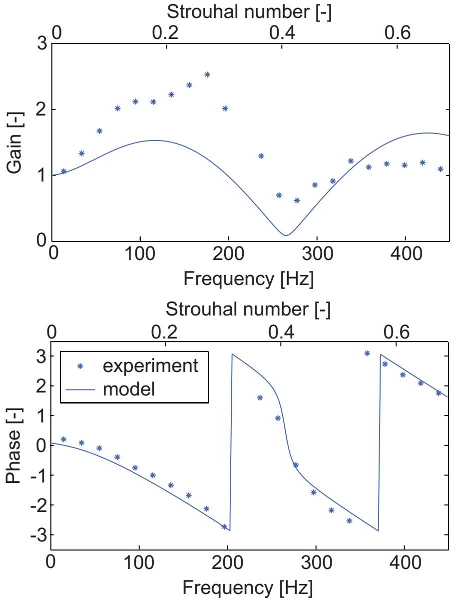

Fig. 11 FTF experiment and model Δx=90 mm

Downloaded 02 Jun 2010 to 171.66.16.96. Redistribution subject to ASME license or copyright; see http://www.asme.org/terms/Terms_Use.cfm

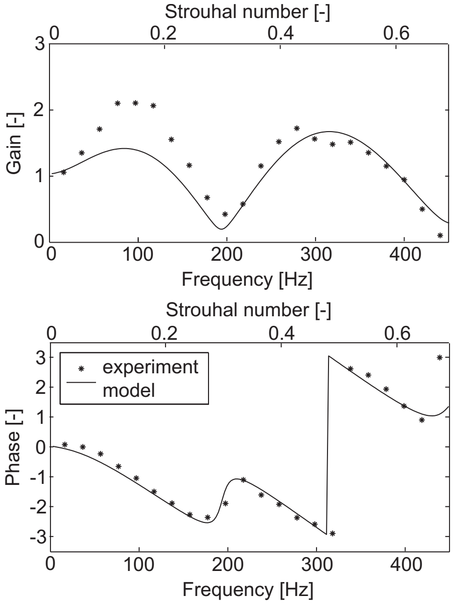

Fig. 12 FTF experiment and model $\Delta x = 130$ mm

because first the disturbance has to travel to the root of the flame. τ_2 increases with an extended distance between the swirl generator and burner exit. The transport velocity that was calculated from the time lags and the distances between swirl generator and burner exit exceeds the bulk velocity in the burner by approximately 40%.

8 Conclusions

In this paper the effect of swirl number fluctuations on the dynamic flame response was studied. A perfectly premixed swirl stabilized burner with variable position of the axial swirl generator was investigated experimentally, numerically, and analytically. The burner is equipped with an axial swirl generator with variable axial position. This makes it possible to change the time lag of swirl number fluctuations, while other effects remain unchanged. In experiments a strong impact of the position of the swirl generator on the dynamic flame response has been observed. The effect of swirl number fluctuations was investigated in detail using CFD simulations in combination with system identification methods (CFD/SI). The generation of fluctuations of swirl number, their propagation to the flame, and their effect on the dynamic flame response were examined. Additionally, a convective time lag model for the different effects was developed and successfully validated with experimental results.

Current models for the flame response can be improved by the inclusion of the model for the impact of swirl fluctuations on the heat release. This improvement will reduce the uncertainty in the prediction of the dynamic flame response further and improve the prediction quality of thermo-acoustic instabilities. It should also help to explain the differences in the stability behavior, as observed by Straub and Richards [9].

Table 1 Parameters of the time lag model

$P=70$ kW, $\phi=0.77$	τ_1 (ms)	σ_1 (ms)	τ_2 (ms)	σ_2 (ms)	τ_3 (ms)	σ_3 (ms)
$\Delta x=30$	1.7	0.27	2.8	0.32	3.6	0.32
$\Delta x=90$	1.7	0.27	4.1	0.45	4.9	0.45
$\Delta x=130$	1.7	0.27	5.1	0.57	6.0	0.57

Acknowledgment

The support of Alstom Power Generation AG, Bayerische Forschungsstiftung, Bayerisches Staatsministerium für Wirtschaft, Forschung und Kunst, Bayerisches Staatsministerium für Wirtschaft, Infrastruktur und Technologie, and Siemens AG—Power Generation in the framework of KW21 is gratefully acknowledged.

Nomenclature

CTA = constant temperature anemometer
FTF = flame transfer function
UIR = unit impulse response
c = reaction progress
d = burner exit diameter
C = cross-correlation of the signal and the response
f = frequency
F = frequency response
G = stretch factor
h = unit impulse response
l_t = integral length scale
Q = heat release
r = radius
S_l = laminar burning velocity
S_t = turbulent burning velocity
Sr = Strouhal number
u = axial velocity
v = velocity
Δx = distance swirl generator to burner exit
Δt = time increment
χ_u = thermal diffusivity
ϕ = equivalence ratio
ρ_u = density of the unburnt mixture
Γ = autocorrelation matrix of the signal
Γ_F = circulation
σ = standard deviation
τ = time lag
ω = angular frequency
$\dot{\omega}$ = source term

Superscripts

$'$ = acoustic fluctuation
$''$ = turbulent fluctuation
$\bar{\ }$ = mean value
$\vec{\ }$ = vector

Subscripts

1 = axial velocity fluctuation
2 = swirl number fluctuation a
3 = swirl number fluctuation b

References

[1] Kopitz, J., Huber, A., Sattelmayer, T., and Polifke, W., 2005, "Thermoacoustic Stability Analysis of an Annular Combustion Chamber With Acoustic Low Order Modeling and Validation Against Experiment," ASME Paper No. GT2005-68797.
[2] Reddy Alemela, P., Fanaca, D., Ettner, F., Hirsch, C., and Sattelmayer, T., 2008, "Flame Transfer Matrices of a Premixed Flame and a Global Check With Modeling and Experiments," ASME Paper No. GT2008-50111.
[3] Huber, A., and Polifke, W., 2008, "Impact of Fuel Supply Impedance on Combustion Stability of Gas Turbines," ASME Paper No. GT2008-51193.
[4] Keller, J., 1995, "Thermoacoustic Oscillations in Combustion Chambers of Gas Turbines," AIAA J., **33**(12), pp. 2280–2287.
[5] Lawn, C., and Polifke, W., 2004, "A Model for the Thermoacoustic Response of a Premixed Swirl Burner, Part II: The Flame Response," Combust. Sci. Technol., **176**, pp. 1359–1390.
[6] Richards, G., Straub, D., and Robey, E., 2008, "Control of Combustion Dynamics Using Fuel System Impedance," ASME Paper No. GT2003-38521.
[7] Schuermans, B., Bellucci, V., Guethe, F., Meili, F., Flohr, P., and Paschereit, C., 2004, "A Detailed Analysis of Thermoacoustic Interaction Mechanisms in a Turbulent Premixed Flame," ASME Paper No. GT2004-53831.
[8] Polifke, W., 2001, "Combustion Instabilities," VKI Lecture Series.

Downloaded 02 Jun 2010 to 171.66.16.96. Redistribution subject to ASME license or copyright; see http://www.asme.org/terms/Terms_Use.cfm

[9] Straub, D., and Richards, G., 1999, “Effect of Axial Swirl Vane Location on Combustion Dynamics,” ASME Paper No. 99-GT-109.

[10] García-Villalba, M., Fröhlich, J., and Rodi, W., 2005, “Large Eddy Simulation of an Annular Swirling Jet With Pulsating Inflow,” Turbulence and Shear Flow Phenomena 4, Williamsburg, VA.

[11] Hirsch, C., Fanaca, D., Reddy, P., Polifke, W., and Sattelmayer, T., 2005, “Influence of the Swirler Design on the Flame Transfer Function of Premixed Flames,” ASME Paper No. GT2005-68195.

[12] Polifke, W., Poncet, A., Paschereit, C., and Döbbeling, K., 2001, “Reconstruction of Acoustic Transfer Matrices by Instationary Computational Fluid Dynamics,” J. Sound Vib., **245**(3), pp. 483–510.

[13] Gentemann, A., Hirsch, C., Kunze, K., Kiesewetter, F., Sattelmeyer, T., and Polifke, W., 2004, “Validation of Flame Transfer Function Reconstruction for Perfectly Premixed Swirl Flames,” ASME Paper No. GT2004-53776.

[14] Polifke, W., and Gentemann, A., 2004, “Order and Realizability of Impulse Response Filters for Accurate Identification of Acoustic Multi-Ports From Transient CFD,” Int. J. Acoust. Vib., **9**(3), pp. 139–148.

[15] Bohn, D., and Deucker, E., 1993, “An Acoustical Model to Predict Combustion Driven Oscillations,” 20th International Congress on Combustion Engines, London.

[16] Krüger, U., Hoffmann, S., Krebs, W., Judith, H., Bohn, D., and Matouschek, G., 1998, “Influence of Turbulence on the Dynamic Behaviour of Premixed Flames,” International Gas Turbine and Aeroengine Congress and Exposition, Stockholm, Sweden.

[17] Sklyarov, V. A., and Furletov, V. I., 1974, “Frequency Characteristics of a Laminar Flame,” Prikl. Mekh. Tekh. Fiz., **1**, pp. 84–94.

[18] Polifke, W., Flohr, P., and Brandt, M., 2002, “Modeling of Inhomogeneously Premixed Combustion With an Extended TFC Model,” ASME J. Eng. Gas Turbines Power, **124**(1), pp. 58–65.

[19] ANSYS, Inc., 2006, “ANSYS CFX-Solver Theory Guide,” ANSYS, Inc.

[20] Zimont, V., and Lipatnikov, A., 1995, “A Numerical Model of Premixed Turbulent Combustion of Gases,” Chem. Phys. Rep., **14**(7), pp. 993–1025.

[21] Wang, S., and Yang, V., 2005, “Unsteady Flow Evolution in Swirl Injectors With Radial Entry,” Phys. Fluids, **17**, p. 045106.

[22] Polifke, W., and Lawn, C. J., 2007, “On the Low-Frequency Limit of Flame Transfer Functions,” Combust. Flame, **151**, pp. 437–451.

Downloaded 02 Jun 2010 to 171.66.16.96. Redistribution subject to ASME license or copyright; see http://www.asme.org/terms/Terms_Use.cfm

Michael T. Timko
e-mail: timko@aerodyne.com

Scott C. Herndon

Ezra C. Wood

Timothy B. Onasch

Megan J. Northway

John T. Jayne

Manjula R. Canagaratna

Richard C. Miake-Lye

Aerodyne Research Inc.,
45 Manning Road,
Billerica, MA 01821-3976

W. Berk Knighton
Department of Chemistry,
Montana State University,
P.O. Box 173400,
Bozeman, MT 59717-3400

Gas Turbine Engine Emissions—Part I: Volatile Organic Compounds and Nitrogen Oxides

The potential human health and environmental impacts of aircraft gas turbine engine emissions during normal airport operation are issues of growing concern. During the JETS/Aircraft Particle Emissions eXperiment(APEX)-2 and APEX-3 field campaigns, we performed an extensive series of gas phase and particulate emissions measurements of on-wing gas turbine engines. In all, nine different CFM56 style engines (including both CFM56-3B1 and -7B22 models) and seven additional engines (two RB211-535E4-B engines, three AE3007 engines, one PW4158, and one CJ6108A) were studied to evaluate engine-to-engine variability. Specific gas-phase measurements include NO_2, NO, and total NO_x, HCHO, C_2H_4, CO, and a range of volatile organic compounds (e.g., benzene, styrene, toluene, naphthalene). A number of broad conclusions can be made based on the gas-phase data set: (1) field measurements of gas-phase emission indices (EIs) are generally consistent with ICAO certification values; (2) speciation of gas phase NO_x between NO and NO_2 is reproducible for different engine types and favors NO_2 at low power (and low fuel flow rate) and NO at high power (high fuel flow rate); (3) emission indices of gas-phase organic compounds and CO decrease rapidly with increasing fuel flow rate; (4) plotting EI-CO or volatile organic compound EIs against fuel flow rate collapses much of the variability between the different engines, with one exception (AE3007); (5) HCHO, ethylene, acetaldehyde, and propene are the most abundant volatile organic compounds present in the exhaust gases that we can detect, independent of engine technology differences. Empirical correlations accurate to within 30% and based on the publicly available engine parameters are presented for estimating EI-NO_x and EI-NO_2. Engine-to-engine variability, unavailability of combustor input conditions, changing ambient temperatures, and complex reaction dynamics limit the accuracy of global correlations for CO or volatile organic compound EIs. [DOI: 10.1115/1.4000131]

1 Introduction

Air travel and freight shipping by air are becoming increasingly important and are expected to continue to expand [1]. The resulting increases in aviation related pollution, including particulate matter (PM) [2], volatile organic compounds (VOCs), and nitrogen oxides ($NO_x \equiv NO+NO_2$), may have negative impacts on human health [3], the local environment, or global climate. The potential human health impact is most acute for airport workers and for people living in the vicinity of airports, many of which are in highly populated areas. Unfortunately, efforts to model the potential impacts of airport activities on local air quality have sometimes conflicted [4,5]. More robust and accurate modeling of potential airport impacts requires improved data sets that (a) provide measurements of engine-to-engine and engine-technology-to-engine-technology variability and (b) includes more detailed chemical speciation of trace gas exhaust constituents than has previously been available.

A number of studies have been conducted over the past 5 years to characterize aircraft emissions by monitoring on-wing gas turbine engines on parked/chocked aircraft [6–14], gas turbine engines mounted on test stands [15–17], and in-use gas turbine engines during actual airport operation [18–22]. The data collected during previous work extend and augment that listed in the International Civil Aviation Organization (ICAO) data bank [23].

A key limitation of previous studies is that they did not investigate sufficient engines or engine technologies to provide an accurate picture of the overall fleet. Here we report the results of dedicated engine tests from two recent field campaigns: JETS/Aircraft Particle Emissions eXperiment (APEX)-2 and APEX-3, henceforth collectively referred to as APEX-2/3. A primary objective of the APEX-2/3 study was to investigate the effect that engine technology exerts over the composition and quantity of gas and particle emissions. This report summarizes some of our most important findings on the speciation of volatile organic compounds and nitrogen oxides present in jet engine exhaust. Because the health and environmental impacts of aircraft emissions depend on their chemical composition, the detailed speciation presented here is expected to improve the accuracy of estimates of aircraft emissions and, subsequently through detailed dispersion, exposure, and toxicology models, their potential impacts. We also present several simple yet accurate correlations (about ±30%) for estimating NO_x and NO_2 emissions that rely only on data publicly available in the ICAO data bank.

2 Experimental Description

2.1 Instrumentation. Table 1 lists the instruments we deployed during the APEX-2/3 campaigns to measure gas-phase species. Concentrations of gas-phase species were measured using LI-COR infrared gas analyzers (CO_2), a chemiluminescence analyzer (for NO/NO_Y, where $NO_Y \approx NO+NO_2$ for these experi-

---

Contributed by the Combustion and Fuels Committee of ASME for publication in the JOURNAL OF ENGINEERING FOR GAS TURBINES AND POWER. Manuscript received April 13, 2009; final manuscript revised July 7, 2009; published online March 19, 2010. Editor: Dilip R. Ballal.

Copyright © 2010 by ASME

Downloaded 02 Jun 2010 to 171.66.16.96. Redistribution subject to ASME license or copyright; see http://www.asme.org/terms/Terms_Use.cfm

Table 1 Instruments deployed in APEX-2/3

Instrument	Species detected	Detection limit[a]	Time resolution	Campaign(s) deployed
LI-COR IR gas analyzer (models 6262 and 820)	CO_2	2 ppm	1 s	APEX-2 and 3
NO_x chemiluminescence analyzer Thermo Electron (model 42C)	NO	0.2 ppb	1 s/20 s	APEX-2 and 3
	NO_Y[b]	0.2 ppb	20 s	APEX-3
QCL-TILDAS[c]	NO_2	1 ppb	1 s	APEX-2 and 3
	C_2H_4	6 ppb	1 s	APEX-2 and 3
	CO	5 ppb	1 s	APEX-2 and 3
	HCHO	1.5 ppb	1 s	APEX-3
TILDAS[d]	HCHO	0.5 ppb	1 s	APEX-2 and 3
	NO	1 ppb	1 s	APEX-3
PTR-MS[e]	Acetaldehyde, propene, benzene, toluene, styrene, C_2-benzenes,[f] phenol, naphthalene, methylnaphthalene, and dimethylnaphthalene	2–5 ppb	8 s	APEX-2 and 3

[a] Defined as three times the noise at the stated time resolution.

[b] $NO_Y \approx NO + NO_2$ for these experiments.

[c] Quantum-cascade tunable infrared laser differential absorption spectrometer (Aerodyne Research, Inc.).

[d] Tunable infrared laser absorption spectrometer (Aerodyne Research, Inc.).

[e] Proton-transfer reaction mass spectrometer.

[f] C_2-benzene implies *o*-xylene, *m*-xylene, *p*-xylene, and ethylbenzene.

ments), a proton transfer reaction mass spectrometer (PTR-MS) [12] (for volatile organic compounds), a lead-salt tunable infrared laser differential absorption spectrometer (TILDAS) [24] (for HCHO and NO), and a quantum cascade tunable infrared laser differential absorption spectrometer (QCL-TILDAS) [25] (for NO_2, C_2H_4, and CO). During APEX-3, HCHO was measured by both TILDAS and QCL-TILDAS, and the measurements agreed to within about 3%.

2.2 Dedicated Engine Tests. Dedicated engine tests were performed during the JETS/APEX-2 campaign at Oakland International Airport (Oakland, CA; August 23–26, 2005) and the APEX-3 campaign at Cleveland Hopkins International Airport (Cleveland, OH; November 1–7, 2005). In all, detailed power cycles were tested in 12 different airframes/airplanes and 17 different engines. Table 2 lists ambient conditions and chemical compositions of the fuels that were used, and Table 3 provides ICAO certification data for the APEX-2/3 engines [23]. All of the engines studied were turbofans except for the turbojet CJ6108A mounted on the N616NA Lear jet airframe. ICAO data is not available for the turbojet as its rated thrust is below the level required for certification [23]. The airplanes remained grounded and chocked during all tests while the engine thrust was varied to simulate operation at ground idle (4%), idle (7%), approach (30%), climbout (85%), takeoff (100%), and some intermediate power conditions (e.g., 15 and 65%). In practice, measuring takeoff emissions from a stationary airplane is challenging, so we

Table 2 Summary of jets/jet engines studied during APEX-2/3 field campaigns. Ambient pressure was always 760±6 torr.

Tail No.	Engine model	Campaign	*T* (K)	RH %	Fuel sulfur[a] (ppm)	Total aromatics[b] (vol %)	Notes
N435WN[c]	CFM56-7B22	APEX-2	286	93	130	19.6	Turbofan
N429WN[c]	CFM56-7B22	APEX-2	286	92	420	20.2	Turbofan
N695SW[c]	CFM56-3B1	APEX-2	285	93	350	22.7	Turbofan
N353SW	CFM56-3B1	APEX-2	285	93	220	20.4	Turbofan
N14324	CFM56-3B1	APEX-3	281	87	700	18	Turbofan
N70330	CFM56-3B1	APEX-3	286	49	400	13.6	Turbofan
N75853	RB211-535E4-B	APEX-3	290	78	300	21.8	Three-spool internally mixed turbofan
N74856	RB211-535E4-B	APEX-3	283	68	300	20.3	Three-spool internally mixed turbofan
N729FD	PW4158	APEX-3	292	69	600	16.2	Turbofan
N11193	AE3007A1E	APEX-3	286	47	300	20.7	Forced mixed turbofan
N16927	AE3007A	APEX-3	282	67	200	19.4	Forced mixed turbofan
N616NA	CJ6108A	APEX-3	291	45	<100	14.2	Turbojet

[a] On a mass basis, as determined by ASTM method D5453 (JETS/APEX-2) and D4294 (APEX-3).

[b] As determined by ASTM method D5186 (JETS/APEX2) and D1319 (APEX-3).

[c] Both the starboard and port side engines were monitored using 1 m sample rakes. Downfield measurements were taken on the starboard engine only.

Downloaded 02 Jun 2010 to 171.66.16.96. Redistribution subject to ASME license or copyright; see http://www.asme.org/terms/Terms_Use.cfm

Table 3 Summary of EIs measured for some gas-phase species during APEX-2/3 and from ICAO certification data

				EI-CO[c] (g kg^{-1})			EI-NO$_x$[d] (g kg^{-1})			EI-HCHO[e] (mg kg^{-1})		
Engine model/Tail No.	Engine location	π_{00}[a]	F_{00}[b] (kN)	7%	30%	85%	7%	30%	85%	7%	30%	85%
CFM56-3B1 (ICAO)		22.44	89.41	34.4	3.8	0.95	3.9	8.3	15.5	2280	80	50
CFM56-3B1/N353SW	Stbd			30 ± 1	3.6 ± 0.5	1.0 ± 0.3	2.8 ± 0.6	7.0 ± 0.4	17 ± 1	164 ± 6		1.7 ± 0.5
	Port			28 ± 2	3.7 ± 0.1		3.4 ± 0.1	7.8 ± 0.3		283 ± 17	ND	
CFM56-3B1/N14324	Stbd			34 ± 1	4 ± 1	1.4 ± 0.1	3.3 ± 0.2	6.8 ± 0.4	14 ± 1	540 ± 170		22 ± 3
CFM56-3B1/N70330	Stbd			40.0 ± 0.8	5.1 ± 0.3	1.6 ± 0.1	2.99 ± 0.07		13.2 ± 0.7		ND	ND
CFM56-3B1/N695SW	Stbd			27 ± 1	4.1 ± 0.5	1.5 ± 0.3	2.9 ± 0.4	6.5 ± 0.6	17 ± 2	528 ± 39	11.5 ± 0.8	0.5 ± 0.4
	Port			28 ± 1[g]	3.8 ± 0.3[g]		3.2 ± 0.1	7.0 ± 0.7		410 ± 30	ND	
CFM56-7B22 (ICAO)		24.41	100.97	22.8	2.50	0.60	4.50	10.00	19.00	2500	100	100
CFM56-7B22/N435WN	Stbd			24 ± 7	1.9 ± 0.7	0.40 ± 0.03	4.3 ± 0.3	9.5 ± 0.6	19 ± 4	270 ± 40	15 ± 8	7.3 ± 0.5
	Port			23.3 ± 3.1	1.71 ± 0.05		4.2 ± 0.8	11 ± 1		380 ± 60	12 ± 7	
CFM56-7B22/N429WN	Stbd			19 ± 4	1.2 ± 0.1	0.6 ± 0.2	4.2 ± 0.3	10.1 ± 0.5	24 ± 5	280 ± 50	2.5 ± 0.8	1.8 ± 0.2
	Port				1.5 ± 0.05			9.1 ± 0.3			4.3 ± 0.7	
RB211-535E4-B[l] (ICAO)		27.9	191.7	18.24	2.43	0.26	4.58	8.65	19.3	140	50	0
RB211-535E4-B[l]/N75853	Stbd			18 ± 8	2.9 ± 1.4	0.22 ± 0.08	5 ± 1	9.3 ± 0.8	24 ± 5	80 ± 2	ND	11 ± 3
RB211-535E4-B/N74856	Stbd			19 ± 1	2.1 ± 0.2	0.20 ± 0.03	5.0 ± 0.6	10 ± 1	23.9 ± 0.7	219 ± 9	ND	ND
PW4158 (ICAO)		30.7	258.0	20.99	1.88	0.54	4.8	11.8	23.7	1780	140	20
PW4158[f]/N729FD	Stbd			39 ± 3	2.2 ± 0.5		3.5 ± 0.3	9.6 ± 0.8	22.4 ± 2	1010 ± 70	ND	
AE3007-A1E (ICAO)		19.06	37.16	37.97	5.63	0.64	4.26	7.42	14.91	3520	30	30
AE3007-A1E[g]/N11193	Stbd			29 ± 12	3 ± 1	0.267 ± 0.004	3.7 ± 0.7	7.7 ± 0.5	13.2 ± 0.6	400 ± 100	12 ± 1	ND
	Port			35 ± 1	4.4 ± 0.1	0.30 ± 0.01	3.43 ± 0.09	7.3 ± 0.2	12.1 ± 0.7	660 ± 20	ND	ND
AE3007-A (ICAO)		18.08	33.73	33.73	17.35	3.28	3.83	7.79	17.47	2510	640	290
AE3007-A[g]/N16927	Stbd			32.8 ± 0.7	4.0 ± 0.4	0.33 ± 0.03	3.4 ± 0.3	6.7 ± 0.5	10.4 ± 0.8	520 ± 20	ND	17.1 ± 1.2
CJ6108A (ICAO)		8.3	13.1									
CJ6108A[g]/N616NA	Stbd			140 ± 7	45 ± 7	21 ± 2	2.4 ± 1.6	3.2 ± 0.5	4.6 ± 0.3	2500 ± 500	400 ± 130	47 ± 11

[a] π_{00} is the pressure ratio.
[b] F_{00} is the rated thrust.
[c] EI-CO measurements averaged over all available downstream sampling locations. Port side engine emissions data for N435WN, N429WN, and N695SW reflect 1 m measurements only.
[d] EI-NO$_x$ measurements averaged over all available sampling locations. EI-NO$_x$ equals the sum of EI-NO$_2$ and EI-NO, both in units of mass of NO$_2$.
[e] EI-HCHO reflects average value of all available 1 m data. ICAO values are for unburned hydrocarbons—EI-HC. ICAO does not speciate hydrocarbon data.
[f] The 85% thrust conditions was not studied for this engine–data measured at 80% thrust.
[g] The 7% thrust setting was not studied for this engine–data measured at 8% rated thrust.
ND indicates that the species concentration was less than the detection limits of the instrument.
Blank spaces indicate missing data.

Downloaded 02 Jun 2010 to 171.66.16.96. Redistribution subject to ASME license or copyright; see http://www.asme.org/terms/Terms_Use.cfm

Table 4 Equations used to calculate emission ratios

No.	Equation	Use	Validity
(2)	$\mathrm{ER}=\frac{C_{\mathrm{X,exhaust}}}{C_{\mathrm{CO_2,exhaust}}}$	Defines the emission ratio (ER)	Universal
(3a)	$C_{\mathrm{X},M}=\left(1-\frac{1}{D}\right)C_{\mathrm{X,dil}}+\left(\frac{1}{D}\right)C_{\mathrm{X,exhaust}}=\frac{C_{\mathrm{X,exhaust}}}{D}$	Mass balance relationships between measured and exhaust gas concentrations of pollutant, X, and CO_2	1 m
(3b)	$C_{\mathrm{CO_2,M}}=\left(1-\frac{1}{D}\right)C_{\mathrm{CO_2,dil}}+\left(\frac{1}{D}\right)C_{\mathrm{CO_2,exhaust}}=\frac{C_{\mathrm{CO_2,exhaust}}}{D}$		
(3c)	$\mathrm{ER}(1\ \mathrm{m})=\frac{C_{\mathrm{X,exhaust}}}{C_{\mathrm{CO_2,exhaust}}}$		
(4a)	$C_{\mathrm{X},M}=(1-f)C_{\mathrm{X,amb}}+fC_{\mathrm{X,exhaust}}$	Mass balance relationships between measured, exhaust, and ambient concentrations of pollutant and CO_2	>15 m
(4b)	$C_{\mathrm{CO_2},M}=(1-f)C_{\mathrm{CO_2,amb}}+fC_{\mathrm{CO_2,exhaust}}$		
(5a)	$\mathrm{ER}(>15\ \mathrm{m})=\frac{\bar{C}_{\mathrm{X},M}-\bar{C}_{\mathrm{X,amb}}}{\bar{C}_{\mathrm{CO_2},M}-\bar{C}_{\mathrm{CO_2,amb}}}$	Time-averaged definition of ER, used when winds did not influence the plume dispersion	>15 m
(5b)	$C_{\mathrm{X},M}=(\mathrm{ER\text{-}X})C_{\mathrm{CO_2},M}+\{C_{\mathrm{X,amb}}-(\mathrm{ER\text{-}X})C_{\mathrm{CO_2,amb}}\}$	"Slope" definition of ER, used when winds influenced plume dispersion	>15 m

emphasize our climbout data (85% power) instead. The power cycle during a typical experiment was as follows: (1) the engines were started and allowed to warm-up for roughly 5–10 min; (2) measurements commenced as the engines were operated at ground idle; (3) the test continued as the power was increased in a stepwise fashion (e.g., from 4% to 7% to 15%, etc.) up to either climbout power or takeoff power; (4) the power was directly reduced to either idle or ground idle; (5) after several minutes at idle, the power was increased directly to either climbout or takeoff; (6) the power was reduced in stepwise fashion back to ground idle and the test concluded. Exhaust gas samples were taken continuously throughout the entire experiment and each stable point lasted for 2–5 min. Engine transients were also captured in the data stream, but these data are not discussed here. Fuel flow rates were recorded at all power conditions for all engines/airframes except CFM56-7B22/N435WN (both port and starboard) and CFM56-3B1/N14324. For these two engine/airframe combinations, we used ICAO fuel flow rates.

For every engine studied, measurements were made approximately 1 m from the engine exit plane and at several downstream locations (>15 m) for most engines. For 1 m measurements, the exhaust gas was immediately diluted with dry nitrogen within the probe tip; the dilution ratio varied from 8:1 to about 40:1 such that the concentration of CO_2 was typically 1000–2000 ppm. Forced nitrogen dilution ensured that the sample gas temperature was reduced to $<150^\circ\mathrm{C}$ in less than 2 ms even for measurements made at takeoff powers [11]. During JETS/APEX-2, heating of the 1 m probe tip was minimized by forced cooling water convection, a procedure that was not used during APEX-3. Some of the engine exit plane measurements may have been affected by chemical conversion in the hot probe tips used during APEX-3, and probe effects is a topic in the Results section. The downstream probe stands consisted of a single undiluted probe tip and a 1.5 cm i.d. unheated stainless steel sample line. Mixing with the ambient air typically provided about 20–60 fold dilution of the exhaust gas.

2.3 Data Analysis. The emission index (EI-X ≡ mass of pollutant, X, emitted per mass fuel consumed) is the accepted method to report aircraft emissions

$$\mathrm{EI\text{-}X}\left[\frac{\mathrm{g\ X}}{\mathrm{kg\ fuel}}\right]=\mathrm{ER\text{-}X}\left(\frac{\mathrm{MW_X}}{\mathrm{MW_{CO_2}}}\right)\mathrm{EI\text{-}CO_2} \tag{1}$$

where ER-X is the emission ratio (ER) (mol pollutant/mol CO_2) of pollutant X (i.e., the concentration ratio of the pollutant to aircraft CO_2). $\mathrm{MW_X}$ and $\mathrm{MW_{CO_2}}$ ($\mathrm{g\ mol^{-1}}$) are the molecular weights of pollutant and CO_2, respectively, and EI-CO_2 is the emission index of CO_2 (g/kg fuel). Prior to dilution, the concentration of CO_2 present in the exhaust gas is always significantly (>10×) greater than that present in the ambient air. Because the gas turbine combustor efficiencies were always greater than 95% and generally greater than 99%, the error associated with assuming complete combustion is smaller than our estimates of experimental uncertainty. Correction factors that take into account CO and measured volatile organic compound concentrations can easily be applied [26]. For reporting EI-NO, the molecular weight of NO_2 was used for $\mathrm{MW_X}$ so that EI-NO and EI-NO_2 are reported on the same molecular weight basis.

Evaluation of Eq. (1) requires calculating the emission ratio [20]. Table 4 lists equations for calculating ER for 1 m exhaust samples, Eq. (3), and for >15 m downfield plume samples, Eqs. (4) and (5). Section 6 defines all mathematical symbols used in Table 4. Calculation of ER at 1 m is straight forward; Yelvington et al. [11] and Herndon et al. [21] described the derivation in detail. Two methods were used to calculate ERs for >15 m

Downloaded 02 Jun 2010 to 171.66.16.96. Redistribution subject to ASME license or copyright; see http://www.asme.org/terms/Terms_Use.cfm

plume measurements, one valid for low-wind conditions, Eq. (5a), the other valid for windy conditions, which introduced time dependent structure into the emissions data, Eq. (5b). Equation (5a) simply takes the time-average value of exhaust gas species concentrations during the time interval of interest to calculate ER and is most useful when the concentrations are stable ($<10\%$ variation). Equation (5b) involves plotting the pollutant concentration as a function of CO_2 concentration during the time interval of interest. Equation (5b) is most accurate when exhaust gas concentrations fluctuate during the time interval of interest ($>10\%$ variation). We have found that Eqs. (5a) and (5b) yield similar absolute EI values, though the uncertainties calculated by Eq. (5b) are generally about half those estimated from the Eq. (5a) under windy conditions [11]. We calculate EIs for all species with 1 Hz response time (see Table 1) using either Eq. (5a) or Eq. (5b) and report only the value with the lower estimated uncertainty.

2.4 Internal Forced Mixing. Equation (3) is valid only for engines with no internal ducting. The data analysis procedures described by Eq. (3) need to be modified for calculating exit plane EIs for engines that employ internal forced mixing of the core and bypass flows. The AE3007s are the only APEX-2/3 engines to employ forced mixing. For internally mixed engines, such as the AE3007s, the two-stream problem implied by Eq. (3) (nitrogen dilution gas and core-flow exhaust gas) becomes a three-stream problem (nitrogen dilution, bypass flow, and core-flow exhaust gas). Unlike nitrogen dilution gas, the bypass air contains ambient levels of carbon dioxide, water, and trace gas pollutants. Analyzing all available data including CO_2 concentrations in the raw exhaust gas (data not presented here), the estimated error in calculated EIs varies from slightly less than 9% (at idle) to 3% (at takeoff). The estimated error is less than 4% for half of the available data set. Given the small magnitude of the correction and the uncertainties inherent in both the correction and the data themselves, we have opted not to correct AE3007 EIs for bypass air dilution.

3 Results

3.1 Measurement Reproducibility and Accuracy. We collected a total of 582 stable data points for 21 gas-phase species (see Table 1). Table 3 lists representative CO, NO_x, and HCHO (a representative volatile organic compound) EIs for all of the engines studied in APEX-2/3. Idle (either 7% or 8% depending on the engine), approach (30%), and climb out (85%) power conditions are emphasized in Table 3. EIs for takeoff power conditions are generally not available due to the difficulty in obtaining such data for stationary aircraft. EI-NO_x reported in Table 3 have been normalized to account for the effects of relative humidity variation [13]. The humidity correction factor was always less than 6%. Each EI reported in Table 3 is the average of all available replicate points (typically 3–6) taken at a given set of conditions (i.e., downstream distance, engine setting, etc.). Experimental uncertainties were estimated in two ways. In the first method, the uncertainty was set equal to the standard deviation of all available data points at a given set of conditions. In the second, the uncertainties in each of the experimental quantities in Eq. (1) were propagated as a Taylor series expansion following the standard method [27]. The larger of these two estimates of the uncertainty are reported here.

3.1.1 Engine Temperature Effects. During a typical test cycle, measurements were taken at a given thrust rating both as the engine thrust was increased and as it was decreased to the set point. That test order was intended to reveal potential emissions dependences on engine temperature. With the RB211-535E4-B providing a notable exception, no systematic biases were found; EI-CO for the RB211-535E4-B engines was about half as much when the power was decreased to ground idle (4%) after a period of operation at power greater than 30%. EI-CO for the RB211-535E4-B did not exhibit hysteresis at power settings other than 4%, though the power was never rapidly decreased to any powers except ground idle. Volatile organic compounds (including HCHO), NO_x (low when EI-CO is high, and vice versa), and some of the particulate measurements (e.g., total number count) also showed dependencies on the ordering of the engine test matrix. The unusually low EI-CO recorded during 4% idle periods, which follow high power operation, is seemingly due to increased engine temperature (and/or fuel/air flows) relative to that experienced during cold starts or when idling follows low power (e.g., 15%) operation. Based on decreased EI-CO and increased EI-NO_x, the engine/inlet flows seem to retain a higher temperature for several minutes following high power operation. The importance of engine warm-up and hysteresis is an area of on-going interest, and the impact of these effects on the overall emissions inventories has not been fully quantified. The data presented here indicate that additional work should be performed to understand potential engine temperature effects on emissions performance.

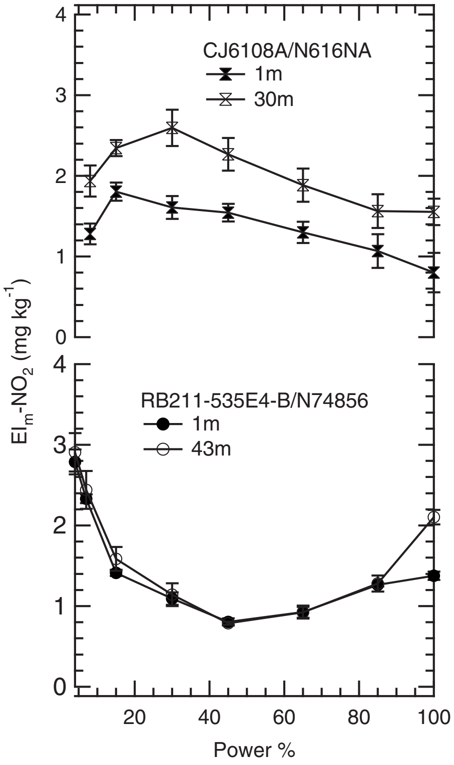

Fig. 1 Comparison of 1 m and >15 m EI-NO_2 data for an engine, which showed a large discrepancy (CJ6108A/N616NA), and one that did not (RB211-535E4-B/N74856)

3.1.2 Probe Effects. During APEX-3, EI-NO_2 was often higher downstream than at the engine exit plane. In contrast, during JETS/APEX-2, the difference between upstream and downstream EI-NO_2 measurements was less significant ($<12\%$). Figure 1 plots 1 m and >15 m EI-NO_2 data for the CJ6108A/N616NA (which had much larger EI-NO_2 at >15 m than 1 m) and the RB211-535E4-B/N74856 (which did not). Table 5 summarizes the calculated differences between 1 m and >15 m measurements of EI-NO_2 measured at 7% idle, as NO_2 discrepancy data at this power are representative of other powers. Interestingly, the NO_2 discrepancy is much more variable for the APEX-3 measurements, ranging from -56% to -5%, than for APEX-2, where it ranges from +10% to -12%. As a rule, the NO_2 discrepancy was less than about 10% for engines with internal mixing (RB211-535E4-B/N74856 and the AE3007 engines), though the RB211-535E4-B/N75853 engine violates this generalization

Downloaded 02 Jun 2010 to 171.66.16.96. Redistribution subject to ASME license or copyright; see http://www.asme.org/terms/Terms_Use.cfm

Table 5 Idle (7%) NO_2 and NO_x discrepancy data between 1 m and >15 m

			EI-NO_2 ($g\ kg^{-1}$)			EI-NO_X ($g\ kg^{-1}$)		
Tail No.	Engine	Campaign	1 m	>15 m	%Δ (%)	1 m	>15 m	%Δ
N435WN	CFM56-7B22	JETS/APEX-2	1.9	2.1	−12	3.9	3.8	2.6
N429WN	CFM56-7B22	JETS/APEX-2	2.1	1.9	10	4.0	3.9	2.5
N353SW	CFM56-3B1	JETS/APEX-2	1.9	1.9	2	3.1	2.9	6.5
N695SW	CFM56-3B1	JETS/APEX-2	2.5	2.3	7	3.0	3.1	−3.3
N14324	CFM56-3B1	APEX-3	1.9	3.0	−56	3.1	3.4	−10
N616NA	CJ6108A	APEX-3	1.3	1.9	−51	1.7	3.8	−120
N729FD	PW4158	APEX-3	2.3	3.1	−35	2.8	3.2	−14
N11193	AE3007-A1E	APEX-3	2.6	2.6	−9	3.6	3.7	−3.0
N16927	AE3007-A	APEX-3	2.5	2.8	−12	3.4	3.3	3.0
N75853	RB211-535E4-B	APEX-3	1.7	2.1	−24	4.5	4.4	3.0
N74856	RB211-535E4-B	APEX-3	2.3	2.4	−5	4.9	5.0	−2.0

(−24% difference).

Conversion of NO_2 to NO in the 1 m probe tips (on the heated metal surfaces) and conversion of NO to NO_2 in the exhaust plume are likely explanations for the upstream/downstream NO_2 behavior in the two campaigns. During JETS/APEX-2, the 1 m probe tip was water cooled. As a result, conversion of NO_2 to NO may have been suppressed in the JETS/APEX-2 sampling system. Water cooling was not used during APEX-3, resulting in higher probe tip temperatures and possibly more conversion of NO_2 to NO. Internal mixing in the engine should decrease the exhaust gas temperature, thereby reducing NO_2 to NO conversion in 1 m samples extracted from these engines. Exhaust gas temperatures were not measured for most of the engines studied in this work; however, Wey and Wey [13] reported exhaust gas temperatures for a CFM56-2C1 engine. The Hunderup and Roby mechanism [28] predicts oxidation of NO to NO_2 when sampling emissions at temperatures only slightly greater than those expected for aircraft gas turbine exhaust (500–700°C compared with 450–750°C for a CFM56-2C1 [13]). Wood et al. [29] discussed nitrogen oxide emissions and NO/NO_2 intraconversion in more detail for aircraft gas turbine engines, focusing specifically on NO to NO_2 conversion in the exhaust plume.

The EI-NO_x data in Table 5 are consistent with NO_2 conversion to NO during sampling of externally mixed engine exhaust using uncooled probes. For internally mixed engines or when a water-cooled sampling probe is used to sample exhaust, EI-NO_x varies usually less than 3% and always less than 6.5% between the 1 m and >15 m sampling location. For externally mixed engines sampled using uncooled probes, the difference is on the order of −10% for the CFM56-3B1 (N14324) and PW4148 (N729FD) engines. The 10% NO_x difference is much less than the 50% difference in NO_2, indicating that additional NO accounts for most of the lost NO_2. The CJ6108A (N616NA) engine is a striking outlier as the 1 m EI-NO_x is 120% less than the 15 m EI, even though the NO_2 discrepancy is only 30%. NO/NO_2 intraconversion alone cannot explain the CJ6108A nitrogen oxide data. The chief difference between the CJ6108A and the CFM56-3B1 and PW4158 engines is that the CJ6108A has the greatest EIs for volatile organic compounds (see Table 3, using HCHO as an indicator) by a factor of 2.5. Hunderup and Roby [28] indicated that nitrogen oxide chemistry may be coupled to hydrocarbon chemistry, and we speculate that the enhanced hydrocarbon concentrations in the CJ6108A exhaust may play a role in the apparent disappearance of NO_x in its 1 m exhaust gas samples when sampled with an uncooled probe. To reduce the impacts of potential probe chemistry, we focused NO_2 analysis on measurements made at >15 m in the downstream plume.

3.2 Effects of Power Condition and Engine Technology on EIs

3.2.1 Emissions Performance Trends. As a rule, combustion efficiency generally increases with power setting, thus reducing EI-CO and EI-HCHO. At the same time, increasing power condition increases the combustion temperature, leading to an increase in EI-NO_x. Qualitatively, the expected power setting trends are observed; EI-CO and EI-HCHO decrease monotonically with engine thrust, whereas EI-NO_x increases monotonically with engine thrust. Quantitatively, the data in Table 3 show that EI-CO and EI-NO_x data within the set of four CFM56-3B1 engines agree nearly to the limits of experimental uncertainty. EI-CO for the CFM56-3B1/N70330 engine is an apparent outlier. Similarly, duplicate measurements of EI-CO and EI-NO_x for the other engines agree to within the estimated limits of experimental reproducibility. The port engine (AE3007A1E) on the N11193 airframe may have emitted more CO than the starboard engine, but the discrepancies are only slightly larger than the estimated uncertainties. The large uncertainties for the N75853/RB211-535E4-B EI-CO are related to the hysteresis effects described earlier; all valid data points were weighted equally in Table 3.

3.2.2 Engine and Engine-Technology Comparisons. When comparisons between classes of engines are made, EI-NO_x is generally higher for the higher-thrust larger engines (PW4158 and RB211-535E4-B), which is expected as the certification process makes allowances for maximum rated thrust. EI-CO does not follow the engine thrust trend and takes values at 7% thrust that ranges from about 20 $g\ kg^{-1}$ (RB211-535E4-B) to about 30–40 $g\ kg^{-1}$ (CFM56) for the turbofan engines. The turbojet technology (CJ6108A/N616NA) has the lowest EI-NO_x and largest EI-CO by a factor of about 2. It has the largest EI-HCHO by a factor of about 5. This older example of turbojet technology is much less fuel efficient and has a much lower combustor inlet temperature than the more modern turbofan engines studied during APEX-2/3, accounting for the differences in the NO_x/CO and emissions between the two engine types (e.g., turbofan and turbojet).

Table 3 suggests that EI-HCHO within a class of engines is much more variable than either EI-CO or EI-NO_x. The most sensitive comparisons of EI-HCHO can be made at idle (7%) conditions. An example of this, EI-HCHO variability is seen within the CFM56-3B1 family of engines at idle power, where EI-HCHO ranges from 211 ± 18 (N353SW, starboard) to 540 ± 170 $mg\ kg^{-1}$ (N14324, starboard). The variability of EI-HCHO partly reflects the influence of ambient temperatures on volatile organic compound emissions, an effect that Yelvington et al. [11] documented

Downloaded 02 Jun 2010 to 171.66.16.96. Redistribution subject to ASME license or copyright; see http://www.asme.org/terms/Terms_Use.cfm

in the APEX-1 data set for a CFM56-2C1 engine. Table 2 lists average ambient temperature for the various tests for reference, and we highlight several test cases here. The N353SW CFM56-3B1 engine was tested at an ambient temperature of 13°C, while the N14324 CFM56-3B1 test was at 8°C, and the trend in the volatile organic compound EIs for these two engines is consistent with the CFM56-2C1 observations reported by Yelvington et al. [11]. The two RB211-535E4-B engines show a distinct temperature effect: EI-HCHO for N75853 equals 80 mg kg^{-1} (17°C) while that of N74856 (10°C) is 219 mg kg^{-1}. The ambient temperature, however, cannot be the sole source of EI-HCHO variability as the port and starboard EI-HCHO measurements of neither the N353SW (CFM56-3B1) nor the N11193 (AE3007-A1E) agree to within our estimated limits of uncertainty—despite the fact that both sets of engines were tested on the same day and at similar temperatures. The source of the remaining HCHO variability (engine maintenance condition, ambient humidity, systematic sampling errors, or instrumental biases) is uncertain at this time.

3.3 Comparison With Certification Data. The ICAO certification data listed in Table 3 can be compared with the measured EIs. ICAO certification data are sometimes used in models that predict the impact of airport activities on regional air quality [30], and deviations between the database and actual measurements may have important ramifications for the accuracy of the air quality predictions.

3.3.1 Comparison With ICAO NO_x. Measured EI-NO_x is generally lower than the ICAO value by about 10% for all of the engines studied, but in good overall agreement. The AE3007 engines are the exceptions as NO_x EIs measured at climbout are about 50% smaller than the corresponding ICAO values. Experimental fuel flow rate data provide the likely explanation for most of the deviations observed for the AE3007 engines as both the AE3007A1E (0.302 kg s^{-1} compared with the ICAO value of 0.3425 kg s^{-1}) and the AE3007A (0.277 kg s^{-1} versus 0.315 kg s^{-1}) were studied at lower fuel flow rates than the ICAO ratings. The dependence of EI-NO_x on fuel flow rate is considered later in this report. Incorrect calculation of dilution factors for the internally mixed AE3007 engines would tend to reduce EI-NO_x; however, we estimate a 10% correction rather than the 50% discrepancy observed.

3.3.2 Comparison With ICAO CO. Measurements of EI-CO agree with the ICAO values within the limits of experimental uncertainty for most of the engines, though the variability in the data is large enough (generally about 25%) to obscure small differences. Additionally, ICAO certification data are tabulated based on at least three engine tests and may include data from more than one engine. Therefore, ICAO data may include engine-to-engine variability, making direct comparisons less straight forward. The PW4158 engine is an exception to the otherwise good agreement with ICAO EI-CO data. The PW4158 engine emitted twice as much CO as listed in the ICAO databank at idle conditions (39 3 ± 3 compared with 20.99 g kg^{-1}). The EI-CO discrepancy for the PW4158 engine may be due to a small, but significant (0.21 kg s^{-1} versus 0.189 kg s^{-1}) difference in the ICAO and actual fuel flows. EI-CO increases strongly with decreasing power at conditions near idle so the slightly lower experimental fuel flow rate used in the experiments may explain the observed CO discrepancy. Interestingly, EI-CO for the AE3007 engines tends to be somewhat lower than the ICAO values (especially at 30% and 85% power), despite the fact that incorrect calculation of exhaust gas dilution should introduce a positive EI bias for the expected relative concentrations of CO and CO_2 in the exhaust, dilution nitrogen, and ambient air.

3.3.3 Comparison With ICAO Unburned Hydrocarbon. ICAO does not have a direct equivalent to EI-HCHO; however, ICAO does tabulate the emission indices of total unburned hydrocarbons (EI-HC). Flame-ionization detection is the ICAO method for measuring EI-HC [23], and Yelvington et al. [11] showed that the ratio of experimental measurements of EI-HCHO and EI-HC are relatively constant for a CFM56-2C1 engine—even as the power condition and EIs change. Consistent with the observation of Yelvington et al. [11], we see that EI-HCHO tends to scale with EI-HC for all of the engine types. As expected, EI-HCHO is always less than or equal to EI-HC; EI-HCHO and EI-HC are effectively equal for the RB211-535E4-B engines. For a given engine, both ICAO EI-HC and EI-HCHO decrease sharply with increasing power. When different classes of engines are compared, EI-HC and EI-HCHO follow similar trends. Engines that have the lowest values of EI-HCHO (e.g., about 100–200 mg kg^{-1} for the RB211-535E4-B engines at idle) also have the lowest certification values of EI-HC (140 mg kg^{-1} for idling RB211-535E4-B engines), and engines with higher values of EI-HCHO have higher values of EI-HC (e.g., the CFM56-3B1 engines).

3.4 Speciation of Nitrogen Oxides Emissions. While ICAO certification specifies the total NO_x emissions (that is the sum of NO and NO_2), the local and regional effects of NO and NO_2 may be quite different [31] from one another. NO_2 is generally considered to be more toxic than NO [32,33] and rapidly photolyzes to contribute to ozone—the primary constituent of photochemical smog and a criterion pollutant. For this reason, understanding the apportionment of NO_x into NO and NO_2 in gas turbine exhaust is a subject of increasing importance. Past studies have focused on NO_x speciation [13,14] for a limited range of gas turbine engines. The APEX-2/3 results are broadly consistent with previous studies and greatly expand the $NO_x/NO/NO_2$ data set. Figure 2 contains a plot of NO_2 and NO for the RB211-535E4-B. The NO_2 to total NO_x tends with respect to engine power were similar for all of the turbofan engines, and the RB211-535E4-B engines were selected as representatives. As discussed previously, the probe tip temperature (water cooled in JETS/APEX-2, uncooled in APEX-3) introduces some uncertainty into EI-NO_2. Nonetheless, the qualitative features present in Fig. 2 are essentially correct and the indicated magnitudes are correct to within about 25%. For the turbofan engines, NO dominates EI-NO_x at high power conditions, but NO_2 makes an important contribution (up to about 75% for the RB211-535E4-B and over 95% for the CFM56-3B1 engines) at 4% idle. Similar NO_2 emissions behavior was reported for the CFM56-2C1 during APEX-1 [13,14] and is discussed further by Wood et al. [29]. The turbojet CJ6108A engine is shown in Fig. 2 for comparison with the turbofan. For the turbojet, the ratio of NO_2 to total NO_x is about 80% at ground idle and remains greater than 25% even at takeoff conditions. In Fig. 2, NO and NO_2 EIs are plotted such that the height of the curve corresponds to total NO_x, and ICAO certification values are shown for reference.

3.5 Speciation of Volatile Organic Compound Emissions. Volatile organic compound EIs fall off sharply with increasing power, and idle organic compound emissions dominate the overall budget. In addition to the 7% ICAO idle point that is listed in Table 3, we measured EIs at a lower "ground" idle at 4% rated thrust for some engines. Figure 3(*a*) plots representative volatile organic compound data (formaldehyde, benzene, and naphthalene) as a function of power for a CFM56-3B1 engine. Figure 3(*a*) shows that volatile organic compound EIs are maximized for 4% idle conditions and rapidly decrease with increasing power. For power conditions greater than about 15%, volatile organic compound concentrations were at or below instrumental detection limits (see Table 1; $\text{EI} \leq 0.01$ g kg^{-1}) for many of the engines tested.

We find that HCHO, ethylene, acetaldehyde, and propene are the most abundant volatile organic compound species emitted—regardless of engine technology or power condition. Figure 3(*b*) contains volatile organic compound data for three very different engines operating at idle (4%): the low thrust turbojet CJ6108A (13.1 kN), the intermediate thrust turbofan CFM56-3B1 (89.4 kN), and the high thrust RB211-535E4-B (191.7 kN). The volatile

Downloaded 02 Jun 2010 to 171.66.16.96. Redistribution subject to ASME license or copyright; see http://www.asme.org/terms/Terms_Use.cfm

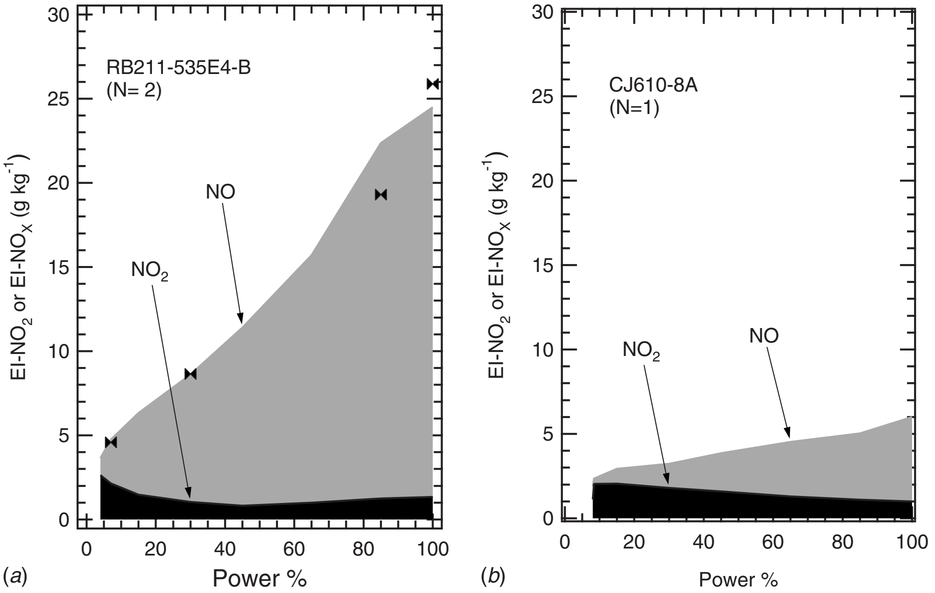

Fig. 2 NO$_x$ speciation for (*a*) RB211-535E4-B and (*b*) CJ6108A engines. ICAO data points (▶◀) are shown for reference.

organic compound data shown in Fig. 3(*b*) for these three engines are representative of the entire APEX-2/3 data set—even though the absolute volatile organic compound EIs vary by a factor of 25 (e.g., RB211-535E4-B compared with CJ6108A). Under all conditions and for all engines, HCHO, ethylene, acetaldehyde, and propene account for 75% or more of the volatile organic compound emissions that we can detect using our instrument suite. Benzene, toluene, styrene, xylenes, and other substituted benzene compound, oxygenates (methanol, acrolein, acetone, glyoxal, propanal, phenol, and benzaldehyde), olefins (butene, pentene, and hexene), and naphthalenes constitute the remaining exhaust gas volatile organic compounds that we can detect. Paraffins [34], including methane, have also been detected in idling aircraft engine exhaust, and our measurements do not include paraffin contributions. Knighton et al. [12,35] and Yelvington et al. [11] provided more detailed information regarding the composition of the trace volatile organic compound emissions based on a study of the CFM56-2C1 engine, including a comparison of PTR-MS/QCL data to flame-ionization detector hydrocarbon measurements [11].

The PTR-MS detects butene and acrolein at the same mass (m/z 57) and cannot distinguish between them; hence, we report m/z 57 as the sum of the two compounds. Spicer et al. [34] used cryogenic preconcentration and gas chromatographic analysis to identify volatile organic compounds in jet engine exhaust, and report that the ratio of butene to acrolein is of order 1. Recently, Timko et al. [36] reported a technique that couples a PTR-MS to a gas chromatograph and that should allow near real-time differentiation of the m/z 57 signal.

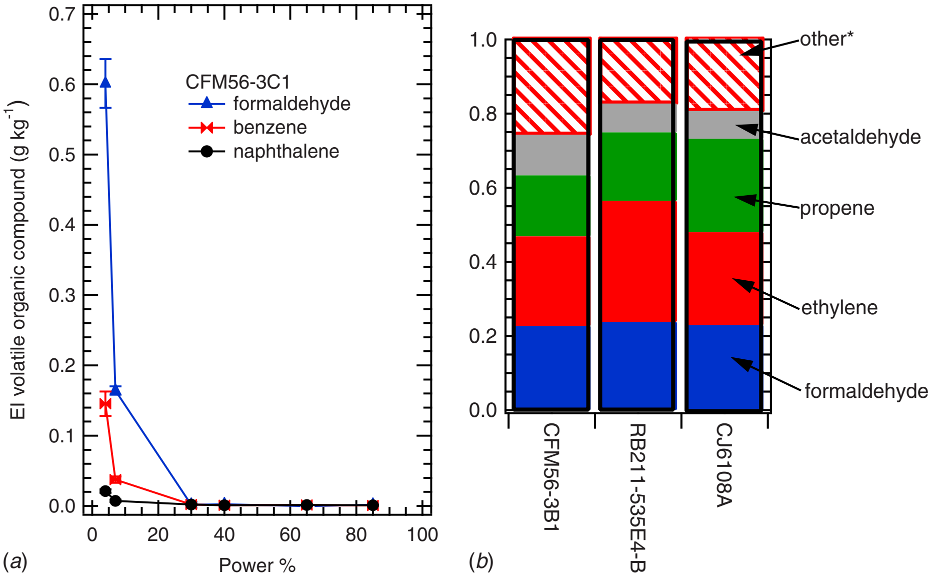

Fig. 3 Emission indices of several representative volatile organic compounds measured during the engine tests (*a*) EIs for formaldehyde, benzene, and naphthalene plotted as functions of engine power for a CFM56–3B1 engine (N353SW). (*b*) Relative ratios of important volatile organic compound emissions for several representative engines operating at idle for the measurement suite available to us.

Downloaded 02 Jun 2010 to 171.66.16.96. Redistribution subject to ASME license or copyright; see http://www.asme.org/terms/Terms_Use.cfm

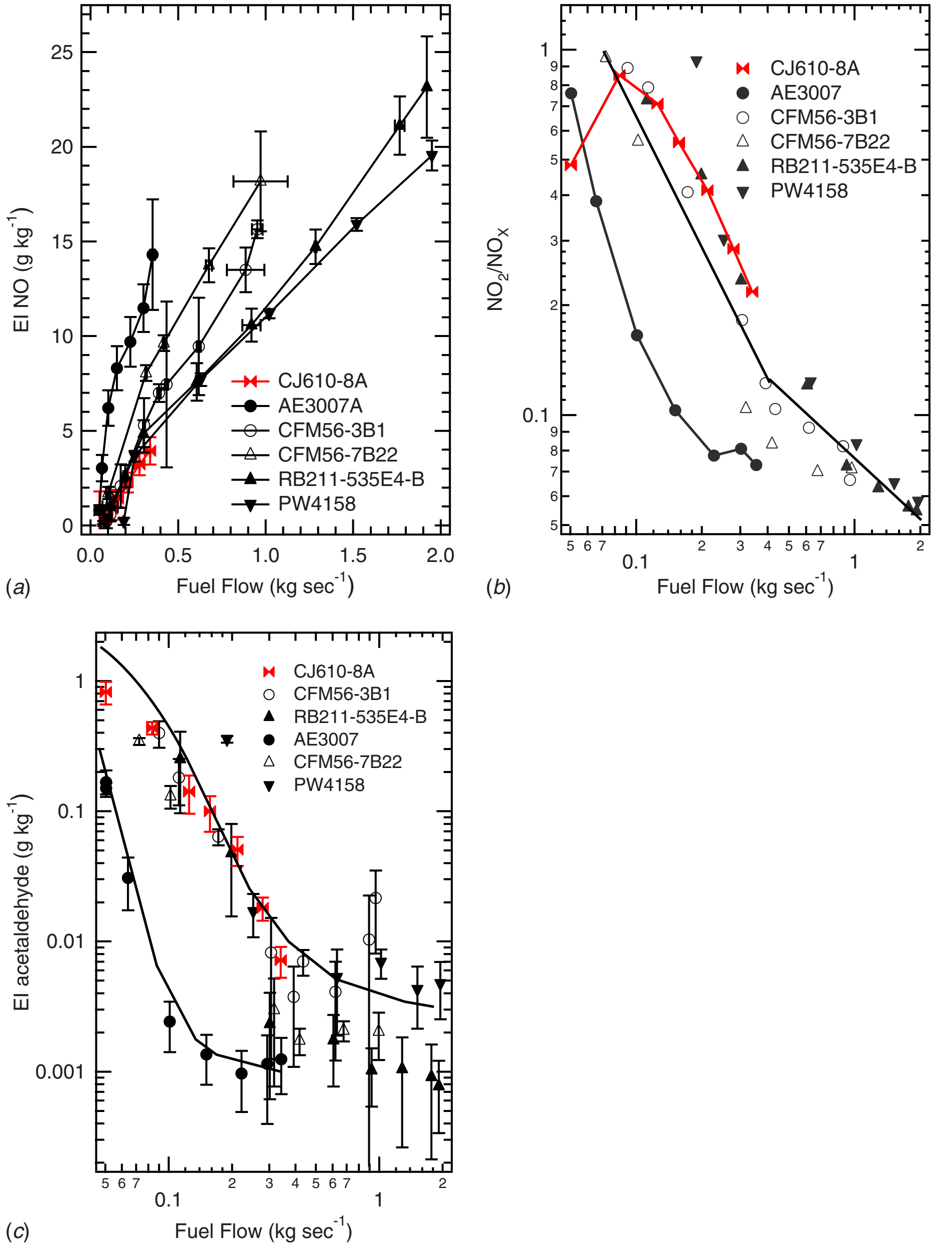

Fig. 4 Emission indices of gaseous pollutants plotted as functions of fuel flow rate for APEX-2/3 engines: (*a*) NO; (*b*) the NO_2/NO_x emission index ratio; (*c*) acetaldehyde, a representative volatile organic compound. Lines are shown to guide the eye and are not intended to convey physical significance.

3.6 Fuel Flow Rate as a Scaling Variable. Previous researchers have used fuel flow rate as a scaling variable for NO_x [13], CO [37], and volatile organic compound [11,12] emissions, and we were encouraged to explore plotting experimental EIs against fuel flow rate to test whether this variable would collapse engine-to-engine variability. Figure 4 contains plots of NO (a), the ratio of NO_2 to total NO_x (b), and acetaldehyde (c). As shown in Fig. 4(*a*), plotting NO emission indices for multiple engines against fuel flow rate does not result in a universal curve. For clarity of presentation, all EIs of a particular engine type (i.e., CFM56-7B22) have been averaged together in Fig. 4(*a*) showing that higher-thrust engines (e.g., PW4158) tended to have lower EI-NO at a given fuel flow rate than lower-thrust engines (e.g., AE3007A1E) as mentioned earlier. The turbojet CJ6108A engine is an exception, as it is has both the lowest rated thrust and the lowest EI-NO.

Plots of NO_2 (not shown here) were similar to Fig. 4(*a*), in that (a) fuel flow rate did not remove engine-to-engine variability and (b) higher-thrust engines had larger EI-NO_2 at a given fuel flow rate than lower-thrust engines. Despite not collapsing variability in either absolute values of EI-NO_2 or EI-NO, fuel flow rate does remove much of the variability in the ratio of NO_2 to total NO_x. Figure 4(*b*) plots the ratio of EI-NO_2 to EI-NO_x for the APEX-2/3 engines as a function of fuel flow rate. Figure 4(*b*) suggests that, while formation of NO is engine dependent, the conversion of NO to NO_2 is engine independent. The AE3007 engines are apparent outliers in the NO_2/NO_x fuel flow scaling rule, as they convert less NO to NO_2; the lower conversion may be a consequence of internal mixing that quenches the NO to NO_2 reaction. Interestingly, the turbojet CJ6108A engine falls on the same curve as the other turbofans except the data point at idle (8% thrust, fuel flow

Downloaded 02 Jun 2010 to 171.66.16.96. Redistribution subject to ASME license or copyright; see http://www.asme.org/terms/Terms_Use.cfm

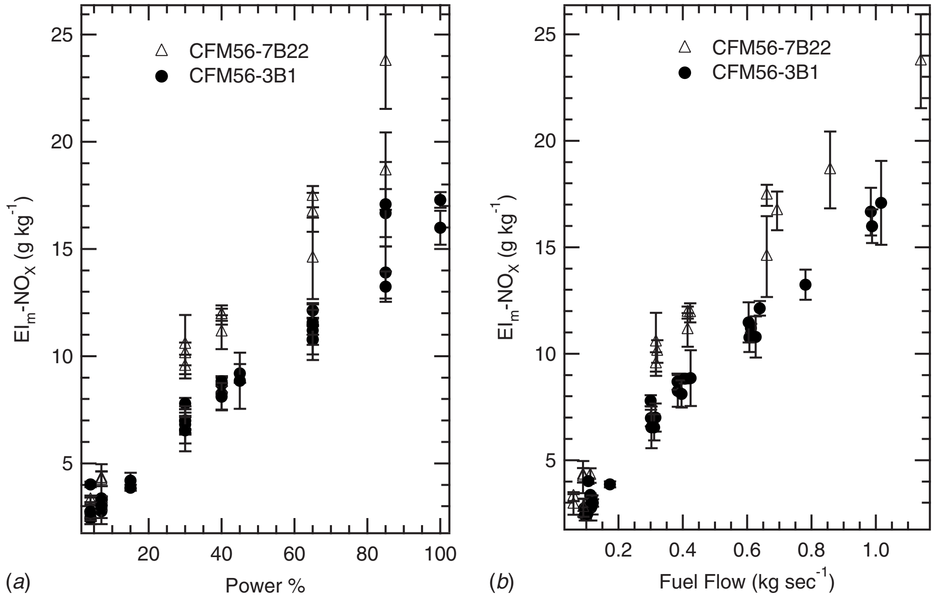

Fig. 5 EI_m-NO_x data for the CFM56 engines: (*a*) EI_m-NO_x plotted against power condition; (*b*) EI_m-NO_x plotted against fuel flow rate to remove engine-to-engine variability for CFM56 type engines

rate=0.05 kg s^{-1}) is lower than expected based on the overall trend line. Unlike the other engines studied, the nitrogen oxide ratio for the CJ6108A goes through a maximum at 15% rated thrust (fuel flow=0.11 kg s^{-1}). Whether the unusual behavior of the CJ6108A is due to the fact that it operated at lower absolute fuel flow rates than the turbofan engines (except the AE3007s which we readily identify as outliers) or marks a more fundamental combustion difference between an older turbojet and more modern turbofan technologies is not known.

Figure 4(*c*) contains plots of EI-acetaldehyde as functions of fuel flow rate for the APEX-2/3 engines. Unlike NO_x, much of the variability in EI-acetaldehyde was removed by plotting against the fuel flow rate. As with Fig. 4(*b*), the AE3007 engines are conspicuous outliers in the EI-acetaldehyde plot. Three separate AE3007 engines were tested on two separate days. When EI-acetaldehyde for the replicate measurements is plotted against fuel flow rate, the three engines fall on the same curve, indicating that the AE3007 volatile organic compound behavior was reproducible. Error introduced by incorrect calculation of dilution ratios can only account for about 10% of the discrepancy between the AE3007s and the other engines. The observed discrepancy is closer to a factor of 10, which is more than can be accounted for by any known source of experimental error. Figure 4(*c*) is representative of a number of species—including the behavior of the outlying AE3007 emissions—such as CO and other volatile organic compounds (HCHO, etc.).

The APEX-2/3 data set contains six examples of CFM56-3B1 engines, affording an opportunity to examine fuel flow rate as a NO_x scaling variable for a single engine technology. Figure 5(*a*) contains a plot of EI_m-NO_x as a function of power, and Fig. 5(*b*) plots EI_m-NO_x as a function of fuel flow rate. Figure 5 includes data for both CFM56-3B1 and -7B22 engines. NO_x data for the N14324/CFM56-3B1 engine is not included in Fig. 5 since we lacked accurate fuel flow rate data for that engine. Visual inspection of Fig. 5 suggests that plotting as a function of fuel flow rate decreases apparent scatter for both types of CFM56 engine. We infer that the fuel flow rate accounts for small test differences (for example, engine temperature, ambient conditions, and operator differences) that are not controlled by engine power setting alone.

4 Discussion

The breadth and depth of the APEX-2/3 NO_x data set provides the opportunity to develop correlations between measured EIs and engine operating parameters. Correlations for NO_2 and specific volatile organic compounds are especially desirable since most correlations [37–40] and the ICAO data bank [23] focus on total NO_x and total unburned hydrocarbons. We sought to complement rather than replace the more sophisticated emissions models currently available [41] and, at this time, we have not pursued more sophisticated modeling approaches for the trace gas data.

4.1 NO_x and NO_2 Correlations. Due to its familiarity, we used NO_x as the starting point of our analysis, even though accurate total NO_x correlations already exist [38–40]. Because plotting EI-NO_x and EI-NO_2 against fuel flow rate did not reduce engine-to-engine variability (Fig. 4(*a*)), we needed additional variables to account for engine operational parameters. T_3/P_3 data are typically used for correlating combustor emissions data, but T_3/P_3 are proprietary and were not available for correlating the APEX-2/3 data. The ratio of engine thrust to fuel flow rate is roughly proportional to residence time [38], while the pressure ratio should be proportional to combustor temperature [42]. The physicality of equating engine volume with thrust is questionable but, since engine NO_x certification accounts specifically for engine thrust, it is clearly an important scaling variable. These considerations suggest the following form for an empirical NO_x correlation

$$\text{EI-NO}_x = \kappa \dot{m}^{\alpha} \pi_{00}^{\beta} F_{00}^{\gamma} \tag{6}$$

where $\dot{m}$ is the mass fuel flow rate (kg s^{-1}), π_{00} is the pressure ratio, and F_{00} is the rated thrust (kN); κ, α, β, and γ are fitting parameters. The best fit of Eq. (6) to the data is shown in Fig. 6(*a*) as a parity plot. The majority of data points (90%) fell within 30% of the best-fit estimate. The best-fit line shown between measured and fit EI-NO_x data has a slope of 1.08 ± 0.03 (instead of 1.0 for a perfect correlation) and a Pearson's *r* value of 0.97.

We then applied Eq. (6) to the EI-NO_2 data. The probe-tip-related sampling issues introduced about 25% uncertainty into the EIs, and the accuracy of an empirical correlation may benefit from

Downloaded 02 Jun 2010 to 171.66.16.96. Redistribution subject to ASME license or copyright; see http://www.asme.org/terms/Terms_Use.cfm

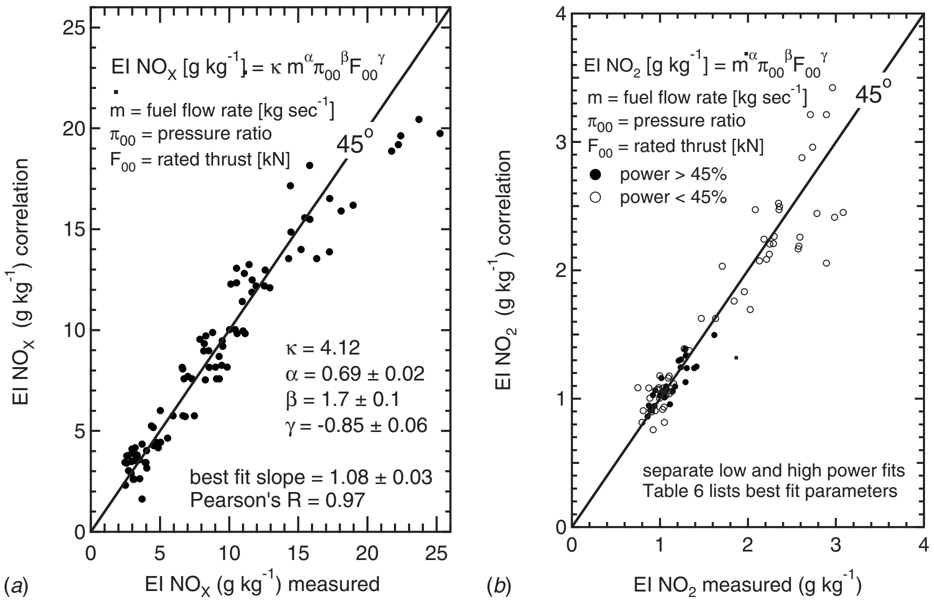

Fig. 6 Comparison of nitrogen oxide measurements to the Eq. (6) fit: (*a*) NO$_x$; (*b*) NO$_2$. Each data point is the average of all available replicate measurements at a given set of conditions (i.e., sample rake, power, etc.). Error bars are defined in the text. EI-NO$_2$ was divided into two regimes based on power, ≤45% and >45%. Values of best-fit parameters are listed in Table 6. CJ6108A (not shown) is an outlier in the NO$_2$ analysis.

an improved EI-NO$_2$ data set. Nonetheless, the available data provided a test for the Eq. (6) correlation form and resulted in some useful observations. Equation (6) could not fit the entire turbofan EI-NO$_2$ data set simultaneously. To improve the fit, we separated the turbofan NO$_2$ data into low and high power populations for separate fitting to Eq. (6). The results of the two-part correlation fit shown in Fig. 6(*b*) as a parity plot. The global best-fit line between measured and fit EI-NO$_2$ data has a slope of 0.93 ± 0.03 (instead of 1.0, as expected for a perfect correlation), a Pearson's r value of 0.95, and 95% of the predictions fall within 25% of the measurements. The error of the furthest outlying point is 52%. Table 6 lists all of the Eq. (6) best-fit parameters used to generate Fig. 6. Interestingly, the fit parameters for the low power NO$_2$ data ($<45\%$) are of the same magnitude but have the opposite sign as for the high power NO$_2$ data ($>45\%$), including the logarithm of κ (+0.536 for low powers and -0.630 for high power).

Upon initial consideration, the requirement of two separate NO$_2$ correlations seems a distinct shortcoming. In fact, while the physical significance of the separate NO$_2$ power regimes—or why percent rated thrust is the appropriate variable for dividing the data set rather than fuel flow rate—is uncertain, the recent study by Wood et al. [29] provides some insight. The report of Wood et al. [29] suggests that the relative importance of key formation/consumption reactions varies with engine operating condition: Low-power NO$_2$ formation is dominated by HO$_2$ oxidation of NO, while high power NO$_2$ formation is dominated by oxidation of NO by O. The need for two separate NO$_2$ correlations may be linked to the two distinct chemical regimes for NO$_2$ formation.

4.2 CO Correlation. Historically, EI-CO has been more difficult to correlate than EI-NO$_x$ [43], and our findings are consistent with that observation. Fitting Eq. (6) directly to the CO data set yielded unphysical values for the fitting parameters (e.g., EI-CO was found to vary with $\pi_{00}{}^8$). We then examined a number of variants of Eq. (6), systematically removing and then coupling the independent parameters—fuel flow rate, pressure ratio, and engine thrust. We found that removing π_{00} from Eq. (6) yielded the best fit to the data and reasonable values for the fitting parameters, resulting in Eq. (7)

$$\text{EI-CO} = \kappa \dot{m}^{\alpha} F_{00}{}^{\gamma} \tag{7}$$

In fact, Eq. (7) performed nearly as well as Eq. (6) (average absolute error 47% versus 37%). The best-fit CO parameters are provided in Table 6. The EI-CO correlation is shown in Fig. 7(*a*) as a log-log parity plot. The best-fit slope for the data is 0.77 and Pearson's R value is 0.85. Clearly, the CO fit is inferior to the NO$_x$ and NO$_2$ fits. The CJ6108A (shown, but excluded from the fit) was an outlier in the CO correlation, as was the first plane from APEX-3 (N14324, CFM56-3B1). The CFM56-3B1/N14324 engine may have been an outlier for the CO analysis as we lacked accurate fuel flow data for this test and used ICAO fuel flow rate data instead.

4.3 Volatile Organic Compound Correlations. A robust correlation for volatile organic compound EIs would improve the accuracy of models to predict potential health and environmental impacts of aircraft emissions. The APEX-2/3 data set includes

Table 6 Best-fit parameters used for correlations

Species	Equation	κ	σ	β	γ
NO$_x$	6	4.12	0.69 ± 0.02	1.7 ± 0.1	-0.85 ± 0.06
NO$_2$ (thrust $<45\%$)	6	3.434	-0.653	-2.07	1.018
NO$_2$ (thrust $>45\%$)	6	0.234	0.652	2.11	-1.082
CO	7	0.0017	-1.77 ± 0.08	NA	1.2 ± 0.2
HCHO	8	2.3×10^{-6}	-2.1 ± 0.2	1.4 ± 0.3	NA

Downloaded 02 Jun 2010 to 171.66.16.96. Redistribution subject to ASME license or copyright; see http://www.asme.org/terms/Terms_Use.cfm

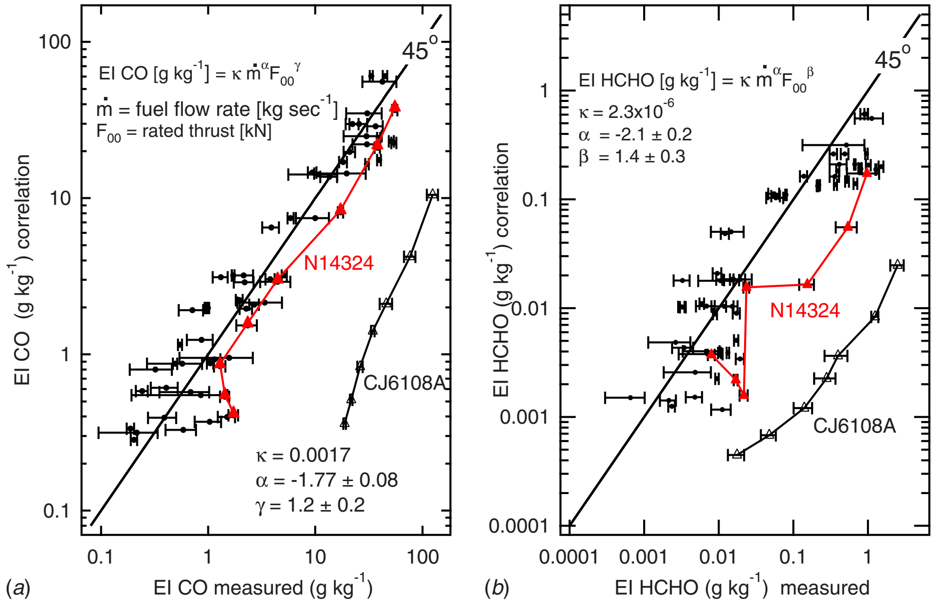

Fig. 7 Comparison of (*a*) CO and (*b*) HCHO measurements with the correlations of Eqs. (7) and (8), respectively. Each data point is the average of all available replicate measurements at a given set of conditions (i.e., sample rake, power, etc.). Error bars are defined in the text. The CJ6108A (△) is an outlier in both regressions, as is the first plane in APEX-3 (▲, N14324). Values of best-fit parameters are listed in the figure and in Table 6.

accurate volatile organic compound EIs for many candidate species including HCHO, acetaldehyde, ethylene, and propene. Because of the high instrumental sensitivity to HCHO (0.5 ppb detection limit), we decided that data for this species would provide the best opportunity to develop a volatile organic compound emissions engine correlation. EI-HCHO contributes 20–25% of the total measured EI-HC independent of the absolute EIs, and developing an accurate EI-HCHO correlation would be the equivalent to developing an EI-HC correlation. As with EI-NO_x and EI-CO, we started with Eq. (6) but found no variation of this correlation, which fit the data to better than an order of magnitude. Removing F_{00} from Eq. (6) resulted in the following correlation:

$$\text{EI-HC} = \kappa \dot{m}^{\alpha} \pi_{00}{}^{\beta} \tag{8}$$

which provided the best fit for EI-HCHO. Table 6 provides the best-fit parameter values for Eq. (8). Figure 7(*b*) depicts the Eq. (8) EI-HCHO correlation as a log-log parity plot. The correlation in Fig. 7(*b*) is poor, though all of the best-fit parameters have physical values. In all of the correlations tested, EI-HCHO varied with $\dot{m}^{-2}$, and this may be the most useful result of the volatile organic compound correlation exercise. As with CO, both the CJ6108A engine (excluded) and the CFM56-3B1 mounted on the N14324 airframe (included) were outliers in the HCHO correlation. Accurate prediction of EI-HCHO may require a more detailed model than the empirical ones tested here. Based on the known effect of ambient temperature on volatile organic compound EIs [11], we attempted to augment Eq. (8) using an additional term for ambient absolute temperature

$$\text{EI-HC} = \kappa \dot{m}^{\alpha} \pi_{00}{}^{\beta} T^{\delta} \tag{9}$$

but found that the additional term did not improve the fit.

5 Conclusions

We report trace gas emissions measurements of in-use gas turbine engines. In addition to NO_x and CO, we measured NO_2 and a range of speciated volatile organic compounds (including HCHO, C_2H_4, propene, benzene, and substituted benzene compounds, naphthalene, etc.). The data set includes measurements over a range of power conditions for 16 different engines including CFM56-3B1 (N=6), CFM56-7B22 (N=3), RB211-535E4-B (N=2), PW4158 (N=1), CJ6108A (N=1), AE3007A (N=1), and AE3007A1E (N=2). Based on this data, we arrive at the following conclusions.

- Measured EIs behaved qualitatively as expected—NO_x increased monotonically with engine thrust, while CO and volatile organic compounds decreased with thrust.
- HCHO, ethylene, acetaldehyde, and propene account for roughly 75% of the volatile organic compounds that we can detect, and this observation is independent of engine technology.
- Benzene, toluene, xylenes, and other substituted benzene compounds, oxygenates (acetone, glyoxal, and propanal), olefins (butene, pentene, hexene), and naphthalenes constitute the remaining 20% of the speciated exhaust gas volatile organic compound content that we can detect using our instrument suite.
- NO_2 was an important contribution to the total NO_x at idle power, and the proportion of NO_2 steadily decreased with engine thrust.
- Plotting EIs against fuel flow rate reduced apparent engine-type-to-engine-type variability for CO and volatile organic compounds, but not for NO_x.
- For CFM56 engines, plotting EIs against fuel flow rate reduced engine-to-engine variability for NO_x.
- Simple correlations, which use data publicly available in the ICAO data bank, were able to describe the NO_x and NO_2 data sets but were less successful for CO and volatile organic compounds.
- Volatile organic compounds and CO EIs scaled with the inverse square of fuel flow rate ($\dot{m}$).

The following outstanding issues remain.

- For unknown reasons, volatile organic compound and CO data for the AE3007 engines differ from the others, following a slightly different trend when plotted against fuel flow rate.

Downloaded 02 Jun 2010 to 171.66.16.96. Redistribution subject to ASME license or copyright; see http://www.asme.org/terms/Terms_Use.cfm

- The effects of engine start-up and warm-up need to be quantified.
- NO_2 emissions measurements may be influenced by probe chemistry effects that need to be understood more carefully.
- The temperature dependence of volatile organic compound EIs requires further study.
- The empirical correlations presented here must be supplemented by mechanistic understanding and accurate physical models, especially for volatile organic compounds.

Acknowledgment

NASA Cooperative Agreement No. NCC3-1084, PARTNER/FAA Grant No. 03-C-NE-UMR, and the California Air Resources Board via the Missouri University of Science and Technology Center of Excellence supported this work. We gratefully acknowledge the contributions of Southwest Airlines, Continental Airlines, FedEx, and NASA Glenn Research Center. We are very grateful to Renee Dowlin (formerly at Oakland International Airport) and Dana Ryan (Cleveland Hopkins International Airport). The entire APEX, JETS/APEX-2, and APEX-3 team contributed to the success of these missions. Paul Yelvington (Mainstream Engineering), Hsi-Wu Wong (ARI), Luwi Oluwole (ARI), Elena de la Rosa Blanco (ARI), and Joda Wormhoudt (ARI) generously provided technical advice and editorial commentary. Changlie Wey (NASA Glenn Research Center) shared gas-phase measurements made at 1 m using an undiluted probe.

Nomenclature

$\bar{C}_{X,\mathrm{amb}}$ = time-averaged ambient gas concentration of pollutant, X (ppm)
$\bar{C}_{X,M}$ = time-averaged sample gas concentration of pollutant, X (ppm)
$\dot{m}$ = fuel flow rate (kg s^{-1})
$\bar{C}_{CO_2,\mathrm{amb}}$ = time-averaged ambient gas concentration of CO_2 (ppm)
$\bar{C}_{CO_2,M}$ = time-averaged sample gas concentration of CO_2 (ppm)
C_2-benzene = *o*-xylene, *m*-xylene, *p*-xylene, and ethylbenzene
$C_{CO_2,\mathrm{exhaust}}$ = exhaust gas concentration of CO_2 (ppm)
$C_{CO_2,M}$ = sample gas concentration of CO_2 (ppm)
$C_{X,\mathrm{exhaust}}$ = exhaust gas concentration of pollutant, X (ppm)
$C_{X,M}$ = sample gas concentration of pollutant, X (ppm)
D = dilution factor for 1 m exhaust gas samples
EI = emission index, mass of pollutant emitted per gram of fuel burned (g kg^{-1})
ER = emission ratio, concentration of pollutant in the exhaust divided by exhaust gas CO_2 concentration (ppm ppm^{-1})
f = exhaust gas fraction in >15 m plume samples
F_{00} = engine rated thrust (kN)
MW_{CO_2} = molecular weight of CO_2 (g mol^{-1})
MW_X = molecular weight of pollutant, X (g mol^{-1})
NO_x = $NO+NO_2$
NO_Y = $NO+NO_2+HONO$
T = ambient temperature (K)
α = exponential fit parameter used in Eqs. (6)–(9) in conjunction with $\dot{m}$
β = exponential fit parameter used in Eqs. (6)–(9) in conjunction with π_{00}
γ = exponential fit parameter used in Eqs. (6)–(9) in conjunction with F_{00}
δ = exponential fit parameter used in Eq. (9) in conjunction with T
κ = prefactor fit parameter used in Eqs. (6)–(9)
π_{00} = engine pressure ratio

References

[1] Federal Aviation Administration, 2007, "FAA Aerospace Forecasts: Fiscal Years 2007-2020."

[2] Lighty, J. S., Veranth, J. M., and Sarofim, A. F., 2000, "Combustion Aerosols: Factors Governing Their Size and Composition and Implications to Human Health," J. Air Waste Manage. Assoc., **50**, pp. 1565–1618.

[3] Yang, C. Y., Wu, T. N., Wu, J. J., Ho, C. K., and Chang, P. Y., 2003, "Adverse Respiratory and Irritant Health Effects in Airport Workers in Taiwan," J. Toxicol. Environ. Health A, **66**, pp. 799–806.

[4] Unal, A., Hu, Y. T., Chang, M. E., Odman, M. T., and Russell, A. G., 2005, "Airport Related Emissions and Impacts on Air Quality: Application to the Atlanta International Airport," Atmos. Environ., **39**, pp. 5787–5798.

[5] Yu, K. N., Cheung, Y. P., Cheung, T., and Henry, R. C., 2004, "Identifying the Impact of Large Urban Airports on Local Air Quality by Nonparametric Regression," Atmos. Environ., **38**, pp. 4501–4507.

[6] Anderson, B. E., Branham, H. -S., Hudgins, C. H., Plant, J. V., Ballenthin, J. O., Miller, T. M., Viggiano, A. A., Blake, D. R., Boudries, H., Canagaratna, M., Miake-Lye, R. C., Onasch, T. B., Wormhoudt, J. C., Worsnop, D. R., Brunik, K. E., Culler, C., Penko, P., Sanders, T., Han, H.-S., Lee, P., Pui, D. Y. H, Thornhill K. L., and Winstead, E. L., 2005, "Experiment to Characterize Aircraft Volatile Aerosol and Trace-Species Emissions (EXCAVATE)," NASA Report No. NASA/TM-2005-213783.

[7] Anderson, B. E., Chen, G., and Blake, D. R., 2006, "Hydrocarbon Emissions From a Modern Commercial Airliner," Atmos. Environ., **40**, pp. 3601–3612.

[8] Miller, T. M., Ballenthin, J. O., Viggiano, A. A., Anderson, B. E., and Wey, C. C., 2005, "Mass Distribution and Concentrations of Negative Chemiions in the Exhaust of a Jet Engine: Sulfuric Acid Concentrations and Observation of Particle Growth," Atmos. Environ., **39**¸ pp. 3069–3079.

[9] Wey, C. C., Anderson, B. E., Hudgins, C., Wey, C., Li-Jones, X., Winstead, E., Thornhill, L. K., Lobo, P., Hagen, D., Whitefield, P., Yelvington, P. E., Herndon, S. C., Onasch, T. B., Miake-Lye, R. C., Wormhoudt, J. W., Knighton, B., Howard, R., Bryant, D., Corporan, E., Moses, C., Holve, D., Dodds, W., 2006, "Aircraft Particle Emissions eXperiment (APEX)," NASA Report No. NASA/TM-2006-214382.

[10] Wey, C. C., Anderson, B. E., Wey, C., Miake-Lye, R. C., Whitefield, P., and Howard, R., 2007, "Overview on the Aircraft Particle Emissions Experiment (APEX)," J. Propul. Power, **23**, pp. 898–905.

[11] Yelvington, P. E., Herndon, S. C., Wormhoudt, J. C., Jayne, J. T., Miake-Lye, R. C., Knighton, W. B., and Wey, C., 2007, "Chemical Speciation of Hydrocarbon Emissions From a Commercial Aircraft Engine," J. Propul. Power, **23**, pp. 912–918.

[12] Knighton, W. B., Rogers, T. M., Anderson, B. E., Herndon, S. C., Yelvington, P. E., and Miake-Lye, R. C., 2007, "Quantification of Aircraft Engine Hydrocarbon Emissions Using Proton Transfer Reaction Mass Spectrometry," J. Propul. Power, **23**, pp. 949–958.

[13] Wey, C., and Wey, C. C., 2006, "Aircraft Particle Emissions eXperiment (APEX)," Appendix, NASA Report No. NASA/TM-2006-214382.

[14] Wormhoudt, J., Herndon, S. C., Yelvington, P. E., Miake-Lye, R. C., and Wey, C., 2007, "Nitrogen Oxide (NO/NO2/HONO) Emissions Measurements in Aircraft Exhausts," J. Propul. Power, **23**, pp. 906–911.

[15] Petzold, A., Fiebig, M., Fritzsche, L., Stein, C., Schumann, U., Wilson, C. W., Hurley, C. D., Arnold, F., Katragkou, E., Baltensperger, U., Gysel, M., Nyeki, S., Hitzenberger, R., Giebl, H., Hughes, K. J., Kurtenbach, R., Wiesen, P., Madden, P., Puxbaum, H., Vrchoticky, S., and Wahl, C., 2005, "Particle Emissions From Aircraft Engines—A Survey of the European Project PartEmis," Meteorol. Z., **14**, pp. 465–476.

[16] Wilson, C. W., Petzold, A., Nyeki, S., Schumann, U., and Zellner, R., 2004, "Measurement and Prediction of Emissions of Aerosols and Gaseous Precursors From Gas Turbine Engines (PartEmis): An Overview," Aerosp. Sci. Technol., **8**, pp. 131–143.

[17] Nyeki, S., Gysel, E., Weingartner, U., Baltensperger, R., Hitzenberger, A., Petzold, A., and Wilson, C. W., 2004, "Properties of Jet Engine Combustion Particles During the PartEmis Experiment: Particle Size Spectra ($d>15$ nm) and Volatility," Geophys. Res. Lett., **31**, p. L18105.

[18] Herndon, S. C., Shorter, J. H., Zahnhiser, M. S., Nelson, D. D., Jayne, J., Miake-Lye, R. C., Waitz, I., Silva, P., Lanni, T., Demerjian, K., and Kolb, C. E., 2004, "NO and NO_2 Emission Ratios Measured From in-Use Commercial Aircraft During Taxi and Takeoff," Environ. Sci. Technol., **38**, pp. 6078–6084.

[19] Herndon, S. C., Onasch, T. B., Frank, B. P., Marr, L. C., Jayne, J. T., Canagaratna, M. R., Grygas, J., Lanni, T., Anderson, B. E., Worsnop, D., and Miake-Lye, R. C., 2005, "Particulate Emissions From in-Use Commercial Aircraft," Aerosol Sci. Technol., **39**, pp. 799–809.

[20] Herndon, S. C., Rogers, T., Dunlea, E. J., Jayne, J. T., Miake-Lye, R., and Knighton, B., 2006, "Hydrocarbon Emissions From in-Use Commercial Aircraft During Airport Operations," Environ. Sci. Technol., **40**, pp. 4406–4413.

[21] Herndon, S. C., Jayne, J. T., Lobo, P., Onasch, T. B., Fleming, G., Hagen, D. E., Whitefield, P. D., and Miake-Lye, R. C., 2008, "Commercial Aircraft Engine Emissions Characterization of in-Use Aircraft at Hartsfield-Jackson Atlanta International Airport," Environ. Sci. Technol., **42**, pp. 1877–1883.

[22] Herndon, S. C., Wood, E. C., Northway, M. J., Miake-Lye, R. C., Thornhill, L., Beyersdorf, A., Anderson, B. E., Dowlin, R., Dodds, W., and Knighton, W. B., 2009, "Aicraft Hydrocarbon Emissions at Oakland International Airport,"

Downloaded 02 Jun 2010 to 171.66.16.96. Redistribution subject to ASME license or copyright; see http://www.asme.org/terms/Terms_Use.cfm

Environ. Sci. Technol., **43**, pp. 1730–1736.
[23] International Civil Aviaton Organization (ICAO), 1995, "Engine Exhaust Emissions Data Bank," Montreal, Quebec, Canada, Document No. 9646-AN/943.
[24] Nelson, D. D., Zahniser, M. S., McManus, J. B., Kolb, C. E., and Jimenez, J. L., 1998, "A Tunable Diode Laser System for the Remote Sensing of on-Road Vehicle Emissions," Appl. Phys. B: Lasers Opt., **67**, pp. 433–441.
[25] Nelson, D. D., Shorter, J. H., McManus, J. B., and Zahniser, M. S., 2002, "Sub-Part-Per-Billion Detection of Nitric Oxide in Air Using a Thermoelectrically Cooled Mid-Infrared Quantum Cascade Laser Spectrometer," Appl. Phys. B: Lasers Opt., **75**, pp. 343–350.
[26] Society of Automotive Engineering, 1996, "Aerospace Recommended Practice," Paper No. ARP1533.
[27] Bevington, P. R., and Robinson, D. K., 1992, *Data Reduction and Error Analysis in the Physical Sciences*, 2nd ed., McGraw-Hill, New York.
[28] Hunderup, J. W., and Roby, R. J., 1996, "An Experimental Investigation of the Conversion of NO to NO_2 at High Pressure," ASME J. Eng. Gas Turbines Power, **118**, pp. 756–764.
[29] Wood, E. C., Herndon, S. C., Timko, M. T., Yelvington, P., and Miake-Lye, R., 2008, "Speciation and Chemical Evolution of Nitrogen Oxides in Aircraft Exhaust," Environ. Sci. Technol., **42**, pp. 1884–1891.
[30] Farias, F., and ApSimon, H., 2006, "Relative Contributions From Traffic and Aircraft NO_X Emissions to Exposure in West London," Environ. Modell. Software, **21**, pp. 477–485.
[31] Kado, N., Delao, A., Fruin, S., Garcia, C., Hughett, N., Luo, D., McDougal, E., Motallebi, N., Propper, R., Sahota, R., Shimer, D., Shimp, D., Takemoto, B., Dodge, D., Green, S., Kim, J., Ostro, B., Frampton, M. W., Forastiere, F., Peters, A., and Temple, P. J., 2006, "Review of the California Ambient Air Quality Standard for Nitrogen Dioxide," California Environmental Protection Agency. Available at: http://www.arb.ca.gov/research/aaqs/no2-rs/no2-rs.htm.
[32] Last, J. A., Sun, W.-M., and Witschi, H., 1994, "Ozone, NO, and NO_2: Oxidant Air Pollutants and More," Environ. Health Perspect., **102**, pp. 179–184.
[33] United States Environmental Protection Agency, 1993, "Air Quality Criteria for Oxides of Nitrogen," Document No. EPA/600/8-91/049aF.
[34] Spicer, C. W., Holdren, M. W., Smith, D. L., Hughes, D. P., and Smith, M. D., 1992, "Chemical Composition of Exhaust From Aircraft Turbine Engines," ASME J. Eng. Gas Turbines Power, **114**, pp. 111–117.
[35] Knighton, W. B., Herndon, S. C., Jayne, J. T., Miake-Lye, R. C., Northway, M., Onasch, T. B., Timko, M. T., and Wood, E. C., "Selected VOC Analysis of Jet Engine Exhaust by Proton Transfer Reaction Mass Spectrometry and Tunable Infrared Laser Differential Absorption Spectroscopy," to be published.
[36] Timko, M. T., Herndon, S. C., de la Rosa Blanco, E., Wood, E. C., Yu, Z., Miake-Lye, R. C., and Knighton, W. B., 2009, "Combustion Products of Jet Fuel, Fischer Tropsch Synthetic Fuel, and Biomass Jet Fuel for a Gas Turbine Engine," to be published.
[37] Dubois, D., and Paynter, G. C., 2006, "Fuel Flow Method 2 for Estimating Aircraft Emissions," SAE Technical Paper No. 2006-01-1987.
[38] Kerrebrock, J. L., 1992, *Aircraft Engines and Gas Turbines*, MIT, Cambridge, MA, Chap. 4.
[39] Lifbert, F. W., 1972, "Correlation of Gas Turbine Emissions Data," ASME Paper No. 72-GT-60.
[40] Yamamoto, T., Furuhata, T., Arai, N., and Gupta, A. K., 2002, "Prediction of NO_X Emissions From High-Temperature Gas Turbines: Numerical Simulation for Low-NO_X Combustion," JSME International, **45**, pp. 221–230.
[41] Lentini, D. D., 2003, "Prediction of NO_X Emissions of in Gas Turbine Combustors Inclusive of the NO_2 Contribution," Proc. Inst. Mech. Eng., Part A, **217**, pp. 83–90.
[42] Kerrebrock, J. L., 1975, "The Effect of Compression Ratio on NO_X Production by Gas Turbines," J. Aircr., **12**, pp. 752–753.
[43] Lefebvre, A. H., 1985, "Influence of Fuel Properties on Gas Turbine Combustion Performance," Paper No. AFWAL-TR-84-2104.

Downloaded 02 Jun 2010 to 171.66.16.96. Redistribution subject to ASME license or copyright; see http://www.asme.org/terms/Terms_Use.cfm

Michael T. Timko
Timothy B. Onasch
Megan J. Northway
John T. Jayne
Manjula R. Canagaratna
Scott C. Herndon
Ezra C. Wood
Richard C. Miake-Lye
Aerodyne Research Inc.,
45 Manning Road,
Billerica, MA 01821-3976

W. Berk Knighton
Department of Chemistry,
Montana State University,
P.O. Box 173400,
Bozeman, MT 59717-3400

Gas Turbine Engine Emissions—Part II: Chemical Properties of Particulate Matter

The characterization of volatile and nonvolatile particle materials present in gas turbine exhaust is critical for accurate estimation of the potential impacts of airport activities on local air quality, atmospheric processes, and climate change. Two field campaigns were performed to collect an extensive set of particle and gaseous emission data for on-wing gas turbine engines. The tests included CFM56, RB211-535E4-B, AE3007, PW4158, and CJ610 engines, providing the opportunity to compare emissions from a wide range of engine technologies. Here we report mass, number, composition, and size data for the nonvolatile (soot) and volatile particles present in engine exhaust. For all engines, soot emissions (EI_m-soot) are greater at climbout (85% power) and takeoff (100%) power than idle (4% or 7%) and approach (30%). At the engine exit plane, soot is the only type of particle detected. For exhaust sampled downwind (15–50 m) and diluted by ambient air, total particle number emissions (EI_n-total) increases by about one or two orders of magnitude relative to the engine exit plane, and the increase is driven by volatile particles that have freshly nucleated in the cooling exhaust gas both in the free atmosphere and in the extractive sample lines. Fuel sulfur content is the determining factor for nucleation of new particles in the cooling exhaust gases. Compositional analysis indicates that the volatile particles consist of sulfate and organic materials (EI_m-sulfate and EI_m-organic). We estimate a lower bound S[IV] to S[VI] conversion efficiency of (0.08 ± 0.01)%, independent of engine technology. Measurements of EI_m-organic ranged from about 0.1 mg kg^{-1} to 40 mg kg^{-1}. Lubrication oil was present in particles emitted by all engines and accounted for over 90% of the particulate organic mass under some conditions. The products of incomplete combustion are a likely source of the remaining volatile organic particle material. [DOI: 10.1115/1.4000132]

1 Introduction

The potential health and environmental impacts of aviation related emissions may become increasingly important as automobiles and other modes of transportation become cleaner and the use of air travel grows. Unlike most other anthropogenic particle material (PM) emission sources, the application of end-of-pipe treatments [1] (e.g., particle traps) is not a feasible emissions reduction strategy for aircraft engines. The effects of airport operations on local air quality [2]—and potentially the health of airport workers [3] and nearby residents—deserve special attention due to the steady increase in air travel and commensurate expansion of airports [4]. Likewise, the global environmental impacts of aviation are incompletely understood [5,6]. The International Civil Aviation Organization (ICAO) regulates gas turbine PM as the "smoke number," a metric devised to reduce plume visibility [7]. Smoke number fails to capture the physical, chemical, and optical properties of gas turbine particles that influence their potential impact on global climate change, local environment, and human health.

Two recent measurement campaigns to characterize the PM emitted from gas turbine engines have greatly advanced the state of understanding: (1) experiment to characterize aircraft volatile aerosol and trace-species emissions (EXCAVATE) [8–11] and (2) the first aircraft particle emission experiment (APEX-1) [12–19]. EXCAVATE and APEX-1 measurements included trace gas and PM emission measurements of on-wing gas turbine engines mounted to stationary aircraft that were run at power settings characteristic of normal airport operation [20,21]. Combustor studies [22–29], military engines tests [29–32], and flight studies [33–39] provide additional particle emission data for gas turbine engines.

Previous studies have focused on a narrow range of gas turbine engine technologies, many of which are representative of neither the modern civilian nor military fleets. Here, we report new measurements of total soot mass (EI_m-soot), total particle number (EI_n-total), and particle composition made during dedicated tests of 16 separate commercial gas turbine engines in two recent field campaigns: JETS/APEX-2 and APEX-3, henceforth referred to collectively as APEX-2/3. A primary objective of this paper is to identify which particle emission data trends are technology dependent and which are not. This paper is the second of a two-part series; the first paper [40] describes gas-phase emissions. The data presented in the two papers greatly increase the level of detail of the data sets available for use in local and global air quality models and provides guidelines for which emission performance parameters can be generalized for different engine technologies and which cannot. As a result, the enhanced emission data set provides a more complete characterization for understanding the environmental impacts of aviation on global climate change and local air quality than has been available previously.

2 Experimental Description

2.1 Experimental Setup. The first paper in this series [40] and a review of the APEX-1 campaign [41] provide detailed descriptions of the APEX-2/3 experimental setup; only the most pertinent details are provided here. We characterized the nonvolatile and volatile PM emissions of a total of 16 on-wing gas turbine engines (7 during JETS/APEX-2 and 9 during APEX-3) using a suite of trace gas and particle characterization instruments. Table

---

Contributed by the Combustion and Fuels Committee of ASME for publication in the JOURNAL OF ENGINEERING FOR GAS TURBINES AND POWER. Manuscript received April 13, 2009; final manuscript received July 7, 2009; published online March 19, 2010. Editor: Dilip R. Ballal.

Copyright © 2010 by ASME

Downloaded 02 Jun 2010 to 171.66.16.96. Redistribution subject to ASME license or copyright; see http://www.asme.org/terms/Terms_Use.cfm

Table 1 Engine, fuel, and engine test data[a]

Tail No.	Engine model	Thrust (kN)	T (K)	RH (%)	Sulfur[b] (ppm)	Aromatics[c,d] (vol %)	Sampling locations (m)	Notes
N435WN[e]	CFM56-7B22	100.97	286	93	130	19.6	stbd: 1, 30, 50 port: 1	Turbofan
N429WN[e]	CFM56-7B22	100.97	286	92	420	20.2	stbd: 1, 30, 50 port: 1(30%)	Turbofan
N695SW[e]	CFM56-3B1	89.41	285	93	350	22.7	stbd: 1, 30, 50 port: 1	Turbofan
N353SW[e]	CFM56-3B1	89.41	285	93	220	20.4	stbd: 1, 30, 50 port: 1	Turbofan
N14324[f]	CFM56-3B1	89.41	281	87	700	18	stbd: 1, 30	Turbofan
N70330[f]	CFM56-3B1	89.41	286	49	400	13.6	stbd: 1, 30	Turbofan
N75853[e]	RB211-535E4-B	191.7	290	78	300	21.8	stbd: 1, 30, 43	Three-spool turbofan
N74856[e]	RB211-535E4-B	191.7	283	68	300	20.3	stbd: 1, 30, 43	Three-spool turbofan
N729FD[f]	PW4158	258.0	292	69	600	16.2	stbd: 1, 30, 43	Turbofan
N11193[f]	AE3007A1E	37.16	286	47	300	20.7	stbd: 1, 15, 30 port: 1, 15, 30	Externally mixed turbofan
N16927[f]	AE3007A	33.73	282	67	200	19.4	stbd: 1, 15, 30	Externally mixed turbofan
N616N[f]	CJ6108A	13.1	291	45	0	14.2	stbd: 1, 15, 30	Turbojet

[a] Ambient pressure was always 760 ± 6 torr

[b] On a mass basis, as determined by ASTM method D5453 (JETS/APEX-2) and D4294 (APEX-3).

[c] As determined by ASTM method D5186 (JETS/APEX2) and D1319 (APEX-3).

[d] Distillation curve (ASTM D86) and density (ASTM D4052, JETS/APEX-2, and D1298, APEX-3) data available for all fuels.

[e] Additional fuel composition data available for JETS/APEX-2 only: polycyclic aromatic hydrocarbon content (ASTM D5186).

[f] Additional fuel composition data available for APEX-3 only: viscosity (ASTM D445), freezing point (ASTM D5972), flash point (ASTM D56), smoke point (ASTM D1322), heat of combustion (ASTM D3338), mercaptan sulfur (ASTM D3227), hydrogen content (ASTM D3343), naphthalene content (ASTM D1840), and olefin content (ASTM D1319).

1 provides descriptions of the engines and of the emission test conditions. The ICAO [7] landing/takeoff cycle guided the selection of idle (7%), approach (30%), climbout (85%), and takeoff (100%) power conditions. Several additional power settings (e.g., ground idle 4%, cruise 65%, and occasionally 15%) completed the test matrix. Obtaining data from stationary aircraft at takeoff conditions was not always possible, and we do not have takeoff data for all engines. For AE3007 engines, aircraft operators recommended testing at 8% power to simulate idle conditions more closely than the standard 7%.

PM laden exhaust gas samples were obtained both at the engine exit plane (nominally 1 m from the exit nozzle) and at specific locations in the evolving exhaust plume (15–50 m). At the engine exit plane, a series of individually addressed sample probes continuously extracted exhaust gas samples. Engine exit plane exhaust gas was immediately diluted with dry nitrogen by a factor of between 10 and 40 at the probe tip and conveyed to the instruments via roughly 30 m of 1.35 cm i.d. stainless steel tubing. Transport times between the engine exit plane and the instruments were on the order of 5–10 s.

Measurements of the downstream exhaust plumes were made to obtain data on the evolution of volatile PM in the cooling gas stream. Two specific downstream locations were selected for each engine based on the engine thrust and space constraints. Larger distances (30 m and 43 m or 50 m) were used for the higher thrust engines (RB211-535E4-B and PW4158), and shorter distances (15 m and 30 m) were used for the lower thrust engines (AE3007 and CJ6108A). For a given engine, no systematic statistically significant difference was observed between the samples obtained at the two downstream sampling locations and we accordingly averaged downstream data collected at the two sampling locations. Turbulent mixing with ambient air typically diluted the downstream exhaust plume samples by a factor of about 10–20 before reaching the sampling probes, though strong winds sometimes increased the dilution factor to as large as 100. No additional dilution was supplied in the downstream probes. Cross winds sometimes interfered with sampling at distances greater than 15 m, thus introducing some data gaps. In both campaigns, the downstream plume gases were conveyed to the instruments via approximately 40 m of 3.8 cm i.d. stainless steel tubing. Transport times between the >15 m extraction points and the instruments were on the order of 5–8 s.

2.2 Particle Line Loss. A fraction of the sampled exhaust particles are lost due to collisions with the walls of the tubing used to convey samples to the instruments. For a similar experimental system used during APEX-1 [41], particle line loss was estimated to be about 30% (i.e., 70% penetration) for particles ranging from 30 nm to 300 nm. For smaller particles, the line loss due to particle diffusion increases sharply and reaches a value of roughly 80% (i.e., 20% penetration) for 10 nm particles. The effects of particle shape and composition on line loss have yet to be characterized fully. Due to uncertainties in the line-loss estimates, we have elected not to apply a line-loss correction to the data presented here. For this reason, data dominated by small particles (e.g., the total number of particles) may be underestimated by as much as a factor of 5 or more. Mass based particle data, which are dominated by particles larger than 30 nm, are less effected by line loss than number based metrics and may be underestimated by about 30%—depending on the particle size distribution. Accurately estimating particle line loss is an area of continuing effort for all of the research teams involved with the APEX series of studies and was the subject of comprehensive tests held at NASA Glenn Research Center (GRC) in October 2006. We expect the results of the GRC study to be definitive, allowing accurate calculation of line-loss correction factors [42].

2.3 Instrumentation

2.3.1 General Description of Instruments. Table 2 lists the particle instruments deployed by our team during the APEX-2/3 campaigns. For particle characterization, we deployed a multi-

Downloaded 02 Jun 2010 to 171.66.16.96. Redistribution subject to ASME license or copyright; see http://www.asme.org/terms/Terms_Use.cfm

Table 2 Particle instruments deployed during aviation field campaigns (APEX-2/3)

Instrument	Species detected	Quantity measured	Detection specifications[a]	Time resolution
CPC[b]	Total particle number	EI_n-total	7 nm–2.5 μm $(0-1)\times 10^7\ \mathrm{m}^{-3}$	1 s
SMPS[c]	Size-resolved particle number	$dN/d\log D_p$ $dV/d\log D_p$	15–600 nm[f]	Full scan ~1 min
C-ToF-AMS[d]	Size-resolved particle mass and chemical speciation	$d\mathrm{EI}_m/d\log D$ composition, EI_m-organic, EI_m-sulfate	30 nm–800 nm[g] $>100\ \mathrm{ng\ m}^{-3}$	10 s
MAAP[e]	Back carbon mass	EI_m-soot	$>5\ \mu\mathrm{g/m}^3$	~1.5 s

[a] Detection limits defined for the specified time resolution.

[b] Condensation particle counter, model 3022A (TSI).

[c] Scanning mobility particle sizer, consisting of a differential mobility analyzer, model 3080 (TSI), and condensation particle counter, model 3022A (TSI).

[d] Time-of-flight aerosol mass spectrometer (ARI) with a time-of-flight spectrometer in the "C" configuration.

[e] Multi-angle absorption photometer (Thermo) [43,44].

[f] The SMPS registers particle size as mobility diameter D_M, defined as the diameter of a spherical particle with the same velocity as the particle of interest as measured in a constant electric field.

[g] The C-ToF-AMS measures particle size as the vacuum aerodynamic diameter D_{VA}, defined as the diameter of a sphere with standard density that settles at the same terminal velocity as the particle of interest.

angle absorption photometer (MAAP) (mass of black carbon soot) [43,44], a scanning mobility particle sizer (SMPS) (particle size distribution), a condensation particle counter (CPC) (total particle number density), and an aerosol mass spectrometer (AMS) (size resolved particle composition) [45–47] equipped with a compact time-of-flight (C-ToF) mass spectrometer detector.

The small-size cut-offs for each instrument are especially important for quantitative interpretation of the PM data. The particle counting detector (CPC) is rated for detection of the smallest particles (~7 nm). The size distribution instrument (SMPS) was operated for detection of particles larger than 15 nm. The C-ToF-AMS detects nearly 100% of the 100 nm particles, 50% of the 80 nm particles, and 5% of the 30 nm particles [48–50]. The MAAP soot measurement is sensitive to soot mass and its precise transmission window for particles smaller than 20 nm is poorly defined. Because the different size cut-offs for the different instruments can be of critical importance, we describe how the size cut-off affects quantitative interpretation in more detail where appropriate.

The MAAP, CPC, and SMPS are all commercially available equipment and are not described in further detail here. Our interpretation of SMPS data, which is consistent with Onasch et al. [14], requires some description as does the C-ToF-AMS. Focusing first on the SMPS data, Fig. 1 provides representative size distribution data gathered during the emissions tests for a CFM56-7B22 engine operating at 65% power. The volume-weighted data in Fig. 1 have been plotted on a log-normal horizontal axis and after division by the logarithm of the particle size distribution bin size—hence the units of $d(\text{volume})/d\log Dp$. The data collected from both 1 m and 50 m exhaust gas samples are shown for comparison. In both size distributions, a clear peak is visible at approximately 90 nm. We assign the 90 nm feature to soot particles. In the 50 m sample, a second peak at apparently 20 nm is present. We assign the 20 nm feature to particles that have been formed via nucleation and condensational growth. The actual peak diameter for nucleation/growth mode particles is likely to be smaller than 20 nm; incomplete penetration of <50 nm particles and the SMPS size cut-off (15 nm) result in the apparent 20 nm peak. Noise at larger diameters is due to entrainment of ambient particles in the exhaust gas.

2.3.2 *Aerosol Mass Spectrometer*.

The C-ToF-AMS provides size-resolved particle composition data for volatile PM (e.g., organic material, sulfuric acid, etc.) [45–52]. The C-ToF-AMS first sorts particles based on their vacuum aerodynamic diameter D_{VA} [53,54], and then quantifies the composition by mass spectrometry. The inlet to the AMS consists of a critical orifice and aerodynamic lens [48–50], which achieve 10^7-fold concentrating of particles relative to gas-phase species and focuses the particles into a narrow beam. The mass/charge (m/z) resolution of the C-ToF-AMS, defined by the ratio $m/\Delta m$, is about 400 at $m/z=30$ and 800 at $m/z=180$ [47]. The C-ToF-AMS differentiates between species based on their characteristic mass-to-charge ratios (m/z). Observed mass spectra in the AMS are converted into speciated mass concentrations according to the algorithm described by Allan et al. [52].

Electronic noise from an unknown source at the Oakland Airport introduced uncertainty into the JETS/APEX-2 data set. Dur-

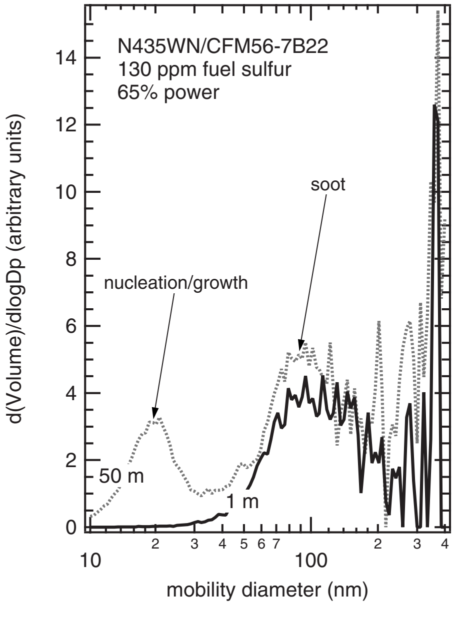

Fig. 1 Representative scanning mobility particle sizer (SMPS) data obtained during testing of a CFM56-7B22 engine (65% power). Data from samples collected at both 1 and 50 m are shown.

Downloaded 02 Jun 2010 to 171.66.16.96. Redistribution subject to ASME license or copyright; see http://www.asme.org/terms/Terms_Use.cfm

ing the APEX-3 campaign, great care was taken to shield the instrument using standard grounding techniques, and the noise was reduced to the point that low-threshold operation was possible. Careful comparison of the JETS/APEX-2 AMS data set with that obtained during earlier campaigns [11,14] and APEX-3 suggests that most sulfate measurements are low by about 10–20% while the JETS/APEX-2 organic loadings are systematically low by about 20–40%. The qualitative implications of the JETS/APEX-2 underestimation are discussed later in the text when the results are presented.

2.4 Data Handling

2.4.1 Emission Indices. In this report, all PM data are recorded as emission indices (mass or number of pollutant, X, emitted per mass fuel consumed—EI). The definition of EI is

$$\mathrm{EI}\ X\left[\frac{\mathrm{g\ \ or\ \ \#}X}{\mathrm{kg\ \ fuel}}\right]=\frac{\Delta M_X}{\Delta C_{\mathrm{CO}_2}}\frac{T}{P}(0.06236)\left[\frac{1}{44.01}\right](3160) \qquad (1)$$

where ΔC_{CO_2} is the difference between the measured exhaust gas CO_2 concentration and the ambient CO_2 concentration (in ppm), ΔM_X is the difference between the concentration of particles in the exhaust gas and that in the dilution or ambient gas (in $\mu\mathrm{g\ m}^{-3}$ for mass EIs, EI_m, or particle number m^{-3} for number EIs, EI_n), T and P are the sample temperature and pressure in K and torr, the factor of $0.06236\ \ \mathrm{m}^3\ \mathrm{torr\ K}^{-1}\ \mathrm{mol}^{-1}$ is a unit conversion based on ideal gas behavior, $44.01\ \ \mathrm{g\ mol}^{-1}$ is the molecular weight of carbon dioxide, and 3160 ($\mathrm{g\ \ CO}_2/\mathrm{kg\ \ fuel}$) is the emission index of carbon dioxide based on a C/H ratio of 1.9 and ignoring combustion inefficiencies. More details are provided in the companion to this report [40] and a previous publication [55].

Experimental uncertainties were estimated in two ways. In the first method, the uncertainty was set equal to the standard deviation of all available data points measured at a given set of conditions (i.e., downstream distance, engine setting, etc.). The number of replicate points was typically between 3 and 6. In the second, the uncertainties in each of the experimental quantities in Eq. (1) were propagated as a Taylor series expansion following the standard method [56]. The uncertainty based on the sample standard deviation was typically the larger of these two estimates of the uncertainty; in all cases, we report the larger of these two uncertainty estimates.

2.4.2 Ambient Background. At the engine exit plane, nitrogen dilution was used for exhaust gas samples and ΔC_{CO_2} and ΔM_X in Eq. (1) are simply equal to their measured values. For samples diluted by ambient air (i.e., samples obtained at $\geq 15\ \ \mathrm{m}$ from the engine exit plane), ΔC_{CO_2} and ΔM_X are defined relative to their ambient backgrounds. The measurements of ambient air before and after each engine test were used to calculated ΔC_{CO_2} and ΔM_X for downstream exhaust samples. In general, ambient levels of particle number density and soot particle mass were much smaller ($<10\%$) than their exhaust gas concentrations. Ambient CO_2 ranged from 380 ppm to 420 ppm during the tests. Uncertainty and intra-test variability in these values introduce no more than 5% error into the experimental data.

To improve the accuracy of the ambient background corrections to PM sulfate and PM organic, we used the fact that the mass weighted diameters of ambient organic and sulfate particles are typically larger than about 300 nm while aviation exhaust PM is generally smaller than 300 nm. Based on this observation and consistent with APEX-1 measurements [14], we divided the size resolved composition data into three size bins based on vacuum aerodynamic diameter [14,53,54]: <50 nm (referred to as nucleation/growth mode), 50–300 nm (referred to as the soot condensation mode, or simply the soot mode for short), and 300–1000 nm (referred to as the ambient mode). We applied size distribution weighting factors to full measured values of EI_m-organic and EI_m-sulfate and treated each bin as a separate species using the following expression:

$$\mathrm{EI}_m X,\mathrm{nucleation}=\frac{\int_{10}^{50}M_X(D_{\mathrm{va}})dD_{\mathrm{va}}}{\int_{10}^{1000}M_X(D_{\mathrm{va}})dD_{\mathrm{va}}}(\mathrm{EI}_m X,\mathrm{total}) \qquad (2a)$$

and

$$\mathrm{EI}_m X,\mathrm{soot}=\frac{\int_{50}^{300}M_X(D_{\mathrm{va}})dD_{\mathrm{va}}}{\int_{10}^{1000}M_X(D_{\mathrm{va}})dD_{\mathrm{va}}}(\mathrm{EI}_m X,\mathrm{total}) \qquad (2b)$$

where M_X is the size-resolved mass of particle species X (either organic or sulfate), in units of $\mu\mathrm{g\ m}^{-3}\ \mathrm{nm}^{-1}$. In practice, we measured $\mathrm{EI}_m X$,total using the AMS mass spectral mode and extract the integrands from particle time-of-flight data. In general, we report EI_m-organic and EI_m-sulfate as the sum of the first two size bins (nucleation/growth and soot coating), except in several specific cases that we highlight. Based on careful analysis of the contribution of various ambient aerosols to calculated EIs, we estimate that the uncertainty introduced by improper background subtraction in downstream measurements of EI_m-sulfate and EI_m-organic is about 20% at most.

2.5 Summary of Experiments. During the APEX-2/3 studies, we collected a total of 582 stable data points, where each stable data point is characterized by the engine and sampling location (1 m, 15 m, 30 m, 43 m, or 50 m), and roughly 200 engine power transitions. Engine stability was evaluated using feedback from the technicians operating the aircraft and from the real-time emission data streams themselves. Gas turbine PM emissions can be described as either nonvolatile (i.e., particles present at the elevated temperatures of the engine exit plane) or volatile (i.e., particle mass initially present in the gas phase, which later converts to the particle phase during exhaust gas cooling). Following this distinction, we divided the description of results into two sections that focus on (1) nonvolatile PM emissions, including particle mass and engine exit plane particle number; and (2) volatile PM emissions based primarily on analysis of samples extracted $>15\ \ \mathrm{m}$ from the diluting exhaust plume.

3 Nonvolatile Particle Characteristics: Mass and Number

3.1 General Description of Nonvolatile Particle Data. We characterized nonvolatile PM emissions by both their mass and number. Table 3 contains EI_n-total measured only at the engine exit plane and EI_m-soot averaged over all probe distances while the engines were operating at idle (7%), approach (30%), and climbout (85%) conditions. The blanks in Table 3 indicate that the experiment was not conducted, and "ND" denotes that the concentration was below instrument detection limits.

3.2 Nonvolatile Soot Mass Emissions. Soot is the primary form of nonvolatile PM emitted by gas turbine engines that we have been able to identify. To the best of our ability to measure particle mass, we find that EI_m-nonvolatile equals EI_m-soot. By definition, the emission index of nonvolatile PM mass should not vary as the exhaust gases cool and dilute with ambient air, and within the limits of experimental uncertainty ($\pm 20\%$) the APEX-2/3 measurements are consistent with this expectation. Here, we report EI_m-soot averaged over all available data points, including both engine-exit-plane and downstream measurements. Quantitatively, EI_m-soot varies over a wide range from below instrument detection limits ($<1\ \ \mathrm{mg\ kg}^{-1}$) to $800\ \ \mathrm{mg\ kg}^{-1}$ (RB211-535E4-B at 65% thrust, data not presented in Table 3).

3.2.1 Analysis of Engine Technology Dependent EI_m*-Soot Variability*. Comparisons of EI_m-soot provide a good test case to identify particle emission trends that are technology driven. Figure 2 plots EI_m-soot as a function of power for the various engine

Downloaded 02 Jun 2010 to 171.66.16.96. Redistribution subject to ASME license or copyright; see http://www.asme.org/terms/Terms_Use.cfm

Table 3 Nonvolatile PM EIs measured for three power conditions during APEX-2/3

Engine model/tail No.	Engine location[a]	EI_m-soot[b] $(\mathrm{mg\ kg^{-1}})$ 7%	30%	85%	EI_n-total[c] $(\mathrm{x10^{13}\ kg^{-1}})$ (1 m downstream) 7%	30%	85%
CFM56-3B1/N353SW	stbd	3 ± 2	5 ± 3	140 ± 20	8.3 ± 3.3	10 ± 4	80 ± 8
	port	2 ± 1	ND[d]		7.6 ± 2.5	8.2 ± 1.7	
CFM56-3B1/N14324	stbd	16 ± 4	18 ± 2	320 ± 50	55 ± 14	35 ± 7	230 ± 20
CFM56-3B1/N70330	stbd	19 ± 4	13 ± 3	300 ± 100	60 ± 5	34 ± 2	84 ± 6
CFM56-3B1/N695SW	stbd	14 ± 3	15 ± 4	360 ± 40	16 ± 2	18 ± 6	94 ± 6
	port	4 ± 2	6 ± 2				
CFM56-7B22/N435WN	stbd	ND	2 ± 1	80 ± 20	2.5 ± 0.6	4.4 ± 1.2	16 ± 1
	port	ND	1.4 ± 0.6		1.5 ± 0.4	2.2 ± 0.2	
CFM56-7B22/N429WN	stbd	0.7 ± 0.5	1.4 ± 0.6	68 ± 8	2.7 ± 0.8	2.9 ± 0.2	17 ± 1
	port					3 ± 0.1	
RB211-535E4-B/N75853	stbd	60 ± 20	140 ± 30	480 ± 60	34 ± 1	140 ± 70	60 ± 20
RB211-535E4-B/N74856	stbd	40 ± 20	90 ± 7	540 ± 20	37 ± 5	54 ± 10	90 ± 2
PW4158[e]/N729FD	stbd	80 ± 20	13 ± 5	220 ± 20	95 ± 7	16 ± 3	130 ± 40
AE3007-A1E[f]/N11193	stbd	40 ± 10	27 ± 3	50 ± 20	130 ± 10	60 ± 5	43 ± 2
	port	47 ± 5[f]	25 ± 2	110 ± 20	170 ± 10	55 ± 3	58 ± 3
AE3007-A[f]/N16927	stbd	54 ± 4	37 ± 2	88 ± 8	90 ± 6	50 ± 4	50 ± 1
CJ6108A[f]/N616NA	stbd	32 ± 6[e]	94 ± 20	290 ± 90	230 ± 60	350 ± 60	260 ± 2

[a] Engine location is either port side (or "engine No. 1") or starboard side (or "engine No. 2"), abbreviated as stbd.

[b] EI_m-soot data are averaged over all available sampling locations (1 m, 15 m, 30 m, 43 m, and 50 m downstream of the engine exit plane, as applicable).

[c] All EI_n-total measurements made at 1 m from the engine exit plane.

[d] ND indicates species concentration less than the detection limits of the instrument. The blank spaces indicate missing data.

[e] The 85% thrust condition was not studied for this engine—data measured at 80% thrust.

[f] The 7% thrust setting was not studied for this engine—data measured at 8% rated thrust.

types studied during APEX-2/3. Error bars have been eliminated from Fig. 2 to improve readability, and Table 3 provides our best estimates of measurement uncertainty. To ease interpretation, the data in Fig. 2 are averaged over all available engines of a particular type (e.g., CFM56-7B22). The AE3007A and A3007-A1E engines are treated as one technology category in Fig. 2 as they did not differ significantly from one another with respect to EI_m-soot. Because EI_m-soot for the CFM56-3B1 and RB211-535E4-B engines is greater than for the other engine types, we plot EI_m-soot data for these two engine types on a separate vertical axis.

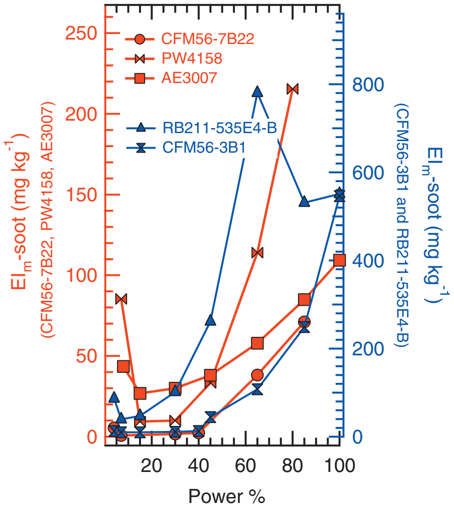

Fig. 2 Comparison of EI_m-soot for the major engine technologies. A separate vertical axis was used to plot EI_m-soot for the RB11-535E4-B so that the low power qualitative trends for the different engine types would be more easily distinguishable. For each engine type depicted, all available data points were averaged.

For all engines we have studied, EI_m-soot is greater at climbout (85%) and takeoff (100%) than at idle (4% or 7%) and approach (30%). Figure 2 shows several different examples of technology dependent trends between EI_m-soot and power. For example, above 7% power, the EI_m-soot for the CFM56 engines increases more or less monotonically with increasing engine power. In contrast, the RB211-535E4-B engines pass through a maximum at 65% power. The PW4158 and AE3007 series engines have greater EI_m-soot at idle/ground idle (4% or 7% rated thrust) than at approach (30% rated thrust).

Quantitative EI_m-soot differences are also apparent between different engine types, and the variation seems to be technology driven. Due to the availability of data, 65% power provides the best comparison point. At 65% power, EI_m-soot ranges 20-fold, from 35 $\mathrm{mg\ kg^{-1}}$ (AE3007) to 800 $\mathrm{mg\ kg^{-1}}$ (RB211-535E4-B). When comparing EI_m-soot for different engine technologies, data variability does not correspond to variations in the measured fuel flow rates as do some trace gas EIs, including acetaldehyde and CO [40]. Different fuel compositions may provide a plausible alternative explanation for some of the variability in EI_m-soot that we have attributed to engine technology differences. Many correlations have been suggested to relate fuel properties to soot production [57–59]. Table 1 contains some pertinent fuel composition data; however, we do not find a strong correlation between EI_m-soot and any of the data listed in Table 1. Additional fuel property data are available for subsets of the engines. For instance, we have smoke point data, olefin content, and naphthalenic content for the APEX-3 engines. For APEX-2 engines, we have polycyclic aromatic content fuel data. No correlations existed between EI_m-soot and any of these secondary fuel properties. EI_m-soot variability between different technology types is likely driven by combustor design differences but engine service life differences, unknown experimental differences, or fuel properties that we did not measure for the APEX-2/3 fuels may also contribute some variability. We note that the dynamic ranges of most of

Downloaded 02 Jun 2010 to 171.66.16.96. Redistribution subject to ASME license or copyright; see http://www.asme.org/terms/Terms_Use.cfm

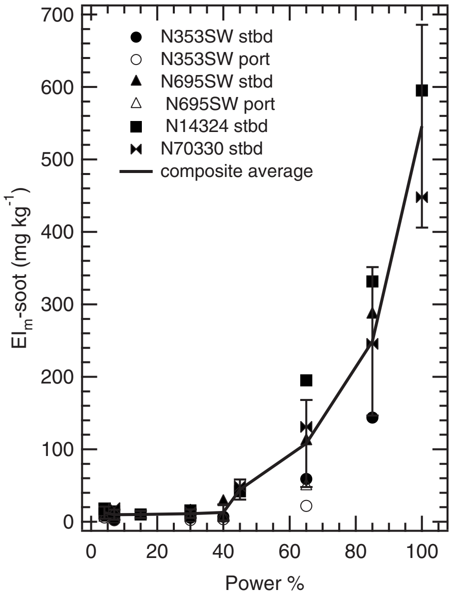

Fig. 3 Comparison of EI_m-soot for just the CFM56-3B1 engines. The composite average for all CFM56-3B1 engines is shown for comparison and to guide the eyes.

the measured fuel properties were less than 25%. More dramatic fuel variations might lead to measurable differences in EI_m-soot.

3.2.2 Analysis of CFM56 EI_m*-Soot Variability*. The APEX-2/3 data set contains more examples of CFM56 engines than any other engine type, thus encouraging a quantitative comparison of the EI_m-soot data for this engine type. Two distinct CFM56 combustor types were studied in APEX-2/3: an "older" technology -3B1 and a more "modern" -7B22. For both categories of CFM56 engines, EI_m-soot increases monotonically with engine power (see Table 3 and Fig. 2) above 7%. Quantitatively, the average (40 mg kg^{-1} for three engines, 65% power) EI_m-soot for the CFM56-7B22 engines is at most 50% the average (100 mg kg^{-1} for six engines, 65% power) EI_m-soot for CFM56-3B1 engines, consistent with the observations of Petzold et al. [27] for a combustor operating under "old" and "new" conditions. Beyond this general designation of technology "age," the ICAO databank [7] provides no specific engine differences that might be expected to lead to substantial differences in EI_m-soot. The -7B22 engine has a slightly higher thrust rating (101 kN versus 89.41 kN), bypass ratio (5.3 versus 5.1), and pressure ratio (24.41 versus 22.44) than the -3B1 engine; however, none of these differences would appear to be significant enough to account for the substantial differences in EI_m-soot that we observe.

Figure 3 plots the EI_m-soot data for the six CFM56-3B1 engines where the composite average EI_m-soot of all six CFM56-3B1 engines has been shown as a reference. The qualitative trend with respect to power is similar for all six CFM56-3B1 engines—increasing EI_m-soot with increasing engine power. Quantitatively, the engine-to-engine CFM56-3B1 soot data exhibit some variability, but less than the engine-type-to-engine-type EI_m-soot variability shown in Fig. 2. EI_m-soot for idling CFM56-3B1 engines varies by about a factor of 5 and falls into two categories. Three of the CFM56-3B1 engines (N14324, N70330, and starboard N695SW) have EI_m-soot in the 15–20 mg kg^{-1} range, while the value for the other three CFM56-3B1 engines (port and starboard engines of N695SW and the port engine of N695SW) is less than 5 mg kg^{-1}. The range in CFM56 EI_m-soot is about a factor of 2 at 85% power and a factor of 6 at 65% power. Plotting EI_m-soot as a function of fuel flow rate (not shown) does not remove engine-to-engine variability for the CFM56-3B1 class of engines, even though plotting against fuel flow rate removed apparent test-to-test variability in a EI_m-soot data set generated from a study of two CFM56-2C1 engines [14]. The underlying source of EI_m-soot variability for CFM56-3B1 engines—experimental error, engine maintenance history, etc.—is not known; plotting against measured fuel property data did not reveal any correlations. Thus, Fig. 2 indicates that engine technology differences account for some of the EI_m-soot variation, while Fig. 3 indicates that engine technology independent factors may also play an important role. Regardless of the underlying mechanism, accurate calculations of airport emission budgets and their respective uncertainties may need to account for the observed EI_m-soot variability.

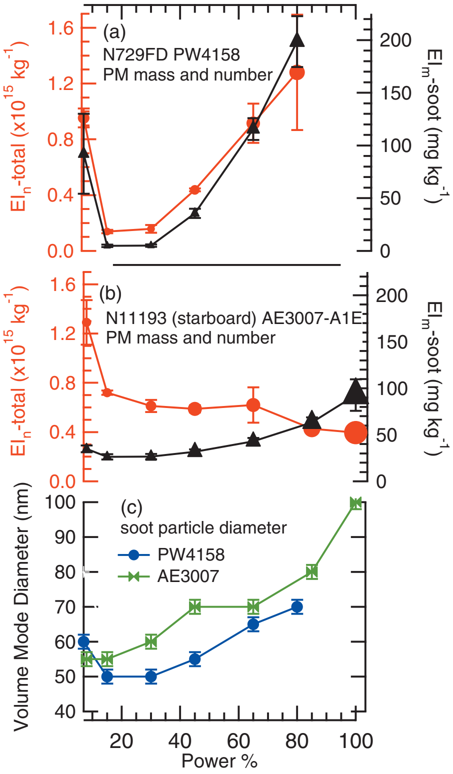

Fig. 4 EI_n-total (measured at 1 m) and EI_m-soot (averaged over all available sampling locations) for an (*a*) AE3007-A1E and an (*b*) PW4158 engine. Panel (*c*) shows volume weighted peak diameters for the SMPS particle size distributions measured at 1 m.

As part of the engine test study, we collected trace gas data [40], which we consulted to help interpret engine-to-engine variability in EI_m-soot. We focused our analysis on the two classes of CFM56 engines (-3B1 and -7B22). Timko et al. [40] found that plotting EI_m-NO_X against fuel flow rate reduced apparent engine-to-engine variability; however, fuel flow rate did nothing to collapse engine-type-to-engine-type EI_m-NO_X variability. Plotting hydrocarbon emission indices against fuel flow rate reduced both engine-to-engine and engine-technology-to-engine-technology variability [40]. In contrast to EI_m-NO_X and EI_m-HC, plotting EI_m-soot against fuel flow rate (not shown) did nothing to collapse soot variability. We conclude that EI_m-soot is inherently more variable than the trace gas EIs, but cannot identify the source of the greater uncertainty.

3.3 Nonvolatile Particle Number Emissions. The APEX-2/3 data indicate that dilution by dry nitrogen at the engine exit plane suppresses new particle formation. The 1 m exhaust plane particle size data plotted in Fig. 1 show only soot mode particles, an observation characteristic of the entire 1 m data set. As a result, we assert that EI_n-total $\approx$ EI_n-nonvolatile for engine exit plane samples. Figure 4(*a*) shows that EI_n-total varies directly with

Downloaded 02 Jun 2010 to 171.66.16.96. Redistribution subject to ASME license or copyright; see http://www.asme.org/terms/Terms_Use.cfm

Table 4 Volatile PM EIs[a] measured for three power conditions during APEX-2/3

		EI_n-total ($x10^{15}$ kg^{-1})			EI_m-organic[b] (mg kg^{-1})			EI_m-sulfate (mg kg^{-1})		
Engine model/combustor model		7%	30%	85%	7%	30%	85%	7%	30%	85%
CFM56-3B1 (A)/N353SW (220)	stbd	9.2 ± 2.6	6.8 ± 1.8	1.11 ± 0.09	0.4 ± 0.2	0.2 ± 0.1	1.4 ± 0.1	ND[c]	ND	0.3 ± 0.1
	port[f]									
CFM56-B1 (B)/N14324 (700)	stbd	sat[g]	sat	8.1 ± 0.6	1.3 ± 0.7	0.4 ± 0.3	1.8 ± 0.3	0.22 ± 0.08	0.21 ± 0.08	2.0 ± 0.3
CFM56-3B1 (C)/N70330 (400)	stbd	5 ± 1	15 ± 8	12 ± 1.0	ND	ND	2.1 ± 0.3	ND	ND	0.7 ± 0.1
CFM56-3B1 (D)/N695SW (350)	stbd	14 ± 3	8 ± 2	2.1 ± 0.2	0.6 ± 0.3	0.2 ± 0.1	1.3 ± 0.1	0.14 ± 0.07	ND	0.6 ± 0.05
	port[f]									
CFM56-7B22 (A)/N435WN (130)	stbd	4 ± 2	3 ± 2	0.53 ± 0.08	0.3 ± 0.1	0.2 ± 0.1	0.5 ± 0.2	ND	ND	0.02 ± 0.004
	port[f]									
CFM56-7B22 (B)/N429WN (420)	stbd	14 ± 2	9 ± 1	3.2 ± 0.1	0.4 ± 0.1	0.3 ± 0.1	0.5 ± 0.05	0.13 ± 0.03	0.07 ± 0.03	0.25 ± 0.04
RB211-535E4-B (A)/N75853 (300)	stbd	10 ± 7	5 ± 4	2.4 ± 0.2	10 ± 2	18 ± 2	20 ± 1	ND	ND	0.8 ± 0.2
					(22 ± 5)	(30 ± 3)	(28 ± 1)			
RB211-535E4-B (B)/N74856 (300)	stbd	1.3 ± 0.5	0.8 ± 0.2	0.7 ± 0.1	10 ± 4	25 ± 4	24 ± 1	ND	ND	0.7 ± 0.1
					(27 ± 4)	(38 ± 4)	(33 ± 2)			
PW4158[d]/N729FD (600)	stbd	28 ± 5	1.3 ± 0.8	1.8 ± 0.3	2 ± 1	ND	0.6 ± 0.2	0.7 ± 0.5	0.4 ± 0.2	0.7 ± 0.1
AE3007-A1E[e]/N11193 (300)	stbd		1.0 ± 0.3	0.7 ± 0.1	2 ± 1	1.7 ± 1.2	1.6 ± 0.8	ND	ND	
	port			0.77 ± 0.07	ND	ND	2 ± 1	ND	ND	
AE3007-A[e]/N16927 (200)	stbd	9 ± 2	2 ± 1	1.2 ± 0.4	1.1 ± 0.6	1.2 ± 1	0.9 ± 0.4	ND	ND	0.5 ± 0.2
CJ6108A[e]/N616NA (~0)	stbd	16 ± 13	11 ± 3	4.8 ± 0.2	4 ± 1	1.6 ± 0.5	2 ± 1	ND	0.3 ± 0.1	0.34 ± 0.06

[a] All measurements made at locations further than 1 m downstream of the engine exit plane (with exceptions noted below).

[b] Particulate organic material (10–300 nm diameter) as measured by the AMS—except for paranthetical values which include 10-1000 nm diameter PM mass. Section 2.4.2 describes the procedure used for extracting EIs from AMS data.

[c] ND indicates species concentration less than the detection limits of the instrument. Blank spaces indicate missing data. See Sec. 2.3.2 for a discussion of the operation AMS during JETS/APEX-2.

[d] The 85% thrust condition was not studied for this engine—data measured at 80% thrust.

[e] The 7% thrust setting was not studied for this engine—data measured at 8.4% rated thrust.

[f] Measurement made only at 1 m upstream location.

[g] Measurement exceeded capacity of CPC, sat indicates sample saturation.

EI_m-soot—as would be expected if the particles were primarily nonvolatile and since the particle sizes were relatively invariant with engine power for this engine. Engine exit plane particle size distributions show evidence only for soot particles with volume-weighted diameters ranging from 30 nm to 50 nm at idle to 70–150 nm at climbout. Without exception, volume-weighted modes peaking at less than 20 nm are never observed in the APEX-2/3 engine exit plane size distribution data. We cannot rule out the presence of nucleation mode particles in engine exit plane samples, but if present their diameters must be smaller than the lower size cut-offs than particle-size distribution SMPS or particle density CPC instruments (~15 nm and ~7 nm, respectively).

The direct, positive relationship between EI_m-soot and EI_n-total shown in Fig. 4(*a*) is representative of all engine exit plane exhaust data in the APEX-2/3 data set except for the AE3007s—and to a lesser extent the CJ6108A (data not shown). As shown in Fig. 4(*b*) for a representative AE3007 engine, EI_m-soot and EI_n-total vary inversely for power >20%. The data in Table 3 show a minimum in EI_n-total for the CJ6108A at 30% power (ICAO approach), even though EI_m-soot increases monotonically with increasing power. We suspect that the critical difference between the engines is the size of soot particles they produce at different powers. In Fig. 4(*c*) we plot volume weighted peak diameters for the PW4158 and AE3007 engines. All data presented in Fig. 4(*c*) were extracted from particle size distributions measured by the SMPS for exhaust samples withdrawn at 1 m from the engine exit plane—as shown in Fig. 1 and further described by Onasch et al. [14]. The AE3007 particle size varies more strongly with engine thrust than the PW4158, which allows EI_n-total to decrease with increasing power, even as EI_m-soot increases. By comparison, the PW4158 particles are relatively constant in size with respect to power; increasing EI_m-soot implies an increase in EI_n-total for the PW4158 engine.

4 Volatile Particle Characterization: Mass, Composition, and Number

4.1 General Description of Volatile Particle Emission Data. Our analysis of particle number, soot mass, and particle size data suggests that gas-to-particle conversion of volatile material does not contribute significantly to particle characteristics for exhaust gas samples extracted at the engine exit plane. Particle mass measurements of volatile PM provide further evidence that gas-to-particle conversion is suppressed in the 1 m sample extraction probe. We have two metrics of volatile particle mass, each measured by the aerosol mass spectrometer: EI_m-sulfate and EI_m-organic. In general, EI_m-sulfate is just at or below detection limits (<0.05 mg kg^{-1} for a CO_2 concentration of 2000 ppm) in the 1 m samples. EI_m-organic is generally greater than EI_m-sulfate at the engine exit plane, ranging from below detection limits (<0.1 mg kg^{-1} for a CO_2 concentration of 2000 ppm) to about 2 mg kg^{-1} for the RB211-535E4-B engines. When engine exit plane samples contain volatile PM, it seems to be a coating on the soot particles as EI_m-sulfate and EI_m-organic increase as EI_m-soot increases. EI_m-sulfate for the AE3007 engines are the only outliers, as EI_m-sulfate decreases as EI_m-soot increases. Forced internal mixing in the AE3007 engines apparently leads to entrainment of ambient sulfate in the exhaust at the engine exit plane consistent with their unusual EI_m-sulfate behavior.

Table 4 reports three volatile PM measurements made at >15 m: EI_m-organic, EI_m-sulfate, and EI_n-total. Reported values of EI_m-organic and EI_m-sulfate are restricted to the 10–300 nm size bin characteristic of nucleation/growth particles and soot coatings. In fact, the restricted 10–300 nm size range underestimates EI_m-organic for RB211-535E4-B engines by about a factor of 2, as these engines emitted a substantial amount of mass in the form of particles that were greater than 300 nm. Parenthetical

Downloaded 02 Jun 2010 to 171.66.16.96. Redistribution subject to ASME license or copyright; see http://www.asme.org/terms/Terms_Use.cfm

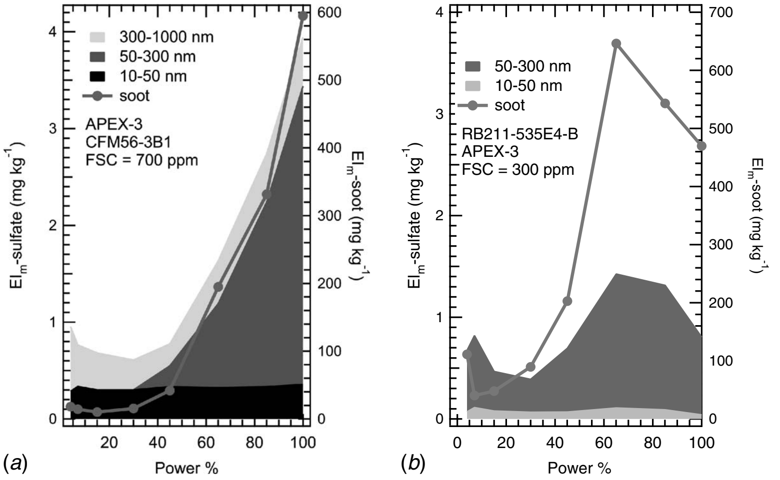

Fig. 5 EI_m-sulfate (30/43 m sampling probe) for two engines: (*a*) N14324 and CFM56-3B1, and (*b*) N74856 and RB211-535E4-B. Size-resolution data were used to apportion the organic PM mass to the nucleation/growth mode (10–50 nm), a soot condensation mode (50–300 nm), and an ambient mode (300–1000 nm)

values provided for the RB211-535E4-B engines reflect total EI_m-organic with no attempt to size-bin the data. The remainder of this section describes in turn EI_m-organic, EI_m-sulfate, and EI_n-total (>15 m).

4.2 PM Sulfate Emissions

4.2.1 Accuracy and Reproducibility of PM Sulfate Data. We find that sulfate and organic materials are the primary volatile species present in gas turbine PM. Fuel sulfur compounds contained in jet fuel supply the sulfur. Combustion in the gas turbine engine[60] quantitatively converts fuel sulfur compounds to S[IV] in the form of SO_2. A fraction of the S[IV] is further oxidized to S[VI] (in the form of SO_3) in the secondary combustor zone and in the turbines [61]. S[VI] rapidly converts from SO_3 to H_2SO_4 [62], which can then nucleate fresh particles or coat existing ones. Nucleated sulfuric acid provides a new surface area for condensation of organic species and may activate the existing soot surface area so that other sulfuric acid molecules and possibly organic materials can stick to it more efficiently [63,64]. In this cascade of microphysical processes, the most uncertain parameter is the fraction of S[IV] that is converted to S[VI]. Most recent reports estimate that the conversion efficiency is in the 1–5% range [28,33,59,65], with only a weak dependence on power condition [61]. Data on the influence of engine technology on sulfur conversion efficiency are sparse [27], but Katragkou et al. [28] reported higher S[IV] conversion for operation of a combustor under simulated modern conditions (i.e., higher bypass ratio and lower air/fuel ratio) compared with old conditions. The APEX-2/3 EI_m-sulfate data set provides an independent and direct lower-bound estimate of the S[IV] conversion efficiency for a range of gas turbine engines technologies.

Before considering S[IV] conversion directly, we describe the accuracy of the EI_m-sulfate measurement. The AMS transmission efficiency is the most important source of uncertainty. The AMS inlet is optimized for 30–800 nm size particles; volatile material present on soot (roughly 50–100 nm diameter) is detected quantitatively while nucleation/growth mode particles are not. As a result, we expect that our measurement of EI_m-sulfate should capture more of the condensed sulfate as conditions favor formation of sulfur acid coatings on the soot rather than nucleation of fresh particles—in other words, conditions that maximize EI_m-soot. Figures 5(*a*) and 5(*b*) show the EI_m-sulfate and EI_m-soot data for the CFM56-3B1/N14324 and RB211-535E4-B/N74856 engines, respectively. As expected from the transmission efficiency argument, EI_m-sulfate closely mirrors EI_m-soot—even when EI_m-soot does not monotonically increase with thrust. Since S[IV] to S[VI] conversion is not anticipated to closely mirror soot production [61], the correlation between EI_m-soot and EI_m-sulfate can be attributed to optimized transmission of soot-sized particles and their coatings into the measurement device. Therefore, based on Fig. 5, we conclude that the aerosol mass spectrometer measurements of EI_m-sulfate should capture the largest fraction of the condensed sulfate at conditions that maximize EI_m-soot.

Figure 6 plots EI_m-sulfate as equivalent sulfur mass

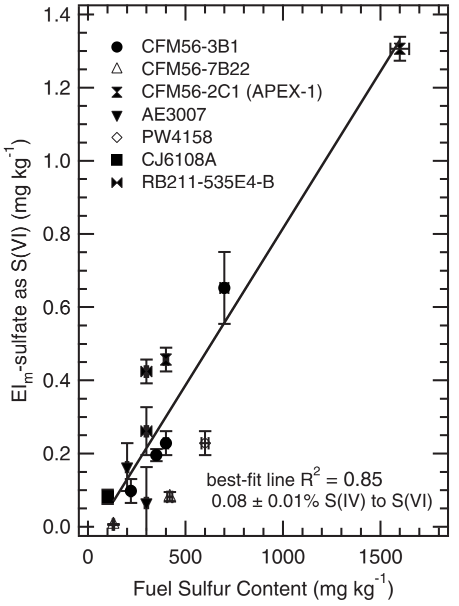

Fig. 6 EI_m-sulfate (30/43 m sampling probe) for all of the APEX-2/3 turbofan engines except AE3007s (internally mixed engines) and CJ6108A plotted as a function of measured fuel sulfur content. Only data at high power (80% or 85%) are included, as the capture efficiency of the aerosol mass spectrometer is maximized at these conditions. The data from APEX-1 are included for completeness and to expand the fuel sulfur content range. A best fit line for the entire data set is shown (R^2=0.85).

Downloaded 02 Jun 2010 to 171.66.16.96. Redistribution subject to ASME license or copyright; see http://www.asme.org/terms/Terms_Use.cfm

(EI_m-sulfate $\times 32/98$) at maximized EI_m-soot (i.e., either 65%, 80/85%, or 100% power, as appropriate and as data are available) as a function of measured fuel sulfur content. In addition to the APEX-2/3 engines, two data points (one for combustion of high sulfur fuel and the other for base fuel) from the CFM56-2C1 engine studied in APEX-1 were included for completeness. Fuel sulfur content error bars are ±3% of the actual value, estimated from the reported reproducibility of the detection method [66]. For low sulfur fuels ($<200\ \mathrm{mg\ kg^{-1}}$), the fuel sulfur measurement error is likely greater than ±3%, and this uncertainty and the uncertainty in measuring low values of EI_m-sulfate likely contribute to the scatter in the low sulfur data.

The overall correlation between EI_m-sulfate and fuel sulfur content shown in Fig. 6 is good ($R^2=0.85$, $N=14$). Limiting the analysis to CFM56 engines improves the fit slightly ($R^2=0.89$, $N=8$), but does not change the slope. Whether the improved CFM56 correlation is due to an engine dependent S[IV] conversion or is simply an experimental uncertainty is not clear based on the available data. After unit conversions, the slope of the best fit line shown in Fig. 6 provides the S[IV] to S[VI] conversion as $(0.08 \pm 0.01)\%$.

4.2.2 Conversion of S[IV] to S[VI]. The data contained in Fig. 6 provide a true lower bound to the S[IV] conversion efficiency. All known sources of experimental error (incomplete particle detection, particle loss in the sampling lines, etc. [11,45–50]) would correct the 0.08% figure upwards. Moreover, the soot coating layer is just one form that S[VI] can take in the exhaust gas. S[VI] that remains in the gas phase would not have been detected by the AMS, and sulfate present in nucleation/growth mode particles would have been detected incompletely. Two sets of literature data, one based on total measurements of S[VI] (both liquid and gas phases) and the other based on gaseous S[VI] only, provide a comparison for the sulfate data. Katragkou et al. [28] measured gaseous S[VI] directly, and conversion efficiencies ranged from as low as about $(0.9 \pm 0.5)\%$ to $(2.3 \pm 1.4)\%$, depending on exhaust gas age and engine operating condition. Curtius et al. [65] measured total S[VI] (both gaseous and condensed) and reported an S[IV] conversion efficiency of $(3.3 \pm 1.8)\%$. Taking the difference between the measurements of Katragkou et al. [28] and Curtius et al. [65] as the conversion efficiency of S[IV] to particle-bound sulfur results in a range of values ($(1 \pm 2)\%$ to $(2.4 \pm 1.9)\%$) that is consistent with that reported here, though the uncertainty of the lower bound estimated from literature data is twice its absolute value. Furthermore, we note that our analysis is restricted to high power and does not provide information about the power dependence of S[IV] conversion—or lack thereof.

In addition to providing a lower bound on the engine S[IV] to S[VI] conversion, Fig. 6 provides an important insight. The APEX-2/3 engines represent a wide range of technologies, including both qualitative (e.g., internally mixed AE3007 versus the other externally mixed engines, or the three spool design of the RB211-535E4-B versus the other engines that are two spool designs) and quantitative (maximum rated thrust, bypass ratio, and pressure ratio—see Table 1) differences. Despite the significant technological differences represented in the APEX-2/3 engine set, the aerosol mass spectrometer estimate of the S[IV] to S[VI] conversion does not vary substantially. In other words, we find that fuel sulfur content is the driver for EI_m-sulfate, independent of engine technology.

4.3 PM Organic Emissions

4.3.1 General Discussion of PM Organic. Table 4 includes downstream EI_m-organic data for the APEX-2/3 engines. In general, EI_m-organic is less than about $3\ \mathrm{mg\ kg^{-1}}$, though the RB211-535E4-B engines are notable outliers. EI_m-organic was frequently minimized at 30% power (ICAO approach), though EI_m-organic for both the RB211-535E4-B engines and CJ6108A engines did not follow this trend. Instead, RB211-535E4-B EI_m-organic is roughly constant with respect to power condition while CJ6108A EI_m-organic is maximized at idle. Quantitatively, the EI_m-organic data in Table 4 are somewhat variable, even when the analysis is restricted to a certain engine type (e.g., CFM56 engines vary by about a factor of 5). The RB211-535E4-B engines are an exception since EI_m-organic for these two engines generally agrees to within our estimated limits of experimental uncertainty

We considered several variables that might be expected to capture the variability in the EI_m-organic data, including EI_m for unburned hydrocarbons (EI_m-HC), fuel sulfur content, and EI_m-soot. A relationship between EI_m-HC and EI_m-organic would be expected if the organic PM were dominated by partially burned hydrocarbons. The high idle EI_m-organic of the CJ6108A engine is consistent with its large value of EI_m-HCHO ($2500 \pm 500\ \mathrm{mg\ kg^{-1}}$ at idle compared with roughly $100-1000\ \mathrm{mg\ kg^{-1}}$ for all other engines) as reported in the first part of this series [40]. Thus, in some instances, the same combustion (in)efficiencies, which lead to large values of EI_m-HC and related species, may also contribute to the PM measurement of EI_m-organic. Because EI_m-HC is typically 100 times larger [7,40] than our measurements of EI_m-organic (at least at engine idle conditions), only a small percentage of the total hydrocarbon emissions would need to condense in the cooled exhaust gas to account for the measured organic PM.

The relationship between EI_m-HC and EI_m-organic cannot be generalized for all engines; RB211-535E4-B engines have low EI_m-HCHO ($100-200\ \mathrm{mg\ kg^{-1}}$) and high EI_m-organic. Moreover, EI_m-organic often increases from approach (30% power) to climbout (85% power), but EI_m-HC always decreases. We also considered fuel sulfur content and EI_m-soot as means to remove apparent EI_m-organic variability, but neither quantity was adequate for the purpose.

To understand the EI_m-organic variability and trends better, we analyzed the exhaust particle mass spectra to identify classes of molecules present in the organic PM. Figure 7 provides normalized mass spectra for three classes of engines operating at climbout power (85%): CJ6108A, CFM56-3B1, and RB211-535E4-B. Important m/z signals are highlighted in Fig. 7 to facilitate discussion. Present in all three spectra is a series of peaks that includes m/z 27 and 29 ($C_2H_3^+$ and $C_2H_5^+$), 41 and 43 ($C_3H_5^+$ and $C_3H_7^+$), and 55 and 57 ($C_4H_7^+$ and $C_4H_9^+$) and that is characteristic of fragmentation of large hydrocarbon molecules. Also present in all three spectra is a series containing $m/z=85$, 113, 127, and 155. The $m/z=85$ series is strongest in the RB211-535E4-B exhaust and is nearly absent from the CJ6108A exhaust. The $m/z=85$ content of the CFM56-3B1 exhaust is intermediate to the other two engines. The two sets of peaks present in the spectra in Fig. 7 are evidence of at least two primary exhaust gas components, which we conclude are (a) products of incomplete combustion and (b) lubrication oil. We describe these two components in Secs. 4.3.2 and 4.3.3.

4.3.2 Lubrication Oil. Identifying the lubrication oil signature was relatively straightforward. Figure 7 provides mass spectra for pure two lubrication oil samples obtained in the laboratory by aerosolizing pure oil taken from the field and feeding it directly into the AMS. Air BP lubrication oil was obtained from the CFM56-3B1/N14324 engine and the Mobil II lubrication oil was obtained from the RB211-535E4-B/N74856 engine. Both lubrication oil samples contain the characteristic $m/z=85$ series. Moreover, both lubrication oil spectra shown in Fig. 7 contain only small amounts of $m/z=69$ and 71; a typical hydrocarbon mixture like raw or partially burned jet fuel would be expected to have strong signals at m/z 69 and 71 [45–47].

The spectra of the two oil samples show important similarities, though some differences are apparent. Most noticeably, the Mobil II sample has a much stronger $m/z=85$ signal relative to the 113, 127, and 155 signals than the Air BP sample. The composition of lubrication oil explains both the common features and the differ-

Downloaded 02 Jun 2010 to 171.66.16.96. Redistribution subject to ASME license or copyright; see http://www.asme.org/terms/Terms_Use.cfm

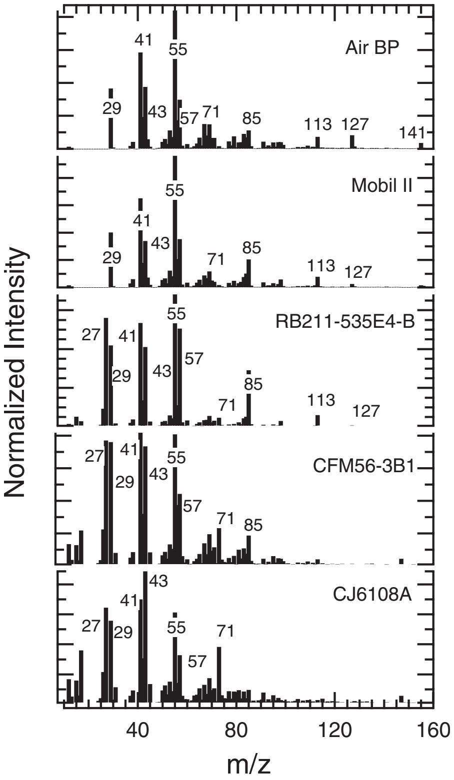

Fig. 7 Mass spectra of exhaust gas samples from three engines (CJ6108A, CFM56-3B1, and RB211-535E4-B) and two lubrication oils (Mobil II and Air BP). Mass spectra of the lubrication oils were obtained by aerosolizing oil samples obtained from the engines (Mobil II from the RB211-535E4-B and Air BP from CFM56-3B1). Characteristic m/z signals are highlighted for easy reference. The $m/z=27/29$, 41/43, 55/57 series is due to hydrocarbons. The $m/z=85$, 113, 127 series is likely due to the synthetic esters in lubrication oil.

ences in the two spectra. The C_5-C_{10} esters of pentaerythritol and dipentaerythritol account for about 95% of the ingredients in gas turbine lubrication oils, with tricresylphosphate isomers contributing roughly half the remainder [67–71]. Based on this insight, we suspect that the $m/z=85$ signal is due to either $C_6H_{11}^+$ or $C_5H_9O^+$ fragments originating from the parent esters. The other signals in the series reflect subsequent addition of CH_2^+ groups, as expected for a blend of C_5-C_{10} esters. The different ratios of $m/z=85$ to the other important peaks are likely due to different blends of synthetic esters in the two samples or partial pyrolysis of the lubrication oil during use or analysis.

4.3.3 Products of Incomplete Combustion. Identification of a lubrication oil signature allowed us to consider separately the remainder of the spectrum. The key to this analysis was that the intensities of m/z 69 and 71 in the lubrication oil spectra were less than 10% that of m/z 85. The source of $m/z=71$ in the field spectra was likely a hydrocarbon mixture separated from lubrication oil. We considered two candidates for the unknown hydrocarbon: raw jet fuel and products of incomplete combustion. Because gas turbine combustor efficiencies are generally $>99\%$, only trace raw jet fuel molecules can possibly remain in the exhaust gas. Furthermore, laboratory mass spectra of jet fuel did not match the residual field spectra minus the lubrication oil contribution. Therefore, we conclude that products of incomplete combustion (i.e., partially burned fuel) are the second important component of the organic PM, with the possible exception of emissions close to idle where comustor efficiencies are lower and emission of unburned fuel may occur.

4.3.4 Quantitative Apportionment of Organic PM. The three field spectra in Fig. 7 can be ordered in terms of the relative ratios of incomplete combustion products to lubrication oil in their exhaust. Because its spectrum is characterized by a strong $m/z=85$ signal and a weak m/z 71 signal, lubrication oil appears to be the primary component of the organic PM in RB211-535E4-B exhaust. Exhaust from the other two engines contains much less lubrication oil than the RB211-535E4-B exhaust. Four qualitative differences between the RB211-535E4-B organic PM composition and the other engines studied support the lubrication oil assignment: (a) the RB211-535E4-B combustor is the most efficient at low powers in the APEX-2/3 data set as indicated by its low idle value of EI_m-HCHO [40] yet it has the highest EI_m-organic; (b) EI_m-organic for the other engines depends on power condition—as would be expected for combustion particles, but not for the RB211-535E4-B engines—as might be expected of a non-combustion related particle emission; (c) unlike the other engines studied, the RB211-535E4-B emits particles larger than 300 nm, possibly consistent with vented or leaked oil; (d) the lubrication oil was detected only in small quantities (≤ 2 mg kg^{-1}) at the 1 m extraction point and we surmise that the lubrication oil most likely entered the exhaust gas at the engine periphery—rather than from the core combustor flow.

Because its spectrum has a very weak $m/z=85$ and very strong $m/z=71$ signal, products of incomplete combustion appear to dominate EI_m-organic for the CJ6108A. The CJ6108A assignment is consistent with the low efficiency at idle and high EI_m-HCHO [40] (or EI_m-HC) of this engine. Because the $m/z=85$ and $m/z=71$ peaks are roughly equal in intensity in the CFM56 spectrum, we conclude that its exhaust contains roughly equal parts of lubrication oil and products of incomplete combustion.

Following the qualitative ordering in terms of lubrication oil content, we quantified the PM analysis using the procedure described by Canagaratna et al. [72] for heavy-duty-diesel engine PM analysis. For the quantitative analysis, we assumed that $m/z=85$ was due entirely to lubrication oil and the ratio of m/z 85 to m/z 71 was the same for lubrication oil measured in the field as it was in the laboratory (about 20:1). We found that lubrication oil was most important at high power and products of incomplete combustion were most important at low power—consistent with the known variation of combustor efficiency with thrust condition. Specifically, about 75–90% of the particulate organic in the RB211-535E4-B low-power exhaust is lubrication oil, and the lubrication oil portion increases to more than 90% at takeoff. For other engines, lubrication oil is a less significant component, constituting about 10–20% of the organic mass at low power and about 50% at climbout/takeoff. The organic PM in CJ6108A engine exhaust contains less than 10% lubrication oil even at takeoff. The presence of lubrication oil in the RB211-535E4-B exhaust accounts for its unusually large value of EI_m-organic (>20 mg kg^{-1} compared with $0-3$ mg kg^{-1} for the other engines). Subtracting our best estimate for the lubrication oil mass from the total RB211 EI_m-organic leads to an EI_m-organic of about $1-5$ mg kg^{-1} for unburned hydrocarbons—in reasonable agreement with the figure measured for other engines during this study.

4.3.5 Origin of Lubrication Oil Differences Between Engines. We considered differences in engine technology that might account for the enhanced contribution of lubrication oil in the RB211-535E4-B engines relative to the rest of those studied. The CFM56 engines provide a useful contrast to the RB211-535E4-B since we studied many versions of the CFM56 technology and observed only a modest ($<50\%$) lubrication oil contribution to their overall organic PM loading in all cases. We considered two potential differences between the CFM56 and RB211-535E4-B engines: (1) differences in lubrication oil vent locations and (2) different size distributions for the lubrication oil PM emissions. The CFM56 engine lubrication vents are located on the engine radial center line. At 1 m, we sample the CFM56 exhaust several

Downloaded 02 Jun 2010 to 171.66.16.96. Redistribution subject to ASME license or copyright; see http://www.asme.org/terms/Terms_Use.cfm

centimeters away from the center line to avoid lubrication oil. When sampling >15 m downstream, the exhaust should be well mixed and—if present in a size mode for which we have sensitivity—should be detected. That we do not detect a substantial lubrication oil signature indicates that either none is present in the CFM56 exhaust or that it is present in a size mode or phase that we cannot detect.

The lubrication oil PM in RB211-535E4-B exhaust ranges in size from about 80 nm to 500 nm. Due to instrument sensitivity, the actual distribution may extend to both smaller and larger sizes. If the CFM56 emits lubrication oil as a gas (for which we have no sensitivity) or as particles larger than about 1000 nm, we would fail to detect it. Based on our current data set, we cannot rule out CFM56 emission of vapor phase or large droplet lubrication oil. We are currently performing tests to characterize lubrication oil emission properties and to understand better the underlying differences in engine technology, which lead to the differences in behavior.

4.4 Volatile Particle Number Emissions

4.4.1 General Discussion of Volatile Particle Number Emissions. Downstream measurements of EI_n-total are the final volatile PM metric to be considered. Downstream EI_n-total are generally 10–100 times greater than their engine exit plane values, and this difference can only be attributed to formation of new particles in the cool sample extraction probe. In accord with this assertion, particle size measurements (SMPS) indicate the presence of a large number of particles smaller than 30 nm (mobility diameter) in downstream exhaust gas samples that are not present at the engine exit plane—as shown in Fig. 1. As a result of nucleation and growth, at downstream locations EI_n-total $\approx EI_n$-volatile and $EI_n\text{-volatile} \gg EI_n$-nonvolatile. The equality is most accurate at low powers for which the increase in EI_n-total between the engine exit plane and downstream locations is most pronounced

Depending on the engine operating and ambient conditions, nucleation of new particles likely initiates either in the plume or in the sampling lines, and their condensational growth and particle coagulation continue in the sampling lines. Microphysical processing in the sampling lines cannot be avoided. Wong et al. [73] modeled both sample line and exhaust plume microphysics and found that particle characteristics are determined primarily by exhaust gas process time, regardless of whether the particles spend that time in the plume or in a sample line. Here, we show that while the microphysical processes that occur in the sample line are not entirely controlled, PM measurements indicate that the processes occur reproducibly and therefore provide a consistent set of data for engine intercomparisons.

4.4.2 Role of Fuel Sulfur for Volatile Particle Number Emissions. Qualitatively, the downstream EI_n-total data in Table 4 generally decrease with engine power. EI_n-total is roughly 1×10^{16} kg^{-1} at idle, and at climbout it is about 1×10^{15} kg^{-1}. Beyond general trends, however, the EI_n-total data in Table 4 vary considerably from engine to engine, even when a subset of engines is considered separately (e.g., only CFM56-3B1 engines). The engine-to-engine variability found at idle can be attributed nearly entirely to variation in fuel sulfur content. Data obtained at downstream sample locations are first separated into high (65% RB211-535E4-B only, and 85% or 100% rated thrust) or low power (4%, 7%, or 15% rated thrust) regimes and then plotted as a function of the fuel sulfur content. Data from all of the APEX-2/3 engines are plotted in Fig. 8 as are two APEX-1 data points (fuel sulfur=400 and 1600 ppm). Best-fit lines are shown in Fig. 8 to guide the eyes and are not intended to imply a definitive physical significance. Regression analysis of the low power data set indicates a linear relationship between EI_n-total and fuel sulfur content (R^2=0.96, N=9). For high power data, the relationship between EI_n-total and fuel sulfur content is much weaker (R^2=0.17, N=9) and the trend line is nearly flat. The low-power EI_n-total (>15 m) data set is uniformly greater than the high-power EI_n-total data. The inverse relationship between EI_n-total and power and the lack of a correlation between EI_n-total and fuel sulfur content at high powers are both consistent with processes favored at high power: 1) partial suppression of new particle formation by the existing soot particles, 2) coagulation of nucleation/growth mode particles with the soot particles, 3) lower combustion efficiencies typical of low power operation compared to high power operation. The N14324/CFM56-3B1 engine is an outlier for the high-power data trend, a possible consequence of its relatively high EI_m-soot or due to a combination of the (a) low temperature (281 K compared with an average of about 286 for the other tests), (b) high humidity (87%), and (c) the relatively low dilution ratio of the sample (about 30:1 compared with 40:1 for the other CFM56 engines at low power). With the possible exception of the N14342/CFM56-3B1, we did not notice a strong influence of ambient conditions on particle characteristics. However, the APEX-2/3 tests did not explore a very wide range of temperatures (281–292 K, see Table 1), and the effects of ambient conditions on particle microphysics may require further study at more extreme conditions to be noticeable.

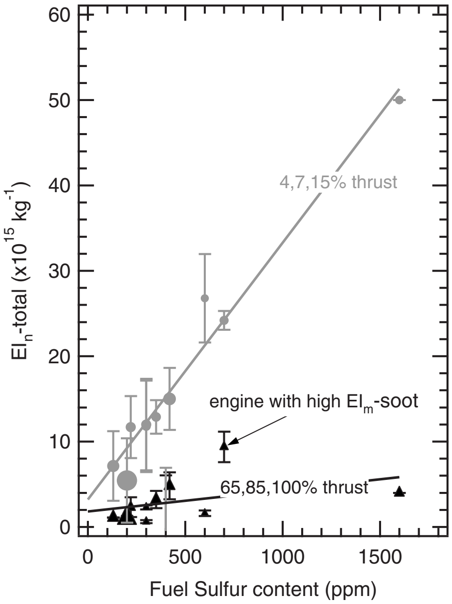

Fig. 8 Downstream measurements of EI_n-total plotted as a function of fuel sulfur content for all of the engines studied in APEX-2/3 and the high sulfur data from APEX-1 (1600 ppm fuel sulfur). The outlying high-power data point (N14324/CFM56-3B1) had high EI_m-soot. The lines are intended to guide the eyes, not to imply a definitive physical relationship. The marker size is proportional to dilution ratio—larger markers have a lower percentage of exhaust gas relative to ambient air.

4.4.3 Unburned Hydrocarbon and Sulfate Composition of Nucleation/Growth Mode Particles. The APEX-2/3 data can help answer an important question related to nucleation/growth mode particles: What is their composition and how does it compare with the composition of the soot coatings? Nucleation/growth mode particle composition may influence their potential human health and environmental impacts. Moreover, understanding nucleation/growth mode particle composition might help assist efforts to model their formation.

Although nucleation/growth mode particles are rarely large enough to be collected quantitatively by the AMS, we were able to extract qualitative information in many instances. Perhaps due to the relatively high sulfur content of the fuel used (700 ppm) and the low temperature and high humidity encountered during the

Downloaded 02 Jun 2010 to 171.66.16.96. Redistribution subject to ASME license or copyright; see http://www.asme.org/terms/Terms_Use.cfm

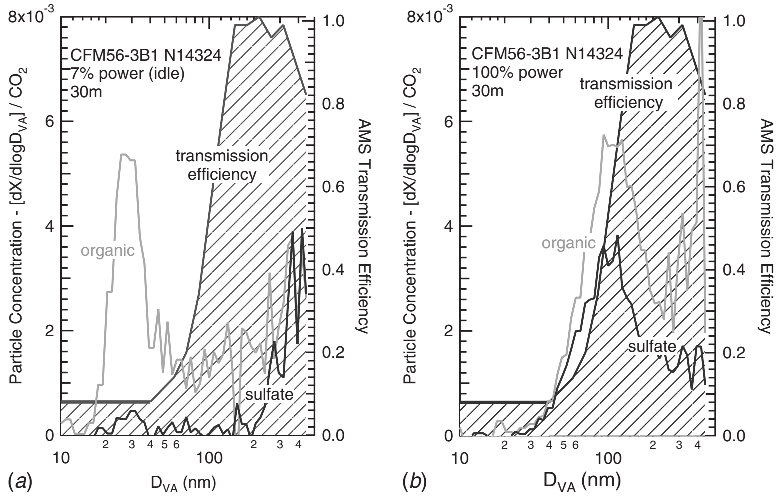

Fig. 9 Downstream AMS measurements of condensed organic and sulfate materials emitted by the CFM56-3B1 engine of a B737 aircraft (N14324). The calculated particle transmission efficiency is shown based on the data from Ref. [50]. In (*a*) at idle, a significant nucleation mode is visible at about 25 nm. The AMS is unable to detect particles smaller than about 30 nm, so the peak depicted at about 25–30 nm appears as a result of limited transmission of particles <50 nm—the true peak is almost certainly smaller.

test, the N14324/CFM56-3B1 engine provided the most intense composition signal for nucleation/growth mode particles. Figures 9(*a*) and 9(*b*) contain plots of size-resolved sulfate and organic particle loadings for the N14324/CFM56-3B1 engine obtained at both idle and takeoff power. For convenience, the AMS particle size dependent sensitivity [50] is included in Fig. 9 on the same horizontal axis as the size-resolved chemical data. Figure 9(*a*) shows a distinct peak at approximately 30 nm, while the maximum in Fig. 9(*b*) occurs at approximately 80–100 nm. Figure 9(*a*) depicts nucleation/growth mode particles, and the PM shown in Fig. 9(*b*) is a coating on soot. These assignments are consistent with values of EI_m-soot at idle and takeoff powers and in size distributions measured at the engine exit plane (where the exhaust gas should contain soot only) and downstream of the CFM56-3B1 engine. Because the particles in the sample depicted in Fig. 9(*a*) were collected under conditions of rapidly decreasing AMS transmission efficiency, the nucleation/growth mode particle size distribution probably peaks at a diameter smaller than 30 nm.

Using Fig. 9, we can determine the relative quantities of organic and sulfate in both the nucleation/growth particles and soot coatings. Figure 9(*a*) indicates that volatile PM emitted at idle is dominated by an organic material with the sulfur content accounting for less than about 10% of the total mass. In contrast, the volatile PM emitted at takeoff is composed of roughly equal parts of organic and sulfate materials. Figure 9 indicates that the power dependence of organic PM formation is much stronger than that of sulfate PM An examination of the EI_m-organic and EI_m-sulfate data in Table 4 suggests that the sulfate/organic power dependence behavior is universal for the engines we have studied, with the exception of the RB211-535E4-B. In fact, after removing contributions due to lubrication oil, the ratio of EI_m-organic for unburned hydrocarbon PM to EI_m-sulfate is always greater at low power than at high power by a factor of about 5.

While Fig. 8 clearly implicates the role of fuel sulfur in new particle formation, Fig. 9 indicates that sulfur is a minority component in these particles at idle. We therefore conclude that sulfur plays an important role in the initial nucleation process, although certain organic molecules may play a secondary role in particle nucleation [74]. Once a sulfuric acid nucleus is formed, organic material may condense onto it, causing its growth. The result is that (especially at low power conditions) organic material dominates the particle mass, while fuel sulfur drives volatile particle number.

5 Conclusions

The trace gas and PM emissions of 16 separate gas turbine engines were measured during the APEX-2/3 field campaigns, greatly increasing the detail available in the aircraft PM emission data set. In all, nine CFM56 engines were tested as well as RB211-535E4-B (2), AE3007 (3), PW4158, and CJ6108A engines. Specific particle measurements reported here include total particle number (EI_n-total), total mass of black carbon (EI_m-soot), mass of organic PM (EI_m-organic), and mass of sulfate material (EI_m-sulfate). Determining which particle emission trends are independent of engine technology and which are dependent on engine technology was an objective of this paper. We find that the following emission data trends are independent of engine technology.

- For 1 m exhaust samples, EI_n-total depends only on EI_m-soot.
- For (>15 m) exhaust samples, EI_n-total depends only on fuel sulfur content (low powers) or EI_m-soot (high power)—at least for the conditions studied in this work.
- For downstream (>15 m) exhaust samples of engines operating at 85% or 100% power, EI_m-sulfate depends only on fuel sulfur content.
- The S[IV] to S[VI] conversion factor is engine technology independent for the range of engines studied.
- EI_m-soot and soot particle size are always greater at climbout (85% power) and takeoff (100% power) than at idle (either 4% or 7%) or approach (30% power).
- Organic material is the most abundant component of volatile PM detected at idle.
- Lubrication oil is a component of organic PM for all the engines studied.
- When considering a single class of engines (e.g., CFM56-3B1), EI_m-soot exhibits variability that cannot be attributed to engine technology differences.

Downloaded 02 Jun 2010 to 171.66.16.96. Redistribution subject to ASME license or copyright; see http://www.asme.org/terms/Terms_Use.cfm

The following observations are dependent on engine technology.

- The magnitude of EI_m-soot varies when comparing different engine types (e.g., RB211-535E4-B versus CFM56-7B22) and when comparing different engines of the same type but different combustors (e.g., CFM56-7B22 versus CFM56-3B1).
- The qualitative relationship between EI_m-soot and engine power varies with engine technology. For example, unlike any other engine studied, the RB211-535-E4-B engines exhibit a maximum in EI_m-soot at 65%.
- At low power, abundance of nonlubrication oil organic PM depends on combustor efficiency—less efficient combustors emit more nonlubrication oil organic PM at low power than do more efficient combustors.
- The quantity of lubrication oil emissions depends strongly on engine technology. For some engines, lubrication oil constitutes 90% of the organic PM mass.

Acknowledgment

NASA Cooperative Agreement No. NCC3-1084, PARTNER/FAA Grant No. 03-C-NE-UMR, and the California Air Resources Board via the Missouri University of Science and Technology Center of Excellence supported this work. We gratefully acknowledge the contributions of Southwest Airlines, Continental Airlines, FedEx, and NASA Glenn Research Center. We are very grateful to Renee Dowlin (formerly at Oakland International Airport) and Dana Ryan (Cleveland Hopkins International Airport). The entire APEX, JETS/APEX-2, and APEX-3 team contributed to the success of these missions. Paul Yelvington (Mainstream Engineering), Hsi-Wu Wong (ARI), Luwi Oluwole (ARI), Elena de la Rosa Blanco (ARI), James Hileman (MIT), and Joda Wormhoudt (ARI) generously provided technical advice and editorial commentary. John Kinsey (U.S. EPA) donated lubrication oil samples that he collected during the two field missions. Changlie Wey shared his CO_2 data, which he obtained from heated raw exhaust lines positioned at the engine exit plane; Dr Wey's data permitted our estimation of dilution ratios. Zhenhong Yu (ARI) analyzed lubrication oil samples using the AMS.

Nomenclature

APEX = aircraft particle emissions experiment; to date, three APEX campaigns have been conducted: APEX-1 took place at Dryden Air Force Base in April 2004; APEX-2 was at Oakland International Airport, August 2005; And APEX-3 was at Cleveland-Hopkins International Airport, November 2005; in this report, APEX-2 and APEX-3 are jointly referred to as "APEX-2/3"
D_M = mobility diameter
D_{VA} = vacuum aerodynamic diameter
EI = emission index, quantity of pollutant emitted per mass of fuel burned
EI_n = number based emission index, number of particles emitted per mass fuel burned
EI_n-total = number based emission index for the total number of particles $\mathrm{EI}_n\text{-total} \equiv \mathrm{EI}_n\text{-volatile} + \mathrm{EI}_n\text{-nonvolatile}$
EI_n-volatile = number based emission index for volatile particles
EI_n-nonvolatile = number based emission index for nonvolatile particles (e.g., soot)
EI_m = mass based emission index, mass of pollutant emitted per mass of fuel burned
EI_m-organic = mass based emission index of organic PM
EI_m-sulfate = mass based emission index of sulfate PM
EI_m-soot = mass based emission index of soot
EXCAVATE = experiment to characterize aircraft volatile aerosol and trace-species emissions; EXCAVATE took place at NASA Langley Research Center, Langley VA in January, 2002
m/z = mass to charge ratio, measured by mass spectrometry
P = pressure
T = temperature

References

[1] Maricq, M. M., 2007, "Chemical Characterization of Particulate Emissions From Diesel Engines: A Review," J. Aerosol Sci., **38**, pp. 1079–1118.
[2] Unal, A., Hu, Y., Chang, M. E., Odman, M. T., and Russel, A. G., 2005, "Airport Related Emissions and Impacts on Air Quality: Application to the Atlanta International Airport," Atmos. Environ., **39**, pp. 5787–5798.
[3] Tesseraux, I., 2004, "Risk Factors of Jet Fuel Combustion Products," Toxicol. Lett., **149**, pp. 295–300.
[4] Federal Aviation Administration, 2007, FAA Aerospace Forecasts: Fiscal Years 2007–2020.
[5] International Panel on Climate Change (IPCC), 2007, *Climate Change 2007*, Cambridge University Press, New York.
[6] Lee, D. S., Fahey, D. W., Forster, P. M., Newton, P. J., Wit, R. C. N., Lim, L. L., Owen, B., and Sausen, R., 2009, "Aviation and Global Climate Change in the 21st Century," Atmos. Environ., **43**, pp. 3520–3537.
[7] International Civil Aviation Organization (ICAO), 1995, Engine Exhaust Emissions Data Bank, Document No. 9646-AN/943, Montreal, QC, Canada.
[8] Anderson, B. E., Branham, H. -S., Hudgins, C. H., Plant, J. V., Ballenthin, J. O., Miller, T. M., Viggiano, A. A., Blake, D. R., Boudries, H., Canagaratna, M., Miake-Lye, R. C., Onasch, T. B., Wormhoudt, J. C., Worsnop, D. R., Brunik, K. E., Culler, C., Penko, P., Sanders, T., Han, H. -S., Lee, P., Pui, D. Y. H., Thornhill, K. L., and Winstead, E. L., 2005, "Experiment to Characterize Aircraft Volatile Aerosol and Trace-Species Emissions (EXCAVATE)," Report No. NASA/TM-2005-213783.
[9] Anderson, B. E., Chen, G., and Blake, D. R., 2006, "Hydrocarbon Emissions From a Modern Commercial Airliner," Atmos. Environ., **40**, pp. 3601–3612.
[10] Miller, T. M., Ballenthin, J. O., Viggiano, A. A., Anderson, B. E., and Wey, C. C., 2005, "Mass Distribution and Concentrations of Negative Chemiions in the Exhaust of a Jet Engine: Sulfuric Acid Concentrations and Observation of Particle Growth," Atmos. Environ., **39**, pp. 3069–3079.
[11] Boudries, H., Canagaratna, M., Onasch, T., Worsnop, D., Wormhoudt, J., Miake-Lye, R., and Anderson, B., 2005, "Real Time Characterization of Aircraft Particulate Emission by an Aerosol Mass Spectrometer During EXCAVATE 2002," Report No. NASA/TM-2005-213783.
[12] Wey, C. C., Anderson, B. E., Wey, C., Miake-Lye, R. C., Whitefield, P., and Howard, R., 2007, "Overview on the Aircraft Particle Emissions Experiment," J. Propul. Power, **23**, pp. 897–905.
[13] Lobo, P., Hagan, D. E., Whitefield, P. D., and Alofs, D. J., 2007, "Physical Characterization of Aerosol Emissions From a Commercial Gas Turbine Engine," J. Propul. Power, **23**, pp. 919–929.
[14] Onasch, T. B., Jayne, J. T., Herndon, S. C., Mortimer, I. P., Worsnop, D. R., Miake-Lye, R. C., 2009, "Chemical Properties of Aircraft Engine Particulate Exhaust Emissions Sampled During APEX," J. Propul. Power, **25**, 1121–1137.
[15] Wormhoudt, J., Herndon, S. C., Yelvington, P. E., Miake-Lye, R. C., and Wey, C., 2007, "Nitrogen Oxide ($NO/NO_2/HONO$) Emissions Measurements in Aircraft Exhausts," J. Propul. Power, **23**, pp. 906–911.
[16] Yelvington, P. E., Herndon, S. C., Wormhoudt, J. C., Jayne, J. T., Miake-Lye, R. C., Knighton, W. B., and Wey, C., 2007, "Chemical Speciation of Hydrocarbon Emissions From a Commercial Aircraft Engine," J. Propul. Power, **23**, pp. 912–918.
[17] Dakhel, P. M., Lukachko, S. P., Waitz, I. A., Miake-Lye, R. C., and Brown, R. C., 2007, "Postcombustion Evolution of Soot Properties in an Aircraft Engine," J. Propul. Power, **23**, pp. 942–948.
[18] Knighton, W. B., Rogers, T. M., Anderson, B. E., Herndon, S. C., Yelvington, P. E., and Miake-Lye, R. C., 2007, "Quantification of Aircraft Engine Hydrocarbon Emissions Using Proton Transfer Reaction Mass Spectrometry," J. Propul. Power, **23**, pp. 949–958.
[19] Wey, T., and Liu, N.-S., 2007, "Modeling Jet Engine Aerosols in the Postcombustor Flow Path and Sampling System," J. Propul. Power, **23**, pp. 930–941.
[20] Herndon, S. C., Onasch, T. B., Frank, B. P., Marr, L. C., Jayne, J. T., Canagaratna, M. R., Grygas, J., Lanni, T., Anderson, B. E., Worsnop, D., and Miake-Lye, R. C., 2005, "Particulate Emissions From In-Use Commercial Aircraft," Aerosol Sci. Technol., **39**, pp. 799–809.
[21] Herndon, S. C., Jayne, J. T., Lobo, P., Onasch, T. B., Fleming, G., Hagen, D. E., Whitefield, P. D., and Miake-Lye, R. C., 2008, "Commercial Aircraft Engine Emissions Characterization of In-Use Aircraft at Hartsfield-Jackson Atlanta International Airport," Environ. Sci. Technol., **42**, pp. 1877–1883.
[22] Gysel, M., Nyeki, S., Weingartner, E., Baltensperger, U., Giebl, H., Hitzenberger, R., Petzold, A., and Wilson, C. W., 2003, "Properties of Jet Engine

Downloaded 02 Jun 2010 to 171.66.16.96. Redistribution subject to ASME license or copyright; see http://www.asme.org/terms/Terms_Use.cfm

Combustion Particles During the PartEmis Experiment: Hygroscopicity at Subsaturated Conditions," Geophys. Res. Lett., **30**, p. 1566.

[23] Petzold, A., Fiebig, M., Fritzsche, L., Stein, C., Schumann, U., Wilson, C. W., Hurley, C. D., Arnold, F., Katragkou, E., Baltensperger, U., Gysel, M., Nyeki, S., Hitzenberger, R., Giebl, H., Hughes, K. J., Kurtenbach, R., Wiesen, P., Madden, P., Puxbaum, H., Vrchoticky, S., and Wahl, C., 2005, "Particle Emissions From Aircraft Engines—A Survey of the European Project PartEmis," Meteorol. Z., **14**, pp. 465–476.

[24] Wilson, C. W., Petzold, A., Nyeki, S., Schumann, U., and Zellner, R., 2004, "Measurement and Prediction of Emissions of Aerosols and Gaseous Precursors From Gas Turbine Engines (PartEmis): An Overview," Aerosp. Sci. Technol., **8**, pp. 131–143.

[25] Nyeki, S., Gysel, M., Weingartner, E., Baltensperger, U., Hitzenberger, R., Petzold, A., and Wilson, C. W., 2004, "Properties of Jet Engine Combustion Particles During the PartEmis Experiment: Particle Size Spectra ($d > 15$ nm) and Volatility," Geophys. Res. Lett., **31**, p. L18105.

[26] Petzold, A., Stein, C., Nyeki, S., Gysel, M., Weingartner, E., Baltensperger, U., Giebl, H., Hitzenberger, R., Dopelheuer, A., Vrchoticky, S., Puxbaum, H., Johnson, M., Hurley, C. D., Marsh, R., and Wilson, C. W., 2003, "Properties of Jet Engine Combustion Particles During the PartEmis Experiment: Microphysics and Chemistry," Geophys. Res. Lett., **30**, pp. 1719.

[27] Petzold, A., Gysel, M., Vancassel, X., Hitzenberger, R., Puxbaum, H., Vrochticky, S., Weingartner, E., Baltensperger, U., and Mirabel, P., 2005, "On the Effects of Organic Matter and Sulphur-Containing Compounds on the CCN Activation of Combustion Particles," Atmos. Chem. Phys., **5**, pp. 3187–3203.

[28] Katragkou, E., Wilhelm, S., Arnold, F., and Wilson, C., 2004, "First Gaseous Sulfur [VI] Measurements in the Simulated Internal Flow of an Aircraft Engine During Project PartEmis," Geophys. Res. Lett., **31**, p. L02117.

[29] Rogers, F., Arnott, P., Zielinska, B., Sagebiel, J., Kelly, K. E., Wagner, D., Lighty, J. S., and Sarofim, A. F., 2005, "Real-Time Measurements of Jet Aircraft Engine Exhaust," J. Air Waste Manage. Assoc., **55**, pp. 583–593.

[30] Corporan, E., Monroig, O., Wagner, M., and DeWitt, M. J., 2004, "Influence of Fuel Chemical Composition on Particulate Matter Emissions of a Turbine Engine," *Proceedings of the ASME Turbo Expo*, pp. 1–11.

[31] Corporan, E., DeWitt, M. J., Belovich, V., Pawlik, R., Lynch, A. C., Gord, J. R., and Meyer, T. R., 2007, "Emissions Characteristics of a Turbine Engine and Research Combustor Burning a Fischer-Tropsch Jet Fuel," Energy Fuels, **21**, pp. 2615–2626.

[32] Corporan, E., Quick, A., and DeWitt, M. J., 2008, "Characterization of Particulate Matter and Gaseous Emissions of a C-130H Aircraft," J. Air Waste Manage. Assoc., **58**, pp. 474–483.

[33] Schumann, U., Arnold, F., Busen, R., Curtius, J., Karcher, B., Kiendler, A., Petzold, A., Schlager, H., Schroder, F., and Wohlfrom, K. H., 2002, "Influence of Fuel Sulfur on the Composition of Aircraft Exhaust Plumes: The Experiments SULFUR 1-7," J. Geophys. Res., **107**, p. 4247.

[34] Busen, R., and Buck, A. L., 1995, "Visible Contrail Formation From Fuels With Different Sulfur Contents," Geophys. Res. Lett., **22**, pp. 1357–1360.

[35] Schumann, U., Ström, J., Busen, R., Baumann, R., Gierens, K., Krautstrunk, M., Schröder, F., and Stingl, P. J., 1996, "In Situ Observations of Particles in Jet Aircraft Exhausts and Contrails for Different Sulfur-Containing Fuels," J. Geophys. Res., **101**, pp. 6853–6869.

[36] Brock, C. A., Schröder, F., Karcher, B., Petzold, A., Busen, R., and Fiebig, M., 2000, "Ultrafine Particle Size Distributions Measured in Aircraft Exhaust Plumes," J. Geophys. Res., **105**, pp. 26555–26567.

[37] Paladino, J., Whitefield, P., Hagen, D., Hopkins, A. R., and Trueblood, M., 1998, "Particle Concentration Characterization for Jet Engine Emissions Under Cruise Conditions," Geophys. Res. Lett., **25**, pp. 1697–1700.

[38] Toon, O. B., and Miake-Lye, R. C., 1998, "Subsonic Aircraft: Contrail and Cloud Effects Special Study (SUCCESS)," Geophys. Res. Lett., **25**, pp. 1109–1112.

[39] Anderson, B. E., Cofer, W. R., Bagwell, D. R., Barrick, J. W., Hudgins, C. H., and Brunke, K. E., 1998, "Airborn Observations of Aircraft Aerosol Emissions 1: Total Nonvolatile Particle Emission Indices," Geophys. Res. Lett., **25**, pp. 1689–1692.

[40] Timko, M. T., Herndon, S. C., Wood, E. C., Onasch, T. B., Northway, M. J., Jayne, J. T., Canagaratna, M. R., Miake-Lye, R. C., and Knighton, W. B., 2010, "Gas Turbine Engine Emissions—Part I: Volatile Organic Compounds and Nitrogen Oxides," ASME J. Eng. Gas Turbines Power, **132**(6), p. 061504.

[41] Wey, C. C., Anderson, B. E., Hudgins, C., Wey, C., Li-Jones, X., Winstead, E., Thornhill, L. K., Lobo, P., Hagen, D., Whitefield, P., Yelvington, P. E., Herndon, S. C., Onasch, T. B., Miake-Lye, R. C., Wormhoudt, J., Knighton, W. B., Howard, R., Bryant, D., Corporan, E., Moses, C., Holve, D., and Dodds, W., 2006, "Aircraft Particle Emissions Experiment (APEX)," Report No. NASA/TM-2006-214382.

[42] Liscinsky, D., and Anderson, B. E., "Particle Matter Measurement Methodology for Aircraft," unpublished.

[43] Petzold, A., Schloesser, H., Sheridan, P. J., Arnott, W., Ogren, J. A., and Virkkula, A., 2005, "Evaluation of Multiangle Absorption Photometry for Measuring Aerosol Light Absorption," Aerosol Sci. Technol., **39**, pp. 40–51.

[44] Petzold, A., and Schönlinner, M., 2004, "Multi-Angle Absorption Photometry: A New Method for the Measurement of Aerosol Light Absorption and Atmospheric Black Carbon," J. Aerosol Sci., **35**, pp. 421–441.

[45] Jayne, J. T., Leard, D. C., Zhang, X. F., Davidovits, P., Smith, K. A., Kolb, C. E., and Worsnop, D. R., 2000, "Development of an Aerosol Mass Spectrometer for Size and Composition Analysis of Submicron Particles," Aerosol Sci. Technol., **33**, pp. 49–70.

[46] Canagaratna, M. R., Jayne, J. T., Jimenez, J. L., Allan, J. D., Alfarra, M. R., Zhang, Q., Onasch, T. B., Drewnick, F., Coe, H., Middlebrook, A., Delia, A., Williams, L. R., Trimborn, A. M., Northway, M. J., DeCarlo, P. F., Kolb, C. E., Davidovits, P., and Worsnop, D. R., 2007, "Chemical and Microphysical Characterization of Ambient Aerosols With the Aerodyne Aerosol Mass Spectrometer," Mass Spectrom. Rev., **26**, pp. 185–222.

[47] Drewnick, F., Hings, S. S., DeCarlo, P. F., Jayne, J. T., Gonin, M., Fuhrer, K., Weimer, S., Jimenez, J. L., Demerjian, K. L., Borrmann, S., and Worsnop, D. R., 2005, "A New Time-of-Flight Aerosol Mass Spectrometer (ToF-AMS)—Instrument Description and First Field Deployment," Aerosol Sci. Technol., **39**, pp. 637–658.

[48] Liu, P., Ziemann, P. J., Kittelson, D. B., and McMurry, P. H., 1995, "Generating Particle Beams of Controlled Dimensions and Divergence: I. Theory of Particle Motion in Aerodynamic Lenses and Nozzle Expansions," Aerosol Sci. Technol., **22**, pp. 293–313.

[49] Liu, P., Ziemann, P. J., Kittelson, D. B., and McMurry, P. H., 1995b, "Generating Particle Beams of Controlled Dimensions and Divergence: II. Experimental Evaluation of Particle Motion in Aerodynamic Lenses and Nozzle Expansions," Aerosol Sci. Technol., **22**, pp. 314–324.

[50] Liu, P. S. K., Deng, R., Smith, K. A., Williams, L. R., Jayne, J. T., Canagaratna, M. R., Moore, K., Onasch, T. B., Worsnop, D. R., and Deshler, T., 2007, "Transmission Efficiency of an Aerodynamic Focusing Lens System: Comparison of Model Calculations and Laboratory Measurements for the Aerodyne Aerosol Mass Spectrometer," Aerosol Sci. Technol., **41**, pp. 721–733.

[51] DeCarlo, P. F., Kimmel, J. R., Trimborn, A., Northway, M. J., Jayne, J. T., Aiken, A. C., Gonin, M., Fuhrer, K., Horvath, T., Docherty, K. S., Worsnop, D. R., and Jimenez, J. L., 2006, "Field-Deployable, High-Resolution, Time-of-Flight Aerosol Mass Spectrometer," Anal. Chem., **78**, pp. 8281–8289.

[52] Allan, J. D., Coe, H., Bower, K. N., Alfarra, M. R., Delia, A. E., Jimenez, J. L., Middlebrook, A. M., Drewnick, F., Onasch, T. B., Canagaratna, M. R., Jayne, J. T., and Worsnop, D. R., 2004, "Technical Note: Extraction of Chemically Resolved Mass Spectra From Aerodyne Aerosol Mass Spectrometer Data," J. Aerosol Sci., **35**, pp. 909–922.

[53] DeCarlo, P., Slowik, J. G., Worsnop, D. R., Davidovits, P., and Jiménez, J. L., 2004, "Particle Morphology and Density Characterization by Combined Mobility and Aerodynamic Diameter Measurements. Part 1: Theory," Aerosol Sci. Technol., **38**, pp. 1185–1205.

[54] Slowik, J. G., Stainken, K., Davidovits, P., Williams, L. R., Jayne, J. T., Kolb, C. E., Worsnop, D. R., Rudich, Y., DeCarlo, P., and Jiménez, J. L., 2004, "Particle Morphology and Density Characterization by Combined Mobility and Aerodynamic Diameter Measurements. Part 2: Application to Combustion Generated Soot Aerosols as a Function of Fuel Equivalence Ratio," Aerosol Sci. Technol., **38**, pp. 1206–1222.

[55] Herndon, S. C., Rogers, T., Dunlea, E. J., Jayne, J. T., Miake-Lye, R., and Knighton, B., 2006, "Hydrocarbon Emissions From In-Use Commercial Aircraft During Airport Operations," Environ. Sci. Technol., **40**, pp. 4406–4413.

[56] Bevington, P. R., and Robinson, D. K., 1992, *Data Reduction and Error Analysis in the Physical Sciences*, 2nd ed., McGraw-Hill, New York, Chap. 3.

[57] Yang, Y., Boehman, A. L., and Santoro, R. J., 2007, "A Study of Jet Fuel Sooting Tendency Using the Threshold Sooting Index (TSI) Model," Combust. Flame, **149**, pp. 191–205.

[58] Sampath, P., Gratton, M., Kretschmer, D., and Odgers, J., 1986, "Fuel Property Effects Upon Exhaust Smoke and the Weak Extinction Characteristics of the Pratt and Whitney PT6A-65 Engine," ASME J. Eng. Gas Turbines Power, **108**, pp. 175–181.

[59] Pande, S. G., and Hardy, D. R., 1995, "An In-Depth Evaluation of Combustion Performance Predictors of Aviation Fuels Sooting Tendencies," Energy Fuels, **9**, pp. 448–457.

[60] Lefebvre, A. H., 1998, *Gas Turbine Combustion*, Taylor & Francis, Ann Arbor, MI, Chap. 9.

[61] Lukachko, S. P., Waitz, I. A., Miake-Lye, R. C., and Brown, R. C., 2008, "Engine Design and Operational Impacts on Particulate Matter Precursor Emissions," ASME J. Eng. Gas Turbines Power, **130**, p. 021505.

[62] Kolb, C. E., Jayne, J. T., Worsnop, D. R., Molina, M. J., Meads, R. F., and Viggiano, A. A., 1994, "Gas Phase Reaction of Sulfur Trioxide With Water Vapor," J. Am. Chem. Soc., **116**, pp. 10314–10315.

[63] Zhang, D., and Zhang, R., 2005, "Laboratory Investigation of Heterogeneous Interaction of Sulfuric Acid With Soot," Environ. Sci. Technol., **39**, pp. 5722–5728.

[64] Karcher, B., 1998, "Physicochemistry of Aircraft-Generated Liquid Aerosols, Soot, and Ice Particles. 1. Model Descriptions," J. Geophys. Res., **103**, pp. 17111–17128.

[65] Curtius, J., Arnold, F., and Schulte, P., 2002, "Sulfuric Acid Measurements in the Exhaust Plume of a Jet Aircraft in Flight: Implications for the Sulfuric Acid Formation Efficiency," Geophys. Res. Lett., **29**, pp. 1113.

[66] American Society for Testing and Materials (ASTM), 1998, "Standard Test Method for Sulfur in Petroleum and Petroleum Products by Energy-Dispersive X-Ray Fluorescence Spectrometry," ASTM Paper No. 4294-98, pp. 1–5.

[67] Winder, C., and Balouet, J. C., 2002, "The Toxicity of Commercial Jet Oils," Environ. Res., **89**, pp. 146–164.

[68] van Netten, C., and Leung, V., 2001, "Hydraulic Fluids and Jet Engine Oil: Pyrolysis and Aircraft Air Quality," Arch. Environ. Health, **56**, pp. 181–186.

[69] Craig, P. H., and Barth, M. L., 1999, "Evaluation of the Hazards of Industrial Exposure to Tricresyl Phosphate: A Review and Interpretation of the Literature," J. Toxicol. Environ. Health, **2**, pp. 281–300.

[70] Mackerer, C. R., Barth, M. L., Krueger, A. J., Chawla, B., and Roy, T. A., 1999, "Comparison of Neurotoxic Effects and Potential Risks From Oral Administration or Ingestion of Tricresyl Phosphate and Jet Engine Oil Containing

Downloaded 02 Jun 2010 to 171.66.16.96. Redistribution subject to ASME license or copyright; see http://www.asme.org/terms/Terms_Use.cfm

Tricresyl Phosphate," J. Toxicol. Environ. Health A, **56**, pp. 293–328.

[71] Wyman, J., Pitzer, E., Williams, F., Rivera, J., Durkin, A., Gehringer, J., Serve, P., Vonminden, D., and Macys, D., 1993, "Evaluation of Shipboard Formation of a Neurotoxicant (Trimethylpropane Phosphate) From Thermal Decomposition of Synthetic Aircraft Engine Lubricant," Am. Ind. Hyg. Assoc. J., **54**, pp. 584–592.

[72] Canagaratna, M. R., Jayne, J. T., Ghertner, D. A., Herndon, S., Shi, Q., Jimenez, J. L., Silva, P. J., Williams, P., Lanni, T., Drewnick, F., Demerjian, K. L., Kolb, C. E., and Worsnop, D. R., 2004, "Chase Studies of Particulate Emissions From In-Use New York City Vehicles," Aerosol Sci. Technol., **38**, pp. 555–573.

[73] Wong, H.-W., Yelvington, P. E., Timko, M. T., Onasch, T. B., and Miake-Lye, R. C., 2008, "Microphysical Modeling of Ground-Level Aircraft-Emitted Aerosol Formation: Roles of Sulfur-Containing Species," J. Propul. Power, **24**, pp. 590–602.

[74] Zhang, R., Suh, I., Zhao, J., Zhang, D., Fortner, E. C., Tie, X., Molina, L. T., and Molina, M. J., 2004, "Atmospheric New Particle Formation Enhanced by Organic Acids," Science, **304**, pp. 1487–1490.

Downloaded 02 Jun 2010 to 171.66.16.96. Redistribution subject to ASME license or copyright; see http://www.asme.org/terms/Terms_Use.cfm

Detailed Numerical Simulations of the Primary Atomization of a Turbulent Liquid Jet in Crossflow

Marcus Herrmann
Department of Mechanical and Aerospace Engineering,
Arizona State University,
Tempe, AZ 85287
e-mail: marcus.herrmann@asu.edu

This paper presents numerical simulation results of the primary atomization of a turbulent liquid jet injected into a gaseous crossflow. Simulations are performed using the balanced force refined level set grid method. The phase interface during the initial breakup phase is tracked by a level set method on a separate refined grid. A balanced force finite volume algorithm together with an interface projected curvature evaluation is used to ensure the stable and accurate treatment of surface tension forces even on small scales. Broken off, small scale nearly spherical drops are transferred into a Lagrangian point particle description allowing for full two-way coupling and continued secondary atomization. The numerical method is applied to the simulation of the primary atomization region of a turbulent liquid jet ($q=6.6$, $We=330$, $Re=14,000$) injected into a gaseous crossflow ($Re=570,000$), analyzed experimentally by Brown and McDonell (2006, "Near Field Behavior of a Liquid Jet in a Crossflow," ILASS Americas, 19th Annual Conference on Liquid Atomization and Spray Systems). The simulations take the actual geometry of the injector into account. Grid converged simulation results of the jet penetration agree well with experimentally obtained correlations. Both column/bag breakup and shear/ligament breakup modes can be observed on the liquid jet. A grid refinement study shows that on the finest employed grids (flow solver 64 points per injector diameter, level set solver 128 points per injector diameter), grid converged drop sizes are achieved for drops as small as one-hundredth the size of the injector diameter. [DOI: 10.1115/1.4000148]

1 Introduction

The atomization of turbulent liquid jets injected into fast moving subsonic gaseous crossflows is an important application for example in gas turbines, ramjets, and augmentors. It is a highly complex process that has been extensively studied experimentally over the past decades. Early studies of the atomization of nonturbulent liquid jets in crossflows have recently been reviewed in Ref. [1], whereas newer studies of this case include the work reported in Refs. [1–8]. Most experimental work has focused on jet penetration, including both the column trajectory and the resulting spray penetration. Some recent jet penetration correlations can be found in Refs. [4,8]. Unlike turbulent liquid jets atomized either by injection into still air or by a coflowing fast moving gas stream, experimental access to the primary atomization region of liquid jets injected into crossflows is relatively straightforward. This is due to the fact that at least the windward side of the liquid jet is typically not surrounded by many drops that could otherwise conceal the jet phase interface geometry. This is not, however, typically the case for the leeward side. Still, experimental studies of nonturbulent liquid jets injected into subsonic crossflows have concluded that depending on the momentum flux ratio and the crossflow Weber number, essentially two different breakup modes can be observed [8]. For low momentum flux ratios and crossflow Weber numbers, the liquid jet breaks up as a whole some distance downstream of the injector. For high momentum flux ratios and crossflow Weber numbers, on the other hand, surface breakup or stripping at the sides of the liquid jets is observed prior to column breakup [8]. Unlike nonturbulent jets, turbulent liquid jets do not exhibit this clear separation of breakup modes [9]. Stripping at the sides of the liquid column occurs even at low Weber numbers, where nonturbulent jets exhibit only the column-breakup mode. Turbulence initiates the generation of ligaments that then break up due to the Raleigh mechanism [9].

Even though at least some level of consensus exists concerning the dominant breakup modes, modeling attempts of the atomization process have had mixed results. While correlations for jet penetration derived from experimental data give good agreement for parameter ranges and configurations for which they were developed, numerical simulations predicting the jet penetration, drop sizes, and liquid volume fluxes have had mixed success [1,10,11]. This is in part due to the fact that under most operating conditions, turbulence interaction is strong and several different atomization mechanisms occur on the jet's surface at the same time. Detailed numerical simulations can help study these simultaneously occurring mechanisms, even in regions of the liquid jet where traditional experimental methods cannot observe the phase interface dynamics.

Although detailed simulations solve the Navier–Stokes equations directly, it is incumbent on any numerical simulation to demonstrate that spatial and temporal discretization errors are not unduly impacting the obtained results. It is this required grid independence of the numerical results that has yet to be demonstrated in numerical simulations of the primary atomization of high speed liquid jets [12–16]. Besides the enormous resolution requirement, detailed numerical simulations are challenging because one not only has to track the position of the liquid/gas interface and handle a large number of topology changes, but one also has to account for the fact that the phase interface is a discontinuity and the surface tension force represents a singular force [17]. Treating the surface tension force numerically in a stable and accurate manner is of crucial importance, since breakup by definition involves small scales where capillary forces are dominant.

The outline of this paper is as follows: after summarizing the governing equations, the numerical methods employed to solve them are briefly outlined. Finally detailed simulation results of the

---

Manuscript received May 5, 2009; final manuscript received May 6, 2009; published online March 30, 2010. Review conducted by Dilip R. Ballal.

Copyright © 2010 by ASME

Downloaded 02 Jun 2010 to 171.66.16.96. Redistribution subject to ASME license or copyright; see http://www.asme.org/terms/Terms_Use.cfm

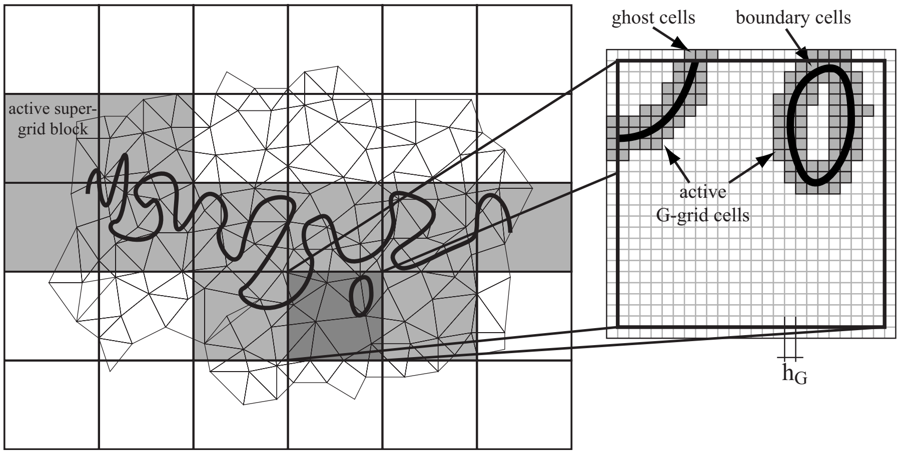

Fig. 1 RLSG grid structure

primary atomization of a turbulent liquid jet ($q=6.6$, We $=330$, Re$=14,000$) injected into a gaseous crossflow (Re $=570,000$) analyzed experimentally in Ref. [2] will be presented and discussed.

2 Governing Equations

The equations governing the motion of an unsteady incompressible immiscible two-fluid system are the Navier–Stokes equations

$$\frac{\partial u}{\partial t} + u \cdot \nabla u = -\frac{1}{\rho}\nabla p + \frac{1}{\rho}\nabla \cdot (\mu(\nabla u + \nabla^T u)) + \frac{1}{\rho}T_\sigma \qquad (1)$$

where u is the velocity, ρ is the density, p is the pressure, μ is the dynamic viscosity, and T_σ is the surface tension force, which is nonzero only at the location of the phase interface x_f. Furthermore, the continuity equation results in a divergence-free constraint on the velocity field, $\nabla \cdot u=0$. The phase interface location x_f between the two fluids is described by a level set scalar G, with

$$G(x_f,t) = 0 \qquad (2)$$

at the interface, $G(x,t)>0$ in fluid 1, and $G(x,t)<0$ in fluid 2. Differentiating Eq. (2) with respect to time yields

$$\frac{\partial G}{\partial t} + u \cdot \nabla G = 0 \qquad (3)$$

Assuming ρ and μ are constant within each fluid, density and viscosity at any point x can be calculated from

$$\rho(x) = H(G)\rho_1 + (1 - H(G))\rho_2 \qquad (4)$$

$$\mu(x) = H(G)\mu_1 + (1 - H(G))\mu_2 \qquad (5)$$

where indices 1 and 2 denote values in fluid 1, respectively, 2, and H is the Heaviside function. From Eq. (2) it follows that

$$\delta(x - x_f) = \delta(G)|\nabla G| \qquad (6)$$

with δ the Dirac delta function. Furthermore, the interface normal vector n and the interface curvature κ can be expressed in terms of the level set scalar as

$$n = \frac{\nabla G}{|\nabla G|}, \quad \kappa = \nabla \cdot n \qquad (7)$$

Using Eqs. (6) and (7), the surface tension force T_σ can thus be expressed as

$$T_\sigma(x) = \sigma\kappa\delta(x - x_f)n = \sigma\kappa\delta(G)|\nabla G|n \qquad (8)$$

with σ the surface tension coefficient.

3 Numerical Methods

In this section, we first briefly summarize the refined level set grid (RLSG) method used to track the phase interface during primary atomization. Then, the level set-based balanced force algorithm is reviewed that allows for the accurate and stable treatment of surface tension forces. Finally the coupling procedure of the RLSG tracked phase interface to the Lagrangian point particle method is described.

4 Refined Level Set Grid Method

In the RLSG method, all level set-related equations are evaluated on a separate equidistant Cartesian grid using a dual-narrow band methodology for efficiency. This so-called G-grid is overlaid onto the flow solver grid on which the Navier–Stokes equations are solved and can be independently refined, providing high resolution of the tracked phase interface geometry, see Fig. 1. Details of the method, i.e., narrow band generation, level set transport, re-initialization, curvature evaluation, and its performance compared with other interface tracking methods in generic advection test cases, can be found in Ref. [18].

In the current simulations, refinement of the G-grid is limited to a factor two in each spatial direction as compared with the flow solver grid. While higher refinements are feasible from an efficiency standpoint, they would require the use of a subflow solver grid model to correctly capture the otherwise nonresolved phase interface dynamics on the G-grid scale [19]. Instead, here, the refined G-grid simply serves to increase the accuracy of the level set-based phase interface tracking scheme.

5 Balanced Force Algorithm

In the Navier–Stokes equations, the position of the phase interface influences two different terms. The first term is due to Eqs. (4) and (5), since $H(G)$ is a function of the position of the phase interface. For finite volume formulations, the volume fraction ψ_{cv} of a control volume is defined as

$$\psi_{\text{cv}} = 1/V_{\text{cv}} \int_{V_{\text{cv}}} H(G)dV \qquad (9)$$

with V_{cv} the volume of the control volume cv. In the RLSG method, the above integral is evaluated using the high-resolution G-grid, see Refs. [18,20] for a detailed description. Then both control volume density and viscosity are simply

$$\rho_{\text{cv}} = \psi_{\text{cv}}\rho_1 + (1 - \psi_{\text{cv}})\rho_2 \qquad (10)$$

$$\mu_{\text{cv}} = \psi_{\text{cv}}\mu_1 + (1 - \psi_{\text{cv}})\mu_2 \qquad (11)$$

Downloaded 02 Jun 2010 to 171.66.16.96. Redistribution subject to ASME license or copyright; see http://www.asme.org/terms/Terms_Use.cfm

The second term that is a function of the interface position is the surface tension force term, Eq. (8). Here it is critical for stability and accuracy that the surface tension force can be balanced by the pressure gradient (jump) across the phase interface exactly on the discrete level. This is ensured by the balanced force approach [18,21] based on the continuum surface force (CSF) model [22]. Then the surface tension force at the control volume face f is

$$T_{\sigma_f} = \sigma \kappa_f (\nabla \psi)_f \tag{12}$$

with the phase interface curvature at the control volume face

$$\kappa_f = \frac{\alpha_{\mathrm{cv}} \kappa_{\mathrm{cv}} + \alpha_{nbr} \kappa_{nbr}}{\alpha_{\mathrm{cv}} + \alpha_{nbr}} \tag{13}$$

where nbr is the control volume sharing the face with cv, and

$$\alpha_{\mathrm{cv}} = \begin{cases} 1 & : \quad 0 < \psi_{\mathrm{cv}} < 1 \\ 0 & : \quad \text{otherwise} \end{cases} \tag{14}$$

The control volume curvature κ_{cv} is calculated from the phase interface geometry on the high-resolution G-grid using a second-order accurate interface projected curvature calculation method [18]. A detailed description of the balanced force algorithm for the RLSG level set method and its performance compared with alternative numerical methods in a range of test cases involving capillary forces can be found in Ref. [18].

6 Coupling to Lagrangian Spray Model

Atomization typically produces a vast number of both large and small scale drops. Resolving the geometry by tracking the phase interface associated with each of the resulting drops quickly becomes prohibitively expensive, such that a different numerical description has to be employed. An alternative approach is to introduce simplifying assumptions concerning the drop shape and treat all drops smaller than a cut-off length scale in a point particle, Lagrangian frame. One of the typical prerequisite of such standard spray models is that the drop size be smaller that the flow solver grid size. Note that the RLSG approach can resolve and track subflow solver sized liquid structures. Drop transfer is initiated if a separated liquid structure has a liquid volume

$$V_D \le V_{\mathrm{trans}} \tag{15}$$

and its shape is nearly spherical

$$r_{\max} \le \alpha \left(\frac{3}{4\pi} V_D \right)^{1/3} \tag{16}$$

with typically $\alpha=2$ and $r_{\max}$ the maximum distance of the liquid structure's surface to its center of mass. This second criterion ensures that small scale detached ligament structures that would fulfill the first criterion are not transferred and replaced by spherical drops, since these ligaments often continue to break up by capillary instabilities producing a range of small scale drops. Not prematurely transferring stretched out structures thus allows this breakup process to be simulated directly instead of relying on secondary atomization models for the Lagrangian description. Further details concerning the application of the Lagrangian spray model coupling procedure can be found in Refs. [23,24].

In the Lagrangian description, full two-way momentum coupling between the drop and continuous phase is used including a stochastic secondary atomization model [25]. However, the cell volume occupied by the Lagrangian drops is not explicitly taken into account and neither drop/drop nor drop/tracked phase interface collisions are modeled. But as long as liquid structures have not been transferred into the Lagrangian description, i.e., they are still tracked by the level set scalar, secondary breakup, cell volume effects, and all collisions are fully captured.

7 Employed Solvers

In this work we use the flow solver CDP/CHARLES that solves the incompressible two-phase Navier–Stokes equations on unstructured grids using the finite volume balanced force algorithm [18]. In the single phase regions, the employed scheme conserves the kinetic energy discretely. Turbulence in the single phase regions of the flow is modeled using a dynamic Smagorinsky large eddy simulations (LES) model, however, none of the terms arising from filtering the phase interface are modeled. The approach instead relies on resolving all relevant scales at the phase interface, thus, ideally reverting to a direct numerical simulation (DNS) at the phase interface. As such, the current simulation approach is a combination of LES in the single phase regions and ideally DNS at the phase interface. A Lagrangian particle/parcel technique is employed to model the small scale liquid drops of the atomizing liquid spray [26].

Table 1 Operating conditions and characteristic numbers

	Experiment	Simulation
Jet exit diameter D (mm)	1.3	1.3
Crossflow density ρ_c (kg/m^3)	1.225	1.225
Jet density ρ_j (kg/m^3)	1000	12.25
Crossflow velocity u_c (m/s)	120.4	120.4
Jet velocity u_j (m/s)	10.83	97.84
Crossflow viscosity μ_c (kg/ms)	1.82×10^{-5}	1.82×10^{-5}
Jet viscosity μ_j (kg/ms)	1.0×10^{-3}	1.11×10^{-4}
Surface tension coeff. σ (N/m)	0.07	0.07
Momentum flux ratio q	6.6	6.6
Crossflow Weber number We_c	330	330
Jet Weber number We_j	2178	2178
Crossflow Reynolds number Re_c	5.7×10^5	5.7×10^5
Jet Reynolds number Re_j	14,079	14,079

The liquid/gas phase interface during primary atomization is tracked by the interface tracking software LIT, using the RLSG method [18]. The solver uses a fifth-order WENO scheme [27] in conjunction with a third order TVD Runge–Kutta time discretization [28]. The phase interface's curvature on the level set grid is evaluated using a second-order accurate interface projection method [18].

The flow solver CDP/CHARLES and the interface tracking software LIT are coupled using the parallel multicode coupling library CHIMPS [18,29]. In order to couple the level set equation to the Navier–Stokes equation, u in Eq. (3) is calculated from the flow solver velocity by trilinear interpolation. To achieve overall second-order accuracy in time, the level set equation is solved staggered in time with respect to the Navier–Stokes equations.

8 Computational Domain and Operating Conditions

The case analyzed in this paper is one studied experimentally by Brown and McDonell [2]. Table 1 summarizes the operating conditions and resulting characteristic numbers. Note that although the density ratio is artificially reduced from the experimental values, all relevant characteristic numbers, i.e., momentum flux ratio q, crossflow Weber number We_c, jet Weber number We_j, crossflow Reynolds number Re_c, and jet Reynolds number Re_j, are the same as in the experiment.

Figure 2 depicts the computational domain and the used boundary conditions, as well as a zoom into the near-injector region to show the mesh detail used in the simulations. The chosen computational domain $(-25D \ldots 50D \times 0 \ldots 25D \times -10D \ldots 10D)$ is smaller than the channel used in the experiment $(-77D \ldots 127D \times 0 \ldots 54D \times -27D \ldots 27D)$. However, simulations using the full experimental channel geometry were conducted to verify that the reduced computational domain does not impact the reported results.

The injector geometry used in the experiments consists of a long initial pipe section of diameter 7.49 mm, followed by a 138 deg angled taper section, followed by a short pipe section of diameter D with $L/D=4$, whose exit is mounted flush with the

Downloaded 02 Jun 2010 to 171.66.16.96. Redistribution subject to ASME license or copyright; see http://www.asme.org/terms/Terms_Use.cfm

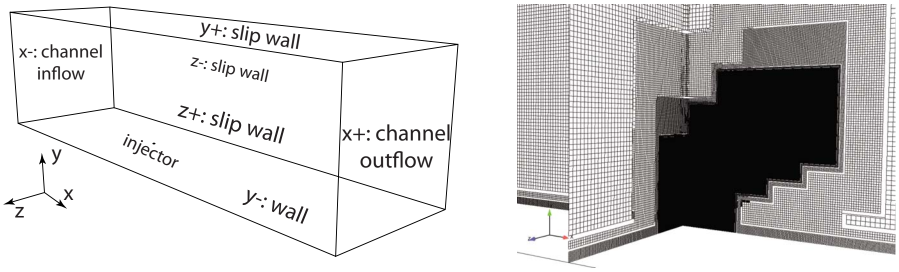

Fig. 2 Computational domain and boundary conditions (left) and mesh detail near the injector (right)

lower channel wall. The experiments conducted for this injector geometry suggest that the specifics of the liquid velocity distribution in the injector exit plane can have a large impact on the resulting atomization process of the liquid jet [2,3]. Both the discharge coefficient of the nozzle and the geometry of the taper region are critical. To account for their effect in the atomization simulations, detailed single phase large eddy simulations of the pretaper pipe, the taper, the post-taper pipe, and the crossflow channel in the vicinity of the injector exit were performed using a dynamic Smagorinsky model. The channel section was included in these simulations to capture the effect of the crossflow on the injector exit plane velocity distribution. The simulations were performed using the correct experimental momentum flux ratio and Reynolds number, see Table 1. Inflow boundary conditions for the pretaper pipe were taken from a precomputed LES pipe flow simulation database at the appropriate Reynolds number. The injector exit plane velocity distributions were then stored as a time sequence in a database to be used in the subsequent two-phase atomization simulations.

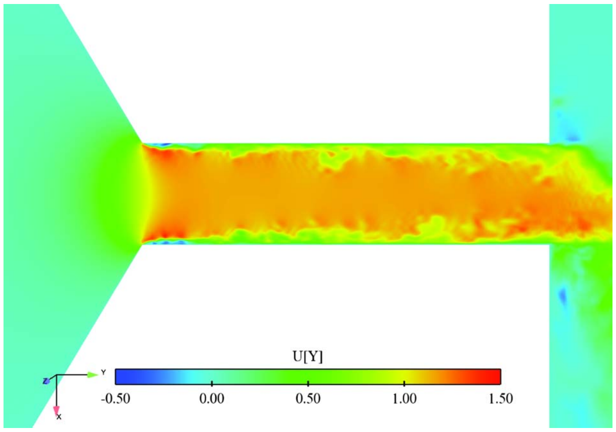

Fig. 3 Zoom of the instantaneous axial velocity distribution in the injector midplane

Figure 3 shows part of the injector simulation depicting the axial velocity distribution in the post-taper pipe section of the injector. All velocities are made dimensionless with the corresponding bulk jet velocity u_j. The effect of the sharp corners at the end of the taper are clearly visible, generating both recirculation regions in the pipe immediately following the corners and significant velocity fluctuations further downstream.

Figure 4 shows an example of the velocity distributions in the injector exit plane that are stored in the database for use as inflow boundary conditions in the crossflow atomization simulations. The effect of the channel crossflow is clearly visible in the shift of the axial velocity distribution in the downstream channel direction.

The two-phase atomization simulations were performed using three different grids of increasing resolution in order to address the important question of how much the employed grid resolution impacts the atomization results. Table 2 summarizes the meshes employed in the three cases c01, c12, and c23. The flow solver grid consists of hexahedra of edge length $D/4$, which are isotropically refined in layers near the injector and lower channel walls, such that the spatial region where the phase interface is tracked is completely filled with equidistant grid cells of the minimum cell size Δx reported in Table 2, see also Fig. 2. Note that in each case, the G-grid is a factor 2 finer than the flow solver grid in order to enhance numerical accuracy of the interface tracking scheme. Separate simulations were conducted to ensure that this does not negatively impact the resulting drop size distributions, i.e., using a flow solver minimum grid size equal to the respective G-grid size yielded virtually identical drop size distributions.

At $t=0$, the liquid jet is initialized in the computational domain by a small cylindrical section of length D capped by a half-sphere protruding into the crossflow channel.

9 Results and Discussion

Figure 5 shows the temporal evolution of the level set tracked liquid mass for the three different grid resolutions. All cases show an initial linear increase. This is due to the fact that at this early stage, almost no small scale drops are generated that would be transferred out of the tracked and into the Lagrangian representa-

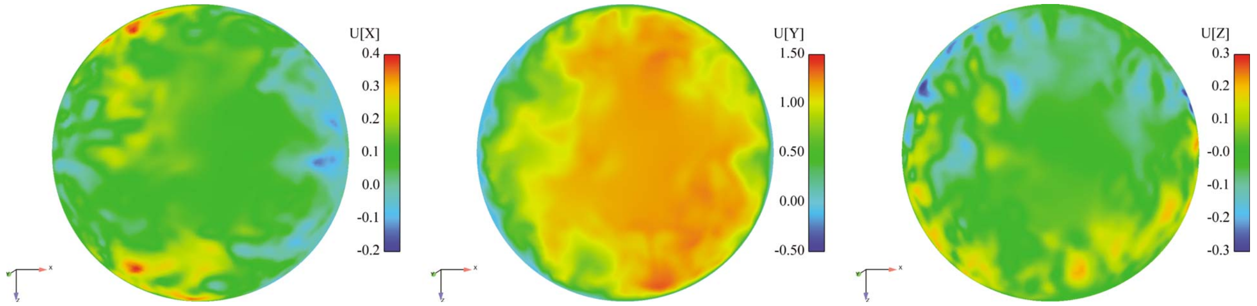

Fig. 4 Instantaneous injector exit plane velocity distributions. From left to right: crossflow direction, axial direction, and transverse direction.

Downloaded 02 Jun 2010 to 171.66.16.96. Redistribution subject to ASME license or copyright; see http://www.asme.org/terms/Terms_Use.cfm

Table 2 Grid resolution and mesh sizes

Case	c01	c12	c23
Flow solver min Δx	$D/16$	$D/32$	$D/64$
RLSG Δx_G	$D/32$	$D/64$	$D/128$
Flow solver mesh size (1×10^6)	8.7	21	110
RLSG max active cells (1×10^6)	3.5	13	66

tion. Then at around $t=5$, significant numbers of small scale drops that fulfill the transfer criterion start to be generated resulting in a slower increase in the tracked mass until at around $t=20$ a statistically steady state is reached. From this point on, a balance exists between the injected liquid mass and the atomized liquid mass that is transferred into the Lagrangian description. It is interesting to note that the coarse grid simulation c01 tends to a larger value of the tracked liquid mass, whereas the two higher resolution cases result in slightly smaller but similar values. This appears to be due to the fact that for the coarse grid simulations, small scale unresolved turbulent eddies cannot initiate atomization, thus, resulting in a smaller transfer rate per phase interface area. The higher resolution cases, on the other hand, do resolve significantly more small scale turbulent eddies that can corrugate the interface and thus initiate atomization quicker. This conjecture is supported by analyzing the instantaneous phase interface geometries shown in Figs. 7–9 that show significantly more small scale structures with increasing grid resolution. Since Fig. 5 indicates that a steady state is reached for $t>20$, all statistics presented in the following are evaluated only for $t>20$ for a total of 43 time units for case c01, 35 time units for case c12, and 8.1 time units for case c23.

Figure 6 shows averaged side views of the atomizing liquid jets evaluated for $t>20$. The jet penetration is compared with the predictions of two common correlations for the penetration of the upper edge of the liquid jet derived by fitting experimental data, namely

$$\frac{y}{D} = 1.37\left(q\frac{x}{D}\right)^{1/2} \tag{17}$$

due to work of Wu et al. [8] valid in the near-injector region only (shown in upper curve) and

$$\frac{y}{D} = 2.63q^{0.442}\left(\frac{x}{D}\right)^{0.39}\mathrm{We}^{-0.088}\left(\frac{\mu_l}{\mu_{\mathrm{H_2O}}}\right)^{-0.027} \tag{18}$$

due to the work of Stenzler et al. [4] (shown in lower curve). Recent experimental observations reported in Ref. [2] show better agreement with the latter correlation even in the near-injector region. This is the case in the simulation results as well. Figure 6 shows better agreement with the correlation of Stenzler et al. [4] and thus also to the experimental results [2]. Note that there is virtually no difference between the three different resolution cases, indicating that even for coarse grids, good jet penetration results can be obtained.

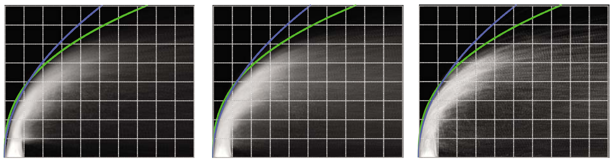

Fig. 6 Impact of grid resolution on averaged side view of the liquid jet; case c01 (left), c12 (center), and c23 (right). Jet penetration is compared with correlations due to Wu et al. [8] (upper curve) and Stenzler et al. [4] (lower curve).

Figures 7–9 show snapshots of the atomizing liquid jets at different times and different grid resolutions viewed from the side, the front, and the top. Two main simultaneous atomization mechanisms can be observed. All cases show instability waves being generated, predominantly visible on the windward side. These instabilities generate role-ups and continue to grow along the jet axis until they form bag like structures that rupture resulting in a broad range of drop sizes, not unlike the column-breakup mode. It is speculated that this instability mode is due to a Kelvin–Helmholtz instability, however, this conjecture is still to be verified using the generated simulation data. The larger scale instability mode is most clearly visible in the lowest resolution case c01. It is equally present in the higher resolution cases, but there it is overlaid by significant turbulence induced surface corrugations and thus not as visibly pronounced.

In addition to the conjectured column-breakup mode, ligaments are formed at the sides of the liquid jets near the injector exit that stretch out and then break up forming a range of drop sizes. At the current stage, the above description of the breakup mechanism is speculative and still requires a detailed, yet to be performed, quantitative study of the generated time dependent simulation data.

Note that due to the turbulent (chaotic) nature of the flow, it cannot be expected that the instantaneous phase interface geometry shown in Figs. 7–9 converges under grid refinement. Only statistical quantities, such as the mean jet penetration or the drop size distribution, should converge. However, it can be seen that many of the larger scale structures on the liquid jet appear to be similar for all three grid resolutions, indicating that the large scale instability mode generated on the upstream pointing side of the liquid jet might be deterministic and sufficiently resolved even on the coarser grids. However, the higher resolution cases show significantly more fine scale structure on the liquid jet and maintain the thin liquid sheets associated with the bag breakup mode in the upper half of the jet slightly longer. This is due to the fact that unlike on the coarse grid, the artificial grid induced topology

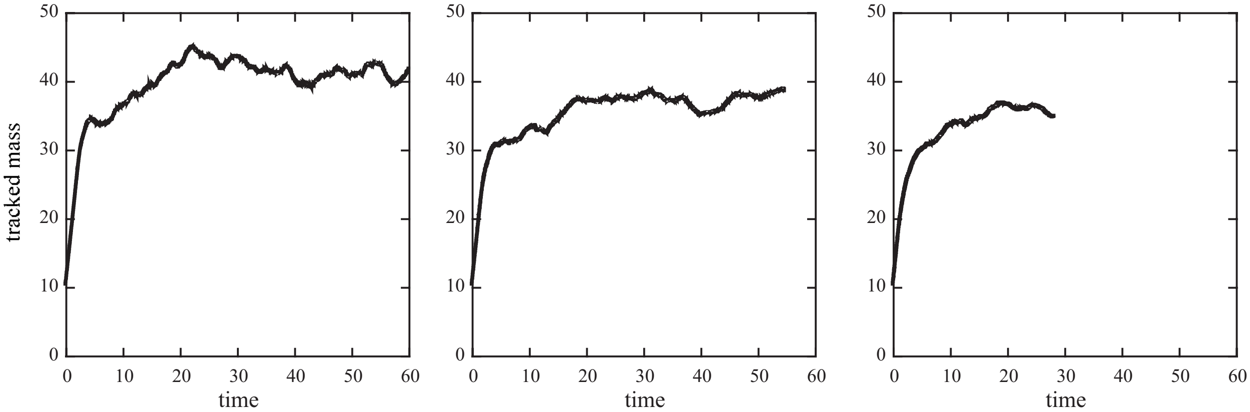

Fig. 5 Temporal evolution of tracked liquid mass for different grid resolutions: case c01 (left), c12 (center), and c23 (right)

Downloaded 02 Jun 2010 to 171.66.16.96. Redistribution subject to ASME license or copyright; see http://www.asme.org/terms/Terms_Use.cfm

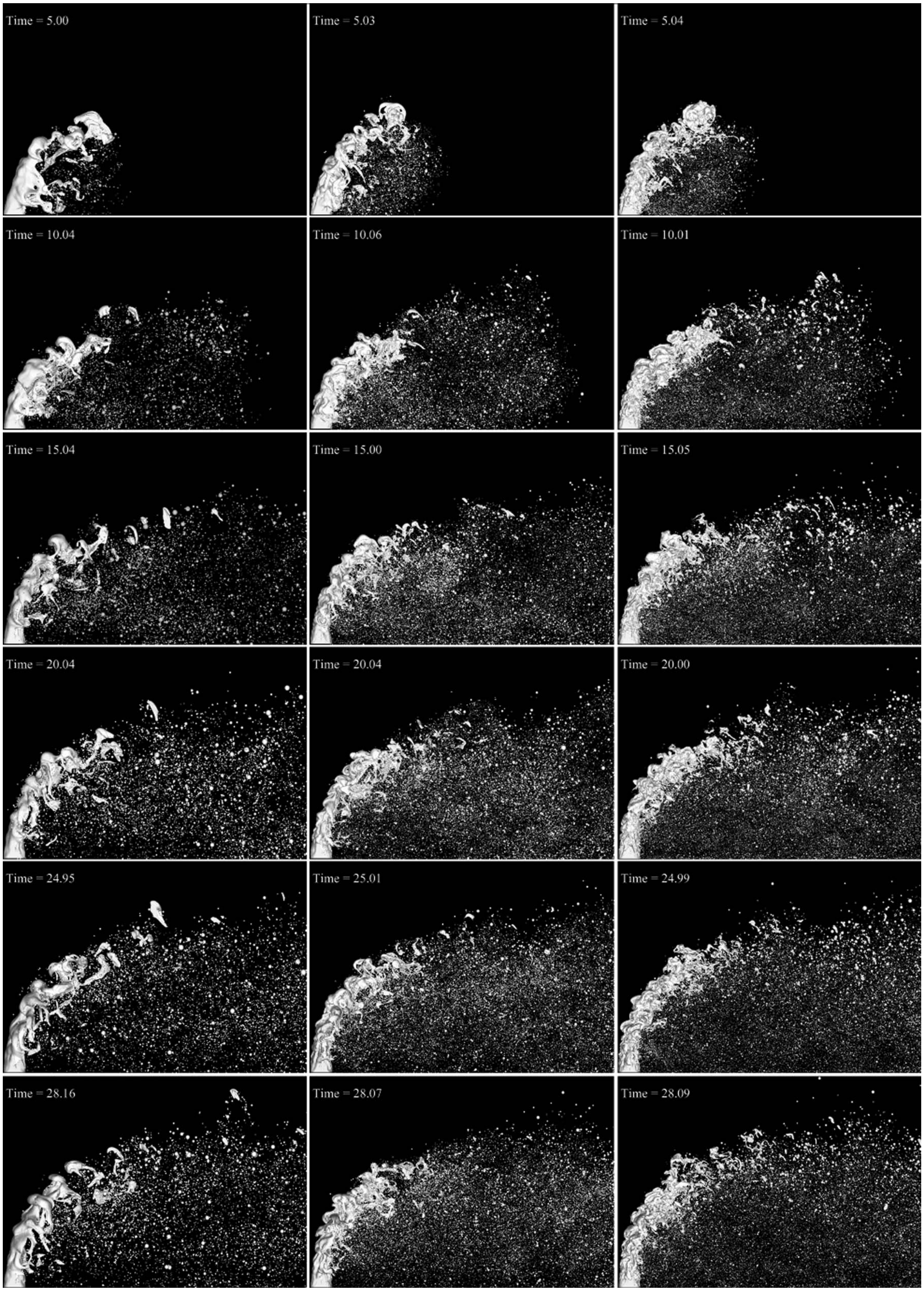

Fig. 7 Side view snapshots of jet in crossflow atomization at $t=5$, 10, 15, 20, 25, and 28.1 time units (top to bottom); case c01 (left), c12 (center), and c23 (right)

change event is slightly delayed because the level set inherent breakup length scale (being equal to the grid size) is reduced. Moreover, the higher resolution cases generate significantly more small scale drops.

Besides mean jet penetration and observed breakup modes, the key quantity to ascertain the quality of a numerical simulation is the grid dependency/independency of the resulting atomized drop size distribution. Figure 10 depicts the calculated drop size distri-

Downloaded 02 Jun 2010 to 171.66.16.96. Redistribution subject to ASME license or copyright; see http://www.asme.org/terms/Terms_Use.cfm

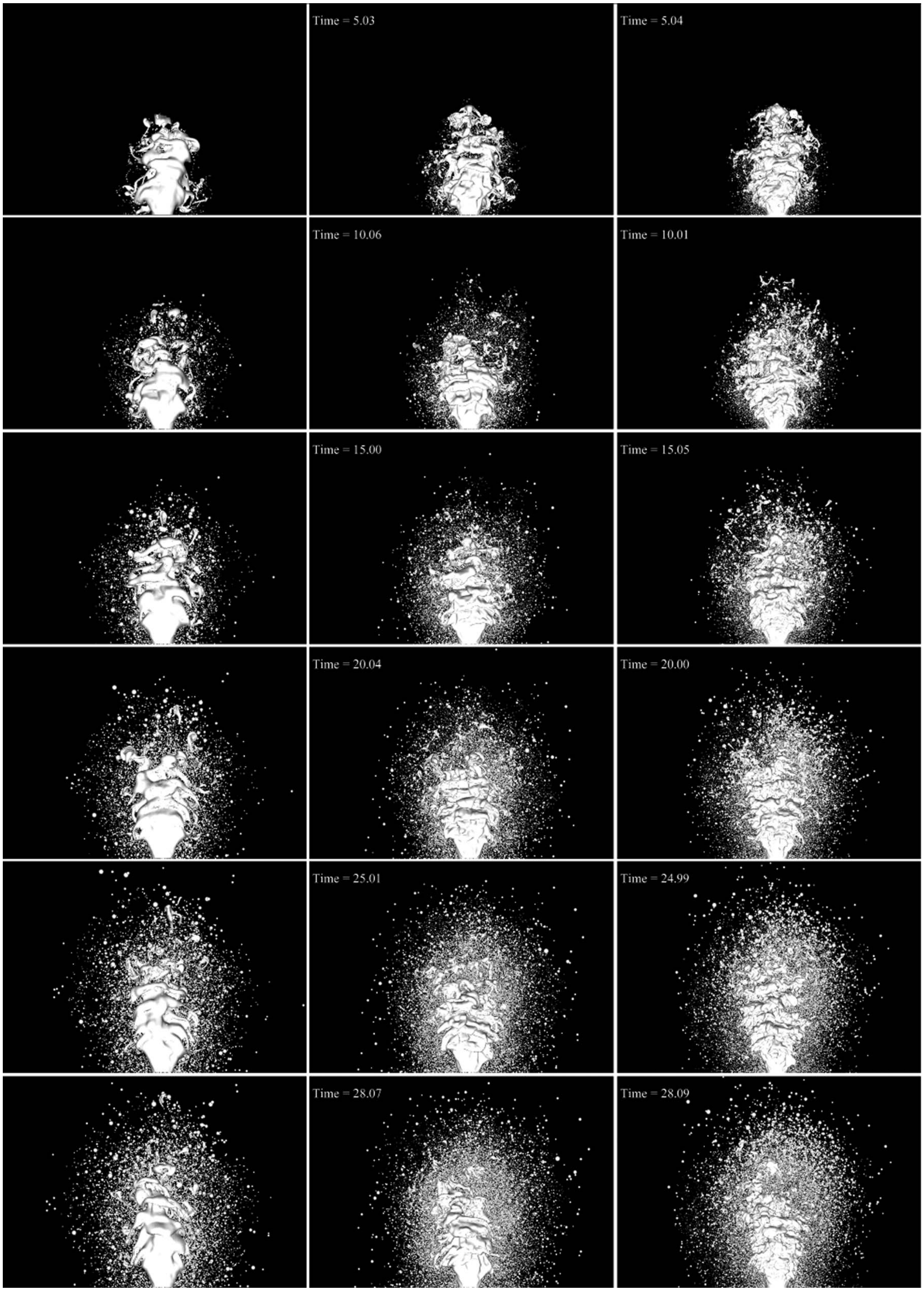

Fig. 8 Front view snapshots of jet in crossflow atomization at $t=5$, 10, 15, 20, 25, and 28.1 time units (top to bottom); case c01 (left), c12 (center), and c23 (right)

butions obtained from the primary atomization at $t>20$ for the three different grid resolutions analyzed in this study. Shown are only those drops that are generated directly from the liquid jet, i.e., drops that are transferred from the level set tracked phase interface representation to the Lagrangian point particle description. Note that these drops can continue to atomize via secondary atomization mechanisms further downstream; however, within the computational domain, only a limited number of these secondary atomization events occur.

The drop size distributions in Fig. 10 were generated by bin-

Downloaded 02 Jun 2010 to 171.66.16.96. Redistribution subject to ASME license or copyright; see http://www.asme.org/terms/Terms_Use.cfm

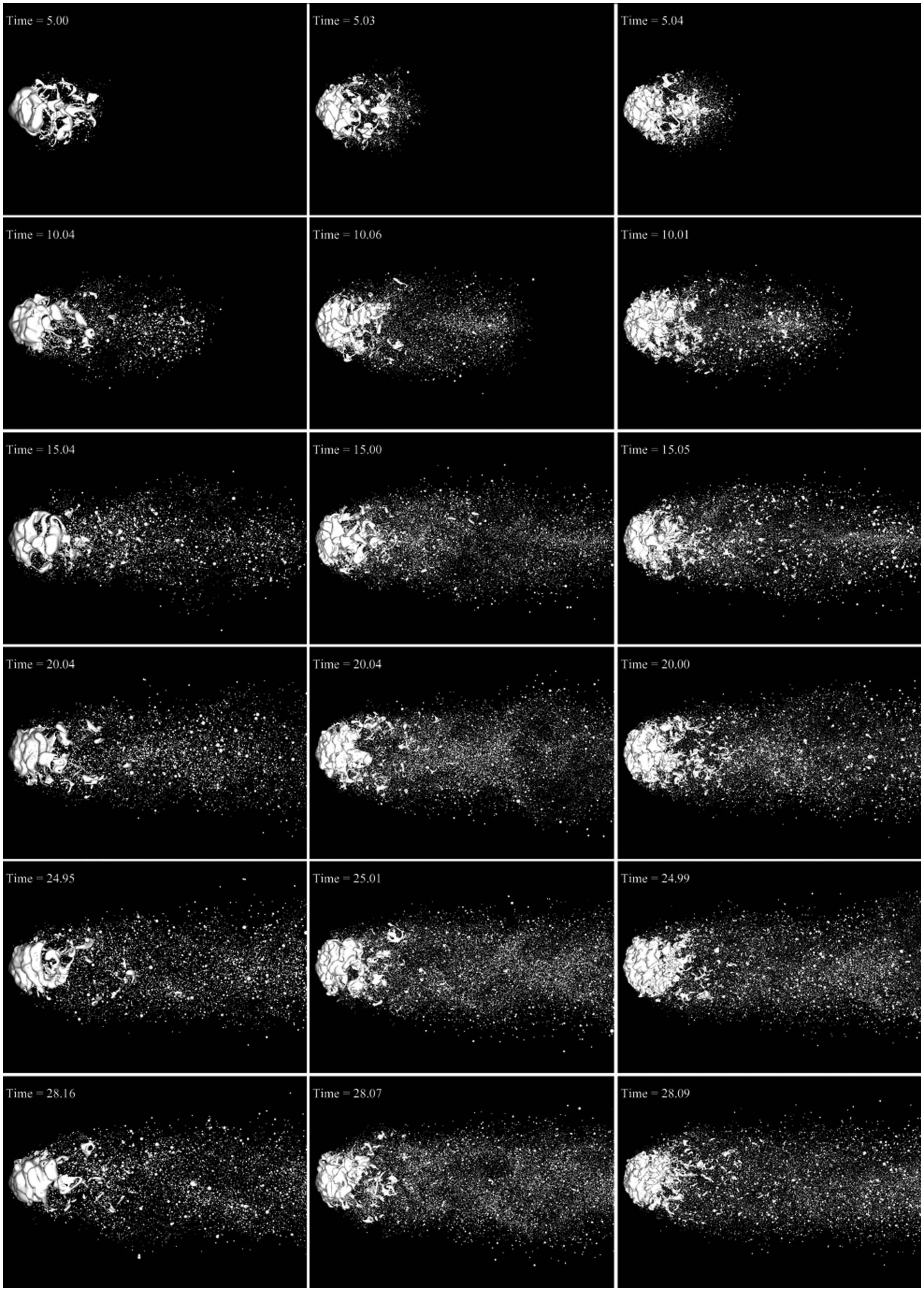

Fig. 9 Top view snapshots of jet in crossflow atomization at $t=5$, 10, 15, 20, 25, and 28.1 time units (top to bottom); case c01 (left), c12 (center), and c23 (right)

ning the data into 20 bins of equal size in terms of $\log(D)$. The approximate total number of drops used to calculate each distribution was 40,000 (c01), 176,000 (c12), and 193,000 (c23). To be able to compare the three probability density functions (pdfs), the coarser grid pdfs were normalized using a single bin of the finest grid pdf. Also shown in Fig. 10 is a log-normal fit to the larger drop sizes of the finest grid results. All three cases show a similar behavior. Larger drop sizes collapse well to the log-normal fit,

Downloaded 02 Jun 2010 to 171.66.16.96. Redistribution subject to ASME license or copyright; see http://www.asme.org/terms/Terms_Use.cfm

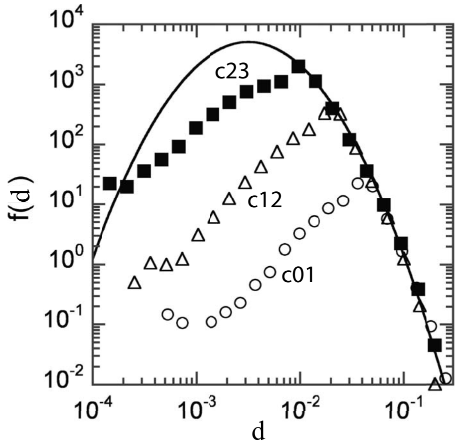

Fig. 10 Grid convergence study of pfd of drop diameters *d* generated directly by primary atomization: case c01 (open circles), c12 (open triangles), and c23 (solid squares). Solid line is log-normal fit to large drop sizes on finest grid.

however, for each grid there is a distinct departure point from the fit from which point on smaller drop sizes do not collapse and fail to match the log-normal fit. This departure point d_p decreases in value proportional to the employed grid size, with $d_p = 1.6\Delta x_G$ for the coarse and medium grids and $d_p = 1.3\Delta x_G$ for the fine grid. The key result of Fig. 10 is the fact that larger drops, i.e., those resolved by at least 1.6 G-grid cells, collapse to a single pdf, in this case a log-normal distribution independent of the employed grid resolution. These drop sizes can thus be considered grid independent. Drops smaller than about $d = 1.6\Delta x_G$, however, show a strong grid dependency. The reason for this behavior is the following: fixed grid methods used to track interfaces, like the level set method used here, have an inherent topology change length scale that is proportional to the local grid size. As soon as two front segments enter the same grid cell, a topology change event is automatically triggered. The exact moment of breakup is thus always a function of the employed grid size. However, for larger drops, the error introduced by missing the exact moment of breakup due to the inherent grid size dependency is small compared with the generated drop size. Thus larger drop sizes are grid independent, as demonstrated in Fig. 10. For smaller drops, the exact moment of breakup is however the dominant source of error; thus, smaller drops are dominated by the employed grid resolution. The cut-off appears to occur at drops resolved by about 1.6 G-grid cells. This number is surprisingly low and appears to decrease with increasing grid resolution. This seems to indicate that the numerically induced topology change starts to mimic the physical breakup mechanism on small scales.

10 Conclusion

Detailed simulation results of the primary atomization of a turbulent liquid jet injected into a subsonic gaseous crossflow previously analyzed experimentally by Brown and McDonell [2] have been presented. The simulations match all key nondimensional numbers, except for the density ratio, which is artificially reduced to study its impact on jet penetration and atomization.

A preliminary qualitative analysis of the simulation results indicates that breakup of the liquid jet occurs via two main simultaneous atomization mechanisms. In the first, instability waves on the liquid column, predominantly visible on the windward side, generate role-ups and continue to grow along the jet axis until they form baglike structures that rupture resulting in a broad range of drop sizes, not unlike the column-breakup mode. It is speculated that this instability mode is due to a Kelvin–Helmholtz instability. In the second mode, corrugations on the liquid jet surface are stretched out into ligaments at the sides of the liquid jet near the injector exit. The stretched out ligaments then break up and form a range of drop sizes. At the current stage, the above description of the breakup mechanisms is speculative and still requires a detailed, yet to be performed, quantitative study of the generated time dependent simulation data.

Grid independent predictions of the jet penetration in agreement with experimental observations can be achieved on relatively coarse grids ($D/\Delta x = 16$). Moreover, the large scale instability mode conjectured to be responsible for the first atomization mechanism is sufficiently resolved even on these coarse grids. Analysis of the temporal evolution of the pre-atomization tracked mass indicates that it is important to resolve turbulent eddies at least up to the maximum flow solver resolution considered ($D/\Delta x = 64$), since these turbulent eddies can generate significant surface corrugations to initiate the second atomization mechanism. The grid independent prediction of atomized drop sizes requires significant computational resources. Grid independent drop sizes on the finest grids have been achieved for drops as small as 13 μm, or one-hundredth of the injector exit diameter.

While the reduced density ratio analyzed in this paper appears to have no significant impact on the jet penetration determined from averaged side views of the jet geometry, it is conceivable that the atomization mechanism and resulting drop sizes are a function of the chosen density ratio. Currently ongoing simulations employing higher density ratios will focus on this question.

Acknowledgment

This work was supported in part by CASCADE Technologies Inc. under the NavAir SBIR Project No. N07-046. The author would like to thank S. Hajiloo and Y. Khalighi for valuable help in generating the fluid solver meshes, and F. Ham for many valuable discussions concerning the flow solver CDP/CHARLES.

Nomenclature

d = drop diameter
d_p = minimum grid independent drop diameter
D = injector diameter
G = level set scalar
H = Heaviside function
n = phase interface normal vector
p = pressure
q = momentum flux ratio
r = radius
Re = Reynolds number
u = velocity
t = time
T_σ = surface tension force
V = volume
V_D = drop volume
We = Weber number
x_f = location of phase interface
x = crossflow direction
Δx = flow solver grid size
Δx_G = level set grid size
y = jet direction

Greek Symbols

δ = Dirac delta function
κ = phase interface curvature
μ = dynamic viscosity
Ψ = volume fraction
ρ = density
σ = surface tension coefficient

Subscripts

1 = fluid 1, i.e., liquid
2 = fluid 2, i.e., gas
c = crossflow

Downloaded 02 Jun 2010 to 171.66.16.96. Redistribution subject to ASME license or copyright; see http://www.asme.org/terms/Terms_Use.cfm

cv = control volume
f = control volume face
j = jet

References

[1] Aalburg, C., van Leer, B., Faeth, G. M., and Sallam, K. A., 2005, "Properties of Nonturbulent Round Liquid Jets in Uniform Gaseous Cross Flows," Atomization Sprays, **15**(3), pp. 271–294.

[2] Brown, C. T., and McDonell, V. G., 2006, "Near Field Behavior of a Liquid Jet in a Crossflow," ILASS Americas 19th Annual Conference on Liquid Atomization and Spray Systems.

[3] Brown, C. T., Mondragon, U. M., and McDonell, V. G., 2007, "Investigation of the Effect of Injector Discharge Coefficient on Penetration of a Plain Liquid Jet Into a Subsonic Crossflow," *ILASS Americas 20th Annual Conference on Liquid Atomization and Spray Systems*, ILASS Americas, Chicago, IL.

[4] Stenzler, J. N., Lee, J. G., Santavicca, D. A., and Lee, W., 2006, "Penetration of Liquid Jets in a Cross-Flow," Atomization Sprays, **16**, pp. 887–906.

[5] Mazallon, J., Dai, Z., and Faeth, G. M., 1999, "Primary Breakup of Nonturbulent Round Liquid Jets in Gas Crossflows," Atomization Sprays, **9**(3), pp. 291–312.

[6] Sallam, K. A., Aalburg, C., and Faeth, G. M., 2004, "Breakup of Round Nonturbulent Liquid Jets in Gaseous Crossflow," AIAA J., **42**(12), pp. 2529–2540.

[7] Fuller, R. P., Wu, P.-K., Kirkendall, K. A., and Nejad, A. S., 2000, "Effects of Injection Angle on Atomization of Liquid Jets in Transverse Ai," AIAA J., **38**(1), pp. 64–72.

[8] Wu, P. K., Kirkendall, K. A., Fuller, R. P., and Nejad, A. S., 1997, "Breakup Processes of Liquid Jets in Subsonic Crossflows," J. Propul. Power, **13**(1), pp. 64–73.

[9] Lee, K., Aalburg, C., Diez, F. J., Faeth, G. M., and Sallam, K. A., 2007, "Primary Breakup of Turbulent Round Liquid Jets in Uniform Crossflows," AIAA J., **45**(8), pp. 1907–1916.

[10] Madabhushi, R. K., 2003, "A Model for Numerical Simulation of Breakup of a Liquid Jet in Crossflow," Atomization Sprays, **13**(4), pp. 413–424.

[11] Arienti, M., Madabhusi, R. K., Slooten, P. R. V., and Soteriou, M. C., 2005, "Numerical Simulation of Liquid Jet Characteristics in a Gaseous Crossflow," ILASS Americas 18th Annual Conference on Liquid Atomization and Spray Systems.

[12] de Villiers, E., Gosman, A. D., and Weller, H. G., 2004, "Large Eddy Simulation of Primary Diesel Spray Atomization," SAE Technical Report No. 2004-01-0100.

[13] Menard, T., Beau, P. A., Tanguy, S., Demoulin, F. X., and Berlemont, A., 2006, "Primary Break Up Modeling, Part A: Dns, a Tool to Explore Primary Break Up," ICLASS-2006, pp. 1–7, Paper No. ICLASS06-034.

[14] Menard, T., Tanguy, S., and Berlemont, A., 2007, "Coupling Level Set/Vof/Ghost Fluid Methods: Validation and Application to 3d Simulation of the Primary Break-Up of a Liquid Jet," Int. J. Multiph. Flow, **33**(5), pp. 510–524.

[15] Bianchi, G. M., Pelloni, P., Toninel, S., Scardovelli, R., Leboissetier, A., and Zaleski, S., 2007, "3d Large Scale Simulation of the High-Speed Liquid Jet Atomization," SAE Technical Paper No. 2007-01-0244.

[16] Desjardins, O., Moureau, V., and Pitsch, H., 2008, "An Accurate Conservative Level Set/Ghost Fluid Method for Simulating Turbulent Atomization," J. Comput. Phys., **227**(18), pp. 8395–8416.

[17] Gorokhovski, M., and Herrmann, M., 2008, "Modeling Primary Atomization," Annu. Rev. Fluid Mech., **40**(1), pp. 343–366.

[18] Herrmann, M., 2008, "A Balanced Force Refined Level Set Grid Method for Two-Phase Flows on Unstructured Flow Solver Grids," J. Comput. Phys., **227**(4), pp. 2674–2706.

[19] Herrmann, M., and Gorokhovski, M., 2008, "An Outline of a LES Subgrid Model for Liquid/Gas Phase Interface Dynamics," *Proceedings of the 2008 CTR Summer Program*, Center for Turbulence Research, Stanford University, pp. 171–181.

[20] Herrmann, M., 2007, "On Simulating Primary Atomization Using the Refined Level Set Grid Method," *ILASS Americas 20th Annual Conference on Liquid Atomization and Spray Systems*, ILASS Americas, Chicago, IL.

[21] Francois, M. M., Cummins, S. J., Dendy, E. D., Kothe, D. B., Sicilian, J. M., and Williams, M. W., 2006, "A Balanced-Force Algorithm for Continuous and Sharp Interfacial Surface Tension Models Within a Volume Tracking Framework," J. Comput. Phys., **213**, pp. 141–173.

[22] Brackbill, J. U., Kothe, D. B., and Zemach, C., 1992, "A Continuum Method for Modeling Surface Tension," J. Comput. Phys., **100**, pp. 335–354.

[23] Herrmann, M., 2006, "Simulating Two-Phase Flows Using the Refined Level Set Grid Method," *ILASS Americas 19th Annual Conference on Liquid Atomization and Spray Systems*, ILASS Americas, Toronto, Canada.

[24] Kim, D., Desjardins, O., Herrmann, M., and Moin, P., 2007, "The Primary Breakup of a Round Liquid Jet by a Coaxial Flow of Gas," ILASS Americas 20th Annual Conference on Liquid Atomization and Spray Systems.

[25] Apte, S. V., Gorokhovski, M., and Moin, P., 2003, "Les of Atomizing Spray With Stochastic Modeling of Secondary Breakup," Int. J. Multiphase Flow, **29**(9), pp. 1503–1522.

[26] Moin, P., and Apte, S. V., 2006, "Large-Eddy Simulation of Realistic Gas Turbine Combustors," AIAA J., **44**(4), pp. 698–708.

[27] Jiang, G.-S., and Peng, D., 2000, "Weighted ENO Schemes for Hamilton-Jacobi Equations," SIAM J. Sci. Comput. (USA), **21**(6), pp. 2126–2143.

[28] Shu, C. W., 1988, "Total-Variation-Diminishing Time Discretization," SIAM (Soc. Ind. Appl. Math.) J. Sci. Stat. Comput., **9**(6), pp. 1073–1084.

[29] Alonso, J. J., Hahn, S., Ham, F., Herrmann, M., Iaccarino, G., Kalitzin, G., LeGresley, P., Mattsson, K., Medic, G., Moin, P., Pitsch, H., Schluter, J., Svard, M., der Weide, E. V., You, D., and Wu, X., 2006, "CHIMPS: A High-Performance Scalable Module for Multi-Physics Simulation," 42nd AIAA/ASME/SAE/ASEE Joint Propulsion Conference & Exhibit, AIAA Paper No. 2006-5274.

Downloaded 02 Jun 2010 to 171.66.16.96. Redistribution subject to ASME license or copyright; see http://www.asme.org/terms/Terms_Use.cfm

Dirk Riechelmann
e-mail: dirk_riechelmann@ihi.co.jp

Masahiro Uchida

Department of Heat and Fluid Dynamics,
Research Laboratory,
IHI Corporation,
Yokohama,
Shin-Nakahara-cho 235-8501, Japan

Three-Stream Flamelet Model for Industrial Applications

Efficient turbulent combustion models are typically designed for the numerical simulation of two-stream problems, namely, the combustion of fuel in air. There are applications, however, where large amounts of a diluent such as water steam or recirculated exhaust gas is supplied to the combustor independent of fuel and air supplies. In such cases, classical approaches become quite time-consuming. In the present paper, a new three-stream flamelet model is presented, which is essentially an extension of the two-stream flamelet model for diffusion flames. Key points of the approach are the introduction of a second mixture fraction variable and the efficient establishment of the flamelet library. After presentation of the theory, the applicability of the new model is demonstrated by comparison with experimental results for the lift-off height of jet diffusion flames.
[DOI: 10.1115/1.4000247]

1 Introduction

Combined cycle power plants are often preferred over simple gas turbine systems for their flexibility to respond to customer needs. Not only can the customer use the steam according to his requirements, but also can the steam generated be used to increase power when not needed otherwise.

Different to water injection systems, where the water is supplied to the system upstream of the compressor (see Ref. [1] for a discussion on its efficiency), the steam may be injected directly to the combustor (Fig. 1). In this case, steam, as generated in the heat recovery system by use of the gas turbine exhaust gas, is mixed with air. Then it is supplied to the casing from where it enters the combustor through swirler or dilution holes. This leads to locally different concentrations of fresh air and steam/air mixture in the combustor.

In general, the combustion process in industrial applications is turbulent. Most numerical solution schemes proposed so far are dedicated to the calculation of either premixed flame or diffusion flame. Hence, one has to choose the appropriate model depending on the actual burner concept. For liquid fuels, the diffusion flame concept is often chosen; this choice appears appropriate considering the fact that the fuel spray is approximated by a certain amount of droplets which evaporate in air. The time needed for droplet evaporation is longer than the reaction time. In prevaporized-premixed combustion systems, on the other hand, the premixed flame concept is the natural choice. Similarly, for gaseous fuels, one has to choose the model depending on the combustion concept.

This paper is concerned with the diffusion flame concept. In many simulations of industrial burners and/or combustors the eddy-breakup model [3] or eddy-dissipation concept [4,5] is used for the reason of efficiency and robustness. However, it is known to produce erroneous results close to burner rims, which may have a large impact on the temperature distribution in the combustor [6]. Flamelet models [7–9] are attractive because they overcome this shortcoming. After the first presentations around the 1980s flamelet PDF models are now standard and, accordingly, one of the supported options in commercial computational fluid dynamics (CFD) codes.

However, when a second air or fuel stream is supplied to the system, the numerical modeling becomes quite difficult; many codes are restricted to equilibrium assumptions for this case. In some codes in situ adaptive tabulation (ISAT) [10] is provided, although this approach still appears quite expensive for industrial applications with larger mechanisms. In other codes, the effect of the secondary fuel or air stream on composition is neglected. In the present context, however, this neglect appears inappropriate since large amounts of steam are supplied to the combustor, which may lead to local extinction. Hasse and Peters [11] introduced a two-mixture fraction model for the simulation of common rail-like fuel injection as found in Diesel engines. This two-mixture fraction model, however, involves the solution of two-dimensional flamelet equations with scalar dissipation rates very difficult to model.

In this paper an extension of the common two-stream flamelet PDF model to a three-stream model is presented. It is simpler than the two-mixture fraction model; this is achieved by the assumption that third stream and oxidizer are to a large degree mixed before getting in touch with fuel. In this model, the dilution effect of the third stream is implemented by affecting the critical dissipation rate for extinction. Furthermore, the effect of the third stream on gas composition, and consequently on local density and temperature, is not neglected. After the presentation of the flamelet PDF model in Sec. 2 and a description of the flamelet library establishment in Sec. 3, preliminary validation tests of the new model by comparison with experiments for CO_2 diluted diffusion flames are presented.

2 Flamelet Model

Turbulent flow is made up of turbulent eddies of various sizes, which cause local flow velocities to vary irregularly around the local mean. The entire, instantaneous flame is regarded as constituted of small strained, plane flames with fuel on one side and air on the other (Fig. 2). The flame is considered thin in comparison to turbulent length scales of the flow, an assumption which is valid for most industrial flames.

Since the flame is thin, it may be wrinkled or distorted by the turbulent eddies and caused to make irregular movements in physical space like a flag flattering in the wind. The eddies, however, are too large to affect the structure of the reacting zone. Therefore, it is reasonable to evaluate the flame structure in advance and store the results in a flamelet library. Scalars such as temperature, density, and chemical species are obtained as functions of mixture fraction, which will be defined below, and dissipation rate. In the actual combustor simulation, the mixture fraction is calculated along with the dissipation rate as a measure of the local time scale. Here, the dissipation rate is modeled in the same way for both two-stream and three-stream models according to Eq. (1), as follows:

Contributed by the International Gas Turbine Institute of ASME for publication in the JOURNAL OF ENGINEERING FOR GAS TURBINES AND POWER. Manuscript received October 30, 2008; final manuscript received September 2, 2009; published online March 30, 2010. Assoc. Editor: Thomas Sattelmayer.

Copyright © 2010 by ASME

Downloaded 02 Jun 2010 to 171.66.16.96. Redistribution subject to ASME license or copyright; see http://www.asme.org/terms/Terms_Use.cfm

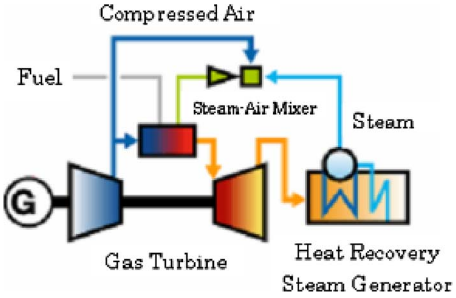

Fig. 1 Example of combined cycle gas turbine power generation system [2]

$$\tilde{\chi} = c_3\frac{\tilde{\varepsilon}}{\tilde{k}}\widetilde{Z''^2} \tag{1}$$

The dissipation rate is a measure for the stretch imposed on the flame locally by the shear between the fuel and the oxidizer. The injected steam affects the flame strength, namely, the critical dissipation rate leading to extinction. It will not, however, affect the flame stretch, which is predominated by the fluid dynamical shear; based on this assumption steam mixture fraction does not enter Eq. (1).

2.1 Two-Stream Model. In the standard two-stream flamelet model a mixture fraction Z may be defined as [8]

$$Z = \frac{\beta - \beta_{Z_0}}{\beta_F - \beta_{Z_0}}; \quad \beta = Y_F - \frac{\nu_F W_F}{\nu_{O_2} W_{O_2}} Y_{O_2} \tag{2}$$

The flame is established at the location, where the mixture fraction becomes stoichiometric. This value is readily obtained by setting $Y_F = Y_{O_2} = 0$ in the above equation, yielding the stoichiometric mixture fraction Z_C.

$$Z_C = \left(1 + \frac{\nu_{O_2} W_{O_2}}{\nu_F W_F}\frac{Y_{F,0}}{Y_{O_2,0}}\right)^{-1} \tag{3}$$

The Favre averaged conservation equations for the mean and variance are given by Eqs. (4) and (5), respectively, which are derived from the conservation equations for chemical species [8]

$$\frac{\partial}{\partial x_j}(\bar{\rho}\tilde{u}_j\tilde{Z}) = \frac{\partial}{\partial x_j}\left[\left(\frac{\mu_t}{\sigma_t} + \overline{\rho D}\right)\frac{\partial \tilde{Z}}{\partial x_j}\right] \tag{4}$$

$$\frac{\partial}{\partial x_j}(\bar{\rho}\tilde{u}_j\widetilde{Z''^2}) = \frac{\partial}{\partial x_j}\left[\left(\frac{\mu_t}{\sigma_t} + \overline{\rho D}\right)\frac{\partial \widetilde{Z''^2}}{\partial x_j}\right] + \frac{c_1}{\sigma_t}\mu_t\left(\frac{\partial \tilde{Z}}{\partial x_j}\right)^2 - c_3\bar{\rho}\frac{\tilde{\varepsilon}}{\tilde{k}}\widetilde{Z''^2} \tag{5}$$

In the diffusion term of the above equations, $\overline{\rho D}$ is typically neglected against turbulent viscosity. The model coefficients in the above equations are set to the common values, namely, $c_1 = c_3 = 2$ and $\sigma_t = 0.7$. Boundary conditions for Eq. (4) are typically $\tilde{Z} = 0$ for the oxygen supply stream, and $\tilde{Z} = 1$ for the fuel supply stream with no variance in both supply streams, accordingly.

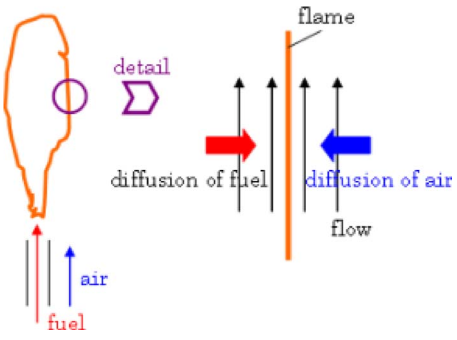

Fig. 2 Phenomenological view of turbulent diffusion flame

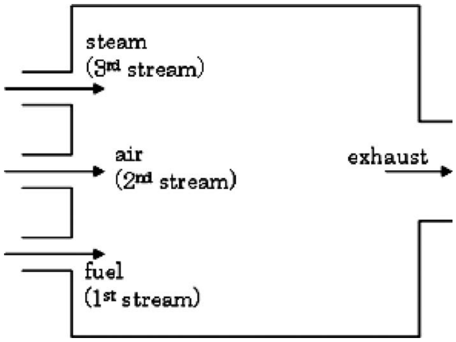

Fig. 3 Supplying stream arrangements in the three-stream flamelet model

2.2 Three-Stream Model. For the three-stream flamelet model presented in this paper we assume an arrangement as indicated in Fig. 3. It is important to note that the steam supplying feed is separated from the fuel supply by the air supplying feed. Then it appears reasonable to assume that the steam first mixes with air before getting in touch with fuel. We may use a second mixture fraction Z_S to describe the degree of mixing between steam and air. Then, the mixture fraction Z, slightly differently defined as in Sec. 2.1, can be used to describe the mixing of steam/air mixture with the fuel.

In the actual applications we are interested in here, the third stream may be any nonreacting gas such as steam, exhaust gas, or even fuel containing gas, as long as the equivalence ratio in the resulting steam/air mixture is below the flammability limit.

Figure 4 shows the mass fractions of the main species as functions of the mixture and second mixture fractions. The typical relations for the classical two-stream flamelet model are seen in the plane $Z_S = 0$, while the mixing of steam and air is given in the plane $Z = 0$. As has been mentioned before, the steam supply may contain small amounts of a fuel F_2, as long as the steam/air mix-

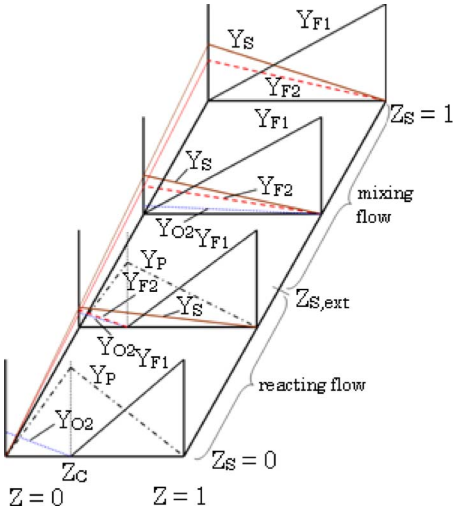

Fig. 4 Change in main species mass fractions with mixture Z and second mixture Z_S fractions. Z_S: mixing of steam (third stream) with air (second stream); Z: mixing of steam/air mixture with main fuel (first stream). Steam may contain small amounts of fuel.

Downloaded 02 Jun 2010 to 171.66.16.96. Redistribution subject to ASME license or copyright; see http://www.asme.org/terms/Terms_Use.cfm

ture will remain below the flammability limit. Then, in the plane $Z=0$, oxygen mass fraction changes, for example, from 0.233 at $Z_S=0$ to zero at $Z_S=1$. On the other hand, fuel mass fraction changes from $Y_{F_2,0}$ at $Z_S=1$ to zero at $Z_S=0$. For the condition of too low fuel concentration, there exists no second mixture fraction, at which a flame could be established. Only after addition of main fuel (named "F_1" in Fig. 4), i.e., for $Z>0$, a flame will exist at mixture fraction $Z=Z_C$. This stoichiometric mixture fraction depends on the second mixture fraction and fuel F_2 (if any fuel is contained in the third stream), as will be shown below (Eq. (10)). For second mixture fractions $Z_S>Z_{S,\text{ext}}$, the oxygen concentration becomes too low; the steam/air/fuel mixture exceeds the rich flammability limit and pure mixing will prevail (indicated as "mixing flow" in Fig. 4).

We define the second mixture fraction Z_S as

$$Z_S=\frac{\beta-\beta_{Z_0}}{\beta_S-\beta_{Z_0}}; \quad \beta=Y_S \tag{6}$$

Note that this expression is simpler than Eq. (2) for the mixture fraction in the two-stream model, since no reaction between the oxidizer and the fuel, eventually contained in the steam supplying feed, can occur.

For the three-stream flamelet model it becomes necessary to redefine the mixture fraction. For simplicity we assume equal diffusivities for all species, although more general derivations are possible [12]. The conservation equations for fuels F_1, F_2 and oxygen are written as

$$\frac{\partial}{\partial t}(\rho Y_{F_1})+\frac{\partial}{\partial x_i}(\rho u_i Y_{F_1})=\frac{\partial}{\partial x_i}\left(D\frac{\partial}{\partial x_i}(\rho Y_{F_1})\right)+\nu_{F_1}W_{F_1}\omega \tag{7a}$$

$$\frac{\partial}{\partial t}(\rho Y_{F_2})+\frac{\partial}{\partial x_i}(\rho u_i Y_{F_2})=\frac{\partial}{\partial x_i}\left(D\frac{\partial}{\partial x_i}(\rho Y_{F_2})\right)+\nu_{F_2}W_{F_2}\omega \tag{7b}$$

$$\frac{\partial}{\partial t}(\rho Y_{\mathrm{O}_2})+\frac{\partial}{\partial x_i}(\rho u_i Y_{\mathrm{O}_2})=\frac{\partial}{\partial x_i}\left(D\frac{\partial}{\partial x_i}(\rho Y_{\mathrm{O}_2})\right)+\nu_{\mathrm{O}_2}W_{\mathrm{O}_2}\omega \tag{7c}$$

For the consideration here, let us assume one overall reaction in the following form

$$\nu_{F_1}F_1+\nu_{F_2}F_2+\nu_{\mathrm{O}_2}\mathrm{O}_2\rightarrow\nu_P P \tag{8}$$

Then, the source terms in Eqs. (7) can be eliminated by addition of the three equations, after multiplying Eq. (7*c*) with the term

$$-\left(\frac{\nu_{F_1}W_{F_1}}{\nu_{\mathrm{O}_2}W_{\mathrm{O}_2}}+\frac{\nu_{F_2}W_{F_2}}{\nu_{\mathrm{O}_2}W_{\mathrm{O}_2}}\right)$$

From the result, the following Shvab–Zeldovich parameter for definition of the mixture fraction in the three-stream model is found

$$\beta'=Y_{F_1}+Y_{F_2}-\left(\frac{\nu_{F_1}W_{F_1}}{\nu_{\mathrm{O}_2}W_{\mathrm{O}_2}}+\frac{\nu_{F_2}W_{F_2}}{\nu_{\mathrm{O}_2}W_{\mathrm{O}_2}}\right)Y_{\mathrm{O}_2} \tag{9}$$

Now, the mixture fraction is defined with this Shvab–Zeldovich parameter. The stoichiometric mixture fraction is obtained as

$$\begin{aligned}Z_C&=\frac{\beta'_C-\beta'_{Z_0}}{\beta'_{F_1}-\beta'_{Z_0}}=\left(1-\frac{Y_{F_1,0}}{Y_{F_2,Z_0}-\left(\frac{\nu_{F_1}W_{F_1}}{\nu_{\mathrm{O}_2}W_{\mathrm{O}_2}}+\frac{\nu_{F_2}W_{F_2}}{\nu_{\mathrm{O}_2}W_{\mathrm{O}_2}}\right)Y_{\mathrm{O}_2,Z_0}}\right)^{-1}\\&=\left(1-\frac{Y_{F_1,0}}{Y_{F_2,0}Z_S-\left(\frac{\nu_{F_1}W_{F_1}}{\nu_{\mathrm{O}_2}W_{\mathrm{O}_2}}+\frac{\nu_{F_2}W_{F_2}}{\nu_{\mathrm{O}_2}W_{\mathrm{O}_2}}\right)(1-Z_S)Y_{\mathrm{O}_2,0}}\right)^{-1}\end{aligned} \tag{10}$$

When no fuel is present in the third stream, $Y_{F_2,0}=0$ and $\nu_{F_2}=0$. Furthermore it can readily be seen that Eq. (10) reduces to Eq. (3) for the two-stream model when no third stream is present, since $Z_S=0$ in that case.

The steam may be directly supplied to the combustor or indirectly to the outer casing, from where it enters the combustor through the dilution or effusion holes and, perhaps, from upstream close to the burner. Within the combustor, local steam concentrations are independent of fuel concentration (the supplied steam, not the steam, which might be produced by reaction of hydrocarbon fuels). Although, by definition, the sum of all mass fractions must add up to unity, it appears appropriate to consider mixture and second mixture fractions as two independent variables.

$$\frac{\partial}{\partial x_j}(\bar{\rho}\tilde{u}_j\tilde{Z}_S)=\frac{\partial}{\partial x_j}\left[\left(\frac{\mu_t}{\sigma_t}+\overline{\rho D}\right)\frac{\partial\tilde{Z}_S}{\partial x_j}\right] \tag{11}$$

$$\frac{\partial}{\partial x_j}(\bar{\rho}\tilde{u}_j\widetilde{Z_S''^2})=\frac{\partial}{\partial x_j}\left[\left(\frac{\mu_t}{\sigma_t}+\overline{\rho D}\right)\frac{\partial\widetilde{Z_S''^2}}{\partial x_j}\right]+\frac{c_1}{\sigma_t}\mu_t\left(\frac{\partial\tilde{Z}_S}{\partial x_j}\right)^2-c_3\bar{\rho}\frac{\tilde{\varepsilon}}{\tilde{k}}\widetilde{Z_S''^2} \tag{12}$$

The constants appearing in the above equations for second mixture fraction are the same as in Eqs. (4) and (5). Boundary conditions are typically $\tilde{Z}_S=1$ for the mean and $\widetilde{Z_S''^2}=0$ for the variance in the third stream and $\tilde{Z}_S=\widetilde{Z_S''^2}=0$ at the other inlets. It is important here to emphasize that the mean and variance of the second mixture fraction should always be set to the same values at the air and fuel inlets. This arises from the idea to describe the mixing of steam with air. If the values differ at the air and fuel inlets, this would cause variances in the second mixture fraction inconsistent with the model.

When the three-stream model is applied, Eqs. (4), (5), (11), and (12) are solved along with the conservation equations for mass and momentum iteratively. Density is the only variable needed during the iterations, same as in the common two-stream flamelet model. However, in the three-stream model, the library is extended by two new entries, namely, the mean and variance of the second mixture fraction. The establishment of the flamelet library will be discussed in Sec. 3.

3 Flamelet Library

As in the common two-stream flamelet model the library is built in two steps. First, the flame structure, i.e., temperature, density, and species, are calculated in counterflow geometry (Fig. 5). Then, these data are processed such that they are readily accessible in the calculation of the actual combustor.

In the two-stream model, the counterflow diffusion flame is calculated for the oxidizer and fuel streams at pressure and temperatures of the actual operating conditions of the combustor with dissipation rate as parameter. For the three-stream model under consideration in this paper, air is doped with certain amounts of the third stream, i.e., water steam. It can be shown that the flamelet equations to be solved under the present assumptions are identical to those for the two-stream model (refer to Appendix B). In the actual combustor, there is a continuous mixing of air and steam; thus, the second mixture fraction will also vary continuously. However, similar to the mixture fraction in the two-stream model, there will be only a limited number of entities in the library, between which the data actually needed are to be interpolated.

As a result of the (laminar) counterflow flame calculations, temperature, density, and species concentrations are known as function of mixture fraction, second mixture fraction, and dissipation rate. The variation in the scalars due to turbulence is statistically modeled by presuming a distribution function. As is often used in PDF methods, the beta-function (Eq. (13)) is adopted here; its parameters *a* and *b* are obtained from the mean and variance of

Downloaded 02 Jun 2010 to 171.66.16.96. Redistribution subject to ASME license or copyright; see http://www.asme.org/terms/Terms_Use.cfm

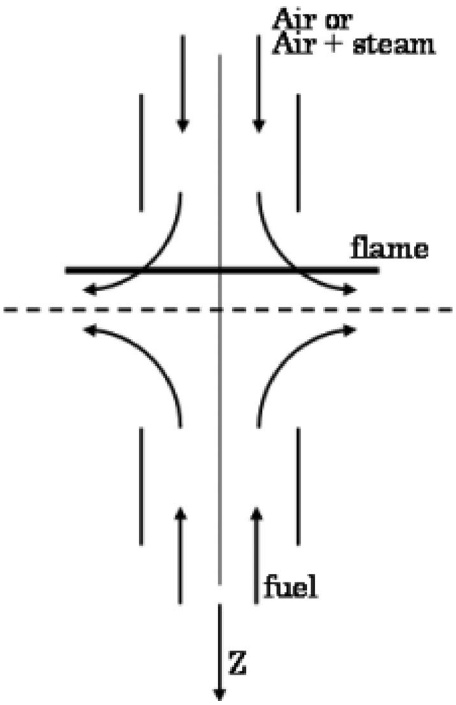

Fig. 5 Geometry of counterflow diffusion flame

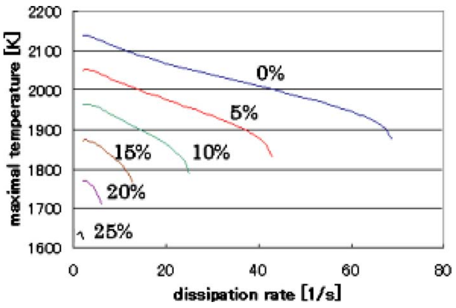

Fig. 6 Maximal temperature versus dissipation rate for various CO_2 mass fractions in oxidizer stream ($T_{\text{oxidizer}}=573$ K, $T_{CH4}=300$ K, $p=0.1$ MPa)

the mixture fraction. Similarly, a second beta-function with two other parameters is defined by the mean and variance of the second mixture fraction.

$$B(a,b)=\int_0^1 Z^{a-1}(1-Z)^{b-1}dZ \tag{13}$$

with

$$a=\tilde{Z}\left\{\frac{\tilde{Z}}{\widetilde{Z''^2}}(1-\tilde{Z})-1\right\},\quad b=a\left(\frac{1}{\tilde{Z}}-1\right)$$

The distribution function is then defined as

$$P(Z;a,b)=\frac{Z^{a-1}(1-Z)^{b-1}}{\int_0^1 Z^{a-1}(1-Z)^{b-1}dZ}=\frac{Z^{a-1}(1-Z)^{b-1}}{B(a,b)} \tag{14}$$

Note that generally the distribution functions for mixture and second mixture fractions are different. When a Dirac function is assumed for the dissipation rate, the mean temperature, for example, is obtained by integration over the mixture and second mixture fractions, as shown by Eq (15).

$$\begin{aligned}\tilde{T}(\tilde{\chi},\tilde{Z},\widetilde{Z''^2},\tilde{Z}_s,\widetilde{Z_s''^2}) &= \int\int\int T(Z_s,\chi,Z)\cdot P(Z)P_s(Z_s)dZdZ_sd\chi\\ &= \int_0^1\left(\int_0^1 T(Z_s,\tilde{\chi},Z)\cdot P(Z;\tilde{Z},\widetilde{Z''^2})dZ\right)\\ &\quad \cdot P_s(Z_s;\tilde{Z}_s,\widetilde{Z_s''^2})dZ_s\\ &= \int_0^1 \tilde{T}_I(Z_s,\tilde{\chi},\tilde{Z},\widetilde{Z''^2})\cdot P_s(Z_s;\tilde{Z}_s,\widetilde{Z_s''^2})dZ_s\end{aligned} \tag{15}$$

By examination of Eq. (15) it is readily seen that statistical independence of the mixture and second mixture fractions is assumed. Typically steam is supplied to the casing, where it mixes to a certain extent with air before entering the combustor. Then, it appears reasonable to suppose that fluctuations in the second mixture fraction are considerably smaller than those in the mixture fraction. Hence, the covariance of mixture fractions $\widetilde{Z''Z_S''}$ is supposed to be negligible. The correctness of this assumption cannot be judged in general, but has to be verified for each actual simulation individually. If it turns out to be inappropriate, more sophisticated modeling is required. Research in this direction is on the way [13,14].

In the common two-stream flamelet model, Eq. (15) implies a single integration when a Dirac function is assumed for the dissipation rate, or a twofold integration otherwise. For the three-stream flamelet model, the integration in Eq. (15) is twofold or threefold, which is very time-consuming if done straightforward. An efficient integration method is outlined in Appendix A.

The mixing of air with a diluent will narrow the flammability limits of the fuel/air mixture. The effect becomes evident when looking at the result of counterflow diffusion flame calculations, where air has been diluted with carbon dioxide (which is easier to handle in the experiments reported later in this paper). These calculations have been performed with the code RUN1DL [15]; for the chemistry the GRI3.0 mechanism [16] has been used. The decrease in flame temperature with dissipation rate and CO_2 content is shown in Fig. 6. It is seen that the flame temperature close to extinction decreases significantly for higher degree of dilution. The change in critical dissipation rate with CO_2 dilution of air is shown in Fig. 7; the combustion limit in counterflow geometry is found to be somewhat above 25 mass % at 0.1 MPa and 300 K and 573 K for fuel and air temperatures, respectively. This may be compared with the flammability limit of 33.2 mass % reported in Ref. [17] for the premixed gas at 300 K.

For the calculation of mean temperature, density, and species concentrations the effect of flame extinction may be implemented following the suggestion in Ref. [7]. In this case, mean scalars are obtained as indicated in Eq. (16), where again a Dirac function is assumed for the dissipation rate

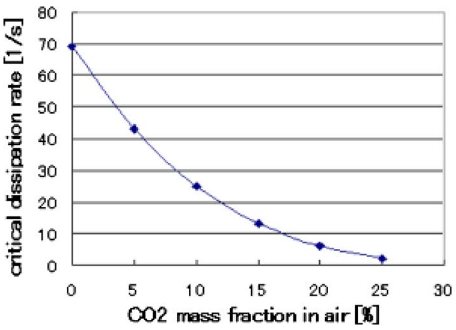

Fig. 7 Critical dissipation rate for extinction of methane in air doped with CO_2 (0.1 MPa, $T_{\text{oxidizer}}=573$ K, $T_{CH4}=300$ K)

Downloaded 02 Jun 2010 to 171.66.16.96. Redistribution subject to ASME license or copyright; see http://www.asme.org/terms/Terms_Use.cfm

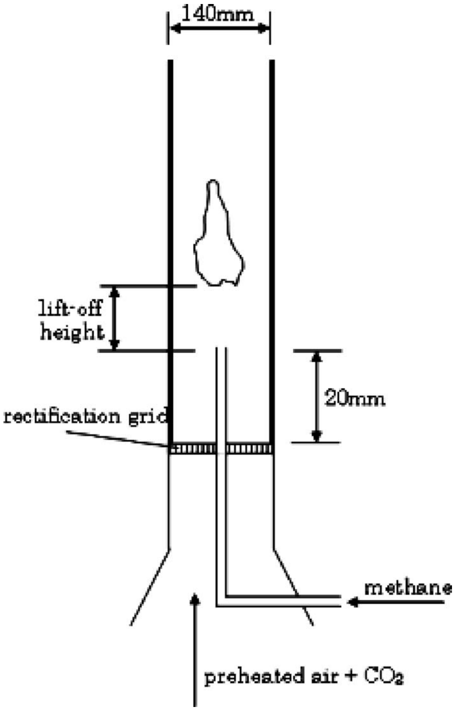

Fig. 8 Experimental apparatus for model evaluation

$$\tilde{T}(\tilde{\chi},\tilde{Z},\widetilde{Z''^2},\tilde{Z}_s,\widetilde{Z_s''^2}) = \int_0^{Z_{s,q}(\tilde{\chi})} \tilde{T}_I(Z_s,\tilde{\chi},\tilde{Z},\widetilde{Z''^2}) \cdot P_s(Z_s;\tilde{Z}_s,\widetilde{Z_s''^2})dZ_s + \int_{Z_{s,q}(\tilde{\chi})}^{1} \tilde{T}_{\mathrm{mf}}(Z_s,\tilde{Z},\widetilde{Z''^2}) \cdot P_s(Z_s;\tilde{Z}_s,\widetilde{Z_s''^2})dZ_s \tag{16}$$

In the above equation, $Z_{s,q}(\tilde{\chi})$ represents the quenching second mixture fraction. Gas temperatures for the burning and quenched, i.e., mixed unburnt gas, are denoted by $\tilde{T}_I$ and $\tilde{T}_{\mathrm{mf}}$, respectively. These temperatures are the mean temperatures as obtained by integration in the mixture fraction space and resemble the temperatures one would have for constant steam concentration.

4 Validation Test

The three-stream flamelet model, as presented above, has been tested by a series of jet diffusion flame experiments with carbon dioxide as diluent. The lift-off height of the flame base from the nozzle exit is measured to examine the ability of the above model to capture the physical phenomena. The tests are qualitative in nature and presented here to demonstrate the applicability of the model. It should be noted that rigorous validation would include local temperature and species concentration measurements within the flame; this is beyond the scope of this paper and left for future work. The flames shown in Fig. 9 can also be computed with the common two-stream flamelet model; however, for each flame another library would be required. The results presented below are obtained with the three-stream model by simply changing the boundary conditions; the same library data are used for all calculations.

The experimental apparatus consists of a 1200 mm long pipe with 140 mm inner diameter made of quartz glass (Fig. 8). Air and carbon dioxide are mixed in a mixing chamber, then heated to 573 K, and supplied to the glass pipe through a punched metal for flow rectification. Methane is supplied through a nozzle of 4.62 mm inner diameter. The nozzle tip is 20 mm raised from the punched metal surface to ensure uniform air supply around the fuel jet. Air or air/carbon dioxide mixture and methane are supplied with 0.47 m/s and 8.74 m/s, respectively. The fuel velocity is large enough to ensure turbulent flow (Re=2338); it causes a lifted flame even without carbon dioxide dilution. Although the air flow velocity is small, there has been large entrainment of surrounding air, which disturbed the flame a lot. So the glass enclosure became necessary.

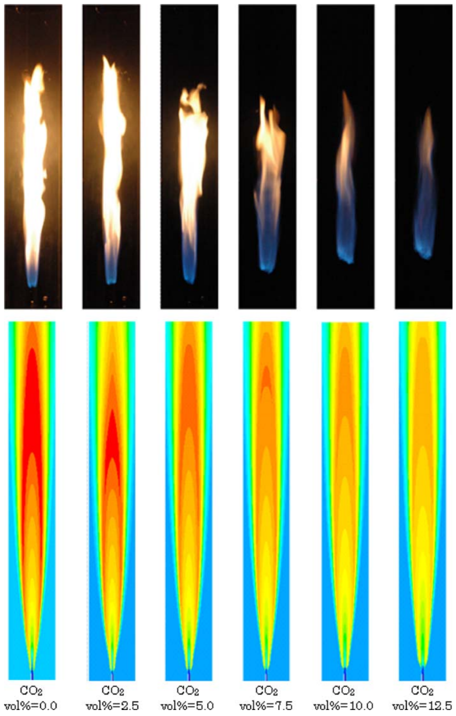

Fig. 9 Images and numerical result for temperature distribution in methane-air flame, where air is diluted with carbon dioxide

The numerical simulations have been performed for the domain just downstream of the rectification grid (Fig. 8) with the standard k-ε model. Since carbon dioxide and air are mixed upstream of the rectification grid in a mixing chamber, the mixed gas enters the computational domain. Therefore, in the present test cases, there are only two inlets, namely, carbon dioxide/air inlet and methane inlet. Regarding the boundary conditions, $\tilde{Z}=0$, $\tilde{Z}_S=\tilde{Y}_{\mathrm{CO}_2}$, and $\widetilde{Z''^2}=\widetilde{Z_S''^2}=0$ at the carbon dioxide/air inlet, $\tilde{Z}=1$, $\tilde{Z}_S=\tilde{Y}_{\mathrm{CO}_2}$, and $\widetilde{Z''^2}=\widetilde{Z_S''^2}=0$ at the methane inlet. As already explained in Sec. 2.2, the mean and variance of the second mixture fraction at the fuel inlet are set to the same values as those at the air inlet. Turbulence level of the flow is assumed to be 1%.

Figure 9 shows images of the flame for different carbon dioxide dilutions. The flame base clearly rises with increased CO_2 content. Furthermore, it is readily seen that the brightness of the flame as well as the flame height decreases with increased carbon dioxide dilution. Similarly, the numerical results show a decrease in flame temperature with CO_2 dilution. The increase in lift-off height is caused by the lower critical dissipation rate for extinction. Near the nozzle exit the dissipation rates are higher than downstream; therefore, the flame lifts further when dilution is increased. The decrease in brightness and temperature may be attributed to various phenomena. First, dilution by CO_2 decreases the oxygen concentration, causing the reaction rate to decrease and resulting in a lower temperature. Second, the heat capacity of CO_2 is large; a large heat capacity of the gas yields lower temperature for the same heat input. Third, it is known [18,19] that even at small lift-off heights a certain amount of air mixes with fuel. The more the flame moves away from the nozzle exit, the more air mixes

Downloaded 02 Jun 2010 to 171.66.16.96. Redistribution subject to ASME license or copyright; see http://www.asme.org/terms/Terms_Use.cfm

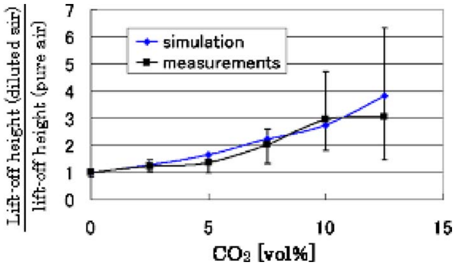

Fig. 10 Measured and calculated lift-off heights versus CO_2-content in air

with the fuel before burning, leading to less unburnt gas in the upper region of the flame; hence, the diffusion flame height becomes shorter because less oxygen is needed. From these results it is seen that the flamelet model qualitatively resembles the experimental evidence.

For quantitative evaluation, the flame height is determined as ensemble average of video records. In the experiments, the oxygen-rich, blue flame base moves up and down and this irregular motion becomes stronger the higher the dilution becomes. The images shown in Fig. 9 are chosen as representative for the mean location of the flame. In the numerical results, the lift-off height is defined here as the distance from the nozzle where the gas temperature gradient in axial direction changes significantly. For the conditions investigated here, this occurred at 1600°C. If we use this point to measure the lift-off height, a value of 17.9 mm is found for the flame without dilution. This height must be compared with a value of 30.1 mm found experimentally. The temperature at the height of 30.1 mm found experimentally could be used to try to achieve agreement with the experimental results. Such a choice, however, is questionable for the other cases with air dilution. So, in this paper, the quantitative result is presented in nondimensional form, where the lift-off height is divided by the lift-off height obtained for the flame without dilution (Fig. 10). The bars denote minimal and maximal locations of the blue flame base, measured as the distance to the fuel nozzle. Comparison shows that the numerical results are in good agreement with the experimental data up to air dilution of 10%. For higher dilution the experimental data show very large up-and-down fluctuations of the flame base. It may be presumed that for large lift-off heights the mixture enters the flammable region; the location of the flame base becomes rather a problem of flame propagation in a gas mixture than flame extinction of a strained diffusion flame. The diffusion flame model, as presented here, cannot mimic this feature.

5 Conclusions

In this paper the conventional two-stream flamelet model, which considers the diffusion flame of fuel with oxidant, is extended to a three-stream flamelet model, where the third stream might be any nonreacting gas, i.e., a diluent such as carbon dioxide; the third stream may eventually contain fuel to such an amount, that the resulting third stream/air mixture is below the flammability limit. Key point is the observation that for the applications considered here, oxidizer and diluting streams are highly mixed before entering the reaction zone.

It is shown that the model can predict the right trend for flame lift-off up to a certain degree of dilution (which is found to be 10 vol % of carbon dioxide in air in the present case). The limitation is due to high degree of premixing prior to combustion, which is not considered in this paper. However, this model can be used in the context of the so-called partially premixed flame approach; it is expected that the trend will be captured correctly also for higher dilutions then.

Nomenclature

a = coefficient in definition of beta-function (Eq. (13))
b = coefficient in definition of beta-function (Eq. (13))
$B(a,b)$ = beta-function (Eq. (13))
$B_I(a,b;X)$ = incomplete beta-function (Eq. (A2))
c = model coefficient
D = diffusion coefficient (m^2/s)
k = turbulent energy (m^2/s^2)
$P(X;\widetilde{X},\widetilde{X''^2})$ = probability density function (Eq. (14))
S = linear polynomial for approximation of density, temperature, or chemical species as function of the mixture fraction (Eq. (A1))
T = gas temperature (K)
u = flow velocity (m/s)
W = molecular weight (g/mole)
x = coordinate (m)
Y = mass fraction (g/g)
$Y_{F,0}, Y_{F_1,0}$ = mass fraction of fuel in fuel supplying stream (g/g)
$Y_{F_2,0}$ = mass fraction of fuel in steam supplying stream (g/g)
$Y_{O_2,0}$ = mass fraction of oxygen in air supplying stream (g/g)
Z = mixture fraction as defined by Eq. (2)
Z_C = stoichiometric mixture fraction (Eqs. (3) and (10))
Z_S = second mixture fraction as defined by Eq. (6)

Greek Symbols

β = Shvab–Zeldovich parameter
β' = Shvab–Zeldovich parameter for mixture fraction in three-stream model (Eq. (9))
δ = expansion parameter (Eq. (B2))
ε = dissipation of turbulent energy (m^2/s^3)
μ = kinematic viscosity (Pa s)
ν = stoichiometric coefficient
ρ = density (kg/m^3)
σ = Prandtl number

Subscripts

C = stoichiometric condition
ext = extinction
F = fuel supply stream
F_1 = fuel supplied in fuel stream
F_2 = fuel supplied in third stream
i = counter index in polynomial
I = incomplete
j = axis direction
mf = mixing flow
q = quenching
s = steam, second
t = turbulent
Z_0 = value at $Z=0$

Superscripts

$\bar{X}$ = time average of variable X
$\widetilde{X}$ = Favre average of variable X
$\widetilde{X''^2}$ = variance of variable X

Appendix A: Efficient Evaluation of Integrals Including the Beta-Function

Straightforward integration of the beta-function over the mixture fraction is very time-consuming since very small steps must be used in order to obtain accurate results. Single integration is a matter of hours; twofold integrations would require days or even

Downloaded 02 Jun 2010 to 171.66.16.96. Redistribution subject to ASME license or copyright; see http://www.asme.org/terms/Terms_Use.cfm

weeks. For this reason, twofold integrations as indicated by Eq. (15) in the paper are too slow for actual applications.

Below, an efficient way to obtain the necessary integrals is outlined for the gas temperature. When statistical independence is assumed, evaluation of the twofold integral (or threefold, if a function other than the Dirac function is assumed for dissipation rate) can be done in two steps. First, an intermediate mean temperature is obtained by integration over mixture fraction (Eq. (A3)). In a second step, this result is integrated over the steam mixture fraction in order to obtain the mean temperature (Eq. (15)). When the second step is done, care must be taken because the critical dissipation rate at which extinction occurs changes with diluent concentration; therefore, the integration bounds in Eq. (16) change with the second mixture fraction. To circumvent any problems with this, the library is built in nondimensional form, where the dissipation rate is normalized by the critical dissipation rate for a given second mixture fraction. Hence, burning occurs for nondimensional dissipation rates less than one; mixing flow is assumed for dissipation rates larger than one. If for the dissipation rate a distribution function different from the Dirac function is assumed, there is a continuous change in the temperature profile from reacting to mixing flow rather than a discontinuous jump.

In order to accelerate the numerical integration, profiles for temperature, species, or density are approximated by three piecewise linear polynomials; then, by use of the incomplete beta-function, the integration is rendered to a simple summation.

For example, consider the temperature $T(Z_s,\widetilde{\chi},Z)$, which is computed in counterflow diffusion flame calculations for mixture fraction in the range $[0,1]$ under condition of the given second mixture fraction and imposed dissipation rate. As preparation for the integration procedure, mixture fraction is divided into three subranges, namely, $[0,X_1]$, $[X_1,X_2]$ and $[X_2,1]$, where the borders X_i are determined such that the temperature profile within each subrange can reasonably well be approximated by a linear polynomial of the form

$$S(Z)=\sum s_i Z^i \tag{A1}$$

Order of the polynomial is determined by best fit; typically it is less than seven. The incomplete beta-function is defined as

$$B_I(a,b;X)=\int_0^X Z^{a-1}\cdot(1-Z)^{b-1}dZ, \quad (0<X\leq 1) \tag{A2}$$

It is readily seen that the following relation holds

$$\int_0^X Z^i\cdot P(Z)dZ=\int_0^X Z^i\cdot Z^{a-1}(1-Z)^{b-1}dZ=B_I(a+i,b;X) \tag{A3}$$

Hence, when the temperature is piecewise approximated by a linear polynomial, the integration for the first subrange, for example, can be evaluated as

$$\begin{aligned}\widetilde{T}_{X_1}(Z_s,\widetilde{\chi},\widetilde{Z},\widetilde{Z''^2})&=\int_0^{X_1}T(Z_s,\widetilde{\chi},Z)\cdot P(Z;\widetilde{Z},\widetilde{Z''^2})dZ\\&=\int_0^{X_1}S(Z)\cdot Z^{a-1}(1-Z)^{b-1}dZ\\&=\int_0^{X_1}\left(\sum s_iZ^i\right)\cdot Z^{a-1}(1-Z)^{b-1}dZ\\&=\sum_i s_iB_I(a+i,b;X_1)\end{aligned} \tag{A4}$$

So, the integral renders to a simple summation. Similarly, for the second subrange, the temperature is evaluated as

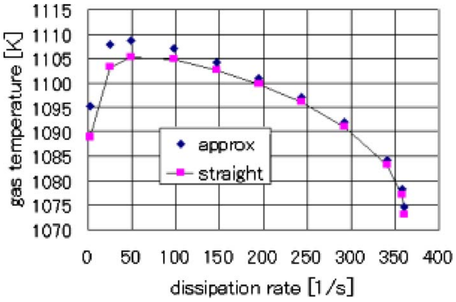

Fig. 11 Accuracy of flamelet library: comparison of straight forward integration with approximated integration

$$\begin{aligned}\widetilde{T}_{X_2}(Z_s,\widetilde{\chi},\widetilde{Z},\widetilde{Z''^2})&=\int_{X_1}^{X_2}T(Z_s,\widetilde{\chi},Z)\cdot P(Z;\widetilde{Z},\widetilde{Z''^2})dZ\\&=\int_{X_1}^{X_2}S(Z)\cdot Z^{a-1}(1-Z)^{b-1}dZ\\&=\int_{X_1}^{X_2}\left(\sum s_iZ^i\right)\cdot Z^{a-1}(1-Z)^{b-1}dZ\\&=\sum_i s_i(B_I(a+i,b;X_2)-B_I(a+i,b;X_1))\end{aligned} \tag{A5}$$

Effective calculation of the incomplete beta-function can be found in the literature [20]. After having performed the first integration over the mixture fraction space as indicated above, the second integration over the second mixture fraction space is carried out in the usual way. Once, the flamelet library is established, density, temperature, and species are retrieved by simple, multidimensional linear interpolation [20].

The accuracy of the integration scheme is demonstrated in Fig. 11. It shows the gas temperature for pure methane/oxygen reaction at mean mixture fraction of 0.02 and variance of 0.09 under real gas turbine working conditions. It is readily seen that temperature is accurate within 6 K.

Appendix B: Flamelet Equations for the Three-Stream Model

In the paper we propose a three-stream model under the assumption that a third stream mixes with the oxidizer stream before burning. In this context, the third stream may be any nonreacting diluent or a mixture of diluent and fuel, as long as the fuel concentration is well below the lower flammability limit after mixing with the oxidizer stream.

Here, we show that the flamelet equations for the chemical species are exactly the same as those for the two-stream model. Changes are to be made only in the boundary conditions for the oxidizer stream (which means the oxidizer/third stream mixture in the three-stream model). For each flamelet calculation, the third stream content in the oxidizer stream will be kept fixed; it can readily be calculated from Eq. (6) in the paper. Note that the temperature of the oxidizer/third stream mixture is to be evaluated appropriately.

In what follows we first have recourse to the derivation of Hasse and Peters [11]. Then, assuming that the third stream is in large portions mixed before entering the reaction zone, the resulting flamelet equations are seen to reduce to the classical ones.

The equation for conservation of chemical species $Y_i=Y_i(x_\alpha,t)$ can be written as

Downloaded 02 Jun 2010 to 171.66.16.96. Redistribution subject to ASME license or copyright; see http://www.asme.org/terms/Terms_Use.cfm

$$\rho\frac{\partial Y_i}{\partial t}+\rho v_\alpha\frac{\partial Y_i}{\partial x_\alpha}=\frac{\partial}{\partial x_\alpha}\left(\rho D_i\frac{\partial Y_i}{\partial x_\alpha}\right)+\omega_i \tag{B1}$$

Two short scales ζ and ζ_s are introduced as

$$\zeta=\frac{Z-Z_{\text{ref}}}{\delta},\quad \zeta_s=\frac{Z_s-Z_{s,\text{ref}}}{\delta_s} \tag{B2}$$

The long scale is the spatial coordinate x_α, which will be replaced by ξ_α. Time is scaled as

$$\tau=\frac{t}{\delta\delta_s} \tag{B3}$$

Then, after variable transformation, the species will be a function of the two stretched variables, long scale spatial coordinate and scaled time, i.e., $Y_i=Y_i(\zeta,\zeta_s,\xi_\alpha,\tau)$; derivations are to be performed according to

$$\begin{aligned}\frac{\partial}{\partial t}&=\frac{\partial\zeta}{\partial Z}\frac{\partial Z}{\partial t}\frac{\partial}{\partial\zeta}+\frac{\partial\zeta_s}{\partial Z_s}\frac{\partial Z_s}{\partial t}\frac{\partial}{\partial\zeta_s}+\frac{\partial\tau}{\partial t}\frac{\partial}{\partial\tau}\\&=\frac{1}{\delta}\frac{\partial Z}{\partial t}\frac{\partial}{\partial\zeta}+\frac{1}{\delta_s}\frac{\partial Z_s}{\partial t}\frac{\partial}{\partial\zeta_s}+\frac{1}{\delta\delta_s}\frac{\partial}{\partial\tau}\end{aligned} \tag{B4a}$$

$$\begin{aligned}\frac{\partial}{\partial x_\alpha}&=\frac{\partial\zeta}{\partial Z}\frac{\partial Z}{\partial x_\alpha}\frac{\partial}{\partial\zeta}+\frac{\partial\zeta_s}{\partial Z_s}\frac{\partial Z_s}{\partial x_\alpha}\frac{\partial}{\partial\zeta_s}+\frac{\partial}{\partial\xi_\alpha}\\&=\frac{1}{\delta}\frac{\partial Z}{\partial x_\alpha}\frac{\partial}{\partial\zeta}+\frac{1}{\delta_s}\frac{\partial Z_s}{\partial x_\alpha}\frac{\partial}{\partial\zeta_s}+\frac{\partial}{\partial\xi_\alpha}\end{aligned} \tag{B4b}$$

The transformation yields

$$\begin{aligned}&\rho\left(\frac{1}{\delta}\frac{\partial Z}{\partial t}\frac{\partial Y_i}{\partial\zeta}+\frac{1}{\delta_s}\frac{\partial Z_s}{\partial t}\frac{\partial Y_i}{\partial\zeta_s}+\frac{1}{\delta\delta_s}\frac{\partial Y_i}{\partial\tau}\right)\\&\quad+\rho v_\alpha\left(\frac{1}{\delta}\frac{\partial Z}{\partial x_\alpha}\frac{\partial Y_i}{\partial\zeta}+\frac{1}{\delta_s}\frac{\partial Z_s}{\partial x_\alpha}\frac{\partial Y_i}{\partial\zeta_s}+\frac{\partial Y_i}{\partial\xi_\alpha}\right)\\&=\frac{1}{\delta}\frac{\partial Z}{\partial x_\alpha}\frac{\partial}{\partial\zeta}\left[\rho D_i\left(\frac{1}{\delta}\frac{\partial Z}{\partial x_\alpha}\frac{\partial Y_i}{\partial\zeta}+\frac{1}{\delta_s}\frac{\partial Z_s}{\partial x_\alpha}\frac{\partial Y_i}{\partial\zeta_s}+\frac{\partial Y_i}{\partial\xi_\alpha}\right)\right]\\&\quad+\frac{1}{\delta_s}\frac{\partial Z_s}{\partial x_\alpha}\frac{\partial}{\partial\zeta_s}\left[\rho D_i\left(\frac{1}{\delta}\frac{\partial Z}{\partial x_\alpha}\frac{\partial Y_i}{\partial\zeta}+\frac{1}{\delta_s}\frac{\partial Z_s}{\partial x_\alpha}\frac{\partial Y_i}{\partial\zeta_s}+\frac{\partial Y_i}{\partial\xi_\alpha}\right)\right]\\&\quad+\frac{\partial}{\partial\xi_\alpha}\left[\rho D_i\left(\frac{1}{\delta}\frac{\partial Z}{\partial x_\alpha}\frac{\partial Y_i}{\partial\zeta}+\frac{1}{\delta_s}\frac{\partial Z_s}{\partial x_\alpha}\frac{\partial Y_i}{\partial\zeta_s}+\frac{\partial Y_i}{\partial\xi_\alpha}\right)\right]+\omega_i\end{aligned} \tag{B5}$$

After multiplying Eq. (B5) with $\delta\delta_s$ and only retaining the leading orders and the chemical source term, one obtains

$$\begin{aligned}\rho\frac{\partial Y_i}{\partial\tau}&=\frac{\partial Z}{\partial x_\alpha}\frac{\partial}{\partial\zeta}\left[\rho D_i\left(\frac{\delta_s}{\delta}\frac{\partial Z}{\partial x_\alpha}\frac{\partial Y_i}{\partial\zeta}+\frac{\partial Z_s}{\partial x_\alpha}\frac{\partial Y_i}{\partial\zeta_s}\right)\right]\\&\quad+\frac{\partial Z_s}{\partial x_\alpha}\frac{\partial}{\partial\zeta_s}\left[\rho D_i\left(\frac{\partial Z}{\partial x_\alpha}\frac{\partial Y_i}{\partial\zeta}+\frac{\delta}{\delta_s}\frac{\partial Z_s}{\partial x_\alpha}\frac{\partial Y_i}{\partial\zeta_s}\right)\right]+\delta\delta_s\omega_i\end{aligned} \tag{B6}$$

By setting $\delta=\delta_s$, introducing the Lewis number, and noting that $\partial Z_s/\partial x_\alpha$ and $\partial Z/\partial x_\alpha$ vary only in long scales, the result of Hasse and Peters [11] is readily obtained.

In the present context, we assume that the third stream is in large portions mixed with the oxidizer stream. More precisely, in industrial applications, the third stream is rather supplied to the outer casing than directly to the inner combustor. Therefore, the third stream is likely to mix with the oxidizer before entering the combustor, at least to a large amount. Thus, it appears reasonable to expect that variations in the third stream concentration should be smaller compared with the oxidizer stream concentrations within the combustor. Hence, we stretch only ζ by setting $\delta_s=1$. Then, in Eq. (B6) the first term on the right side becomes the dominant one compared with the second and third (of order unity) and the fourth (much smaller than unity). When scaling time as $\tau=t/\delta^2$ instead of Eq. (B3), the reaction term in Eq. (B6) is retained as before and the resulting equation is

$$\rho\frac{\partial Y_i}{\partial t}=\frac{\rho}{2Le_i}\left(2D\left(\frac{\partial Z}{\partial x_\alpha}\right)^2\frac{\partial^2 Y_i}{\partial Z^2}\right)+\omega_i=\frac{\rho}{Le_i}\frac{\chi}{2}\frac{\partial^2 Y_i}{\partial Z^2}+\omega_i \tag{B7}$$

This is the flamelet equation for the two-stream model (QED).

References

[1] Chiang, H.-W. D., Wang, P.-Y., and Li, H.-L., 2008, "Power Augmentation Study of an Existing Combined Cycle Power Plant by Overspray Inlet Fogging," ASME Paper No. GT2008-50058.

[2] http://www.ihi.co.jp/powersystems/english/technology/flecs.html

[3] Spalding, D. B., 1971, "Mixing and Chemical Reaction in Steady Confined Turbulent Flames," Proc. Comb. Inst., **13**, pp. 649–657.

[4] Magnussen, B. F., 1981, "On the Structure of Turbulence and a Generalized Eddy Dissipation Concept for Chemical Reaction in Turbulent Flow," 19th AIAA Meeting, St. Louis, MO.

[5] Ertesvag, I. S., and Magnussen, B. F., 2000, "The Eddy Dissipation Turbulence Energy Cascade Model," Combust. Sci. Technol., **159**, pp. 213–235.

[6] Riechelmann, D., Fujimori, T., and Prud'homme, F., 2004, "Numerical Simulation on Combustion of Low-Calorific Fuel in Gas Turbines," 24th CIMAC, Kyoto, Japan, Paper No. 225.

[7] Peters, N., 1983, "Local Quenching Due to Flame Stretch and Non-Premixed Turbulent Combustion," Combust. Sci. Technol., **30**, pp. 1–17.

[8] Peters, N., 2000, *Turbulent Combustion*, Cambridge University Press, Oxford.

[9] Klimenko, A. Y., and Bilger, R. W., 1999, "Conditional Moment Closure for Turbulent Combustion," Prog. Energy Combust. Sci., **25**, pp. 595–687.

[10] Yang, B., and Pope, S. B., 1998, "Treating Chemistry in Combustion With Detailed Mechanisms—In Situ Adaptive Tabulation in Principal Directions—Premixed Combustion," Combust. Flame, **112**, pp. 85–112.

[11] Hasse, C., and Peters, N., 2005, "A Two Mixture Fraction Flamelet Model Applied to Split Injections in a DI Diesel Engine," Proc. Comb. Inst., **30**, pp. 2755–2762.

[12] Williams, F. A., 1985, *Combustion Theory*, 2nd ed., Addison-Wesley, Reading, MA.

[13] Brandt, M., Polifke, W., and Flohr, P., 2006, "Approximation of Joint PDFs by Discrete Distributions Generated With Monte Carlo Methods," Combust. Theory Modell., **10**(4), pp. 535–558.

[14] Ivancic, B., Flohr, P., Paikert, B., Brandt, M., and Polifke, W., 2004, "Auto-Ignition and Heat Release in a Gas Turbine Burner at Elevated Temperature," ASME Paper No. GT-2004-53339.

[15] http://www.lstm.ruhr-uni-bochum.de

[16] http://www.me.berkeley.edu/gri_mech/releases.html

[17] Coward, H. F., and Jones, G. W., 1952, "Limits of Flammability of Gases and Vapors," Bureau of Mines Bulletin No. 503.

[18] Schefer, R. W., and Goix, P. J., 1998, "Mechanism of Flame Stabilization in Turbulent, Lifted-Jet Flames," Combust. Flame, **112**, pp. 559–574.

[19] Janicka, J., and Peters, N., 1982, "Prediction of Turbulent Jet Diffusion Flame Lift-Off Using a PDF Transport Equation," Symp. (Int.) Combust., [Proc.], **19**, pp. 367–374.

[20] 2007, *Numerical Recipes: The Art of Scientific Computing*, 3rd ed., Cambridge University Press, Cambridge.

Downloaded 02 Jun 2010 to 171.66.16.96. Redistribution subject to ASME license or copyright; see http://www.asme.org/terms/Terms_Use.cfm

Combined Cycles With CO_2 Capture: Two Alternatives for System Integration

Nikolett Sipöcz
e-mail: nikolett.sipocz@uis.no

Mohsen Assadi

Department of Mechanical and Structural
Engineering and Material Science,
University of Stavanger,
N-4036 Stavanger, Norway

As carbon capture and storage technology has grown as a promising option to significantly reduce CO_2 emissions, system integration and optimization claim an important and crucial role. This paper presents a comparative study of a gas turbine cycle with postcombustion CO_2 separation using an amine-based absorption process with monoethanolamine. The study has been made for a triple pressure reheated 400 MWe natural gas-fuelled combined cycle with exhaust gas recirculation (EGR) to improve capture efficiency. Two different options for the energy supply to the solvent regeneration have been evaluated and compared concerning plant performance. In the first alternative heat is provided by steam extracted internally from the bottoming steam cycle, while in the second option an external biomass-fuelled boiler was utilized to generate the required heat. With this novel configuration the amount of CO_2 captured can be even more than 100% if the exhaust gas from the biofuelled boiler is mixed and cleaned together with the main exhaust gas flow from the combined cycle. In order to make an unprejudiced comparison between the two alternatives, the reduced steam turbine efficiency has been taken into consideration and estimated, for the alternative with internal steam extraction. The cycles have been modeled in the commercial heat and mass balance program IPSEPRO™ using detailed component models. Utilizing EGR can double the CO_2 content of the exhaust gases and reduce the energy need for the separation process by approximately 2% points. Using an external biomass-fuelled boiler as heat source for amine regeneration turns out to be an interesting option due to high CO_2 capture effectiveness. However the electrical efficiency of the power plant is reduced compared with the option with internal steam extraction. Another drawback with the external boiler is the higher investment costs but nevertheless, it is flexibility due to the independency from the rest of the power generation system represents a major operational advantage.

[DOI: 10.1115/1.4000122]

1 Introduction

The increasing anthropogenic CO_2 emissions and possible global warming have challenged countries all over the world to find new and better ways to meet the world's increasing need for energy while reducing greenhouse gas (GHG) emissions. Since it is envisaged that alternative energy sources will only provide part of the world's energy needs in the near-term future, fossil fuels will remain a key energy source [1]. Combustion of fossil fuels for power generation currently accounts for approximately one-third of the total CO_2 emissions in EU-25 and this share is likely to increase in the future due to growth in demand for electricity [2]. Hence, increased energy conversion efficiency in combination with carbon capture and storage (CCS) is essential to reduce CO_2 emissions considerably while permitting the continuing use of fossil fuels in power generation. Among the three generally considered categories for carbon capture technologies, postcombustion, precombustion, and oxyfuel combustion, special attention has historically been devoted to postcombustion systems and in particular chemical absorption. In addition to its advantages of being retrofittable onto existing power plants and the most suitable technology for future capture ready plants, it is also the most viable CO_2 capture technology today as two commercialized processes exist [3–7]. However, one of the main obstacles is the large amount of heat required for solvent regeneration, due to large volumetric flows. This is consequently leading to considerable penalty in net electric efficiency of around 8–10% points for natural gas combined cycles [8,9].

Fundamental research concerning the retrofit of existing power plants has been performed in the recent past as a need to explore the best near-term plan for CO_2 capture. These studies include analysis of different alternatives to reduce the reboiler duty [10–12] and integration of the absorption process into conventional power cycles [6,7,13–17]. These process integration studies have principally been conducted on coal-fired power plants emphasizing the location of turbine steam extractions. It has been revealed that the optimal option is to extract saturated steam in between the intermediate- and low pressure turbines [4,17,18] with a pressure corresponding to a steam saturation temperature of approximately 132°C, depending on the reboiler pinch point, using the lowest quality steam available to fulfill the reboiler requirements [18]. However, conventional steam turbines (STs) do not have an extraction point in this pressure range; hence, modifications of the steam cycle are necessary. Several options for the steam extraction are presented in a study by Zachary and Titus [5], concluding that integration of a noncondensing turbine for the steam extraction from the intermediate pressure (IP)/low pressure (LP) turbine crossover pipe is the most efficient.

Nonintegrated solutions for the heat supply to the capture plant are enabling alternatives when the design basis of the power plant requires a constant export of electricity. In a comparative study of different humid air turbine (HAT) cycles with CO_2 capture by Fredriksson Möller et al. [19], including an option with an external biomass-fuelled boiler as steam supply to the reboiler, it was

---

Contributed by the International Gas Turbine Institute of ASME for publication in the Journal of Engineering for Gas Turbines and Power. Manuscript received April 8, 2009; final manuscript received April 14, 2009; published online March 17, 2010. Editor: Dilip R. Ballal.

Copyright © 2010 by ASME

Downloaded 02 Jun 2010 to 171.66.16.96. Redistribution subject to ASME license or copyright; see http://www.asme.org/terms/Terms_Use.cfm

Table 1 Assumptions for the reference NGCC [25,27,33]

Parameter	Value	Unit
Ambient air temperature	15	°C
Economizer pinchpoint	15	°C
Evaporator pinchpoint	10	°C
Approach point temp.	5	°C
HRSG pressure drop hot side	0.04	bar
Steam superheating temperature	560	°C
Steam reheat temperature	560	°C
Isentropic efficiency HP/IP ST	0.92	-
Isentropic efficiency LP ST	0.89	-
Condenser pressure	0.04	bar
Turbine inlet temperature (TIT)	1328	°C
GT total pressure ratio	33	-
Fuel	100% CH_4	-
Exhaust gas mass flow	623	kg/s

revealed that the nonintegrated option has a significantly lower efficiency than the alternative with internal steam extraction.

An approach that could reduce capital cost of CO_2 separation units in natural gas-fuelled combined cycles (NGCCs) with integrated postcombustion CO_2 capture is by recirculation of the exhaust gases. Exhaust gas recirculation (EGR) allows for CO_2 separation at elevated partial pressure, and consequently reduces the efficiency penalty and capture equipment costs [20–22]. Nonetheless, recirculation of flue gases affects the combustion process where the most significant aspect is the low oxygen concentration, which has an negative impact on the oxidation of CO to CO_2. In a recent study by ElKady et al. [23] performed at an existing dry low NO_x GE gas turbine burner, it is stated that EGR levels of up to 35% are feasible without major modifications of existing combustion technology.

The scope of the present paper is to investigate a natural gas-fired combined cycle with exhaust gas recirculation, CO_2 post-combustion capture and two different options for the heat supply to the reboiler. The first alternative encompasses thermal integration of the CO_2 capture plant into the steam cycle while the second option utilizes an external biomass-fuelled boiler to raise steam to the stripper. The purpose with this work is to asses the thermodynamic performance of the two concepts along with addressing major technical constraints and opportunities concerning the two different configurations. The present study is aimed to serve as basis for further studies currently in progress considering the crucial issue of precise modeling of both power plant components and the CO_2 capture process for accurate plant design and economical appraisals.

2 Case Study

As reference a “conventional” combined cycle based on the gas turbine (GT)26 from ALSTOM Power [24,25] was simulated in the heat and mass balance program IPSEPRO. The GT26 machine is a heavy duty industrial gas turbine with the special feature of sequential combustion. The two stage combustion system consequently leads to low NO_x emissions and high turbine exit temperatures, which is favorable for combined cycle applications. The heat recovery steam generator (HRSG) is a triple-pressure steam cycle with a single reheat and pressure levels chosen at 120/27/4.6 bar. The steam is condensed in a condenser, cooled with an abundance of water at 10°C. The deaerator system operates at a pressure of 1.2 bar, 105°C with a condensate feed water temperature of 90°C. Deaeration and heating of the condensate is attained by use of LP steam. The condensate from the condenser is heated by means of a closed water loop, which is using the flue gas heat to preheat the condensate in order to utilize as much of the low temperature heat in the exhaust as possible. The input data used for the reference NGCC without CO_2 capture is shown in Table 1, all calculations are based on the lower heating value of the fuel (50.04 MJ/kg).

Table 2 Settings for the CO_2 separation plant

Parameter	Value	Unit
Amine regeneration temperature	120	°C
Pressure drop absorber	0.15	bar
Reboiler pinch point	10	°C
Heat of reaction MEA	85	kJ/mol CO_2
Lean/rich amine HTX pinch point	10	°C
Regenerator reflux ratio	1.0	mol H_2O/mol CO_2

3 Integration of Power Plant and CO_2 Recovery

If CO_2 capture is applied to a NGCC power plant in terms of chemical post-treatment of the flue gases, the main changes of the process layout are an additional cooling unit bringing the temperature of the flue gases down to approximately 50°C, an additional fan to overcome pressure drops in the system, the CO_2 separation plant with the key components, namely, absorber column, lean/rich heat exchanger (HTX) and stripper column, and at last a multistage CO_2 compression unit.

In this work the reference combined cycle has been adapted with chemical absorption removal of CO_2 ahead of the stack. The model used for CO_2 separation is based on the calculation model proposed by Kohl and Nielsen [26] and has been developed by Fredriksson Möller [27]. The model has been used in several studies of gas turbine-based power plants with CO_2 capture and is not further described here [9,27]. An initial condition of the simulations has been to capture 90% of CO_2 produced by means of an aqueous solution of monoethanolamine (MEA), with 30% MEA by weight. The main purpose of the CO_2 separation model is to calculate the heat required for regeneration of the amine solution at a given temperature. However, the reboiler temperature is limited to 122°C, above which thermal degradation of MEA and corrosion becomes intolerable [19]. Prediction of the necessary steam flow to the reboiler requires information about the flue gas such as composition, flow rate, and pressure. These parameters serve as input data to the capture model. A summary of the assumptions for the CO_2 separation plant can be found in Table 2.

In order to reduce the flow rate of exhaust gases to be treated and to increase the CO_2 concentration, the concept of EGR has been added to the reference cycle. EGR is a well known method that has been used earlier for anti-icing purposes in compressors as well as an option to reduce NO_x emissions [21–23]. Due to combustion related issues such as efficiency, flame stability, incomplete oxidation of CO, etc., a maximum level of recirculation of 35–40% is recommended [22,23]. In this work, a recirculation rate of 40% is considered, (after condensation of the water content). This decision was based upon the recommendations by Bolland and Mathieu [22], meaning that EGR levels less than 40% are acceptable reaching a minimum oxygen concentration (MOC) of 16–18 vol % in the combustion air (16.6 vol % in the current study). In order to maintain a high cycle efficiency, the recirculated flue gas is cooled down to 25°C in a flue gas condenser (FGC), which gives an inlet temperature of the compressor of about 20°C after being mixed with ambient air. Besides, an additional blower is required to compensate for the pressure drop in the FGC. The modified combined cycle with EGR has a higher total power output than the reference cycle as a result of elevated turbine exit temperature, but the efficiency is slightly lower due to increased fuel consumption. The performance of the NGCC with EGR in comparison with the reference cycle is presented in Table 3. The input data used for this system are the same as for the reference system, with addition of the FGC and the flue gas blower as described above.

Downloaded 02 Jun 2010 to 171.66.16.96. Redistribution subject to ASME license or copyright; see http://www.asme.org/terms/Terms_Use.cfm

Table 3 Performance parameters of the NGCC with and without EGR

Parameter	Value		Unit
	w/o EGR	w/EGR	
Net power output	410	414	MW
Net LHV efficiency	58.4	57.8	-
Exhaust gas temperature	626	632	°C
Exhaust gas massflow	623	622	kg/s
CO_2 emissions	6.2	10.9	vol%
Power, flue gas blower	-	1033	kW
Cooling duty for EGR	-	20.2	$MW_{thermal}$

The large amount of thermal energy needed for amine scrubbing is one of the main drawbacks of solvent-based CO_2 capture. In order to supply this energy, two different options have been integrated into the reference power plant with EGR for comparison, Figs. 1 and 2.

- The first option includes extraction of steam from the LP section of the steam turbine. This option affects the original plant steam cycle efficiency and power output.
- The second alternative utilizes a biomass boiler to produce the steam needed for regeneration of the amines, without interfering with the original power plant. This option enables under certain conditions for capture efficiencies above 100%.

3.1 Internal Steam Extraction. For the amine-based capture plant used in this study, the most ideal solution would be to extract steam with a pressure of 2.8 bar corresponding to a saturation temperature of 130°C. Nevertheless, the modeled steam cycle doesn't have an extraction point in agreement with the required conditions; hence some necessary modifications of the steam cycle have been made. By extracting steam in between the IP/LP steam turbines, required conditions for the stripping process could be achieved. In order to avoid large throttle losses the LP live steam pressure was reduced to 2.9 bar. The condensate from the capture plant is partly mixed with the steam going to the stripper; to cool the reboiler entry steam down to approximately 130°C [14], the remaining condensate is returned back to the high pressure (HP) feed water circuit Due to the nature of the CO_2 separation plant model the condensate leaving the capture plant is free from undesirable contaminants; hence pretreatment of the condensate before re-injection into the steam cycle has been disregarded.

In addition, the influence by means of reduced steam turbine efficiency due to reduced mass flow expanded through the LP steam turbine has been taken into consideration and estimated, however these effects might be neglected, since the efficiency reduction is less then 2% points. The methodology used to calculate this effect is presented in Ref. [28] and shortly described below.

A turbine section could mainly be described by two parameters; isentropic efficiency and swallow capacity. The isentropic efficiency is defined as

$$\eta_s = \frac{\Delta h_0}{\Delta h_{0,s}} = \frac{h_{0,\mathrm{in}} - h_{0,\mathrm{out}}}{h_{0,\mathrm{in}} - h_{0,s,\mathrm{out}}} \tag{1}$$

When a turbine section is considered, the stage loading parameter, also known as isentropic velocity number, is replaced by the Parson number. The Parson number is defined as [28]

$$X = \frac{\Sigma u^2}{\Delta h_s} \tag{2}$$

A method to further simplify this equation is by correlating the efficiency to relative Parson number, which results in the elimination of the sum of the blade speed squared in the numerator, due to the fact that the turbine rotational speed is the same for both cases. This results in a correlation where the efficiency is only dependent on relative isentropic enthalpy drop [28]:

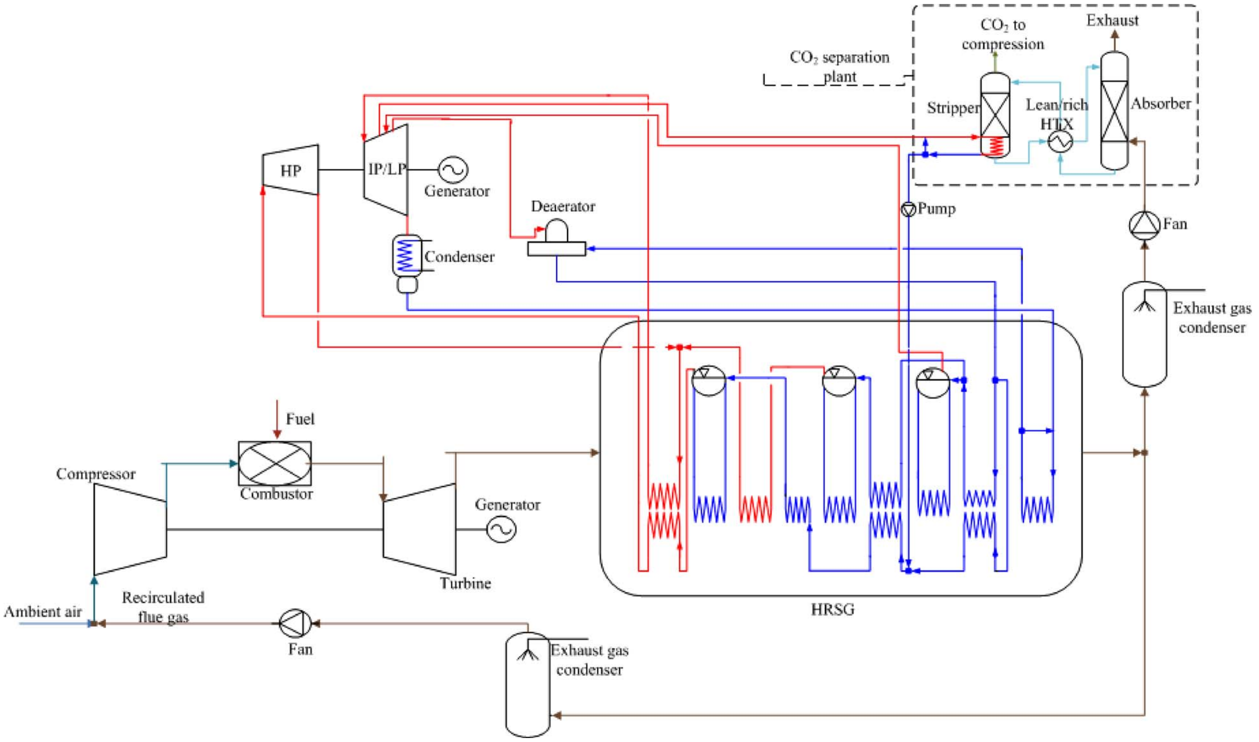

Fig. 1 Layout of the NGCC with EGR and CO_2 separation by internal steam extraction

Downloaded 02 Jun 2010 to 171.66.16.96. Redistribution subject to ASME license or copyright; see http://www.asme.org/terms/Terms_Use.cfm

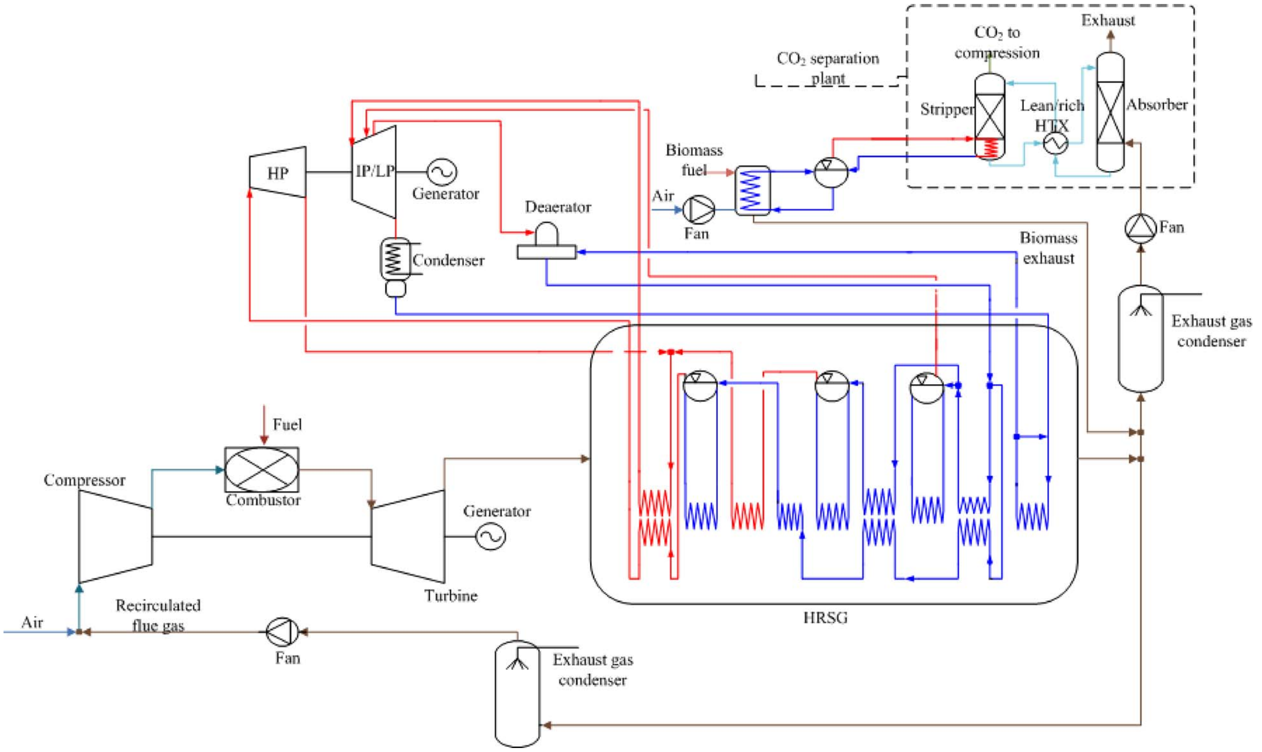

Fig. 2 Layout of the NGCC with EGR and CO$_2$ separation by the utilization of a biomass boiler

$$\eta_{s,\mathrm{act}}^{\mathrm{dry}} = \eta_{s,\mathrm{des}}^{\mathrm{dry}} \cdot f\left(\frac{\Delta h_{s,\mathrm{des}}}{\Delta h_{s,\mathrm{act}}}\right) \tag{3}$$

The actual (denoting the case when steam is extracted) and the design enthalpy drop (denoting the case when capture is not applied and no steam is extracted) for the LP steam turbine are calculated by simulation of the two cases. By knowing the relationship between actual and design enthalpy drop the actual efficiency could be derived using characteristic curves presented in Ref. [28]. For further information the readers are referred to p. 426 in Ref. [28].

3.2 Biomass Boiler. As a second alternative, a biomass boiler has been modeled to produce the steam required for the absorption process. Prior to entering the CO$_2$ capture plant the exhaust from the boiler is mixed with the flue gases from the combined cycle. In this way 100% of the fossil fuelled-based CO$_2$ and a part of the CO$_2$ generated by biomass could be treated. The fuel composition used in the simulations was chosen as 32.74% C, 28.44% O, 4.13% H, 0.89% N, 0.09 S, 30% moist, and 2.9% ash [29]. The outlet exhaust temperature from the boiler was set to 150°C.

One of the main operational burdens for chemical absorption of CO$_2$ is the breakdown of the amines in the presence of large quantities of oxygen in the flue gas stream. These breakdown processes, also known as oxidative degradation, lead to solvent losses and formation of undesirable degradation products, which have to be removed to uphold the separation of CO$_2$. In addition, the oxidative degradation of amines is highly affected by the sulfur content in the exhaust gas, i.e., SO$_2$, which results in the formation of heat-stable salts. SO$_2$ levels below 10 ppm are considered as acceptable without the need for additional flue gas treatment prior to the CO$_2$ capture unit [30]. Low levels of SO$_2$ are achievable by a proper selection of the biomass fuel. In this work, a wood-based fuel has been chosen, for which the SO$_2$ level in the exhaust gases is well below the European Union (EU) daily limit levels of 50 mg/Nm^3 [31].

4 Results and Discussion

The performance of the modeled NGCC with EGR and chemical absorption separation of CO$_2$ along with two different options for the heat supply for amine regeneration is presented in Table 4. The comparison shows a decrease in net efficiency for both options, but the efficiency drop for the external biomass boiler option is twice as high, 11.5%, as for the modified steam cycle alternative. The high efficiency penalty for the external boiler is due to increase in fuel thermal energy input. However, the biomass option has major advantages that should not be disregarded. An important benefit in this context is the anticipated implementation of countermeasures against CO$_2$ emissions like the recognition of CCS within the EU emission trading scheme (ETS) [32].

Table 4 Technical performance of the studied cycles

Parameter	Ref. NGCC w/EGR	Alt. 1 steam cycle	Alt. 2 bio boiler	Unit
Net power output[a]	414	371.8	405.8	MW
Net LHV efficiency[a]	57.8	52.0	46.4	%
ST shaft power	154.2	119.4	153.8	MW
LP ST efficiency	89	87	89	%
Overall capture efficiency	-	90	91.2	%
Additional fuel consumption	-	-	160.3	MW
EGR rate	40	40	40	%
EGR fan power	1033	1033	1033	kW
Capture unit fan power	-	6877	6948[b]	kW
Cooling duty for EGR	20.2	26.7	21.0	MW$_{\mathrm{thermal}}$
Cooling duty prior capture	-	32.93	25.2	MW$_{\mathrm{thermal}}$

[a] The net power output and the net LHV efficiency are calculated without including the additional energy needed to compress the captured CO$_2$ to suitable transport conditions.

[b] The calculated fan power prior capture includes the power needed for the air blower before the biomass boiler.

Downloaded 02 Jun 2010 to 171.66.16.96. Redistribution subject to ASME license or copyright; see http://www.asme.org/terms/Terms_Use.cfm

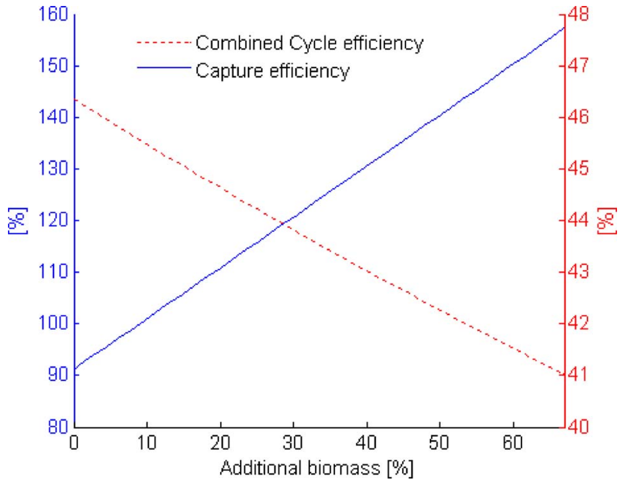

Fig. 3 The effects on net combined efficiency and capture efficiency for increased steam generation by additional combustion of biomass fuel in the biomass boiler

Capturing the CO_2 derived from the combustion of biomass in addition to CO_2 from fossil fuels results under certain circumstances in negative net emissions, providing an opportunity for additional revenues for power producers in a future ETS market. Nevertheless, this is only achievable at the expense of even lower cycle efficiency, as seen in Fig. 3, along with increased amount of CO_2 needed to be stored. Furthermore, the exhaust gases leaving the biomass boiler at approximately 150°C can be used for heat production to be integrated into a district heating net improving the energy efficiency of the plant. Another option could be to utilize the heat in the biomass exhausts in an organic Rankine cycle (ORC) for additional electricity production, thus improving the electrical efficiency of the plant. However, the additional investment costs for the ORC cycle should be evaluated in a thermo-economical study.

As the results reveal the most convenient integration option of the CO_2 chemical absorption plant is by modification of the existing steam cycle. If the power plant is not built as a capture ready plant major changes of the steam cycle will be necessary due to the changed cycle properties at the time when capture is to be applied. The main issue is the modification of the steam turbines, as a result of the 50% reduction in mass flow entering the LP turbine. The steam extraction will not only influence the LP turbine, but also the IP in terms of reduced backpressure at the turbine outlet that in turn reduces the flow. Additional losses encountered due to this reduction need to be further investigated, hence the estimated LP steam turbine efficiency drop of 1.9% points is most probably underestimated.

The component models used in this study are standard models of the IPSE model library, except for the CO_2 separation plant and the biomass boiler. It is well known that process modeling and simulation play an important role for system optimization as well as for evaluation of different plant process alternatives. Therefore the use of advanced models with detailed information such as component geometry, performance, characteristics, etc., is crucial to perform results with high accuracy.

However, physical models built up by heat and mass balance equations require and provide a high level of knowledge of a process. At the same time, a convergent solution of such a process requires iterations, which for a high accuracy model is achieved at the cost of computational time due to complex program code. Moreover, it is also known that the complexity of a physical model is limited by the fact that it is impossible to include all parameters that real systems typically possess. Another approach, which could maintain both the accuracy of a complex model and reduce the time needed for computation considerably, is by the use of statistical models such as artificial neural networks (ANN).

The research group has many years of experience in developing advanced physical component models of gas turbines, steam turbines, heat exchangers, condensers, etc. In an ongoing study, the same cycles as evaluated in this work are modeled with advanced component models in order to gain deeper understanding about the significance of using high accuracy models. Nevertheless, our previous experience of developing and integrating component models with detailed information to perform power plant simulations has shown to be difficult in some respects, due to too high complexity. Therefore, an ANN model of the CO_2 separation plant has been developed and integrated into our existing heat and mass balance models in IPSEPRO. The results from the thermo-economical studies based on above described models will soon be published.

5 Conclusions

The performance of a triple-pressure reheat natural gas combined cycle with postcombustion CO_2 capture and EGR has been evaluated. Two different alternatives for the heat supply to the amine regeneration were analyzed and compared based on their technical performance.

The study has shown that integration of the CO_2 separation plant by modifying the existing steam cycle to the conditions required by the stripper is the best option with regard to the overall power plant efficiency. It has also been concluded that the decrease in LP steam turbine efficiency due to the steam extraction after the IP turbine is approximately 2% points and has only a marginal influence on the net combined cycle efficiency.

Using an external biomass boiler to supply the necessary steam to the CO_2 capture process is the least efficient option with an estimated net efficiency reduction of 11.5% points compared with the reference NGCC with EGR. Nonetheless, the external boiler has one important feature that cannot be reproduced by the performance parameter net cycle efficiency, which is the operational independency. The external boiler option assures a near 100% power output, relative to a plant without CO_2 capture, whether the CO_2 separation process is in operation or not. Additionally, economical benefits could be gained by allocations of green certificates, CO_2 emission allowances, etc., since the biomass boiler allows for capture efficiencies above 100%.

The main focus of this paper has been to evaluate the technical performance of the two options. Apparently the best technical solution is not always the best one from an economical point of view. At the end of the day the best solution is the one showing the best economy over the plants lifetime. Accordingly, an economical analysis is necessary to evaluate which option is the most profitable and will be further investigated.

Nomenclature

f = function of
h = enthalpy
u = blade speed
Δ = difference
η = efficiency
X = Parson number

Subscripts

0 = stagnation properties
act = actual
des = design
in = inlet
out = outlet
s = isentropic

Superscripts

dry = expansion in dry zone

Downloaded 02 Jun 2010 to 171.66.16.96. Redistribution subject to ASME license or copyright; see http://www.asme.org/terms/Terms_Use.cfm

References

[1] 2007, IEA World Energy Outlook.

[2] European Commission Directorate-General for Research, 2006, "World Energy Technology Outlook-2050."

[3] Reddy, S., Scherffius, J., Freguia, S., and Roberts, C., 2003,"Fluor's Econamine FG Plus^{SM} Technology: An Enhanced Amine-Based CO_2 Capture Process," Second National Conference on Carbon Sequestration, Alexandria, VA, May 5–8.

[4] Alstom, 2001, "Engineering Feasibility and Economics of CO_2 Capture on an Existing Coal-Fired Power Plant," US DOE NETL Report No. PPL-01-CT-09.

[5] Zachary, J., and Titus, S., 2008, "CO_2 Capture and Sequestration Options: Impact on Turbo-Machinery Design," ASME Paper No. GT2008-50642.

[6] Desideri, U., and Paolucci, A., 1999, "Performance Modelling of a Carbon Dioxide Removal System for Power Plants," Energy Convers. Manage., **40**, pp. 1899–1915.

[7] Singh, D., Croiset, E., Douglas, P. L., and Douglas, M. A., 2003, "Techno-Economic Study of CO_2 Capture From an Existing Coal-Fired Power Plant: MEA Scrubbing Vs. O_2/CO_2 Recycle Combustion," Energy Convers. Manage., **44**, pp. 3073–3091.

[8] Kvamsdal, H. M., Jordal, K., and Bolland, O., 2007, "A Quantitative Comparison of Gas Turbine Cycles With CO_2 Capture," Energy, **32**, pp. 10–24.

[9] Fredriksson Möller, B., Assadi, M., Linder, U., 2003, "CO_2 Free Power Generation—A Study of Three Conceptually Different Plant Layouts," ASME Paper No. GT2003-38413.

[10] Tobiesen, A., Svendsen, H. F., and Hoff, K. A., 2005, "Desorber Energy Consumption Amine-Based Absorption Plants," International Journal of Green Energy, **2**, pp. 201–215.

[11] Abu-Zahra, M. R. M., Schneiders, L. H. J., Niederer, J. P. M., Feron, P. H. M., and Versteeg, G. F., 2007, "CO_2 Capture From Power Plants. Part I. A Parametric Study of the Technical Performance Based on Monoethalonamine," Int. J. Greenh. Gas Control, **1**, pp. 37–46.

[12] Aroonwilas, A., and Veawab, A., 2007, "Integration of CO_2 Capture Unit Single- and Blended-Amines Into Supercritical Coal-Fired Power Plant: Implications for Emission and Energy Management," Int. J. Greenh. Gas Control, **1**, pp. 143–150.

[13] Romeo, L. M., Espatoleroa, S., and Bolea, I., 2008, "Designing a Supercritical Steam Cycle to Integrate the Energy Requirements of CO_2 Amine Scrubbing," Int. J. Greenh. Gas Control, **2**, pp. 563–570.

[14] Romeo, L. M., Bolea, I., and Escosa, J. M., 2008, "Integration of Power Plant and Amine Scrubbing to Reduce CO_2 Capture Costs," Appl. Therm. Eng., **28**(8-9), pp. 1039–1046.

[15] Alie, C., 2006, "Simulation and Optimization of a Coal-Fired Power Plant With Integrated CO_2 Capture Using MEA Scrubbing," *Proceedings of the Eighth International Conference on Greenhouse Gas Control Technologies*, Trondheim, Norway.

[16] Mimura, T., Shimojo, S., Suda, T., Iijima, M., and Mitsuoka, S., 1995, "Research and Development on Energy Saving Technology for Flue Gas Carbon Dioxide Recovery and Steam System in Power Plant," Energy Convers. Manage., **36**, pp. 397–400.

[17] Mimura, T., Simayoshi, H., Suda, T., Iijima, M., and Mituoka, S., 1997, "Development of Energy Saving Technology for Flue Gas Carbon Dioxide Recovery in Power Plant by Chemical Absorption Method and Steam System," Energy Convers. Manage., **38**, pp. S57–S62.

[18] Alie, C., 2004, "CO_2 Capture With MEA: Integrating the Absorption Process and Steam Cycle of an Existing Coal-Fired Power Plant," M.Sc. thesis, University de Waterloo, Canada.

[19] Fredriksson Möller, B., Obana, M., Assadi, M., and Mitakakis, A., 2004, "Optimisation of HAT-Cycles-With and Without CO_2 Capture," ASME Paper No. GT2004-53734.

[20] Chiesa, P., and Consonni, S., 2000, "Natural Gas-Fired Combined Cycles With Low CO_2 Emissions," Trans. ASME: J. Eng. Gas Turbines Power, **122**, pp. 429–436.

[21] Finkenrath, M., Ursin, T. P., Hoffmann, S., Bartlett, M., Evulet, A., Bowman, M. J., Lynghjem, A., and Jakobsen, J., 2007, "Performance and Cost Analysis of Novel Gas Turbine Cycle With CO_2 Capture," ASME Paper No. GT2007-27764.

[22] Bolland, O., and Mathieu, P., 1998, "Comparison of Two CO_2 Removal Options in Combined Cycle Power Plants," Energy Convers. Manage., **39**(16–18), pp. 1653–1663.

[23] ElKady, A. M., Evulet, A., Brand, A., Ursin, T. P., Lynghjem, A., 2008, "Exhaust Gas Recirculation in DLN F-Class Gas Turbines for Post-Combustion CO_2 Capture," ASME Paper No. GT2008-51152.

[24] Alstom Power webpage: http://www.power.alstom.com

[25] Kjellberg, T., "Evaluation of a CO_2 Capture Ready Combined Cycle," M.Sc. thesis, Lund University, Sweden. 2007.

[26] Kohl, A. L., and Nielsen, R. B., 1997, *Gas Purification*, 5th ed., Gulf Publishing Co., Houston, TX.

[27] Fredriksson Möller, B., 2005, "A Thermoeconomic Evaluation of CO_2 Capture With Focus on Gas Turbine-Based Power Plants," Ph.D. thesis, Lund University, Sweden.

[28] Schobeiri, M., 2005, *Turbomachinery Flow Physics and Dynamic Performance*, Springer-Verlag, Berlin, Heidelberg.

[29] Simon, D., 2008, StandardKessel GmbH, Duisburg, Germany, personal communication.

[30] Chapel, D. G., and Mariz, C. L., 1999, "Recovery of CO_2 From Flue Gases: Commercial Trends," Canadian Society of Chemical Engineers Annual Meeting, Saskatoon, Saskatchewan, Canada, Oct. 4–6.

[31] European Commission, IP/07/1537, 2007, "Air Pollution: Commission Takes Action Over Levels of Sulphur Dioxide and PM10 in Member States," Brussels, Belgium, October.

[32] European Commission, 2007, "Limiting Global Climate Change to 2 Degrees Celsius: The Way Ahead for 2020 and Beyond," Brussels, Belgium, January.

[33] IEA Greenhouse Gas R&D Programme, 2005, "Retrofit of CO_2 Capture to Natural Gas Combined Cycle Power Plants."

Downloaded 02 Jun 2010 to 171.66.16.96. Redistribution subject to ASME license or copyright; see http://www.asme.org/terms/Terms_Use.cfm

Ramón F. Colmenares Quintero
School of Engineering,
Cranfield University,
Cranfield, Bedfordshire MK43 0AL, UK
e-mail: r.f.colmenaresquintero@cranfield.ac.uk
Gas Turbine Engineering Group,
Aeronautical Engineering Programme,
Faculty of Engineering,
Universidad de San Buenaventura,
Carrera 8H No. 172-20, Bogotá, Colombia
e-mail: gtegroup@docentes.usbbog.edu.co

Rob Brink
e-mail: rob.brink@gmail.com

Stephen Ogaji
e-mail: s.ogaji@cranfield.ac.uk

Pericle Pilidis
e-mail: p.pilidis@cranfield.ac.uk

School of Engineering,
Cranfield University,
Cranfield, Bedfordshire MK43 0AL, UK

Juan C. Colmenares Quintero
Department of Chemistry,
Olah and Prakash Group,
Loker Hydrocarbon Research Institute,
University of Southern California,
837 Bloom Walk,
Los Angeles, CA 90089-1661
e-mail: jcarlos@wp.pl
Institute of Physical Chemistry,
Polish Academy of Sciences,
ul. Kasprzaka 44/52, 01–224 Warszawa, Poland
e-mail: jcarlos@ichf.edu.pl

Alexander García Quintero
Faculty of Industrial Engineering,
Escuela Colombiana de Carreras Industriales,
Cra. 19 No. 49-20,
Bogotá, Colombia
e-mail: betolisto1@hotmail.com

Application of the Geared Turbofan With Constant Volume Combustor on Short-Range Aircraft: A Feasibility Study

Recently a considerable effort was made to understand the gas- and thermodynamics of wave rotor combustion technology. Pressure-gain combustors potentially have superior performance over conventional combustors due to their unsteady flow behavior. Wave rotor combustion provides semiconstant volume combustion and could be integrated in the steady-flow gas turbine. However, a feasibility study to assess the economical and environmental aspects of this concept has not been conducted for short-range missions. Preliminary multidisciplinary design framework was developed to assess novel and radical engine cycles. The tool comprises modules to evaluate noise, emissions, and environmental impact. Uncertainty can be accounted for with Monte Carlo simulation. The geared turbofan with constant volume combustor is simulated and benchmarked against a baseline geared turbofan engine. Results indicate that the former complies with CAEP/6 and FAR Part 36 regulations for noise and emissions. Furthermore, the acquisition cost of the engine is higher, but the engine direct operating cost decreases by 25.2%. The technology requires further development to meet future noise and emission requirements. [DOI: 10.1115/1.4000135]

Keywords: environment, economics, innovative turbofans, multidisciplinary design optimization

1 Introduction

Aviation forms a vital part of the transportation system required for today's globalized economy. Furthermore, it generates revenue and provides jobs. The annual growth of air transport raises concerns about noise pollution and emissions. Soaring fuel prices affect airline operation and have an impact on the affordability of air transport.

Noise pollution is an issue for inhabitants of the airport's hinterland. The growth of air traffic and the probability of congestion near airports drive the call of local governments and residents for more stringent regulations. Furthermore, legislators consider extension of emission regulations to include cruise. Implementation of such legislation could have a considerable impact on airline operation and economics. Noise and emission charges have been introduced on several (mainly European) airports. Besides, the European Union plans to add aviation to its greenhouse gas emission trading scheme. These measures are put in place to encourage airlines to operate clean and quiet aircraft.

The Advisory Council for Aviation Research in Europe (ACARE) has formulated a vision for the year 2020. Objectives set, for engines, are a 20% decrease in fuel burn and CO_2 emissions, 80% NO_x emission reduction, and 6 dB less noise. The ACARE vision comprises a roadmap for the research-and-development effort required to achieve those aims. Novel and

---

Contributed by the International Gas Turbine Institute (IGTI) of ASME for publication in the Journal of Engineering for Gas Turbines and Power. Manuscript received April 15, 2009; final manuscript received April 21, 2009; published online March 24, 2010. Editor: Dilip R. Ballal.

Copyright © 2010 by ASME

Downloaded 02 Jun 2010 to 171.66.16.96. Redistribution subject to ASME license or copyright; see http://www.asme.org/terms/Terms_Use.cfm

Table 1 Main performance parameters of baseline GTF

Parameter	Units	GTF	GTF CVC
TET	K	1650	1650
BPR	-	8.2	8.2
FPR	-	1.45	1.45
OPR	-	38.6	38.6
Mass flow	kg/s	445.64	420.55

radical engine cycles are developed under several programs (e.g., VITAL, NEWAC, and DREAM) to achieve these ambitious goals.

Colmenares et al. [1–4], Pascovici et al. [5–7], and Kyprianidis et al. [8] did techno-economic analyses of multiple novel cycles including intercooled, intercooled-recuperated, contrarotating turbofan (CRTF), and geared turbofan (GTF) cycles. The multidisciplinary design framework TERA was utilized for the analyses.

A radical cycle under research is the combustion wave rotor (CVC). Considerable effort has been invested to understand its unsteady flow behavior [9–11]. However, only one study is known to the authors that assesses the operational feasibility of a conventional turbofan with CVC combustor [12]. In this paper a geared turbofan mounted with a CVC is considered. The main question is as follows: Compared with a baseline geared turbofan is the GTF CVC cycle feasible to match noise and emission regulations for an acceptable performance and cost of ownership?

Since the low pressure system of the geared turbofan can operate at its optimum speed, the stage count is reduced and the SFC is lower. Besides, the pressure gain over the CVC—due to semi-constant volume combustion—potentially contributes to the reduced stage count. The main disadvantage of the GTF CVC cycle is its complexity. For a comprehensive description of the CVC cycle the reader is referred to research undertaken in the past [13].

2 Research Methodology

First, a parametric study is performed to explore the design space. The objectives are minimum fuel burn, cruise SFC, NO_x emissions, noise, and engine direct operating cost (DOC). Both the baseline GTF and GTF CVC have a TET of 1650 K, since the technology level of both engines is assumed similar. The optimum FPR is determined with the design parameters BPR and OPR. The main performance parameters of the baseline GTF and GTF CVC are listed in Table 1. A roadmap of the optimization study is provided in Fig. 1.

Subsequently, five single-objective optimizations and one multi-objective optimization are performed. The GTF CVC cycle is optimized for every individual objective. Then a multi-objective trade case is run for fuel burn versus cruise SFC versus NO_x emissions versus noise versus engine DOC. The Kreisselmeier–Steinhauser method combined with the Davidon–Fletcher–Powell optimization algorithm is used.

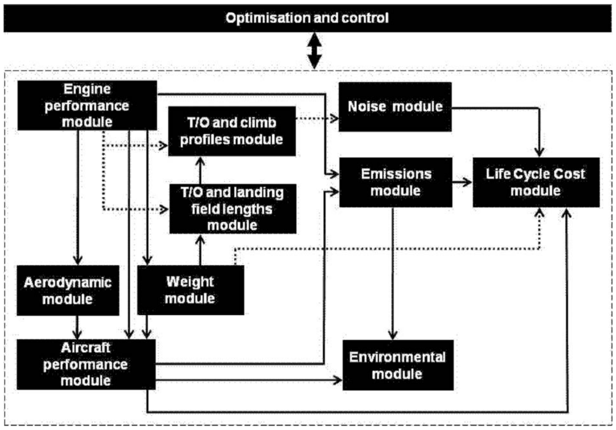

Fig. 2 Overview of PMDF

Ultimately, a risk assessment is carried out on the engine DOC with Monte Carlo simulation.

The simulations for this paper are run for a “rubber aircraft” with fixed payload-range performance. If the engine design parameters are varied, the aircraft geometry changes [14]. All results for the GTF CVC are given relative to the baseline GTF.

3 Preliminary Multidisciplinary Design Framework

A tool was developed for the assessment of novel and radical cycles. The preliminary multidisciplinary design framework (PMDF) consists of several interconnected modules, which are linked to an optimization and control unit. Figure 2 provides an overview of PMDF. The reader is referred to Ref. [15] for detailed description of this tool.

The emission, environmental, and weight modules were developed by Cranfield University. An existing life cycle cost module was modified, and the remaining models were obtained from NASA.

4 Validation

PMDF is validated with the data of an Airbus A320 mounted with CFM56-5 engines. A selection of validation results is listed in Table 2. The data for the validation are obtained from the public domain. The reliability of these data cannot be guaranteed.

However, the validation gives a good indication of the accuracy of PMDF results. Best engineering judgment is used where no validation data are available.

5 Results and Discussion

The feasibility of the GTF CVC cycle is assessed with a multidisciplinary design optimization (MDO) study. The results pre-

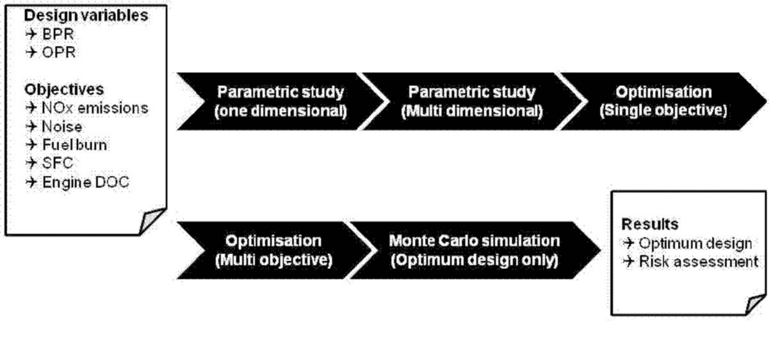

Fig. 1 Roadmap optimization study

Downloaded 02 Jun 2010 to 171.66.16.96. Redistribution subject to ASME license or copyright; see http://www.asme.org/terms/Terms_Use.cfm

Table 2 Validation results

Parameter	Units	PMDF	PD
SFC$_{sls}$	g/kN s	8.98	-
SFC$_{cr}$	g/kN s	16.60	17.00[a]
FN$_{sls}$	kN	120	120
FN$_{cr}$	kN	19	-
Engine weight	kg	2,381	2,382
Engine length	m	2.76	2.60
Fan diameter	m	1.76	1.73
Design range	km	4,847	4,815[b]
Block fuel	kg	15,778	-
Block time	h	6.08	-
MTOW	kg	78,259	73,920[c]
ZFW	kg	61,651	61,025
Climb time to FL350	min	19.50	-
Climb distance	km	236.87	-
Climb fuel	kg	1,549	-
Descent time	min	22.4	-
Descent distance	km	202.24	-
Descent fuel	kg	259	-
Flyover noise	EPNdB	82	88
Sideline noise	EPNdB	93.6	94.4
Combined noise	EPNdB	175.6	182.4
LTO EI$_{NO_x}$	g/kN	30.8	29.57[d]
Total RF	W/m^2	1.27×10^{-5}	-
Price CFM56	USD	6.98	6.95[e]
Price Airbus A320	USD	77.17	76.9
Total maintenance	$ct/ASM	2.02	2.01[f]
Engine maintenance	$ct/ASM	0.68	0.67

[a] Source: Jane's Aero Engines, 21st ed.
[b] Source: Airbus.
[c] Source: Jane's All the World's Aircraft, 2006–2007 ed.
[d] Source: ICAO, Annex 16, Vol. 2.
[e] Source: CFM International.
[f] Source: Aircraft Commerce February/March 2007.

sented in this section are relative to the baseline GTF cycle. They represent the percentage increase or decrease compared with the baseline GTF.

5.1 Parametric Study. Variation of nondimensional block fuel and LTO NO$_x$ is presented in Fig. 3. LTO NO$_x$ decreases, if the BPR becomes larger. This is mainly due to the reduction in SFC caused by higher BPRs. On the other hand, the LTO NO$_x$ of the GTF CVC is lower than the value found for the baseline GTF despite high values of NO$_x$ emission index, which arise from constant volume combustion process.

Block fuel diminishes with rising BPR until an optimum value is reached at BPR equals to 7.2. This reduction in fuel burn is because of a propulsive efficiency improvement. For BPRs greater than 7.2 the engine weight and the nacelle drag become dominant and the block fuel increases. The GTF CVC burns almost 17% less fuel than a baseline GTF engine.

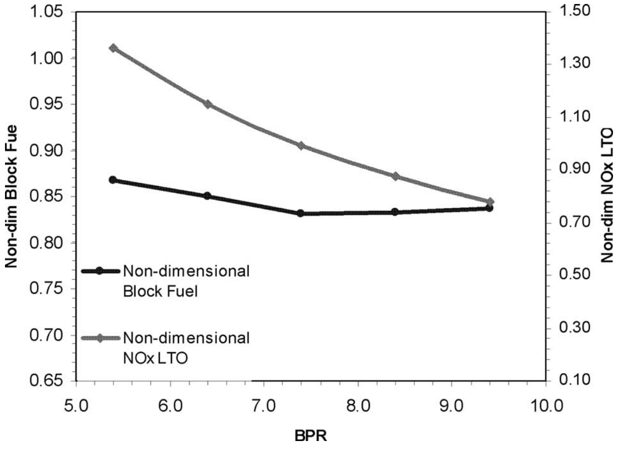

Fig. 3 Parametric study of nondimensional block fuel and LTO NO$_x$ versus BPR (FPR=1.45, OPR=38.6, and TET=1650 K)

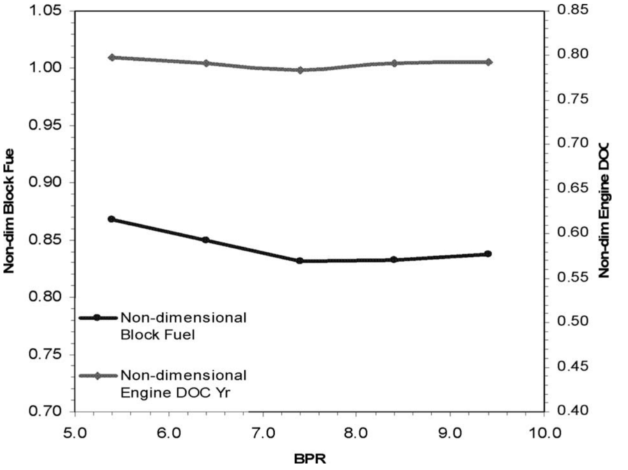

Fig. 4 Parametric study of nondimensional block fuel and engine DOC versus BPR (FPR=1.45, OPR=38.6, and TET =1650 K)

Engine DOC (see Fig. 4) has a relatively constant value at 0.80 approximately. However, an optimum engine DOC can be identified, which coincides with the optimum block fuel for BPR equals to 7.2. The engine DOC curve levels off for BPR ranging from 8.3 to 9.4, since the combined noise levels are lower. Hence, the noise charges—which have a significant influence on the engine DOC—decrease and offset the raising fuel cost.

Nondimensional flyover, sideline, and combined noise are presented in Fig. 5. If BPR increases, the exhaust jet velocity drops and jet noise decreases. However, the fan diameter increases with BPR, which results in higher fan noise levels. Sideline noise is mainly controlled by fan broadband noise (i.e., the turbulence that develops in the wakes of the fan blades). Figure 5 shows that jet and fan noise balance over almost the complete BPR-domain. Flyover noise is dominated by the eighth power of the jet velocity (Lighthill's theory), which in turn reduces as the BPR does. In case of flyover the GTF CVC produces more noise than the baseline GTF. Since the flyover noise is more dominant for higher

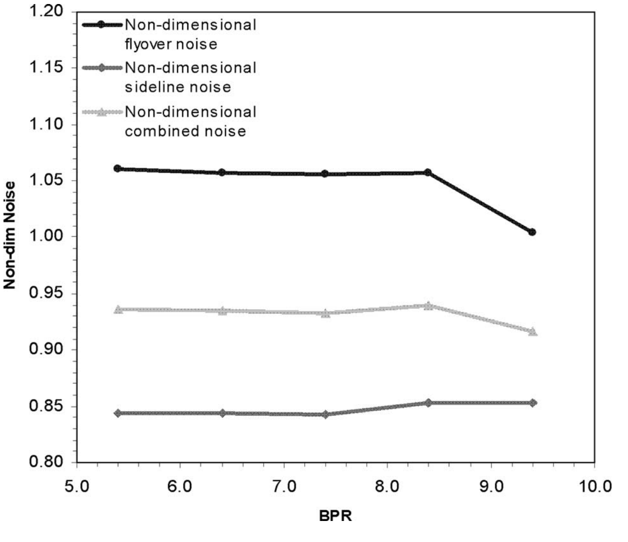

Fig. 5 Parametric study of nondimensional EPNL versus BPR

Downloaded 02 Jun 2010 to 171.66.16.96. Redistribution subject to ASME license or copyright; see http://www.asme.org/terms/Terms_Use.cfm

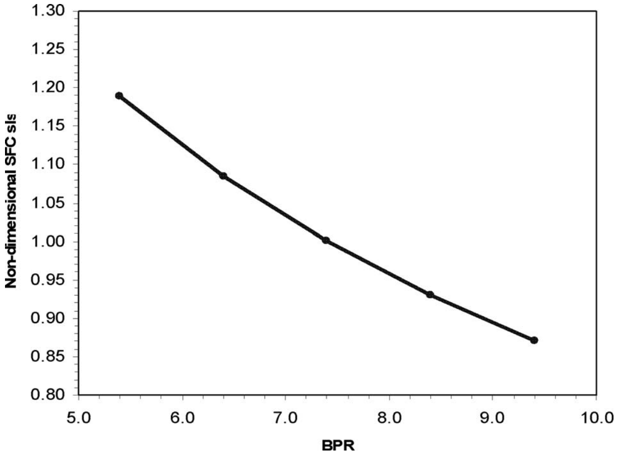

Fig. 6 Parametric study of nondimensional SFC versus BPR (FPR=1.45, OPR=38.6, and TET=1650 K)

values of BPR, the combined noise follows its trend leading to a drop in cumulative noise.

SFC in nondimensional values as a function of BPR is provided in Fig. 6. If BPR rises, the SFC decreases because of an improvement of the propulsive efficiency. For BPR values above 7.2 the GTF CVC has a lower SFC than the baseline GTF.

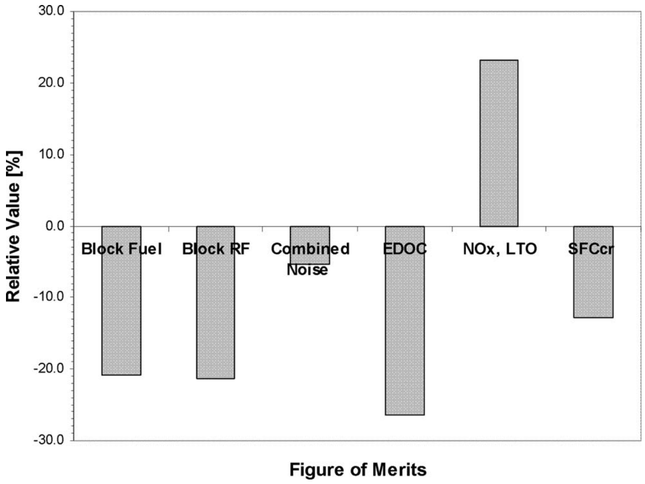

Fig. 7 Single-objective optimization for minimum fuel burn (BPR=7.5, FPR=1.45, OPR=53.9, and TET=1650 K)

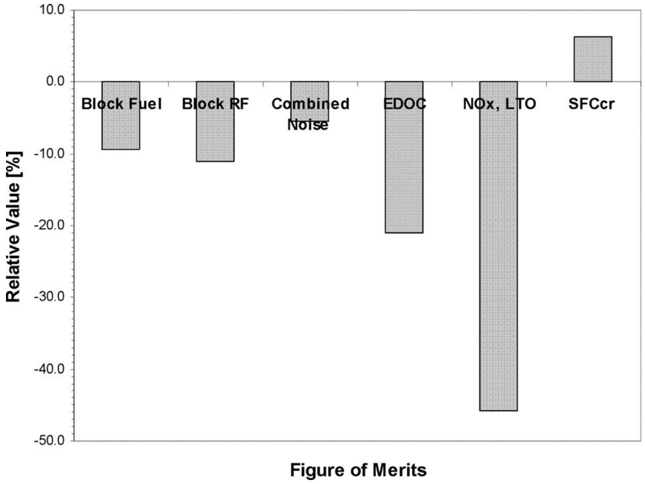

Fig. 8 Single-objective optimization for minimum NO_x emissions (BPR=5.5, FPR=1.45, OPR=30.0, and TET=1650 K)

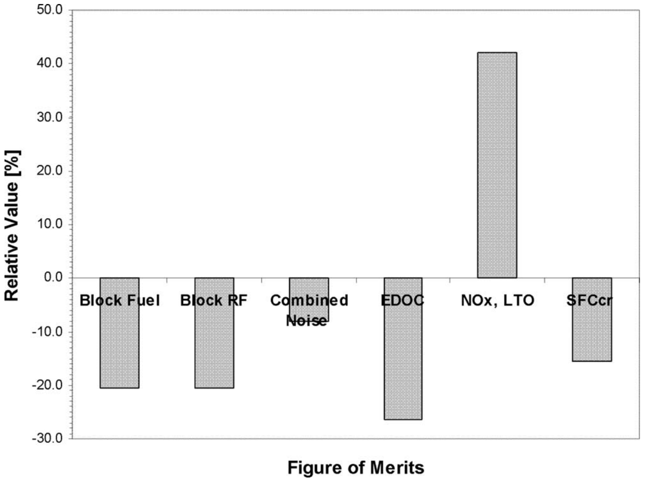

Fig. 9 Single-objective optimization for minimum cruise SFC/noise (BPR=8.5, FPR=1.45, OPR=54.0, and TET=1650 K)

5.2 Single-Objective Optimization. Single-objective optimization is performed for minimum fuel burn, cruise SFC, NO_x emissions, noise, and engine DOC. Figures 7–10 display the results of the optimization runs. Aero-engine design requires a compromise between NO_x and CO/CO_2 emissions (fuel burn) to find the overall optimum. The single-objective optimization minimum for fuel burn, cruise SFC, and NO_x emissions demonstrate this trade-off.

Optimization of the GTF CVC cycle for fuel burn results in a 20.9% reduction compared with the baseline GTF (see Fig. 7). Besides, the cruise SFC improves with 12.8% due to the high OPR. This improvement of cruise SFC is offset by the lower BPR (GTF BPR=8.2 and GTF CVC BPR=7.5). The lower fuel burn is reflected in the engine DOC as a cost advantage. Combined noise is lower than the baseline, since the fan is smaller. Radiative forcing (RF) contributions for CO_2 and NO_x are calculated by PMDF. Block RF is over 21% lower because of the significant reduction in fuel burn, but is offset by higher NO_x emissions.

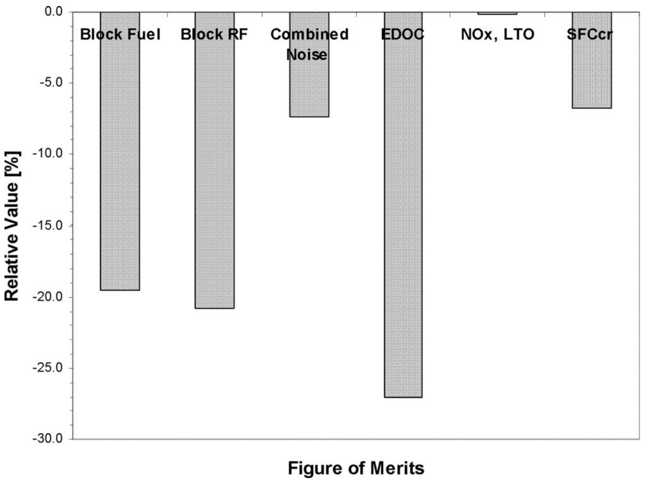

Fig. 10 Single-objective optimization for minimum engine DOC (BPR=5.8, FPR=1.45, OPR=54.0, and TET=1650 K)

Downloaded 02 Jun 2010 to 171.66.16.96. Redistribution subject to ASME license or copyright; see http://www.asme.org/terms/Terms_Use.cfm

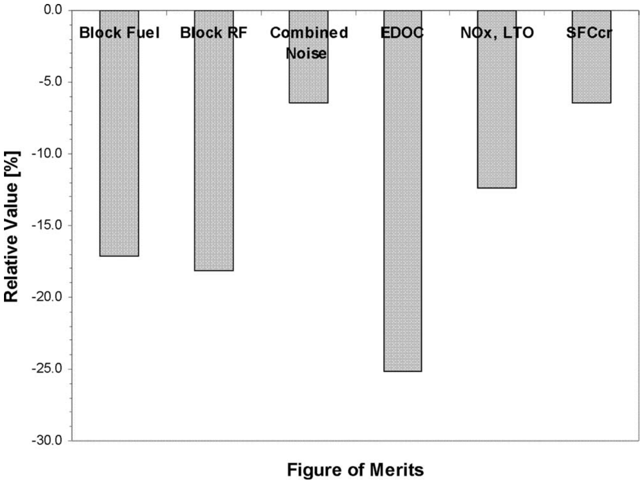

Fig. 11 Multi-objective optimization for FB versus NO_x versus cruise SFC versus noise versus engine DOC ($BPR=6.9$, $FPR=1.46$, $OPR=41.6$, and $TET=1650$ K)

If the engine is optimized for minimum NO_x emissions, a 45.7% reduction is obtained (see Fig. 8). The OPR and combustion temperature are moderate, which results in low NO_x formation. Fuel burn decreases by 9.3% but the cruise SFC is higher than the baseline value. This trend may appear controversial on first sight. However, the cruise schedule selected for the mission (optimum altitude for given Mach number and range) allows the aircraft with a GTF CVC engine to fly higher. Therefore, fuel burn in cruise is less than baseline, although the SFC is higher. Again, the reduction in fuel burn and noise results in a decrease in engine DOC. Block RF reduces under the influence of lower fuel burn and NO_x emissions.

The optimization for minimum SFC (see Fig. 9) shows a trend similar to the optimization for minimum fuel burn (see Fig. 7). A lower cruise SFC is obtained at the expense of a substantial increase in NO_x emissions.

Optimizations for minimum cruise SFC and minimum combined noise result in a similar engine (see Fig. 9). High BPR is favorable for both high propulsive efficiency and a low exhaust jet velocity. The high TET and OPR provide a favorable thermal efficiency. In this single-objective optimization case an engine DOC reduction of 26.5% is obtained. A 20.5% block-RF reduction is obtained due to a significant reduction in fuel burn (read CO_2 emissions).

Figure 10 demonstrates that the main contributors to engine DOC are fuel cost and noise charges. The 27% cost reduction is obtained with a 19.5% decrease in fuel burn, almost 21% less RF, and 7.3% less noise. Interestingly, NO_x emissions remain virtually unchanged. The engine design for minimum operational cost gives a 6.8% reduction in cruise SFC. This decrease is the product of a high OPR and a modest BPR.

5.3 Multi-Objective Optimization. A multi-objective optimization run is done to find the optimum design compromise. A trade-off is made for fuel burn versus cruise SFC versus NO_x emissions versus combined noise versus engine DOC. Figure 11 presents the results of the optimum design compromise.

Table 3 Ranges of *K*-factors

K-factor	Range
Maintenance labor rate	1.0–1.03
Noise charges	1.0–1.2
Emission charges	1.0–1.2
Cost technology factors	0.9–1.1

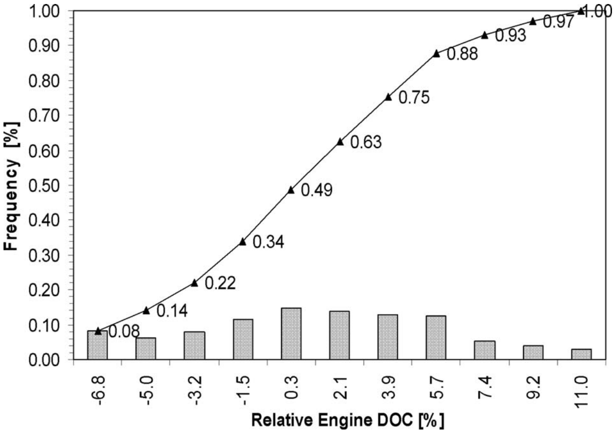

Fig. 12 Cumulative curve EDOC

Table 4 Quartiles and median of the cumulative curve

Parameter	EDOC (%)
Median	0.95
Lower quartile	−2.01
Upper quartile	3.90
Interquartile range	5.91

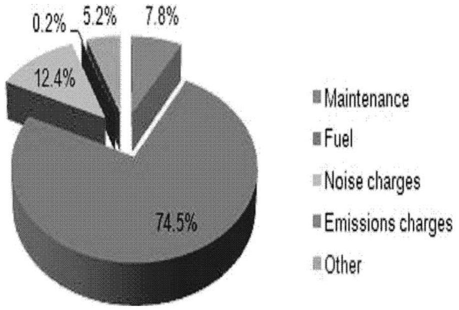

Fig. 13 Breakdown of the engine DOC for the baseline GTF

The optimized design induces a 17.2% decrease in fuel burn, 18.2% decline of radiative forcing, 6.4% lower cruise SFC, 12.4% reduction in NO_x emissions, 6.5% less noise, and 25.2% lower engine DOC. Potential advantages over the baseline for individual figures of merit are higher in the case of the single-objective optimization cases. Obviously, the design optimized for several figures of merit is a compromise to achieve the best overall result.

NO_x emissions are mainly driven by flame temperature, residence time, and the homogeneity of the fuel-air mixture. The unsteady flow behavior of the combustion wave rotor potentially allows for short residence times. However, the CVC adiabatic flame temperature is higher due to the constant volume combustion process. No work is done on the flow during combustion. Therefore, the internal energy of the flow is higher than in the case of the baseline GTF. Consequently, the SFC of the GTF CVC cycle is lower but NO_x emissions are potentially higher. Ultimately, the balance of SFC reduction and emission index rise determines the NO_x emissions per unit net thrust. Therefore, compromise is required to achieve the optimum design.

5.4 Cumulative Curves. An uncertainty assessment is performed for the engine DOC. Monte Carlo simulation is applied to the optimized GTF CVC cycle ($BPR=6.9$, $FPR=1.45$, OPR

Downloaded 02 Jun 2010 to 171.66.16.96. Redistribution subject to ASME license or copyright; see http://www.asme.org/terms/Terms_Use.cfm

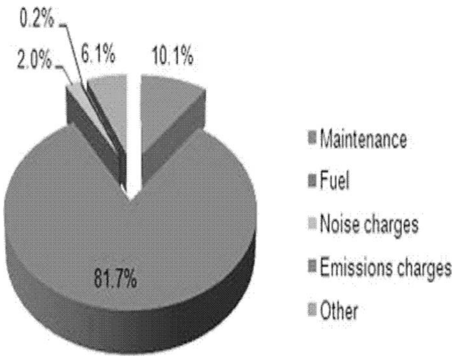

Fig. 14 Breakdown of the engine DOC for the GTF CVC

=41.6, and TET=1650 K) for this purpose. *K*-factors are used to access the uncertainty of noise and emission charges, maintenance labor rate, and cost technology factors for engine R&D, production, and maintenance (see Table 3). The range for the fuel price is set from \$3.57 to \$6.00 per gallon, based on the kerosene price of June 2008.

The cumulative curve for the relative engine DOC is presented in Fig. 12. Furthermore, Table 4 shows the median, quartile, and interquartile ranges. The probability is 50% that the engine DOC has a value between −3.2% and 3.9%. Besides, the chance is 25% that the relative engine DOC is higher than 3.9%.

5.5 Breakdown of Engine DOC. Engine DOC is broken down into categories for the baseline GTF and optimized[1] GTF CVC in Figs. 13 and 14. The category "other" comprises depreciation and insurance cost. Three major items in the engine DOC of the baseline GTF are maintenance and fuel costs as well as noise charges. The optimized GTF CVC produces slightly less noise, which is reflected in the engine DOC. Main contributors to the engine DOC of the GTF CVC are fuel (81.7%) and maintenance (10.7%) costs. Emission charges have a similar contribution for both engines. Depreciation and insurance cost shares differ 0.85% between the GTF and GTF CVC engines.

The lower contribution of fuel cost for the baseline GTF (74.5% compared with 81.7% for the GTF CVC) may seem controversial at first sight. However, the baseline GTF has a lower contribution of fuel cost due to the high (12.4%) noise charge. The lower contribution of noise charges for the GTF CVC drives the fuel contribution up to 81.7%. Also, a small shift can be identified in maintenance cost. In absolute figures, the GTF CVC burns less fuel and therefore its fuel cost is lower.

5.6 Pareto Front. The Pareto front is an effective methodology to validate feasible aero-engine designs. An *n*-parameter design space is defined and *k* criteria are applied to assess all design points. Each design space point *x* is assigned a criteria space point $f(x)$. The dimensions of criterion vector *X* have to be minimized to find feasible criterion points for the Pareto front. Therefore, image vector *Y* must be strictly dominated by criterion vector *X*. Mathematically the process is expressed as follows:

$$f: R^n \rightarrow R^k \tag{1}$$

X is a set of feasible designs in R^n.

$$Y = f(X) \tag{2}$$

$$X \succ Y \tag{3}$$

Figure 15 shows the Pareto front of the nondimensionalized fuel burn versus NO_x emissions. A reduction in NO_x emission can be obtained at the cost of a higher fuel burn. If NO_x emissions are reduced by 20% (from 1.0 to 0.8 for the GTF CVC), fuel burn increases 4%. Hence, compliance with future emissions and economical requirements could imply a design compromise.

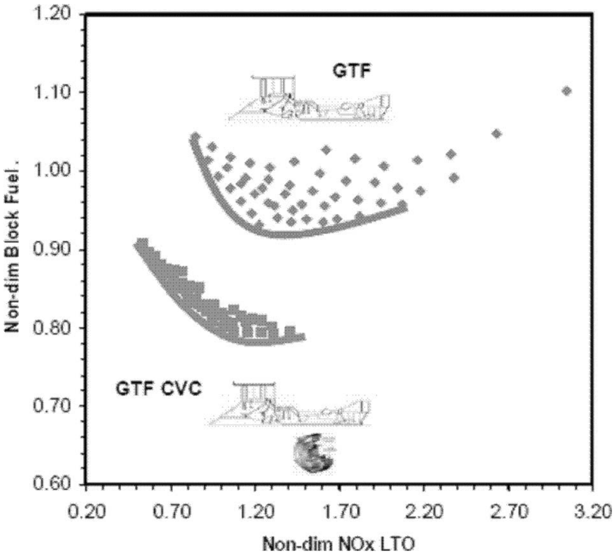

Fig. 15 Pareto front nondimensional FB versus NO_x

The Pareto fronts for nondimensionalized fuel burn and noise versus engine DOC are shown in Fig. 16. Note that the Pareto front for EDOC versus FB of the GTF CVC is small. Hence, variations in fuel burn have a small impact on engine DOC for the design points on the Pareto front. In case of the GTF CVC, a modest reduction in noise (e.g., 2 EPNdB) results in 2.7% higher engine DOC due to increased maintenance cost. The BPR rises from 5.5 to 8.5.

Figure 16 shows that compared with a baseline geared turbofan (EDOC=1.0, FB=1.0, and delta noise=0.0 EPNdB), the GTF CVC cycle consumes less fuel and produces less noise for lower engine DOC.

5.7 Comparison Baseline GTF and Optimized GTF CVC. The main cycle and performance parameters of the baseline GTF and optimized GTF CVC engines are listed in Table 5. FPR, TET, and FN of the engines are similar. BPR and mass flow of the GTF CVC are lower. Conversely, the engine with a combustion wave

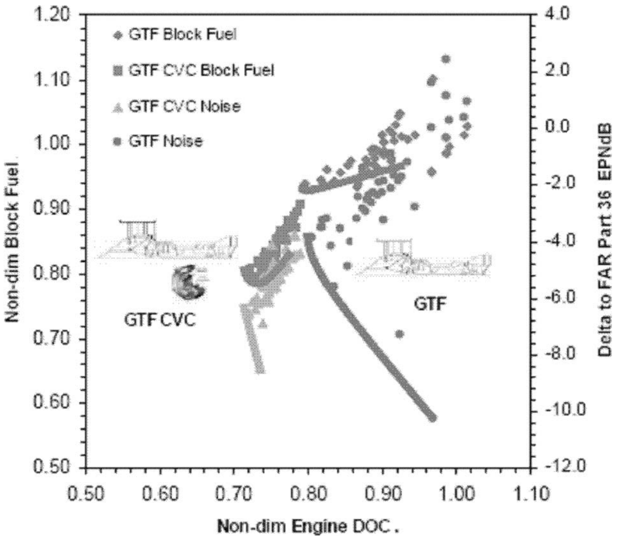

Fig. 16 Pareto front nondimensional FB/noise versus EDOC

---

[1] Optimized for fuel burn, cruise SFC, NO_x, noise, and engine DOC.

Downloaded 02 Jun 2010 to 171.66.16.96. Redistribution subject to ASME license or copyright; see http://www.asme.org/terms/Terms_Use.cfm

Table 5 Main cycle and performance parameters of the baseline GTF and optimized GTF CVC

Parameter	Units	GTF (BL)	GTF CVC
TET	K	1650	1650
BPR	-	8.2	6.9
FPR	-	1.45	1.45
OPR	-	38.6	41.6
Mass flow	kg/s	446	401
FN[a]	kN	121	121

[a] Net thrust at ISA SLS.

Table 6 Dimensions and weight delta to baseline of the GTF CVC

Parameter	Δ to BL (%)
Bare engine weight	−18.0
Bare engine length	15.7
Bare engine maximum radius	−1.7
Nacelle length	5.6
Nacelle weight	4.5
Power plant weight	−13.2

Table 7 Compliance of the optimized GTF CVC to noise and emission requirements

Noise[a] Δ to FAR36 (EPNdB)	NO_x emission LTO fraction of CAEP/6 (%)
−5.25	56.6

[a] Combined noise.

rotor has a higher overall pressure ratio.

Deviations in dimensions and weight of the GTF CVC from the baseline GTF are listed in Table 6. Bare engine, as well as powerplant, weight is lower. However, the nacelle weight has increased by 4.5%. Supplementary ducting and a longer burner (CVC) contribute to additional length and weight. Conversely, the GTF CVC's fan and gear system are 23.9% lighter. Therefore, the overall powerplant weight diminishes by 13.2%.

5.8 Compliance to Noise and Emission Requirements. Apart from cost of ownership, compliance to noise and emission requirements is an important consideration in aero-engine design. Noise pollution is a local problem confined to the vicinity of airports. However, pollutant emissions have both a local and global impact. Noise and emission regulations become more stringent as air traffic increases. Emissions have an environmental as well as an economical impact. The European Union decided to add aviation to the EU greenhouse gas emission trading scheme. Besides, ICAO considers emission legislation for cruise. These measures could have a considerable economical impact on airline operations. Table 7 shows that the GTF CVC cycle complies with FAR36 and CAEP/6 regulations. Furthermore, the cycle has development potential to meet future noise and emission requirements.

6 Conclusions

The GTF CVC has a significant cost of ownership advantage over geared turbofans. Acquisition and maintenance costs of GTF CVC engines are higher. A substantially lower fuel burn offsets these costs though. Hence, the life cycle cost of the GTF CVC engines is lower.

Replacement of the annular combustor with a CVC allows for a reduction in HPC size for a given net thrust. Furthermore, lower stage count for the HPT and LPT can be achieved. However, the relative weight of individual stages could be higher due to elevated pressures and temperatures. Careful design of ducting between the turbomachinery and CVC is required to curb its weight.

NO_x emissions of the GTF CVC are lower than the baseline. A higher EI is offset by a lower SFC. The net result is lower NO_x production.

The results of the multi-objective trade case study show that the GTF CVC complies with FAR36 and CAEP/6 noise and emission requirements. Also, a substantial cost of ownership reduction has been identified. However, a considerable R&D effort is required before GTF CVC engines can enter service.

Design, production, and development of a CVC cycle test setup could contribute to the effort undertaken to understand its behavior. Furthermore, this test setup could provide detailed data and component maps, which can be used for further MDO studies.

Acknowledgment

We would like to express our acknowledgments to Arnie McCullers and Karl Geiselhart for the advice on the models NASA provided. Their support was very helpful in understanding and using the models.

Nomenclature

ASM = available seat mile
BPR = by-pass ratio
CAEP = Committee on Aviation Environmental Protection
CO = carbon monoxide
CO_2 = carbon dioxide
CVC = constant volume combustion
DREAM = validation of radical engine architecture systems
EDOC = engine direct operating cost
EI = emission index
EPNL = effective perceived noise level
EU = European Union
FAR = federal aviation regulation
FB = fuel burn (block fuel)
FN = net thrust
FPR = fan pressure ratio
GTF CVC = geared turbofan with constant volume combustion
HPC/HPT = high pressure compressor/turbine
ICAO = International Civil Aeronautics Organization
K = scaling factor
LPT = low pressure turbine
LTO = landing and take-off
MTOW = maximum take-off weight
NASA = National Aeronautics and Space Administration
NEWAC = new aero-engine core concepts
NO_x = nitrogen oxides
OPR = overall pressure ratio
R&D = Research and Development
SFC = specific fuel consumption
TERA = techno-economical risk assessment
TET = turbine entry temperature
USD = American dollar
VITAL = environmentally friendly aero-engine (EU project)
X = vector of design variables
ZFW = zero fuel weight

Subscripts

cr = cruise condition
sls = sea level static

Downloaded 02 Jun 2010 to 171.66.16.96. Redistribution subject to ASME license or copyright; see http://www.asme.org/terms/Terms_Use.cfm

References

[1] Colmenares, F., Pascovici, D. S., Ogaji, S., and Pilidis, P., 2007, "A Preliminary Parametric Study for Geared, Intercooled and/or Recuperated Turbofan for Short Range Civil Aircraft," ASME Paper No. GT2007-27234.

[2] Colmenares, F., Gomez, J., Pascovici, D., and Ogaji, S., 2007, "A Preliminary Feasibility Study for Future Aero Engines," *Proceedings of the 18th ISABE Conference*, ISABE, Blacksburg, VA, Paper No. ISABE 2007-1194.

[3] Colmenares, F., Kyprianidis, K., Gomez, J., Ogaji, S., Pilidis, P., and Latorre, S., 2008, "Future Aero-Engines' Optimisation for Minimal Fuel Burn," ASME Paper No. GT2008-50126.

[4] Colmenares, F., Pascovici, D., Ogaji, S., Pilidis, P., Garcia, A., and Latorre, L., 2008, "Future Aero-Engines' Optimisation for Minimal Operating Costs," ASME Paper No. GT2008-50127.

[5] Pascovici, D. S., Colmenares, R. F., Ogaji, S. O. T., and Pilidis, P., 2007, "An Economic and Risk Analysis Model for Aircraft and Engines," ASME Paper No. GT2007-27236.

[6] Pascovici, D. S., Colmenares, F., Ogaji, S. O. T., and Pilidis, P., 2007, "Analysis of Direct Operating Costs of Future Engines," *Proceedings of the 18th ISABE Conference*, ISABE, Blacksburg, VA, Paper No. ISABE 2007-1106.

[7] Pascovici, D. S., Colmenares, F., Kyprianidis, K. G., Ogaji, S. O. T., and Pilidis, P., 2008, "Weibull Distributions Applied to Cost and Risk Analysis for Aero Engines," ASME Paper No. GT2008-51060.

[8] Kyprianidis, K., Colmenares, F., Pascovici, D., Ogaji, S. O. T., Pilidis, P., and Kalfas, A. I., 2008, "EVA—A Tool for Environmental Assessment of Novel Propulsion Cycles," ASME Paper No. GT2008-50602.

[9] Akbari, P., Nalim, M. R., and Li, H., 2006, "Analytic Aerothermodynamic Cycle Model of the Combustion Wave Rotor in a Gas Turbine Engine," *Proceedings of the Fourth International Energy Conversion Engineering Conference and Exhibit*, AIAA, Reston, VA, Paper No. AIAA 2006-4176.

[10] Akbari, P., Nalim, M. R., and Snyder, P. H., 2006, "Numerical Simulation and Design of a Combustion Wave Rotor for Deflagrative and Detonative Propagation," *Proceedings of the 42nd AIAA/ASME/SAE/ASEE Joint Propulsion Conference and Exhibit*, AIAA, Reston, VA, Paper No. AIAA 2006-5134.

[11] Akbari, P., Szpynda, E., and Nalim, M. R., 2007, "Recent Developments in Wave Rotor Combustion Technology and Future Perspectives: A Progress View," *Proceedings of the 43rd AIAA/ASME/SAE/ASEE Joint Propulsion Conference and Exhibit*, AIAA, Reston, VA, Paper No. AIAA 2007-5055.

[12] Won, H. T., and Waters, M., 2003, "Constant Volume Combustor Implementation on a 50 Passenger Commercial Regional Transport Mission Simulation," *Proceedings of the 39th AIAA/ASME/SAE/ASEE Joint Propulsion Conference and Exhibit*, AIAA, Reston, VA, Paper No. AIAA 2003-4413.

[13] Smith, C. F., Snyder, P. H., Emmerson, C. W., and Nalim, M. R., 2002, "Impact of the Constant Volume Combustor on a Supersonic Turbofan Engine," *Proceedings of the 38th AIAA/ASME/SAE/ASEE Joint Propulsion Conference and Exhibit*, AIAA, Reston, VA, Paper No. AIAA 2002-3916.

[14] Hertel, J., and Albers, M., 1993, "The Impact of Engine and Aircraft Interrelations on DOC and Its Application to Engine Design," *Proceedings of the AIAA Aircraft Design, Systems and Operations Meeting*, AIAA, Reston, VA, Paper No. AIAA 1993-3930.

[15] Colmenares Quintero, R. F., 2009, "Techno-Economic and Environmental Risk Assessment of Innovative Propulsion Systems for Short-Range Civil Aircraft," Ph.D. thesis, Cranfield University, Cranfield, Bedfordshire.

Downloaded 02 Jun 2010 to 171.66.16.96. Redistribution subject to ASME license or copyright; see http://www.asme.org/terms/Terms_Use.cfm

Comparison of Preanode and Postanode Carbon Dioxide Separation for IGFC Systems

Eric Liese
National Energy Technology Laboratory,
P.O. Box 880 Morgantown,
WV 26507
e-mail: eric.liese@netl.doe.gov

This paper examines the arrangement of a solid oxide fuel cell (SOFC) within a coal gasification cycle, this combination generally being called an integrated gasification fuel cell cycle. This work relies on a previous study performed by the National Energy Technology Laboratory (NETL) that details thermodynamic simulations of integrated gasification combined cycle (IGCC) systems and considers various gasifier types and includes cases for 90% CO_2 *capture (2007, "Cost and Performance Baseline for Fossil Energy Plants, Vol. 1: Bituminous Coal and Natural Gas to Electricity," National Energy Technology Laboratory Report No. DOE/NETL-2007/1281). All systems in this study assume a Conoco Philips gasifier and cold-gas clean up conditions for the coal gasification system (Cases 3 and 4 in the NETL IGCC report). Four system arrangements, cases, are examined. Cases 1 and 2 remove the* CO_2 *after the SOFC anode. Case 3 assumes steam addition, a water-gas-shift (WGS) catalyst, and a Selexol process to remove the* CO_2 *in the gas cleanup section, sending a hydrogen-rich gas to the fuel cell anode. Case 4 assumes Selexol in the cold-gas cleanup section as in Case 3; however, there is no steam addition, and the WGS takes places in the SOFC and after the anode. Results demonstrate significant efficiency advantages compared with IGCC with* CO_2 *capture. The hydrogen-rich case (Case 3) has better net electric efficiency compared with typical postanode* CO_2 *capture cases (Cases 1 and 2), with a simpler arrangement but at a lower SOFC power density, or a lower efficiency at the same power density. Case 4 gives an efficiency similar to Case 3 but also at a lower SOFC power density. Carbon deposition concerns are also discussed.* [DOI: 10.1115/1.4000140]

1 Introduction

Gasification technologies, along with new cleanup and sequestration technologies, allow for an environmentally advantageous use of coal for energy production, as well as the coproduction of other beneficial products such as hydrogen, liquid fuels, etc. Given the vast quantities of coal resources, it is logical to advance these technologies as part of a secure energy future. To support this advancement, this paper considers plant configurations that combine a solid oxide fuel cell (SOFC)+gas turbine (GT) (a "hybrid") in a way that includes carbon separation and capture, *assuming cold-gas cleanup and a pressurized gasifier currently considered for integrated gasification combined cycle (IGCC) systems* [1]. There have been numerous studies of hybrids without CO_2 separation [2,3] and some studies of hybrids with CO_2 separation considering a natural gas fuel source [4,5]. For an integrated gasification fuel cell (IGFC) system, there are currently some general system outlines given, i.e., a presentation given by GE at the 2006 Solid State Energy Conversion Alliance (SECA) meeting [6] and papers by Tucker et al. [7] and VanOsdol et al. [8] (Refs. [7,8] assume warm-gas cleanup). A chemical looping example with CO_2 capture is shown by Lisbona and Romeo [9]. There are also IGFC studies that employ low-temperature catalytic gasification [10,11], and *it should be noted that such assumed differences could very likely produce different conclusions from this study regarding a preferred cycle layout*.

The SOFC provides an interesting opportunity with regard to CO_2 separation. After the fuel passes through the anode, the spent fuel can be oxidized, with mostly water vapor and CO_2 remaining; the water can be condensed leaving mostly CO_2. Thus a CO_2 physical or chemical separation process is not needed. However, there are drawbacks to this option in contrast to using a CO_2 separation process (with or without water-gas-shift (WGS)) upstream to the anode. In this work, thermodynamic comparisons of such option systems will be shown, along with consideration for other issues such as carbon deposition.

To begin the paper, the fuel inlet assumption to the models will be defined. Then an overview of four system concept cases will be presented. The remaining assumptions will then be discussed along with the basic calculation routine. Then results and conclusions will be given.

2 Fuel Inlet Assumption

The gasifier island is not modeled in this paper. The work here relies on previous work performed in a National Energy Technology Laboratory (NETL) Office of Systems Analysis and Planning (OSAP) study of IGCC systems that compares various gasifiers and syngas cleanup with and without CO_2 removal [1]. In particular, results from the Conoco Philips E-Gas gasifier were used (OSAP Cases 3 and 4 in the report), with results taken after the syngas cooler (convective boiler). The syngas state variables and molar composition input to the inlet of the cold-gas cleanup process are given in Table 1. The coal mass flow rate to the gasifier is 210,417 kg/h with a high heating value (HHV) of 27,134 kJ/kg (the energy input result being 1586 MW).

The removal point of CO_2 will be shown on a case by case basis. To summarize, there will either be CO_2 removal after the anode, CO_2 separation upstream of the anode with steam added WGS of the CO, or CO_2 separation upstream of the anode *without* steam added WGS. Other assumptions will be given, but first an overview of the four cases is presented.

Contributed by the International Gas Turbine Institute (IGTI) of ASME for publication in the Journal of Engineering for Gas Turbines and Power. Manuscript received April 21, 2009; final manuscript received April 23, 2009; published online March 24, 2010. Editor: Dilip R. Ballal.

Copyright © 2010 by ASME

Downloaded 02 Jun 2010 to 171.66.16.96. Redistribution subject to ASME license or copyright; see http://www.asme.org/terms/Terms_Use.cfm

Table 1 Fuel conditions for model inlet

State variables	
Temperature	370°C
Pressure	37 bar
Mass flow rate	545,525 kg/h
Mole fractions	
N_2	0.0102
Ar	0.0190
H_2	0.2738
CO	0.3851
CO_2	0.1473
H_2O	0.1246
CH_4	0.0400

3 Case 1 Overview

The first case begins with the idea that CO_2 will be removed postanode, and thus no CO_2 removal process is necessary. However, due to the need to remove sulfur, cold-gas cleanup is still necessary, shown by the "Fuel Conditioning" box in Fig. 1.

The syngas is cooled and water condensed prior to fuel cleaning. A methyldiethanolamine (MDEA) process is assumed for H_2S removal, as in Case 3 of the NETL OSAP study. Some internal reheating is done along with supplemental fuel reheating to 350°C. The fuel reheat temperature is limited to 350°C, since the low water content of the syngas makes carbon dusting a concern [12]. Since this temperature is so limited, no syngas expander is used to produce power via syngas expansion. Instead a jet ejector is assumed since anode recycle is used to re-introduce water in order to prevent carbon deposition in the fuel cell, and to heat the anode inlet gas to a temperature of 650°C. It is assumed that the pressure of the syngas (around 37 bar) is enough motive pressure to recycle the anode exhaust (at pressures from 2 bar to 4 bar) by using a jet ejector [13,14]. A small fraction of the anode exhaust goes to the GT combustor. The remaining "waste" is expanded in a turbine (producing power) to atmospheric pressure. This fuel is oxidized (with oxygen from the air separation unit (ASU)), and the latent heat is used to preheat the anode inlet fuel to 350°C and to raise steam for power generation and auxiliary applications (as elaborated on in Sec. 7). The water vapor is condensed, with mostly CO_2 remaining. This is compressed to 150 bar.

On the cathode side, air is compressed and then preheated to 650°C via a GT exhaust recuperator (dotted line is a heat stream). The SOFC utilizes oxygen and heats the cathode air to 800°C, and the cathode exhaust is then joined with a fraction of the anode waste prior to expansion in the turbine. It is noted that in practice the recuperator would have to be larger than any current recuperator designed as a GT air recuperator, or multiple recuperators would have to be used.

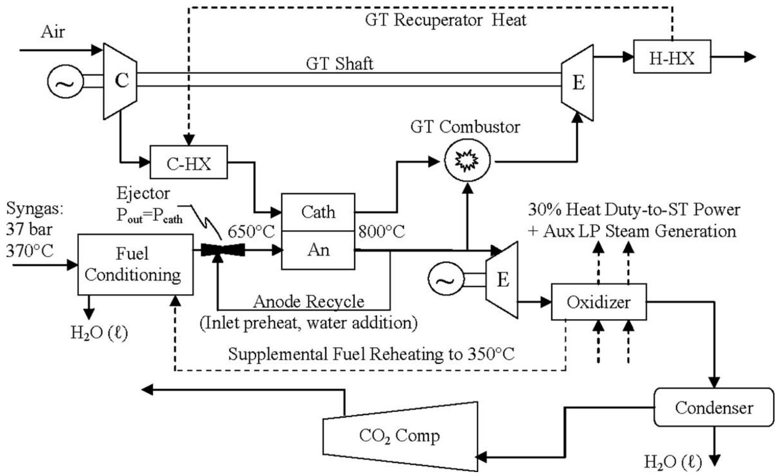

Fig. 1 Case 1: postanode CO_2 capture with cathode recuperator

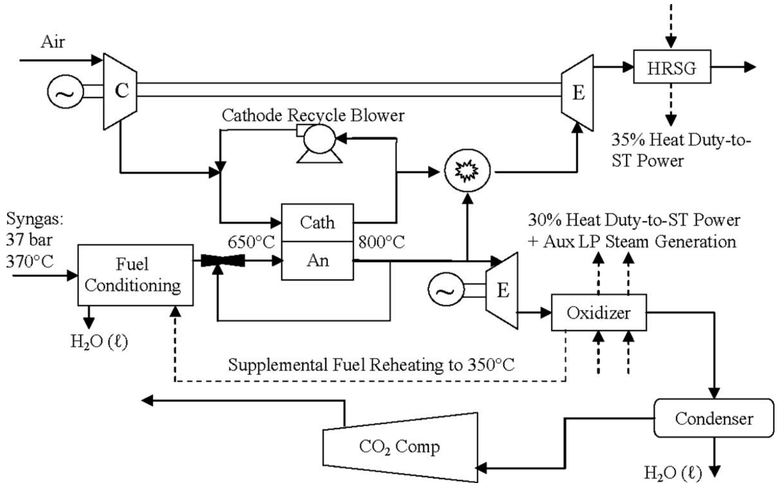

Fig. 2 Case 2: postanode CO_2 capture with cathode recycle

Downloaded 02 Jun 2010 to 171.66.16.96. Redistribution subject to ASME license or copyright; see http://www.asme.org/terms/Terms_Use.cfm

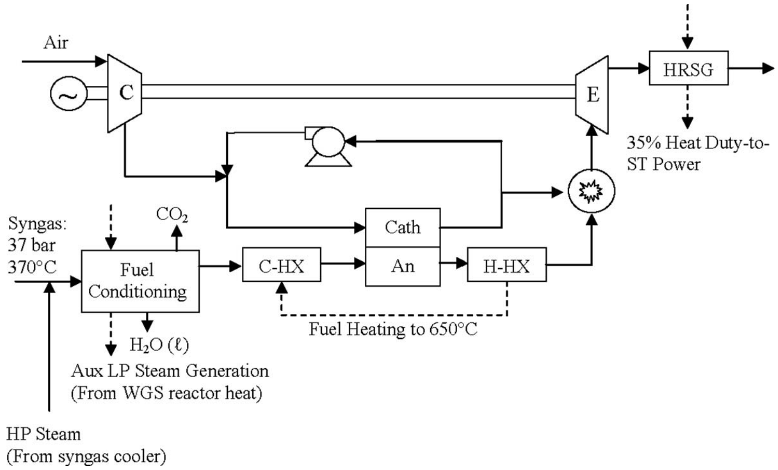

Fig. 3 Case 3: preanode CO_2 capture with steam addition and WGS

4 Case 2 Overview

Case 2, shown in Fig. 2, is similar to Case 1 except that instead of a recuperator to preheat the cathode inlet air, the cathode exhaust is recycled with a blower, and this preheats the inlet air. This removes the need for a recuperator, but it is noted that such high-temperature blowers are just being developed and currently on a distributed generation scale. Recycling will have a negative effect on SOFC performance (i.e., a lower Nernst voltage) by lowering the oxygen concentration in the cathode. By using cathode recycle, a higher turbine exhaust temperature than the configuration of Case 1 can be achieved; high enough (600°C) to have a heat recovery steam generator (HRSG), also shown in Fig. 2. The 35% heat duty-to-steam turbine (ST) power assumption is further discussed in Sec. 7.

5 Case 3 Overview

For Case 3 (Fig. 3), the cathode configuration of Case 2 is used (cathode recycle and a HRSG), but CO_2 is removed in the Fuel Conditioning section (before the anode). Instead of a MDEA process, a Selexol process is assumed for H_2S and CO_2 removal (as in Case 4 of the NETL OSAP report). High pressure (HP) steam from the syngas cooler is added; the steam produced from it being a good match for the required steam needed for the WGS reactor (steam/CO=1.8). The exothermic WGS reaction is kept at a constant temperature with the low pressure (LP) steam generator. Typically, a high-temperature and low-temperature WGS reactor is used to maximize the shift and availability of the gas, but only a low-temperature shift is used here for simplicity. 95% CO_2 removal in the Selexol unit is then assumed. It is noted that the end CO_2 capture result for this case is 87%, not 90%, as attained by the other cases. This is due to the methane content of the syngas. Some further means, such as gas recycling or a polishing step, would be needed.

In this case, since a hydrogen-rich syngas is produced, carbon dusting is not a concern and thus preheating to 650°C for the anode inlet is done with heat exchange from the anode exhaust. The entire anode exhaust then goes to the GT combustor.

6 Case 4 Overview

Here (Fig. 4), the cathode configuration is maintained, and CO_2 is still removed upstream to the anode. However, in this case, there is no HP steam addition or WGS reactor in the Fuel Conditioning block. Thus CO will remain as part of the syngas composition, with WGS occurring in the SOFC, as in Cases 1 and 2. Anode recycle is again employed for preheating and to prevent carbon deposition. Additional LP steam addition (Fig. 4) and a postanode WGS reactor are also employed to help avoid carbon deposition (to be discussed in Sec. 8). As in Cases 1 and 2, a small fraction of the anode exhaust goes to the GT combustor, and the remainder is expanded to atmospheric pressure. However, the ex-

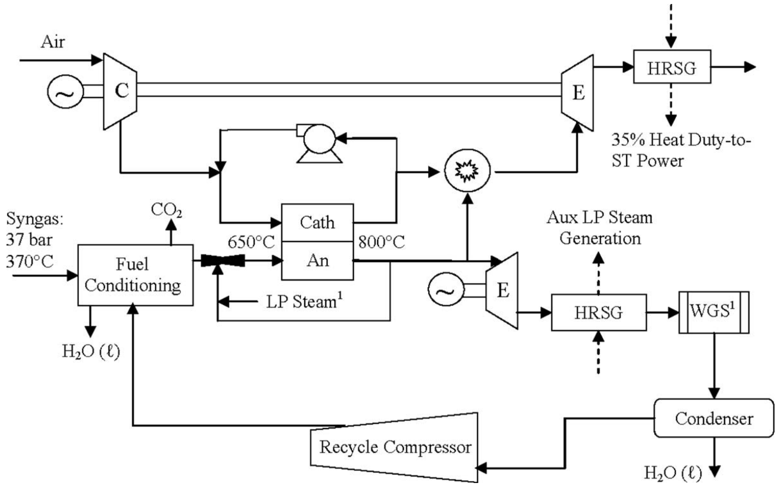

Fig. 4 Case 4: preanode CO_2 capture with second fuel recycle

Downloaded 02 Jun 2010 to 171.66.16.96. Redistribution subject to ASME license or copyright; see http://www.asme.org/terms/Terms_Use.cfm

Table 2 Pressure drop, turbomachinery efficiency

ΔP cathode	0.1 bar
ΔP anode	0.1 bar
ΔP GT combustor	0.25 bar
ΔP GT recuperator	0.05 bar
ΔP other heat exchangers	0.025 bar
Compressor efficiency	80%
Expander efficiency	85%
Blower efficiency	70%
Four-stage I.C. CO_2 compressor efficiency	85%

panded fuel is not oxidized. The heat is used to produce LP steam. After the WGS reactor, water is condensed and so H_2, CO, and CO_2 remain, along with N_2 and Ar. This gas is recycled to the Fuel Conditioning block upstream to the CO_2 removal process.

The previous configurations are fairly straightforward and have similar outlines as in previous literature [6–8,15], so the reason for the configuration of Case 4 may seem a bit curious. The motivation for the second fuel recycle in this configuration is as follows. First, the HP steam addition needed in Case 3 for the WGS is a significant energy penalty, so eliminating this requirement would be valuable. Second, it is beneficial to utilize as much H_2 in the SOFC as possible, since it is the most efficient device. Yet the gas composition can have a limiting effect, i.e., too much CO_2 will limit the WGS reaction (and thus the production of H_2 from CO) and too little H_2 or too much H_2O will effect the SOFC electrochemical performance, which can be generalized by observing the anode outlet ratio of H_2/H_2O. The placement of the second recycle effectively allows for increased fuel utilization, since the SOFC performance is not affected, the indicator being the ratio of H_2/H_2O. This will be demonstrated in Sec. 8. Also, for Case 4, taking out CO_2 upstream allows more WGS in the SOFC compared with Cases 1 and 2. Not only can more CO be shifted to H_2, but the exothermic reaction takes place in the SOFC, thus, producing a high grade waste heat.

7 Additional Assumptions and Calculation Routine

Assumptions not discussed in the case overviews are as follows. Turbomachinery efficiencies and pressure drops are given in Table 2. The pressure drop does not vary with operating pressure but is fixed.

The ASPEN PLUS® simulation software is used, with a user model for the SOFC. The fuel cell electrochemistry is based on a model given in previous references [7,8,15] and includes the pressure benefit to the Nernst potential; logarithmic with respect to pressure. In previous work, the SOFC model calculated the Nernst potential and overpotentials based on the cell outlet conditions; but in the work to be shown in this paper, the model was modified to use an average of inlet and outlet conditions, called the 0D-average model. An external one-dimensional (1D) model (i.e., not incorporated into the system model) will also be used to help corroborate power density results. The SOFC model in this work has the following baseline settings, unless otherwise noted: a single cell voltage of 0.75 V, a global fuel utilization of 80%, an air and fuel inlet temperature of 650°C, and an air and fuel outlet temperature of 800°C. Internal steam-methane reforming is accounted for and internal WGS equilibrium is assumed. The dc/ac conversion efficiency is 95%.

The work in this paper does not model a steam turbine system, but assumes that heat duty can be used to produce ST power at a certain "efficiency." For cases with a HRSG, this is assumed to be 35% of the heat duty assuming a temperature inlet of 600°C and outlet of 132°C (the operating pressure of the turbine adjusted to set the 600°C inlet temperature). The temperature is a compromise of data taken from two sources. These data are listed in Table 3.

Table 3 ST power from HRSG assumption. Assumes an average $C_p = 1.15$ kJ/kg K.

	W501G (Ref. [16])	S107FA (Ref. [17])	This work
HRSG T_{in} (°C)	595	601	600
HRSG T_{out} (°C)	156	93	132
Flow (kg/s)	546.7	445	Dependent
ST power (MW)	95.5	90.9	Calculated
Efficiency (%)	34.6	35	35

The W501G case is a repowering feasibility study example shown for electric power research institute's (EPRI's) SOAPP software [16]. The GE S107FA CC and their three-pressure HRSG are from GE public information [17].

The syngas cooler (convective boiler) generates HP steam. Since the fuel composition and flow rate are fixed, the heat available from the syngas cooling amounts to 163 MW of heat duty. For cases where this steam is used in the steam cycle, 30% of this heat (49 MW) will produce electric power. For Case 3, which uses steam for WGS, this steam is used since it will supply a sufficient amount. This number is based on a comparison of Cases 3 and 4 of the NETL OSAP report, where the effect of the steam subtraction from the ST to the WGS reactor is seen. Furthermore, it is assumed that heat recovered from the anode exhaust oxidizer (Cases 1 and 2) can generate steam for the ST and generate power at 30% of the heat duty.

The LP auxiliary steam requirements (needed for the sour stripper, ASU, slurry heater, and amine reboiler or Selexol regenerator) can be estimated from the NETL OSAP report. The requirement is about the same for both Case 3 (MDEA) and Case 4 (Selexol with CO_2 removal) of the OSAP report. The auxiliary LP steam flow rate is 159,000 kg/h at 4.6 bar and 155°C (with supply at 135°C from the deaerator). This LP steam requirement is produced in all four cases.

Auxiliary power requirements for the gasification-cleanup are estimated from the NETL report OSAP Cases. In the NETL report, these are given as Exhibits 3–51 for the IGCC without CO_2 removal and Exhibits 3–67 for the IGCC plant with 90% CO_2 removal. All cases in this paper scale the OSAP Case 4 ASU air and oxygen compressor, since it does not use extracted GT compressor air. Nitrogen compression is not needed as it would be for an IGCC and, thus, is subtracted from the auxiliary power need. The estimate for the total auxiliary power is 121.1 MW for Cases and 1 and 2, and 110.0 MW for Cases 3 and 4 (including the results for power needed to produce and supply extra oxygen for Cases 1 and 2). Four-stage intercooled CO_2 compression to 150 bar is included and will be listed as a separate result from the auxiliary. The recycle compressor for Case 4 is also four-stage intercooled.

Decisions for certain model operating parameters are made in the following manner. Flow rate to the cathode is adjusted to maintain a temperature difference of 150°C across the SOFC (800°C at the outlet). For the recuperated GT (Case 1), the pressure ratio of the GT is adjusted until an SOFC inlet temperature of 650°C (assuming an 88% effectiveness) is reached. For the cathode recycle cases, the pressure ratio is adjusted to give a 600°C temperature at the turbine exhaust (HRSG inlet), and the recycle blower is adjusted to maintain 650°C. For Cases 1, 2, and 4, the fraction of fuel sent from the anode exhaust to the GT combustor is varied to meet the 90% CO_2 capture (generally this is 6 to 9% of the anode exhaust mass flow).

8 Results

The investigation will begin with IGFC system performance results given a constant SOFC single cell voltage (or SOFC efficiency). This will be followed by some thought regarding the power density results, including consideration of an external 1D

Downloaded 02 Jun 2010 to 171.66.16.96. Redistribution subject to ASME license or copyright; see http://www.asme.org/terms/Terms_Use.cfm

Table 4 A summary of power and efficiency

	Case 1	Case 2	Case 3	Case 4
Power unit	MW	MW	MW	MW
SOFC(*95% dc/ac)	621.6	620.5	627.1	753.1
GT	81.9	52.4	189.1	70.7
ST	140.8	229.3	152.8	171.5
Expander, postanode	26.9	46.4	N/A	68.0
Blower	N/A	−18.9	−7.4	−20.9
CO_2 compressor	−63.8	−62.3	−25.2	−25.2
Recycle compressor	N/A	N/A	N/A	−66.8
Auxiliaries	−121.1	−121.1	−110.0	−110.0

model. Then, a comparison will be made to an IGFC system that does not include CO_2 capture. Finally carbon deposition concerns will be examined.

8.1 Constant Voltage. First, it was stated previously that a low anode outlet ratio of H_2/H_2O could limit electrochemical performance. Values above 0.22 are likely reasonable [4]. Case 1 results produce a ratio of 0.232, Case 2=0.224, Case 3=0.257, and Case 4=0.226.

Table 4 shows a comparison of the primary power production and consumption equipment, and Table 5 gives the total power, system efficiency (based on the HHV of coal input), and operating pressure (pressure in the SOFC). Results for the IGCC analysis from Ref. [1] are also shown in Table 5 for comparison.

In Table 4, a comparison of the SOFC power for Cases 1 and 2, show similar results. Since the voltage was kept constant, any advantage in performance (due to pressure, gas composition, etc.) will be realized in terms of fuel cell power density, not power. Next, it can be seen that Case 1 has a higher GT power and lower ST power. This is not unexpected given the strategy. The resulting system pressure ratio for Case 2, 3.8 bar, is different from some previous works that compare recuperated and cathode recycle options [7,8]; however, these references did not consider a HRSG at the GT outlet for the cathode recycle case (Case 2). Note that Case 2 results give a higher total power and efficiency than Case 1, with only a moderately higher operating pressure (Table 5).

For Case 3, the fuel cell power is again about the same with the advantage in performance from the hydrogen-rich gas taken in terms of increased power density. The GT power is higher, since all the unutilized fuel is burned in the GT combustor, increasing the turbine inlet temperature. Note that with the exception of Case 3, 48.9 MW of power results from the HP steam generation via the gasifier's syngas cooler (also called the convective syngas boiler). For Case 3, the HP steam from the syngas cooler is used for the WGS reactor, thus, all the ST power produced is from the HRSG. This, in combination with heat not being recovered after the anode exhaust results in lower ST power production. But the total power and efficiency are significantly higher, as shown in Table 5. The operating pressure is also higher since the higher turbine inlet temperature requires an increased pressure ratio to obtain the 600°C turbine exhaust temperature. Note that lowering the SOFC fuel utilization would result in an increased operating pressure since the turbine inlet temperature would be higher. The system efficiency would decrease only slightly, as demonstrated by VanOsdol et al. [8]. This point is brought up because in this study the resulting turbine conditions are not associated to any particular manufacturer's turbine, but a higher pressure ratio result could be obtained with only a slight efficiency impact by adjusting the SOFC fuel utilization. Also, a higher fraction of the power will come from the GT and ST part of the cycle (presumably, the lower cost power sections).

Table 6 SOFC power density results

Case	Relative SOFC power density 0D model	Relative SOFC power density 1D model
1	0.80	0.56
2	0.81	0.56
3	1	1
4	0.81	0.64

For Case 4, the high SOFC power is due to the high global fuel utilization, approximately 97.5%, a result of the second recycle. For Cases 1 and 2, an 80% fuel utilization leaves a significant amount of CO at the outlet due to limitations of WGS. However, the CO_2 recycle compression power requirement is fairly significant (second to last column of Table 4). In the final analysis, the total power and efficiency is slightly better than Case 3. Also, if the gasifier pressure could be lowered, this would reduce the recycle compressor power; however, the net benefit is slight since 50 mol % of the gas is CO_2, which needs to be compressed to 150 bar regardless. So Cases 3 and 4 appear to compare reasonably with regard to system power and efficiency. However, in order to maintain the fuel cell voltage at 0.75 V for Case 4, the resulting fuel cell power density is lower.

8.2 Power Density Examination Including a 1D Model Consideration. Table 6 compares the power density of Cases 1, 2, and 4, with Case 3 for the 0D-average model used in the ASPEN simulations and a separate 1D model. The 1D model is a coflow dynamic SOFC model developed by Georgia Tech for NETL's Hyper facility, a real-time hardware-in-the-loop hybrid simulator [18] (note: 1D model simulations not yet published). Results from the ASPEN simulation were input to the 1D model in an effort to corroborate the 0D-average model findings. First, in Table 6 the 0D-average model predicts a favorably higher power density for Case 3 compared to the other cases. Furthermore, the difference is greater in the case of the 1D model results. Since the 1D model results are not a part of the system model, they are not used in Tables 4 and 5.

However, it is interesting to make another comparison. The 1D model was run with an increased current density to match the power density of Case 3, resulting in a cell voltage, 0.64 V. Then, the system model with the 0D-average SOFC model was run using this cell voltage value (0.64 V). The results are shown in Table 7 with comparison to Cases 3 and 4 at the original cell voltage of 0.75 V. While the SOFC power is still higher for Case 4, the system power and efficiency are lower than Case 3.

Therefore, while there is some question remaining about power density versus fuel cell efficiency, the higher power density for the hydrogen-rich syngas fuel is not surprising and seems to be con-

Table 5 Comparing operating pressure, total power, and efficiency including IGCC with 90% CO_2 capture

	Case 1	Case 2	Case 3	Case 4	IGCC
SOFC pressure (bar)	2.2	3.8	9	4.0	16
Nernst potential (V/cell)	0.95	0.95	1.00	0.95	N/A
Total power (MW)	686.4	746.4	826.4	841.2	503
HHV efficiency (%)	43.3	47.1	52.1	53.0	31.7

Downloaded 02 Jun 2010 to 171.66.16.96. Redistribution subject to ASME license or copyright; see http://www.asme.org/terms/Terms_Use.cfm

Table 7 Case 4 SOFC power density increased (voltage reduced) to match Case 3 power density

	Case 3: 0.75 V	Case 4: 0.75 V	Case 4: 0.64 V
Power unit	MW	MW	MW
SOFC (*95% dc/ac)	627.1	753.1	671.7
GT	189.1	70.7	88.2
ST	152.8	171.5	198.2
Expander, postanode	N/A	68.0	68.0
Blower	−7.4	−20.9	−26.4
CO_2 compressor	−25.2	−25.2	−25.2
Recycle compressor	N/A	−66.8	−66.8
Auxiliaries	−110.0	−110.0	−110.0
Total power	826.4	841.2	798.7
HHV efficiency (%)	52.1	53.0	50.4

sistent with ongoing lab tests at NETL and elsewhere. While not elaborated on in this work, spatial effects (i.e., the temperature profile) could be an important factor with regards to a preferred fuel composition. Recent work at the National Fuel Cell Research Center (NFCRC) demonstrates this idea [19].

8.3 System Comparison Without CO_2 Capture. For a final comparison, it would be interesting to demonstrate the effect CO_2 capture has on system performance, e.g., in the NETL OSAP study, the IGCC efficiency is 39.3% without CO_2 capture and 31.7% with CO_2 (including compression to 150 bar). In order to do this, the postanode exhaust of Case 2 is modified such that its entire exhaust goes to the GT combustor (after using some heat for auxiliary LP steam generation).

A comparison of this result along with Case 3 is shown in Table 8. The difference in absolute efficiency is 4.4%, compared with 7.6% for the IGCC study. Case 2 still has a lower power density than Case 3 but is better than the Table 6 finding due to the higher pressure operating pressure result of 7.5 bar (the relative power density using the 0D-average model is 0.88 compared with 0.81 in Table 6). An equal power density comparison is not made here, but the system efficiency for Case 2 in Table 8 will decrease as a result.

Table 8 Case 2 without CO_2 removal

	Case 2: $V=0.75$, no CO_2 removal	Case 3: $V=0.75$
Power unit	MW	MW
SOFC (*95% dc/ac)	605.0	627.1
GT	187.7	189.1
ST	211.5	152.8
Expander, postanode	N/A	N/A
Blower	−9.2	−7.4
CO_2 compressor	N/A	−25.2
Recycle compressor	N/A	N/A
Auxiliaries	−98.3	−110.0
Total power	896.7	826.4
HHV efficiency (%)	56.5	52.1

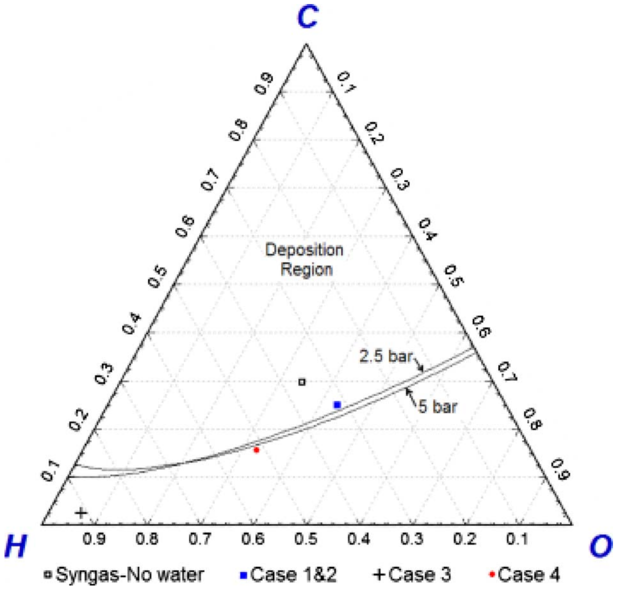

Fig. 5 Ternary diagram for C–H–O equilibrium at 650°C

8.4 Carbon Deposition. The anode inlet and outlet gas compositions are shown in Table 9. In order to determine whether carbon deposition in the SOFC anode is a possibility, the location of the anode inlet gas composition is plotted on a ternary C–H–O equilibrium diagram show in Fig. 5. Each corner of the diagram represents 100 mol % of that specie. The area above the lines at 2.5 bar and 5 bar represents the area where deposition can occur.

First, note that a point is plotted for the syngas after water is removed (Syngas—no water). From a kinetics standpoint, this is acceptable if the syngas temperature is lower than 400°C [12], thus, the limit of 350°C prior to the anode recycle for Cases 1, 2, and 4. The anode recycle is used to move this state via oxygen addition in the form of water. (Water vapor results from the anode reaction; however, there is no net addition of hydrogen atoms but oxygen. Oxygen is transported through the SOFC electrolyte.) However, points plotted for Cases 1 and 2 show that even with the anode recycle, the syngas is still in the carbon deposition region, although much closer to the equilibrium line. Thus, Cases 1 and 2 would still benefit from either more anode recycle or steam addition, but this will also degrade fuel cell performance.

Case 3 shows that the hydrogen-rich syngas is in the noncarbon deposition region. Although the line for a pressure of 9 bar is not shown, the trend of increasing pressure is to expand the noncarbon area at the high hydrogen end of the map. Case 4 would have similar results as Cases 1 and 2; however, this case added some

Table 9 Anode inlet, outlet gas molar composition

	Anode in mol frac.				Anode out mol frac.			
	1	2	3	4	1	2	3	4
N_2	0.011	0.011	0.013	0.063	0.011	0.011	0.012	0.062
Ar	0.021	0.021	0.025	0.118	0.020	0.020	0.023	0.115
H_2	0.167	0.163	0.861	0.191	0.070	0.068	0.179	0.089
CO	0.238	0.234	0.012	0.156	0.105	0.103	0.017	0.058
CO_2	0.363	0.368	0.035	0.178	0.493	0.495	0.073	0.280
H_2O	0.182	0.185	0.001	0.282	0.301	0.303	0.696	0.396
CH_4	0.018	0.018	0.053	0.012	0	0	0	0

Downloaded 02 Jun 2010 to 171.66.16.96. Redistribution subject to ASME license or copyright; see http://www.asme.org/terms/Terms_Use.cfm

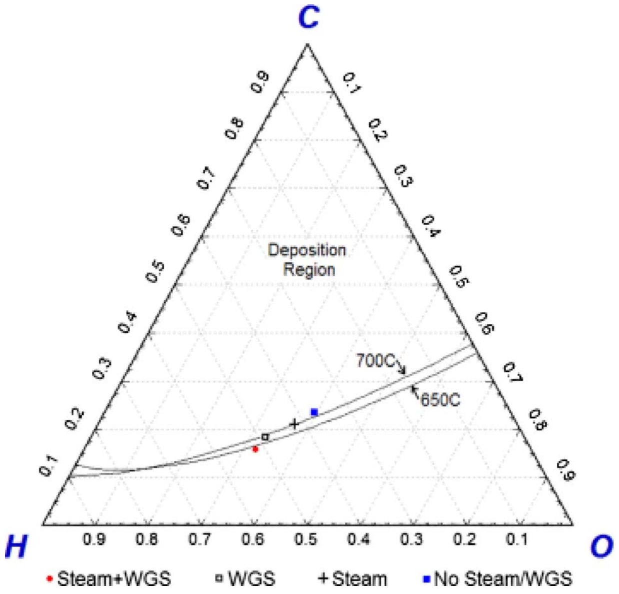

Fig. 6 Ternary diagram for C–H–O equilibrium at 5 bar, Case 4 considerations

LP steam to the anode inlet and a WGS reactor at the anode outlet (as was shown in Fig. 4). This point is plotted in Fig. 6, including tests with and without the LP steam or WGS. The pressure is 5 bar, with lines plotted for temperatures of 650°C and 700°C. Note that at 700°C, the point with only LP steam addition would be sufficient, but it is still a close situation.

9 Conclusions

All cases demonstrate a significantly higher efficiency compared with an IGCC with CO_2 capture. This is understandable since the conversion of a carbon fuel to hydrogen is a normal part of an SOFC process; whereas, there is no benefit to doing so for an IGCC cycle. The operating pressure is moderate for Cases 1, 2, and 4, and 9 bar for Case 3. Cases 2 and 3 are arranged similar to preliminary systems shown by Ref. [6]. The efficiency result for Case 2 is lower (3% absolute), and Case 3 is slightly higher (2% absolute) in this work than in Ref. [6].

Cases 1 and 2 do not require a CO_2 separation process. While Cases 3 and 4 do require this step, the process is quite well known (e.g., in ammonia production). For Case 4, the volume flow rate through the CO_2 separation equipment is roughly double that of the hydrogen-rich syngas case (Case 3). Since the size of the equipment is related to volume flow (e.g., a Selexol process [1]), it can be expected that Case 4 will need larger vessels. Favorably, Cases 3 and 4 require no postanode oxygen combustor. Furthermore, the oxidation of the waste anode fuel for Cases 1 and 2 would likely have to be staged due to temperature constraints, further complicating the heat recovery process.

The advantage of the second recycle in Case 4 is the re-addition of the usable fuel (H_2 and shifted CO) while removing the water (a negative effect on electrochemistry) and CO_2 (a limiter for WGS). In effect, there is a greatly increased H_2 and CO utilization. Also, the addition of HP steam for WGS is not needed. But the recycle compressor needed to compress the gas from 1 bar to 37 bar, offsetting the benefit of HP steam savings when compared with Case 3. Also, it would appear that the system arrangement is simpler and the SOFC area less for Case 3, although the operating pressure is higher.

Whether a particular pressure value is beneficial or detrimental from a risk, design, or cost perspective is not examined in this paper. Notably, the operating pressure for Case 3 can essentially be changed by changing the fuel utilization, without a dramatic effect on efficiency. This cannot be done for the other cases since most of the unutilized anode fuel is not going to the GT cycle. Naturally auxiliary fuel could not be used due to the CO_2 constraint. Thus Case 3 appears to be more flexible in achieving a particular design point pressure; although issues related to the increased volumetric flow in the GT expander would need to be resolved, as demonstrated by Chiesa et al. [20]; the volumetric heating value of the anode exhaust fuel is higher than natural gas, so given the same turbine inlet temperature there will be an increase in the turbine shaft torque, which is limited. Note that for Case 3 lowering the fuel utilization will also decrease the cathode recycle since the compressor outlet temperature will be higher (from gas compression heating).

If the SOFC model in this paper largely overpredicts the performance benefit resulting from the hydrogen-rich syngas, then Case 4 could have more promise, but this does not seem likely given the 1D model comparison results in this work. Since fuel cell power density and fuel cell spatial effects are important factors in determining a preferred system, a dimensional fuel cell model incorporated into the system model will be important for future comparative, conclusive work. Ongoing studies by the NFCRC [19] recognize this fact.

The results presented here make no conclusion regarding IGFC options given other technological assumptions such as warm-gas cleanup. Another example would be the use of a catalytic gasifier that produces a high methane content syngas as demonstrated by Grol [10] and Thijssen [11]; these studies suggested even higher efficiencies due to the high efficiency of the gasifier and high methane content of the syngas. Interestingly, the cycle proposed by Thijssen is similar to Case 4 of this paper.

Acknowledgments

I would like to thank all those who modeled, wrote, and put together the excellent detail listed as Ref. [1]. I would also like to thank Comas Haynes and Kevin Davies at Georgia Tech for developing the 1D MATLAB/SIMULINK® real-time SOFC model, and Tom Smith for it's implementation.

Nomenclature

GT = gas turbine
HHV = higher heating value
HP = high pressure
HRSG = heat recovery steam generator
IGCC = integrated gasification combined cycle
IGFC = integrated gasification fuel cell
LP = low pressure
NETL = National Energy Technology Laboratory
NFCRC = National Fuel Cell Research Center
OSAP = Office of Systems Analysis and Planning—an office within NETL
SECA = Solid State Energy Conversion Alliance
SOFC = solid oxide fuel cell
ST = steam turbine
WGS = water gas shift reaction—$CO+H_2O \leftrightarrow H_2+CO_2$

References

[1] 2007, "Cost and Performance Baseline for Fossil Energy Plants, Vol. 1: Bituminous Coal and Natural Gas to Electricity," National Energy Technology Laboratory Report No. DOE/NETL-2007/1281.

[2] Liese, E. A., and Gemmen, R. S., 2005, "Performance Comparison of Internal Reforming Against External Reforming in a Solid Oxide Fuel Cell, Gas Turbine Hybrid System," ASME J. Eng. Gas Turbines Power, **127**, pp. 86–90.

[3] Campanari, S., 2000, "Full Load and Part Load Performance Prediction for Integrated SOFC and Microturbine Systems," ASME J. Eng. Gas Turbines Power, **122**, pp. 239–246.

[4] Campanari, S., 2002, "Carbon Dioxide Separation From High Temperature Fuel Cell Power Plants," J. Power Sources, **112**, pp. 273–289.

[5] Kvamsdal, H. M., Jordal, K., and Bolland, O., 2007, "A Quantitative Comparison of Gas Turbine Cycles With CO_2 Capture," Energy, **32**, pp. 10–24.

[6] Minh, N., 2006, "SECA Coal Based System Program," Seventh Annual Peer Review Workshop Meeting, Philadelphia, PA.

Downloaded 02 Jun 2010 to 171.66.16.96. Redistribution subject to ASME license or copyright; see http://www.asme.org/terms/Terms_Use.cfm

[7] Tucker, D., VanOsdol, J., Liese, E., Lawson, L., Zitney, S., Gemmen, R., Ford, J. C., and Haynes, C., 2006, "Evaluation of Methods for Thermal Management Is a Coal-Based SOFC Turbine Hybrid Through Numerical Simulation," *Proceedings of the Seventh International Colloquium on Environmentally Preferred Advanced Power Generation*, Irvine, CA, Paper No. ICEPAG2006-24022.

[8] VanOsdol, J., Gemmen, R., and Liese, E., 2008, "Examination of the Effect of System Pressure Ratio and Heat Recuperation on the Efficiency of a Coal Based Gas Turbine Fuel Cell Hybrid Power Generation System With CO_2 Capture," Sixth International Fuel Cell Engineering and Technology Conference, Denver, CO, Paper No. FUEL CELL 2008-65083.

[9] Lisbona, P., and Romeo, L. M., 2008, "Enhanced Coal Gasification Heated by Unmixed Combustion Integrated With an Hybrid System of SOFC/GT," Int. J. Hydrogen Energy, **33**, pp. 5755–5764.

[10] Grol, E., 2008, "Systems Analysis for Integrated Gasification Fuel Cell Combined Cycle," Ninth Annual SECA Workshop, Pittsburgh, PA.

[11] Thijssen, J., 2008, "Coal System Studies: Effects of Methane Content and High-Efficiency Catalytic Gasification," Ninth Annual SECA Workshop, Pittsburgh, PA.

[12] Baker, B.A., and Smith, G.D., 2007, "Alloy Solutions to Metal Dusting Problems in the PetroChemical Industry," Special Metals Corporation, Huntington, WV; see www.specialtymetals.com/documents.

[13] Ferrari, M. L., Traverso, A., Magistri, L., and Massardo, A. F., 2005, "Influence of the Anodic Recirculation Transient Behavior on the SOFC Hybrid Performance," J. Power Sources, **149**, pp. 22–32.

[14] Yi, Y., Rao, A. D., Brouwer, J., and Samuelsen, G. S., 2005, "Fuel Flexibility Study of an Integrated 25 kW SOFC Reformer System," J. Power Sources, **144**, pp. 67–76.

[15] Bove, R., and Ubertini, S., 2008, *Modeling Solid Oxide Fuel Cells—Methods, Procedures and Techniques*, Springer-Verlag, Berlin.

[16] "Electric Power Research Institute's State-of-the Art Power Plant (SOAPP) Software Product Example," see repowering example, SOAPP-REPO.

[17] 2008, "GE Combined Cycle Product Line and Performance," GE Power Product and Services Website Information, Publication Document No. GER3574g.

[18] Liese, E. A., Smith, T. P., Haynes, C. L., and Gemmen, R. S., 2006, "A Dynamic Bulk SOFC Model Used in a Hybrid Turbine Controls Test Facility," ASME Paper No. GT2006-GT90383.

[19] Li, M., Brouwer, J., Powers, J. D., and Samuelsen, G. S., 2009, "A Finite-Volume SOFC Model for Coal-Based Integrated Gasification Fuel Cell System Analysis," *Proceedings of the Seventh International Fuel Cell Science, Engineering, and Technology Conference*, Newport Beach, CA, Paper No. FuelCell2009-85247.

[20] Chiesa, P., Lozza, G., and Mazzocchi, L., 2005, "Using Hydrogen as Gas Turbine Fuel," ASME J. Eng. Gas Turbines Power, **127**, pp. 73–80.

Downloaded 02 Jun 2010 to 171.66.16.96. Redistribution subject to ASME license or copyright; see http://www.asme.org/terms/Terms_Use.cfm

Analysis of Compressor On-Line Washing to Optimize Gas Turbine Power Plant Performance

Ernst Schneider[1]
e-mail: ernst.schneider@power.alstom.com

Saba Demircioglu Bussjaeger

Susana Franco

Dirk Therkorn

Alstom (Switzerland) Ltd.,
Brown-Boveri-Strasse 7, 5401 Baden,
Switzerland

Due to compressor fouling, gas turbine efficiency decreases over time, resulting in decreased power output of the plant. To counteract the effects of compressor fouling, compressor on-line and off-line washing procedures are used. The effectiveness of compressor off-line washing is enhanced if combined with the cleaning of the VIGVs and the first compressor blade row by hand. This paper presents a thorough analysis of the effects of compressor on-line washing on the gas turbine performance. The analysis is based on the measured data of six gas turbines operated at two different plants. Different washing schedules and washing fluids are analyzed and compared. Furthermore, the effects of compressor on-line washing on the load distribution within the compressor are analyzed. The performance benefit of daily compressor on-line washing compared with weekly compressor on-line washing is quantified. As expected, daily compressor on-line washing yields the lowest power degradation caused by compressor fouling. Also, the effect of washing additives is analyzed. It is shown with long term data that compressor on-line washing cleans up to the first 11 compressor stages, as can be detected well in the compressor. With a view to gas turbine performance optimization, the recommendation is to perform compressor off-line washing at regular intervals and to take advantage of occasions such as inspections, when the gas turbine is cooled down anyhow. Especially for gas turbines with a high fouling rate, a daily compressor on-line washing schedule should be considered to reduce the power loss. For gas turbines operating with high fogging, compressor on-line washing has no added benefit. To determine the optimal compressor washing schedule, compressor blade erosion also has to be considered. A reasonable balance between compressor on-line washing and off-line washing improves the gas turbine performance and optimizes the gas turbine availability.

[DOI: 10.1115/1.4000133]

1 Introduction

The condition of a gas turbine compressor is affected by the environmental conditions of the site. With increasing operating time degradation of the compressor can be registered in terms of reduced performance. Apart from abrasion and erosion of the blade surfaces, compressor fouling is the main cause of the reduction in compressor efficiency and compressor inlet air mass flow. The degradation of the gas turbine compressor has a direct influence on the gas turbine power plant efficiency and power.

To prevent degradation, industrial gas turbines are equipped with sophisticated air filter systems. These air filter systems significantly reduce the amount of contaminants the gas turbine is subjected to, but cannot filter out the contaminant particles altogether. Most of the contaminants are of small size; normally 80% are below 2 μm [1]. However, even small concentrations of foreign particles can accumulate to several tons of contaminants that are ingested by the gas turbine during the operating time between two major inspections [1]. (A contaminant concentration of 1 ppm exposes the gas turbine to 12,500 kg of impurities assuming an air mass flow rate of 450 kg/s and 8000 OH.)

The source and the properties of these contaminants can differ greatly. Not only sand, dust, or dirt are registered, but also chemical substances such as oil or salt and natural contaminants such as plant spores or insects [1]. The contaminated air is the cause for compressor fouling. Compressor fouling is the phenomenon caused by small solid or liquid particles starting to adhere to the compressor blades and annulus surfaces [2–4]. Due to their higher mass and higher inertia, these small particles can deviate from the streamline trajectory of the air and impinge the material surfaces. Depending on the flow conditions, the particle mass, and the materials, the small particles may remain stuck to the surfaces after impingement. Oil vapors, high humidity, desert environments, etc., accelerate the fouling process. The result of fouling is an increased surface roughness with negative effects on the flow and a change in the effective flow area. Especially the first compressor stages are affected by the fouling process. Compressor fouling decreases compressor efficiency and the compressor flow capacity [4].

2 Compressor Efficiency

The gas turbine compressor is the greatest consumer of turbine power. The power consumption of the compressor amounts to 60–65% of the turbine power [5]. Hence, even small changes in the compressor efficiency have a significant effect on the overall gas turbine performance and efficiency.

The efficiency of an axial compressor is defined as the ratio between ideal and actual enthalpy increases of the gas due to the compression from the pressure level p_1 up to the pressure level p_2 (see Fig. 1). For an ideal process the compression is isentropic. However, a real process also involves an entropy increase. Hence, the registered enthalpy increase is higher than for the ideal process. If the actual process is approached by infinitesimal isentropic steps the isentropic compressor efficiency is obtained as

---

[1] Corresponding author.

Contributed by the International Gas Turbine Institute (IGTI) of ASME for publication in the JOURNAL OF ENGINEERING FOR GAS TURBINES AND POWER. Manuscript received April 14, 2009; final manuscript received April 28, 2009; published online March 18, 2010. Editor: Dilip R. Ballal.

Copyright © 2010 by Alstom

Downloaded 02 Jun 2010 to 171.66.16.96. Redistribution subject to ASME license or copyright; see http://www.asme.org/terms/Terms_Use.cfm

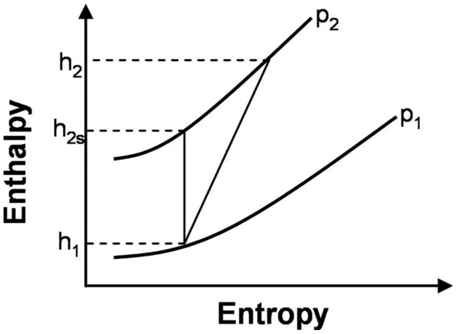

Fig. 1 Enthalpy versus entropy map of a compression

$$\eta_s = \frac{h_{2s} - h_1}{h_2 - h_1} \tag{1}$$

Modern axial gas turbine compressors have efficiencies of about 87% [5]. Assuming the air as an ideal gas, the enthalpies can be expressed as functions of the temperature $h=f(T)$. Hence, the enthalpy differences can be expressed as temperature differences [6]

$$\Delta h_s = c_p(T_{2,s} - T_1) \tag{2}$$

$$\Delta h_n = c_p(T_2 - T_1) \tag{3}$$

and considering that for isentropic processes [6]

$$\Delta h_n = c_p T_1 \left[\left(\frac{p_2}{p_1} \right)^{R/c_p} - 1 \right] \tag{4}$$

the polytropic compressor efficiency can be expressed as

$$\eta_n = \frac{R \ln\frac{p_2}{p_1}}{c_p \ln\frac{T_2}{T_1}} \tag{5}$$

Hence, the polytropic compressor efficiency can be calculated based on the measured flow conditions at the compressor inlet and at the compressor exit.

3 Compressor Cleaning

3.1 Compressor On-Line Washing. Compressor on-line washing is normally done during gas turbine base load operation with the VIGVs in the fully open condition. For compressor on-line washing, an on-line washing system has to be installed at the air inlet of the gas turbine. Generally demineralized water is injected through a configuration of small nozzles in the air flow before the first compressor stage. Examples of such on-line compressor washing injection nozzles are shown in Figs. 2 and 3. In addition to demineralized water, a detergent can be used to increase the cleaning effect of compressor on-line washing. Since a cleaning effect can only be obtained as long as the injected water is liquid and has not evaporated, the cleaning effect of compressor on-line washing is limited to the VIGVs and the first stages of a compressor [7–9]. Compressor on-line washing can diminish the degree of compressor fouling, but it cannot prevent it completely. Hence, from the point of view of performance recovery, the recommendation is to carry out a compressor off-line washing from time to time, because this shows a higher effectiveness for performance recovery.

3.2 Compressor Off-Line Washing. For compressor off-line washing, the gas turbine has to be shut down and cooled. A compressor off-line washing procedure normally consists of several steps. First the gas turbine compressor is flushed with demineralized water. A detergent can also be used. Using the start-up system the gas turbine is accelerated to 20–50% of nominal speed and then allowed to coast to a stop. The flushing may be repeated several times. The procedure ends with several rinse-cycles, which are repeated until the water that pours out of the compressor through the opened blow-off valves does not indicate anymore signs of contamination [5,7]. With compressor off-line washing, the effects of compressor fouling can be removed virtually completely. Compressor off-line washing is recommended at the normal inspection intervals to avoid nonavailability of the gas turbine because of the necessary cool-down periods.

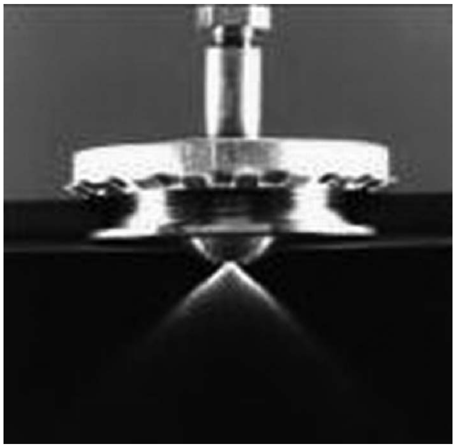

Fig. 2 Turbotect MK1 on-line compressor washing injection nozzle

3.3 Compressor Hand Cleaning. Cleaning the compressor by hand involves cleaning the VIGVs and the blades of the first compressor row with brushes and a detergent. Cleaning the compressor by hand is very effective for removing particles sticking to the blade surface, but has the drawback that it is very time consuming and requires the shutdown and cooling of the gas turbine beforehand [7]. Since cleaning the compressor by hand affects only the VIGVs and the blades of the first compressor row, it should be always done in combination with a compressor off-line washing.

3.4 Abrasive Cleaning. The use of abrasive materials for compressor cleaning, e.g., the injection of rice or walnut-shells into the compressor, is suspended in most plants [5], since the erosion effects are too high and there is the danger that these nonliquid materials collect in the gas turbine and clog the passages of the secondary air system. Particles may enter seals and the lubrication system, or they may damage the coating of the compressor blades [5,7]. Nonetheless, abrasive compressor cleaning may be performed on a removed rotor during a major overhaul.

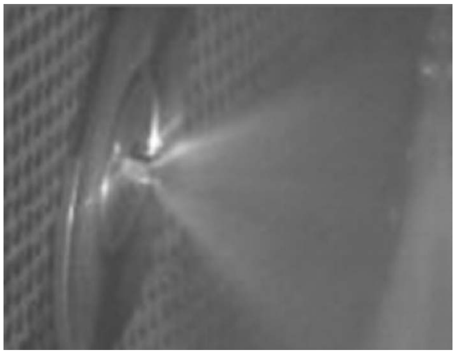

Fig. 3 Turbotect MK3 on-line compressor washing injection nozzle

Downloaded 02 Jun 2010 to 171.66.16.96. Redistribution subject to ASME license or copyright; see http://www.asme.org/terms/Terms_Use.cfm

Table 1 Environmental conditions at Plant A and Plant B

Plant A
• Industrialized area • Petrochemical industry • Maritime conditions
Plant B
• Industrialized area • High air humidity • High concentration of particles $<10\ \mu$m • Maritime conditions

4 Compressor Washing Schedule Analysis

Different on-line washing schedules were investigated to determine the effects on the compressor efficiency and the power plant power output. Measured data of six gas turbines were used. Only operating points at base load conditions were considered. The measured power output was corrected for ambient temperature, ambient pressure, relative humidity, generator power factor, rotor speed, and condenser vacuum. The compressor efficiency was calculated based on the measured data. It was assumed that the compressor inlet conditions correspond to the ambient conditions. Hence, the pressure drop over the air inlet filters is considered in the compressor efficiency value. The compressor efficiency was corrected for ambient conditions and rotor speed.

Three of the gas turbines analyzed are operated at Plant A. The three Alstom GT26 gas turbines will be named PA1, PA2, and PA3. PA1, PA2, and PA3 are three identical single-shaft, combined-cycle power plant units. Plant A is situated in the moderate climate zone. At Plant B, situated in the tropical climate zone, three Alstom GT13E2 gas turbines are operated in a multi-shaft arrangement for a triple pressure water steam cycle. They will be named PB1, PB2, and PB3. In Table 1 is given an overview of the environmental conditions of Plants A and B.

4.1 Analysis Plant A. At Plant A different compressor on-line washing schedules were compared over a period of 7 months. During this time PA1 had no compressor on-line washing, PA2 had a weekly compressor on-line washing schedule with demineralized water and PA3 had a daily compressor on-line washing schedule with demineralized water, too. No detergents were used and the water was not heated.

In Fig. 4 a comparison of the compressor efficiencies of the gas turbines PA1, PA2, and PA3 is given for the period of the compressor on-line washing. Before the start of the test campaign, the compressors of the three gas turbines were cleaned thoroughly with compressor off-line washing.

The general trend of the compressor efficiency degradation is similar for all three units. During the first weeks of the test campaign, the units show no signs of degradation. This phase of relative constant compressor efficiencies is followed by a phase with gradually increasing degradation up to a level where the compressor efficiency values stabilize again at a lower level.

Similar overall trends can also be seen in Fig. 5, where the relative power output of the three units PA1, PA2, and PA3 is plotted for the period of the compressor on-line washing. The exchange rates between compressor efficiency and power, i.e., the effect of a compressor efficiency change on the power output, are known from performance calculations. Based on the exchange rates it is possible to deduce that the power output degradation is caused mainly by the compressor efficiency degradation. At the beginning, the power output remains relatively constant, then it decreases gradually and stabilizes again at a lower level. The relative constant compressor efficiency and power trends during the first weeks after the compressor off-line washing may be explained by nonlinear fouling effects. In the beginning, dirt accumulates on the blades only slowly. Influenced by the dirt already sticking to the compressor blades, the degradation rate increases. After several weeks, a new equilibrium is found, the increased roughness of the blade surfaces abets the further accumulation of dirt, but at the same time dirt particles are transported downstream by the air mass flow. A stable degradation level may be reached after a certain time, as it is also confirmed by the tests of Tarabrin et al. [4] and Stalder [11]. The compressor off-line washing of PA1 performed during the test campaign was without additional compressor hand cleaning. It shows only a small effect on compressor efficiency recovery.

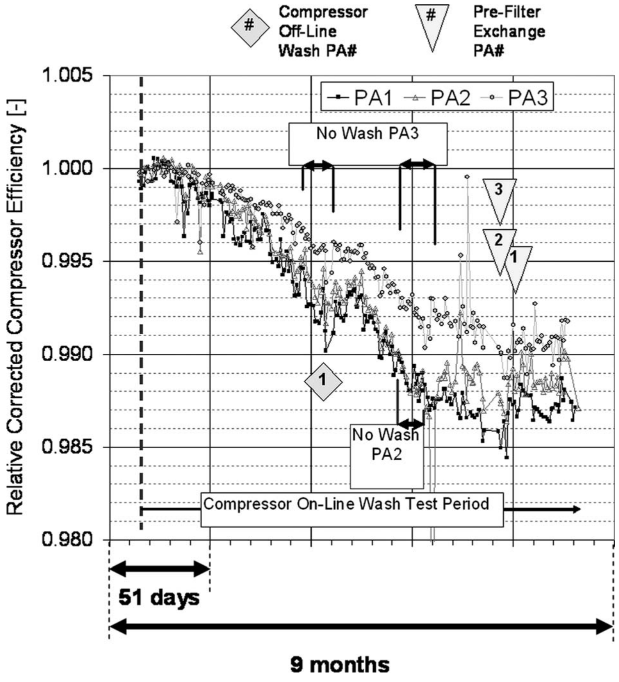

Fig. 4 Relative corrected compressor efficiency Plant A

The small compressor efficiency degradation rate at the beginning of the test campaign is the reason why, during the first weeks,

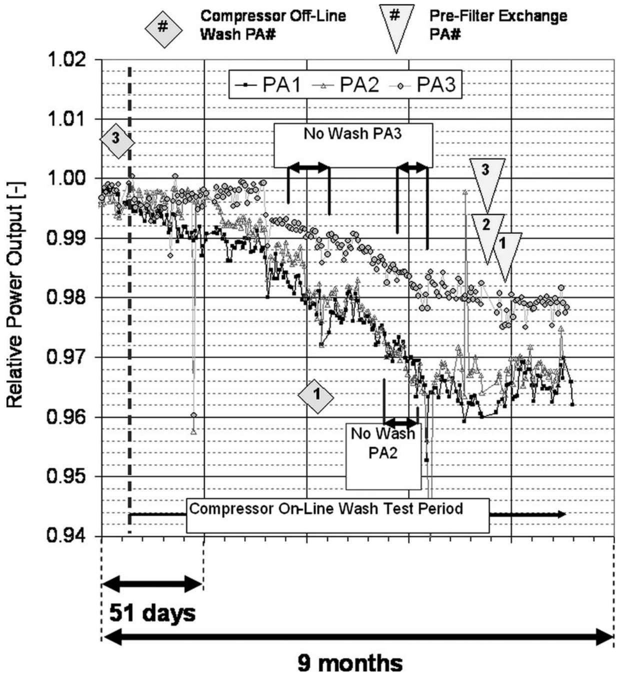

Fig. 5 Relative power output comparison Plant A

Downloaded 02 Jun 2010 to 171.66.16.96. Redistribution subject to ASME license or copyright; see http://www.asme.org/terms/Terms_Use.cfm

the effects of compressor efficiency degradation disappear within the scatter of the compressor efficiency values. The same can be said for the power plant power output. Hence, the first signs of compressor efficiency degradation can be registered for all units only after about 6 weeks. The first signs of power output degradation can be registered for PA1 after 6 weeks, for PA2 after 9 weeks, and for PA3 after 12 weeks following the beginning of the test campaign. The gas turbine without compressor washing shows the highest degradation rate. For the gas turbine with weekly compressor on-line washing, the degradation rate is lower, and the gas turbine with a daily compressor washing schedule has the lowest degradation rate. Compressor on-line washing helps to keep the power output of the plant at a higher level for a longer time. In other words, compressor fouling progresses at a slower rate as a result of compressor on-line washing (see Fig. 4). As can be seen in Figs. 4 and 5, the degradation rate for PA3 increased during the time span when no compressor on-line washing was performed.

At the end of the compressor on-line washing test period, the registered total corrected relative compressor efficiency degradations were about 1.4% for PA1, 1.2% for PA2, and 1.0% for PA3. Based on the empirical exchange rate of 2 for the dependency of power output degradation on compressor efficiency degradation, which is consistent with the values published in literature [2], power output degradations of 2.8% for PA1, 2.4% for PA2, and 2.0% for PA3 were to be expected. The actual registered power output degradations were 3.6% for PA1, 3.4% for PA2, and 2.0% for PA3. Therefore, although compressor efficiency degradation is the main contributor to the degradation of the total power output, it is not the only effect.

The effects of power recovery due to air inlet filter changes are relatively small and have about the same magnitude as the scatter. Nonetheless, it is necessary to change the air inlet filters regularly, since new filters that are not soiled and are undamaged are more effective in preventing the fouling of the compressor. Hence, they reduce the degradation rate of the compressor.

After identifying the daily compressor on-line washing schedule as the most effective from the point of view of power output, further compressor on-line washing tests were performed at PA1, PA2, and PA3. The three units were subsequently operated during a period of 13 months with a daily compressor on-line washing schedule, and the power outputs were compared (see Fig. 6). As expected, the degradation behavior of the three units is comparable, since they are identical and are operating under the same atmospheric conditions and with similar load schedules. After 9 months of the test campaign there is a period of about 2 months during which PA3 accumulated less operating hours than PA1 and PA2. During this period the degradation rate of PA3 is lower. Nonetheless, the results for PA3 obtained during the second test phase confirm the ones obtained during the first phase with daily compressor on-line washing.

4.2 Analysis Plant B. At Plant B different compressor on-line washing schedules and washing fluids were compared during a period of 6 months. During this time PB1 had a twice-a-week compressor on-line washing with a detergent, PB2 had a daily compressor on-line washing with demineralized water plus a weekly compressor on-line washing with a detergent, and PB3 had no compressor on-line washing. The water used was not heated.

In Fig. 7 the relative corrected compressor efficiencies of PB1, PB2, and PB3 are plotted for the time span of the compressor on-line washing tests. In Fig. 8 the relative corrected power output of the units PB1, PB2, and P3 is also given for the time period of the test campaign. As can be seen, the trends of the compressor efficiencies and the power output for each unit are similar. For about 2 months during the test campaign, not all data needed for the calculation of the compressor efficiency for PB1 were available.

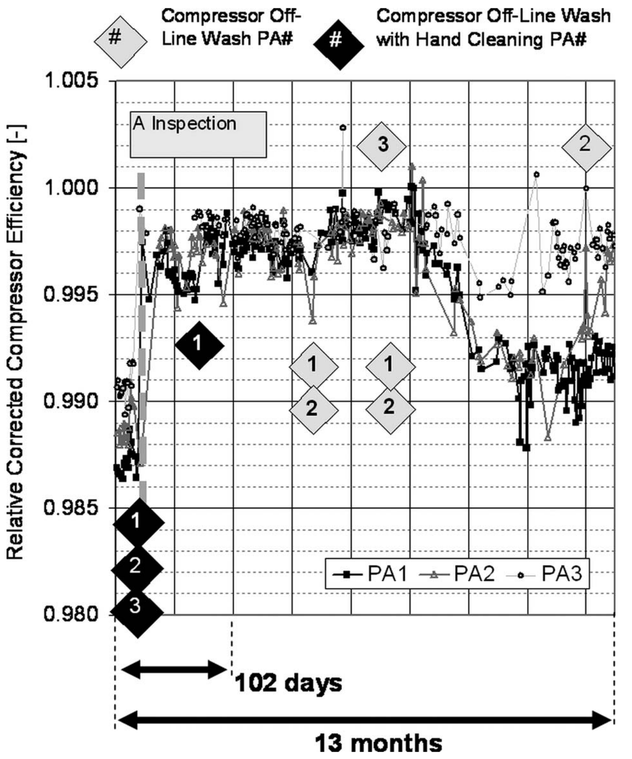

Fig. 6 Power output of the units of Plant A during the period with the same daily washing schedule

In contrast to the compressor efficiency trends observed at Plant A, the compressor efficiency degradation progresses faster at Plant B without a relatively stable phase directly after the compressor off-line washing at the beginning of the test period. Also, the degradation does not reach a stable level as observed at Plant A. The probable reason for the different degradation trends is that the environment at Plant B is more highly polluted, so the rate of compressor fouling is greater than at Plant A.

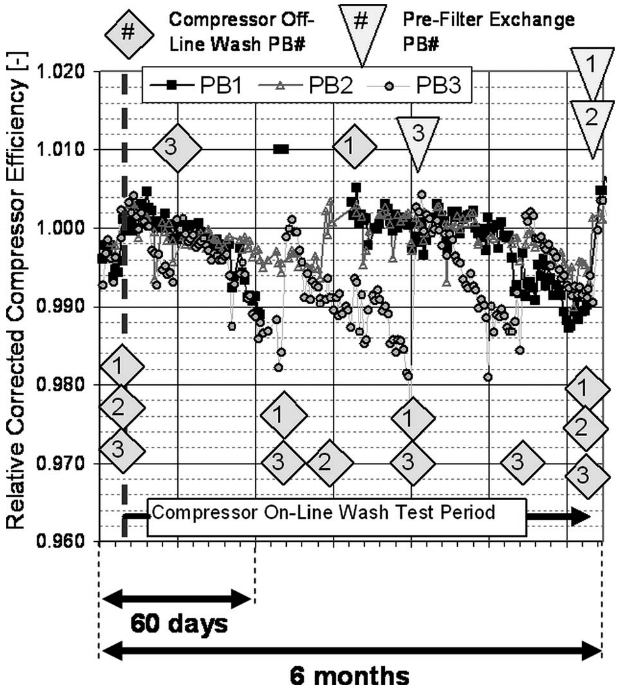

Fig. 7 Relative corrected compressor efficiency Plant B

Downloaded 02 Jun 2010 to 171.66.16.96. Redistribution subject to ASME license or copyright; see http://www.asme.org/terms/Terms_Use.cfm

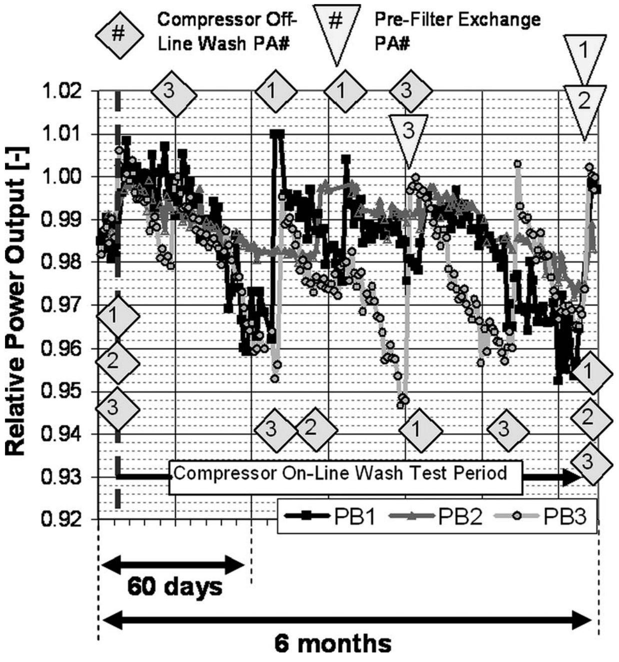

Fig. 8 Relative power output comparison Plant B

As can be seen in Fig. 7, the gas turbine PB2 has the lowest compressor efficiency degradation rate. The effect is also a relatively flat power output degradation trend. The compressor efficiency and power output degradation rate of PB3 are significantly higher. During the test period analyzed, gas turbine PB3 had a power output degradation of about 4% in 6 weeks, whereas PB2 lost only about 1.5% in 11 weeks as shown in Fig. 8.

The data of Plant B allow a comparison of the effectiveness of compressor on-line washing with water and compressor on-line washing with a detergent. As can be seen in Fig. 8, the power output trend of PB1, the compressor of which is washed twice-a-week with a detergent, first follows the power output trend of PB2. Then the PB1 degradation rate becomes higher and is more like that of PB3, the unit without compressor on-line washing. Hence, the effectiveness of the compressor cleaning with a detergent diminishes over time, rendering a daily compressor on-line washing routine with water more effective. But during the first weeks after a compressor off-line washing, the effectiveness of a detergent is higher than that of water only. This is consistent with the results obtained by Boyce and Gonzales [5].

Based on the known exchange rates between compressor efficiency and power output, the conclusion can be drawn that the power output degradation is primarily caused by the compressor efficiency degradation. Hence, compressor fouling is also the main reason for power output degradation at Plant B.

5 Effect of a Single Compressor On-Line Washing

The effect of a single compressor on-line washing on the compressor efficiency and the power output of the gas turbine was analyzed. Averaged data of the time period 2 h before the compressor on-line washing were compared with the data of the time period 2 h after the compressor on-line washing. The data were only considered, if the gas turbine had no load changes during the 4 h period.

The corrected relative compressor efficiency of PA2 before, during, and after one of the weekly compressor on-line washing routines of the test campaign is plotted in Fig. 9. The compressor on-line washing starts at 15:06:00 and ends at 16:06:00. Before the compressor on-line washing, the corrected relative compressor efficiency has an averaged value of about 0.9973. After the compressor on-line washing the averaged value is 0.9980. Hence, the compressor on-line washing produces an increase of 0.07%. The power output of PA2 shows a similar development. Before the compressor on-line washing, the corrected power output level is at 0.9945 and after the compressor on-line washing, the power output increases at 0.9960. Hence, as a result of compressor on-line washing, the power output increases by 0.15%.

During the 60 min of the compressor on-line washing procedure, an increase in the power output up to a value of 0.9995 is recorded. This increase results from the injected water for the compressor washing, which has a similar effect on the gas turbine as high fogging.

The analysis of numerous weekly and daily compressor washing has shown that the averaged value of compressor efficiency recovery due to a weekly compressor on-line washing is 0.112%, whereas the averaged compressor efficiency recovery due to a daily compressor on-line washing is 0.031%. A daily compressor on-line washing has an averaged power recovery of 0.065%, a weekly one of 0.21%.

As expected, the weekly compressor on-line washing has a higher impact compared with a single daily compressor on-line washing procedure, but after 1 week the fouling process is more progressed than after 1 day and more dirt has accumulated on the surfaces that can be washed away. If the effect of compressor on-line washing is compared based on the time interval, the effectiveness of daily compressor on-line washing is about twice as high as that of weekly compressor on-line washing—e.g., the compressor efficiency recovery $7 \times 0.031\% = 0.187\% > 0.112\%$.

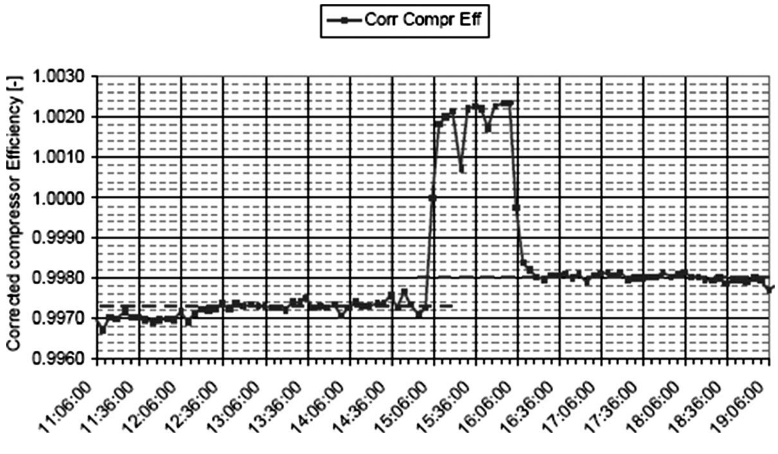

Fig. 9 Effect of a weekly compressor on-line washing

Downloaded 02 Jun 2010 to 171.66.16.96. Redistribution subject to ASME license or copyright; see http://www.asme.org/terms/Terms_Use.cfm

Table 2 Degradation trends of the compressor section pressure ratios for periodswith and without compressor on-line washing

	Compressor section pressure ratio			
	Sec I	Sec II	Sec III	Sec IV
No compressor washing	↗	↗	→	→
Daily compressor washing	↗	↑	↘	→

6 Compressor On-Line Washing Stage Cleaning Capability

As stated, compressor on-line washing can only clean compressor stages where the water used has not yet evaporated. One aim of the analysis was also to determine up to which compressor stage the compressor on-line washing still has a cleaning capability and what the effects of compressor on-line washing are for the different compressor sections.

The analysis was based on measured data of the secondary air system. The pressures and temperatures were measured in the external cooling air pipes of the gas turbine. The cooling air extractions are after the 5th, 11th, 16th, and 22nd stages of the compressor. These data were used for the calculation of the compressor section efficiencies (see Eq. (5)) and the compressor pressure ratios of the compressor stages 1–5 (Section I), 6–11 (Section II), 12–16 (Section III), and 17–22 (Section IV).

Before the analysis the determined compressor efficiencies and compressor pressure ratios were corrected for ambient effects. The analysis was based only on stable base load operating points. The data were measured at Plant A unit PA1. In a first step the aim was to determine qualitatively the differences in the compressor fouling behavior with and without compressor on-line washing.

The results show that the compressor pressure ratio of the high pressure Section IV is in line with the overall compressor ratio over time. That signifies that the loading of Section IV is independent of the washing schedule and follows the overall characteristic of the gas turbine compressor.

For Section III the compressor section efficiency and the compressor section pressure ratio are also in line with the overall compressor values if no compressor on-line washing is performed. Hence, without compressor on-line washing, the degradation of Section III progresses similar to the overall degradation of the compressor. However, for a daily compressor washing schedule, the degradation of Section III is higher than the overall degradation of the compressor. This suggests that dirt particles are flushed from the compressor front to the rear stages.

The fouling process increases the loading of the stages of Section II for both a compressor with and without daily compressor on-line washing. The compressor section efficiency and the compressor section pressure ratio increase whereas the extent of the increase is higher for the compressor with daily compressor on-line washing. The increasing stage efficiency values indicate a compressor rematching due to the fouling.

A similar effect can also be observed for the low pressure Section I. The compressor section efficiency and the compressor section pressure ratio increase because of the fouling effects. Again, the increase in the compressor section pressure ratio is higher for the period with daily compressor on-line washing.

For the period without compressor washing the degradation is more uniformly distributed throughout the compressor in comparison to the period with compressor on-line washing. In Table 2 the degradation trends of the compressor section pressure ratios over time are displayed with arrows, indicating increasing, constant, or decreasing trends compared with the total compressor pressure degradation.

Table 3 Changes in compressor section pressureratios and compressor section efficiencies

Compressor	Sec I	Sec II	Sec III	Sec IV
Section pressure ratio	↗	↗	↓	↓
Section efficiency	↘	↗	↓	↓

In a second step, the changes in the averaged section efficiencies and the averaged section pressure ratio values of PA1 during the compressor on-line washing period were analyzed and compared with the changes in the total compressor efficiency and compressor pressure ratio during the same time period.

For the high pressure Section IV of the compressor, both the compressor section efficiency and the compressor section pressure ratio decrease more than the overall values. This is an indication of the compressor fouling degree in Section IV.

For Section III the relative decrease in compressor section pressure ratio is higher than for Section IV. The relative decrease in compressor section efficiency is elevated, too. Hence, Section III has higher relative fouling than Section IV and higher relative fouling than the overall compressor.

Due to the fouling, the loading within the compressor sections changes. The compressor section pressure ratio of Section II increases. The increase in the section efficiency normally indicates a decrease in the reduced mass flow for the same characteristic line of the compressor.

In Section I a degradation of the compressor section efficiency can be observed. At the same time, the compressor section pressure ratio increases. Hence, the load of Section I increases and partly compensates the fouling of the rear stages. A part of the degradation of Section I might be related to nonrecoverable degradation aspects such as blade erosion as a result of the compressor on-line washing regime.

The analysis has shown that because of the fouling, a tendency exists for the stage loadings to decrease for the rear stages and increase for the front stages. The cleaning effects of compressor on-line washing can be seen up to stage 11. After stage 11 the injected water droplets have evaporated and no cleaning effect can be obtained. To clean the rear stages, compressor off-line washing has to be performed.

In Table 3 are indicated with arrows the changes in the compressor section pressure ratios and the compressor section efficiencies of a fouled compressor with daily compressor on-line washing regime. The relative changes in section pressure ratios and efficiencies are higher for the rear stages than for the front stages.

A similar analysis was also performed for PA2 that had a weekly compressor on-line washing regime. The obtained results were comparable, but the fact that daily compressor on-line washing is more effective must be kept in mind.

7 Conclusions

Compressor on-line washing can reduce the compressor efficiency degradation rate. Compressor on-line washing is no substitute for compressor off-line washing, but it lengthens the time between two compressor off-line washing procedures, if these are performed at fixed power degradation levels. Hence, compressor on-line washing increases the availability of the plant, if a certain level of performance degradation must not be exceeded.

The absolute power recovery of a single compressor on-line washing procedure that is embedded in a daily washing schedule is about a fourth of the absolute power recovery that can be obtained with a single compressor on-line washing procedure that is embedded in a weekly schedule. But analyzing the same time frames and not the single compressor on-line washing procedures, it becomes apparent that a daily compressor on-line washing schedule is more effective by about a factor of 2 than a weekly compressor on-line washing schedule.

Downloaded 02 Jun 2010 to 171.66.16.96. Redistribution subject to ASME license or copyright; see http://www.asme.org/terms/Terms_Use.cfm

For a certain time period, weekly compressor on-line washing with a detergent can be as effective as daily compressor on-line washing with water only. Increasing the compressor on-line washing frequency with a detergent may provide better results than the daily compressor on-line washing with water.

The highest compressor degradation during the period with daily compressor on-line washing is observed in the rear stages of the compressor, especially between stages 11 and 16. Hence, the loading distribution is shifted to the front stages. The degradation without on-line washing is more equally distributed throughout the compressor. At the first stages compressor rematching over time has been observed with and without on-line washing. The cleaning effects of compressor on-line washing can be seen up to the middle of the compressor. Compressor off-line washing can also reach the stages that are more to the rear of the compressor, although it could not be proven that a cleaning effect is given up to the last stage.

To keep the gas turbine performance at a high level, the recommendation is to perform regular compressor off-line washing during shutdowns, e.g., boroscope inspections, etc., of the gas turbine, since the gas turbine has to be cooled down anyhow on such occasions.

From the performance point of view, compressor off-line washing should be performed if the gas turbine has more than 2% power loss. If the gas turbine has a high fouling rate, a daily compressor on-line washing schedule should be considered to reduce the power degradation in the interval between inspections.

Compressor on-line washing has no additional benefit during high fogging operations of the gas turbine. High humidity in the inlet air mass flow can have a certain self-cleaning effect on the compressor because of condensing and coalescing water droplets [10]. As was observed in different power plants, compressor on-line washing may increase the erosion of the compressor blades, especially of compressor blade 1 (see also results published by Oosting et al. [10]). The erosion is dependent on blade surface, material, and the design of the compressor on-line washing nozzles. A new generation of compressor on-line washing nozzles that reduces the erosion effects has been developed and is currently undergoing testing. The overall cost benefit optimum needs to be investigated further unless the erosion problem is solved.

Nomenclature

Latin

c = specific heat capacity (J/kg K)
h = enthalpy (J/kg)
OH = operating hour (h)
PA = Plant A
PB = Plant B
p = pressure (Pa)
R = gas constant (J/kg K)
Sec = section
T = temperature (K)
W = work (J/kg)
VIGV = variable inlet guide vane

Greek

Δ = difference
η = efficiency
Π = pressure ratio

Indices

1 = compressor inlet
2 = compressor exit
comp = compression
n = polytropic
p = isobar
s = isentropic

References

[1] Hamed, A., Tabakoff, W., and Wenglarz, R., 2006, "Erosion and Deposition in Turbomachinery," J. Propul. Power, **22**(2), pp. 350–360.

[2] Diakunchak, I. S., 1992, "Performance Deterioration in Industrial Gas Turbines," ASME J. Eng. Gas Turbines Power, **114**, pp. 161–168.

[3] Meher-Homji, C. B., and Bromley, A., 2004, "Gas Turbine Axial Compressor Fouling and Washing," *Proceedings of 33rd Turbomachinery Symposium*, Texas A&M University, Houston, Texas.

[4] Tarabrin, A. P., Schurovsky, V. A., Bodrov, A. I., and Stalder, J.-P., 1998, "An Analysis of Axial Compressor Fouling and a Blade Cleaning Method," ASME J. Turbomach., **120**, pp. 256–261.

[5] Boyce, M. P., and Gonzales, F., 2007, "A Study of On-Line and Off-Line Turbine Washing to Optimize the Operation of a Gas Turbine," ASME J. Eng. Gas Turbines Power, **129**, pp. 114–129.

[6] Saravanamuttoo, H. I. H., Rogers, G. F. C., and Cohen, H., 2001, *Gas Turbine Theory*, 5th ed., Pearson Education Ltd., Harlow, England.

[7] Demircioglu, S., 2008, "Detail Analysis of Compressor On-Line Wash Impact in the Gas Turbine Performance," Master thesis, FH Offenburg, Offenburg, Germany.

[8] Bromley, A. F., and Meher-Homji, C. B., 2004, "Gain a Competitive Edge With a Better Understanding of GT Compressor Fouling, Washing," Comb. Cycl. J. (CCJ), PSI Media; Fourth Quarter, pp. 37–41.

[9] Stalder, J. P., and van Oosten, P., 1994, "Compressor Washing Maintains Plant Performance and Reduces Cost of Energy Production," ASME Paper No. 94-GT-436.

[10] Oosting, J., Stalder, J., Boonstra, K., Eicher, U., de Haan, A., and van der Vecht, D., 2007, "On Line Compressor Washing on Large Frame 9-FA Gas Turbines Erosion on R0 Compressor Blade Leading Edge Field Performance With a Novel on Line Wash System," Paper No. GT2007-28227.

[11] Stalder, J. P., 2001, "Gas Turbine Compressor Washing State of the Art: Field Experiences," ASME J. Eng. Gas Turbines Power, **123**, pp. 363–370.

Downloaded 02 Jun 2010 to 171.66.16.96. Redistribution subject to ASME license or copyright; see http://www.asme.org/terms/Terms_Use.cfm

Daniel McGuire
Xiao Huang
Department of Mechanical and Aerospace
Engineering,
Carleton University,
Ottawa, Ontario K1S 5B6, Canada

Doug Nagy
Liburdi Engineering,
400 Highway 6 North,
Dundas, Ontario L9H 7K4, Canada

Weijie Chen
NRC Institute for Aerospace Research,
1200 Montreal Road,
Building M-17, Room 104,
Ottawa, Ontario K1A 0R6, Canada

Effect of Tungsten Addition on the Nucleation of Borides in Wide Gap Brazed Joint

Wide gap brazing (WGB) is a cost effective and reliable means to repair gas turbine hot section components with defect sizes exceeding 0.3 mm. However, it has been shown that WGB joints of nickel-based superalloys suffer from reduced ductility and thermal fatigue life due to the presence of brittle intermetallics and porosities in the brazed joint. In order to disperse the brittle intermetallic compounds, potentially increase the ductility of the repaired region, and reduce the risk of the thermomechanical fatigue failure, elemental tungsten (W) was added to the braze additive filler alloy IN738 by mechanical alloying. The alloyed IN738 was then brazed with the addition of 30 wt %, 50 wt %, and 80 wt % of braze alloy (BNi-9). After brazing at 1200°C for 20 min, microstructural analysis of WGB joints showed a decreasing trend of discrete boride size and the amount of eutectic and script-shaped borides with the increases of W. The increase in the braze alloy to additive filler alloy ratio diminished the effect of W addition due the dissolution of W particulates. [DOI: 10.1115/1.4000136]

1 Introduction

Braze repair is a proven approach for reliable, cost effective life extension of gas turbine components. Conventional brazing, or narrow gap brazing, relies on capillary attraction, and as such the joint gaps are limited. Since boron (B) and silicon (Si) are often used as melting point depressants in the nickel- and cobalt-based braze alloys, a small clearance of 50–100 μm is required to prevent formation of brittle intermetallic phases in the form of borides and silicides [1]. Arising from this limitation of narrow gap brazing, in practice when a gap exceeds 0.1–0.3 mm the process falls within the wide gap brazing regime. The braze alloy in wide gap brazing is commonly a mixture of additive filler alloys resembling that of parent material composition and low melting temperature braze alloy [2].

In a wide gap braze repair, the additive filler alloy provides three basic functions: a source for the capillary forces to draw the molten braze alloy; as a gap retainer during brazing; and an additional sink for B or Si to reduce the propensity for the formation of brittle intermetallic phases. To be successful in reducing the brittle intermetallic phases, the filler metal must be able to act as a sink, either with solid-state diffusion of the B and Si or by partial dissolution of the additive alloy by the molted braze alloy [3]. Even with careful control of the braze alloys and brazing processes, formation of intermetallic phases cannot be completely avoided. The formation of brittle intermetallic and eutectic phases during the wide gap braze process results in generally lower mechanical properties than the parent materials [4], particularly the ductility and fatigue life of the joint [5,6]. For example, stage-one low-pressure-turbine (LPT) nozzle-guide-vanes (NVGs) of CFM56 family are frequently braze repaired and returned to service with an expected life of 12,000–15,000 h, or 5,000–7,000 cycles; however it was found that after a test run, the repaired trailing edge cracks have reopened due to thermal shock during start up of the engine. Thermal shock leads to high strain induced stresses and the brittle failure of the braze joints.

It has been shown that thermal-mechanical fatigue crack initiates and propagates along eutectic or large script-type intermetallic compounds in the brazed joint [4,7]. It is expected that the reduced boride size and the occurrence of the eutectic and script-type phases will help reduce the ability for cracks to initiate and propagate, thereby improving the joints ductility and fatigue properties [2,7]. These improvements will also lead to increased component coatability and oxidation resistance of wide gap brazed joints [8].

In our previous work, microstructure was substantially modified, with regards to the size and distribution of borides, as well as the reduction in eutectic phases, by the introduction Rhenium (Re) to the additive filler alloy; the addition of Re was assumed to have provided nucleation sites for boride formation [2]. Yet the same beneficial microstructural change was not seen with the addition of Ru due to the difference in their elemental characteristics [9,10]. In this study, the addition of W to additive filler alloy is used as a low cost alternative to Re addition with the objective to achieve similar microstructure improvements seen with Re addition [2]. W exhibits very similar ionization energy and electronegativity as Re as shown in Table 1.

2 Experimental Procedure

2.1 Materials. The material used in this study consisted of IN738 (NI-284 from PRAXAIR, Indianapolis, IN) additive filler powder alloyed with different concentrations of W; and BNi-9 (NI-276 from PRAXAIR) as the braze alloy. Their compositions are summarized in Tables 2 and 3. The substrate alloy, used to form the cavity for wide gap brazing, is made of stainless steel 304 (chosen for its machinability). The bonding and interface characteristics between the braze materials and base metal were not examined in this study, only the microstructure of the braze region was of interest for this experiment.

2.2 Sample Preparation. Wide gap specimens were machined from stainless steel 304 bar stock to create the cavity in a puck, with dimensions shown in Fig. 1. The stainless steel puck was ultrasonically cleaned for 10 min in alkaline solution and isopropyl alcohol, and dried thoroughly before the addition of additive and braze alloys. The additive filler alloy IN738 was prepared by mechanically alloying it with various amounts of W. The mechanical alloying was accomplished by grinding the IN738 with the W powder in a planetary mill.

This equipment is capable of providing powder mixing and

Contributed by the International Gas Turbine Institute of ASME for publication in the JOURNAL OF ENGINEERING FOR GAS TURBINES AND POWER. Manuscript received April 16, 2009; final manuscript received April 17, 2009; published online March 24, 2010. Editor: Dilip R. Ballal.

Copyright © 2010 by ASME

Downloaded 02 Jun 2010 to 171.66.16.96. Redistribution subject to ASME license or copyright; see http://www.asme.org/terms/Terms_Use.cfm

Table 1 Element properties [10,11]

Property	B	Ru	W	Re
Ground state configuration	$\mathrm{He}:2s^2 2p^1$	$\mathrm{Kr}:5s^1 4d^7$	$\mathrm{Xe}:6s^2 4f^{14} 5d^4$	$\mathrm{Xe}:6s^2 4f^{14} 5d^5$
First ionization energy (kJ/mol)	800	750	510	520
Electronegativity	2.0	2.2	1.7	1.9

powder size reduction to $d < 20\ \mu$m. The IN738 powder was ground using 5 mm diameter stainless balls in a stainless grinding bowl. Maximum sample temperature was controlled to be $<150°$C for safety reasons. Three different weight percentages of W were added to IN738: 2 wt %, 5 wt %, and 8 wt %, each sample was ground for either 2 h or 4 h to create six different powder conditions. The mechanically alloyed additive alloys were then layered into the stainless puck, as shown in Fig. 1, with various amounts of braze alloy to create a total of eight final conditions, as outlined in Table 4.

With the limited volume of the cavity in the stainless puck, the amount of powder added was determined by the weight percentage of each powder type and total volume of the cavity. For samples with 30 wt% and 50 wt% braze alloy, 0.9302 g of additive alloy was placed into the gap, followed by further addition of the braze alloy. For the sample with 70 wt% braze alloy, the additive alloy was reduced to 0.6202 g to accommodate the increased weight percent of braze alloy. Details of the eight conditions investigated in this study are outlined in Table 4. The specimens are referred to by their percent of W addition (P) followed by grind time (G) and amount of braze alloy (B) which they are combined with, such that P8G2B50 specifies a wide gap repair with 8 wt% W in IN738 after 2 h grinding time and braze alloy constitute 50% of the overall alloy mix used to fill the gap.

Binding agent (Nicrobraz 510 from Wall Colmonoy, Madison Heights, MI) was added to the powders placed in the gap. This was accomplished by adding drops of binder to the powder, allowing adequate time for the binder to permeate the powder and permitting any trapped air in the powder mixture to escape [11]. This process was repeated until the surface was completely wetted, at which point the sample was taped against a solid surface to compact the powder further. After all the trapped air having been driven off, three more drops of binder were added to seal the surface and prevent any powder loss during transportation and brazing.

2.3 Braze Cycle. The samples were heated to 1200°C in a vacuum furnace at Liburdi Engineering (Dundas, Ontario), and held isothermally for 20 min before being furnace cooled. As shown by previous studies, the braze temperature greatly influences the microstructure as well as the mechanical properties of the joint [4]. The dependency on braze temperature is more pro-

Table 2 Nominal compositions for braze additive alloy and substrate

Alloy	Al	B	C	Cr	Co	Fe	Mn	Mo	Nb	Ni	S	Si	Ta	Ti	W	Zr
IN738	3.40	0.001	0.17	16.0	8.50	-	0.01	1.75	0.90	Bal.	-	0.01	1.75	3.40	2.60	0.10
SS304	-	-	0.15	19.0	-	Bal.	2.00	-	-	10.0	0.15	1.00	-	-	-	-

Table 3 Properties of braze alloy powder BNi-9

	Composition					
Product name	Ni	Cr	B	Solidus (°C)	Liquidus (°C)	Brazing range (°C)
BNi-9(Ni-276)	Bal.	15	3.5	1020	1050	1066–1149

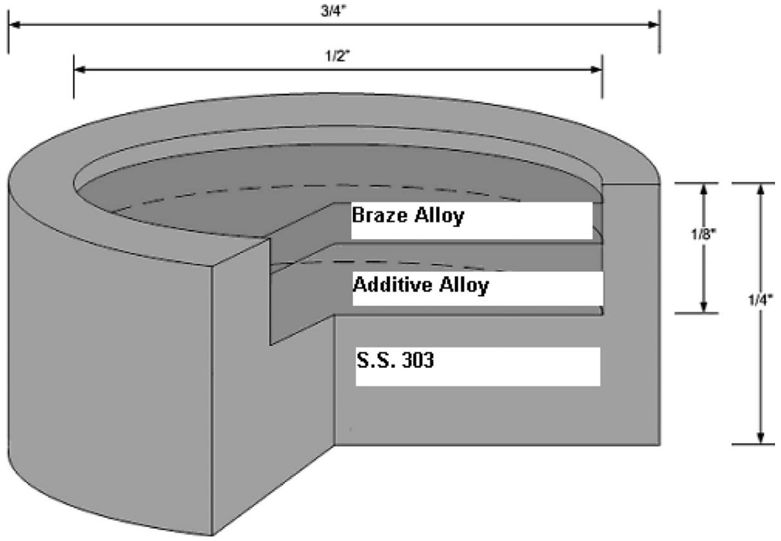

Fig. 1 Specimen cutaway showing typical preparation

Downloaded 02 Jun 2010 to 171.66.16.96. Redistribution subject to ASME license or copyright; see http://www.asme.org/terms/Terms_Use.cfm

Table 4 Wide gap braze repair specimens identifications

Specimens	% addition W	Grind time (h)	Additive alloy (g)	Braze alloy (g)
P8G2B50	8	2	0.9302	0.4651 (50%)
P8G4B50	8	4	0.9302	0.4651 (50%)
P5G2B30	5	2	0.9302	0.2791 (30%)
P5G2B50	5	2	0.9302	0.4651 (50%)
P5G2B70	5	2	0.6202	0.4341 (70%)
P5G4B50	5	4	0.9302	0.4651 (50%)
P2G2B50	2	2	0.9302	0.4651 (50%)
P2G4B50	2	4	0.9302	0.4651 (50%)

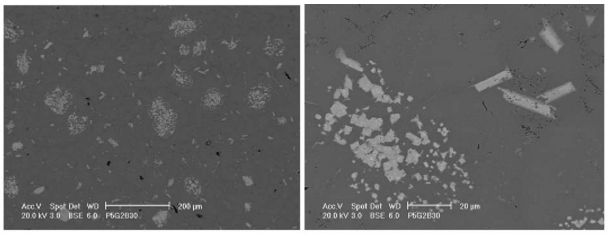

(a) P5G2B30

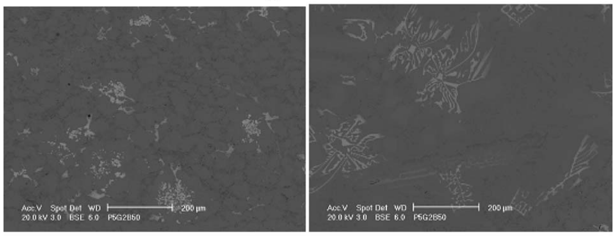

(b) P5G2B50

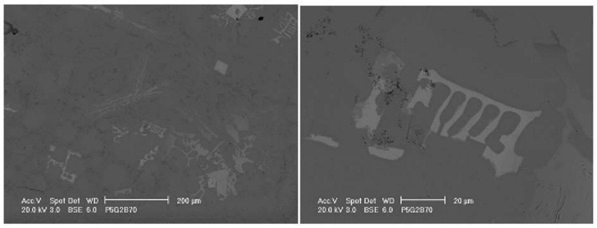

(c) P5G2B70

Fig. 2 Microstructures of samples with varying amount of braze alloy

nounced as the amount of additive alloy is increased. The braze alloy's ability to penetrate the additive alloy depends on the fluidity of the molten braze alloy and the surface wettability of the additive alloy. The ability of the additive alloy to act as a sink for the boron also relies on the extent of boron diffusion from the braze metal. The braze temperature of 1200°C and short holding time of 20 min were expected to provide a good basis from which one could compare the impact of W addition on the boride formation, since limited diffusion was allowed to occur.

2.4 Microstructural Examination. After brazing, the samples were sectioned using a high-speed, liquid cooled, abrasive cutting wheel. The section was then mounted in Bakelite and polished using the Buehler ECOMET IV polisher/grinder. The sample preparation involved wet grinding with 180, 240, 320, 400, and 600 grit silicon carbide abrasive papers, followed by polishing using 6 μm and 3 μm Beta Diamond Products (Yorba Linda, CA) diamond polishing suspensions, and finally, with a colloidal silica suspension. The samples were etched using Marble's reagent to reveal the phases in the brazed region. Microstructure examination was carried out using a Phillips XL30-SFEG ultrahigh resolution scanning electron microscope (SEM). Secondary electron (SE) and backscatter electron (BSE) images, and energy dispersive spectroscopy (EDS) element maps were prepared.

3 Results and Discussion

3.1 Effect of Braze Alloy to Additive Alloy Ratio. The effect of varying the ratio of braze alloy with respect to additive alloy is shown in Fig. 2. It is to be mentioned that all samples shown in the figure contained mechanically alloyed powders ground for 2 h and the amount of W addition to the IN738 additive alloy remained constant (5 wt %). The amount of braze metal has an impact on both the boride formation and the porosity near the borides. With lower concentrations of braze alloy present, the borides tend to be much smaller in size and assume discrete morphology mostly as shown in Fig. 2(*a*). When the braze alloy was increased to 70%, Fig. 2(*c*), eutectic and script-type borides formed in addition to limited discrete borides. With the addition of 50% braze alloy, the microstructure of the brazed joint exhibited a mixed mode of borides: some cluster of discrete borides (left) and distinct eutectic boride (right). It was also evident that the boride clustering was much more severe with lower braze alloy ratio, Fig. 2(*a*), suggesting the possibility of limited mixing between the additive alloy and W, and the lack of complete melting of additive alloy during brazing cycle. The distribution and size of borides were seen to be nonuniform, particularly for those samples containing all types of borides such that in P5G2B30, where two different views were included in Fig. 2(*b*) to illustrate the variations.

To determine if W addition has contributed to the boride formation, EDS analysis was carried out on samples with low and high braze alloy to additive filler alloy ratios: P5G3B30 and P5G2B70. The average EDS results of various particles labeled Figs. 3 and 4 are given in Tables 5 and 6. As anticipated, all secondary phases contained significant boron, although the standardless EDS used could not give accurate measure of the actual boron percentages. The atomic percentages of various elements shown in Tables 5 and 6 are therefore treated as qualitative measurements. Comparing to spot H and I in Fig. 3(*a*), representing γ-Ni matrix, all the secondary phases (A–G) contained significantly higher B and W contents, while had depleted Ni, Co, and Ti. This observation suggests that W (Cr and Mo) partitioned preferentially to borides either as nucleation sites, in the form of unmelted W particles, for boride initiation, or by forming W borides during brazing cycle.

Further examining the particles B and C in Fig. 3(*a*), increased contrast (W gives high contrast in backscatter electron images) was observed in the center of the particle. Higher W content on spot B was determined by EDS as compared with spot A; therefore, it seems that the presence of W in the additive alloy IN738 has contributed to the boride initiation and formation. The participation of W in the formation of eutectic (D) and script-typed (A, B, and E) borides in the sample with higher ratio of braze alloy (P5G2B70) was further examined. EDS spot analysis on spots A–F (labeled in Fig. 3(*b*)) given in Table 6 showed increased W presence in the eutectic phases, in addition to high boron content. While different W contents were observed among the borides analyzed, the contribution of W to the nucleation of eutectic and script-typed boride was not evident.

3.2 Microstructure Variation With Tungsten Addition. The effect of W addition on the formation of borides is demonstrated in Fig. 4, with the primary interest being any change in size and distribution of borides with the addition of W. In this group of samples, both the grinding time and amount of braze alloy were kept unchanged. It is anticipated that the additional nucleation sites provided by the gradual changes in W content will play a role in reducing the size and continuous nature of the borides.

As seen in Fig. 5, there is a trend of increasing number of discrete borides, and reduction in eutectic and script-type of

Downloaded 02 Jun 2010 to 171.66.16.96. Redistribution subject to ASME license or copyright; see http://www.asme.org/terms/Terms_Use.cfm

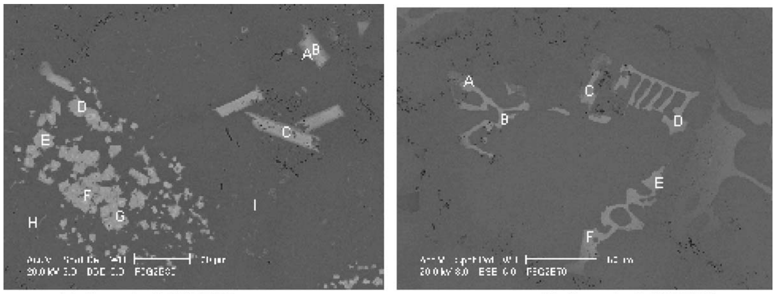

(a) Sample P5G2B30 (b) Sample P5G2B70

Fig. 3 EDS spot analysis of various phases in P5G2B30 (*a*) and P5G2B70 (*b*)

borides with the increase in W addition in three samples. Initially, with low W concentration, the borides tend to form around all the primary γ-Ni phase, as shown in Figs. 4(*a*) and 4(*b*). At the highest concentration of W, 8 wt %, there was a lack of the formation of eutectic and script-type of borides seen in Fig. 4(*c*), where finely dispersed borides were observed. The resulting borides were also much smaller in size, and more homogeneously distributed.

Microstructure variations were also observed in samples P2G4B50 and P5G4B50, depending on the location selected, but overall there were limited discrete boride formation in sample P5G4B50 similar to that observed in P5G2B50 (Fig. 2(*b*)). Clustering of the borides in Fig. 4(*c*) was also noticed; the reason for the clustering was believed to be associated with insufficient mixing during mechanical alloying.

To identify the alloy distribution in relationship to borides, X-ray maps of Ni, Cr, Co, W, and Ti were obtained, shown in Fig. 5. W addition at low concentration (2 wt %) had little effect in modifying the boride formation; although W is heavily segregated to the boride, shown in Fig. 5. Cr is also concentrated in the borides and Ni is depleted from borides. Co shows even distribution throughout the microstructure in the brazed joint. Ti, on the other hand, showed uneven distribution, irrespective of boride distribution. Increasing the W content to 8 wt % in IN738 led to a very different microstructure, seen in Fig. 6. As described earlier, higher concentration of W has the effect of reducing boride sizes. Also, W is observed to distribute preferentially within borides, as illustrated in W map of Fig. 6. It is clear that W may act as the primary nucleation site for boride formation. Observing the Cr maps in Figs. 5 and 6, the addition of W has also increased the homogeneity of Cr distribution in the brazed joint by breaking down the size of various borides. Ni depletion from the borides in sample P8G4B50 is not as noticeable as that in sample P2G4B50 (Fig. 5).

A detailed analysis of the composition of the borides, as shown in Fig. 7 and Table 7, showed that the central region of the boride (spot B) has a higher concentration of W to Cr in comparison to the outer layer (spot A). Comparing the compositions of B to A, C to D, and F to E, the central regions of discrete borides had at least 50% more W than the outer regions. This, along with W map in Fig. 6 further suggests that W can promote boride nucleation in the presence of higher concentration of W (8 wt %) and braze alloy to additive alloy ratio of 0.5.

3.3 Impact of Grinding Time. Using the Pulverisette 6 mechanical alloying facility, mixing of IN738 and W powders was achieved by repeatedly breaking and welding of the powder particles. In our past research, we have observed uniform dispersion of Re particles within IN738 powder after mechanically alloying for several hours [2]. Powder size ranged from 10 μm to 50 μm, similar to that of initial IN738 powder size, however with altered particle shape. In this study, two different grinding times of 2 h and 4 h were utilized. From the microstructural study conducted, it is apparent that the grinding time may not be sufficient to yield homogeneous W distribution as illustrated in Fig. 4(*c*).

When the brazed alloy is greater than 50%, the additive alloy has been found to be in complete liquid state when the joint reaches brazing temperature of 1200°C [8]. Comparing Figs. 8(*a*) and 8(*b*), it can be concluded that despite the different grinding time used, the microstructures of both sample exhibited very similar features and limited influence from W addition. This observation suggests that when W addition was ≤ 5 wt% and braze alloy of 50 wt %, the impact on boride formation was minimal; this may have been attributed to the dissolution of W in the molten braze alloy during brazing. With the increase in W content to 8%, the effect of grinding time on the formation of the borides can be clearly seen in Figs. 8(*c*) and 8(*d*). Using a low grinding time of 2 h, the effect on boride particle size reduction and distribution was very limited, resulting in a formation of large borides, chunks in localized regions. The increased grinding time to 4 h not only provided better distribution of the W, but had the effect of reducing the particle size leading to more uniform and finer boride formation, as shown in Fig. 8(*d*). If grinding time can be further increased, it is expected that the boride clusters seen in Fig. 8(*d*) should be alleviated.

4 Conclusions and Recommendation

In this study, the addition of W to braze additive filler alloy was employed in an attempt to refine the boride formation. A mechanical alloying process was used to add W in the weight percentages

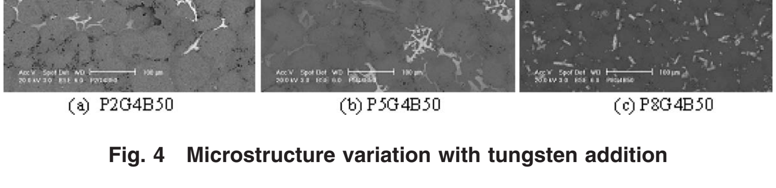

(a) P2G4B50 (b) P5G4B50 (c) P8G4B50

Fig. 4 Microstructure variation with tungsten addition

Downloaded 02 Jun 2010 to 171.66.16.96. Redistribution subject to ASME license or copyright; see http://www.asme.org/terms/Terms_Use.cfm

Table 5 EDS (at. %) analyses of various phases labeled in P5G2B30

Spot	Ni	Cr	W	Ti	Co	Mo	B
A	3.15	16.75	4.26	0.3	0.86	2.99	71.06
B	2.38	9.82	6.47	0.68	0.47	2.59	77.22
C	2.16	11.56	7.04	0.69	0.52	2.76	74.54
D	3.13	11.68	8.4	0.92	1.11	2.63	71.81
E	2.3	9.93	7.7	0.47	0.56	2.12	76.21
F	1.85	8.61	10.18	0.55	0.33	0.65	76.72
G	2.07	9.2	6.85	0.89	1.01	1.53	78.35
H	69.06	17.5	1.32	2.52	8.56	1.05	0
I	72.43	15.99	1.97	2.17	7.43	0	0

of 2, 5, and 8 to IN738 braze additive alloy. After grinding for 2 h and 4 h, the powder mixture were used in combination with BNi-9 to fill wide gap joint. The microstructure of various joint compositions after brazing at 1200°C was studied to determine the effect of W percentages, grinding time, and braze alloy ratios on the boride formation and distribution. From the microstructure observation, it is conclusive that W addition can impart changes to the formation and distribution of borides. Specifically, increasing the braze alloy from 30 wt % to 70 wt %, diminishing the effect of W addition on the nucleation of borides, possibly due to the dissolution of W in molten braze region during brazing cycle. An addition of 2 wt % of W in IN738 yielded little effect on the boride formation; increasing the W addition to 5 wt % but with short grinding time and 50 wt % braze alloy showed similar results. With sufficient grinding time of >4 h and W addition of ~8 wt%, the brazed joint exhibited more optimized microstructural features, with smaller boride size and better distribution. Additionally, with higher W addition, the dissolution of W in braze alloy can be minimized ensuring its effect on the nucleation of borides during brazing.

Table 6 EDS (at. %) analyses of various phases labeled in P5G2B70

Spot	Ni	Cr	W	Ti	Co	Mo	B
A	2.47	12.07	3.63	0.42	0.53	1.5	79.37
B	4.11	17.66	6.73	0.34	0.64	2.22	68.1
C	2.25	11.47	3.8	0	0.67	1.56	79.91
D	2.96	16.87	5.1	0.4	0.38	1.92	72.03
E	2.21	15.64	5.02	0.46	0.67	2.11	73.31
F	2.48	14.75	5.48	0.41	0.46	1.57	74.66

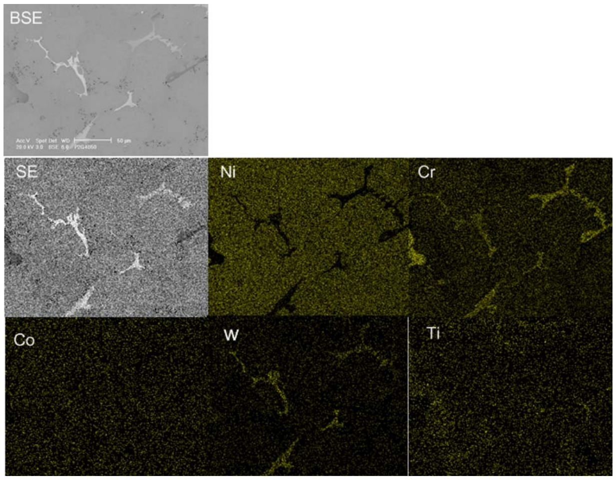

Fig. 5 Elemental maps of sample P2G4B50

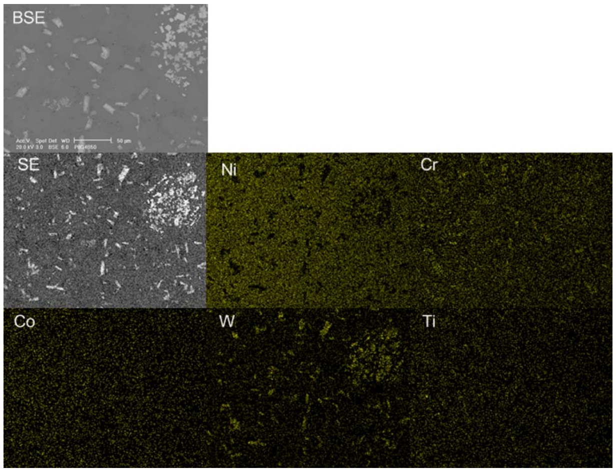

Fig. 6 Element distribution of P8G4B50

While there are many commercially available braze alloys containing W, its addition, in the form of solid solution, is primarily for the purpose of improving mechanical strength of the joint. The addition of W to IN738 through mechanical alloy has the advantage over other alloys in contributing to the nucleation and dispersion of borides. Unlike that in a previous study where costly elemental Re was used to refine discrete boride formation, this study utilized a less costly W to ensure future commercial viability. Future experiments are being planned to test the high temperature tensile and fatigue properties.

Acknowledgment

The authors thank Mr. Thomas Henhoeffer for the preparation of metallographic samples. The W powder was provided by Dr. Matthew Yao of Deloro Stellite Inc.

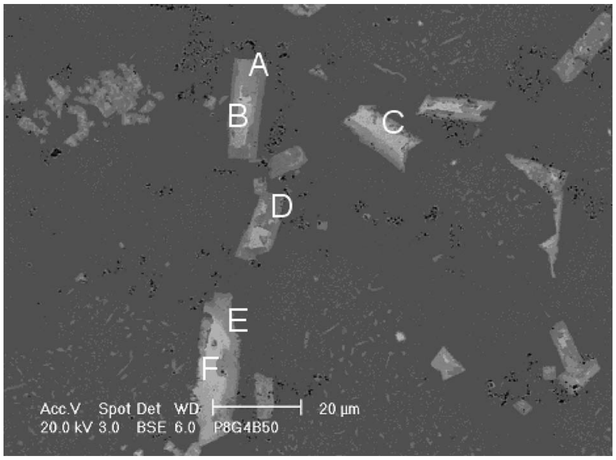

Fig. 7 EDS analysis of sample P8G4B50

Table 7 EDS (at. %) analyses of various phases in P8G4B50

	Ni	Cr	W	Ti	Co	Mo	B
A	2.73	12.43	4.38	0.71	0.78	1.39	77.17
B	2.71	14.25	6.84	0.73	1.05	2.2	71.59
C	4.15	13.72	11.16	0.7	0.66	2.68	66.93
D	3.39	16.21	4.02	0.23	1.21	1.34	73.61
E	3.59	13.34	5.21	0.63	1.01	1.68	74.21
F	2.71	11.69	8.52	0.36	0.57	2.59	72.94

Downloaded 02 Jun 2010 to 171.66.16.96. Redistribution subject to ASME license or copyright; see http://www.asme.org/terms/Terms_Use.cfm

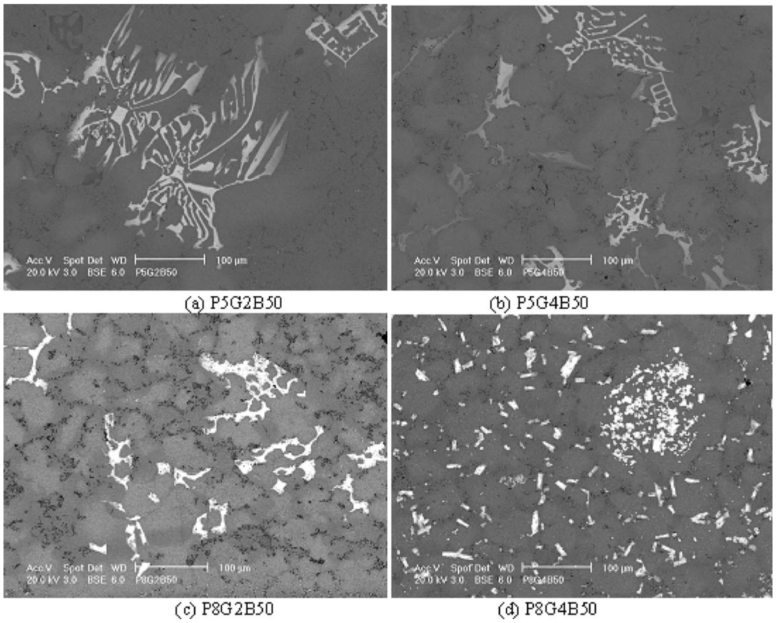

(a) P5G2B50 (b) P5G4B50

(c) P8G2B50 (d) P8G4B50

Fig. 8 Effect of grinding time on the boride formation and distribution

References

[1] Wu, X. W., Chandel, R. S., Seow, H. P., and Li, H., 2001, "Wide Gap Brazing of Stainless Steel to Nickel-Based Superalloy," J. Mater. Process. Technol., **113**, pp. 215–221.

[2] X. Huang, S. Yandt, D. Nagy, M. Yao, 2007, "Effect of Ruthenium, Rhenium and Yttria Additions on the Microstructure of Wide Gap Brazing of IN738," ASME Turbo Expo 2007: Power for Land, Sea and Air, Montreal, Canada, May 14–17.

[3] Su, C. Y., Lih, W. C., Chou, C. P., and Tsai, H. C., 2001, "Activated Diffusion Brazed Repair for IN738 Hot Section Components of Gas Turbines," J. Mater. Process. Technol., **115**, pp. 326–332.

[4] Yu, Y. H., and Lai, M. O., 1995, "Effects of Gap Filler and Brazing Temperature on Fracture and Fatigue of Wide-Gap Brazed Joints," Mater. Sci., **30**(195), pp. 2101–2107.

[5] Su, C. Y., Chou, C. P., Chang, W. J., and Lui, M. H., 2000, "Effect of Mechanical Properties Using Different Filler Metals on Wide Clearance Activated Diffusion Brazed Ni-Based Superalloy," J. Mater. Eng. Perform., **9**(6), pp. 663–668.

[6] Henhoeffer, T., Huang, X., Yandt, S., Seo, D., and Au, P., 2009, "Microstructure and High Temperature Tensile Properties of Narrow Gap Braze Joint Between X-40 and IN738," J. Mater. Sci. Technol., **25**(7), pp. 840–850.

[7] Henhoeffer, T., Huang, X., Yandt, S., Au, P., and Nagy, D., "Microstructure and High Temperature Tensile Properties of Wide Gap Brazed Cobalt Based Superalloy X-40," J. Mater. Sci. Technol., to be published.

[8] Nagy, D., and Huang, X., 2009, "Wide Gap Brazing and New Development of Vertically Laminated Repair Scheme," ASME J. Eng. Gas Turbines Power, **131**(1), p. 012101.

[9] Chang, R., 2007, *Chemistry*, 9th ed., McGraw-Hill, New York.

[10] Nave, R., 2008, "Ionization Energies," http://hyperphysics.phy-astr.gsu.edu/hbase/chemical/ionize.html, accessed April 2008.

[11] Schoonbaert, S., Huang, X., Yandt, S., and Au, P., 2008, "Brazing and Wide Gap Repair of X-40 Using Ni-Base Alloys," ASME J. Eng. Gas Turbines Power, **130**(3), p. 032101.

Downloaded 02 Jun 2010 to 171.66.16.96. Redistribution subject to ASME license or copyright; see http://www.asme.org/terms/Terms_Use.cfm

The Thermal Impact of Using Syngas as Fuel in the Regenerator of Regenerative Gas Turbine Engine

Luciana M. Oliveira
e-mail: luciana@unifei.edu.br

Marco A. R. Nascimento
e-mail: marcoantonio@unifei.edu.br

Genésio J. Menon

Department of Mechanical Engineering,
Itajubá Federal University (UNIFEI/NEST),
37500-903 Itajubá MG, Brazil

Environment and energy are driven forces of human survival and development. Nowadays the use of primary energy comprises mostly mineral fuels, which have limited reserves and whose utilization may cause serious environmental impacts. Attention has been paid to discover clean and renewable resources such as syngas, which is an important renewable source of energy and is environment friendly. The use of syngas from biomass gasification process as fuel in regenerative gas turbine causes an increase in turbine exhaust mass flow and a change in the gas composition due to a low heat value. As a result, the regenerator changes its size, thermal characteristics, weight, and cost compared with the use of natural gas as fuel. The aim of this work is to assess the thermal performance, the size, and the cost of the recuperator of a 600 kW regenerative gas turbine engine when designed for syngas and natural gas. Two different types of surfaces, cross-corrugated and undulated-corrugated, are used for analysis. The results are shown, comparing heat-transfer coefficient, effectiveness, pressure loss, size, and cost for syngas and natural gas. [DOI: 10.1115/1.4000125]

1 Introduction

Gas turbines have been used as primary drivers in the industrial and aeronautic sectors for electric power generation, mechanical driving, and the propulsion of industrial heat exchangers of aircraft. However, the technical evolution of their components and the drop in their prices made the share of industrial gas turbines in the world market increase substantially. Above all, the microturbines, whose features are, for example, easy installation, low costs, and fast investment return, have expanded the market shear.

Recent researches present arrangement alternatives that try to increase the useful life and the efficiency of the gas microturbines. Within this scenario we can highlight the recuperators, which use thermal energy out of the turbine exhaust gases for heating the air before entering the combustion chamber. This causes a reduction in fuel consumption, a rise in the efficiency, and pollution reduction in the microturbine.

However, for the efficiency of the microturbine to reach acceptable values, the recuperator must present effectiveness above 85%. On the other hand, it must also be compact, given that it is part of an extremely small system, and present low a cost, which can be compensated by the rise in the microturbine efficiency. This way, the researchers' greatest challenge has been to design highly efficient, compact, and low-cost recuperators [1,2].

A common target in many researches is the heat-transfer surfaces that are appropriate for the design of recuperators—we can highlight the cross-corrugated (Fig. 1) and the cross-undulated (Fig. 2) primary surfaces.

The cross-corrugated surfaces are also called chevron plates. They have already been used in industrial heat exchangers and are classified as platelike heat-transfer surfaces. In industrial processes the hydraulic diameter that is used is over 5 mm. But in order to be used in recuperators, the hydraulic diameter must be significantly smaller [3]. Savostin and Tikhonov [4] carried out an experimental study of the thermal and hydraulic performances of cross-corrugated surfaces, building heat exchanger modules with diameters as small as 1.54 mm. However, this concept was not commercialized because of its restrict applications [3]. This technology was reassessed for a possible application in recuperators of annular gas microturbines [2].

The cross-undulated surface, Fig. 2, is a variation of the cross-corrugated surface. It was only in the past decade that this surface started to be presented in scientific papers that talked about its use in rotating preheaters [5,6].

This surface can be manufactured in the same way as the cross-corrugated one, using stamping, pressing, and folding of metallic sheets. The disadvantage of the cross-undulated surface in relation to the cross-corrugated one is that it is formed by two different plaques, which leads to higher manufacturing difficulties and higher expenditures with experts during the design phase.

The historical development of these surfaces is summarized by Utriainen and Sundén in Ref. [3].

Both the cross-corrugated and the cross-undulated surfaces have been studied by several authors [7–11], because they can be manufactured with high compactness, which leads to high effectiveness due to the high rate heat-transfer surface per volume, and reduced costs, given that they are entirely interconnected to the volume and to the material weight that is used. Some of these studies are briefly commented below.

Utriainen and Sundén [3] carried out calculations regarding the volume, weight, and dimension of the matrix of recuperators using the cross-corrugated and the cross-undulated surfaces, which allowed the conclusion that these surfaces have great potential to be used in recuperators.

Liang et al. [10] used the genetic algorithm technique to optimize the geometric parameters of a recuperator of a 100 kW microturbine with a cross-corrugated surface. The results showed that this surface presented better performance than the other surfaces that were analyzed.

Traverso and Massardo [1] studied the volume and the cost of the recuperator matrix using cross-corrugated and cross-undulated surfaces. Their use was compared for 50 kW, 100 kW, and 500 kW microturbines.

Contributed by the International Gas Turbine Institute (IGTI) of ASME for publication in the Journal of Engineering for Gas Turbines and Power. Manuscript received April 24, 2009; final manuscript received April 8, 2009; published online March 18, 2010. Editor: Dilip R. Ballal.

Copyright © 2010 by ASME

Downloaded 02 Jun 2010 to 171.66.16.96. Redistribution subject to ASME license or copyright; see http://www.asme.org/terms/Terms_Use.cfm

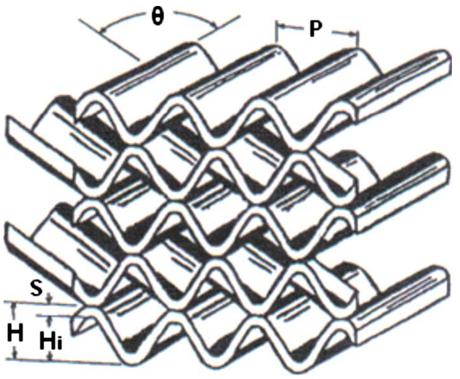

Fig. 1 Cross-corrugated surfaces

Micheli et al. [9] developed a multigoal optimization method in order to optimize the design of a recuperator matrix of a 50 kW microturbine using a cross-corrugated surface. The optimizations aimed at maximizing the heat-transfer area and minimizing load losses.

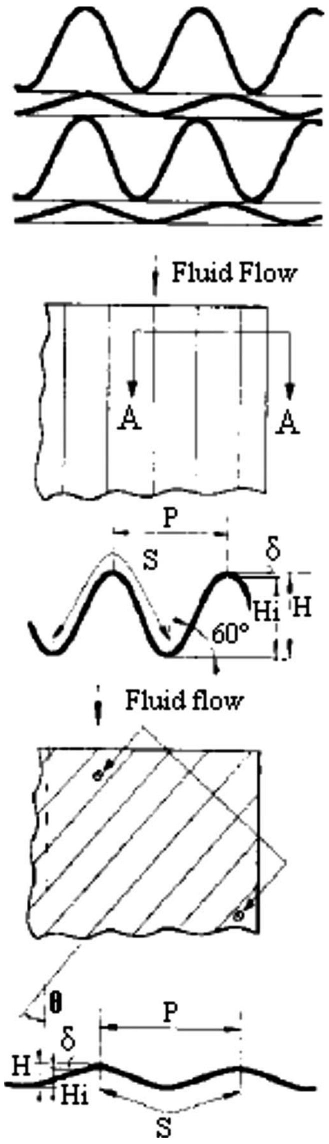

Fig. 2 Cross-undulated surface

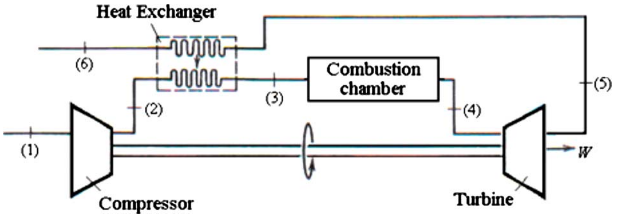

Fig. 3 Regenerative turbine arrangement

The design of recuperators and their costs are entirely interconnected to their material. Such materials must resist to high temperatures, oxidation caused by the water steam present in the exhaust gases, and to a whole complex of tension conditions, which the heat-transfer surface submitted to that could lead to material failure [12]. Materials such as austenitic stainless steels, nickel alloys, superalloys, and even ceramic materials are studied as options for manufacturing the recuperator, depending on the maximum temperature of the cycle and on the complexity of the surface manufacture [13–20].

At the same time, within the past few years, the study of thermal systems has been also focused on the development of alternative fuels [21,22], such as gasified biomass. As the calorific value of syngas from gasified biomass is lower than the natural gas calorific value, it changes the performance and the behavior of the gas turbine significantly. Some of these changes are related to the small increase in the flow of exhaust gases as well as to the change in their chemical composition and a large reduction in compressor air flow. This influences the dimensional design and, consequently, the cost of the recuperators for microturbines.

The aim of this work is to assess the thermal performance, the size, and the cost of the recuperator of a 600 kW regenerative gas turbine engine when designed for syngas and natural gas. Two different types of surfaces, cross-corrugated and undulated-corrugated, are used for analysis. The results are shown, comparing heat-transfer coefficient, effectiveness, pressure loss, size, and cost for syngas and natural gas.

2 Cycle Simulation

In the regenerative cycle the preheating of air before it enters the combustion chamber is carried out by absorbing the heat of the exhaust gases of the turbine. The regenerative cycle differs from the simple cycle because of the inclusion of an extra component: the heat exchanger. Figure 3 presents the arrangement of the gas turbine in a regenerative cycle. Between stages 2 and 3 the air is preheated by using the heat of the exhaust gases represented by stages 5 and 6. This way, the fuel consumption can be reduced and the same temperature can be attained at the turbine inlet and, consequently, the same power outlet. The main purpose is to increase the efficiency of the cycle.

This study was performed using the GATECYCLE GE enter software to simulate the single shaft regenerative cycle in a 600 kW microturbine using natural gas and syngas as fuels for design point only. This program can simulate any existing or new thermal power plant (or cogeneration system), at design point or off design point. The design input parameters used in the GATECYCLE simulation for both fuels are shown in Table 1 [23]. The parameter values selected in Table 1 were based on the current technologies for radial turbomachineries. The turbine inlet temperature (TIT) of 850°C was selected because it is the maximum temperature the material of the radial turbine can support, maintaining the mechanical resistance and the useful life without any blade cooling.

Through the simulations carried out by the GATECYCLE the design point conditions attained for the microturbine recuperator are presented in Table 2.

The chemical composition of the fuels is in Table 3.

Downloaded 02 Jun 2010 to 171.66.16.96. Redistribution subject to ASME license or copyright; see http://www.asme.org/terms/Terms_Use.cfm

Table 1 Design point input parameters

Descrição	Valores	Unidade
Ambient temperature	288	K
Ambient pressure	101.32	kPa
Turbine inlet temperature	1123	K
Temperature of fuel	288	K
Pressure ratio	4	-
Compressor adiabatic efficiency	80	%
Combustion adiabatic efficiency	99	%
Turbine efficiency	85	%
Mechanical efficiency	98	%
Recuperator effectiveness	92	%
Combustion chamber pressure loss	2	%
Recuperator pressure loss (air)	3	%
Recuperator pressure loss (gas)	4	kPa
Air humidity	60	%
Gas turbine power output	600	kW

By analyzing the reactions that take place in the combustion chamber it is possible to attain the chemical composition of the exhaust gases, as well as their molar fractions, as it is shown in Table 4. This way, it is possible to attain the physical properties of the exhaust gases that will be used in the dimensional and thermal calculations of the recuperator.

3 Regenerator Design

This study developed a calculation method implemented in a FORTRAN language program to calculate the dimensions of the recuperator for the 600 kW microturbine. This calculation method was validated using the results published by Utriainen and Sundén [3]. Such program uses the effectiveness/number of transfer units (NUT) method to calculate the dimensions of the recuperator and the correlations derived from Ref. [3] to calculate the heat-transfer convective coefficients and the Fanning friction factor for the cross-corrugated and cross-undulated surfaces. These correlations are used to calculate the Nusselt number and the Fanning friction factor for the air side ($\mathrm{Nu}_{\mathrm{air}}, f_{\mathrm{air}}$) and for the gas side ($\mathrm{Nu}_{\mathrm{gas}}, f_{\mathrm{gas}}$). In these correlations the Re is the Reynolds number for the air side or for the gas side, depending on what side of the recuperator was calculated. These correlations are shown as follows:

Table 2 Recuperator design point conditions

	Natural gas	Syngas	Units
Recuperator air inlet temperature	461.4	461.4	K
Recuperator air outlet temperature	817.1	822.9	K
Recuperator gas inlet temperature	855.0	861.4	K
Recuperator gas outlet temperature	511.6	555.6	K
Air flow	4.6	3.846	kg/s
Gas flow	4.63	4.41	kg/s
Air inlet pressure	405.3	401.2	kPa
Gas outlet pressure	101.3	101.3	kPa
Fuel flow	0.04	0.564	kg/s

Table 3 Fuel compositions

Components	Natural gas	Syngas
CH_4 (%)	87.59	5.6
C_2H_6 (%)	9.13	-
C_3H_8 (%)	0.36	-
N_2 (%)	1.18	56.4
H_2 (%)	-	4
CO (%)	-	14
CO_2 (%)	1.74	20
PCI (MJ/N m^3)	35.6	3.8

Table 4 Molar fractions of exhaust gases

Components	Natural gas	Syngas
O_2	0.17999	0.15707
CO_2	0.01451	0.05314
H_2O	0.02742	0.02195
Ar	0.00926	0.00824
N_2	0.76883	0.75959

Table 5 Coefficients of the correlations

Surfaces	$C1$	$C2$	$C3$	$C4$
CC2.2-60	6.2884	0.1648×10^{-1}	28.3023	0.3952×10^{-1}
UCS-30	6.7538	0.1155×10^{-2}	37.0463	0.1392×10^{-1}

$$\mathrm{Nu} = C1 + C2\ \mathrm{Re} \tag{1}$$

$$f\ \mathrm{Re} = C3 + C4\ \mathrm{Re} \tag{2}$$

Table 5 shows the coefficients used in correlations (1) and (2) for Re smaller than 2000.

In Table 5 the names of surface mean that CC2.2-60 is a surface of type cross-corrugated, which has a corrugation angle of 60 deg, while UCS-30 is a surface of type corrugated-undulated, which presents a corrugation angle of 30 deg.

The simplified algorithm of the program developed for the calculation of the dimensions of the recuperator matrix is presented below. For the algorithm the Reynolds number is fixed and the velocity is constant because the hydraulic diameter is a fixed value.

(1) The dimensions of the unitary cell must be known.
(2) Calculating the physical properties of the air and of the gas in the medium temperature.
(3) Calculating the total heat transferred in the matrix

$$Q = \varepsilon \cdot (\dot{m} \cdot c_p)_{\min}(\mathrm{Te}_{\mathrm{gas}} - \mathrm{Te}_{\mathrm{air}})$$

(4) Calculating the air side velocity

$$W_{\mathrm{air}} = \frac{\mathrm{Re}_{\mathrm{air}}\ \nu_{\mathrm{air}}}{D_{h_{\mathrm{air}}}}$$

(5) Calculating the gas side velocity

$$W_{\mathrm{gas}} = W_{\mathrm{air}} \frac{\dot{m}_{\mathrm{gas}} \rho_{\mathrm{air}} A_{\mathrm{air}}}{\dot{m}_{\mathrm{air}} \rho_{\mathrm{gas}} A_{\mathrm{gas}}}$$

(6) Calculating the Nusselt numbers and the friction factors, for both sides, through correlations (1) and (2).
(7) Calculating the heat-transfer coefficient on both sides.
(8) Calculating the overall heat-transfer coefficient

$$U = 1 \bigg/ \left(\frac{1}{h_{\mathrm{air}}} + \frac{1}{h_{\mathrm{gas}}} + \frac{s}{K_w} \right)$$

(9) Calculating the total heat-transfer area

$$A_{\mathrm{tot}} = \frac{Q}{U \Delta T_m}$$

(10) Calculating the matrix porosity

$$\sigma = \frac{V_s}{V}$$

(11) Calculating the compactness

Downloaded 02 Jun 2010 to 171.66.16.96. Redistribution subject to ASME license or copyright; see http://www.asme.org/terms/Terms_Use.cfm

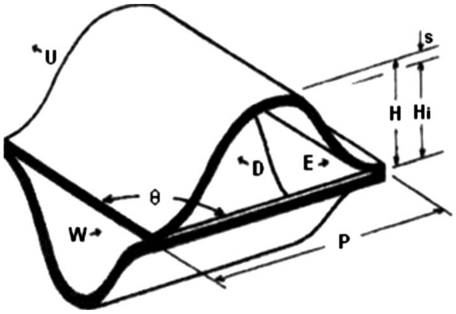

Fig. 4 Unitary cell (perspective view)

$$C=\frac{4\sigma}{D_h}$$

(12) Calculating the recuperator volume

$$V=\frac{A_{\text{tot}}}{C}$$

(13) Calculating the recuperator weight

$$W=\rho_{\text{mat}}Vg$$

(14) Calculating the front area (flow area at the inlet)

$$A_{\text{front}}=A_{\text{air}}+A_{\text{gas}}+A_{\text{metal}}$$

(15) Calculating the length of recuperator matrix

$$L=\frac{V}{A_{\text{front}}}$$

(16) Calculating the pressure losses for both sides

$$\Delta p_{\text{air}}=2f_{\text{air}}\frac{L}{D_{h_{\text{air}}}}\rho_{\text{air}}w^2{}_{\text{air}}$$

$$\Delta p_{\text{gas}}=2f_{\text{gas}}\frac{L}{D_{h_{\text{gas}}}}\rho_{\text{gas}}w^2{}_{\text{gas}}$$

(17) Calculating the total relative pressure losses

$$\bar{\Delta}p_{\text{total}}=\frac{\Delta p_{\text{air}}}{p_{\text{air}}}+\frac{\Delta p_{\text{gas}}}{p_{\text{gas}}}$$

This study calculates the thermal performance, the size, and the cost of the recuperator matrix of a 600 kW microturbine using cross-corrugated and cross-undulated surfaces, shown in Figs. 1 and 2. According to previous comments these surfaces are extremely compact (with a compactness over 1000 m^2/m^3), allowing the recuperator matrix to have a high rate of heat transfer in a small volume.

The matrix of the recuperator that is built with these surfaces is a package of closely packed plates with bearing sine-wave corrugations that delimit open flow passages, which intersect one another at an angle θ. This way, a complex flow and temperature field is established, resulting in an increase in heat-transfer rates compared to low pressure drops.

Considering the repeating geometric characteristics of these surfaces, the matrix of the recuperator will be formed by a significantly large number of identical and small geometric elements called unitary cells. The scheme of a unitary cell of a cross-corrugated surface is shown in Fig. 4. This cell has two inputs (W and D) and two outputs (U and E), and its geometry is completely specified by parameters p (pitch), h (external height), s (wall thickness), and θ (corrugation angle); all of them indicated in Fig. 4. Other units can also be derived from these parameters.

Table 6 Geometrical data surfaces

Surface	P (mm)	H_i (mm)	H (mm)	θ (deg)
CC2.2-60	2.36	1.07	1.15	60
UCS-30	2.24 and 3.17	1.30 and 0.79	1.38 and 3.96	30

In the present study, two surfaces, one cross-corrugated and one cross–undulated, are used for assessing the thermal performance, the size, and the cost of the recuperator. The geometric characteristics of these surfaces are presented in Table 6. The metal sheet thickness is 0.08 mm.

4 Design Assessment

4.1 Pressure Drop Analysis. Figures 5(*a*) and 5(*b*) show the total relative pressure losses in the recuperator matrix when natural gas and syngas are used as fuels for two surfaces.

The variation in the type of fuel influences the quantity of air and exhaust gas and the chemical characteristics of the exhaust gases that go through the recuperator. Consequently, the total relative pressure losses in the recuperator matrix are also influenced. Figures 5(*a*) and 5(*b*) show that the pressure drop of recuperator matrix decreases when the exhaust gases are derived from the combustion of the syngas, in relation to natural gas for both surfaces. This takes place because the turbine mass flow and turbine inlet temperature do not change. Therefore, the use of syngas, which presents a low heat value (LHV) much lower than the natural gas, leads to the necessity to insert more fuel in the chamber, and, because of that, the amount of air used in the combustion chamber is reduced. This way, the air flow that will pass through the air side of the recuperator is reduced much more than the gas side, as it is shown in Table 2, causing the dimensions of the required recuperator to be smaller, which is confirmed in Fig. 7. Consequently, the pressure drop in the core of recuperator is also smaller.

The flow velocities in the core of the recuperator cannot be high because the corrugations of plates lead to a high pressure drop if the flow presents high velocities. Also, the geometry of corrugated plates is very small, as it is shown in Table 6, which leads to a low flow velocity. For these reasons, the Reynolds number in this type of heat exchanger must be low, characterizing a laminar draining flow.

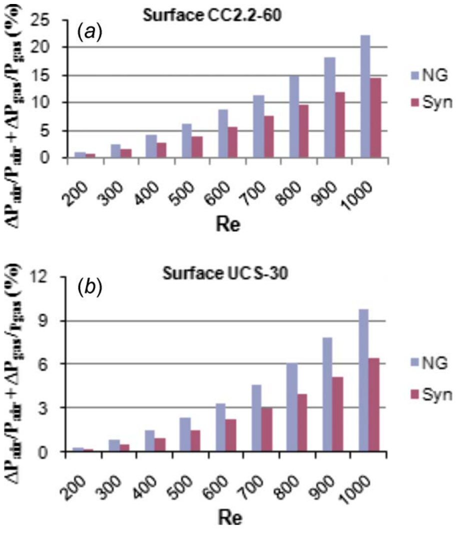

Fig. 5 Total relative pressure drop

Downloaded 02 Jun 2010 to 171.66.16.96. Redistribution subject to ASME license or copyright; see http://www.asme.org/terms/Terms_Use.cfm

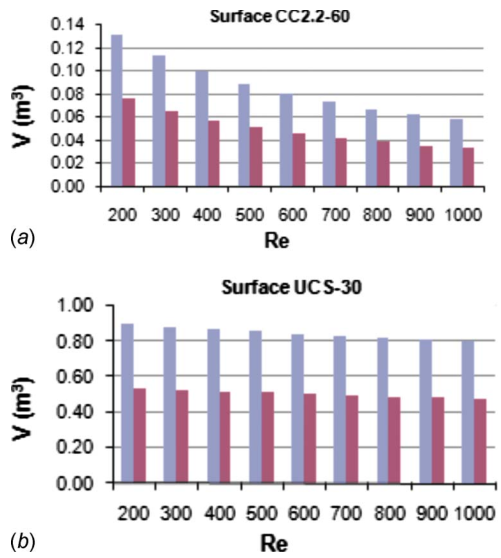

Fig. 6 Matrix volume

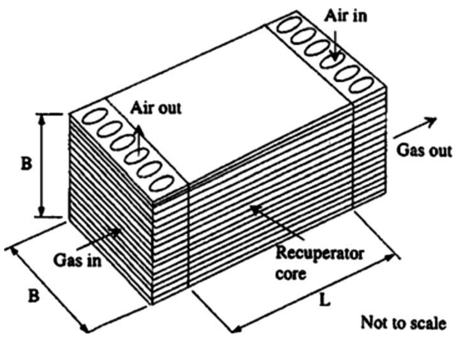

Fig. 7 Cube-shaped recuperator concept [3]

The total relative pressure losses must not surpass a limit of 4%, for higher losses do not justify the insertion of this equipment in the microturbine cycle. Taking this limit into account Fig. 5 shows that by using natural gas as fuel, the Reynolds number must not exceed and must be lower than 500 for a CC2.2-60 surface and must be lower than 700 for a UCS-30 surface. In the same way, it is possible to notice that by using syngas the Reynolds number must be lower than 600 for the C2.2-60 surface and must not exceed 800 for a UCS-30 surface.

It is possible to observe that the use of syngas leads to a reduction in the overall load loss in the studied surfaces. This difference is kept practically constant as the Reynolds number gets higher, ranging about 33% and 35% for the CC2.2-60 and UCS-30 surfaces, respectively.

4.2 Recuperator Size Analysis. The variation in the type of fuel influences the size of recuperator too. Figures 6(*a*) and 6(*b*) show the volume of the recuperator matrix when natural gas and syngas are used as fuels for two surfaces.

The reduction in the pressure drop leads to a reduction in the volume of the matrix, which can be confirmed in Fig. 6. This reduction takes place because, with a smaller loss, the length of the draining of the fluids is reduced, leading to a smaller volume. This observation is very important toward the design of the recuperators, given that the reduction in the load loss allows the attainment of a more compact recuperator. The studied cases showed that these reductions in volume are significant, because, when the natural gas is replaced with syngas as the fuel of the microturbine, the pressure drop is reduced about 33% and 35% for CC2.2-60 and UCS-30 surfaces, respectively, while the reduction in the volume of the matrix ranges about 40% for both surfaces. One can notice that the variation of the volume as the Reynolds number gets higher is more significant when using the CC2.2-60 surface for both fuels. The matrix volume keeps almost constant as the Reynolds number gets higher when the UCS-30 is used.

The reduction in matrix recuperator volume is reflected in its size. Using the design of a recuperator corresponding to the cube shaped recuperator configuration (Fig. 7), the length and the width of matrix were calculated.

Figure 8 shows the results of the length and the width of matrix for a CC2.2-60 surface using the studied fuels.

Figure 9 shows the results of the length and the width of matrix for UCS-30 surface using the studied fuels.

The results show the reduction in both dimensions when natural gas is replaced with syngas as the fuel of the microturbine. However, the variation is more significant in the length of matrix. For the analyzed surfaces, a reduction of about 30% in length matches to a reduction of about 9% in width. Analyzing the variation of size as the Reynolds number increases, it is possible to notice that

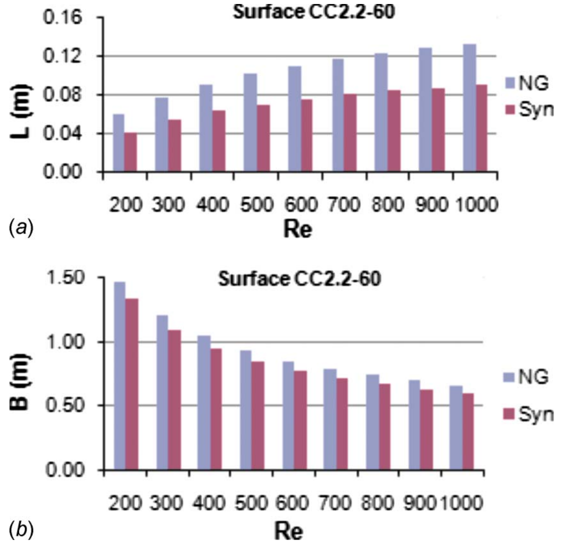

Fig. 8 Recuperator size using the CC2.2–60 surface: (*a*) length and (*b*) width

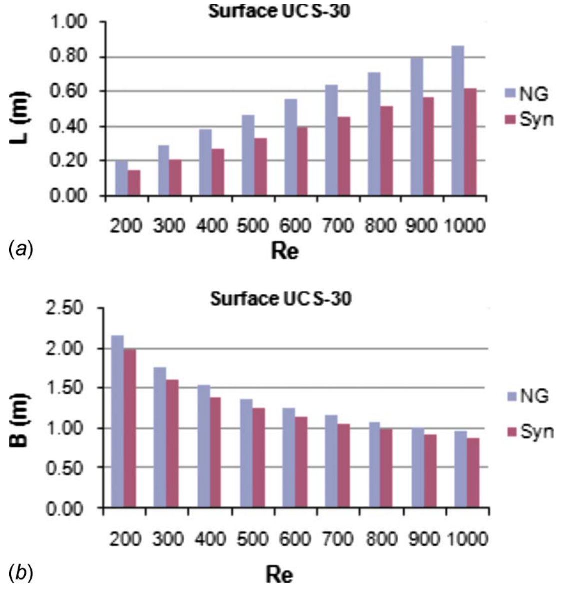

Fig. 9 Recuperator size using the UCS–30 surface: : (*a*) length and (*b*) width

Downloaded 02 Jun 2010 to 171.66.16.96. Redistribution subject to ASME license or copyright; see http://www.asme.org/terms/Terms_Use.cfm

Table 7 Recuperator cost

	347 stainless	Inconel 625	Haynes 230	Haynes 214
Metal cost ($/kg)	12	60	84	108
Fabrication cost ($/kg)	18	90	126	162
Total cost ($/kg)	30	150	210	270

the length increases, whereas the width gets smaller. This takes place because the increase in the Reynolds number leads to a rise in the flow velocity. Since the fluid flow is kept constant, the frontal area is reduced and, consequently, the length increases.

One can also notice the small length of the matrix in the analyzed cases. It is important for this dimension to be small, given that the pressure drop must be small.

In spite of the small dimensions of matrix, the total heat-transfer area is big because of the corrugations of the plates.

4.3 Recuperator Cost Analysis. In relation to the recuperator cost, it is possible to consider the volume and the weight as its indicators. McDonald [12] suggested that the cost of a recuperator matrix is a multiple of the material cost, and the fabrication cost is 1.5 times the material cost.

In addition, the compact recuperators with corrugated plates have characteristics such as good reliability, high thermal performance, compact size, low weight, adjustment capacity to automate, and high producing manufacturing methods. Thus, the matrix that presents the smallest volume and weight will probably contribute toward the design of a cheaper recuperator. On the other hand, the economic gain coming from designing a highly compact recuperator must be balanced with the pressure loss in the matrix, which influences the cycle overall efficiency and, consequently, the fuel consumption. That is the reason why the compactness of the recuperator (smaller volume and weight) will lead to a reduction until the limit of the load loss that was previously established.

McDonald [12] provided information about microturbine recuperator matrix cost (not including pipes, casings, and manifolds) for several candidate recuperator materials. Some of these materials are 347 stainless steel, Inconel 625, Haynes 230, and Haynes 214, presented in ascending order of resistance to high temperature and cost.

Table 7 presents the cost of recuperator matrix for the materials considered. For production of recuperators in very large quantities a factor of 1.5 times the material cost for the complete matrix has been suggested [12].

With the weight of recuperator matrix shown in Figs. 10(*a*) and 10(*b*), it is possible to estimate the cost of recuperator matrix built with the considered materials.

Figures 11 and 12 present a comparison between these costs for both studied cases, with Re=500, and indicate that the use of syngas causes the reduction in the recuperator cost for two of the studied surfaces.

Considering that turbine mass flow and turbine inlet temperature do not change and considering the recuperator input conditions, presented in Table 2, the results show that burning the syngas in the microturbine allows the recuperator dimensions to be smaller and, consequently, the cost is lower as well. This way, from a recuperator designing the point of view, using syngas as fuel presents more advantages.

4.4 Heat Performance Analysis. A comparison of the overall heat-transfer coefficient obtained at the conditions used in this study is presented in Figs. 13(*a*) and 13(*b*).

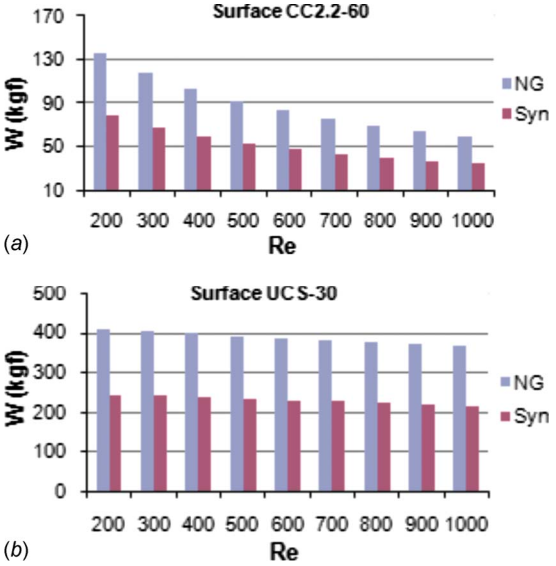

Fig. 10 Matrix recuperator weight

It is possible to notice that the variation in the type of fuel influences this thermal parameter. The use of syngas leads to an increase in the overall heat-transfer coefficient for two surfaces. However, this increase is not considerably significant, lying about 5% for the CC2.2-60 surface and 2% for the UCS-30 surface.

One can also notice that the values of the overall heat-transfer coefficient for two of the analyzed surfaces are very different. For the CC2.2-60 surface the values come close to 500 W/m^2 K, whereas for the UCS-30 surface the values do not exceed 75 W/m^2 K. Such differences occur because the compactness of the CC2.2-60 surface is much higher than the compactness of the UCS-30 surface, which leads the CC2.2-60 surface to have a total heat-transfer area much higher than the UCS-30 surface.

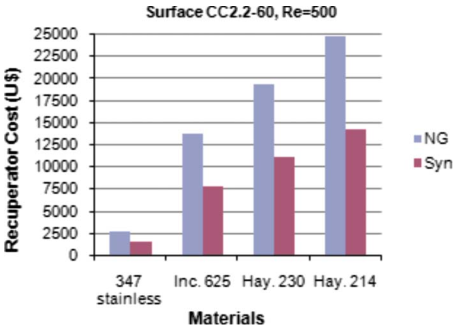

Fig. 11 Recuperator cost for CC2.2-60

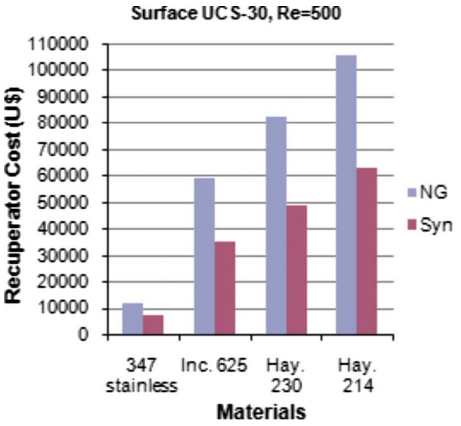

Fig. 12 Recuperator cost for UCS-30 surface

Downloaded 02 Jun 2010 to 171.66.16.96. Redistribution subject to ASME license or copyright; see http://www.asme.org/terms/Terms_Use.cfm

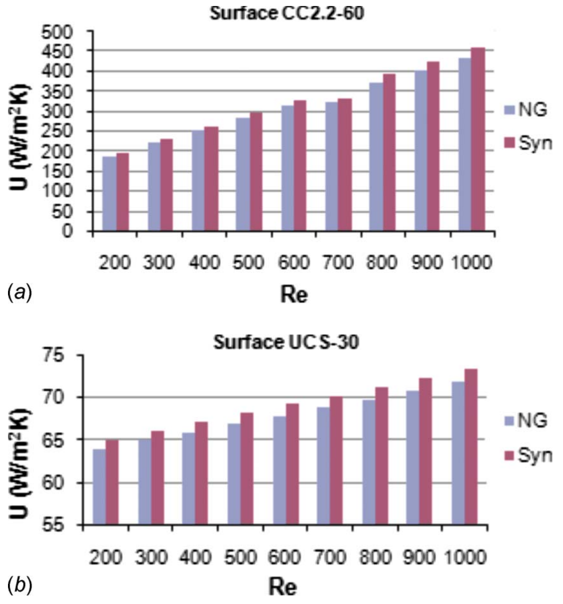

Fig. 13 Overall heat-transfer coefficient

4.5 Surface Analysis. By analyzing the studied surfaces, it is possible to notice that the cross-corrugated surface (CC2.2-60) presents higher compactness (the smallest volume and weight), suggesting a higher capacity of heat transfer and cost reduction, while the cross-undulated surface (UCS-30) showed themselves as less compact, likely to have higher costs. Besides, one must consider that the matrix with a cross-undulated surface is formed by two different surfaces, which leads to difficulties regarding their manufacture, therefore, elevating their cost.

Hence, it is possible to say, based on the analyses that were carried out, that it is possible to attain a good recuperator matrix design for a 600 kW microturbine, using syngas as fuel and cross-corrugated surfaces.

5 Conclusions

This study carried out an assessment regarding the thermal performance, the size, and the cost of the recuperator of a 600 kW regenerative gas turbine engine designed for syngas and natural gas. Two different types of surfaces, cross-corrugated and undulated-corrugated ones, were used for the analysis. The comparison of the pressure drop, size, cost, and overall heat-transfer coefficient was performed.

The results showed that the use of syngas leads to a reduction in the overall relative pressure losses in the studied surfaces. This difference is kept practically constant as the Reynolds number increases, ranging about 33% and 35% for the CC2.2-60 and UCS-30 surfaces, respectively. But the volume of the matrix has a reduction of about 40% for both surfaces.

Considering the recuperator input conditions and that turbine mass flow and turbine inlet temperature do not change, the results show that burning syngas in the microturbine allows the recuperator dimensions to be smaller and, consequently, the cost is lower as well. This way, from a recuperator designing the point of view, using syngas as fuel presents more advantages.

A comparison between the overall heat-transfer coefficients obtained at the conditions used in this study showed that the use of syngas leads to a rise in this parameter.

The studied surfaces analysis has shown that, the Cross Corrugated surface (CC2.2-60) presents a higher compactness (the smallest volume and weight) and consequently, a reduction cost. Therefore, this surface has a great potential for use in compact recuperators of gas microturbines.

Hence, the results showed that the use of syngas as fuel and of Cross Corrugated surfaces allows a good design of recuperator matrix for a 600 kW microturbine.

Despite the analysis in this paper was carried out for a recuperator of a 600 kW gas turbine engine it is applied for all sizes of regenerative gas turbine engine.

Acknowledgment

The authors wish to thank CAPES for financial support.

Nomenclature

A_{air} = inlet flow area for air (m^3)
A_{front} = total front area (m^3)
A_{gas} = inlet flow area for gas (m^3)
A_{tot} = total heat-transfer area (m^3)
B = width of recuperator (m)
C = compactness (m^2/m^3)
c_p = specific heat (J/kg K)
$C1$, $C2$, $C3$, and $C4$ = coefficients of correlations
Dh = hydraulic diameter (mm)
ε = effectiveness (%)
f = Fanning friction factor
g = acceleration of gravity (m/s^2)
h_{air} = air heat-transfer coefficient ($\text{W/m}^2\text{ K}$)
H_i = internal height (mm)
h_{gas} = gas heat-transfer coefficient
K = thermal conductivity (W/m K)
K_w = thermal conductivity of material
L = length of recuperator matrix (m)
$\dot{m}$ = mass flow rate (kg/s)
Nu = Nusselt number
P_{air} = pressure on the air side (kPa)
P_{gas} = pressure on the gas side (kPa)
Q = total heat transferred (kW)
Re = Reynolds number
$T_{e\text{air}}$ = recuperator air inlet temperature (K)
$T_{e\text{gas}}$ = recuperator gas inlet temperature (K)
$T_{s\text{ar}}$ = recuperator air outlet temperature (K)
$T_{s\text{gas}}$ = recuperator gas outlet temperature. (K)
U = overall heat-transfer coefficient ($\text{W/m}^2\text{ K}$)
W = weight of matrix (kg)
W_{air} = air velocity (m/s)
ΔP_{air} = pressure loss on the air side (kPa)
ΔP_{gas} = pressure loss on the gas side (kPa)
ΔP_{tot} = total relative pressure loss (%)
θ = included angle between corrugations (deg)
σ = porosity of matrix

References

[1] Traverso, A., and Massardo, A. F., 2005, "Optimal Design of Compact Recuperators for Microturbine Application," Appl. Therm. Eng., **25**, pp. 2054–2071.

[2] McDonald, C. F., 2000, "Low-Cost Compact Primary Surface Recuperator Concept for Microturbines," Appl. Therm. Eng., **20**, pp. 471–497.

[3] Utriainen, E., and Sundén, B., 2002, "Evaluation of the Cross Corrugated and Some Other Candidate Heat Transfer Surfaces for Microturbine Recuperators," ASME J. Eng. Gas Turbines Power, **124**, pp. 550–560.

[4] Savostin, A. F., and Tikhonov, A. M., 1970, "Investigation of the Characteristics of Plate-Type Heating Surfaces," Teploenergetika (Moscow, Russ. Fed.), **17**(9), pp. 75–78.

[5] Stasiek, J. A., 1998, "Experimental Studies of Heat Transfer and Fluid Flow Across Corrugated-Undulated Heat Exchanger Surfaces," Int. J. Heat Mass Transfer, **41**(6–7), pp. 899–914.

[6] Ciofalo, M., Collins, M. W., and Stasiek, J. A., 1998, "Flow and Heat Transfer Predictions in Flow Passages of Air Preheaters: Assessment of Alternative Modeling Approaches," *Computer Simulations in Compact Heat Exchangers*,

Downloaded 02 Jun 2010 to 171.66.16.96. Redistribution subject to ASME license or copyright; see http://www.asme.org/terms/Terms_Use.cfm

B. Sundén and M. Faghri, eds., Computational Mechanics Publications.

[7] Ciofalo, M., and Stasiek, J. A., 1996, “Investigation of Flow and Heat Transfer in Corrugated Passages-II. Numerical Simulations,” Int. J. Heat Mass Transfer, **39**(1), pp. 165–192.

[8] Stasiek, J. A., Collins, M. W., Ciofalo, M., and Chew, P. E., 1996, “Investigation of Flow and Heat Transfer in Corrugated Passages-I. Experimental Results,” Int. J. Heat Mass Transfer, **39**(1), pp. 149–164.

[9] Micheli, D., Pediroda, V., and Pieri, S., 2007, “Multi-Objective Optimization of a Microturbine Compact Recuperator,” ASME Paper No. GT2007-27636.

[10] Liang, H. X., Xie, G. N., Wang, Q. M., Luo, L. Q., and Feng, Z. P., 2006, “Genetic Algorithm Optimization for Primary Surfaces Recuperator of Microturbine,” ASME Paper No. GT2006-90366.

[11] Shah, R. K., 2005, “Compact Heat Exchangers for Microturbines,” *Micro Gas Turbines*, pp. 2-1–2-18.

[12] McDonald, C. F., 2003, “Recuperator Considerations for Future Higher Efficiency Microturbines,” Appl. Therm. Eng., **23**, pp. 1463–1487.

[13] Rakowski, J. M., and Stinner, C. P., 2004, “The Use and Performance of Oxidation and Creep-Resistant Stainless Steels in an Exhaust Gas Primary Surface Recuperator Application,” ASME Paper No. GT2007-53917.

[14] Lara-Curzio, E., Trejo, R., More, K. L., Maziasz, P. A., and Pint, B. A., 2004, “Screening and Evaluation of Materials for Microturbine Recuperators,” ASME Paper No. GT2004-54254.

[15] Pint, B., 2005, “The Effect of Water Vapor on Cr Depletion in Advanced Recuperator Alloys,” ASME Paper No. GT2005-68495.

[16] Maziasz, P. J., Shingledecker, J. P., Pint, B. A., Evans, N. D., Yamamoto, Y., More, K., and Lara-Curzio, E., 2005, “Overview of Creep Strength and Oxidation of Heat-Resistant Alloy Sheets and Foils for Compact Heat-Exchangers,” ASME Paper No. GT2005-68927.

[17] Pint, B. A., More, R. L., Trejo, R., and Lara-Curzio, E., 2006, “Comparison of Recuperator Alloy Degradation in Laboratory and Engine Testing,” ASME Paper No. GT2006-90194.

[18] Maziasz, P. J., Pint, B. A., and Shingledecker, J. P., 2004, “Austenitic Stainless Steels and Alloys With Improved High-Temperature Performance for Advanced Microturbine Recuperators,” ASME Paper No. GT2004-54239.

[19] McDonald, C. F., 1997, “Ceramic Heat Exchangers=The Key to High Efficiency in Very Small Gas Turbines,” ASME Paper No. GT1997-463.

[20] Wilson, D. G., 2007, “Investigation Into the Use of Ceramic-Honeycomb Rotary Regenerators for Solar Brayton Cycles,” ASME Paper No. GT2007-27216.

[21] Karellas, S., Karl, J., and Kakaras, E., 2008, “An Innovative Biomass Gasification Process and Its Coupling With Microturbine and Fuel Cell Systems,” Energy, **33**(2), pp. 284–291.

[22] Williams, D. W., 2001, “Microturbine Operation With Biogas From a Covered Dairy Manure Lagoon,” ASAE Meeting Presentation, Paper No. 01-6154.

[23] Nascimento, M. A. R., Osvaldo, J. V., Lora, E. S., Sierra, G. A., Rodrigues, L. O., Carvalho, H. M., and Moura, N. R., 2008, “Cycle Selection and Compressor Design of 600 kW Simple Cycle Gas Turbine Engine,” *Proceedings of the TURBOEXPO 2008, ASME Turbo Expo 2008*, Berlin, Germany, Jun. 9–13.

Downloaded 02 Jun 2010 to 171.66.16.96. Redistribution subject to ASME license or copyright; see http://www.asme.org/terms/Terms_Use.cfm

Experimental Evaluation of the Transient Behavior of a Compressor Station During Emergency Shutdowns

J. Jeffrey Moore
Southwest Research Institute,
San Antonio, TX 78238

Rainer Kurz
Solar Turbines Incorporated,
San Diego, CA 92123

Augusto Garcia-Hernandez

Klaus Brun

Southwest Research Institute,
San Antonio, TX 78238

The transient behavior of compressor stations, particularly under rapidly changing conditions, is of vital interest to operators. Predicting transient behavior is an important factor in avoiding damage during events such as emergency shutdowns. A limited number of "accidental" data sets from compressor manufacturers and users are available in the public literature domain. A variety of simulations and modeling approaches have been presented over the last few years at industry conferences. The available experimental data is not of sufficient quality and resolution to properly compare predictions with analytical results or simulations available in current software packages. Necessary information about the compressor, driver, valves, and geometry of the system is often missing. Currently utilized software has not been adequately validated with full-scale realistic benchmark data, as this data is not available in the public domain. Modeling procedures and results of surge control system simulations seldom contain validation data achieved through actual testing. This type of transient test data for a dynamic surge condition is often difficult to obtain. The primary objective of this work is to develop experimental transient compressor surge data on a full-scale test facility, which would facilitate the verification and comparison of existing and future transient surge models. Results of the testing and model comparisons will be documented. Relevant, dimensionless parameters will be presented and validated utilizing the test data. Conclusions from the testing and recommendations for the transient analysis software will be provided.

[DOI: 10.1115/1.4000093]

1 Introduction

The possible operating points of a centrifugal gas compressor operated at variable speeds are shown in the head-flow characteristic in Fig. 1. The operating range is limited by maximum and minimum operating speed, maximum available power, choke flow, and stability (surge) limit. At flows lower than the stability point, the compressor initially shows a reduced capability to generate head with reduced flow, until it experiences reverse flow; that is, the gas now flows from the discharge to the suction side. Once flow reversal occurs, the amount of flow depends on the pressure ratio across the compressor, since in this situation, the compressor acts more or less like an orifice. The flow reversal means that the pressure downstream of the compressor is gradually reduced. The speed of pressure reduction depends largely on the size of the volume downstream of the compressor. Once the pressure is reduced sufficiently, the compressor will recover, and gas will flow again from the suction to the discharge side. Unless action is taken, the events will repeat. Ongoing surge can damage thrust bearings (due to the massive change of thrust loads), seals, and eventually, overheat the compressor. Details of the energy transfer from the compressor into the gas are described in Ref. [1].

Surge has to be avoided to protect the compressor. The usual method for surge avoidance ("antisurge control") consists of one or several recycle loops that can be activated by fast-acting valves ("antisurge valves") when the control system detects that the compressor approaches its surge limit. Typical control systems use suction and discharge pressure and temperature, together with the inlet flow into the compressor, as input to calculate the relative distance ("surge margin") of the present operating point to the predicted or measured surge line of the compressor (Fig. 1). The surge margin (SM) is defined by

$$\mathrm{SM} = \left. \frac{Q_{\mathrm{op}} - Q_{\mathrm{surge}}}{Q_{\mathrm{op}}} \right|_{N=\mathrm{const}} \tag{1}$$

It should be mentioned that the definition of the surge line is somewhat arbitrary, especially due to the fact that it is ultimately a system feature, not an isolated compressor feature. Definitions frequently used to establish this line include a local maximum in the head-flow characteristic, the onset of rotating stall (established usually from vibration signatures or by the use of theoretical criteria), the onset of high vibrations (either broadband or at distinct frequencies), or the point where actual flow reversal is established.

If the surge margin reaches a preset value (often 10%), the antisurge valve (ASV) starts to open, thereby reducing the pressure ratio of the compressor, and increasing the flow through the compressor.

The antisurge control system has to cover the following tasks [2,3].

- Facilitate the starting and normal shutdown process.
- Accommodate slow process changes to prevent process disruption. This requires the capability to precisely control the recycle valve so no oscillations occur, which can be accomplished with precisely positioned valves.
- Accommodate fast process changes and massive system disturbances (for example, during emergency shutdowns). This requires fast system reaction and, among other things, extremely fast-opening valves with sufficiently large flow areas.

Contributed by the International Gas Turbine Institute of ASME for publication in the Journal of Engineering for Gas Turbines and Power. Manuscript received March 19, 2009; final manuscript received August 13, 2009; published online March 16, 2010. Editor: Dilip R. Ballal.

Copyright © 2010 by ASME

Downloaded 02 Jun 2010 to 171.66.16.96. Redistribution subject to ASME license or copyright; see http://www.asme.org/terms/Terms_Use.cfm

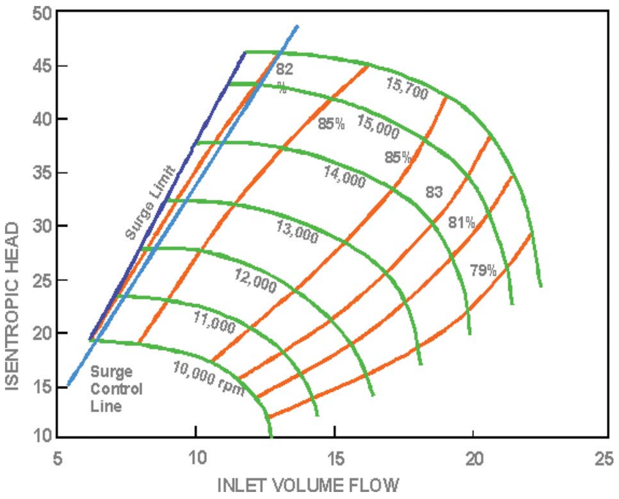

Fig. 1 Typical map of a variable speed centrifugal compressor

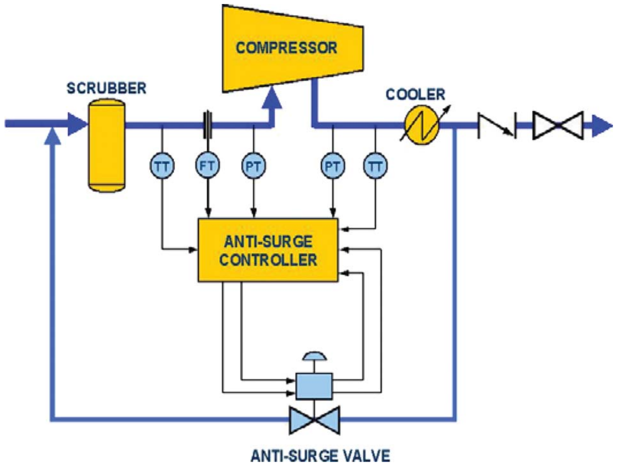

Fig. 2 Surge avoidance system schematic

Emergency shutdowns (ESD) tax the reaction of the entire system. Here, the fuel supply to the gas turbine driver is cut off instantly.[1] In electric, motor-driven installations, the ESD is initiated by tripping the motor. In either case, the compressor train will decelerate rapidly under the influence of the fluid forces counteracted by the inertia of the rotor system. Because the head-making capability of the compressor is reduced by the square of its running speed, while the pressure ratio across the machine is imposed by the upstream and downstream piping system, the compressor would surge if the surge valve could not provide fast relief of the discharge pressure. A 30% loss in speed, which is very common in ESD scenarios [3,4], equates to a loss in head of approximately 50%. Therefore, the valve must reduce the pressure across the compressor by about half in the same time, as the compressor loses 30% of its speed.

The rate at which the discharge pressure can be relieved not only depends on the reaction time of the valve, but also on the time constraints imposed by the piping system. The transient behavior of the piping system depends largely on the volumes of gas enclosed by the various components of the piping system. Besides the piping itself, this may include various scrubbers, knockout drums, and coolers (Fig. 2).

The larger the volumes are in the system, the longer it will take to equalize the pressures. Obviously, the larger the valve, the better is its potential to avoid surge. However, the larger the valve, the poorer is its controllability at partial recycle, and the slower the opening time. The faster the valve can be opened, the more flow can pass through it, especially in the first few critical seconds following an ESD. There are, however, limits to the valve opening speed, dictated by the need to control intermediate positions of the valve and by practical limits to the power of the actuator. The situation may be improved by using a valve that is only boosted to open, thus combining high opening speed for surge avoidance with the capability to avoid oscillations by slow closing.

If the discharge volume is too large, and the recycle valve cannot be designed to avoid surge, a short recycle loop (hot recycle valve) may be considered where the recycle loop does not include the aftercooler.

Other authors have successfully developed transient surge models, which predict the behavior of the compression systems during an ESD [5,6]. However, correlations are made to laboratory-scale compression systems. This paper presents results and predictions for a full-scale natural gas centrifugal compressor that is fully instrumented to provide both accuracy and realism. The data generated will be used to validate the prediction, and parametric studies will be performed to establish the sensitivity of key parameters.

2 Modeling the Piping Surge Control Interaction

The design of the piping and valves, together with the selection and the placement of instruments, will significantly affect the performance of an antisurge control system. This is a major issue during the planning stage, because the correction of design flaws can be very costly once the equipment is in operation. A typical configuration for a recycle system is outlined in Fig. 2.

In its simplest form, the system includes a flow-measuring element in the compressor suction, instruments to measure pressures and temperatures at suction and discharge, the compressor, an aftercooler, a discharge check valve, and a recycle line with a control valve, which is connected upstream of the discharge check valve and compressor flow-measuring device.

The control system monitors the compressor operating parameters, compares them to the surge limit, and opens the recycle valve, as necessary, to maintain the flow through the compressor at a desired margin from the surge. In the event of an ESD, where the fuel to the gas turbine or the power to the motor is shut off instantly, the surge valve should open immediately essentially, at the same time the fuel valve is closing.

For any simulation of the transient behavior of the system, the following features of the system have to be known.

- The geometry of the piping system, in particular, the volumes of the piping and vessels.
- The opening and closing characteristics of the valves (recycle valves, check valve).
- The inertia of the compressor train.
- The thermal inertia of the driver.
- The compressor performance map.
- Any known delays in the surge control system.

One of the key challenges in ESD simulations is to determine the correct deceleration of the train. The rate of deceleration is determined by the inertia of the train J (referenced to compressor speed (N) for geared trains), any residual power generated by the gas turbine ($P_{\mathrm{GT,resid}}$), the friction losses in the system, and the power absorption of the compressor

$$P = P_{\mathrm{compr}} + P_{\mathrm{frict}} - P_{\mathrm{GT,resid}} = T \cdot N = -J \cdot N \cdot \frac{dN}{dt} \qquad (2)$$

---

[1] Some installations maintain fuel flow to the turbine for 1–2 s while the recycle valve opens. However, this can generate a safety hazard.

Downloaded 02 Jun 2010 to 171.66.16.96. Redistribution subject to ASME license or copyright; see http://www.asme.org/terms/Terms_Use.cfm

$$\frac{dN}{dt} = \frac{P_{\text{compr}}(t) + P_{\text{frict}}(t) - P_{\text{GT,resid}}(t)}{-(2\pi)^2 \cdot J \cdot N(t)} \tag{3}$$

Assuming all operating points of the compressor follow the fan law, the compressor power may be expressed as

$$P_{\text{compr}}(t) = P_o\left(\frac{N}{N_o}\right)^3 \tag{4}$$

where P_o and N_o are the steady-state power and speed at the initial operating point, respectively. Another way to determine the compressor power is to know the instantaneous operating point of the compressor (in terms of head, flow, efficiency, and suction density). But this requires a priori knowledge of the locus on the compressor map during shutdown. Assuming a constant Q/N, while not perfect, gives a reasonable assessment for the compression power. It is usually assumed that the steady-state flow-head-efficiency map of the compressor is still accurate enough to determine the consumed power at any transient operating point during the shutdown process.

Substituting and integrating Eq. (4) into Eq. (3) yields the following expression for the speed decay:

$$N(t) = \frac{JN_o^3}{JN_o^2 + P_o t} \tag{5}$$

The residual power generated by the gas turbine after the fuel valve is closed is very difficult to determine in the absence of test data. Even after the fuel valve is closed, the amount of fuel in the system, as well as the thermal inertia of the gas turbine, yield some residual power output.

3 Test Objectives

This project consists of testing actual fast transient events with a full-scale centrifugal compressor in a number of piping geometries under a varying range of surge conditions using natural gas. The piping configurations and operating conditions for the surge tests are selected to be as representative as possible of actual, common compressor ESD events. The selected test conditions produce nondimensional volume, head, and flow parameters that match the actual conditions in terms of similarity.

The instrumentation used to measure the compressor performance and occurrence of the surge was selected, installed, and calibrated so as to minimize test uncertainty. Transient events were tested from a number of operating conditions and different control system settings. The system data points were selected so that the test data represents typical oil and gas applications (e.g., typical relationships between system inertia and gas forces).

The geometry of the system, as well as the valve and compressor behavior, are well defined. Dynamic data of pressure, flow, temperature, and speed were gathered. The goal of the project is to create a set of highly accurate data from a system with well defined geometry that allows the calibration of transient fluid dynamic codes, thus providing a means of assessing the model accuracy and error ranges. Results are subsequently compared with current surge analysis test software.

4 Test Setup

The tests described in this paper were conducted at the Metering Research Facility (MRF) of the Southwest Research Institute in San Antonio, TX. A gas turbine-driven, centrifugal compressor operates here in a closed loop filled with natural gas (Fig. 3). Figure 4 shows the layout of the test facility, together with the installed instrumentation, and Table 1 shows the list of instrumentation installed. The gas turbine is a 1500 hp (1.1 MW) class two shaft gas turbine that directly drives a single stage centrifugal compressor. The train has a maximum speed of 22,300 rpm. The system allows testing for a number of different operating conditions in the high pressure loop (flow rates of 6–150 MMSCFD (160^*10^3–4000^*10^3 m_N^3/d), pressure range of 200–1050 psi (gauge) (13.8–72.4 bar), and temperature range of 60–90°F (15–32°C). All shutdown sequences were initiated from 202 psi (absolute) to 209 psi (absolute) (13.9–14.4 bar) suction pressure.

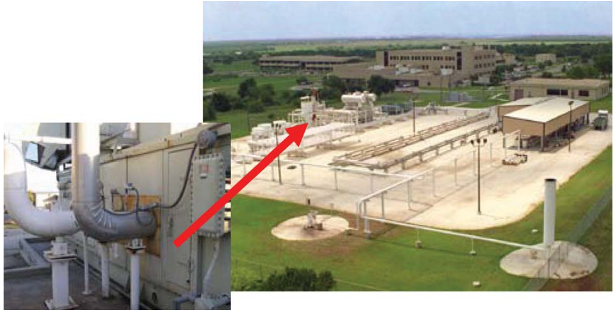

Fig. 3 MRF at SwRI

Although the entire high pressure loop of the MRF was utilized for these tests, the principal component monitored was the C160K centrifugal compressor. This compressor was a single stage centrifugal compressor type C160, with a $7_{1/2}$ inch diameter impeller. The compressor driver was a Solar Saturn 20 2-shaft industrial gas turbine, with a power output of 1150 kW at ISO conditions, directly connected to the centrifugal compressor. The compressor setup included suction and discharge headers, a gas scrubber, aftercooler, isolation valves, vibration monitoring system, and recycle valve.

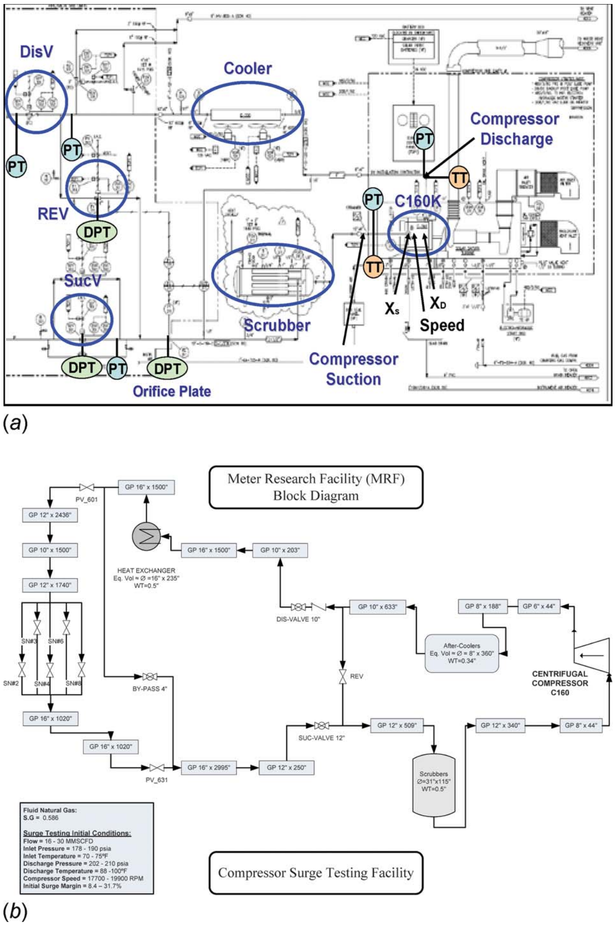

Fluid Natural Gas:
S.G = 0.586

Surge Testing Initial Conditions:
Flow = 16 - 30 MMSCFD
Inlet Pressure = 178 - 190 psia
Inlet Temperature = 70 - 75ºF
Discharge Pressure = 202 - 210 psia
Discharge Temperature = 88 -100ºF
Compressor Speed = 17700 - 19900 RPM
Initial Surge Margin = 8.4 – 31.7%

Fig. 4 Piping and instrumentation diagram for MRF

Downloaded 02 Jun 2010 to 171.66.16.96. Redistribution subject to ASME license or copyright; see http://www.asme.org/terms/Terms_Use.cfm

Table 1 Parameters $\Pi_1-\Pi_4$ for the MRF test setup

Parameter	MRF value (C160K-1E)	C366	Pipeline station 1	Pipeline station 2	Production compressors
Π_1	9,200–12,200	12,000–15,200	1000	1900	3200–3400
Π_2	0.28–0.33	0.23–0.54	3.8	2.3	0.5–0.8
Π_3	0.13–0.16	0.16–0.19	0.02	0.035	0.03–0.04
Π_4	1.5–2.2	0.9–1.9	18.47	7.8	2.5–2.8

The suction header was a 12 in. diameter (schedule 80) pipe connected to an isolating suction valve and to a 31×115 in.^{2} scrubber to finally reach the suction side of the centrifugal compressor. Along its path, the suction header had several taps that were utilized to mount the test instrumentation. From the compressor discharge, an 8 in. diameter pipe is connected to a fin-fan aftercooler. Downstream of this cooler was a recycle loop and a discharge isolation valve. The recycle loop was a small segment of pipe that connected the suction with the discharge header through a control valve. The control valve was part of the surge control system of the machine. This surge control system monitored various parameters such as suction and discharge pressure and flow rate, to control the recycle valve position. All the surge control was accomplished through pneumatic programmable relays. The recycle control valve (REV) was a 6 in. diameter, equal-percentage ($\mathrm{Cv}_{\max}=394\ \mathrm{gpm/psi}^{1/2}=2.99\times10^{-4}\ \mathrm{m}^3/\mathrm{Pa}^{1/2}\ \mathrm{s}$), quick-opening valve that was actuated pneumatically. Its normal position was open. This allowed the possibility of controlling the opening time by adding a valve in the vent of the actuator diaphragm. A general schematic of the compressor setup is presented in Fig. 4, including the locations of the instrumentation used.

This setup allows for transient tests that are intended to collect high fidelity transient data of full-scale ESD (fast stop) of a centrifugal compressor under different initial conditions. The transient data includes static and dynamic pressure (absolute and differential) from different locations, compressor speed, suction and discharge temperatures, and vibration data. The absolute pressure transducers are mounted closely to the piping (Fig. 5), and have a bandwidth (2000 Hz) capable of measuring both the mean (DC) and fluctuating (AC) pressure components. Data acquisition includes the use of a 24-bit A/D high frequency instrument with 16 channels of parallel sampling. In addition, performance tests are conducted to determine the current status of the unit and to obtain its performance curves. The diagram identifies the suction and discharge valves, the recycle valve, the discharge cooler, and the suction scrubber. The test setup includes valves on the suction (Suc *V*) and discharge (Dis *V*) sides of the compressor. These valves will automatically close at the initiation of a shutdown, and travel from fully open to fully closed in 2 s.

Fig. 5 High frequency pressure transducer in discharge pipe

Gas temperature was measured using two thermocouples located at the compressor suction and discharge inside thermowells. Radial shaft vibration data on the compressor were collected from the vibration monitoring system located in the external control panel of the compressor. In addition, two more vibration signals were obtained from vibration probes installed in the unit, resulting in *X-Y* data on both ends. Compressor speed was measured through a magnetic pick-up sensor located on the shaft of the power turbine of the driver. The frequency signal was converted to a voltage signal by using a frequency-to-voltage converter. A linear variable differential transformer (LVDT) was used for measuring linear displacement of the recycle valve, allowing stroke length and travel time of the recycle valve to be measured. In addition, all the instrumentation was calibrated and verified prior to its installation in the MRF.

5 Similarity Considerations

The test setup must allow for conditions that are representative of actual compressor installations to be of value as a benchmark. To evaluate this, certain dimensionless parameters that represent the physics of the emergency shut down process are established:

Deceleration parameter

$$\Pi_1 = \frac{\omega^2 J}{\mathrm{T}} \tag{6}$$

Energy parameter

$$\Pi_2 = \frac{\Delta p V_2}{J\omega^2} \tag{7}$$

Bleed volume parameter

$$\Pi_3 = \frac{t_V \Delta p^{1/2} C_V}{V_2} \tag{8}$$

Time parameter (bleed time deceleration time)

$$\Pi_4 = \frac{t_b}{t_d} = \frac{V_2 T}{\Delta p^{1/2} \omega J C_V} \tag{9}$$

These parameters describe the dynamic behavior of the system in nondimensional terms. In the following table, the parameters established for the test are compared with the parameters of actual installations. The comparison reveals that the available configuration is comparable to actual installations, both for pipeline compressors and production compressors. The purpose of these parameters is not the same as for the parameter established by Botros and Ganesan [6], which is intended to determine whether a system will likely exhibit unstable behavior; that is, whether the recycle valve is sized correctly

$$N_{\mathrm{BG}} = \frac{J \cdot N^2}{W_{\mathrm{surge}} H_{\mathrm{surge}} t_{\mathrm{delay}}} \tag{10}$$

Downloaded 02 Jun 2010 to 171.66.16.96. Redistribution subject to ASME license or copyright; see http://www.asme.org/terms/Terms_Use.cfm

Table 2 Summary of inertia number established by Botros and Ganesan [6] for the MRF compressor facility

Botros and Ganesan inertia number						
Data point	Speed (rpm)	Inertia (kg m^2)	Mass rate at surge (kg/s)	Head at surge (J/kg)	Delay time (s)	Inertia number N_{BG}
MRF No. 1	17,800	0.19	4.49	16,487.1	0.18	50
MRF No. 2	19,800	0.19	4.78	20,532.8	0.18	47

Comparing parameters $\Pi_1 - \Pi_4$ for the MRF installation (Table 1) with a number of actual installations revealed that the test setup is well within the range of actual installations. For comparison purpose, the inertia number, as defined by Botros and Ganesan [6], is shown in Table 2. The value for the MRF falls between 30 and 100, where a detailed simulation is recommended.

6 Test Results

The first set of test data was gathered under steady-state conditions with the purpose of establishing the steady state performance of the compressor at different speeds (Fig. 6). For most simulations, manufacturers' predictions have to be used, but to exclude potential inaccuracies, the compressor was tested. In this particular case, the head-flow characteristics matched the prediction quite well.

The two surge lines in Fig. 6 require some explanation that is rooted in different conventions of setting the surge line of a compressor: The (theoretical) surge line at the right is based on the first horizontal tangent of the head-flow characteristic. It was determined in the previous tests of an identical impeller by the compressor manufacturer and is the setting that is used for production surge control systems. At flows lower than indicated by this surge line, rotating stall can occur. Since this compressor is designed for much higher pressures than encountered during this test, the control system is normally based on this surge line. The surge line to the left is the stability limit for the current installation based on tests. At flows lower than the flow established by this surge line, a surge event (i.e., reversal of flow) was encountered. For this installation, due to the relatively low pressure, aerodynamic forces on the rotor, for example, due to stall events, would be of no consequence to the life of the machine.

With the steady-state performance established, a series of tests to determine the transient performance of the system was performed. The test matrix is outlined in Table 3. The first series of tests involved the initiation of an emergency shutdown with the compressor operating at 17,800 rpm at various surge margins. The second series involved the initiation of emergency shutdowns at a higher speed (19,800 rpm), again with the compressor operating at different surge margins when the emergency shutdown was initiated.

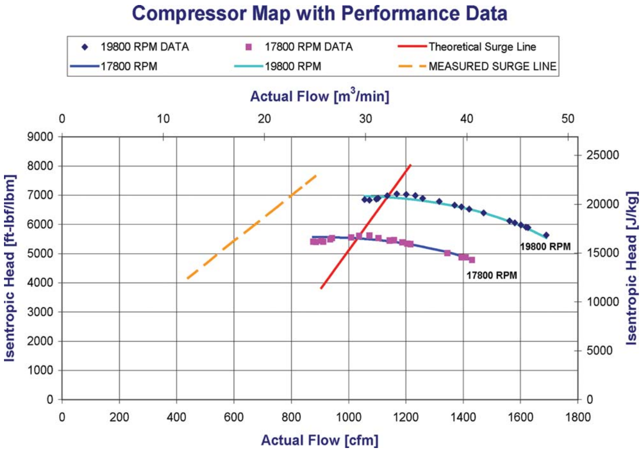

Fig. 6 Steady state compressor head-flow map for two speeds

Figures 7 and 8 show the path (locus) that the compressor followed during each shutdown. The most critical cases occurred when the shutdown was initiated at a low initial surge margin (e.g., transient No. 9 in the 19,800 rpm case). The trace for transient No. 9 in the 19,800 rpm case (Fig. 8) also had markers for significant system events, such as the REV that is starting to open, 35.9% open, and fully open. It showed that the compressor actually operated past its (theoretical) stability line, and reached its lowest flow at 35.9% valve opening. However, due to the system characteristics, no full flow reversal occurred. At this point, the flow through the recycle valve, and thus, the discharge pressure reduction, had become large enough to move the compressor operating point back across the surge line, and into the stable operating region. The minimum flow (600 ACFM) was similar for each speed, but the potential for surge was greater for the higher speed case.

To appreciate the time sequence of the events, Figs. 9–11 provide traces for measured process variables in the time domain for transient No. 9 with 19,800 rpm case, as outlined in Fig. 8.

The discharge pressure rapidly declines after the initiation of the shutdown (Fig. 9), while the suction pressure starts to increase toward the settle out condition. The discharge valve is fully closed (and thus, builds up differential pressure) after about 4 s. This setup does not have a large consequence on surge prevention, as the pressure downstream of the valve also drops.

Data is recorded 8 s prior to the shutdown to determine the initial operating point. The settle out pressure outside the now isolated recycle loop is slightly higher (2 psi), as indicated by the pressure downstream of the discharge valve.

Figure 10 shows the rapid reduction in compressor speed and head after the shutdown is initiated. There is a delay of about 200 ms due to the fact that the gas turbine still produces power even after the fuel is shut off. Then the compressor speed rapidly decreases, and the compressor loses about 15% of its initial speed in the first second. The flow minimum after 1100 ms, and the corresponding valve opening of 36%, can also be identified in Fig. 10.

Figure 11 shows the differential pressure over the suction and discharge side unit valves. This pressure differential is near zero for a fully open valve, and increases when the valve closes. Data indicates that it took 2 s for the discharge valve to close, and almost 3 s for the suction valve to close. The differential pressure through the discharge valve dropped to a negative value due to a reverse flow from the discharge volume to the suction side through the recycle valve. Although there is a discharge check valve, the data indicates that it was not closing in the first few seconds of the transient event. Therefore, the discharge volume flowed backward through the recycle valve to the suction side, which represents a sink due to its lower pressure condition.

7 Modeling

The purpose of the tests is to serve as a benchmark for dynamic simulation software. Because the test geometry and the compressor behavior are well known, it is possible to identify software

Downloaded 02 Jun 2010 to 171.66.16.96. Redistribution subject to ASME license or copyright; see http://www.asme.org/terms/Terms_Use.cfm

Table 3 Test matrix

Initial point data for shutdown sequences (U.S. customary units)

Data point No.	Compressor suction (psi (absolute))	Compressor discharge (psi (absolute))	T_{suc} (°F)	T_{di}s (°F)	Mass row (lb m/s)	Actual flow (cfm)	Standard flow (MMSCFD)	Compressor speed (rpm)	P2/P1	Initial surge margin (%)	Compressor isertropic head (ft)
Transient No. 0	188.3	208.3	70.4	87.8	13.66	1400.8	26.38	17,700	1.106	38.6	4810.0
Transient No. 1	186.2	208.1	70.7	89.3	11.54	1203.2	22.29	17,778	1.118	28.5	5328.6
Transient No. 2	185.1	208.0	71.5	90.7	10.17	1071.6	19.65	17,777	1.124	19.7	5600.7
Transient No. 3	184.6	207.0	72.5	92.2	8.84	938.4	17.08	17,850	1.122	8.4	5519.0
Transient No. 4	185.1	209.2	72.3	93.6	15.52	1618.8	29.98	19,800	1.131	41.0	5903.4
Transient No. 5	182.4	209.3	73.2	96.1	13.12	1399.3	25.34	19,879	1.148	31.7	6650.4
Transient No. 6	180.9	209.3	74.1	98.1	11.45	1237.6	22.11	19,878	1.157	22.8	7044.3
Transient No. 7	180.6	208.3	74.8	99.0	10.12	1100.7	19.56	19,878	1.153	13.2	6920.7
Transient No. 7.1	181.0	208.6	75.4	99.5	10.13	1101.7	19.58	19,801	1.152	13.3	6884.3
Transient No. 8	180.7	202.6	73.7	93.3	8.66	941.1	16.73	17,778	1.121	8.6	5516.5
Transient No. 9	177.5	204.4	72.6	96.8	9.73	1072.9	18.79	19,800	1.152	11.00	6831.6

Data point No.	Compressor suction (KPa)	Compressor discharge (KPa)	T_{suc} (°C)	T_{dis} (°C)	Mass row (kg)	Actual flow (m^3/min)	Standard flow (MMSCFD)	Compressor speed (rpm)	P2/P1	Initial surge margin (%)	Compressor isertropic head (J/kg)
Transient No. 0	1298.3	1435.9	21.3	31.0	6.19	39.7	26.38	17,700	1.106	38.6	14,377.4
Transient No. 1	1283.6	1434.8	21.5	31.8	5.23	34.1	22.29	17,778	1.118	28.5	15,927.6
Transient No. 2	1276.1	1434.1	22.0	32.6	4.61	30.3	19.65	17,777	1.124	19.7	16,740.7
Transient No. 3	1272.4	1427.2	22.5	33.4	4.01	26.6	17.08	17,850	1.122	8.4	16,496.8
Transient No. 4	1275.9	1442.5	22.4	34.2	7.04	45.8	29.98	19,800	1.131	41.0	17,645.8
Transient No. 5	1257.6	1443.2	22.9	35.6	5.95	39.6	25.34	19,879	1.148	31.7	19,878.6
Transient No. 6	1247.6	1442.8	23.4	36.7	5.19	35.0	22.11	19,878	1.157	22.8	21,056.0
Transient No. 7	1245.0	1435.9	23.8	37.2	4.59	31.2	19.56	19,878	1.153	13.2	20,686.4
Transient No. 7.1	1248.0	1438.0	24.1	37.5	4.60	31.2	19.58	19,801	1.152	13.3	20,577.5
Transient No. 8	1245.9	1397.0	23.1	34.1	3.93	26.6	16.73	17,778	1.121	8.6	16,489.3
Transient No. 8	1223.5	1409.4	22.6	36.0	4.41	30.4	18.79	19,800	1.152	11.0	20,420.1

specific inaccuracies that are normally hidden due to the uncertainty in the input parameters. The modeling effort includes two stages:

- modeling based on data that may be known at the beginning of a project (geometry, compressor maps, inertia, valve data); and
- modeling based on the above and, additionally, knowledge of the train's deceleration rate.

The quantitative analysis of the system was based on fluid simulation utilizing the Stoner Pipeline Simulation® (SPS) software [7]. SPS solves nonlinear systems of differential equations at each time step using the method of characteristics. Transient analysis consists of a linearized solution of partial differential equations. The optimum time step for the computations is automatically determined by SPS without sacrificing accuracy. Every time step will depend on the transient sequence and event simulated. The time step varies dynamically depending on hydraulic conditions, but can also be entered manually for validation purposes. Very small time steps are required to model fast transients, but larger time steps are used when the model is relatively steady [7].

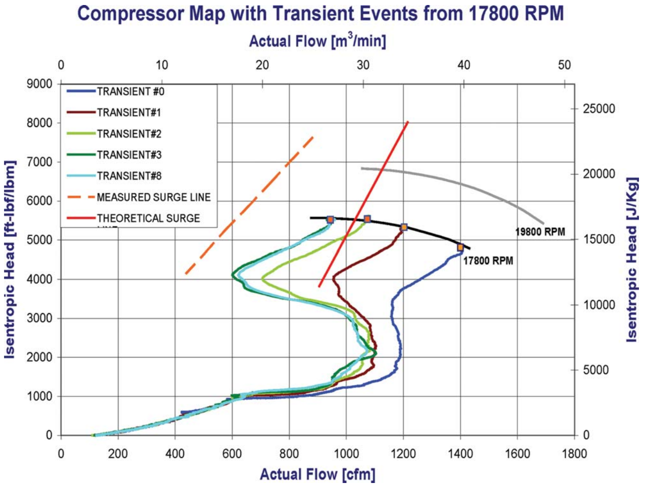

Fig. 7 Transient shutdown loci measurements for 17,800 rpm

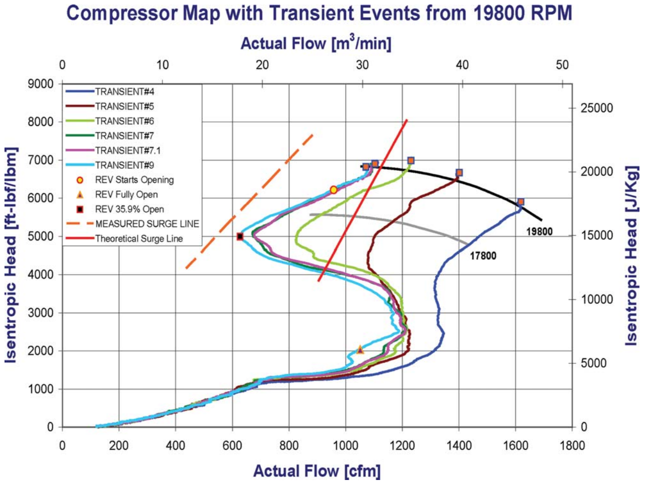

Fig. 8 Transient shutdown loci measurements for 19,800 rpm

Downloaded 02 Jun 2010 to 171.66.16.96. Redistribution subject to ASME license or copyright; see http://www.asme.org/terms/Terms_Use.cfm

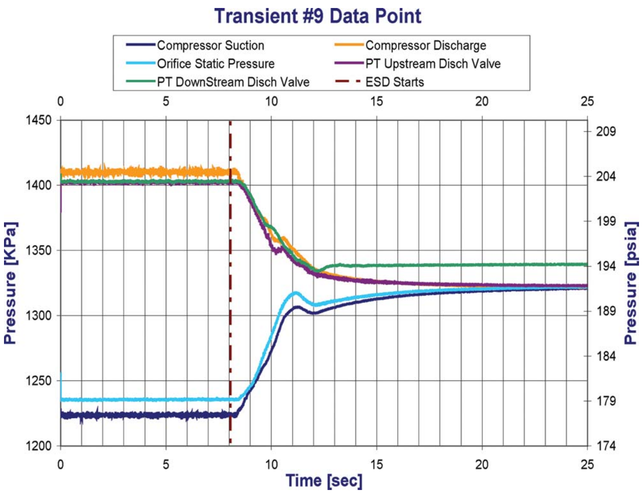

Fig. 9 Pressure versus time at different locations

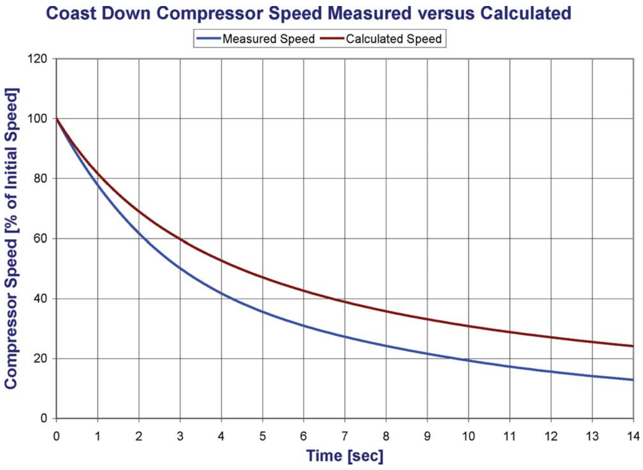

Fig. 12 Measured versus calculated speed decay

The process of creating a system model consists of a review of the available data for the system, creating a functional process block diagram, developing a system model in the SPS software, running the simulation based on initial and boundary operating conditions, model validation, and analysis of the resulting simulation data. This computational model allows for the evaluation and comparison of various conditions of the system.

A functional process block diagram was created, based on the data collected from the experimental facility used to conduct the tests (Fig. 4). This phase of the process also included collecting some basic data that was needed in the computational model such as compressor maps and other operational parameters.

The model was then "tuned" so it accurately predicted known steady-state parameters for a specific operating point. Generally, parameters such as pipe roughness and thermal and flow coefficients are used to adjust the model. The model was validated by comparing the simulation results to known steady-state parameters (e.g., suction and discharge pressures, head, inlet and outlet temperatures, speed, actual flow) at various other operating points. The comparison of the computational model versus real steady-state conditions provided an average uncertainty value of 1.51%.

The compressor coast down speed, as well as the valve opening and closing sequences, were either calculated or obtained from manufacturers' datasheets. These assumed that values will be compared with prediction, and the model will be systematically improved. All those sequences were programmed in a general ESD sequence that was initiated from each SS point for each simulated scenario. In addition, an optimum time step was determined to accurately capture the dynamic behavior of the system and its response. Results of each simulation are presented in a chart of head versus actual flow, including the compressor performance map, for further comparison with the test data. Figure 12 compares the measured and predicted speed decay using Eq. (4). The measured speed decay is slightly faster than the prediction, but provides reasonable correlation despite the simple fan law assumptions discussed earlier. The calculation ignores the residual gas turbine power.

Figure 13 shows a comparison of typical simulation results versus the experimental data. For this simulation, both the calculated and measured speed decay rate were used in the analysis. Both simulations matched the overall shape of the curve compared with the measurements. Surprisingly, the prediction using the calculated speed decay was slightly better than the prediction with the measured speed decay. Clearly, there was an offsetting error in the model. Overall, the predictions matched the shape of the measured curve reasonably well.

Figure 14 shows the transient ESD predictions using both the calculated and the measured speed decay for the 19,800 rpm case. Again, the calculated speed decay provides better agreement with the measured loci, as compared with using the measured speed decay.

Figures 15 and 16 provide a comparison between the predicted and measured temperatures and pressures (at compressor suction

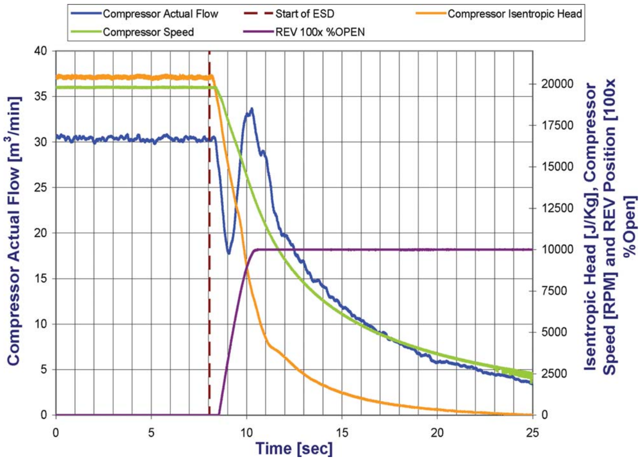

Fig. 10 Compressor actual flow, head and speed, and recycle valve position versus time

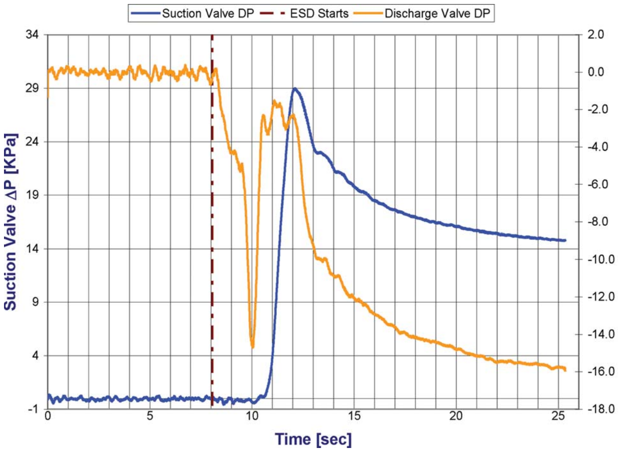

Fig. 11 Differential pressure over unit valves

Downloaded 02 Jun 2010 to 171.66.16.96. Redistribution subject to ASME license or copyright; see http://www.asme.org/terms/Terms_Use.cfm

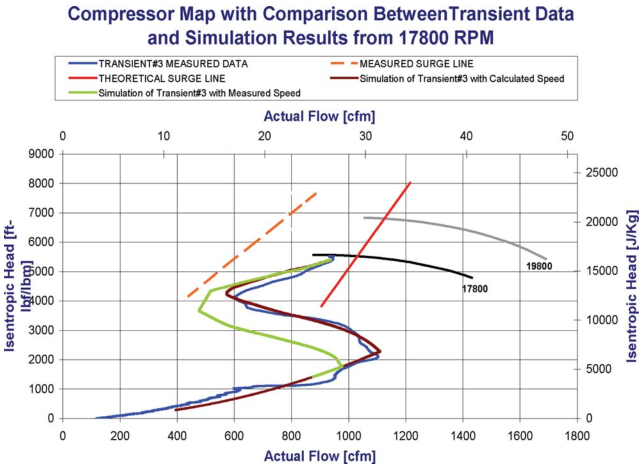

Fig. 13 Compressor map with measured and simulated transient events

and discharge). The measured temperature traces (Fig. 15) indicate an almost constant discharge temperature during the initial 5 s of the shutdown event. This is mostly due to the thermal mass of the compressor and the slow time constant of the thermowell, which keeps the discharge temperature from falling with the reduced head that the compressor produces as it spins down. The suction temperature reacts faster to the inflow of hot gas from the compressor discharge. While the pressures track reasonably well (Fig. 16), the measured temperatures react significantly slower than the temperatures in the simulation. Again, this is likely due to the long time constant of the thermowell used in the testing. However, this measurement error results in less than 3% deviation in the head and flow calculation.

8 Modeling Sensitivity Analysis

A sensitivity analysis provides a better understanding of system behavior when specific parameters are modified. Additionally, it helps to determine the effect of one variable, while others remain unchanged. Figure 17 shows a comparison between the test data for case No. 9 (Table 3) and simulation data. The simulation was conducted with different assumptions about the flow capacity of the recycle valve. The assumptions range from a recycle valve with 50% capacity of the valve actually installed, to 200% capacity. The baseline condition, which models the actual flow characteristics of the valve, shows a good correlation to the measured data. An ASV with half of the flow results in a minimum flow near

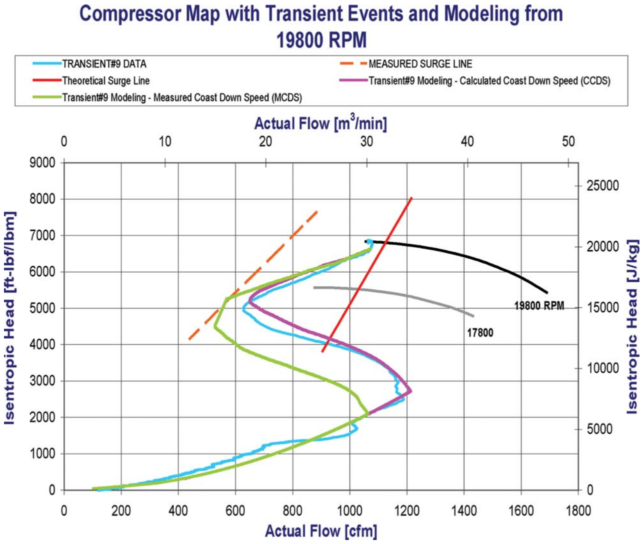

Fig. 14 Predictions using measured and calculated speed decay

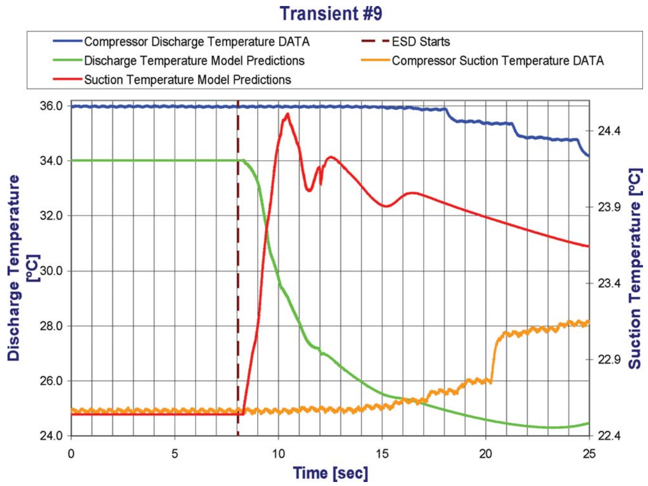

Fig. 15 Temperature model predictions versus measured data

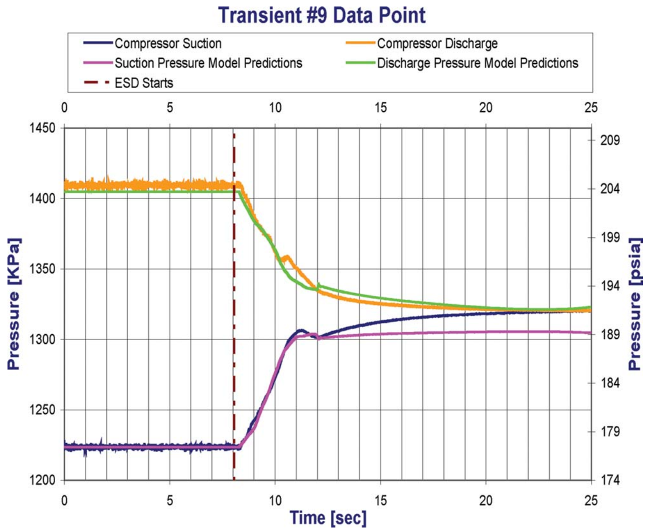

Fig. 16 Pressure model predictions versus measured data

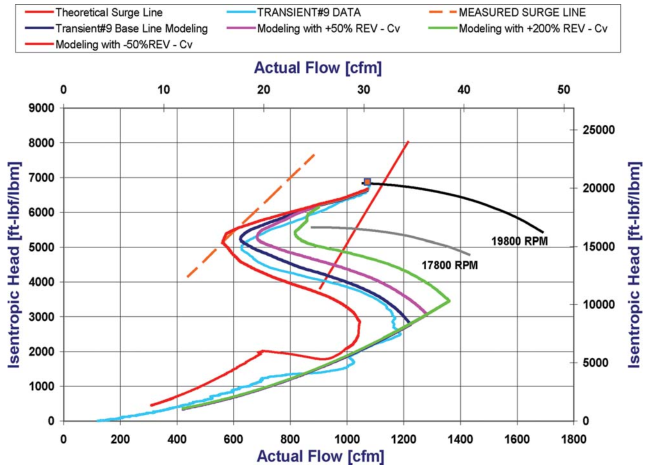

Fig. 17 ASV size sensitivity study from 19,800 rpm

Downloaded 02 Jun 2010 to 171.66.16.96. Redistribution subject to ASME license or copyright; see http://www.asme.org/terms/Terms_Use.cfm

the actual surge line. The system could benefit from a larger valve to reduce likelihood of surge. Overall, the predictions match the measured values well. This was accomplished without specific tuning of the model, and using the calculated speed decay.

9 Conclusions

A highly accurate series of surge test data has been gathered and compared with a state-of-the-art transient simulation. Overall, the code is predicting the transient shutdown behavior of a centrifugal compression station reasonably accurately without specific tuning of the model. The data quality and detail allowed using the transient software without many of the uncertainties usually involved in modeling a new compression system.

The goal of this study, which is to gather highly accurate data of a realistic emergency shutdown, was accomplished, and the use as a benchmark for a typical transient analysis was demonstrated. The analysis underpredicts the speed decay rate during shutdown, and the predictions generally get worse using the measured rather than the predicted speed decay. Some of this difference is likely due to the simple assumptions (fan law) made in the derivation. The SPS code requires an assumption about the rate of speed decrease, and this can be a source of inaccuracy. The analytical model accuracy can also be improved if steady-state test data is gathered in order to refine the pressure drops and pipe friction factors throughout the domain. Further refinement can be obtained from actual valve opening times in the installed operating condition that can be obtained.

Future work will include the investigation of the effect of different ASV sizes and response time.

Acknowledgment

The authors would like to thank the Gas Machinery Research Council, Exxon-Mobil, Solar Turbines, and BP for funding this work. Special thanks go to Mr. Angus Sites of Exxon-Mobil and Ms. Meron Wollie of BP for their technical guidance.

Nomenclature

Cv = valve flow coefficient ($m^3/Pa^{1/2}$ s)
H = head
J = inertia (kg m^2)
N = speed (rpm)
NPT = power turbine speed
P = power (kW)
P = pressure (kPa)
Q = flow (m^3/min)
T = compressor torque (N m)
t_b = time scale for discharge volume to bleed down (s)
t_d = time scale for train to decelerate (s)
t_V = ASV opening time (s)
V_2 = discharge volume between compressor and ASV (m^3)
W = mass flow
Π = dimensionless parameter
ω = rotational speed (rad/s)
GT = gas turbine

References

[1] Ribi, B., and Gyarmathy, G., 1997, “Energy Input of a Centrifugal Stage Into the Attached Piping System During Mild Surge,” ASME Paper No. 97-GT-84.
[2] Brun, K., and Nored, M., 2007, *Application Guideline for Centrifugal Compressor Surge Control Systems*, Gas Machinery Research Council, available at: www.gmrc.org.
[3] White, R. C., and Kurz, R., 2006, “Surge Avoidance in Compressor Systems,” *Proceedings of the Turbomachinery Symposium*, Houston, TX.
[4] Kurz, R., and White, R. C., 2004, “Surge Avoidance in Gas Compression Systems,” ASME J. Turbomach., **126**(4), pp. 501–506.
[5] Morini, M., Pinelli, M., and Venturini, M., 2007, “Application of a One-Dimensional Modular Dynamic Model for Compressor Surge Avoidance,” ASME Paper No. GT2007-27041.
[6] Botros, K. K., and Ganesan, S. T., 2008, “Dynamic Instabilities in Industrial Compression Systems With Centrifugal Compressors,” *Proceedings of the Turbomachinery Symposium*, Houston, TX.
[7] Advantica, Inc., Stoner Pipeline Simulation (SPS) Reference Manual and Software.

Downloaded 02 Jun 2010 to 171.66.16.96. Redistribution subject to ASME license or copyright; see http://www.asme.org/terms/Terms_Use.cfm

Rainer Kurz
Solar Turbines Incorporated,
9330 Skypark Court,
San Diego, CA 92123
e-mail: kurz_rainer_x@solarturbines.com

Klaus Brun
Rotating Machinery and Measurement Technology,
Department of Fluids Engineering,
Mechanical and Materials Engineering Division,
Southwest Research Institute,
San Antonio, TX 78238
e-mail: klaus.brun@swri.org

Assessment of Compressors in Gas Storage Applications

An analytical model is generated that allows the evaluation of the compression system. It is also used to derive general rules for optimizing a system. Several strategies for the compression system (single compressors, multiple compressors with a single driver in series and parallel configuration, and multiple compressors with individual drivers) are evaluated based on the said model. [DOI: 10.1115/1.4000147]

1 Introduction

The first natural gas storage facilities date back to the early 20th century in the United States and Canada. They were used to provide local natural gas supply during the winter heating season. This became necessary because the high demand in winter frequently exceeded the capacity of the local pipeline and production infrastructure. The introduction of a gas spot market in the mid-1980s has led to an increased demand for gas storage facilities. Currently, there are over 400 facilities in North America, and over 130 in Europe in operation. The vast majority of these gas storage facilities use depleted hydrocarbon reservoirs, aquifers, or salt caverns for storage [1]. The former two options involve storage in porous rock layers, while the latter is created by washing a cavity out of a salt dome. These types of storage facilities are very safe, preventing reliably leaks or other safety hazards. In either case, the pipeline company injects natural gas into the storage field when demand is low and withdraws it from the storage field during times of high demand.

Historically, storage was used to respond to the peak needs of cold winter days. Natural gas demand used to be at its highest in winter, primarily due to home heating requirements. In recent years, however, mostly due to increased demand from natural gas fired power plants, demand has become less seasonal. Because of this shift, well-placed natural gas storage has become even more important to natural gas operations.

Today, North American natural gas storage plays a key role in balancing supply and demand, particularly consumption during peak-demand periods.

- Storage can reduce the need for both swing natural gas production deliverability and pipeline capacity by allowing production and pipeline throughput to remain relatively constant.
- Customers may use storage to reduce pipeline demand charges, to hedge against natural gas price increase, or to arbitrage gas price differences.
- Pipelines and local distribution companies use storage for operation flexibility and reliability, providing an outlet for unconsumed gas supplies or a source of gas to meet unexpected gas demand.
- Storage at market trading hubs often provides balancing, parking, and loan services.
- In the future, additional conventional storage will be needed to meet growing seasonal demands and high deliverability storage will be required to serve fluctuating daily and hourly power plant loads.

Gas supply and demand in many pipeline systems shows significant seasonal changes, which is further aggravated by the periodic influx of liquefied natural gas. Gas storage facilities, where gas is stored during times of low demand or high supply and removed during times of high demand or reduced supply, are an important means in managing the gas supply [2].

Gas compressors are required to inject gas from a pipeline into the underground for storage, and to extract gas from the storage and feed it into the pipeline. Typical pipeline pressures range from 40 bar to 100 bar, and from this pressure, the gas has to be compressed to final storage pressure, typically between 100 bar and 200 bar. The compressor duty is cyclical in nature. Traditionally, the cycles were seasonal, with fluctuating pipeline and storage pressures gradually changing during the course of the season. However, under spot market activity conditions, daily demand cycles, market conditions, or short term weather patterns can require a facility to change their operating patterns several times a week.

Gas compression has to be used to fill the storage facility, as well as to recompress gas when the facility is emptied. The compression task is therefore described as filling a large constant volume with gas, with the limiting factor being the available driver power. This yields very uncharacteristic operating conditions for the compressor: Initially, the low pressure (LP) ratio allows for high flow conditions. The pressure ratio has to increase with an increasing amount of gas in the facility, therefore, reducing the possible flow for a power limited compression system (Fig. 1).

Different speed-torque characteristics of different drivers have to be accounted for these applications. A gas turbine with a free power turbine will provide increased torque at lower speeds. Therefore, the compressor limits will be determined by the available power. A electric drive with variable frequency drive is generally torque limited, which may impose and additional boundary. Constant speed drives are not covered in this study, as their operating characteristic is determined by the constant speed, with all possible operating points lying on a single speed line, unless other control mechanisms are employed.

Typical parameters for a storage site involve storage capacities of $0.05-1.5\times10^9\ \text{m}^3$ at storage pressures from 25 bar to about 200 bar. For the larger cavities, the filling can be accomplished at a rate of $250{,}000-700{,}000\ \text{m}^3/\text{h}$ [1].

2 Compressor Behavior

Centrifugal compressors, driven by gas turbines or variable speed electric motors are frequently used in gas storage applications.

Contributed by the International Gas Turbine Institute (IGTI) of ASME for publication in the JOURNAL OF ENGINEERING FOR GAS TURBINES AND POWER. Manuscript received May 5, 2009; final manuscript revised May 22, 2009; published online March 30, 2010. Editor: Dilip R. Ballal.

Copyright © 2010 by ASME

Downloaded 02 Jun 2010 to 171.66.16.96. Redistribution subject to ASME license or copyright; see http://www.asme.org/terms/Terms_Use.cfm

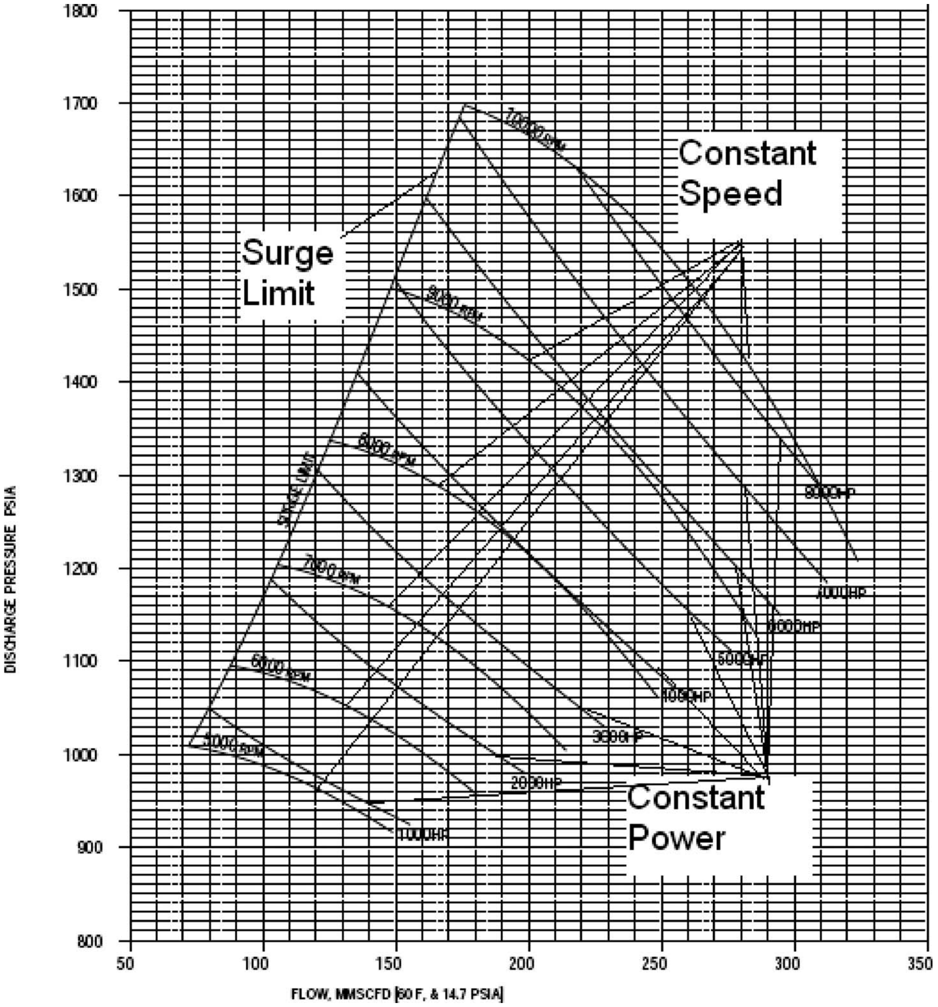

Fig. 1 Compressor map with lines of constant power

Beyond the quest for higher compressor peak efficiencies, the operating requirements require a compressor capable of operating over a wide operating range at high efficiency. Wide operating range in a centrifugal compressor can be achieved by a combination of means. Aerodynamic theory suggests a strong relationship between operating range, efficiency, and impeller backsweep. However, there is a practical limit to the amount of backsweep. In particular, increasing backsweep reduces the capability of an impeller of a given tip speed to make head. With the capability to use two impellers in a casing, this perceived disadvantage could be eliminated. The operating range is further increased by the use of a vaneless diffuser. The amount of backsweep allows for the control of the surge margin at the best efficiency point (BEP).

The performance of centrifugal gas compressors is best displayed in a map showing isentropic efficiency and isentropic head[1] as a function of the actual inlet flow, with the compressor speed as a parameter. Such a map also needs to define the operating limits of the compressor (Fig. 2).

The limitation for lower flow is the surge limit. Some manufacturers also limit the operation of their machines in the choke region, while others allow the operation of their machines anywhere in choke, as long as the head remains positive. Other limits include the maximum and minimum speed and temperature limits. The speed limits are either rotor dynamic limitations or stress limits. It must be noted that a performance map, as described, will not change even if the inlet conditions are changed (within limits).

The performance of a gas compressor can be described by the relationships of actual flow (Q), isentropic head (H_s), and isentropic efficiency (η_s), with the operating speed (N) as a parameter. Typical manufacturer data include a map containing this information.

The compressor actual head (H) can be determined from the suction and discharge pressure and temperature, assuming the gas composition is known. The relationship between the pressure, temperature, and enthalpy (h) is defined by the equations of state described below. By using the equations of state [3], the relevant enthalpies for the suction, the discharge, and the isentropic discharge state can be computed. The isentropic head (H_s) is

$$H_s = h(p_2, \Delta s = 0) - h(p_1, T_1) \tag{1}$$

With the isentropic efficiency

$$\eta_s = \frac{H_s}{H} \tag{2}$$

the actual head (H), which defines the power requirement, as well as the discharge temperature, is

$$H = \frac{H_s}{\eta_s} = h((p_2, T_2) - h(p_1, T_1) \tag{3}$$

---

[1] We prefer isentropic head and efficiency over polytropic head and efficiency because the isentropic head can be directly derived from station design parameters (i.e., gas composition, suction temperature and pressure, and discharge pressure), whereas the definition of the polytropic head requires the additional knowledge of the compressor efficiency or the discharge temperature.

Downloaded 02 Jun 2010 to 171.66.16.96. Redistribution subject to ASME license or copyright; see http://www.asme.org/terms/Terms_Use.cfm

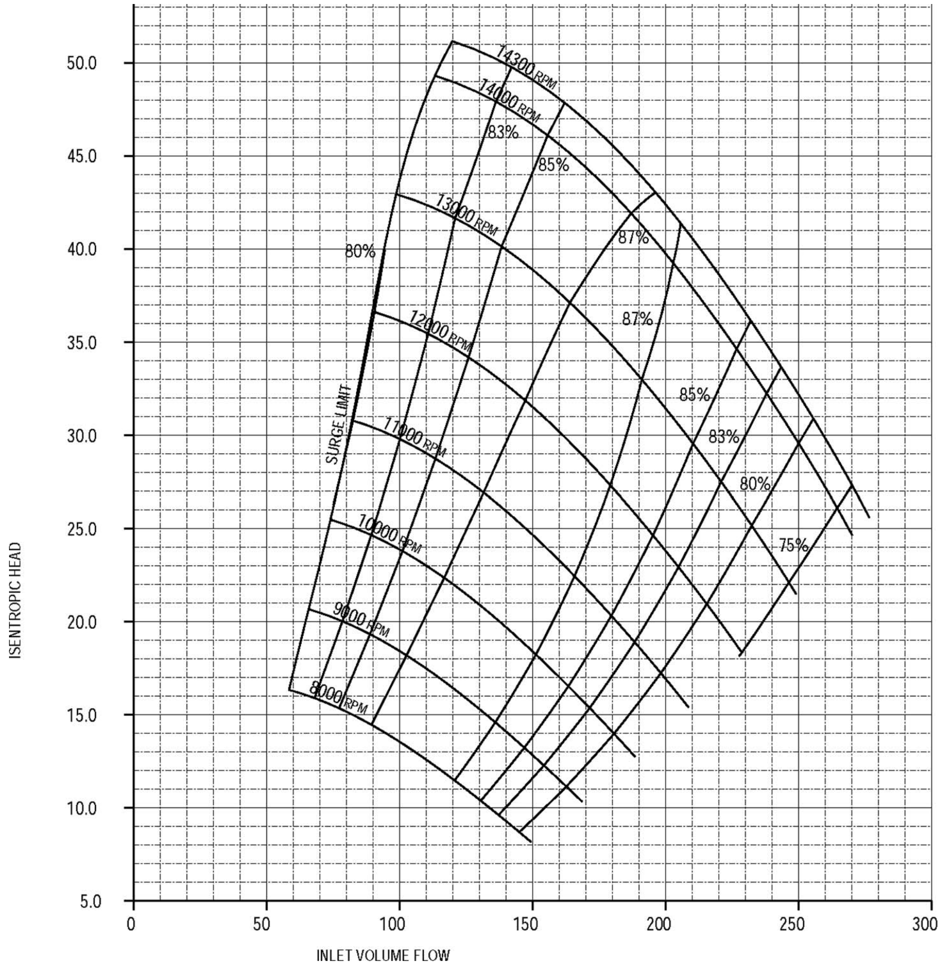

Fig. 2 Typical compressor map

The actual flow (Q) can be calculated from standard flow[2] or mass flow once the density is known (from the equation of state), i.e.,

$$Q(p,T) = \frac{\rho_{\text{std}}}{\rho(p,T)} Q_{\text{std}} = \frac{W}{\rho(\,p,T))} \tag{4}$$

Finally, the aerodynamic or gas power of the compressor, then, is determined to be

$$P_g = \rho_1 Q H = \frac{p_1}{Z_1 R T_1} Q H \tag{5}$$

Mechanical losses occur in the gas compressor and the gearbox (if one is used). The adiabatic efficiency of a compressor does not include the mechanical losses, which typically amount to about 1–2% of the absorbed power. The predicted absorbed power of a compressor should include all mechanical losses. By introducing a mechanical efficiency (η_m), typically 98–99%, to account for bearing losses, the absorbed compressor power (P) becomes

$$P = \frac{P_g}{\eta_m} \tag{6}$$

For directly driven compressors (i.e., without a gearbox between the gas turbine and the compressor), the absorbed power (P) is exactly equal to the required power at the power turbine output shaft.

3 Series and Parallel Arrangements

In general, storage applications require the compression system to operate over a wide range of different operating conditions. The limiting factor for shortest storage times is defined by the available driver power, as well as the operating limits (surge and choke) of the compressor. Since power, head and flow are tied in a fixed relationship

$$P = H \cdot W \tag{7}$$

a power limited compression system can process a high gas flow when the pressure ratio is low (initial part of filling the cavity from a pipeline), and a much lower gas flow when the pressure ratio is high (final part of the filling process). The system obviously has to be sized such that it is capable of meeting the final pressure ratio requirements.

At full load, the speed of the compressor usually does not vary to a large degree. One method to increase the range of the compressor system is to operate two compressors either in a series or a parallel configuration (Fig. 3). In this way, the operation at low pressure ratio would take advantage of the increased capacity of two compressors operating in parallel, while the operation at higher pressure ratios would use the two compressors in a serial configuration (Fig. 4).

The two machines have to be sized such that there is sufficient overlap between coverage of the series and the parallel configurations to allow for a transition from series to parallel operation using external or internal valving. Ideally, this is accomplished without having to shut the units down. The two compressors men-

---

[2] Standard conditions are $p=14.7$ psi (absolute) and $T=60°\text{F}$. Similarly, normal conditions are specified at $p=101.325$ kPa and $T=0°\text{C}$.

Downloaded 02 Jun 2010 to 171.66.16.96. Redistribution subject to ASME license or copyright; see http://www.asme.org/terms/Terms_Use.cfm

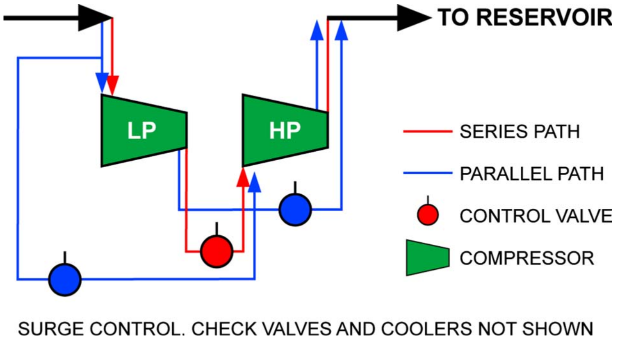

Fig. 3 Compressors operating in series and in parallel. LP and high pressure (HP) compressors can have separate drivers or are part of a train using a single driver.

tioned do not necessarily have to be identical. They also can be either driven by the same driver (in a tandem arrangement), or by separate drivers.

The operation scheme can also be used with three or more compressors. For three compressors, there would be three different modes of operation at full load:

- all three units in parallel
- two units in parallel feeding the third unit
- all three units in series

The latter arrangement would always require dissimilar compressors, while the first two can be accomplished in many cases with identical compressors.

We have not yet discussed the characteristics of the compressors typically used in storage applications. The limitations for a centrifugal compressor are the maximum flow, limited by power or speed, and the minimum flow (at maximum head), limited by the surge control line. Between these, the centrifugal compressor can be operated at maximum available load. The reciprocating compressor will easily allow for the increase in pressure ratio, but it will do so at almost constant flow. This means that initially it will not be able to use full power until the combination of pressure ratio and flow requires maximum power. Then the machine would have to be unloaded (e.g., with clearance pockets) and, again, would operate at a reduced power requirement, until the pressure ratio becomes high enough to require full power. Essentially, while the centrifugal compressor operates along a full load power line, the reciprocating compressor would operate in discrete steps defined by the discrete flow setting.

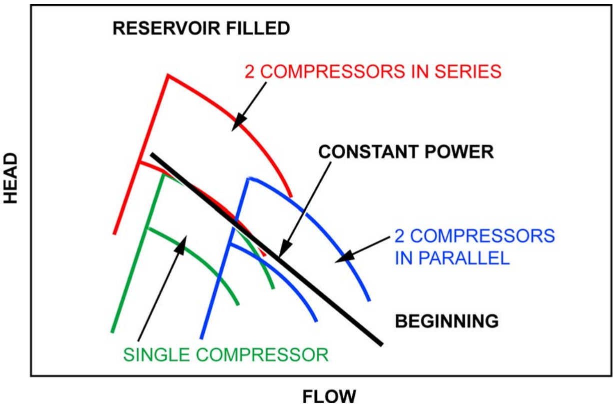

Fig. 4 Composite coverage maps for two compressors capable of operating in series and in parallel

4 Theoretical Model

Assume a path of constant power, P, along a compressor map, as described above

$$P = H \cdot W = \frac{H_s}{\eta_s}\rho_1 Q \tag{8}$$

Along this path, the relationship

$$\begin{aligned} p_2 &= f(Q)|_{P=\text{const}} \\ dp_2 &= f'(Q)dQ \end{aligned} \tag{9}$$

is well defined for a given compressor map, assuming the suction conditions for the compressor (p_1, T_1, and gas) are held constant.

The storage facility has a storage volume V, and the total volume V_c pumped by the compressor between times $t=0$ and $t=t_e$ is

$$V_c = \int_{t=0}^{t_e} g(t)dt \tag{10}$$

where we need to find how the function $g(t)$ is related to $f(Q)$. For the storage volume V, the pressure p_v is determined by the trapped mass M. We will assume a constant temperature of the gas in the storage facility

$$p_V V = M Z_V R T_V \tag{11}$$

Differentiation leads to

$$V dp_v = Z_v R T_v dM \tag{12}$$

and the change in mass is due to the flow through the compressor. The constant

$$C_1 = \rho_1 \frac{Z_v R T_v}{V} \tag{13}$$

includes the gas density at suction conditions and the storage facility volume.

$$\begin{aligned} dM &= \rho_1 \cdot Q \cdot dt \\ dp_v &= C_1 \cdot Q \cdot dt \end{aligned} \tag{14}$$

p_v is approximately equal to the discharge pressure of the compressor, neglecting the small pressure drop in the piping system. Equation (9) defines an expression for p_2 and, thus, p_v, and combining it with the equation above yields

$$\begin{aligned} f'(Q)dQ &= C_1 Q dt \\ dt &= \frac{f'(Q)dQ}{C_1 Q} \end{aligned} \tag{15}$$

which can be integrated to

$$t = \frac{1}{C_1}\int \frac{f'(Q)}{Q} dQ \tag{16}$$

In its simplest form, $f(Q)$ can be approximated by a straight line (although other functions are possible)

$$f(Q) = p_2 = C_2 Q + C_3 \quad f'(Q) = C_2 \tag{17}$$

and the integral yields

$$t = \frac{C_2}{C_1}\int \frac{dQ}{Q} = \frac{C_2}{C_1}\ln Q + C_4\Big|_{t=0}^{T} \tag{18}$$

where the constant C_4 follows from $Q=Q_0$ at $t=0$

$$C_4 = -\frac{C_2}{C_1}\ln Q_0 \tag{19}$$

and we get

Downloaded 02 Jun 2010 to 171.66.16.96. Redistribution subject to ASME license or copyright; see http://www.asme.org/terms/Terms_Use.cfm

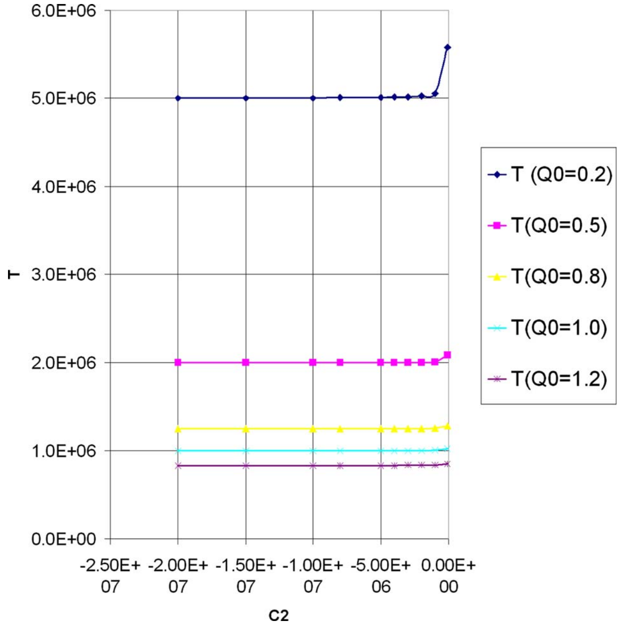

Fig. 5 Influence of C_2 (steepness of the p_2-flow curve at constant power) on filling time T for different choices of initial flow Q_0

$$t = \frac{C_2}{C_1} \ln Q - \frac{C_2}{C_1} \ln Q_0 = \frac{C_2}{C_1} \ln \frac{Q}{Q_0} \tag{20}$$

and the actual flow (which becomes smaller with time due to the increasing pressure):

$$Q(t) = Q_0 e^{(C_1/C_2)t} \tag{21}$$

Thus the volume of gas stored over a given period of time T becomes

$$V_c = \int_0^T Q_0 \cdot e^{(C_1/C_2)t} dt = \frac{C_2}{C_1} Q_0 (e^{(C_1/C_2)T} - 1) \tag{22}$$

Conversely, the time T needed to store a certain volume of gas is

$$T = \frac{C_2}{C_1} \ln\left(\frac{C_1}{C_2} \frac{V_c}{Q_0} + 1 \right) \tag{23}$$

The minimal time necessary for a certain required volume V_c and given C_1 are either determined by Q_0 or by C_2. The equation above shows (not surprisingly) that the larger the Q_0, the shorter the filling time. This indicates that a compressor with a large choke flow is advantageous. For a given amount of available power, a better compressor efficiency will also lead to a larger Q_0. In particular, this also means that a compressor capable of absorbing all of the available driver power for most or all possible operating conditions is advantageous. This sounds trivial, but a compressor operating in choke may be limited by its speed and not by available power. Likewise, a reciprocating compressor may only be able to absorb the full driver power for a few points in its operating range.

Regarding the steepness of the compressor characteristic, we find that the steeper the curve, the faster the filling. Increased steepness leads to an asymptotic approach to a shortest possible time, i.e., beyond a certain steepness, the time reductions become smaller and smaller (Fig. 5). Another aspect is that the steepness and Q_0 are related. For a given minimum flow (surge), the steeper the head (or p_2)-flow relationship, the smaller Q_0 becomes.

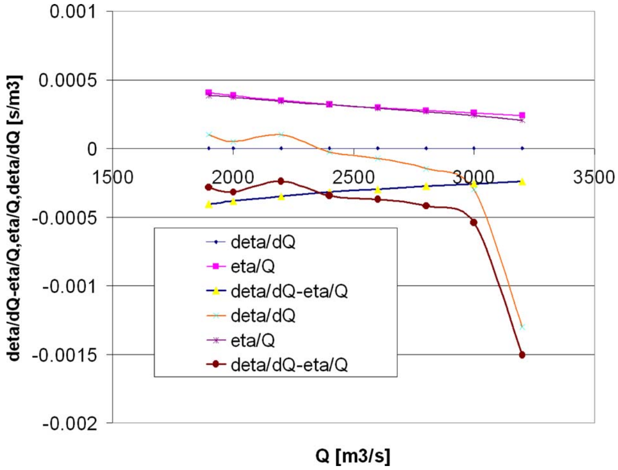

Fig. 6 Evaluation of Eq. (27) for case with constant efficiency (eta=const) and case where efficiency is reduced on either side of BEP(variable eta). The curves show the behavior of the terms $d\eta/dQ$, η/Q, and $d\eta/dQ\text{-}\eta/Q$ in Eq. (27).

5 Insights

The constant C_1 in the equations above is, for unchanged gas inlet conditions, a function of the storage facility (its Volume and its temperature) and always a positive number. The constant C_2, however, is the steepness of the constant power line in the discharge pressure-flow characteristic of the compressor. The larger C_2 the longer it takes to fill a certain volume or the less gas volume enters the storage facility in a given time

$$C_2 = \frac{dp_2}{dQ_{P=\text{const}}} \tag{24}$$

C_2 is thus the steepness of the line of constant power. What makes this line steeper or flatter?

From

$$P(Q) = \rho Q \frac{H_s}{\eta_s} \tag{25}$$

we know that the line of isentropic head versus flow at constant power is, with $C_5 = P/\rho$

$$H_s = C_5 \frac{\eta_s}{Q} \tag{26}$$

with the steepness

$$\frac{dH_s}{dQ} = C_5 \frac{d(\eta_s/Q)}{dQ} = C_5 \left(Q^{-1} \frac{d\eta_s}{dQ} - \eta_s \frac{1}{Q^2} \right) = \frac{C_5}{Q} \left(\frac{d\eta_s}{dQ} - \frac{\eta_s}{Q} \right) \tag{27}$$

The second term (η_s/Q) is always positive, the first term is positive at flows lower than BEP, and negative for flows higher than BEP. From our maps we know that that the slope of dH/dQ is always negative, and gets flatter toward surge and steeper toward choke. At the best efficiency point of the compressor we get $d\eta_s/dQ=0$.

The curious part of this result is that the amount of gas that can be brought into the cavity in a certain time interval not only depends on the efficiency, but also on the rate of efficiency change. At flows higher than BEP, (η_s/Q) will always get smaller, and a faster rate of change in $d\eta/dQ$ counteracts the steepness. If $d\eta/dQ$ were zero, $Hs(Q)$ would become less steep (Fig. 6).

At flows lower than BEP, (η_s/Q) will change slowly because both η_s and Q get smaller. $d\eta_s/dQ$, on the other hand, is positive, thus, counteracting the influence of (η_s/Q). The net result is that dH/dQ is steeper toward choke and less steep toward surge.

Downloaded 02 Jun 2010 to 171.66.16.96. Redistribution subject to ASME license or copyright; see http://www.asme.org/terms/Terms_Use.cfm

Because of the relationship between head and discharge pressure (for constant suction conditions), we know that the steeper the head-flow relationship, the steeper the p_2-flow relationship. Figure 6 indicates that any increase in compressor efficiency will increase the steepness of the head-flow relationship and, therefore, will increase the steepness of the p_2-flow relationship. More particularly, if the efficiency is increased by a constant factor across the board, the steepness will increase at the same rate as the efficiency increase. Interestingly, a compressor with a typical efficiency distribution (i.e., efficiency dropping from peak efficiency both toward surge and choke), compared with a hypothetical machine with constant efficiency will have a steeper more advantageous curve for all operating points at a higher flow than the best efficiency point (Fig. 6).

The integral formulation above allows to approximate the $P(Q)$ relationship as piecewise linear, and each linear piece n contributes a certain amount of time

$$t = \sum_{n=1}^{N} t_n \tag{28}$$

The two operating boundaries of the compressor, maximum flow, and minimum flow also have significant impacts on the time required to fill the cavity. In particular, on the maximum flow side, even at a low efficiency, a compressor with a higher choke flow capability has an advantage over a compressor that chokes earlier or has limitations regarding the operation in “overload.”

Figure 5 indicates that the dominant factor in these evaluations is Q_0, as even extreme values of C_2 lead to small modifications of the filling time. For a given amount of driver power, the compressor efficiency determines Q_0, and the higher the compressor efficiency is, the higher Q_0 becomes and the shorter the filling time.

6 Evaluation of Compression Options

With the relationships derived above, we can evaluate typical options for this type of application. To allow for a comparison, the available driver power was the same for all cases. The analysis of the slope of dH/dQ indicates that it is reasonable to describe the map of a compressor as two segments, where the first segment starts in choke and ends at the flow at best efficiency, while the second segment starts at the best efficiency point and ends at the surge control line.

With the given limitations in operating range, an elegant method is to arrange centrifugal compressors such that can operate either in series or in parallel configurations (Figs. 3 and 4). As indicated earlier, this is both possible using individual drivers for each compressor or by having a single driver for the compressors. In reality, the differences between the individual driver solution and a single driver solution are relatively small, even if the compressors use different stages (i.e., one compressor is sized for lower flows than the other, which is usually necessary due to the volume reduction after the first compressor in a series arrangement. Arrangements with three compressors can sometimes be sized with identical stages by running the compressors such that two compressors feed the third one in the series arrangement).

When the compressors run in parallel, the individual driver solution allows one to run the compressors at different speeds, but force the compressor with the lower flow staging further into choke if the entire driver power is to be used. If both compressors are part of the same train, they have to run at the same speed, but the higher flow compressor will absorb more power than the low flow compressor, which allows the low flow compressor to operate more efficiently.

When the compressors run in series, the requirement to run at identical speeds in the single driver solution may cause the low flow compressor to run closer to surge than for the individual driver solution.

Careful selection of the aerodynamic layout of the compressors involved will make the true differences between these two options very small, if not negligible. In either case, the efficiency will usually be higher than for an attempt to cover the entire operating range with a single compressor. In particular, operation in choke with the double disadvantage of low efficiency, as well as limitations that may not allow one to use all available power, are easier avoided by applying multiple compressors that can be operated either in series or in parallel.

7 Conclusion

Key requirements for the capability to fill the storage cavity fast or, more generally, to increase the amount of stored gas fast are predominantly a function of the driver power and compressor efficiency. An increase in either of the two increases the crucial factor Q_0. It should be noted that the power referenced here is not just the available driver power, but the portion of driver power that can actually be used by the compressor. Another factor that plays usually a secondary role besides the efficiency of the compressor is the slope of the efficiency characteristic.

It becomes clear that arrangements that allow one to switch multiple compressors between series or parallel operation are advantageous. Modern control systems allow the switch without having to shut compressors down.

Depending on the commercial advantage of fast filling times and high flexibility, the added first cost of multiple units may be compensated.

Acknowledgment

The authors would like to thank Ms. Tonya Müller for her thorough review of the derivations in the paper.

Nomenclature

$C_{1,2,3,4,5}$ = constants
SG = specific gravity relative to air
H = head
h = enthalpy
N = speed
P = power
p = pressure
Q = volumetric flow, compr. inlet (capacity)
R = gas constant
T = temperature
T = elapsed time
t = time
W = mass flow
V = volume of storage facility
V_c = compressed volume $V_c = \int Q \cdot dt$
Z = compressibility Factor
ρ = density
η = efficiency

Subscripts

0 = initial
1 = suction
2 = discharge
s = isentropic
v = conditions in the storage cavity

Appendix

Typical orders of magnitude for the constants used

$$C_1 = \frac{50 \ \text{bar} \cdot 0.9 \cdot 489 \frac{\text{J}}{\text{kg K}} \cdot 303 \ \text{K}}{10^9 \ \text{m}^3} = 4 \times 10^{-3} \frac{\text{N}}{\text{m}^5}$$

$$C_2 = \frac{\Delta p_2}{\Delta Q} = -\frac{30 \cdot 10^5 \ \text{N/m}^2}{0.3 \ \text{m}^3\text{/s}} = -10^7 \frac{\text{N s}}{\text{m}^5}$$

Downloaded 02 Jun 2010 to 171.66.16.96. Redistribution subject to ASME license or copyright; see http://www.asme.org/terms/Terms_Use.cfm

$$\frac{C_1}{C_2} = -4 \times 10^{-10}\ \text{s}^{-1} \tag{A1}$$

i.e., the value of C_1/C_2 is very small, C_2/C_1 is very large. This means in particular that

$$\text{abs}\left(\frac{C_1}{C_2} \cdot \frac{V_c}{Q_0}\right)$$

in Eq. (23) will always be much smaller than 1 because V_c/Q_0 is essentially the time it would take to fill volume V_c if the initial flowrate Q_0 could be maintained. For the extent of a month (2.6×10^6 s), or a year (3.1×10^7 s), the overall term is still much smaller than 1

$$C_5 = \frac{10^7\ \text{W}}{30\ \text{kg/m}^3} = 3.3 \cdot 10^5 \frac{\text{J m}^3}{\text{kg s}} \tag{A2}$$

$$\frac{dH_s}{dQ} = \frac{C_5}{Q}\left(\frac{d\eta_s}{dQ} - \frac{\eta_s}{Q}\right) = \frac{3.3 \times 10^5\ \text{J}}{1\ \text{kg}}\left(-\frac{0.03}{0.25\dfrac{\text{m}^3}{\text{s}}} - \frac{0.77}{1\dfrac{\text{m}^3}{\text{s}}}\right) \tag{A3}$$

$$\frac{dH_s}{dQ} = -2.94 \times 10^5 \frac{\text{J s}}{\text{kg m}^3}$$

For this particular set of data, the magnitude of C_2 is almost immaterial because the filling time is dominated by Q_0. However, very small abs (C_2) will increase the time significantly.

References

[1] Ruhrgas, A. G., 1994, Untertagespeicher.
[2] INGAA, 2007, *Interstate Pipeline Desk Book*, 1st ed., Interstate Natural Gas Association of America, Washington, DC.
[3] Kumar, S., Kurz, R., and O'Connell, J. P., 1999, "Equations of State for Compressor Design and Testing," ASME Paper No. 99-GT-12.

Downloaded 02 Jun 2010 to 171.66.16.96. Redistribution subject to ASME license or copyright; see http://www.asme.org/terms/Terms_Use.cfm

Jun Li
Institute of Turbomachinery,
Xi'an Jiaotong University,
Xi'an 71049, P.R.C.;
Department of Mechanical Engineering,
Keio University,
Yokohama 223-8522, Japan
e-mail: junli@mail.xjtu.edu.cn

Shengru Kong

Xin Yan

Institute of Turbomachinery,
Xi'an Jiaotong University,
Xi'an 71049, P.R.C.

Shinnosuke Obi
Department of Mechanical Engineering,
Keio University,
Yokohama 223-8522, Japan

Zhengping Feng
Institute of Turbomachinery,
Xi'an Jiaotong University,
Xi'an 71049, P.R.C.

Numerical Investigations on Leakage Performance of the Rotating Labyrinth Honeycomb Seal

Three-dimensional Reynolds-averaged Navier–Stokes (RANS) solutions from CFX *were utilized to investigate the leakage flow characteristics in the labyrinth honeycomb seal of steam turbines. At first, the accuracy and reliability of the utilized RANS approach was demonstrated using the published experimental data of the honeycomb seal. It showed that the utilized numerical method has sufficient precision to predict the leakage performance in seals. Then a range of sealing clearances, cell diameters, cell depths, rotation speeds, and pressure ratios were investigated to determine how these factors affect the leakage flow rate of the labyrinth honeycomb seal. The computed leakage flow rate increased with increasing sealing clearance and pressure ratios. Furthermore, the results show that the studied labyrinth honeycomb seal has the optimum sealing performance in the case of honeycomb cell diameter equals labyrinth step width, and the ratio of the honeycomb cell depth to honeycomb cell diameter is 0.93 under the designed condition. The flow pattern of each case is also illustrated to describe the leakage flow characteristics in labyrinth honeycomb seals.* [DOI: 10.1115/1.4000091]

Keywords: labyrinth honeycomb seal, leakage flow, numerical simulation

1 Introduction

The increasing demand for aggressive power output, efficiency, and operational life for turbines requires us to pay more attention to the leakage flow between stationary and rotating components. Leakage flow has many disadvantages for a turbine. Leakage flow is one of the main sources of loss in the through flow of a turbine. The leakage flow interacts with the main flow and reduces turbine efficiency [1]. In addition, leakage flows may induce flow excitation and result in rotordynamic instability [2]. Controlling leakage flow, and the corresponding clearance technique, is one of the critical aspects of turbine design and manufacture process. Labyrinth seals, a noncontact dynamic sealing technology, are the key elements to control the amount of leakage flow for through flow in a turbine. Despite advanced sealing technologies, including brush seals, leaf seals, finger seals, and so on, for turbine leakage flow control [1,3], labyrinth seals still play an important role in leakage flow control. Thus, improved design tools are a necessity for a more efficient and reliable turbine [4]. To overcome the leakage flow excitation of labyrinth seals for the recently developed large power output steam turbine, gas turbine, labyrinth honeycomb seals were developed and applied [5]. Figure 1 shows the structural configuration of a labyrinth honeycomb seal. Labyrinth honeycomb seal technology requires that the honeycomb lands installed at the stator component and the rotating components are consistent with the conventional labyrinth seals. To increase labyrinth honeycomb seal utilization for turbines, it is crucial to study the discharge behavior of this kind of sealing technology.

The sealing performance, including the discharge coefficient of labyrinth honeycomb seals, is the subject of the current seal research. There are many factors that can affect leakage flow of the labyrinth honeycomb seal. One of these factors is the sealing clearance. At the same sealing clearance size, the leakage flow rate of the honeycomb seal is higher than that of the labyrinth seal at the same flow condition and axial distance [6]. Another factor is the honeycomb cell size [7]. Empirical results, as well as theoretical analysis, have shown that other factors such as the pressure ratio and rotational speed may impact the discharge characteristics of the labyrinth honeycomb seal [8]. A few simple correction equations based on the experimental data were derived and used to predict the experimental results. Therefore, it is difficult to decide the factors for every new design. At present, the progress of computer and CFD technologies makes it possible to utilize a numerical simulation to predict the performance of rotating seals. Furthermore, it is also convenient to obtain the correction factors directly if the validity of the numerical method has been demonstrated.

To investigate how these factors, such as the sealing clearance, honeycomb cell sizes, pressure ratio, and rotation speed, affect the discharge behavior, numerical investigations were performed in the present study to calculate the leakage flow in the shaft labyrinth honeycomb seal. First of all, the computed leakage flow rate and detailed velocity profiles within the seal chamber were compared with the obtained experimental data for the labyrinth seal with smooth and honeycomb lands. After the accuracy and reliability of the utilized numerical approach have been demonstrated, the influence of sealing clearance, honeycomb cell sizes, pressure ratio, and rotation speeds on the leakage flow characteristics in the shaft labyrinth honeycomb seal were investigated in detail.

2 Literature Review

Labyrinth seals are widely used in steam turbines, gas turbines, and other applications where transient rubbing contact is likely. The labyrinth seal is a noncontacting dynamic seal, and the major advantages of this seal are its simplicity, reliability, and tolerance to large thermal and pressure variations [2]. Labyrinth seals work

---

Manuscript received March 3, 2009; final manuscript received June 17, 2009; published online March 16, 2010. Editor: Dilip R. Ballal.

Copyright © 2010 by ASME

Downloaded 02 Jun 2010 to 171.66.16.96. Redistribution subject to ASME license or copyright; see http://www.asme.org/terms/Terms_Use.cfm

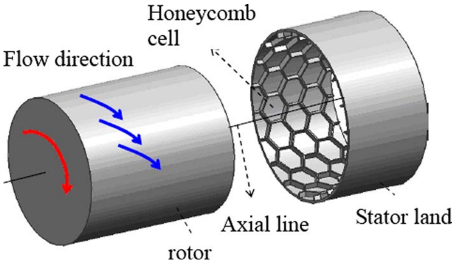

Fig. 1 Structural configuration of the labyrinth honeycomb seal

on the principle that fluid pressure energy is converted at each tooth tip clearance into kinetic energy that is either dissipated into heat by turbulence, or enters the subsequent tooth clearance by kinetic energy carryover [9–11].

The honeycomb seal, whose inner bore consists of many hexagonal or honeycomb pockets, was originally introduced in the 1960s as a replacement for aluminum labyrinth seals, which were being eroded by processing fluids [10]. Stocker et al. [11] comprehensively presented experimental results on the leakage performance of labyrinth seals with honeycomb lands. He used both two-dimensional planar and three-dimensional rotating seal test rigs to measure the air leakage through labyrinths with honeycomb, abradable or solid stator walls. He concluded that the leakage flow rate of the honeycomb land was greatly increased, in comparison with that of the smooth land at a small tooth clearance of a straight-through labyrinth seal with four teeth. The honeycomb seal withstands severe operating conditions in terms of high temperatures and high rotational speeds while allowing limited rubbing of the stator fins at the rotor without the danger of seal failure. Therefore, a significantly tighter seal clearance, which represents a leakage-reducing factor, can be realized [5].

Research on the leakage flow characteristics in labyrinth seals, including honeycomb seals, had initially been based on experimental tests and numerical simulations. Advanced experimental techniques, together with numerical methods, have been applied to obtain detailed information of the complex leakage flow in labyrinth seals, and to identify the relevant parameters influencing the labyrinth leakage flow characteristics. Regarding the effect of rub grooves formed into an abradable surface, Rhode and Allen [12,13] obtained flow visualization digital images for large-scale stepped labyrinths that explain the measured effects on leakage. Wittig et al. [14] investigated the effects of the pressure ratio and Reynolds number on straight-through labyrinth seals by measuring the leakage rates of geometrically similar, two-dimensional plane models. Plots of the nondimensional discharge coefficients against the overall pressure ratio for different scales were presented.

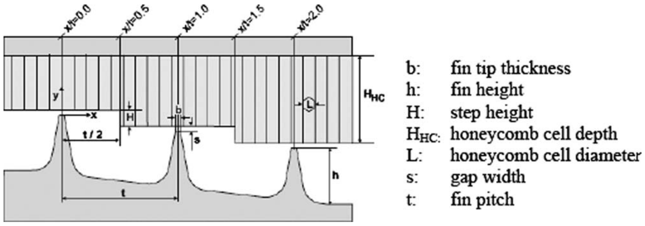

Fig. 2 Geometrical parameters of the labyrinth seal with honeycomb lands [6]

Table 1 Conditions and numerical methods

Inlet total temperature	300 K
Outlet static pressure	101325 Pa
Discretization scheme	High resolution
Computational method	Time marching method
Turbulence model	$k-\varepsilon$, scalable log wall function
Fluid	Air (ideal gas)
Wall properties	Adiabatic, smooth surface

Recently, Schramm et al. [6] obtained CFD results from a commercial code showing the leakage flow entering the honeycomb cells. They also found agreement with laser doppler velocimeter (LDV) measurements regarding the presence of a three-dimensional velocity field near the tooth tips. Choi and Rhode [15] introduced a new approach for employing a two-dimensional CFD model to approximately compute a three-dimensional flow field in a honeycomb labyrinth seal. A numerical study for worn and unworn labyrinth seals with honeycomb land at different radial clearances using the commercial CFD code, CFX, was presented [16]. Yan et al. [17] applied three-dimensional commercially available CFD software, CFX, to predict the leakage performance and windage effects of the labyrinth seal with different sizes of honeycomb lands. They presented results confirming the conclusions of Denecke and co-workers [7,8].

Several investigators report on the high performance of labyrinth honeycomb seals. Paolillo et al. [18] experimentally studied the rotational speed on the discharge characteristics of two kinds of labyrinth honeycomb seals. Soemarwoto et al. [19] numerically investigated the leakage performance of three designs of labyrinth honeycomb seals, and they discussed detailed flow patterns. The obtained results showed that the canted-knife seal design with respect to the straight-knife case has the lower performance. Chougule et al. [20] utilized the three-dimensional CFD numerical approach to investigate the leakage performance of their new design labyrinth honeycomb seal. A staggered honeycomb land and straight teeth with a newly designed inclined notch showed a 17% reduction in seal leakage, compared with the initial design.

However, the influence of sealing clearance and honeycomb cell size on the leakage performance of labyrinth honeycomb seals is seldom presented. Thus, the main objective of the present work was to utilize a 3D numerical method to investigate the discharge behavior in the shaft labyrinth honeycomb seal. The effects of

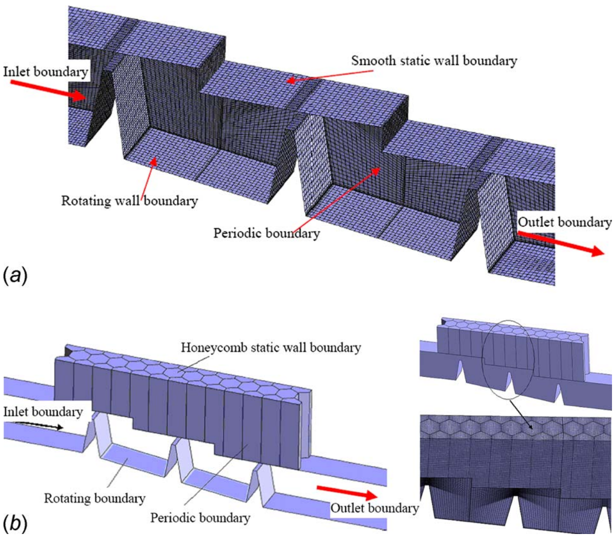

Fig. 3 Boundary condition definitions

Downloaded 02 Jun 2010 to 171.66.16.96. Redistribution subject to ASME license or copyright; see http://www.asme.org/terms/Terms_Use.cfm

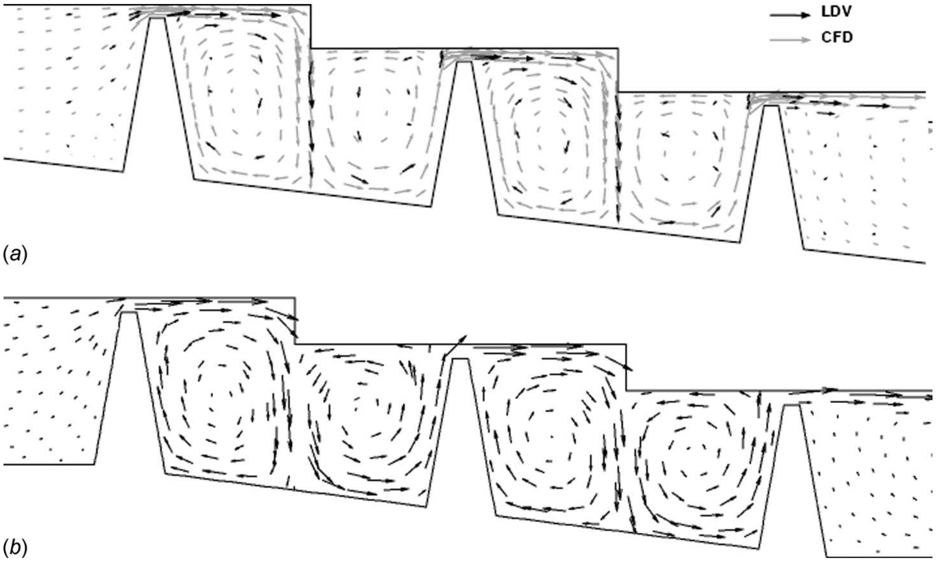

Fig. 4 Velocity flow pattern in the labyrinth smooth seal ($s1=1.204$ mm, $\pi=1.1$)

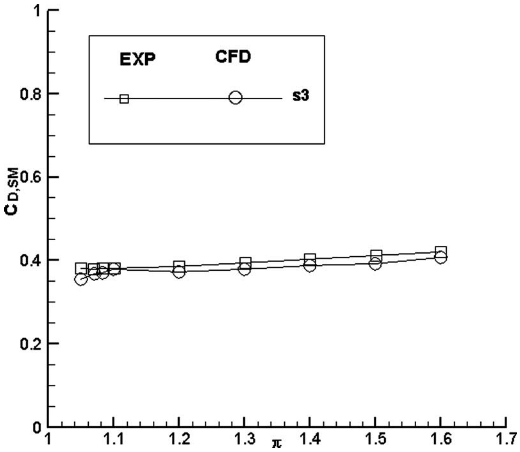

Fig. 5 Comparison of the discharge coefficients between the present CFD results and the experimental data

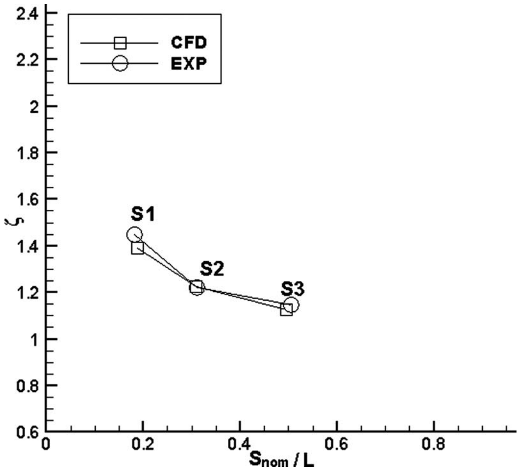

Fig. 6 Comparison of the leakage increase parameter between the present CFD results and the experimental data

many factors such as sealing clearance, honeycomb cell size, pressure ratio, and rotational speed on the leakage flow characteristics were conducted and are discussed here.

3 Numerical Method

3.1 Validation Model. To demonstrate the accuracy and reliability of the numerical approach for predicting the discharge behavior of the labyrinth honeycomb seal, the experimental labyrinth seal with smooth and honeycomb lands was utilized. The computational geometrical parameters of the experimental research were obtained from Schramm et al. [6]. The labyrinth seals with smooth and honeycomb lands configurations are defined in Fig. 2. It features three straight knives on the rotor.

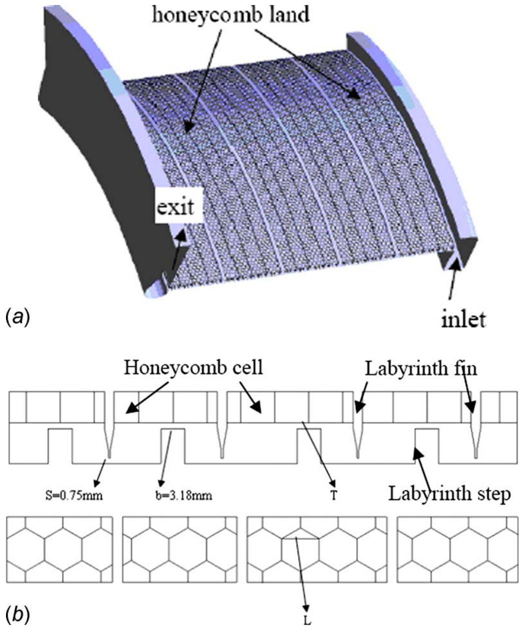

Fig. 7 Configuration and geometrical parameters of the labyrinth honeycomb seal

Downloaded 02 Jun 2010 to 171.66.16.96. Redistribution subject to ASME license or copyright; see http://www.asme.org/terms/Terms_Use.cfm

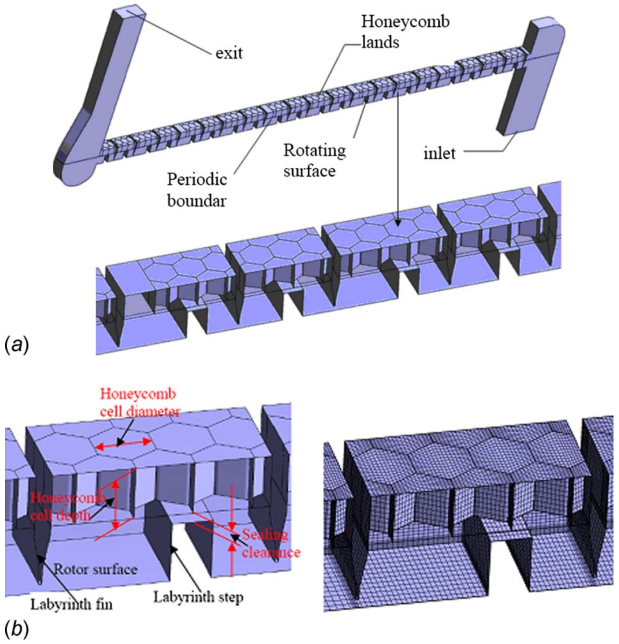

Fig. 8 Boundary condition definitions and the local grid

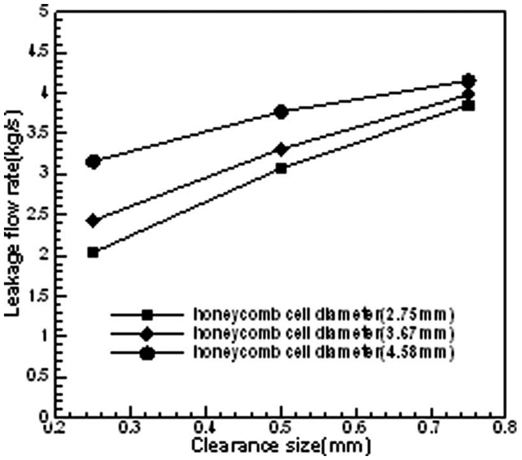

Fig. 10 Leakage flow rate with different sealing clearance sizes (D=4.26 mm)

3.2 Numerical Approach. Since the flow in both the labyrinth smooth seal and labyrinth honeycomb seal is typically three-dimensional (turbulence due to the structure and flow conditions, and there exists a high relative rotation speed), it is necessary to solve 3D Reynolds-averaged Navier–Stokes (RANS) equations to analyze the flow patterns, and to predict the leakage flow rate of the seals.

A multiblock structured grid was generated for the computational case. In order to study the leakage flow characteristics for the labyrinth smooth seal and labyrinth honeycomb seal, the commercial finite element code, CFX5.7 [21], was used. This software solves the compressible time-averaged RANS equations. Additionally, a second order high resolution discretization scheme was used. The turbulence characteristics of the flow are modeled by the standard $k-\varepsilon$ equations. The scalable logarithmic wall func-

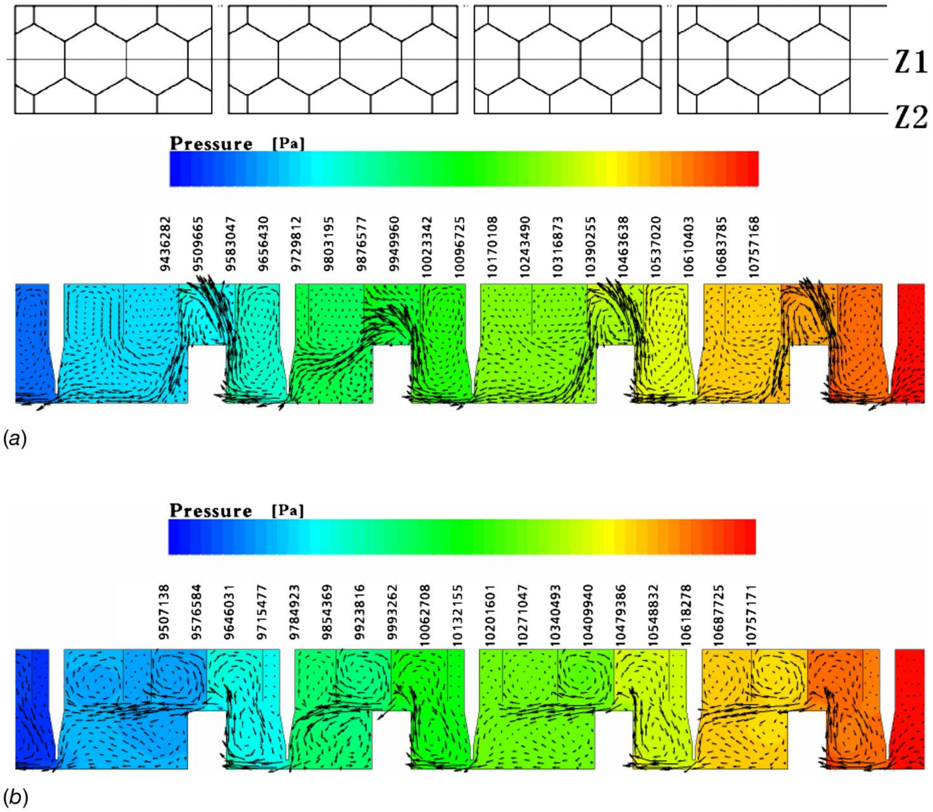

Fig. 9 Flow fields in the labyrinth honeycomb seal at two sections at the designed flow condition (T=0.75 mm, L=4.58 mm, and D=4.26 mm)

Downloaded 02 Jun 2010 to 171.66.16.96. Redistribution subject to ASME license or copyright; see http://www.asme.org/terms/Terms_Use.cfm

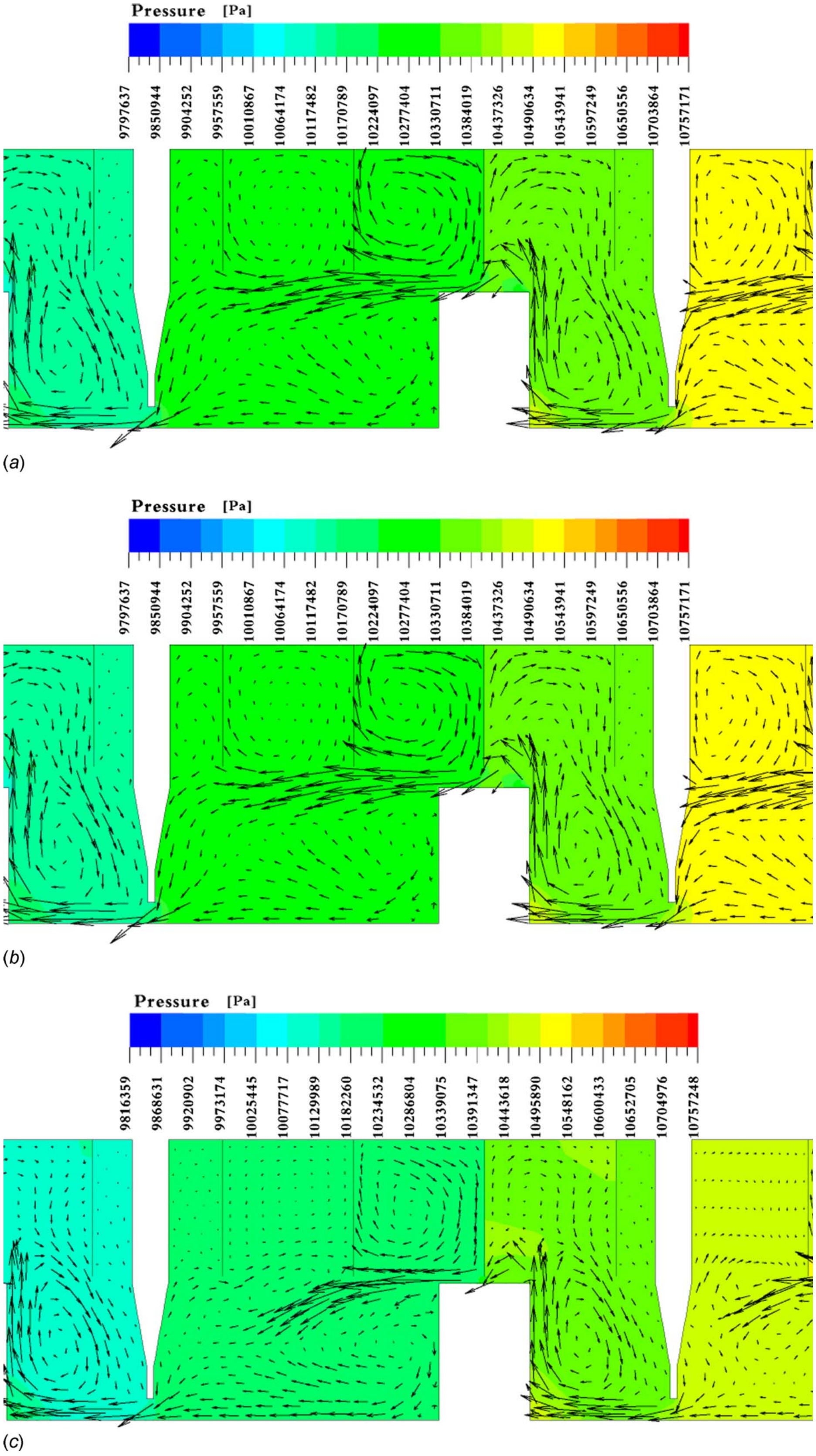

Fig. 11 Static pressure contours and velocity distributions in the labyrinth honeycomb seal with different sealing clearance sizes ($L=4.58$ mm, $D=4.26$ mm): (*a*) $T=0.75$ mm, (*b*) $T=0.05$ mm, and (*c*) $T=0.25$ mm

Downloaded 02 Jun 2010 to 171.66.16.96. Redistribution subject to ASME license or copyright; see http://www.asme.org/terms/Terms_Use.cfm

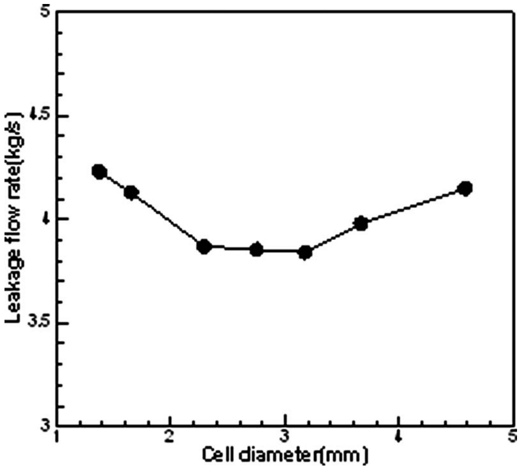

Fig. 12 Leakage flow rate with different honeycomb cell diameters (T=0.75 mm, D=4.26 mm)

tion was used to describe the near wall velocity. The scalable logarithmic wall function is utilized when the $y+$ is greater than 11.06, according to the CFX user guide. The maximum $y+$ in the present honeycomb seal simulation is about 200. The $y+$ criterion is met over almost the entire wall region. The boundary conditions and numerical methods are listed in Table 1. The ideal gas setting was used in this numerical model. Figure 3 shows the boundary conditions defined for the labyrinth smooth seal and the labyrinth honeycomb seal. In addition, the local computational grid for the labyrinth honeycomb seal is given in Fig. 3(*b*). In this simulation, a periodic boundary condition was assumed in the circumferential direction. In the flow direction, specifications at the flow inlet and exit boundaries were needed. The inlet boundary was placed at the seal entrance, and total pressure, total temperature, and turbulence quantities were defined, while the averaged static pressure was specified at the outlet of the seal. The stationary walls were defined to be adiabatic. The desired convergence target of each simulation was that the root mean square (rms) residuals of the momentum and mass equations, energy equations, and turbulence equations reached (or were even lower than) 10^{-6}.

3.3 Discharge Coefficients. To compare the experimental data, a dimensionless discharge coefficient C_D was defined to quantify the leakage behavior. Equations (1) and (2) is adopted from Ref. [6], as follows:

$$C_D = \dot{m}/\dot{m}_{\text{ideal}} \tag{1}$$

where the leakage mass flow rate $\dot{m}$ is taken from the CFD analysis, and $\dot{m}_{\text{ideal}}$ stands for a theoretical mass flow for isentropic conditions

$$\dot{m}_{\text{ideal}} = \frac{p_1 A}{\sqrt{T_1}} \sqrt{\frac{2k}{R(k-1)}\left[\left(\frac{1}{\pi}\right)^{2/k} - \left(\frac{1}{\pi}\right)^{k+1/k}\right]} \tag{2}$$

In this formula, π represents the ratio of the inlet to outlet pressure. The cross sectional area of the gap is calculated as $A = B \cdot s$

The discharge coefficients of two cases at different pressure ratios are calculated using Eq. (1). The leakage mass flow rate $\dot{m}$ is calculated through the sealing clearance by summing the dot product of the density times the velocity vector and the area projections over the faces of the inlet or exit boundary. The specified formulation of $\dot{m}$ is described by the following equation. CFX calculates the inflow and outflow mass flow using Eq. (3) in its postprocessing

$$\dot{m} = \int \rho \vec{v} \cdot d\vec{S} = \sum \rho_i \vec{v}_i \cdot \vec{S}_i \tag{3}$$

To compare the leakage performance between the labyrinth smooth seal and labyrinth honeycomb seal, the leakage increase parameter ξ was used, according to Schramm et al. [6]. The leakage increase parameter was defined as follows:

$$\xi = \frac{C_{D,\text{HC}}}{C_{D,\text{SMOOTH}}} \tag{4}$$

where $C_{D,\text{HC}}$ and $C_{D,\text{SMOOTH}}$ are the dimensionless discharge coefficient of the labyrinth honeycomb seal and labyrinth smooth seal, respectively.

3.4 Numerical Method Validation. The geometrical parameters of the labyrinth and honeycomb seal is adopted from Ref. [6]. Three sizes of clearance of the computational seal equals $s1 = 1.204$ mm, $s2 = 1.988$ mm, and $s3 = 3.192$ mm, respectively. Figure 4 shows the leakage flow pattern in the labyrinth smooth seal. The present numerical result is in good agreement with the experimental data. As shown in Fig. 4, the fluid passes the labyrinth gap, and impinges on the step. The jet is then deflected by almost 90 deg, and directed towards the bottom of the labyrinth chamber beneath the step. Inside the cavity, the jet separates two counter-rotating and equally sized recirculation zones. The comparison of the leakage flow rate between the experimental data and numerical results for labyrinth smooth seal is given in Fig. 5. The leakage increase parameter between the experimental data and calculated results for the labyrinth honeycomb seal is shown in Fig. 6. The reliability and accuracy of the utilized numerical approach is demonstrated in Figs. 5 and 6.

4 Results and Discussions

On the basis of the accuracy and reliability of the utilized numerical approach, the effects of sealing clearance sizes, honeycomb cell sizes, rotational speed, and pressure ratios on the leakage performance of the labyrinth honeycomb seal were calculated and are discussed in detail.

4.1 Problem Description. Figure 7 shows the configuration of the shaft labyrinth honeycomb seal of steam turbines. The labyrinth and honeycomb seal diameter is 907.78 mm. The sealing clearance size s between the labyrinth fins and the rotor surface is 0.75 mm. The height and width of the labyrinth step is designed as H=4.78 mm and b=3.18 mm, respectively. The honeycomb lands are installed at the stator component between neighboring labyrinth fins of the labyrinth seal. To investigate the effect of sealing clearance sizes on the leakage performance, the sealing clearance size between the honeycomb lands and labyrinth step of the rotor surface varied as T=0.75 mm, T=0.5 mm, and T=0.25 mm in this work. At the fixed sealing clearance T=0.75 mm and the honeycomb cell depth D=4.26 mm, seven sizes of honeycomb cell diameters are utilized to study the cell diameter effects on the flow fields. In addition, at the sealing clearance T=0.75 mm and the honeycomb cell diameter L=4.58 mm, five sizes of honeycomb cell depths were used to study the leakage flow fields. Moreover, the effects of the rotation speed and pressure ratios on the leakage performance of the labyrinth honeycomb seal were also investigated at the constant sealing clearance and honeycomb cell sizes, respectively.

The boundary condition definition and local computational grid is shown in Fig. 8. A multiblock structural grid was generated in the labyrinth honeycomb seal for numerical computation. The averaged mesh size for the honeycomb seal simulation is about 1,000,000. The mesh size is set up at about 800,000 for the small-

Downloaded 02 Jun 2010 to 171.66.16.96. Redistribution subject to ASME license or copyright; see http://www.asme.org/terms/Terms_Use.cfm

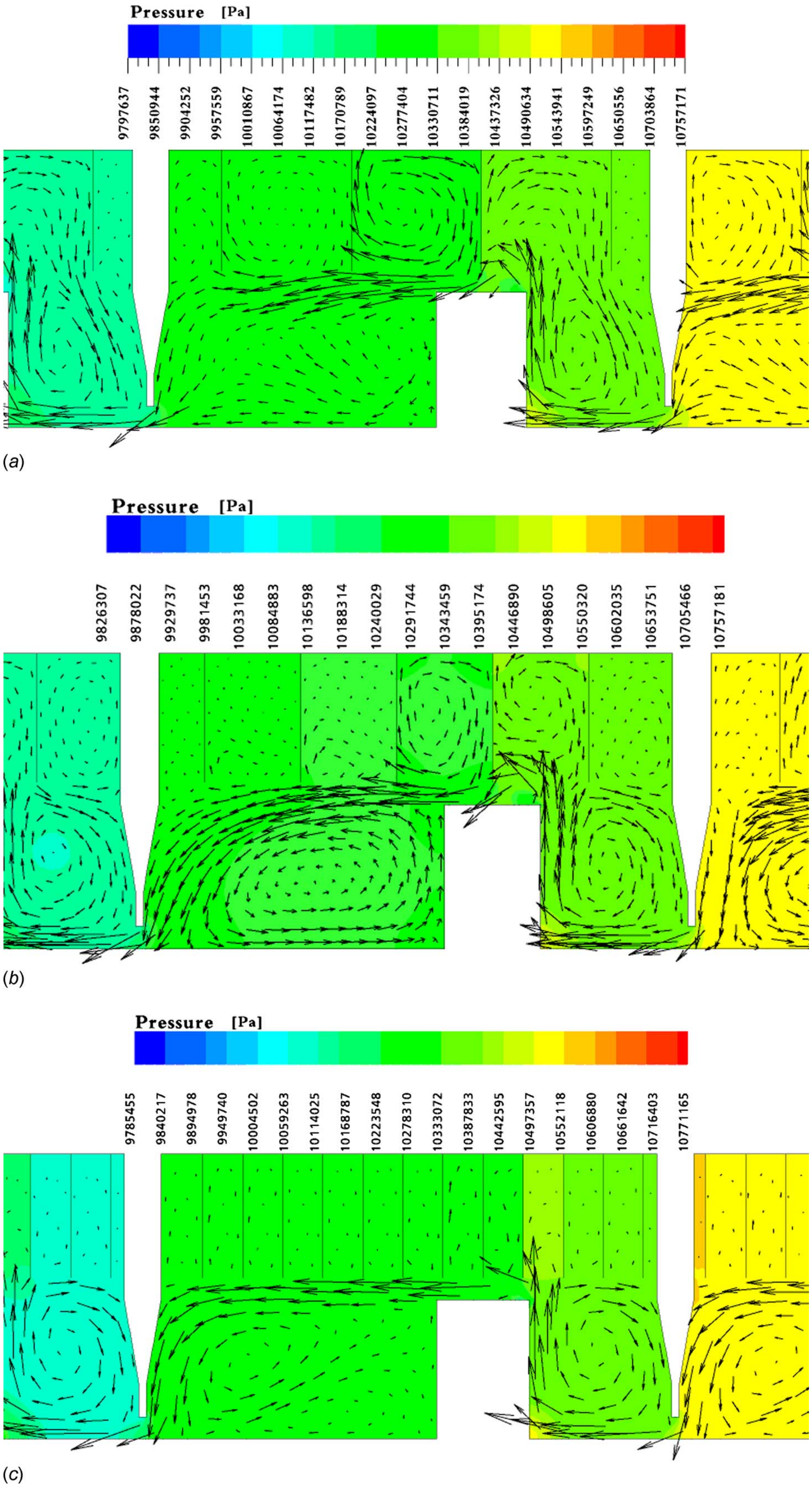

(*a*)

(*b*)

(*c*)

Fig. 13 Static pressure contours and velocity distribution in the labyrinth honeycomb seal with different cell diameters ($T=0.75$ mm, $D=4.26$ mm): (*a*) $L=4.58$ mm ($L/b=1.44$), (*b*) $L=3.178$ mm ($L/b=1.0$), and (*c*) $L=1.37$ mm ($L/b=0.43$)

Downloaded 02 Jun 2010 to 171.66.16.96. Redistribution subject to ASME license or copyright; see http://www.asme.org/terms/Terms_Use.cfm

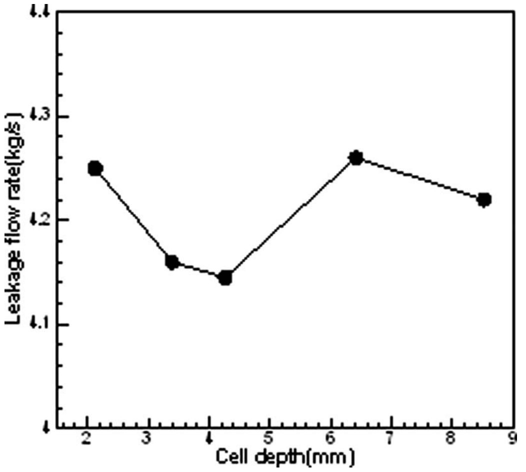

Fig. 14 Leakage flow rate with different honeycomb cell depths ($L=4.58$ mm, $T=0.75$ mm)

est clearance size, and 1,200,000 for the largest clearance size of the honeycomb seal. The same numerical approach delineated above was utilized. At the designed flow condition, a total pressure of 10.757 MPa, and a total temperature of 752.37 K, are given at the inlet. The outlet static pressure is 2.8512 MPa. The rotation speed at the designed condition is set at 3000 rpm. The honeycomb lands and labyrinth fins are defined as the static wall boundary. In addition, the rotor surface is set to be the rotating wall boundary and equals 3000 rpm at the designed flow condition. Each case of the honeycomb seal is conducted on a personal computer with CPU 2.40 GHz and 8G memory. It took about 48 h for each case computation in this work.

Figure 9 shows the computed flow field in the labyrinth honeycomb seal at two lateral positions, $z1$ and $z2$, under the designed flow condition. The gap size was fixed at $T=0.75$ mm. The honeycomb cell diameter and depth were defined as $L=4.58$ mm and $D=4.26$ mm, respectively. Inside each honeycomb cell cavities, recirculation zones occur that are driven by the viscous shear layer at the opening honeycomb cell. The intensity and recirculation flow pattern in each honeycomb cell is influenced by the clearance size and cell geometrical parameters. Further discussion is to be given in later computations. At the lateral position $z1$ where the section is centered at the computational region, the leakage jet impinges into the bottom of the honeycomb cell, and forms a strong clockwise vortex inside the honeycomb cell where the honeycomb cell is located upon the labyrinth step. At the lateral position $z2$ where the section is located at the periodic boundary of the computational region, a different leakage jet pattern is observed, compared with position $z1$. A recirculation zone is observed within each honeycomb cell, and the transfer of the kinetic energy of the leakage jet into heat energy also occurs here. The pressure drop across the labyrinth honeycomb seal is due to this flow pattern. Different honeycomb cell cavity sizes are observed at position $z2$. Thus, the detailed flow pattern in the computed labyrinth honeycomb seals is to be discussed at position $z2$ for each case.

4.2 Effects of Sealing Clearance. Three sizes of sealing clearance between the honeycomb cell and the labyrinth step were calculated to investigate the effects on the leakage characteristics. The honeycomb cell depth was fixed at $D=4.26$ mm. Three honeycomb cell diameters with $L=4.58$ mm, $L=3.67$ mm, and $L=2.75$ mm were studied under three gap sizes. Comparison of the leakage flow rate among the three clearance sizes for the different honeycomb cell diameters is given in Fig. 10. A similar variation in the trend of the clearance size on the leakage flow rate of the labyrinth honeycomb seal is observed. For the fixed honeycomb cell diameter, the leakage flow rate increases with increasing clearance size. According to Fig. 10, the effect of the intensity of the gap size on the leakage flow rate at a small cell size ($L=2.75$ mm) is greater than that at a large cell size ($L=4.58$ mm). For the fixed honeycomb cell diameter, the leakage flow rate increases with increasing clearance size.

Figure 11 shows the static pressure contours and velocity distribution under three different gaps in the local labyrinth honeycomb seal with a 4.58 mm cell diameter and a 4.26 mm cell depth. As to the smallest gap size, $T=0.25$ mm, the angel of the velocity vector toward and away from the honeycomb land (Fig. 11(*c*)) is greater than that of the gap size $T=0.75$ mm (Fig. 11(*a*)). The greater angle of leakage velocity vector at the smallest gap leads to a more distinct deflection of the leakage flow, and impinges on the bottom of the labyrinth cavity directly downstream of the fin tip. The clockwise recirculation zone is observed within each honeycomb cell. The recirculation inside two honeycomb cells located upon the labyrinth step is more obvious than that of other neighboring cells. The leakage jet velocity increases with the increasing size of the gap between the honeycomb cell and the labyrinth step. This results in an increase in the leakage flow rate. A similar flow pattern inside the honeycomb cell chamber is observed for the three gap sizes, according to Fig. 11.

4.3 Effects of Honeycomb Cell Diameter. To investigate the effects of honeycomb cell diameter on the leakage performance, seven sizes of cell diameters were calculated for the fixed clearance size ($T=0.75$ mm) and cell depth ($D=4.26$ mm). Seven dimensionless honeycomb cell diameters L/b with 1.44, 1.15, 1.0, 0.86, 0.72, 0.52, and 0.43 were calculated. The specified honeycomb cell diameter is determined to ensure integral numbers of honeycomb cells along the circumferential direction in the stator component of the studied labyrinth seal.

Figure 12 shows the effect of the cell diameter on the leakage performance of the labyrinth honeycomb seal. During the variation of the cell diameter from 4.58 mm ($L/b=1.44$) to 3.178 mm ($L/b=1.0$), the leakage flow rate decreased with the decrease in

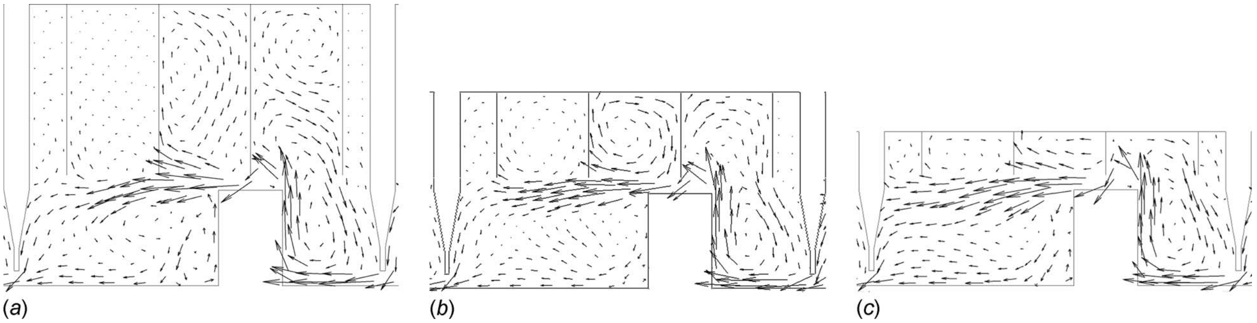
(*a*) (*b*) (*c*)

Fig. 15 Velocity distribution in the labyrinth honeycomb seal with different cell depths ($L=4.58$ mm, $T=0.75$ mm)

Downloaded 02 Jun 2010 to 171.66.16.96. Redistribution subject to ASME license or copyright; see http://www.asme.org/terms/Terms_Use.cfm

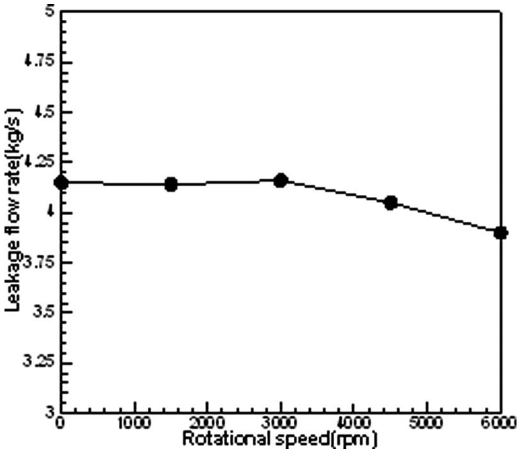

Fig. 16 Leakage flow rate at different rotation speeds (L =4.58 mm, T=0.75 mm, D=4.26 mm)

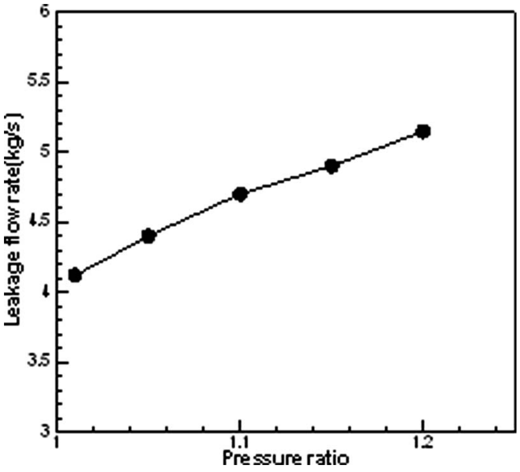

Fig. 18 Leakage flow rate at different pressure ratios (L =4.58 mm, T=0.75 mm, D=4.26 mm)

the cell diameter. However, the leakage flow rate increased with decreasing cell diameter in the range from 3.178 mm ($L/b=1.0$) to 1.37 mm ($L/b=0.43$). That is to say, the leakage flow rate obtains the minimum value at the cell diameter equal to the labyrinth step ($L/b=1$) in seven point calculations. The reason for this is interpreted using the flow pattern in each cell diameter of the labyrinth honeycomb seal.

The flow pattern in three typical cell diameter labyrinth seals is shown in Fig. 13. As shown in Fig. 13(*a*), the leakage jet from the gap between the labyrinth fin and the rotor surface forms a main anticlockwise recirculation zone. The intensity of the recirculation zone inside the cell downstream of the labyrinth fin becomes very weak. In addition, the jet from the clearance between the honeycomb land and the labyrinth step forms a clockwise recirculation zone within the cell. The intensity of the vortex in the downstream labyrinth step becomes weak, due to the interaction of the jet with the vortex inside the large diameter cell cavity. When the cell diameter equals the labyrinth step width, the flow pattern changed greatly, as shown in Fig. 13(*b*). The jet forms two anticlockwise recirculation regions and a clockwise recirculation zone downstream of the labyrinth fin. Further, a strong anticlockwise recirculation region is generated in the chamber downstream of the labyrinth step, compared with that seen in Fig. 13(*a*). The strong recirculation dissipated the kinetic energy of the leakage flow into heat energy. Correspondingly, the leakage flow rate became smaller than that of the 4.58 mm cell diameter case. The intensity of recirculation inside each cell and cavity becomes weak when the cell diameter decreases to 1.37 mm, as shown in Fig. 13(*c*). Therefore, the leakage flow rate is larger than that of the case with the 3.178 mm cell diameter.

4.4 Effects of Honeycomb Cell Depth. Five sizes of cell depth were utilized to investigate its effects on the leakage performance of the labyrinth honeycomb seals with fixed cell diameter and gap size. The specified honeycomb cell depth was set to be 1.86, 1.4, 0.93, 0.74, and 0.47, divided by cell diameter L. Figure 14 shows the dependence of the leakage flow rate upon the cell depth with a fixed cell diameter and clearance size. When the cell depth equals 4.26 mm ($D/L=0.93$), the leakage flow rate obtains a minimum value, according to Fig. 14. The velocity vector distribution inside the honeycomb seal with three typical cell depths is shown in Fig. 15. The leakage jet generates the clockwise recirculation within each cell, and the corresponding kinetic energy is transferred into heat energy due to the recirculation flow in the case of $D/L=0.93$. The recirculation pattern inside the cell is strongly influenced by the cell depth, according to Fig. 15. Regardless of whether D/L is greater than 0.93 or less than 0.93, the kinetic energy of the jet is not sufficiently transferred into heat energy because of recirculation patterns inside each cell. The leakage flow rate is the smallest in the case of $D/L=0.93$ among the five studied cases.

4.5 Effects of Rotational Speed. Figure 16 shows the effects of rotational speed on the leakage flow rate of the labyrinth honeycomb seal with a constant honeycomb cell and clearance size. The leakage flow rate remains approximately constant in the range of 0–3000 rpm. The leakage flow rate decreases with increasing rotation speed when the rotational speed is greater than 3000 rpm. The corresponding reason is illustrated according to the velocity vector distribution inside the seal, according to Fig. 17. A similar flow pattern is observed for the case of rotation speeds of 0 rpm and 3000 rpm. The intensity of recirculation inside the chamber downstream of the labyrinth step in the case of 6000 rpm is stronger than that at 0 rpm and 3000 rpm. The larger viscous shear stress is generated to dissipate the jet kinetic energy efficiently due to the large rotation speed. This results in a decrease in the leakage flow rate.

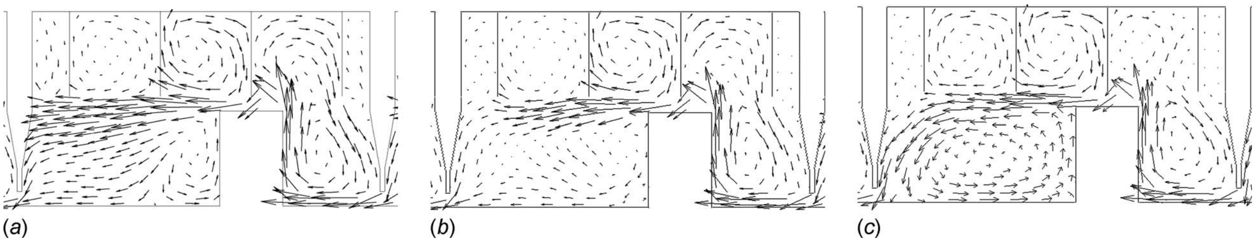
(*a*) (*b*) (*c*)

Fig. 17 Velocity distribution in the labyrinth honeycomb seal at different rotation speeds (L=4.58 mm, T=0.75 mm, D =4.26 mm)

Downloaded 02 Jun 2010 to 171.66.16.96. Redistribution subject to ASME license or copyright; see http://www.asme.org/terms/Terms_Use.cfm

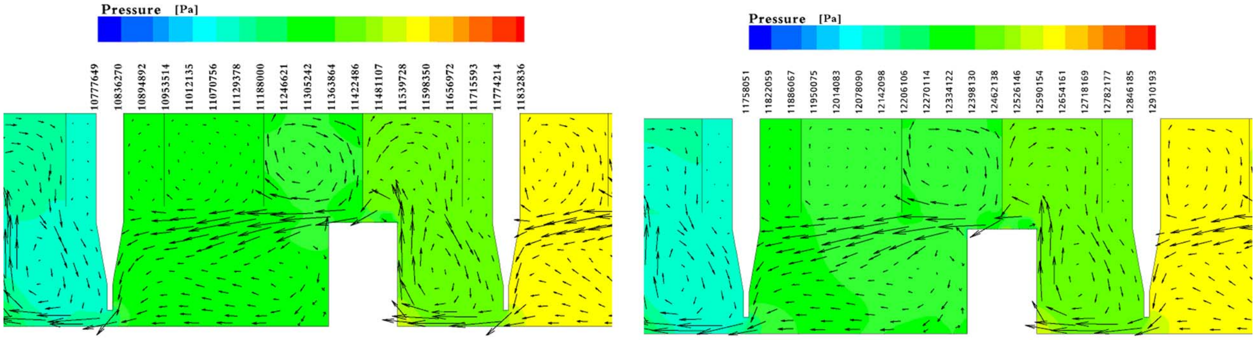

(*a*) (*b*)

Fig. 19 Static pressure contours and velocity distribution in the labyrinth honeycomb seal at different pressure ratios ($L=4.58$ mm, $T=0.75$ mm, $D=4.26$ mm)

4.6 Effects of Pressure Ratio. The dependence of the leakage flow rate upon the pressure ratio of the labyrinth honeycomb seal in the case of fixed cell and clearance size is shown in Fig. 18. The leakage flow rate increases approximately linearly as the pressure ratio increases. The computed flow fields of the labyrinth honeycomb seal with two different pressure ratios are shown in Fig. 19. The pressure decreases along the chamber step by step. The low speed fluid is filled within the honeycomb cells in the forms of vortices, which push the chamber flow to the seal bottom or back into the cells. According to Fig. 19, the influence of the pressure ratio on the leakage flow pattern is omitted. The leakage flow rate increases linearly with the increasing pressure ratio at the fixed geometrical parameters of the labyrinth honeycomb seal.

5 Conclusions

Based on Schramm's experimental data [6], a three-dimensional RANS solution with the commercial CFD software, CFX, was utilized to analyze the influence of clearance size, cell size, pressure ratio, and rotation speed on leakage performance in the labyrinth honeycomb seal for steam turbines.

As for the clearance size factor, the computed leakage flow rate increases with increasing sealing clearance for three kinds of cell diameters in the designed condition.

As for the cell diameter factor, the computed leakage flow rate shows that the labyrinth honeycomb seal displays optimum leakage performance when the cell diameter equals the labyrinth step width. The leakage flow rate becomes large when either the cell diameter is greater or smaller than the corresponding labyrinth step width.

As for the cell depth factor, the investigated labyrinth honeycomb seal with the case of $D/L=0.93$ shows better sealing performance than that of other cases. The strongest intensity of the formed vortex inside the cell was observed in the case of $D/L=0.93$. The obtained results show that the studied labyrinth honeycomb seal displays optimum sealing performance in the case of $L/b=1$ and $D/L=0.93$ under the designed condition.

The leakage flow rate remains approximately constant with the rotational speed variation of 0–3000 rpm. The leakage flow rate decreases with the increasing rotation speed when the rotational speed is greater than 3000 rpm. The computed leakage flow rate increases with increasing pressure ratio at the fixed geometrical parameter of the labyrinth honeycomb seal. The influence of the pressure ratio on the leakage flow pattern is nearly negligible.

Acknowledgment

J.L. is grateful to the Program with Grant No. 50506023 supported by National Natural Science Foundation and New Century Excellent Talents in University with Grant No. NCET-07-0669.

Nomenclature

A = area
b = labyrinth step width
B = seal circumference
C_D = discharge coefficient
D = honeycomb cell depth
h = fin height
H_{HC} = honeycomb cell height
H = seal step height
k = ratio of specific heats
L = honeycomb cell diameter
$\dot{m}$ = mass flow rate
$\dot{m}_{\mathrm{ideal}}$ = ideal mass flow rate
n = rotation speed
p_1 = upstream pressure
p_2 = downstream pressure
R = specific gas constant
s = sealing clearance between fin and rotor surface
t = fin pitch
T = sealing clearance between honeycomb land and step
π = the ratio of the inlet to outlet pressure p_1/p_2
ξ = leakage increase parameter $C_{D,\mathrm{honeycomb}}/C_{D,\mathrm{smooth}}$
ρ = fluid density

References

[1] Lakshminarayana, B., 1996, *Fluid Dynamics and Heat Transfer of Turbomachinery*, Wiley, New York, pp. 339–347.

[2] Chupp, R. E., Hendricks, R. C., Lattime, S. B., and Steinetz, B. M., 2006, "Sealing in Turbomachinery," J. Propul. Power, **22**(2), pp. 313–349.

[3] Chupp, R. E., Ghasripoor, F., Turnquist, N. A., Demiroglu, M., and Aksit, M. F., 2002, "Advanced Seals for Industrial Turbine Applications: Dynamic Seal Development," J. Propul. Power, **18**(6), pp. 1260–1266.

[4] Wittig, S., Dorr, L., and Kim, S., 1983, "Scaling Effects on Leakage Losses in Labyrinth Seals," Trans. ASME: J. Eng. Gas Turbines Power, **105**, pp. 305–309.

[5] Childs, D. W., 1993, *Turbomachinery Rotordynamics Phenomena, Modeling, and Analysis*, Wiley, New York, pp. 290–294.

[6] Schramm, V., Willenborg, K., Kim, S., and Wittig, S., 2002, "Influence of Hoeycomb Facing on the Flow Through Stepped Labyrinth Seal," ASME J. Eng. Gas Turbines Power, **124**(1), pp. 140–146.

[7] Denecke, J., Dullenkopf, K., Wittig, S., and Bauer, H.-J., 2005, "Experimental Investigation of the Total Temperature Increase and Swirl Development in Rotating Labyrinth Seals," ASME Paper No. GT2005-68677.

[8] Denecke, J., Färber, J., Dullenkopf, K., and Bauer, H.-J., 2008, "Interdependence of Discharge Behavior, Swirl Development and Total Temperature Increase in Rotating Labyrinth Seals," ASME Paper No. GT2008-51429.

[9] Stoff, H., 1980, "Incompressible Flow in a Labyrinth Seal," J. Fluid Mech., **100**, pp. 817–829.

[10] Soto, E., and Childs, D., 1999, "Experimental Rotordynamic Coefficient Results for a Labyrinth Seal With and Without Shunt Injection and a Honeycomb Seal," ASME J. Eng. Gas Turbines Power, **121**, pp. 153–159.

[11] Stocker, H., Cox, D., Holle, G., 1977, "Aerodynamic Performance of Conven-

Downloaded 02 Jun 2010 to 171.66.16.96. Redistribution subject to ASME license or copyright; see http://www.asme.org/terms/Terms_Use.cfm

tional and Advanced Design Labyrinth Seals With Solid-Smooth, Abradable and Honeycomb Lands," NASA Technical Report No. NASA-CR-135307.

[12] Rhode, D. L., and Allen, B. F., 1998, "Visualization and Measurements of Rub-Groove Leakage Effects on Straight-Through Labyrinth Seals," ASME Paper No. 98-GT-506.

[13] Rhode, D. L., and Allen, B.F., 1999, "Measurement and Visualization of Leakage Effects of Rounded Teeth Tips and Rub-Groove on Stepped Labyrinth Seals," ASME Paper No. 99-GT-377.

[14] Wittig, S., Schelling, U., Jacobsen, K., and Kim, S., 1987, "Numerical Predictions and Measurements of Discharge Coefficients in Labyrinth Seals," ASME Paper No. 87-GT-188.

[15] Choi, D. C., and Rhode, D. L., 2004, "Development of a Two-Dimensional Computational Fluid Dynamics Approach for Computing Three-Dimensional Honeycomb Labyrinth Leakage," ASME J. Eng. Gas Turbines Power, **126**, pp. 794–802.

[16] Chougule, H. H., Ramerth, D., Ramchandran, D., and Kandala, R., 2006, "Numerical Investigation of Worn Labyrinth Seals," ASME Paper No. GT2006-90690.

[17] Yan, X., Li, J., Song, L., and Feng, Z. P., 2008, "Investigations on the Discharge and Total Temperature Increase Characteristics of the Labyrinth Seals With Honeycomb and Smooth Lands," ASME J. Turbomach., **131**(4), p. 041009.

[18] Paolillo, R., Moore, S., Cloud, D., and Glahn, J. A., 2007, "Impact of Rotational Speed on the Discharge Characteristics of Stepped Labyrinth Seals," ASME Paper No. GT2007-28248.

[19] Soemarwoto, B. I., Kok, J. C., de Cock, K. M. J., Kloosterman, A. B., Kool, G. A., and Versluis, J. F. A., 2007, "Performance Evaluation of Gas Turbine Labyrinth Seals Using Computational Fluid Dynamics," ASME Paper No. GT2007-27905.

[20] Chougule, H. H., Ramerth, D., and Ramchandran, D., , 2008, "Low Leakage Designs for Rotor Teeth and Honeycomb Lands in Labyrinth Seals," ASME Paper No. GT2008-51024.

[21] AEA Technology GmbH, 2004, *CFX-TASCflow User Documentation*, AEA Technology, Software Ltd., Waterloo, ON, Canada.

Downloaded 02 Jun 2010 to 171.66.16.96. Redistribution subject to ASME license or copyright; see http://www.asme.org/terms/Terms_Use.cfm

A Method for Forced Response Analysis of Mistuned Bladed Disks With Aerodynamic Effects Included

E. P. Petrov
Department of Mechanical Engineering,
Centre of Vibration Engineering,
Imperial College London,
South Kensington Campus,
London SW7 2AZ, UK
e-mail: y.petrov@imperial.ac.uk

A method has been developed for high-accuracy analysis of forced response levels for mistuned bladed disks vibrating in gas flow. Aerodynamic damping, the interaction of vibrating blades through gas flow, and the effects of structural and aerodynamic mistuning are included in the bladed disk model. The method is applicable to cases of high mechanical coupling of blade vibration through a flexible disk and, possibly shrouds, to cases with stiff disks and low mechanical coupling. The interaction of different families of bladed disk modes is included in the analysis providing the capability of analyzing bladed disks with pronounced frequency veering effects. The method allows the use of industrial-size sector models of bladed disks for analysis of forced response of a mistuned structure. The frequency response function matrix of a structurally mistuned bladed disk is derived with aerodynamic forces included. A new phenomenon of reducing bladed disk forced response by mistuning to levels that are several times lower than those of their tuned counterparts is revealed and explained. [DOI: 10.1115/1.4000117]

1 Introduction

Blades cannot be manufactured, assembled, and operated in a bladed disk perfectly identically. Because of this, industrial bladed disks are inherently mistuned by inevitable scatters of individual blade natural frequencies and mode shapes, scatters of characteristics of blade root joints, and shroud contact interfaces.

Forced response levels of bladed disks are highly sensitive to mistuning. Even small mistuning ranges restricted by manufacturing tolerances can change forced response levels several times. The problem of analyzing mistuned bladed disks has a major practical importance and has been investigated by many authors during the past 40 years (see surveys in Refs. [1–3]). Significant progress has been made recently in developing mistuning analysis methods employing different condensation techniques for detailed bladed disk models with large numbers of degrees of freedom (see Refs. [4–8]).

Most numerical studies of mistuning effects (e.g., Refs. [9–16]) on bladed disk forced response have been made without accounting for the effects coming from unsteady aerodynamic forces applied to vibrating blades: specific type of damping, blade coupling through gas flow, and change in bladed disk modal characteristics compared with those in a vacuum. The studies reported to date indicate that the mistuning has, as a rule, a worsening effect on bladed disk forced response levels, i.e., it increases forced response amplitudes several times compared with amplitudes of a tuned bladed disk. The magnitude of the mistuning amplification factor is dependent on bladed disk design and excitation conditions and can reach (e.g., see Ref. [10]) the theoretical limit $(1+\sqrt{N_B})/2$ derived in Ref. [11] for a bladed disk with N_B blades. The possibility of alleviating the worsening mistuning effect by the introduction of intentional mistuning patterns and strategies is explored in Refs. [12–16].

In contrast to the reported worsening mistuning effect on forced response levels, it is well known that mistuning has a stabilizing effect for flutter (e.g., see Refs. [17–20])

The apparent importance of the aerodynamic effects for mistuned bladed disk forced response stimulated the devolvement of approaches for analysis of combined action of structural and aerodynamic forces during recent years. High-order linearized aerodynamic models together with rather simplified structural models are considered in Refs. [21,22].

In Refs. [23,24], a fundamental modal model (FMM) (as in Ref. [8]), is applied for structural modeling. The aerodynamic coupling coefficients are calculated for full-scale unsteady Reynolds averaged Navier–Stokes (RANS) model by computational fluid dynamics (CFD) methods. The analysis is performed in modal coordinates of a tuned bladed disk and one family of modes is used, which makes the analysis computationally efficient. However, the use of one family of modes restricts applicability of the method to bladed disks with small mechanical coupling, e.g., when the disks are stiff.

High-fidelity structural model and rather simplified one-passage gas-flow model were considered in Ref. [25]. The approach proposed here requires iterative determination of aeroelastic eigenvalues where a gas flow and structural analysis has to be performed on each iteration. The prohibitively large computation expense is expected, if this method is applied to more complex and complete models of gas flow.

In this paper, a new high-fidelity method is proposed, which allows the use of industrial-size sector models of bladed disks for analysis of forced response of mistuned structures.

The method is developed to deal with the problem of large time expense required for the CFD analysis based on nonlinear RANS equations and millions of grid points. Advanced CFD codes (e.g., Ref. [26]) use multiprocessor computer clusters and such CFD analyses become routine in modern industrial practice. Nevertheless, the computational times required for time-domain CFD analysis is still orders of magnitude larger than these needed for the frequency domain analysis of mistuned forced response (e.g., Ref. [5]).

The method allows separation of two types of analyses: (i) CFD analysis and (ii) mistuned forced response analysis. The modal

---

Contributed by the International Gas Turbine Institute of ASME for publication in the Journal of Engineering for Gas Turbines and Power. Manuscript received April 8, 2009; final manuscript received April 15, 2009; published online March 17, 2010. Editor: Dilip R. Ballal.

Copyright © 2010 by ASME

Downloaded 02 Jun 2010 to 171.66.16.96. Redistribution subject to ASME license or copyright; see http://www.asme.org/terms/Terms_Use.cfm

aerodynamic forces are calculated for a structurally tuned structure vibrating with a frequency of interest, usually the excitation frequency. When the CFD analysis is done, the same CFD characteristics can be used for analysis of multitude of differently mistuned bladed disks, including cases of large mistuning where the blade natural frequencies can differ 10–20% from the nominal values.

The novelty of the approach, along with significant differences in the formulation from those used in earlier papers, is in providing new qualities in the mistuned analysis of bladed disks in gas flow. Among these is the capability of high-fidelity bladed disk frequency response function (FRF) matrix calculation with all aerodynamics effects included. Once the matrix is calculated, any structural modification can be applied including those that change significantly the resonance frequencies and mode shapes. This cannot be achieved by the method developed in Refs. [23,24] where only one family of modes is included in the analysis, and as soon as a blade mode shape is changed by a structural modification, the aerodynamic model become inaccurate. It cannot be achieved also by a method presented in Ref. [25] because of large computational expense required in that approach. Another important feature of the new method is the capability to separate fully CFD and structural analysis. The FRF matrix with aerodynamic effects included is determined only once for a nominal bladed disk and then different mistuned bladed disks can be calculated without returning to CFD analysis. This cannot be done in the method described in Ref. [25] where coupled aeroelastic eigenvalue problem is solved iteratively each time.

In distinction to the FMM-based modeling, the method is also more generic and is applicable to cases of high mechanical coupling of blade vibration through a flexible disk and, possibly shrouds, in addition to cases with stiff disks and low mechanical coupling. The interaction of different families of bladed disk modes and frequency veering effects are included in the analysis.

Aerodynamic damping, the interaction of vibrating blades through gas flow and the effects of both major causes of mistuning, (i) structural mistuning and (ii) aerodynamic mistuning, are included in the model. The FRF matrix of a structurally mistuned bladed disk allowing for all effects of aerodynamic forces is derived for both these cases.

The mode shapes and natural frequencies of a bladed disk in vacuum used in the formulation are calculated from sector models of a bladed disk. The formulation developed here can be directly used for analysis of nonlinear vibration of mistuned bladed disks with friction joints by the application of a method developed in Ref. [27], as it is shown in Ref. [28].

Two major cases are foreseen: (i) a case when gas flow affects bladed disk mode shapes and (ii) a case when effects of gas flow on bladed disk mode shapes are not significant.

Numerical investigation of the effects of blade mistuning on forced response characteristics of a blisk with the inclusion of aerodamping and aerocoupling effects has been carried out.

A new phenomenon has been discovered and explained: a reduction by random mistuning forced response levels for mistuned bladed disks to the levels, which are significantly lower than forced response of their tuned counterparts.

2 Equation of Motion for a Mistuned Bladed Disk

For bladed disks, the steady-state forced response amplitudes are mostly of interest and the equation of motion in gas flow can be written in the frequency domain in the form

$$[\boldsymbol{K} + i\boldsymbol{C} - \omega^2\boldsymbol{M}]\boldsymbol{Q} + \boldsymbol{F}(\boldsymbol{Q}) = \boldsymbol{P} \qquad (1)$$

where $\boldsymbol{K}$, $\boldsymbol{C}$, and $\boldsymbol{M}$ are the stiffness, damping, and mass matrices of a mistuned bladed disk; $\boldsymbol{Q}$, $\boldsymbol{F}$, and $\boldsymbol{P}$ are the vectors of complex amplitudes of displacements, aerodynamic, and excitation forces, respectively; $\omega = k\Omega$ is frequency of vibration, excited by kth engine-order (EO) harmonic of excitation, and Ω is the rotation speed of a rotor. For a common case of small vibrations, the aerodynamic forces are linearly dependent on the vibration amplitudes: $\boldsymbol{F}(\boldsymbol{Q}) = \boldsymbol{G}\boldsymbol{Q}$, which gives the following equation:

$$[\boldsymbol{Z}_0 + \delta\boldsymbol{Z} + \boldsymbol{G}]\boldsymbol{Q} = \boldsymbol{P} \qquad (2)$$

where $\boldsymbol{Z}_0 = \boldsymbol{K}_0 + i\boldsymbol{C}_0 - \omega^2\boldsymbol{M}_0$ is the dynamic stiffness matrix of a tuned bladed disk; $\boldsymbol{K}_0$, $\boldsymbol{C}_0$, and $\boldsymbol{M}_0$ are the stiffness, damping, and mass matrices of the tuned bladed disk, and $\delta\boldsymbol{Z}$ is the structural mistuning matrix characterizing distinctions of the mistuned bladed disk from its tuned counterpart.

3 Calculation of Forced Response Amplitudes

As shown in Ref. [5], any structural mistuning matrix can be represented as multiplication of two matrices:

$$\underset{(N\times N)}{\delta\boldsymbol{Z}} = \underset{(N\times n)}{\boldsymbol{E}}\ \underset{(n\times N)}{\boldsymbol{V}} \qquad (3)$$

where $\boldsymbol{V}$ is a matrix constructed from nonzero rows of the mistuning matrix $\delta\boldsymbol{Z}$, $\boldsymbol{E}$ is a matrix comprising zeros and units corresponding to nonzero rows in $\delta\boldsymbol{Z}$, N is the total number of degrees of freedom (DOFs) in the structure, and n is the number of nonzero rows in $\delta\boldsymbol{Z}$.

Applying the approach developed in Refs. [5,10] to the new case considered here, when aerodynamic forces are included, one can write

$$\boldsymbol{Q} = \boldsymbol{Q}_0 - \boldsymbol{A}\boldsymbol{E}\boldsymbol{h} \qquad (4)$$

$$[\boldsymbol{I} + \boldsymbol{V}\boldsymbol{A}\boldsymbol{E}]\boldsymbol{h} = \boldsymbol{Q}_0 \qquad (5)$$

where $\boldsymbol{A} = [\boldsymbol{Z}_0 + \boldsymbol{G}]^{-1}$ is the FRF matrix including the aerodynamic coupling and damping and $\boldsymbol{Q}_0$ is vector of forced response amplitudes; both are determined for a structurally tuned bladed disk; $\boldsymbol{h}$ is an auxiliary vector. It should be noted that, due to the fact that $n \ll N$, the size of matrices in Eqs. (4) and (5) is much smaller than that of the original equation (2) and the condensation achieved here is exact and does not involve any simplifying assumptions.

Equations (4) and (5) allow efficient determination of $\boldsymbol{Q}$ but direct evaluation of the FRF matrix, $\boldsymbol{A}$, cannot be made due to the prohibitively large size of matrices involved when industrial-size finite element (FE) models are involved, which can contain millions of DOFs. Moreover, the aerodynamic forces are calculated by CFD codes (e.g., Ref. [26]) separately from the forced response analysis and in the form different from requested here. In order to achieve high accuracy, these codes use detailed grids and, accordingly, time of calculation required for CFD analysis can be large.

A method developed below for the calculation of the FRF matrix is aimed at fast and accurate high-fidelity forced response analysis of mistuned bladed disks with aerodynamic coupling and damping. The method has the following features.

(i) A FE sector model of a tuned, cyclically symmetric, bladed disk is only required for analysis of a mistuned assembly.
(ii) Effects of structural and aerodynamic mistuning can be modeled with any accuracy required.
(iii) Time-consuming CFD analysis is performed independently of the forced response analysis and only once for all possible structural mistuning patterns and magnitudes.

4 High-Fidelity FRF Matrix Including Structural and Aerodynamic Forces

The FRF matrix has to describe dynamic properties of the structure vibrating in gas flow with high accuracy in order to achieve high-fidelity analysis of the mistuned forced response.

To calculate the FRF matrix with the structural and aerodynamic forces included, a multistage approach is developed.

4.1 Mode Shapes and Frequencies of a Bladed Disk. At first, an eigenvalue and eigenvector problem is solved for a tuned

Downloaded 02 Jun 2010 to 171.66.16.96. Redistribution subject to ASME license or copyright; see http://www.asme.org/terms/Terms_Use.cfm

structure in the absence of the damping and aerodynamic forces. A sector model of a bladed disk is used and the eigenproblem is solved for all possible numbers, k, of nodal diameters, i.e., from 0 to $N_B/2$ (where N_B is the number of blades in a bladed disk analyzed):

$$\boldsymbol{K}_k^S \boldsymbol{\Phi}_k^S = \boldsymbol{M}_k^S \boldsymbol{\Phi}_k^S \boldsymbol{\Xi}_k, \quad k = 0, \ldots, N_B/2 \tag{6}$$

where $\boldsymbol{K}_k^S(N_S \times N_S)$ and $\boldsymbol{M}_k^S(N_S \times N_S)$ are the stiffness and mass matrices of a bladed disk sector. These matrices are, for $k \neq 0, N_B/2$, complex and Hermitian, since the cyclic symmetry boundary conditions are applied (e.g., see Ref. [5]). $\boldsymbol{\Xi}_k(n_m \times n_m) = \mathrm{diag}\{\chi_1, \ldots, \chi_m\}$ is a diagonal matrix of first n_m eigenvalues, which are equal here to natural frequencies squared, $\chi_j = \omega_j^2$. $\boldsymbol{\Phi}_k^S(N_S \times n_m)$ is a matrix constructed from first n_m eigenvectors—mode shapes of the sector, and $N_S = N/N_B$ is the number of sector DOFs. Calculation of eigenvectors and eigenvalues is a standard procedure, which does not represent a difficulty, even when a realistic FE sector model containing large number of DOFs is used. The mode shapes are mass normalized to satisfy the following equation:

$$(\boldsymbol{\Phi}_k^S)^H \boldsymbol{M}_k^S \boldsymbol{\Phi}_k^S = \boldsymbol{I} \tag{7}$$

where $\boldsymbol{I}$ is the identity matrix and H is a superscript indicating a Hermitian conjugate. Mass-normalized mode shapes for a whole bladed disk can be then expressed through sector mode shapes in the following way:

$$\underset{(N \times n_m)}{\boldsymbol{\Phi}_k} = w_k \{ \underset{(N_S \times n_m)}{\boldsymbol{\Phi}_k^S}, e^{ik\alpha} \underset{(N_S \times n_m)}{\boldsymbol{\Phi}_k^S}, \ldots, e^{ik\alpha(N_B - 1)} \underset{(N_S \times n_m)}{\boldsymbol{\Phi}_k^S} \}^T \tag{8}$$

where w_k is the normalization coefficient, which is equal to $\sqrt{N_B}$ for $k=0$ or $N_B/2$ and $\sqrt{N_B/2}$ for all other k values.

It should be noted that the matrix of structural damping, $\boldsymbol{C}_k^S$, is conventionally expressed as a matrix of proportional damping, i.e., as linear combination of stiffness and mass matrix: $\boldsymbol{C}_k^S = i(\eta_K \boldsymbol{K}_k^S + \eta_M \boldsymbol{M}_k^S)$, where η_K and η_M are the damping factors. The proportional damping does not affect mode shapes obtained from Eq. (6) and the matrix of eigenvalues for a damped structure, $\hat{\boldsymbol{\Xi}}_k$, can be expressed by a simple formula through those of an undamped structure: $\hat{\boldsymbol{\Xi}}_k = (1 + i\eta_K)\boldsymbol{\Xi}_k + i\eta_M \boldsymbol{I}$.

4.2 Aerodynamic Coupling and Damping Matrix. The CFD codes calculate aerodynamic forces in time domain and, usually, separately from the structural analysis. These forces can be determined for any given motion of a bladed disk, including a case of harmonic vibrations with a given frequency, ω, i.e., $\boldsymbol{f}(e^{i\omega t}\boldsymbol{Q})$, where $\boldsymbol{Q}$ is a vector of complex amplitudes of structural DOFs.

The vector of complex amplitudes can be expressed through mode shapes of a tuned bladed disk: $\boldsymbol{Q} = \boldsymbol{\Phi} \boldsymbol{c}_Q$. Therefore, to be able to determine the aerodynamic forces for any displacements the complex amplitudes of aerodynamic forces, $\boldsymbol{f}(\boldsymbol{\phi}_j e^{i\omega t})$ are calculated, using an available CFD code, for each mode shape of a structure in vacuum, $\boldsymbol{\phi}_j$, included in the analysis. The vibration frequency is selected to be equal, for all mode shapes analyzed, to that frequency, ω, for which we want to calculate the FRF matrix. These calculations are made with the assumption that structural vibrations are small, and, therefore, the aerodynamic forces generated by these vibrations are close to linear: $\boldsymbol{f}(\varepsilon \boldsymbol{\phi}_j e^{i\omega t}) = \varepsilon \boldsymbol{f}(\boldsymbol{\phi}_j e^{i\omega t})$, even if the nonlinear RANS equations are used for CFD analysis.

A matrix of modal aerodynamic forces, $\boldsymbol{F}$, is then formed from vectors $\boldsymbol{f}(\boldsymbol{\phi}_j e^{i\omega t}) : \boldsymbol{F} = \cup_{j=1}^{n_m} \boldsymbol{f}(\boldsymbol{\phi}_j e^{i\omega t})$. The matrix, $\boldsymbol{G}$, of physical aerodynamic forces can be also derived in order to express the aerodynamic forces through vector $\boldsymbol{Q}$:

$$\boldsymbol{f}(e^{i\omega t}\boldsymbol{Q}) = \boldsymbol{f}(e^{i\omega t}\boldsymbol{\Phi} \boldsymbol{c}_Q) = \boldsymbol{F}\boldsymbol{c}_Q = [\boldsymbol{F}\boldsymbol{\Phi}^H \boldsymbol{M}]\boldsymbol{Q} = \boldsymbol{G}\boldsymbol{Q} \tag{9}$$

where the following expression for the expansion coefficients, $\boldsymbol{c}_Q = \boldsymbol{\Phi}^H \boldsymbol{M} \boldsymbol{Q}$, is used.

The matrix of aerodynamic forces, $\boldsymbol{G}$, is complex and is generally not symmetric. This matrix includes all effects of aerodynamic forces occurring due to blade vibration including aerodamping and blade interaction through gas flow. Yet for large-scale bladed disk models, its calculation is computationally expensive and further derivation avoids the necessity of its explicit determination.

4.3 FRF Matrix for Aerodynamically Tuned Bladed Disk. For an aerodynamically tuned bladed disk, a vector of aerodynamic forces calculated for a mode shape belonging to a family of modes with a selected number of traveling waves, k, is orthogonal to all mode shapes belonging to families of modes with a different number of waves. Hence, matrix $\boldsymbol{F}(\boldsymbol{\Phi})\boldsymbol{\Phi}^H$ in Eq. (9) has block-diagonal form:

$$\underset{(N \times N)}{\boldsymbol{F}(\boldsymbol{\Phi})\boldsymbol{\Phi}^H} = \mathrm{diag}[\boldsymbol{F}(\boldsymbol{\Phi}^s_{-N_B/2})(\boldsymbol{\Phi}^s_{-N_B/2})^H, \ldots, \boldsymbol{F}(\boldsymbol{\Phi}^s_{N_B/2})(\boldsymbol{\Phi}^s_{N_B/2})^H] \tag{10}$$

and, therefore, modes of vibration for a bladed disk in gas flow can be determined for each family of modes corresponding to a chosen number of nodal diameters, k, individually. Moreover, the aerodynamic forces are dependent on the direction of the traveling waves, and, therefore, negative values of EO number, k, corresponding to backward traveling waves have to be considered in addition to positive ones, which correspond to backward traveling waves.

Eigenvalues $\tilde{\boldsymbol{\Xi}}_k$ and eigenvectors $\tilde{\boldsymbol{\Phi}}_k^S$ for a structurally and aerodynamically tuned bladed disk vibrating in the gas flow can be determined from the following equation, formulated for a bladed disk sector model for each family of modes corresponding to engine-order number, k:

$$[\boldsymbol{K}_k^S + i\boldsymbol{C}_k^S + \boldsymbol{G}_k^S]\tilde{\boldsymbol{\Phi}}_k^S = \boldsymbol{M}_k \tilde{\boldsymbol{\Phi}}_k^S \tilde{\boldsymbol{\Xi}}_k, \quad k = -N_B/2, \ldots, N_B/2 \tag{11}$$

The engine-order number, k, can take negative and positive values from $-N_B/2$ to $N_B/2$, which corresponds to mode shapes with backward and forward traveling waves.

Matrices of the bladed disk in vacuum for forward and backward traveling waves are related by the following equations:

$$\boldsymbol{K}_k^S = (\boldsymbol{K}_{-k}^S)^H, \quad \boldsymbol{C}_k^S = (\boldsymbol{C}_{-k}^S)^H, \quad \boldsymbol{M}_k^S = (\boldsymbol{M}_{-k}^S)^H, \quad \boldsymbol{\Phi}_k^S = (\boldsymbol{\Phi}_{-k}^S)^H \tag{12}$$

However, there is no a general relationship between matrices $\boldsymbol{G}_k^S$ and $\boldsymbol{G}_{-k}^S$, which have to be calculated by CFD codes for both traveling wave directions individually.

One can see that in contrast to the eigenproblem for a bladed disk in vacuum described by Eq. (6): (i) an additional term $\boldsymbol{G}_k^S$ describing aerodynamic coupling and damping is introduced and (ii) k takes not only positive but also negative values.

The order of this eigenproblem can be reduced by expressing mode shapes of the bladed disk in gas flow, $\tilde{\boldsymbol{\Phi}}_k^S$, through mode shapes of the bladed disk in vacuum defined by Eq. (6):

$$\tilde{\boldsymbol{\Phi}}_k^S = \boldsymbol{\Phi}_k^S \boldsymbol{c}_k^S \tag{13}$$

Then Eq. (13) is substituted into Eq. (11) and, after simple transformations involving Eq. (9), one can obtain the following eigenvalue problem:

$$[\hat{\boldsymbol{\Xi}}_k + (\boldsymbol{\Phi}_k^S)^H \boldsymbol{F}_k^S]\boldsymbol{c}_k^S = \boldsymbol{c}_k^S \tilde{\boldsymbol{\Xi}}_k \tag{14}$$

where $\boldsymbol{F}_k^S = \boldsymbol{F}(\boldsymbol{\Phi}_k^s)$ is matrix of aerodynamic forces applied to the bladed disk sector, which are produced on a family of modes traveling with k waves.

Downloaded 02 Jun 2010 to 171.66.16.96. Redistribution subject to ASME license or copyright; see http://www.asme.org/terms/Terms_Use.cfm

The solution of this problem provides eigenvalues, $\tilde{\boldsymbol{\Xi}}$, for the bladed disk vibrating in gas flow and corresponding eigenvectors, $\boldsymbol{c}_k^S$. The latter are used in Eq. (13) to recover mode shapes, $\tilde{\boldsymbol{\Phi}}$, of the structure including the effects of gas flow. In order to obtain mass-normalized mode shapes, $\tilde{\boldsymbol{\Phi}}$, the following normalization condition is used to supplement Eq. (14):

$$\boldsymbol{c}_{\boldsymbol{\Phi}}^H \boldsymbol{c}_k^S = \boldsymbol{I} \tag{15}$$

The square root of real parts of the complex eigenvalues $\tilde{\chi}_j$ give natural frequencies of the bladed disk in gas flow and the modal damping factor of a bladed disk in gas flow can be determined for jth mode as $\tilde{\eta}_j = \mathrm{Im}(\tilde{\chi}_j)/\mathrm{Re}(\tilde{\chi}_j)$.

In practically frequent cases, when the aerodynamic forces do not affect significantly mode shapes of a bladed disk, matrix $(\boldsymbol{\Phi}_k^S)^H \boldsymbol{F}_k^S$ in Eq. (14) has strongly dominant diagonal elements and $\boldsymbol{c}_{\boldsymbol{\Phi}} \simeq \boldsymbol{I}$. Therefore, eigenvalues of the structure in gas flow can be determined without solving the eigenproblem and written in the form

$$\tilde{\boldsymbol{\Xi}}_k = \hat{\boldsymbol{\Xi}}_k + \mathrm{diag}\{(\boldsymbol{\phi}_{k1}^S)^H \boldsymbol{f}(\boldsymbol{\phi}_{k1}^S), \ldots, (\boldsymbol{\phi}_{kn_m}^S)^H \boldsymbol{f}(\boldsymbol{\phi}_{kn_m}^S)\} \tag{16}$$

The found eigenvalues and eigenvectors allow calculation of FRF matrix for a bladed disk vibrating in gas flow, without the need for time-consuming matrix inverse $[\boldsymbol{Z}_0 + \boldsymbol{G}]^{-1}$ for each traveling wave number, k. Moreover, there is no need to calculate matrix $\boldsymbol{G}$. These FRF matrices are generated from eigenvalues and eigenvectors of the structure vibrating in gas flow in the form

$$\boldsymbol{A}_k = \tilde{\boldsymbol{\Phi}}_k^S [\tilde{\boldsymbol{\Xi}}_k - \omega^2 \boldsymbol{I}]^{-1} (\tilde{\boldsymbol{\Phi}}_k^S)^H = \sum_{j=1}^{n_m} \frac{\tilde{\boldsymbol{\phi}}_{kj}^S (\tilde{\boldsymbol{\phi}}_{kj}^S)^H}{\tilde{\chi}_{kj} - \omega^2} \tag{17}$$

The FRF matrix for a whole bladed disk can be constructed from the traveling wave FRF matrices derived above, extending the method developed in Ref. [5] for the case when aerodynamic matrices are included. This matrix takes the following form:

$$\boldsymbol{A} = \begin{bmatrix} \boldsymbol{H}_0 & \boldsymbol{H}_1 & \ldots & \boldsymbol{H}_{N_B-1} \\ \boldsymbol{H}_{-1} & \boldsymbol{H}_0 & \ldots & \boldsymbol{H}_{N_B-2} \\ \ldots & \ldots & \ldots & \ldots \\ \boldsymbol{H}_{-N_B+1} & \boldsymbol{H}_{-N_B+2} & \ldots & \boldsymbol{H}_0 \end{bmatrix} \tag{18}$$

where $\boldsymbol{H}_j = 1/N_B \sum_{k=-N_B/2}^{N_B/2} e^{-i\alpha kj} \boldsymbol{A}_k$. In contrast to the case of a FRF matrix obtained without aerodynamic effects, the matrix derived here is, generally, not symmetric and takes into account aerodynamic stiffness, coupling, and damping, which affect differently waves of deformation traveling forward and backward.

4.4 FRF Matrix for Aerodynamically Mistuned Bladed Disk.

For an aerodynamically mistuned bladed disk, the matrix of mode shapes, $\boldsymbol{\Phi}$, in Eq. (9) comprises mode shapes for all engine orders, including cases for backward traveling wave modes ($k < 0$) and forward traveling wave modes ($k > 0$):

$$\underset{(N \times N_B n_m)}{\boldsymbol{\Phi}} = [\boldsymbol{\Phi}_{-N_B/2}, \boldsymbol{\Phi}_{-N_B/2+1}, \ldots, \boldsymbol{\Phi}_0 \ldots, \boldsymbol{\Phi}_{N_B/2-1}, \boldsymbol{\Phi}_{N_B/2}] \tag{19}$$

For this case, all families of modes are coupled and eigenvalues $\tilde{\boldsymbol{\Xi}}$ and eigenvectors $\tilde{\boldsymbol{\Phi}}$ for a structurally tuned and aerodynamically mistuned bladed are determined from the following equation:

$$[\boldsymbol{K} + i\boldsymbol{C} + \boldsymbol{G}]\tilde{\boldsymbol{\Phi}} = \boldsymbol{M}\tilde{\boldsymbol{\Phi}}\tilde{\boldsymbol{\Xi}} \tag{20}$$

Having expressed mode shapes of the bladed disk in gas flow, $\tilde{\boldsymbol{\Phi}}$, through mode shapes of a tuned bladed disk in vacuum, $\boldsymbol{\Phi}$, we have

$$\tilde{\boldsymbol{\Phi}} = \boldsymbol{\Phi}\boldsymbol{c} \tag{21}$$

Using the above equation, Eq. (20) is then transformed to the form:

$$[\hat{\boldsymbol{\Xi}} + \boldsymbol{\Phi}^H \boldsymbol{F}]\boldsymbol{c} = \boldsymbol{c}\tilde{\boldsymbol{\Xi}} \tag{22}$$

where $\hat{\boldsymbol{\Xi}} = \mathrm{diag}[\hat{\boldsymbol{\Xi}}_{-N_B/2}, \ldots, \hat{\boldsymbol{\Xi}}_{N_B/2}]$ is a diagonal matrix of eigenvalues determined for a bladed disk in vacuum combined from values determined from Eq. (6) and with allowing for structural damping. The following normalization condition is applied to obtain mass-normalized mode shapes:

$$\boldsymbol{c}^H \boldsymbol{c} = \boldsymbol{I} \tag{23}$$

The solution of an eigenproblem given by Eqs. (22) and (23) provides eigenvalues, $\tilde{\boldsymbol{\Xi}}$, for the bladed disk vibrating in gas flow, corresponding eigenvectors, $\boldsymbol{c}$, and, therefore, mass-normalized bladed disk mode shapes in aerodynamically mistuned gas flow, $\tilde{\boldsymbol{\Phi}}$. The order of this eigenproblem is reduced to the total number of modes used in the analysis, $N_B n_m \ll N$.

The FRF matrix of a bladed disk vibrating in gas flow is then calculated using these eigenvalues and mode shapes:

$$\boldsymbol{A} = \tilde{\boldsymbol{\Phi}}[\tilde{\boldsymbol{\Xi}} - \omega^2 \boldsymbol{I}]^{-1} \tilde{\boldsymbol{\Phi}}^H = \sum_{j=1}^{N_B n_m} \frac{\tilde{\boldsymbol{\phi}}_j \tilde{\boldsymbol{\phi}}_j^H}{\tilde{\chi}_j - \omega^2} \tag{24}$$

For a case when bladed disks modes are not affected significantly by the aerodynamic coupling and damping forces, the eigenproblem of Eq. (20) is not required to be solved and the effects of aerodynamic mistuning are fully described by the modified eigenvalues, which can be calculated for each family of modes individually:

$$\tilde{\boldsymbol{\Xi}} = \hat{\boldsymbol{\Xi}} + \mathrm{diag}\{\boldsymbol{\phi}_1^H \boldsymbol{f}(\boldsymbol{\phi}_1), \ldots, \boldsymbol{\phi}_{n_m}^H \boldsymbol{f}(\boldsymbol{\phi}_{n_m})\} \tag{25}$$

For aerodynamically mistuned bladed disk, the traveling wave blade motion does not produce pure traveling aerodynamic forces. Because of this, Eq. (25) requires the evaluation of expressions $\boldsymbol{\phi}_j^H \boldsymbol{f}(\boldsymbol{\phi}_j)$, which involves the use of aerodynamic forces calculated over the whole bladed disk and not only for one sector as it is done in Eq. (16) for aerodynamically tuned bladed disk.

Moreover, when the mode shapes are not significantly changed by gas flow, the FRF matrix for the whole bladed disk can be calculated using the expressions derived in Sec. 4.3 (see Eq. (18)). Mode shapes, $\boldsymbol{\Phi}_k^S$, obtained from a sector model of a bladed disk in vacuum are then used and eigenvalues for a bladed disk in gas flow $\tilde{\boldsymbol{\Xi}}_k$ are simply selected from matrix $\tilde{\boldsymbol{\Xi}}$.

4.5 Advantages of the Proposed Approach.

The following remarks need to be noted with respect to the method proposed here for FRF matrix calculation with aerodynamic forces included.

1. The approach proposed here provides a high-fidelity FRF matrix, which takes into account comprehensively the aerodynamic and structural forces and does not use assumptions on the vibration mode shape of a bladed disk. Once the matrix is calculated, a bladed disk with any structural modifications can be analyzed, including those that change significantly the resonance frequencies and mode shapes.
2. The CFD and structural analysis can be performed separately since the method facilitates combining results of these analyses requiring usually very different computational expenses. The FRF matrix with aerodynamic effects included is determined only once for a nominal bladed disk and then different mistuned bladed disks can be calculated without returning to CFD analysis.
3. When all modes included in analysis the approach is exact and, hence, it does not introduce any simplifications or errors in addition to the errors of the original structural and

Downloaded 02 Jun 2010 to 171.66.16.96. Redistribution subject to ASME license or copyright; see http://www.asme.org/terms/Terms_Use.cfm

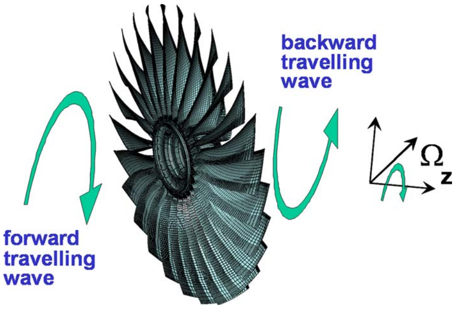

Fig. 1 Forward and backward traveling wave excitations

gas-flow models and solvers. In practical calculations, the number of modes used in the analysis is restricted, but usually high accuracy can be achieved with reasonably small number of modes (example of study of effects of number of modes on accuracy of the modal model is in Ref. [5]).

(4) The approach requires from a CFD solver the calculation of the matrix of modal aerodynamic forces, $\boldsymbol{F}$. This matrix is calculated at the same vibration frequency for all mode shape involved in the analysis. The more computationally expensive matrix $\boldsymbol{G}$ does not need to be evaluated.

(5) Number of modes involved in the matrix of modal aerodynamic forces, $\boldsymbol{F}$, can be selected independently and smaller than the total number of structural modes involved in the mistuning analysis. This allows the reduction in the computational time required for CFD calculations, which are usually the most protracted part of the analysis when high-fidelity nonlinear gas-flow models are applied.

5 Excitation of Forward and Backward Traveling Waves

Aerodynamic pressure, $\boldsymbol{p}(r,z,\varphi)$, caused by the gas flow is inhomogeneous in the circumferential direction, φ, radial direction, r, and axial direction, z. When a bladed disk rotates with rotation speed, Ω, the inhomogeneous aerodynamic pressure, $\boldsymbol{p}(r,z,\varphi+\Omega t)$, produces dynamic excitation forces:

$$\boldsymbol{p}=\sum_{k=0}^{\infty}\boldsymbol{p}_k^c(r,z)\cos(k\Omega t+k\varphi)+\boldsymbol{p}_k^s(r,z)\sin(k\Omega t+k\varphi) \qquad (26)$$

which travel opposite to the rotation direction in the coordinate system fixed to the rotor (see Fig. 1) and therefore such a type of excitation is called a "backward traveling wave" excitation.

It is often assumed that backward traveling aerodynamic excitation can excite in a tuned bladed disk only backward traveling waves and in a mistuned bladed disk, these mode shapes are dominant.

However, excitation by a backward traveling wave can produce, for higher engine orders, such a phase shift between loads applied to neighboring blades which excites the forward traveling waves of displacements and deformations. Direction of the traveling wave of displacements depends on the engine-order number, and for a backward traveling wave excitation, a condition defining the direction of the traveling wave of displacements can be formulated in the following form:

- backward traveling wave for $\mathrm{mod}(k,N_B)\leq N_B/2$
- forward traveling wave for $\mathrm{mod}(k,N_B)>N_B/2$

where $\mathrm{mod}(k,N_B)$ is a remainder of division of k by N_B.

The fact that if engine order k^* excites a backward traveling wave then engine order N_B-k^* produces a forward traveling wave can be seen from Eq. (26) by analyzing a phase shift between neighboring blades. This phase shift is equal to $2\pi k/N_B$ and values $2\pi k^*/N_B>0$ correspond to backward traveling waves. However, even positive engine orders, k, can produce forward traveling wave forced response and, because integer multiples of 2π in a phase are inessential, the engine order N_B-k^* provides phase shift corresponding to a forward traveling wave: $2\pi(N_B-k^*)/N_B=-2\pi k^*/N_B<0$.

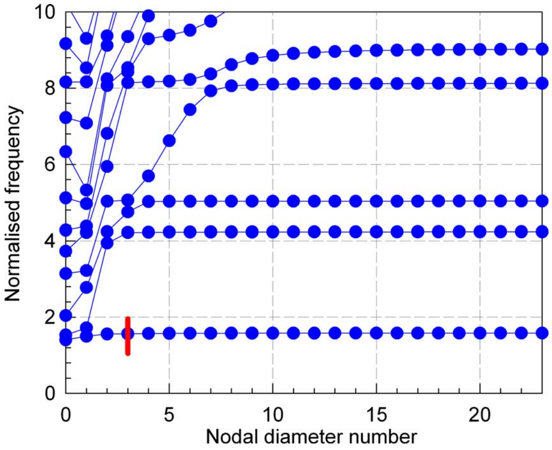

Fig. 2 Natural frequencies of the tuned blisk and a frequency range of interest

It should be noted that the excitation frequency is multiple of the rotation speed, $\omega=k\Omega$, and, hence, the resonance peak vibrations are excited by different engine-order numbers at different rotation speeds.

6 Numerical Studies

The method is implemented in a computer code FORSE developed by the author at Imperial College London. The method and the code have been applied for analysis of different mistuned bladed disks with aerodynamic damping and coupling of blade vibrations. Results of some numerical investigations and validation of the method are reported in Refs. [28–30]. The major focus of a numerical study presented in this paper is to demonstrate and to explain a newly discovered phenomenon, which is strongly associated with the inclusion of aerodynamic effects in the mistuning analysis: a reduction in the forced response amplitude levels in a mistuned bladed disk compared to those for its tuned counterpart.

6.1 A Bladed Disk Analyzed. A forced response analysis is performed for a mistuned blisk for which structural damping is low and the aerodynamic damping is a dominant source of vibration energy dissipation. The blisk contains 46 blades. Natural frequencies and mode shapes have been determined for all possible nodal diameter numbers from 0 to 23 using one bladed disk sector with cyclic symmetry boundary condition applied. The FE model of one sector contains about 146,000 DOFs. For each nodal diameter value, first, 48 modes were determined and used in the analysis for the generation of the FRF matrix of the bladed disk. Lower natural frequencies of the bladed disk are displayed in Fig. 2. Blade frequency mistuning was modeled by mass elements attached to nodes of the FE model (see Ref. [5]). Excitation forces were determined using CFD solver (Ref. [26]) using high-fidelity RANS model with about 350,000 grid points per one passage. Backward traveling wave excitation by −3EO and forward traveling wave excitation by +3EO were of interest. The excitation frequency range includes first flapwise (1F) family of modes and the frequency range analyzed is illustrated in Fig. 2 by a bold vertical line corresponding to 3EO.

Amplitudes of the excitation are assumed to be identical for both traveling wave directions. The aerodamping damping factors and effects of aerocoupling and stiffness on the in-vacuum blisk

Downloaded 02 Jun 2010 to 171.66.16.96. Redistribution subject to ASME license or copyright; see http://www.asme.org/terms/Terms_Use.cfm

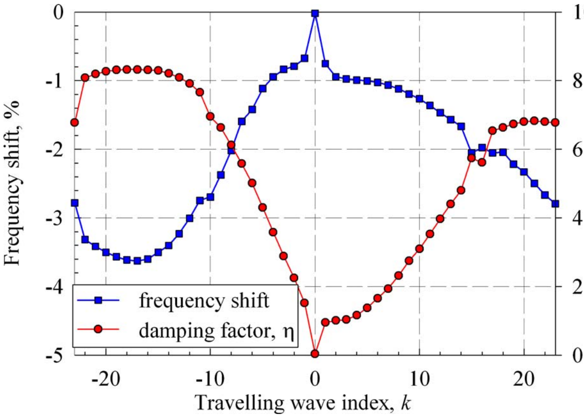

Fig. 3 Resonance frequency shifts and modal damping factors from action of the aerodynamic forces

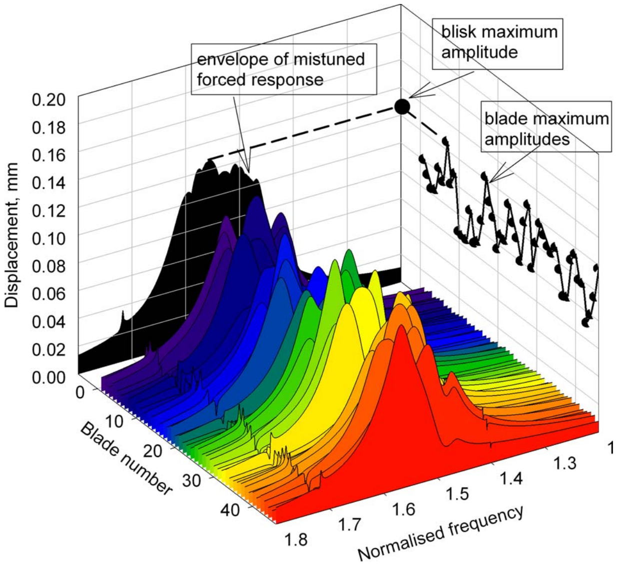

Fig. 5 Forced response for all blisk blades: a case of +3EO

natural frequencies determined from CFD analysis are shown in Fig. 3.

The effects of unsteady aerodynamic forces on mode shapes are neglected for the blisk analyzed. One can see that the modal damping factor for −3EO is close to the minimum among all modal factors and the modal damping factor corresponding to +3EO, although being more than two times larger than for −3EO, also belongs to a group of modes with smaller than average modal damping values.

For the assessment of the effects of magnitudes of blade mistuning on forced response levels, random mistuning patterns were generated with three different ranges of blade mistuning values: (i) 1%, (ii) 5%, and (iii) 10%. For this mistuning generation 1F mode, the blade-alone frequency is controlled. An example of one of such mistuning patterns is shown in Fig. 4.

The forced response is calculated for each blade of the blisk at a node located at blade tip. An example of the blade responses excited by −3EO excitation and calculated for a 5% mistuned pattern is shown in Fig. 5.

In order to provide overall characterization of the forced response for mistuned structures, the following major characteristics, schematically shown in Fig. 5, are used for the following analysis:

- an envelope of forced response searched over all blades for each excitation frequency: $a_{\text{env}}(\omega)= \max\limits_{j=1\ldots N_b} (a_j(\omega))$
- the maximum blade response levels found for each blade over the frequency range, $[\omega^-,\omega^+]$, analyzed: $a_j^{\max} = \max\limits_{\omega\in[\omega^-,\omega^+]} (a_j(\omega))$
- the maximum response level found over all blades and frequencies: $a_{\text{blisk}}^{\max} = \max\limits_{\omega\in[\omega^-,\omega^+]} a_{\text{env}}(\omega) = \max\limits_{j=1,\ldots,N_b} a_j^{\max}$

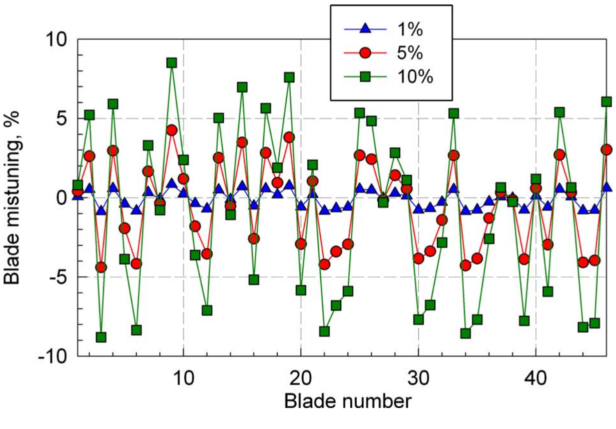

Fig. 4 Random mistuning pattern generated for different levels of mistuning

The mistuned forced response is compared with that of its tuned counterpart $a_{\text{tuned}}^{\max}$, and the amplification coefficient, $a_{\text{blisk}}^{\max}/a_{\text{tuned}}^{\max}$ is used to assess the worsening or improving effect (as it happens here) of mistuning.

6.2 A New Phenomenon: Reduction in Forced Response Levels by Mistuning. Envelopes of the forced response calculated for all mistuned patterns shown in Fig. 4 by +3EO and −3EO excitation are plotted in Fig. 6 together with the forced response of a tuned blisk.

A new phenomenon is observed here: forced response levels for a mistuned bladed disk can be smaller than those of its tuned counterpart by several times for a random mistuning pattern. For the blisk analyzed here, this phenomenon is encountered for the case of forward traveling wave excitation and for ranges of blade frequency scatters 5% and 10%. For these mistuning ranges, the forced response of the mistuned blisk is lower than the forced response of the tuned blisk: (i) by 1.9 times for 5% mistuning and (ii) by 2.4 times for 10% mistuning. For a smaller mistuning range of 1%, the forward traveling wave excitation produces forced response level for the mistuned structure, which is close to the level of its tuned counterpart. In contrast to the case of forward traveling wave excitation, for backward directed excitation, the forced response levels of a mistuned blisk are higher than those of a tuned blisk for all mistuning ranges studied (as found in previous studies).

However, for the backward traveling wave case, increasing the blade mistuning range from 1% to 5% also reduces forced response level by 30% and further mistuning level increase to 10% makes the response level very close to that of the tuned bladed disk. Maximum blade amplitudes are plotted in Fig. 7, where not only a reduction in the response levels due to mistuning can be observed but also a variation in the maximum blade amplitude patterns with a variation in the mistuning range, although the mistuning pattern is unchanged.

The effect of reduction in the forced response levels with the increase in the mistuning intensity is shown in Fig. 8, where the

Downloaded 02 Jun 2010 to 171.66.16.96. Redistribution subject to ASME license or copyright; see http://www.asme.org/terms/Terms_Use.cfm

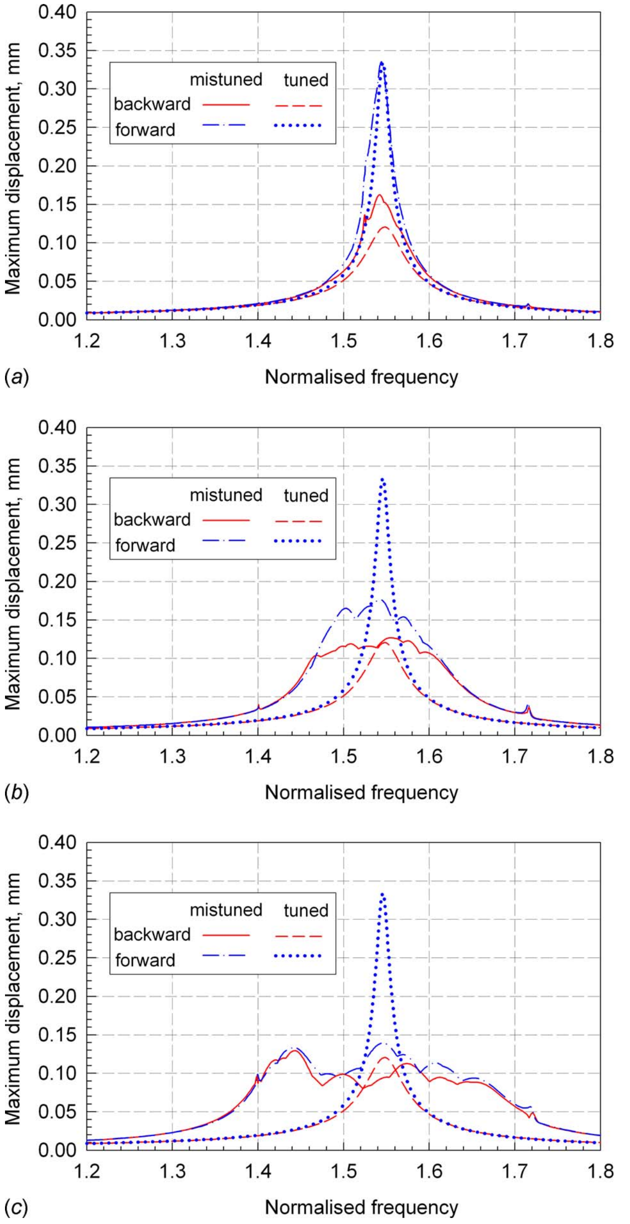

Fig. 6 Envelope of the forced response for tuned and mistuned blisk with different mistuning ranges: (*a*) 1%, (*b*) 5%, and (*c*) 10%

amplification factor is plotted as a function of mistuning range.

In order to demonstrate that the effect of reduction in the forced response level manifests itself for all mistuning patterns and not for one especially generated pattern, the forced response calculations have been performed for other generated randomly mistuning patterns. An example of the amplification factors calculated for ten randomly generated mistuning patterns for three mistuning ranges: ±1%, ±5%, and ±10% are shown in Fig. 9.

These results show that forced response levels of mistuned blisks are significantly lower than those of a tuned blisk for all mistuning patterns generated when forward traveling excitation is applied. The mean values of the amplification factors averaged over all ten mistuning patterns are shown in Table 1. One can see that for forward traveling wave, the averaged forced response level for a mistuned structure is significantly smaller than that of a tuned structure, namely, (i) by 1.7 times for a case of 5% mistuning range and (ii) by 2.2 times for a case of 10% mistuning.

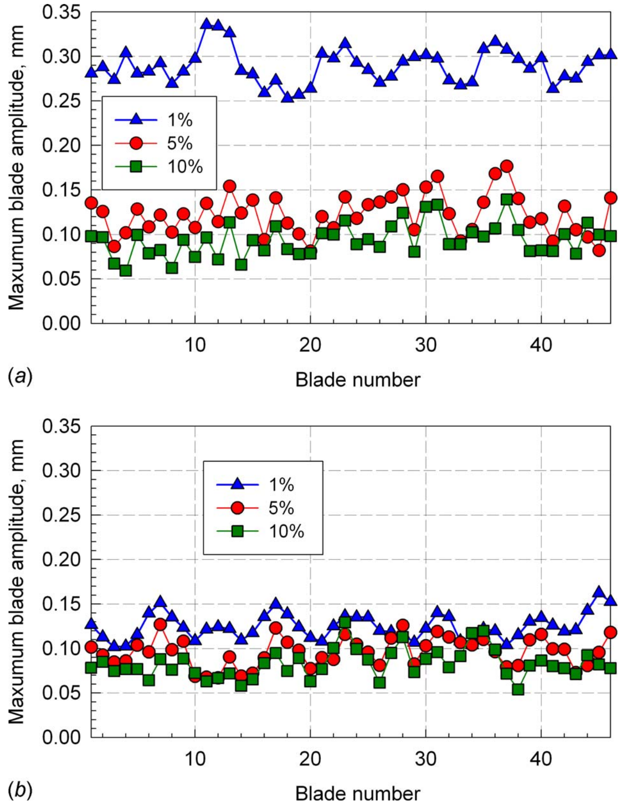

Fig. 7 Blade maximum amplitudes: (*a*) a case of forward traveling wave and (*b*) a case of backward traveling wave

6.3 Discussion of the Phenomenon. The phenomenon of a reduction in the forced response levels for mistuned bladed disks to the levels, which are significantly lower than those of their tuned counterparts, discovered in this study, is new and, to the best author's knowledge, has not been reported in the literature.

To date, there was a point of view, commonly accepted among specialists, that mistuning is generally adverse for forced response levels, although it is favorable for flutter suppression. One of the reasons that this phenomenon has not been probably reported is the absence, until recently, of methods allowing forced response calculation of mistuned bladed disks using realistic structural models and results of CFD calculations. Accordingly, investigations of forced response of mistuned bladed disks have been carried out mostly without accounting for the specific features of the aerodynamic damping and aerocoupling. Studies using an approach developed in Ref. [23] were performed for a bladed disk

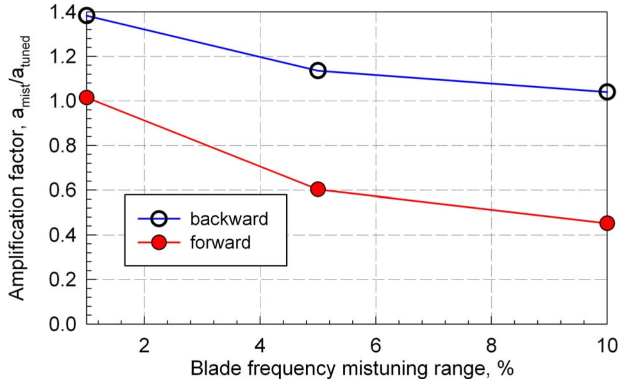

Fig. 8 Dependency of the amplification factor on the mistuning range

Downloaded 02 Jun 2010 to 171.66.16.96. Redistribution subject to ASME license or copyright; see http://www.asme.org/terms/Terms_Use.cfm

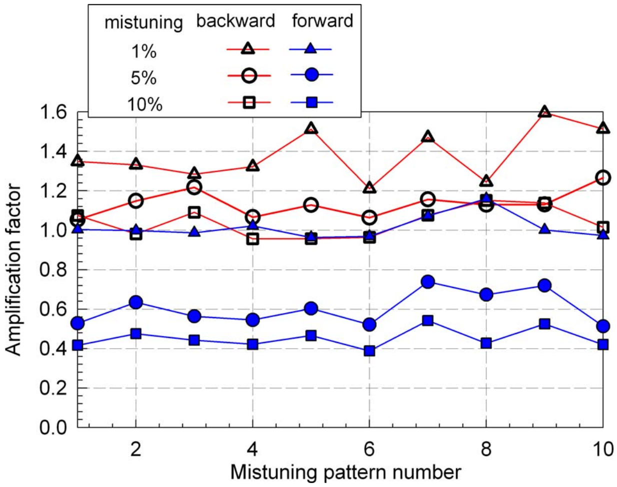

Fig. 9 Amplification factors for cases of forward and backward traveling waves

with a stiff disk and low structural blade vibration coupling. Applications of the method, reported in Refs. [29,30] were aimed at a statistical analysis of the forced response characteristics of mistuned bladed disks.

Due to the novelty of this result, and its high practical importance, there is a need to address a set of questions, such as the following.

- What are the causes and conditions of its appearance?
- Is this phenomenon specific for the blisk analyzed or occurs for the majority of practical bladed disks?
- What are the practical implications?

The answer for the first question follows from the fundamental difference in the forced responses for tuned and mistuned bladed disks.

The effects of gas flow on natural frequencies and mode shapes of a tuned bladed are summarized in Table 2.

For a tuned bladed disk, the traveling wave excitation excites only modes from one family of modes: modes with the same number and the same direction of a traveling wave as the excitation. If, as it happens in the test case considered here, the damping factors for forward and backward traveling waves differ significantly, then the resonance peak forced response levels are also different.

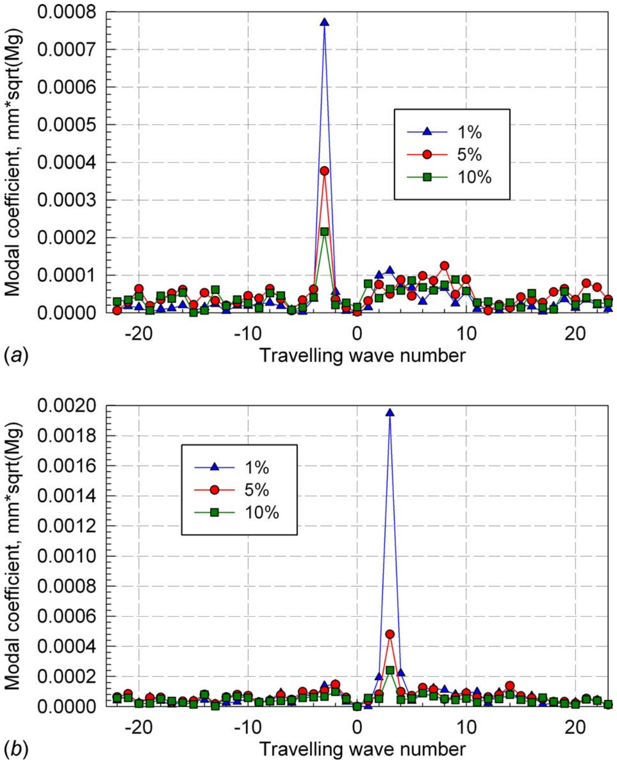

Fig. 10 Modal coefficients for maximum response amplitudes the mistuned blisk excited by (*a*) −3EO and (*b*) +3EO

Mistuning distorts a forced response mode shape and, as a result, modes with all traveling wave numbers are excited even by a single EO-traveling wave excitation. Therefore, in the expansion of a mode shape of the mistuned bladed disk over mode shapes of a tuned bladed disk (see Eq. (21)), contributions of modes corresponding to modes with numbers of traveling waves different from excitation EO can be significant. In other words, if the modal expansion of the forced response amplitudes is expressed in the form

$$\boldsymbol{Q}(\omega)=\sum_{k=-N_B/2}^{N_B/2}\sum_{j}^{n_m}\boldsymbol{c}_{kj}(\omega)\tilde{\boldsymbol{\phi}}_{kj} \tag{27}$$

where $c_{kj}(\omega)=\hat{c}_{kj}/((1+\eta_{kj})\omega_{kj}^2-\omega)$ are the modal coefficients. Then, for a tuned bladed disk, the modal coefficients are equal to zero for all k different in a value and a sign from the EO exciting the forced vibrations. For a mistuned bladed disk, they all are generally not zero.

Table 1 Amplification factors averaged over mistuning patterns

	Mistuning range		
Traveling wave	1%	5%	10%
Backward	1.3832	1.1357	1.0406
Forward	1.0150	0.6039	0.4526

Table 2 Modal properties of a tuned bladed disk

	Forward and backward traveling waves	
Modal property	In a vacuum	In gas flow
Frequency	Identical	Different
Mode shape	Complex conjugate	Different
Damping	Identical	Different

The modal coefficients of the modal expansion of a mistuned forced response over tuned mode shapes are plotted in Fig. 10. The modal coefficients are determined for the first mode in each family at the frequency where the maximum mistuned blisk amplitude is the largest. Significant contributions of all traveling wave modes for higher mistuning are evident. For +3EO excitation, their relative contributions are larger than for −3EO. These relative contributions increase by several times with the mistuning range increase from 1% to 5% and 10%.

A major cause of the reported phenomenon of a reduction in the response for mistuned bladed disk compared with its tuned counterpart are the differences in modal damping values for modes with different numbers of nodal diameters and directions of traveling waves, which are introduced by the action of aerodynamic forces. When mode shapes corresponding to the EO excitation have smaller damping values than the rest of the modes, then the excitation of modes with higher modal damping factors makes the resultant damping factor higher than that for a tuned bladed disk. To illustrate this, the relative contributions into the total energy

Downloaded 02 Jun 2010 to 171.66.16.96. Redistribution subject to ASME license or copyright; see http://www.asme.org/terms/Terms_Use.cfm

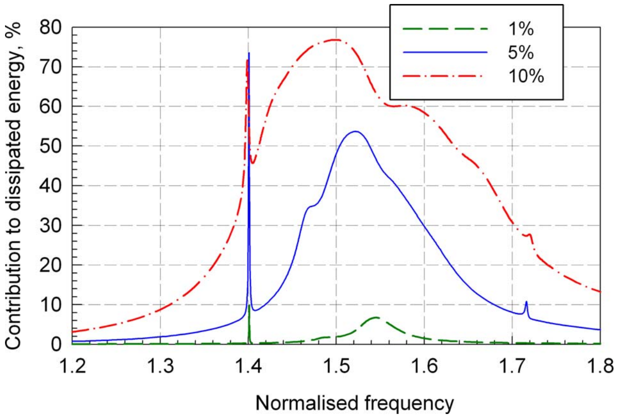

Fig. 11 Contribution to the total dissipated energy of modes with traveling wave numbers different from +3EO excitation

dissipated in gas flow are plotted in Fig. 11 for a sum of energy dissipated by all the modes with traveling wave numbers, which differ from the excitation considered here: +3EO. It is evident that these contributions become dominant when the mistuning intensity becomes 5% and 10%. The aerodynamic damping for +3EO mode is close to the minimum (see Fig. 3); therefore, distortion of the tuned mode shape by mistuning causes large contributions of other modes. This distortion results in a higher value of the resultant damping factor.

This increase in energy dissipation can overcome two other mistuning factors, which are usually the major causes of the mistuned forced response increase: localization of the forced response and the interference "overlap" of resonances. As a result, forced response of a mistuned bladed disk can become lower than the response of its tuned counterpart, and this happens for the blisk analyzed here, where the amplification factor is made 0.4 by a randomly generated mistuning pattern.

It should be noted that this phenomenon is expected to occur for most industrial bladed disks for which aerodynamic damping is significant. Due to the fact that the dependency of the modal damping factor on traveling wave number shown in Fig. 3 is typical (see also Refs. [29,30,23]), and there are always wave numbers that have damping factor values smaller than majority of modes, it is expected that the effect of reduction in the forced response level owing to mistuning can manifest in many other bladed disks. Moreover, it is expected also that for EO excitation corresponding to wave numbers with maximum damping factors, mistuning can produce much higher amplification factors than are conventionally estimated when aerodamping and aerocoupling are not included in the analysis.

7 Conclusions

An effective method has been developed to include coupling, damping, and elastic effects of gas flow in the forced response analysis of mistuned bladed disks.

The method is applicable to cases of high mechanical coupling of blades (cases of flexible disk and, possibly, shrouded blades) and to cases with low mechanical coupling (a stiff disk). The interaction of different families of modes and frequency veering effects are included in the analysis.

The method allows the aerodynamic characteristics of the gas flow to be calculated separately from forced response analysis using the existing CFD program codes. This calculation is performed only for one configuration: a structurally tuned bladed disk. Its results can be used for the analysis of multitude different structurally mistuned bladed disks and cases of large mistuning, when mode shapes are significantly distorted, can be analyzed. The effects of aerodamping, aerocoupling, and aerostiffening on forced response of mistuned bladed disks are included with high accuracy and using cyclically symmetric structural models.

Two major cases are considered: (i) a case when gas flow affects bladed disk mode shapes and (ii) a case when the effects of gas flow on bladed disk mode shapes are not significant.

The efficiency of the developed method allows analysis of the mistuned forced response with aeroelastic effects to be performed without a significant increase in computation time compared with a case when the aerodynamic effects are not included.

The method allows the use of industrial-size sector models of bladed disks for the analysis of forced response of a mistuned structure.

The frequency response function matrix of a structurally mistuned bladed disk is derived with the aerodynamic effects. Cases of aerodynamically tuned and mistuned gas flow are considered.

Numerical investigations of the effects of blade mistuning on forced response characteristics of a blisk with inclusion of aerodamping and aerocoupling effects have been carried out.

A new phenomenon has been discovered and explained: a reduction in resonance peak levels owing to mistuning of the forced response levels for mistuned bladed disks to the levels, which are significantly lower than the forced response of their tuned counterparts.

Acknowledgment

The author is grateful to Rolls-Royce plc. for providing the financial support for this project and for giving permission to publish this work.

References

[1] Ewins, D. J., 1991, "The Effects of Blade Mistuning on Vibration Response—A Survey," IFToMM Fourth International Conference on Rotordynamics, Prague, Czechoslovakia.
[2] Slater, J. C., Minkiewicz, G. R., and Blair, A. J., 1999, "Forced Response of Bladed Disk Assemblies—A Survey," Shock Vib. Dig., **31**(1), pp. 17–24.
[3] Castanier, M., and Pierre, C., 2006, "Modelling and Analysis of Mistuned Bladed Disk Vibration: Status and Emerging Directions," J. Propul. Power, **22**(2), pp. 384–396.
[4] Yang, M.-T., and Griffin, J. H., 2001, "A Reduced-Order Model of Mistuning Using a *Subset* of Nominal System Modes," ASME: J. Eng. Gas Turbines Power, **123**, pp. 893–900.
[5] Petrov, E. P., Sanliturk, K. Y., and Ewins, D. J., 2002, "A New Method for Dynamic Analysis of Mistuned Bladed Discs Based on Exact Relationship Between Tuned and Mistuned Systems," ASME: J. Eng. Gas Turbines Power, **124**(3), pp. 586–597.
[6] Bladh, R., and Pierre, C., 2002, "Dynamic Response Predictions for a Mistuned Industrial Turbomachinery Rotor Using Reduced-Order Modeling," ASME: J. Eng. Gas Turbines Power, **124**, pp. 311–324.
[7] Moyroud, F., Fransson, T., and Jacquet-Richardet, G., 2002, "A Comparison of Two Finite Element Reduction Techniques for Mistuned Bladed Disks," ASME: J. Eng. Gas Turbines Power, **124**, pp. 942–952.
[8] Feiner, D. M., and Griffin, J. H., 2002, "A Fundamental Model of Mistuning for a Single Family of Modes," ASME J. Turbomach., **124**, pp. 597–605.
[9] Ewins, D. J., 1969, "Effect of Detuning Upon the Forced Vibration of Bladed Discs," J. Sound Vib., **9**(1), pp. 65–79.
[10] Petrov, E., and Ewins, D., 2003, "Analysis of the Worst Mistuning Patterns in Bladed Disc Assemblies," ASME J. Turbomach., **125**(4), pp. 623–631.
[11] Whitehead, D. S., 1966, "Effect of Mistuning on the Vibration of Turbomachines Induced by Wakes," J. Mech. Eng. Sci., **8**(1), pp. 15–21.
[12] Nikolic, M., Petrov, E. P., and Ewins, D. J., 2008, "Robust Strategies for Forced Response Reduction of Bladed Discs Based on Large Mistuning Concept," ASME: J. Eng. Gas Turbines Power, **130**, p. 022501.
[13] Jones, W. J., and Cross, C. J., 2002, "Reducing Mistuned Bladed Disk Forced Response Below Tuned Resonant Amplitudes," Seventh National Turbine Engine High Cycle Fatigue Conference, Palm Beach, FL.
[14] Castanier, M. P., and Pierre, C., 1997, "Consideration on the Benefits of Intentional Blade Mistuning for the Forced Response of Turbomachinery Rotors," *Proceedings of the ASME Aerospace Division*, AD-Vol. 55, pp. 419–425.
[15] Kenyon, J. A., and Griffin, J. H., 2000, "Intentional Harmonic Mistuning for Robust Forced Response of Bladed Disks," Fifth National Turbine Engine High Cycle Fatigue Conference, Chandler, AZ.
[16] Mignolet, M. P., Hu, W., and Jadic, I., 2000, "On the Forced Response of Harmonically and Partially Mistuned Bladed *Disks*, Part I: Harmonic Mistuning; Part II: Partial Mistuning and Applications," Int. J. Rotating Mach., **6**(1), pp. 29–56.
[17] Kielb, R. E., and Kaza, K. R. V., 1984, "Effects of Structural Coupling on Mistuned Cascade Flutter and Response," ASME: J. Eng. Gas Turbines Power, **106**, pp. 17–24.

Downloaded 02 Jun 2010 to 171.66.16.96. Redistribution subject to ASME license or copyright; see http://www.asme.org/terms/Terms_Use.cfm

[18] Hoyniak, D., and Fleeter, S., 1986, “The Effect of Circumferential Aerodynamic Detuning on Coupled Bending-Torsional Unstalled Supersonic Flutter,” ASME J. Turbomach., **108**, pp. 253–260.

[19] Nowinski, M., and Panovsky, J., 1998, “Flutter Mechanisms in Low-Pressure Turbine Blades,” ASME Paper No. 98-GT-573.

[20] Bendiksen, O., 1984, “Flutter of Mistuned Turbomachinery Rotors,” ASME J. Eng. Gas Turbines Power, **106**, pp. 25–34.

[21] Kahl, G., 1998, “Structural Mistuning and Aerodynamic Coupling in Turbomachinery Bladings,” *Unsteady Aerodynamics and Aeroelasticity of Turbomachines*, T. H. Fransson, ed., Kluwer Academic, Dordrecht, pp. 335–346.

[22] Willcox, K., and Peraire, J., 2002. “Application of Reduced-Order Aerodynamic Modeling to the Analysis of Structural Uncertainty in Bladed Disks,” *Proceedings of ASME Turbo Expo 2002*, Amsterdam, The Netherlands, Jun.

[23] Kielb, R. E., Feiner, D. M., Griffin, J. H., and Miyakozava, T., 2004, “Probabilistic Analysis of Mistuned Bladed Disks and Blisks With Aerodynamic and FMM Structural Coupling,” *Proceedings of the Ninth National Turbine Engine HCF Conference*, Pinehurst, NC, Mar. 16–19.

[24] Kielb, R. E., Miyakozava, T., and Hall, K. C., 2008, “The Effects of Aerodynamic Asymmetric Perturbations on Forced Response of Bladed Disks,” ASME Paper No. GT2008-50719.

[25] He, Z., Epureanu, B., and Pierre, C., 2007, “Fluid-Structural Coupling Effects on the Dynamics of Mistuned Bladed Disks,” AIAA J., **45**(3), pp. 552–561.

[26] Sayma, A., Vahdati, M., Sbardella, L., and Imregun, M., 2000, “Modeling of Three-Dimensional Viscous Compressible Turbomachinery Flows Using Unstructured Hybrid Grids,” AIAA J., **38**(6), pp. 945–954.

[27] Petrov, E. P., and Ewins, D. J., 2005, “Method for Analysis of Nonlinear Multiharmonic Vibrations of Mistuned Bladed Discs With Scatter of Contact Interface Characteristics,” ASME J. Turbomach., **127**(1), pp. 128–136.

[28] Petrov, E., Di Mare, L., Hennings, H., and Elliott, R., 2010, “Forced Response of Mistuned Bladed Disks in Gas Flow: A Comparative Study of Predictions and Full-Scale Experimental Results, ASME J. Eng. Gas Turbines Power, **132**(5), p. 052504.

[29] Sladojevic, I., Petrov, E., Sayma, A., and Imregun, M., 2006, “Forced Response Variation of Aerodynamically and Structurally Mistuned Turbo-Machinery Rotors,” ASME Paper No. GT2006-90948.

[30] Sladojevic, I., Petrov, E., Sayma, A., Imregun, M., and Green, J., 2005, “Investigation of the Influence of Aerodynamic Coupling on Response Levels of Mistuned Bladed Discs With Weak Structural Coupling,” ASME Paper No. GT2005-69050.

Downloaded 02 Jun 2010 to 171.66.16.96. Redistribution subject to ASME license or copyright; see http://www.asme.org/terms/Terms_Use.cfm

Experimental Study on Fault Caused by Partial Arc Steam Forces and Its Economic Solution

Daren Yu
e-mail: yudaren@hcms.hit.edu.cn

Yanfeng Duan[1]
e-mail: duanyanfeng@gmail.com

Jinfu Liu
e-mail: liujinfu@hcms.hit.edu.cn

Zhansheng Liu
e-mail: lzs@hit.edu.cn

Qinghua Hu
e-mail: huqinghua@hcms.hit.edu.cn

Department of Energy Science and Engineering,
Harbin Institute of Technology,
Harbin 150001, P.R.C.

It is noticed in a few steam turbines that there are a pad temperature rise of more than 10°C and a radial journal movement of more than 50 μm in the bearings adjacent to control stage when they operate under partial arc admission at 60–80% of their full load. It is found through fault mechanism analysis and experimental study that the fault is caused by partial arc steam forces acting on control stage. A fault characteristic is concluded to help identify this fault. Diagonal admission is therefore proposed as an economic solution for elimination of this fault and it is proved to be effective through practical test. [DOI: 10.1115/1.4000090]

Keywords: partial arc admission, partial arc steam forces, fault diagnosis, diagonal admission

1 Introduction

A large number of steam turbines are being used at partial loads and varying loads. In order to maintain a high operating efficiency over a wide range of loads, these turbines are designed to operate under partial arc admission. In a modern steam turbine design, the effects of partial arc admission are evaluated, and bearings are selected to avoid fault occurring [1]. However, a class of faults may occur in high-pressure rotor bearings of some steam turbines and they feature bearing pad temperature rise and radial journal movement when the turbines operate at 60–80% of their full load in sequential valve mode (partial arc admission).

Although the general picture of the effects of partial arc admission has been established, only few experiments have been found regarding this issue [2,3]. Therefore, it is necessary to analyze this fault through practical cases, and extract fault characteristics for fault diagnosis in practice. The fault can be eliminated by applying full arc admission, which results in more throttle loss; hence, a solution to the fault is needed, which can be used to reduce throttle loss while eliminating the fault.

In this paper, the fault was analyzed theoretically and experimentally through some practical cases. We found that the fault is caused by partial arc steam forces, and so concluded a fault characteristic and proposed an economic solution to the problem.

2 Description of Case

A number of cases were studied with a 210 MW steam turbine operating in sequential valve mode during its routine operation. Figure 1 shows the operation data of the unit in 1 day. When the load fluctuates between 130 MW and 210 MW, the pad temperature (denoted by T_{P2}), the 0-to-peak values of the 1X amplitude component of journal vibration (denoted by V_{J2}), and the journal location (denoted by L_{J2}) in bearing 2 vary significantly. Bearing 2 is one of the high-pressure (HP) rotor bearings and close to the control stage in this case. L_{J2H} and L_{J2V} in Fig. 1 denote the horizontal and vertical components of L_{J2}, respectively, and they are highly related to T_{P2}. The positive directions of them are indicated in Fig. 2. T_{P2}, V_{J2}, and L_{J2H} get very high when the load is between 140 MW and 180 MW (60–80% of the full load 230 MW). Consequently, rubbing accidents shown in Fig. 3 may occur between journal and pad due to overloading resulting from the fault. Until now, this fault occurring in HP rotor bearings has been found in many large steam turbines.

3 Fault Analysis

The fluctuations of T_{P2} and V_{J2} imply the variation in the load of bearing 2. The significant variations in L_{J2} and the load of bearing 2 show that there are external forces acting on the rotor. Since the fault occurs in the HP rotor bearings at partial loads and these signals vary with the load, it is reasonable to consider that the external forces are related to partial arc admission.

Under partial arc admission, the steam forces acting on the control stage are not uniform [4]. Figure 2 qualitatively shows the tangential steam forces acting on control stage rotor blades when GV1 and GV2 are widely open, GV3 has a small opening, and GV4 is closed. The sequential valve scheme of this type of 210 MW turbines can be denoted by GV1+GV2→GV3→GV4, which means GV1 and GV2 are opened first, then GV3, and finally GV4 if the load increases. A resultant force passing through the shaft centerline is composed of the unbalanced tangential steam forces and it acts on control stage only while all the other stages are under full arc admission. As shown in Fig. 2, the tangential steam forces in the arcs of each GV are denoted by F_{GV1}, F_{GV2}, F_{GV3}, and F_{GV4}, respectively. The resultant force, denoted by F_{PA}, is the combination of F_{GV1}–F_{GV4}.

The horizontal and vertical components of F_{PA} are denoted by F_{PAH} and F_{PAV}. Both of them shown in Fig. 4 are calculated under the premise of the rated main steam pressure (MSP) [5,6]. The maximum value of F_{PAH} is about 77 kN, which is too great for the weight of HP rotor of about 100 kN. F_{PAV} varies in the range of 14 kN, which is within the tolerance of the bearings and so it can be neglected in this work. F_{PAH} mainly has influences on bearings 1 and 2. There are remarkable additional loads caused by F_{PAH}, denoted by F_{B1H} and F_{B2H}, respectively, acting on the two bearings in the horizontal direction. These additional loads have great effect on the pad temperature and the radial rotor position in the bearings [7].

If F_{PA} is the cause of fault, it should be related to journal locations, pad temperatures, and journal vibrations in HP rotor bearings. Accordingly, F_{PA} during the above case is necessary to be calculated for analyzing the relationships between it and the signals. However, F_{PA} is significantly influenced by the MSP. It is difficult to precisely estimate F_{PA}, while the MSP fluctuates in a wide range in this case. Therefore, we conducted an experiment with another 210 MW turbine of the same type. As shown in Fig. 5, keeping the MSP basically stable at the rated value, we first gradually decrease the load from 210 MW to 150 MW, and then gradually increase it to 210 MW. The variation in F_{B2H} during the experiment can be calculated according to the load.

---

[1] Corresponding author.

Manuscript received February 8, 2009; final manuscript received July 10, 2009; published online March 16, 2010. Editor: Dilip R. Ballal.

Copyright © 2010 by ASME

Downloaded 02 Jun 2010 to 171.66.16.96. Redistribution subject to ASME license or copyright; see http://www.asme.org/terms/Terms_Use.cfm

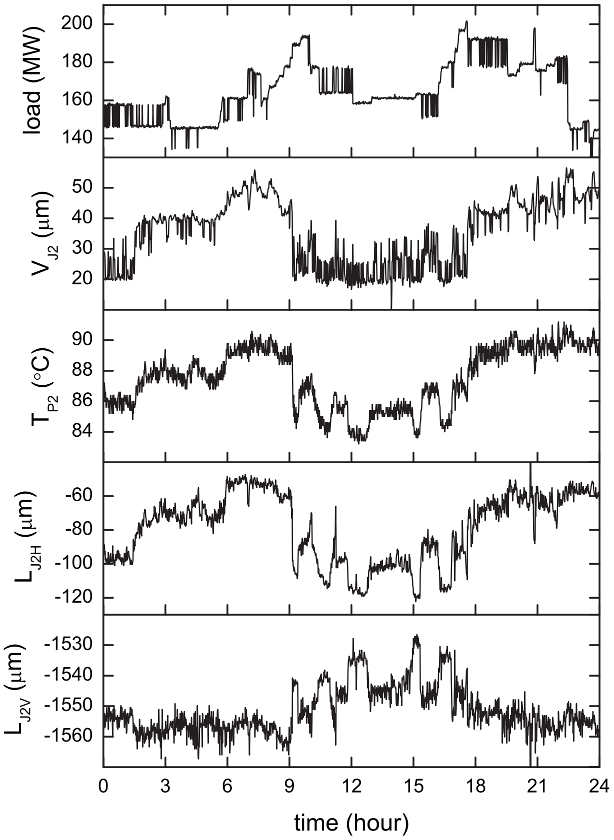

Fig. 1 Variations in load, V_{J2}, T_{P2}, L_{J2H}, and L_{J2V} during routine operation

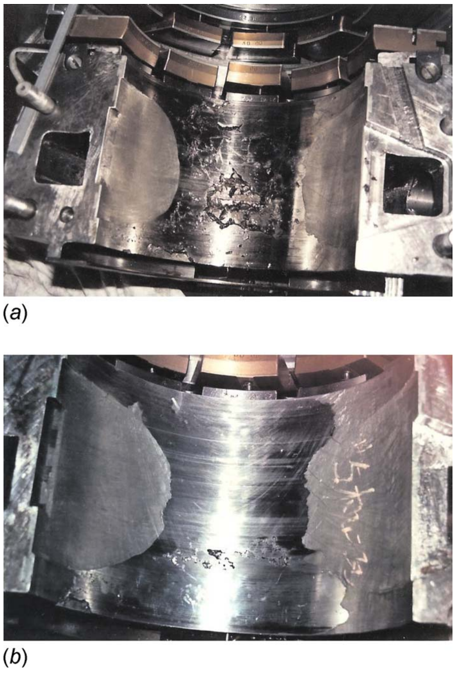
(*a*)

(*b*)

Fig. 3 Rubbing accidents in bearing 2

It can be seen from Figs. 5 and 6 that T_{P2} and L_{J2H} are highly correlated with F_{B2H}. The correlation coefficient between T_{P2} and F_{B2H} is 0.8823 and that between L_{J2H} and F_{B2H} is 0.8800. The maximum value of F_{B2H} is more than 40 kN. It increases the load of bearing 2 and causes significant variation in L_{J2H}, which will result in the deviation of the bearing from its design condition and lead to the distortion of the oil wedges. Consequently, the oil gap will be squeezed thinner, the inlet height of oil wedge will decrease, and T_{P2} will increase. The oil film may partially break up in the heavily loaded zone and cause rubbing between journal and pad.

Therefore, the cause of this class of faults is partial arc steam forces acting on control stage due to valve-opening sequence. A notable characteristic of this fault is that pad temperature and journal location in HP rotor bearing are highly correlated with the resultant force of partial arc steam forces. This characteristic is helpful to identify this fault in practice.

4 An Economic Solution

The problem can be addressed by applying full arc admission. However, it is not an economic solution as it causes more throttle loss. We give an economic solution for the elimination of the fault by changing the valve-opening sequence.

Considering two pairs of valves (GV1/GV3 and GV2/GV4) diagonally positioned, the steam forces in the diagonal arcs can be totally counteracted if the diagonally positioned valves have the same opening. Therefore, the sequential valve scheme can be improved by opening a pair of diagonally positioned valves first and then the other valves in sequence. Taking GV2+GV4→GV3 →GV1 as an example, F_{GV2} and F_{GV4} are counteracted totally, while F_{GV3} can be partially counteracted by F_{GV1}. For the purpose of distinction, the new scheme is referred to as the diagonal admission, and the old one is called the sequential admission. The

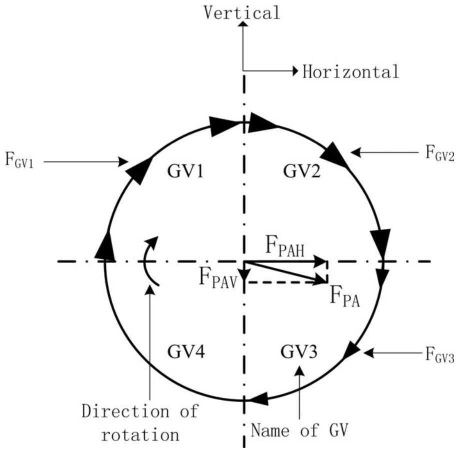

Fig. 2 Steam forces acting on control stage and layout of GVs

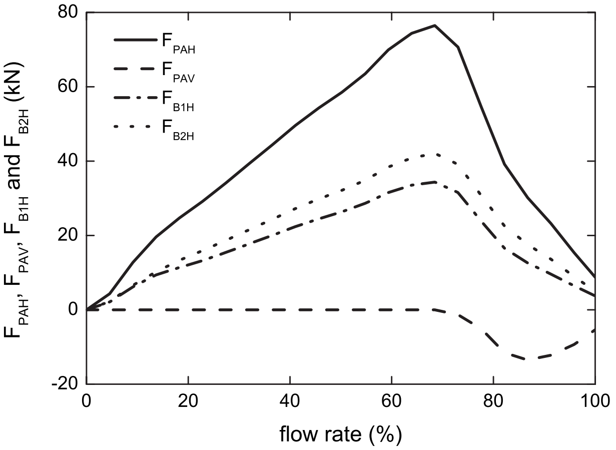

Fig. 4 F_{PAH}, F_{PAV}, F_{B1H}, and F_{B2H} of 210 MW turbine

Downloaded 02 Jun 2010 to 171.66.16.96. Redistribution subject to ASME license or copyright; see http://www.asme.org/terms/Terms_Use.cfm

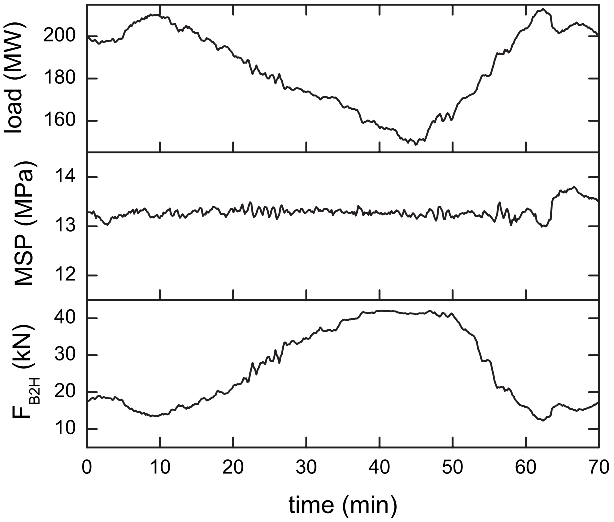

Fig. 5 Variations in load, MSP and F_{B2H} during experiment

opening of the third opened valve GV3 is decisive for F_{PA}. Consequently, F_{PA} is much less under diagonal admission. Because diagonal admission comes under the category of partial arc admission, it is more economic than full arc admission.

Diagonal admission may result in new problems. For example, if the bearing is heavily loaded, the choice of GV2 or GV3 as the third opened valve will increase the bearing load and the pad temperature; if the bearing is lightly loaded, choosing GV1 or GV4 will reduce the stability of rotor-bearing system. This fault can be eliminated by one of the four solutions: (a) GV1+GV3→GV2→GV4, (b) GV1+GV3→GV4→GV2, (c) GV2+GV4→GV1→GV3, and (d) GV2+GV4→GV3→GV1, depending on the loading of the bearing. In addition, schemes (b) and (d) are conductive to maintain the oil wedge.

According to the discussion above, the sequential valve scheme of the 210 MW turbine is modified from GV1+GV2→GV3→GV4 to GV2+GV4→GV3→GV1. As shown in Fig. 7, although the load varies between 120 MW and 220 MW, the increment of T_{P2} is only about 4°C, which is much less than 21°C shown in Fig. 6. Compared to full arc admission, diagonal admission can eliminate the fault and reduce throttle loss.

5 Conclusions

This paper focuses on a class of faults occurring in HP rotor bearings of steam turbines that operate under sequential admission. As to those steam turbines, the worst case working condition is at two-valve-point. Due to the amount of those steam turbines that is considerable, the results of this paper have wide applicability.

The cause of fault is found to be partial arc steam forces acting on control stage and a fault characteristic is concluded for the purpose of fault diagnosis. The solution of diagonal admission is effective for fault elimination and is more economic than full arc admission.

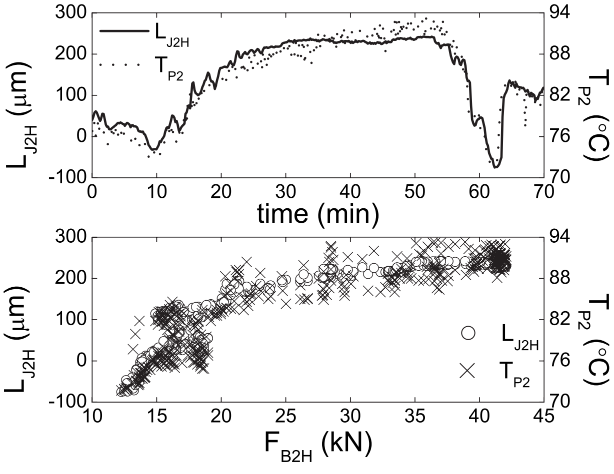

Fig. 6 Variations in L_{J2H} and T_{P2} during experiment

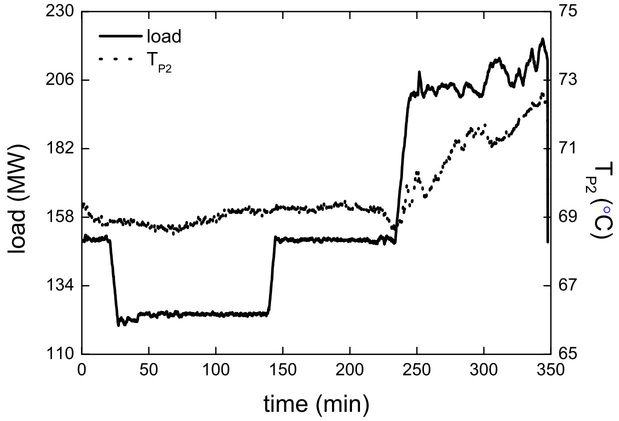

Fig. 7 Variation in T_{P2} under diagonal admission

Acknowledgment

The authors would like to thank Dr. Tao Cui, Dr. Juntao Chang, Dr. Rui Zhou, Dr. Ying Cui, Mr. Xiaonan Sun, Mr. Xianfang Wen, Professor Songjing Li, and Mrs. Jing Zhao for their constructive suggestions and/or assistant provided. This work is supported by the Chang Jiang Scholars Program and the National Natural Science Foundation of China (Grant No. 50606008).

Nomenclature

F_{GV1} = steam forces on rotor blades in the arc of governing valve 1
F_{GV2} = steam forces on rotor blades in the arc of governing valve 2
F_{GV3} = steam forces on rotor blades in the arc of governing valve 3
F_{GV4} = steam forces on rotor blades in the arc of governing valve 4
F_{B1H} = additional loads acting on bearing 1 in horizontal direction
F_{B2H} = additional loads acting on bearing 2 in horizontal direction
F_{PA} = resultant force of unbalanced tangential steam forces on control stage
F_{PAH} = horizontal component of F_{PA}
F_{PAV} = vertical component of F_{PA}
L_{J2} = journal location in bearing 2
L_{J2H} = horizontal component of L_{J2}
L_{J2V} = vertical component of L_{J2}
T_{P2} = pad temperature of bearing 2
V_{J2} = 0-to-peak value of 1X amplitude component of journal vibration in bearing 2

References

[1] Bloch, H. P., 1995, *A Practical Guide to Steam Turbine Technology*, McGraw-Hill, New York.
[2] Fridh, J. E. A., 2002, "Partial Admission in Axial Turbines," SNEA Technical Report No. P12457-2.
[3] Boulbin, F., Penneron, N., Kermarec, J., and Pluviose, M., 1992, "Turbine

Downloaded 02 Jun 2010 to 171.66.16.96. Redistribution subject to ASME license or copyright; see http://www.asme.org/terms/Terms_Use.cfm

Blade Forces Due to Partial Admission," Revue Francaise de Mecanique, **1992**(3), pp. 203–208.

[4] Elliott, T. C., Chen, K., and Swanekamp, R. C., 1998, *Standard Handbook of Powerplant Engineering*, McGraw-Hill, New York.

[5] Lakshminarayana, B., 1996, *Fluid Dynamics and Heat Transfer of Turbomachinery*, Wiley, New York.

[6] Lampart, P., Szymaniak, M., and Rzadkowski, R., 2004, "Unsteady Load of Partial Admission Control Stage Rotor of a Large Power Steam Turbine," *ASME Conference Proceedings*, 2004(41707), pp. 237–246.

[7] TCE, 2003, "Partial Arc Admission in Steam Turbines," Turbo Components & Engineering, Technical Report, URL: http://www.tce1.com/Newsletters/5-2.pdf

Downloaded 02 Jun 2010 to 171.66.16.96. Redistribution subject to ASME license or copyright; see http://www.asme.org/terms/Terms_Use.cfm

Spreadsheet Calculations for Jets in Crossflow From Single and Opposed Rows With Alternating Hole Sizes

J. D. Holdeman[1]
National Aeronautics and Space Administration,
Glenn Research Center,
Cleveland, OH 44135
e-mail: jjdholdeman@aol.com

J. R. Clisset[2]
University of Florida,
Gainesville, FL 32611

J. P. Moder
Aerospace Engineer
Combustion Branch,
Propulsion Systems Division,
National Aeronautics and Space Administration,
Glenn Research Center,
Cleveland, OH 44135

The primary purpose of this study was to show the expected results for cases of single and opposed rows of jets from alternating large and small round holes. Previous publications demonstrated that the NASA empirical model gave results that were an excellent representation of mean experimental scalar results and that the model could confidently be used to investigate configurations for which results have not been published in the open literature. Calculations for cases of opposed rows of jets that would overpenetrate slightly in an inline configuration showed that better mixing was attained when one row was shifted to make a staggered configuration so that a small hole was opposite from a larger one. However, the result was no better than for an optimum inline configuration with all the holes of the same size. Staggering the rows does not make much difference in an optimum inline configuration. For all cases investigated, the dimensionless variance of the mixture fraction decreased significantly with increasing downstream distance, but, at a given downstream location, the variation between cases was small. [DOI: 10.1115/1.4000129]

1 Introduction

Jets in crossflow (JICs) have been extensively investigated in the literature. The studies of multiple jets that are summarized in Ref. [1] were motivated by mixing of dilution jets in conventional gas turbine combustors, and the studies summarized in Refs. [2,3] focused on optimizing the mixing section in the rich burn/quick mix/lean burn (RQL) combustor scheme. References to many of the JIC studies that were published prior to Refs. [1–3] can be found in their citations.

Because these reference lists are extensive, older reports and papers are not referenced in this publication unless specific results are mentioned. Note that it was shown in Refs. [1–3] that trends of a conserved scalar were independent of the duct shape and were similar whether they were from experimental or analytical studies. Thus, trends were the same from probe measurements, nonintrusive species measurements, empirical model calculations, or computational fluid dynamics (CFD) calculations for nonreacting or reacting flows in a rectangular, annular, or cylindrical duct.

The Excel® spreadsheets posted with Refs. [4,5] are functionally equivalent to the Applesoft® BASIC programs used in Refs. [6,7]. Discussions of spreadsheet specifics, several additional cases of jet mixing in a confined crossflow, a listing of the correlation equations in the NASA empirical model, and a slideshow were published in Refs. [4,5]. Suggested design procedures for cylindrical and rectangular ducts are given in Refs. [2,3]. Both NASA and Cranfield design methods are discussed in Ref. [8].

The spreadsheet used in this paper is the same as that posted with Ref. [5] except that contour plots were added. The contour plots in the spreadsheet have considerably less resolution than those in Figs. 4–14 in Ref. [5] that were done with a graphics postprocessor using data exported from the spreadsheet. Results are shown as profile plots for all calculations in Ref. [4] and in Figs. 15–24 and the slideshow in Ref. [5].

Figure 1 is a schematic of the basic flow field for jets in a confined crossflow. The jets are shown entering the mainstream flow through orifices in the top duct wall. The primary independent geometric variables are the lateral spacing between similar locations of adjacent orifices S, the duct height H, and the orifice diameter d. S/H and H/d were chosen as independent variables. The product of them, the ratio of the orifice spacing to orifice diameter S/d, is a frequently cited dimensionless variable.

Downstream distances are specified in intervals of x/H because the objective in combustor design is usually to identify orifice configurations to optimize the mixing within a given length and the downstream locations of interest are usually independent of the orifice diameter. The ratio of the downstream distance to the orifice diameter x/d is a common dimensionless parameter, particularly in unconfined flows.

The dimensionless scalar is

$$\theta = (T_M - T)/(T_M - T_J) \tag{1}$$

Note that unmixed jet fluid is $\theta=1$ and unmixed mainstream fluid is $\theta=0$. A physically realistic θ should be neither <0 nor >1. Although θ was originally formulated from temperature data in an

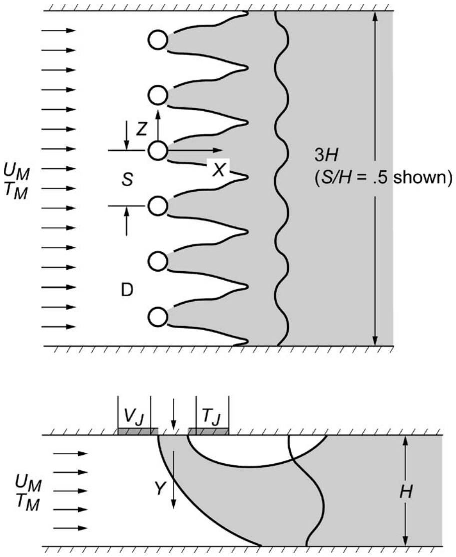

Fig. 1 Schematic for flow field for one-side injection of a row of jets in a confined crossflow, shown for injection from the top duct wall

---

[1] Corresponding author. Retired.

[2] Present address: U.S. Army Proving Grounds, Yuma, AZ.

Contributed by the International Gas Turbine Institute of ASME for publication in the JOURNAL OF ENGINEERING FOR GAS TURBINES AND POWER. Manuscript received April 9, 2009; final manuscript: May 14, 2009; published online March 18, 2010. Editor: Dilip R. Ballal.

Copyright © 2010 by ASME

Downloaded 02 Jun 2010 to 171.66.16.96. Redistribution subject to ASME license or copyright; see http://www.asme.org/terms/Terms_Use.cfm

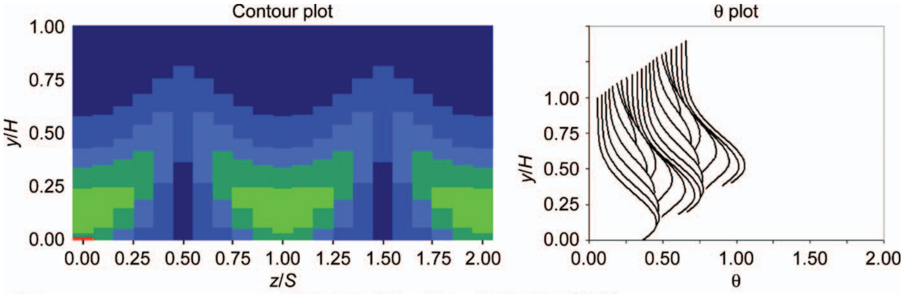

(a) $S/H = 1.0$, $H/d = 4$ ($c = 5.14$); $Us = 0.099$

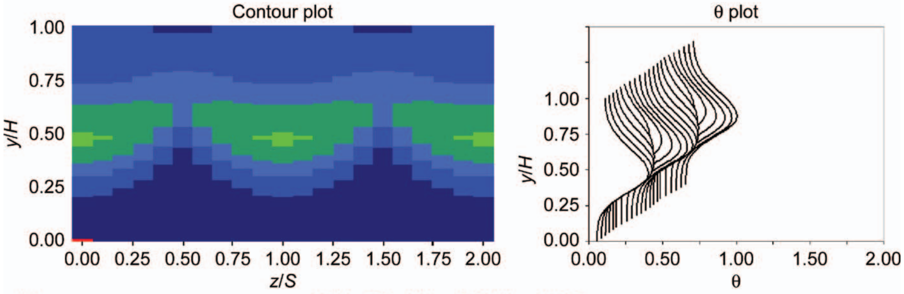

(b) $S/H = 0.5$, $H/d = 5.66$; $Us = 0.078$

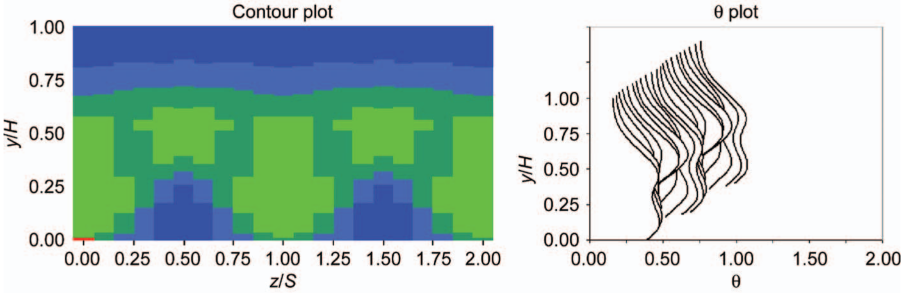

(c) $S/H = 1.0$, $H/d = 4$ for large holes and $S/H = 0.5$, $H/d = 5.66$ for small holes; $Us = 0.099$

Fig. 2 Variation in scalar profile and contour plots for one-side injection from alternating size holes at $x/H=0.5$ for $DR=2.2$, $J=26.4$, $C_d=0.64$, with $S_x/H=0$

incompressible flow, θ applies to any conserved scalar. For example, species concentration was often used in the isothermal experimental studies summarized in Refs. [2,3] and a carbon balance was used in the reacting flow experiments reported in Ref. [2]. The specifics and operation of the spreadsheet, the correlations in the NASA empirical model, the "closest" experimental data, and listings of the original BASIC programs are given in Ref. [4].

The correlation equations for each of the scaling parameters are given in Refs. [1,4]. The ones in Ref. [1] are written in terms of H_{eq} rather than H. For all the cases considered here, $H_{\text{eq}}=H$. Most of the cases for this application are in the near field of the JIC, so, although the trajectory becomes asymptotic in the axial direction, characterization of the flow depends on both downstream distance and JIC configuration.

For all calculations, the dimensionless flow and geometric variables that must be specified are the jet-to-mainstream density ratio DR, jet-to-mainstream momentum-flux ratio J, jet discharge coefficient C_d, orifice-spacing-to-duct-height ratio S/H, duct-height-to-orifice-diameter ratio H/d, and the dimensionless downstream distance x/H. If there are multiple rows of jets, the axial distance between their centers S_X/H must also be specified.

Three-dimensional oblique plots (herein called profile plots) and low resolution contour plots are the native displays in the spreadsheet. The dependent variable θ is shown on the horizontal axis in the profile plots and θ is the plotted variable in the contour plots. The vertical and oblique axes in the profile plots are the y and z directions, which are, respectively, in the direction of the jet injection and along the orifice row in a y-z plane. These are the axes of ordinates and abscissas in the contour plots. There are 21 profiles in the z-span shown in the figures, but less than half of the jet profiles are calculated directly. The others are generated by assuming cyclic boundary conditions at the jet centerplanes or midplanes as appropriate. (The x-y planes through the orifice center and halfway between orifices in each row are called the centerplane and the midplane.)

Because of the positive results using the superposition model for inline jets shown in Ref. [5], the superposition model was used for all opposed row conditions. To invoke the superposition model, one must not have the same configurations on both top and bottom in any row. The "solution" to get superposition for two opposed rows of jets with their centerlines aligned is to use row 1 top and row 2 bottom (or row 2 top and row 1 bottom) and to specify $S_X/H=0$.

The NASA JIC empirical model assumes that the flows of interest will be confined and cannot be used for unconfined jet flows because the relations used for orifice size and spacing do not extrapolate properly as jet spacing and/or the distance to the opposite wall becomes large. Although it may work, the spreadsheet should not be used upstream of the trailing edge of the orifices.

Downloaded 02 Jun 2010 to 171.66.16.96. Redistribution subject to ASME license or copyright; see http://www.asme.org/terms/Terms_Use.cfm

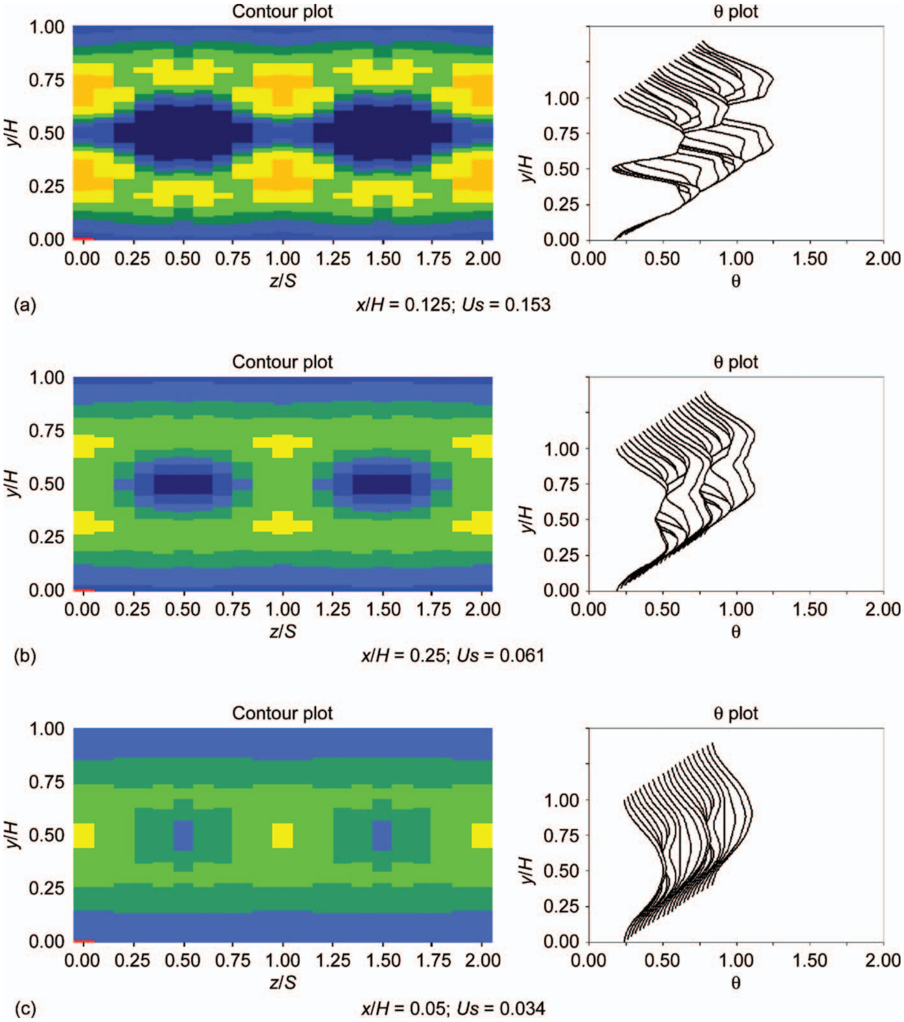

(a) $x/H = 0.125$; $Us = 0.153$

(b) $x/H = 0.25$; $Us = 0.061$

(c) $x/H = 0.05$; $Us = 0.034$

Fig. 3 Variation in scalar profile and contour plots for opposed rows of alternating hole sizes with similar holes opposite each other for $S/H=0.5$, $H/d=8$ and $S/H=0.25$, $H/d=11.31$ on each side with $S_x/H=0$ (total $A_J/A_M=0.098$), $DR=2.2$, $J=26.4$, and $C_d=0.64$

Per Ref. [9], the unmixedness U_s is defined as

$$U_s = \frac{\theta_{\text{var}}}{\theta_{\text{ave}}(1-\theta_{\text{ave}})} \tag{2}$$

where θ_{var} is the mean squared deviation from θ_{ave} of all 2121 θ values at each axial x location for which calculations are performed. θ_{ave} is the fully mixed mean value (usually$=m_J/m_T$) and is not a function of x.

The objective of this study was to investigate opposed rows of jets with alternating hole sizes. There are no data for opposed rows of jets from alternating large and small holes in the open literature, but there were previous experiments in Ref. [10] for the case of one-side injection from mixed holes sizes, and the results were published in Ref. [9] for opposed rows of inline jets from different size holes on opposite sides.

2 Results and Discussion

The cases calculated are a single row and opposed rows of jets from alternating large and small holes. The conditions investigated computationally are identified in the titles of Figs. 2–6. These figures show both profile and contour plots. The $x=0$ location is at the center of the holes, and the trailing edge of round holes is at $x/H= (0.5)/(H/d)$).

The unmixedness U_s is given in the subtitle for each part of each figure. There is a considerable decrease in U_s with downstream distance for each case shown in Figs. 2–6. However, at a given downstream location there is also a smaller difference in U_s between cases

2.1 One-Side Injection From Orifices With Mixed Hole Sizes. The cases shown in Fig. 2 are similar to those in Ref. [10]. In addition to the alternating size holes in Fig. 2(*c*), these include the cases of only large holes at the spacing between holes of the same size in the mixed configuration (Fig. 2(*a*)) and uniform size holes at the spacing between adjacent holes in the mixed configuration (Fig. 2(*b*)). Note that the case shown in Fig. 2(*c*) is a combination of the cases shown in Figs. 2(*a*) and 2(*b*) so the total area for the case in Fig. 2(*c*) is $A_J A_M=0.098$.

The penetration of the jets was shown previously, e.g., Refs. [1,4–7], to be largely independent of orifice size, so the jet penetration would be expected to be about the same for adjacent holes; independent of their size, if the same spacing was used for both the large and small holes. This is contrary to the data in Ref. [10] that shows that jets from the large holes penetrate farther. To implement mixed hole sizes in the JIC spreadsheet, we used both rows on top with the axial spacing $S_x/H=0$ and the spacing between large holes for the large holes and the spacing between all holes for the small holes. Although the lateral spacing S/H can be

Downloaded 02 Jun 2010 to 171.66.16.96. Redistribution subject to ASME license or copyright; see http://www.asme.org/terms/Terms_Use.cfm

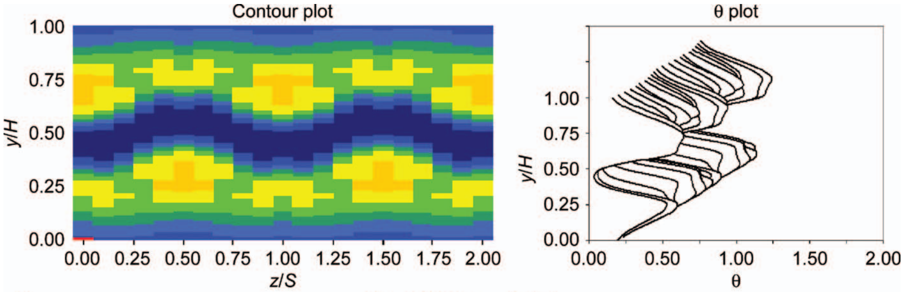

(a) $x/H = 0.125$; $Us = 0.149$

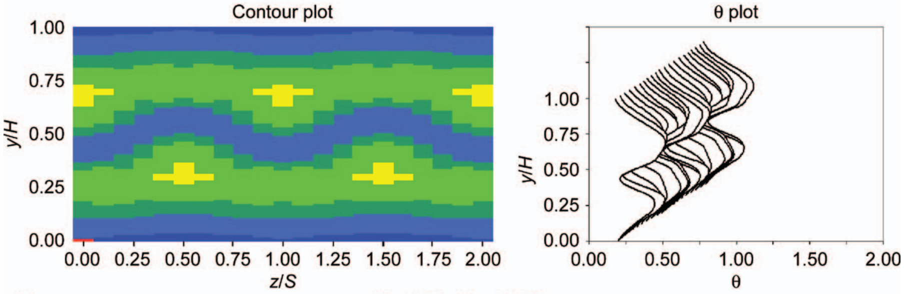

(b) $x/H = 0.25$; $Us = 0.047$

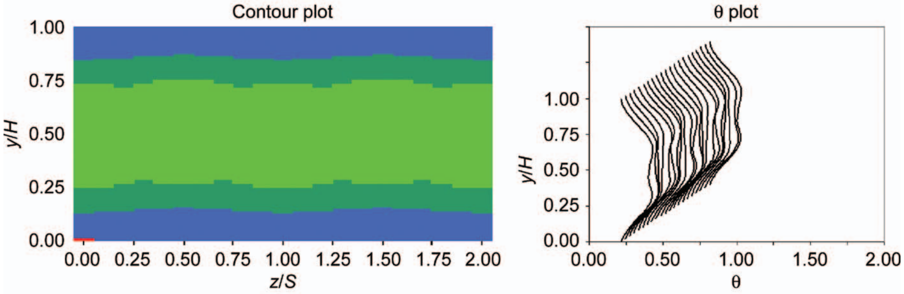

(c) $x/H = 0.5$; $Us = 0.029$

Fig. 4 Variation in scalar profile and contour plots for opposed rows of alternating hole sizes with large and small holes opposite each other for $S/H=0.5$, $H/d=8$ and $S/H=0.25$, $H/d=11.31$ on each side with $S_x/H=0$ (total $A_J/A_M=0.098$), $DR=2.2$, $J=26.4$, and $C_d=0.64$

input for only row 1 top in the spreadsheet, it is divided by two for the smaller holes by specifying four holes for them and two holes for the larger ones. This significantly changes the penetration of adjacent jets although they have the same J.

This is shown in the spreadsheet calculations in Fig. 2(*c*) for alternating size holes for injection from one side (here the top) at $x/H=0.5$. Each row of the mixed hole size configuration in this simulation is half of the total area. However, because there are only half as many large holes and because a larger hole is coresident with a smaller one in the simulation, the area of the large holes is really three times that of the small ones. The jets from the large holes overpenetrate as expected, because the S/H between large holes is too big ($S/H=1.0$), whereas the spacing of the uniform size holes is optimum ($S/H=0.5$) for this momentum-flux ratio ($J=26.4$).

2.2 Opposed Rows of Jets With Mixed Hole Sizes. The results in Fig. 2 for one-side injection of jets in crossflow agree with the experimental data in Ref. [10], so the JIC spreadsheet was used to calculate expected results for opposed rows of jets with mixed hole sizes. For these we used both rows on top and bottom with $S_x/H=0$ and again used the spacing between large holes for the large holes and the spacing between all holes for the small holes.

For opposed rows with holes of mixed sizes, there are two options—holes of similar size can be opposite each other or a larger hole can be opposite a smaller one. These are shown in Figs. 3 and 4 for a total $A_J/A_M=0.098$. Although the θ distributions suggest significantly better mixing in the staggered configuration, the U_s values are only slightly lower for the staggered configuration in Fig. 4. The limiting cases are as follows: (1) All holes are of the same size and (2) only the large holes exist. The case where all the holes are the same size in shown in Figs. 5(*a*) and 6(*a*). This is a nearly optimum configuration for opposed rows of inline jets. Note that $C=1.28$ for the configuration shown and that the jets penetrate to $\sim H/4$. The configuration in Figs. 5(*b*) and 6(*b*) has double the S/H, as do the larger holes in the mixed configuration, but the diameter of the holes is increased in this case to give the same total area ($A_J/A_M=0.098$). For this one, $C=2.57$ and the jets penetrate to $\sim H/2$. As this is a nearly optimum configuration for one-side injection, it would be expected to overpenetrate for opposed rows of inline jets with $S/H=0.5$ (Figs. 5(*b*) and 6(*b*)). The case shown in Figs. 5(*c*) and 6(*c*) is of staggered jets that overpenetrate if opposed jets are inline. The staggered configuration has a row shifted such that the centerplane of the jets from one side is opposite from the midplane of jets from the opposite side. θ distributions for these suggest that the staggered

Downloaded 02 Jun 2010 to 171.66.16.96. Redistribution subject to ASME license or copyright; see http://www.asme.org/terms/Terms_Use.cfm

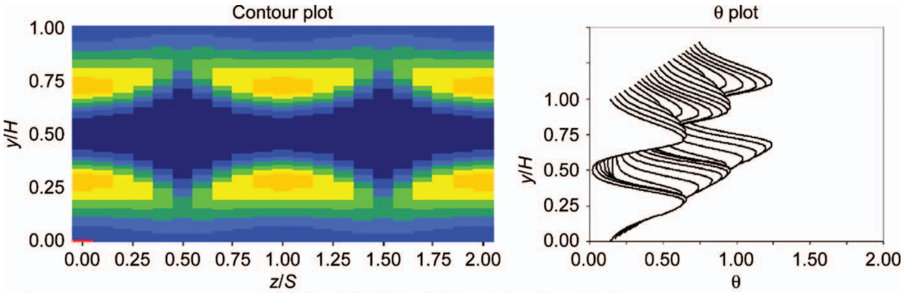

(a) $S/H = 0.25$, $H/d = 8$ ($C = 1.28$); $Us = 0.197$

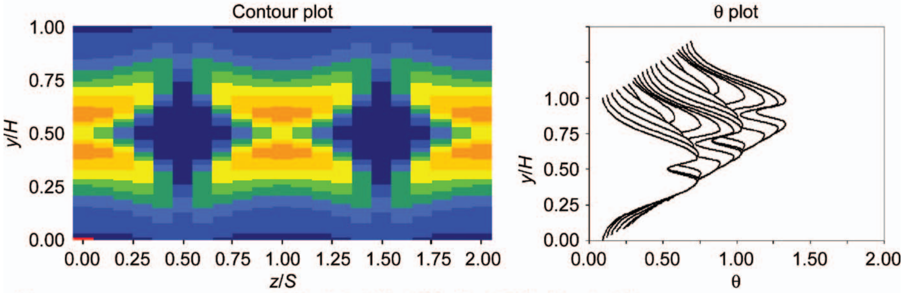

(b) $S/H = 0.5$, $H/d = 5.66$ ($C = 2.57$); $Us = 0.194$

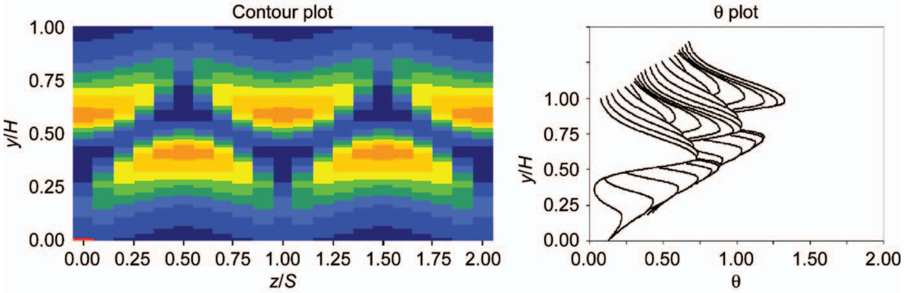

(c) $S/H = 0.5$, $H/d = 5.66$ ($C = 2.57$); $Us = 0.173$

Fig. 5 Variation in scalar profile and contour plots for opposed rows of inline jets (total $A_J/A_M=0.098$) at $x/H=0.125$ with $DR=2.2$, $J=26.4$, and $C_d=0.64$

jets in a nearly optimum configuration for one-side injection mix better than inline ones. Although the θ distributions in Figs. 5(*c*) and 6(*c*) suggest this, the U_s values for the staggered cases are only slightly less than for the inline cases. The cyclical nature of the results shown in Fig. 6(*c*) is confirmed by unpublished measurements [11] for the staggered jet case described in Ref. [12]. The staggered configuration for the opposed row inline optimum ($C=1.28$) is not shown as shifting makes very little difference for that one.

3 Conclusions

A spreadsheet that displays 3D plots of the distributions of a conserved scalar downstream of jets mixing with a confined crossflow was used to investigate the cases of single and opposed rows of alternating large and small holes. The spreadsheet used in this paper is the same as that posted with NASA/TM-2006-214226 except that contour plots were added to the Excel® spreadsheet.

Previous publications showed that the NASA empirical model gave results that were an excellent representation of mean experimental results and that the model could confidently be used to investigate configurations for which results have not been published in the open literature such as opposed rows of mixed size holes. The larger holes penetrated farther and dominated the mixture fraction. For all cases investigated, the dimensionless variance of the mixture fraction decreased significantly with increasing downstream distance, but the variation between cases, at a given downstream location, was smaller.

Acknowledgment

The authors would particularly like to thank Mr. Richard E. Walker (Aerojet Liquid Rocket Co., retired) and Dr. Ram Srinivasan (then of Garrett Turbine Engine Co.) for their contributions to the NASA JIC empirical model, and to Professor William E. Lear of the University of Florida for suggesting that the original computer code, written in Applesoft® BASIC on a 64K Apple //e®, could be rendered in an Excel® spreadsheet and for directing the development of the spreadsheet at UF. The authors also wish to acknowledge the contributions to the spreadsheet made by Mr. Gilbert F. Canton (then at UF) and Mr. Joel P. Scheuer (then a LERCIP participant at NASA Glenn) and appreciate the support and encouragement from Mr. Timothy D. Smith, Dr. Clarence T. Chang, and Dr. C. John Marek (retired) at the NASA Glenn Research Center, Mr. David S. Liscinsky of the United Technologies Research Center, Professor John F. Foss of Michigan State University, Professor G. Scott Samuelsen of the University of California-Irvine, and the late Professor Arthur H. Lefebvre, author of *Gas Turbine Combustion*.

Downloaded 02 Jun 2010 to 171.66.16.96. Redistribution subject to ASME license or copyright; see http://www.asme.org/terms/Terms_Use.cfm

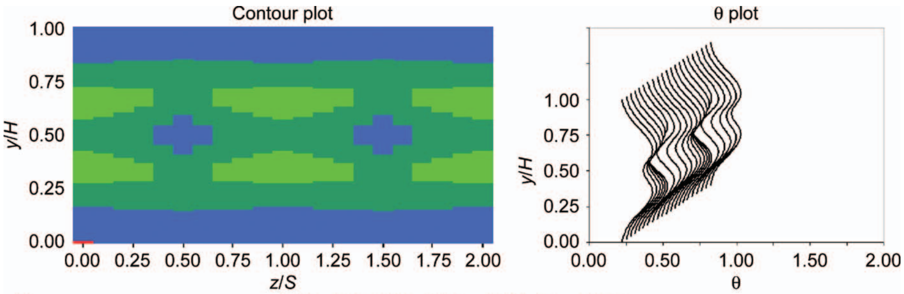

(a) $S/H = 0.25$, $H/d = 8$ ($C = 1.28$); $Us = 0.019$

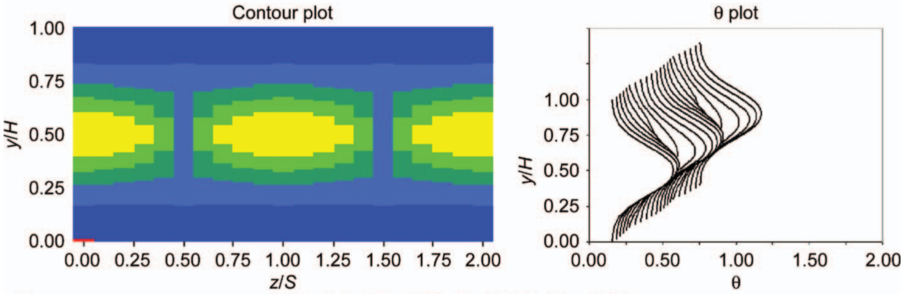

(b) $S/H = 0.5$, $H/d = 5.66$ ($C = 2.57$); $Us = 0.091$

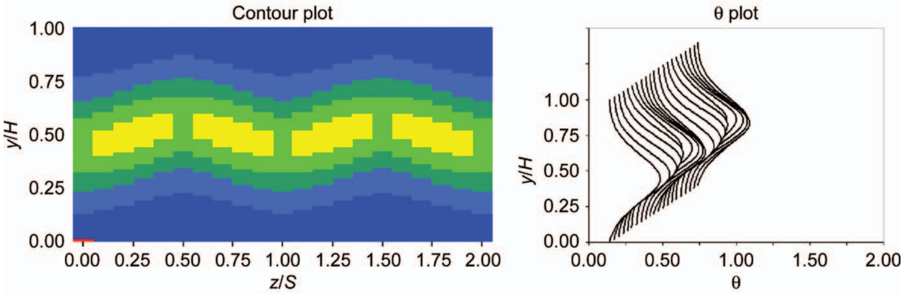

(c) $S/H = 0.5$, $H/d = 5.66$ ($C = 2.57$); $Us = 0.088$

Fig. 6 Variation in scalar profile and contour plots for opposed rows of inline jets (total $A_J/A_M=0.098$) at $x/H=0.5$ with $DR=2.2$, $J=26.4$, and $C_d=0.64$.

Nomenclature

A_J/A_M = jet-to-mainstream area ratio$=(\pi/4)/((S/d)\times(H/d))=(\pi/4)/((S/H)(H/d)^2)$
C = $(S/H)(\mathrm{sqrt}(J))$
C_d = orifice discharge coefficient=(effective area)/(physical area)
d = actual physical diameter of a round hole
d_j = effective diameter$=(d)(\mathrm{sqrt}(C_d))$
DR = jet-to-mainstream density ratio, ρ_J/ρ_M
H = duct height at center of row of holes (called H_0 in several previous publications)
H/d = ratio of duct height to orifice diameter
H_{eq} = effective duct height (=H except in the symmetry model for opposed rows of inline jets)
J = jet-to-mainstream momentum-flux ratio $(\rho_J V_J^2)/(\rho_M U_M^2)$
m_J = jet mass flow
m_M = mainstream mass flow
m_T = total mass flow, m_J+m_M
m_J/m_M = jet-to-mainstream mass-flow ratio= $(\rho_J/\rho_M)\times(V_J/U_M)(C_d)(A_J/A_M))=(m_J/m_T)/(1-m_J/m_T)$
m_J/m_T = jet-to-total mass-flow ratio
S = lateral spacing between equivalent locations of adjacent orifices
S/d = ratio of orifice spacing to orifice diameter $=(S/H)(H/d)$
S/H = ratio of orifice spacing to duct height
T = local scalar variable
T_J = scalar variable at jet exit
T_M = scalar variable in unmixed mainstream flow
U = axial velocity
U_M = unmixed mainstream velocity
U_s = unmixedness= $\theta_{\mathrm{var}}/(\theta_{\mathrm{ave}}(1-\theta_{\mathrm{ave}})))$, same as Eq. (2)
V_J = jet exit velocity
x = downstream coordinate; $x=0$ at center of the first row of orifices
y = cross-stream coordinate; $y=0$ at wall
z = lateral coordinate; $z=0$ at centerplanes
θ = dimensionless scalar, $(T_M-T)/(T_M-T_J)$; same as Eq. (1)
θ_{ave} = fully mixed scalar difference ratio$=\theta_{\mathrm{EB}}$
θ_{EB} = equilibrium θ (called TB in Ref. [6]) $\sim m_J/m_T$
θ_{var} = variance of scalar difference ratio

References

[1] Holdeman, J. D., 1993, "Mixing of Multiple Jets With a Confined Subsonic Crossflow," Prog. Energy Combust. Sci., **19**, pp. 31–70.

Downloaded 02 Jun 2010 to 171.66.16.96. Redistribution subject to ASME license or copyright; see http://www.asme.org/terms/Terms_Use.cfm

[2] Holdeman, J. D., Liscinsky, D. S., Oechsle, V. L., Samuelsen, G. S., and Smith, C. E., 1997, "Mixing of Multiple Jets With a Confined Subsonic Crossflow: Part I—Cylindrical Ducts," ASME J. Eng. Gas Turbines Power, **119**, pp. 852–862.
[3] Holdeman, J. D., Liscinsky, D. S., and Bain, D. B., 1999, "Mixing of Multiple Jets With a Confined Crossflow: Part II—Opposed Rows of Orifices in Rectangular Ducts," ASME J. Eng. Gas Turbines Power, **121**, pp. 551–562.
[4] Holdeman, J. D., Smith, T. D., Clisset, J. R., and Lear, W. E., 2005, "A Spreadsheet for the Mixing of a Row of Jets With a Confined Crossflow," NASA Report No. NASA/TM-2005-213137.
[5] Holdeman, J. D., Clisset, J. R., Moder, J. P., and Lear, W. E., 2006, "On the Mixing of Single and Opposed Rows of Jets With a Confined Crossflow," NASA Report No. NASA/TM-2006-214226.
[6] Holdeman, J. D. 1983, "Perspectives on the Mixing of a Row of Jets With a Confined Crossflow," AIAA Paper No. 83-1200.
[7] Holdeman, J. D., and Srinivasan, R., 1986, "Perspectives on Dilution Jet Mixing," AIAA Paper No. 86-1611.
[8] Lefebvre, A. H., 1999, *Gas Turbine Combustion*, 2nd ed., Taylor & Francis, London.
[9] Liscinsky, D. S., True, B., and Holdeman, J. D., 1996, "Effect of Inlet Flow Conditions on Crossflow Jet Mixing," AIAA Paper No. 96-2881.
[10] Walker, R. E., and Kors, D. L., 1973, "Multiple Jet Study Final Report," NASA Report No. CR-121217.
[11] Liscinsky, D. S., 2008, private communication.
[12] Kobayashi, H., Ham, F., and Wu, X., 2008, "Application of a Local SGS Model Based on Coherent Structures to Complex Geometries," Int. J. Heat Fluid Flow, **29**, pp. 640–653.

Downloaded 02 Jun 2010 to 171.66.16.96. Redistribution subject to ASME license or copyright; see http://www.asme.org/terms/Terms_Use.cfm

Comparative Performance, Emission, and Combustion Characteristics of Rice-Bran Oil and Its Biodiesel in a Transportation Diesel Engine

Avinash Kumar Agarwal[1]
e-mail: akag@iitk.ac.in

Atul Dhar

Engine Research Laboratory,
Department of Mechanical Engineering,
Indian Institute of Technology Kanpur,
Kanpur 208016, India

The methyl esters of vegetable oils known as biodiesel are becoming increasingly popular because of their low environmental impact and potential as a green alternative fuel for diesel engines. Methyl ester of rice-bran oil (RBOME) is prepared through the process of transesterification. In the present investigation, experiments have been carried out to examine the performance, emission, and combustion characteristics of a direct-injection transportation diesel engine running with diesel, 20% blend of rice-bran oil (RBO), and 20% blend of RBOME with mineral diesel. A four-stroke, four-cylinder, direct-injection transportation diesel engine (MDI 3000) was instrumented for the measurement of the engine performance, emissions, in-cylinder pressure-crank angle history, rate of pressure rise, and other important combustion parameters such as instantaneous heat release rate, cumulative heat release rate, mass fraction burned, etc. A careful analysis of the performance, emissions, combustion, and heat release parameters has been carried out. HC, CO, and smoke emissions for RBO and RBOME blends were lower than mineral diesel while NO_x emissions were almost similar and brake specific fuel consumption (BSFC) was slightly higher than mineral diesel. Combustion characteristics were quite similar for the three fuels.

[DOI: 10.1115/1.4000143]

Keywords: biodiesel, rice-bran oil, combustion, pressure-crank angle diagram, heat release analysis, emissions

1 Introduction

Depletion of petroleum reserves, rising vehicle population, increasing fuel prices, and uncertainties concerning petroleum availability, stringent emission standards, and global warming due to carbon dioxide emissions, have forced the development of alternate energy sources, which are becoming increasingly important. Vegetable oils have comparable energy density and cetane number as that of mineral diesel [1]. Physical and chemical characteristics of the vegetable oil can be improved by transesterification process, leading to reduction in fuel viscosity, which would otherwise cause problems in fuel injection and may cause nozzle wear [2–4]. The resultant product, i.e., biodiesel, has higher cetane number and heating value closer to mineral diesel. Also, carbon cycle time for fixation of CO_2 from biodiesel is quite small compared with mineral diesel. This means that biodiesel usage will effectively reduce greenhouse gas emissions [5].

Some researchers reported improved engine performance, particularly thermal efficiency for biodiesel fuelled engines [2–4,6–17]. With the use of biodiesel as a fuel in the engine, there is considerable reduction in harmful emissions like CO, HC, and smoke, but NO_x emissions increase [2–4,6–16]. Most of the western countries use edible oils such as soybean, sunflower, saffola, etc., for the production of biodiesel. In South Asia, variety of nonedible oils like linseed, mahua, karanja, rice-bran, and jatropha are available in abundance, which can be utilized for the production of biodiesel. Some of these oils have already been evaluated as substitute diesel fuels [2,3,6,8,18]. Agarwal and Das [2] used linseed oil methyl ester as a fuel in stationary engines. They found that 20% blend of linseed oil methyl ester was optimum blend, and it gave maximum benefit in terms of thermal efficiency. Similar results were found in our earlier study for rice-bran oil on a transportation diesel engine [3]. This study showed improved performance of the engine with reduction in the exhaust emissions except NO_x [3]. Zhang and Van Gerpan [13] investigated the combustion characteristics of turbocharged direct-injection diesel engine using blends of methyl, isopropyl, and winterized methyl ester of soybean oil with diesel as fuel. They found that all fuel blends except isopropyl ester had similar combustion behavior. Ignition delay for ester/diesel blend was shorter than mineral diesel as a fuel. Senatore et al. [14] showed that with rapeseed oil methyl ester, heat release is advanced as compared with diesel. Also injection starts earlier in the case of biodiesel as a fuel and average cylinder gas temperature was higher for biodiesel. Senthil Kumar et al. [18] found that for jatropha oil methyl ester, ignition delay was higher as compared with ignition delay for diesel in a constant speed diesel engine. Selim et al. [4] tested jojoba oil methyl ester (JME) as a fuel on Ricardo compression swirl diesel engine and found that the pressures and pressure rise rates for JME are almost similar to those of gas oil. JME, however, exhibits slightly lower pressure rise rate than gas oil, and esters seem to have slightly delayed combustion.

Blending of vegetable oils in small concentration ($<20\%$) with diesel is found to reduce the viscosity to acceptable American Society of Testing and Materials (ASTM) limits. Various governments in their transport/biodiesel policy have targeted to replace about 20–30% petroleum based fuels with biofuels due to availability issues (e.g., European Union (EU) 10% petrol and diesel from renewable sources until 2020; India has targeted 20% biodiesel and ethanol content until 2017, etc.). In this scenario, many sources of biodiesel need to be utilized simultaneously and rice-bran oil is one of the major surplus oil available for this purpose. It was realized that very little information is available on the performance, emission, and combustion behavior of rice-bran oil and rice-bran oil ester blends. The objective of this study is to critically evaluate and compare the performance of 20% blend of rice-bran oil methyl ester (RBOME20) and 20% blend of rice-bran oil (RBO20), vis-à-vis, mineral diesel.

2 Fuel Preparation and Characterization

Rice-bran oil was transesterified using methanol in the presence of an alkaline catalyst (NaOH). Process parameters like temperature, catalyst amount, molar ratio of alcohol to oil, and reaction temperature were optimized and it is found that 9:1 molar ratio of alcohol to oil, 55°C temperature, 0.75% (w/w) catalyst, and 1 h reaction time is optimum for the transesterification of rice-bran oil [9]. Characterization of rice-bran oil, rice-bran oil methyl ester, and diesel were done in the laboratory as per the relevant ASTM norms. Some fuel properties are shown in Table 1.

3 Experimental Setup

A transportation direct injection (DI) diesel engine (MDI 3000, Mahindra & Mahindra Ltd., India) was used for conducting the engine experiments. The specifications of the engine are given in Table 2.

---

[1] Corresponding author.

Manuscript received April 30, 2009; final manuscript received May 14, 2009; published online March 24, 2010. Editor: Dilip R. Ballal.

Copyright © 2010 by ASME

Downloaded 02 Jun 2010 to 171.66.16.96. Redistribution subject to ASME license or copyright; see http://www.asme.org/terms/Terms_Use.cfm

Table 1 Properties of the fuels

Characteristics	Rice-bran oil (RBO)	Mineral diesel (D)	Rice-bran oil methyl ester (RBOME)	20% rice-bran oil blend (RBO20)	20% biodiesel blend (RBOME20)
Specific gravity at 30°C	0.928	0.839	0.877	0.887	0.847
Viscosity (cS) at 40°C	42	3.18	5.3	4.9	3.48
Calorific value (MJ/Kg)	40.3	44.8	42.2	43.9	44.3
Flash point (°C)	316	68	183	–	–
Fire point (°C)	337	103	194	–	–
C:H:O (%)	74:11:12	82:13:1	73:13:11.6	–	–

The engine was coupled with an eddy current dynamometer (ASE 70, Schenck Avery Ltd., India). A piezoelectric pressure transducer (GU21C, AVL, Austria) was installed in the engine cylinder head to measure the combustion pressure. Signals from the pressure transducer were given to the charge amplifier. A high-precision shaft encoder was used for delivering signals for top dead center (TDC) and the crank angle with a precision of 0.1 deg crank angle. The signals from the charge amplifier and shaft encoder were supplied to a high-speed data acquisition system (Indimeter-619, AVL, Graz, Austria).

Three fuels, namely, RBO20, RBOME20, and mineral diesel were tested at different engine load conditions at two speeds (1800 rpm and 2400 rpm). Cylinder pressure data were acquired for 50 consecutive cycles and then the average was taken for eliminating the effect of cycle-to-cycle variations. All tests were carried out under steady state engine operating conditions.

4 Performance and Emission Tests

Experiments were conducted using RBO20, RBOME20, and mineral diesel. BSFC was found to be highest for RBO20 followed by RBOME20 (Fig. 1) at 1800 rpm; however, at 2400 rpm, BSFC for RBOME20 is better than even mineral diesel. Brake thermal efficiency (BTE) is affected differently by the engine speed variation for different fuels. Thermal efficiency of mineral diesel is highest at 1800 rpm while at 2400 rpm it is highest for RBOME blend followed by mineral diesel. Oxygen present in biodiesel molecules leads to improved combustion of fuel, therefore resulting in lower emission formation. In the case of RBO, higher viscosity prevents adequate fuel atomization (due to relatively higher fuel viscosity), which leads to inferior combustion compared with mineral diesel. Calorific value of RBO is lowest followed by RBOME; therefore this trend of BSFC (Fig. 1) is expected. Exhaust gas temperatures for all the fuels are quite close at 1800 rpm (Fig. 2) but slightly higher for mineral diesel followed by RBO20 and RBOME20 at 2400 rpm. Since all other results at 2400 rpm are similar to that at 1800 rpm, the experimental results at 2400 rpm have not been shown/discussed in the interest of space. The smoke opacity was analyzed using smoke opacimeter (AVL437, AVL, Austria). Smoke opacity was highest for mineral diesel and lowest for RBOME20. Smoke opacity increases with increasing engine speed and increasing engine load (Fig. 2).

The emission tests were conducted on these fuels using raw exhaust gas emission analyzer (EXSA 1500, Horiba, Japan). All the observed raw emission values are converted into mass emissions. Lowest CO_2 emissions were observed for mineral diesel (Fig. 3) at 1800 rpm. CO_2 emissions for mineral diesel were quite close to RBOME20, however slightly higher for RBO20. NO_x emissions for mineral diesel and RBOME20 were almost comparable (Fig. 3). The emissions of CO slightly decrease both for RBO20 and RBOME20 at lower engine loads (Fig. 4); however, at higher engine load conditions, CO emissions for all the fuels

Table 2 Specifications of the engine

Type of engine	Four-stroke, naturally aspirated, water cooled engine
Number of cylinders	Four
Bore/stroke (mm)	88.9/101.6
Displacement volume (cc)	2520
Compression ratio	18:1
Rated power	40.4 kW at 3000 rpm
Maximum torque	152 N m at 1800 rpm
Injection system	In-line reciprocating mechanical pump
Injection timing	17 ± 1 deg BTDC
Injector opening pressure	214–194 kg/cm^2

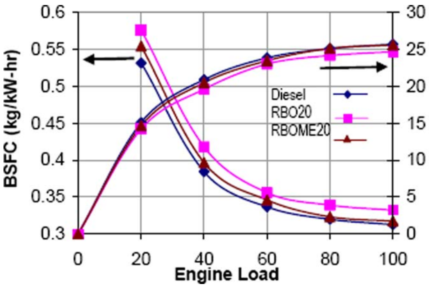

Fig. 1 BSFC and thermal efficiency at 1800 rpm

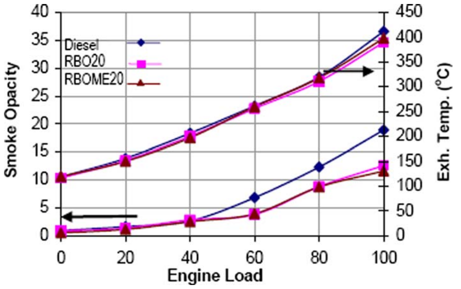

Fig. 2 Smoke opacity and exhaust temperature at 1800 rpm

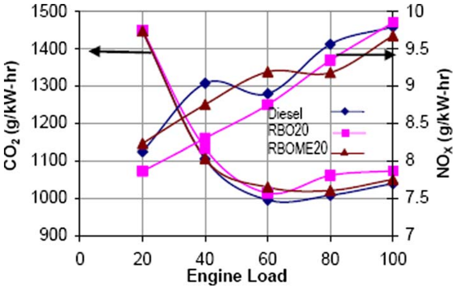

Fig. 3 CO_2 and NO_x emissions at 1800 rpm

Downloaded 02 Jun 2010 to 171.66.16.96. Redistribution subject to ASME license or copyright; see http://www.asme.org/terms/Terms_Use.cfm

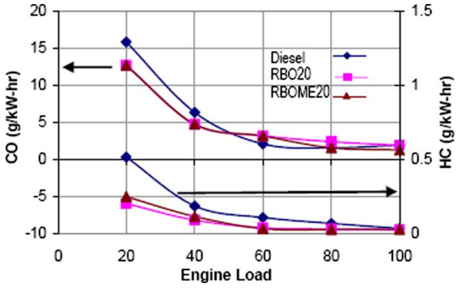

Fig. 4 CO and HC emissions at 1800 rpm

were approximately similar. HC emissions were highest for mineral diesel followed by RBOME20 and lowest for RBO20 (Fig. 4).

5 Combustion Analysis

In a compression ignition engine, cylinder pressure depends on the burned fuel fraction during the premixed combustion phase, i.e., initial stage of combustion. Cylinder pressure characterizes the ability of the fuel to mix well with air and burn. High peak pressure and maximum rate of pressure rise correspond to large amount of fuel burned in the premixed combustion stage. The cylinder pressure-crank angle history is obtained at different loads for mineral diesel, RBO20, and RBOME20. Peak pressure and maximum rate of pressure rise are obtained at different loads from these measurements.

Representative results of cylinder pressure and instantaneous rate of heat release at no load and full load at 1800 rpm are discussed in the following paragraphs (Figs. 5 and 6). At all engine loads, in-cylinder pressure curves for mineral diesel, RBOME20, and RBO20 are almost the same except that RBO20 shows slightly earlier start of combustion. As engine load increases, this difference in the start of combustion timing among the three fuels reduces. Earlier start of combustion for RBOME20 may be caused by shorter ignition delay (high cetane number), and for RBO20, it may be caused by advancing of fuel injection due to higher bulk modulus of the RBO20.

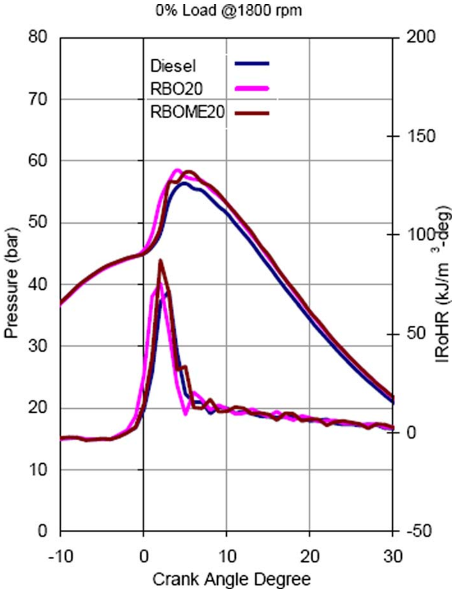

Fig. 5 Comparison of in-cylinder pressure and heat release rate variation at no load condition

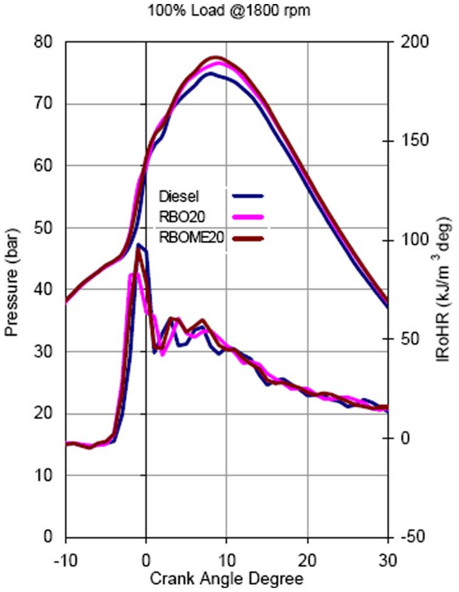

Fig. 6 Comparison of in-cylinder pressure and heat release rate variation at full load condition

Peak pressure for all the fuels occur between 4–8 deg crank angle after top dead center (ATDC) at 1800 rpm and 4–9 deg crank angle ATDC at 2400 rpm. Peak pressure is slightly higher for RBOME20 at 1800 rpm in all the engine loads. From the heat release diagram it is evident that the initial rate of heat release is slightly higher for mineral diesel in the beginning of the combustion. All fuels experience rapid premixed burning, followed by diffusion combustion as is typical of naturally aspirated diesel engines. After the ignition delay period, the premixed fuel-air mixture burns rapidly, releasing heat at a very rapid rate, after which diffusion combustion takes place, where the burning rate is controlled by the availability of combustible fuel-air mixture.

It can be noted that at no load condition, most of the heat releases take place in the premixed combustion phase, whereas at full load, significant amount of heat release also take place in the diffusion combustion phase. This diffusion combustion phase heat release is relatively higher for RBO20 and RBOME20 compared to mineral diesel.

Figure 7 shows the cumulative heat release curve for no load and full load conditions at 1800 rpm. Cumulative heat release is marginally higher for both RBO20 and RBOME20 at low load compared with mineral diesel (Fig. 7). At medium and high load the cumulative rate of heat release for RBO20 and RBOME20 are almost the same as with mineral diesel.

Mass burn rate of the fuel can be found out from the cumulative heat release diagram. Figure 8 shows the crank angle at which 10% and 90% mass of fuel is burned. This figure shows that 10%

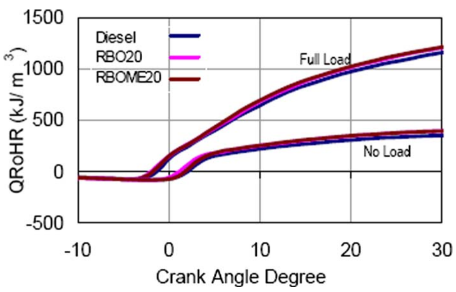

Fig. 7 Comparison of cumulative heat release rate variation at idle and full load conditions

Downloaded 02 Jun 2010 to 171.66.16.96. Redistribution subject to ASME license or copyright; see http://www.asme.org/terms/Terms_Use.cfm

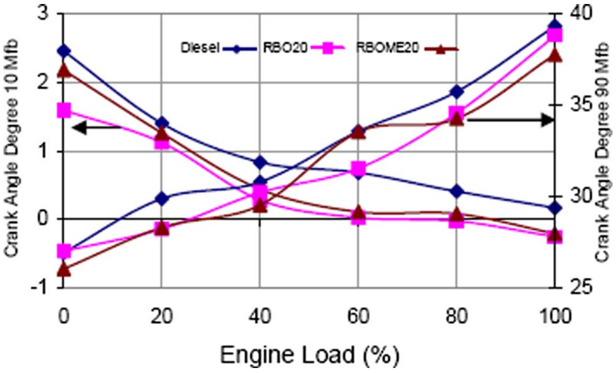

Fig. 8 Crank angle for 10% and 90% mass burns at 1800 rpm

of fuel burns earlier for the RBO20 and 90% of the fuel is burned earlier in case of RBOME20, showing faster burning of RBOME20 compared to mineral diesel and RBO20. Combustion duration for all the fuels increases as the load is increased due to the increase in the quantity of fuel injected. From all these diagrams and discussions, it is amply clear that RBO20 and RBOME20 have shorter ignition delay compared with mineral diesel; however, the burning speed of RBO20 is relatively slower.

6 Conclusions

A detailed experimental analysis for finding out the performance, emission, and combustion characteristics of RBO20 and RBOME20, vis-à-vis, mineral diesel was carried out. HC and CO emissions for both RBO20 and RBOME20 were lower than mineral diesel. NO_x emissions are comparable for all the three fuels at all load and speed conditions. BSFC for RBO20 was higher than mineral diesel but BSFC for RBOME20 was quite close to mineral diesel. Combustion of RBOME20 was found to be more efficient than mineral diesel but thermal efficiency of RBO20 was inferior to mineral diesel. CO_2 emissions for RBO20 were slightly higher than mineral diesel but almost similar for RBOME20 and mineral diesel. Smoke opacity for both RBO20 and RBOME20 was better than mineral diesel.

Various combustion parameters such as pressure-crank angle diagram, peak pressures, crank angle for peak pressure, crank angle for 10% mass burn, crank angle for 90% mass burn, instantaneous heat release rate, cumulative heat release, etc., were evaluated for different engine loads in the transportation diesel engine. The experimental investigations revealed that the overall combustion characteristics were quite similar for RBOME20, RBO20, and mineral diesel. For RBO20 and RBOME20, ignition delay is lower compared to mineral diesel. RBO20 and RBOME20 did not cause any fuel/combustion related problems. The ignition delay was shorter for RBO20 and RBOME20 compared with mineral diesel; however, the burning rate was relatively slower for RBO20. This detailed experimental investigation suggests that 20% blend of biodiesel as well as 20% rice-bran oil can substitute mineral diesel without any significant modification in medium duty transportation DI diesel engine.

References

[1] Agarwal, A. K., 2007, "Biofuels (Alcohols and Biodiesel) Applications as Fuels for Internal Combustion Engines," Prof. Energy Combust. Sci., **33**(3), pp. 233–271.

[2] Agarwal, A. K., and Das, L. M., 2001, "Biodiesel Development and Characterization for Use as a Fuel in Compression Ignition Engine," ASME J. Eng. Gas Turbines Power, **123**(2), pp. 440–447.

[3] Sinha, S., and Agarwal, A. K., "Performance Evaluation of a Biodiesel (Rice-Bran Oil Methyl Ester) Fuelled Transport Diesel Engine," SAE Paper No. 2005-01-1730.

[4] Selim, M. Y. E., Radwan, M. S., and Elfeky, S. M. S., 2003, "Combustion of Jojoba Methyl Ester in an Indirect Injection Diesel Engine," Renewable Energy, **28**, pp. 1401–1420.

[5] Van Gerpan, J., 2005, "Biodiesel Processing and Production," Fuel Process. Technol., **86**, pp. 1097–1107.

[6] Raheman, H., and Ghadge, S. V., 2008, "Performance of Diesel Engine With Biodiesel at Varying Compression Ratio and Ignition Timing," Fuel, **87**, pp. 2659–2666.

[7] Canakci, M., 2007, "Combustion Characteristics of a Turbocharged DI Compression Ignition Engine Fueled With Petroleum Diesel Fuels and Biodiesel," Bioresour. Technol., **98**, pp. 1167–1175.

[8] Raheman, H., and Ghadge, S. V., 2007, "Performance of Compression Ignition Engine With Mahua (Madhuca Indica) Biodiesel," Fuel, **86**, pp. 2568–2573.

[9] Lin, C.-Y., and Lin, H.-A., 2006, "Diesel Engine Performance and Emission Characteristics of Biodiesel Produced by the Peroxidation Process," Fuel, **85**, pp. 298–305.

[10] Scholl, K. W., and Sorenson, S. C., "Combustion of Soybean Oil Methyl Ester in a Direct Injection Diesel Engine," SAE Paper No. 930934.

[11] da Silva, F. N., Prata, A. S., and Teixeira, J. R., 2003, "Technical Feasibility Assessment of Oleic Sunflower Methyl Ester Utilization in Diesel Bus Engine," Energy Convers. Manage., **44**, pp. 2857–2878.

[12] Al-Widyan, M., Tashtoush, G., and Abu-Qudais, M., 2002, "Utilization of Ethyl Ester of Waste Vegetable Oils as Fuel in Diesel Engines," Fuel Process. Technol., **76**, pp. 91–103.

[13] Zhang, Y., and Van Gerpan, J. H., "Combustion Analysis of Esters of Soyabean Oil in a Diesel Engine," Transactions of SAE, SAE 960765.

[14] Senatore, A., Cardone, M., Rocco, V., and Prati, M. V., 2000, "A Comparative Analysis of Combustion Process in D.I. Diesel Engine Fueled With Biodiesel and Diesel Fuel," Transactions of SAE, SAE 2000-01-0691.

[15] Shi, X., Pang, X., Mu, Y., He, H., Shuai, S., Wang, J., Chen, H., and Li, R., 2006, "Emission Reduction Potential of Using Ethanol-Biodiesel-Diesel Fuel Blend on a Heavy-Duty Diesel Engine," Atmos. Environ., **40**, pp. 2567–2574.

[16] Usta, N., 2005, "An Experimental Study on Performance and Exhaust Emissions of a Diesel Engine Fuelled With Tobacco Seed Oil Methyl Ester," Energy Convers. Manage., **46**, pp. 2373–2386.

[17] Laforgia, D., and Ardito, V., 1995, "Biodiesel Fueled IDI Engines: Performances, Emissions and Heat Release Investigation," Bioresour. Technol., **51**, pp. 53–59.

[18] Senthil Kumar, M., Ramesh, A., and Nagalingam, B., 2003, "An Experimental Comparison of Methods to Use Methanol and Jatropha Oil in a Compression Ignition Engine," Biomass Bioenergy, **25**, pp. 309–318.

Downloaded 02 Jun 2010 to 171.66.16.96. Redistribution subject to ASME license or copyright; see http://www.asme.org/terms/Terms_Use.cfm

Improved Three-Dimensional Crowning Profiles for Dovetail Attachments

J. R. Beisheim
Development Group,
ANSYS Inc.,
Canonsburg, PA 15317

G. B. Sinclair
Department of Mechanical Engineering,
Louisiana State University,
Baton Rouge, LA 70803

*Dovetail attachments in gas turbines are subject to fatigue failures. These fatigue failures occur as a result of large fluctuations in hoop stresses near the edges of contact in attachments. The high hoop stresses available for fluctuating are, in turn, the result of high contact stress peaks near the edges of contact. One means of alleviating these stresses is via crowning. Such crowned configurations are inherently three-dimensional and consequently present some challenges to obtaining convergent contact stresses with finite elements. Such challenges are met in the work of Beisheim and Sinclair (2008, "Three-Dimensional Finite Element Analysis of Dovetail Attachments With and Without Crowning," ASME J. Turbomach., **130**, pp. 021012-1–021021-8), and crowning is shown to reduce contact stresses by about 40%. The crowning profile used in that paper is the natural Hertzian profile of a segment of an ellipsoid. This note investigates an alternative profile with a view to increasing the area of contact, and thereby further reducing contact stresses. Converged contact stresses are obtained for both profiles, and demonstrate that the alternative profile can indeed reduce contact stresses by an additional 10%.* [DOI: 10.1115/1.4000142]

1 Introduction

Single tooth attachments or "dovetails" are used to secure fan and compressor blades to disks in gas turbines. A section through a typical dovetail is shown in Fig. 1(*a*). Therein, the base of the blade is pulled, as a result of the centripetal acceleration of its remainder, while it is restrained by contact with the disk on two flats (e.g., $C-C'$ in Fig. 1(*a*)). At the edges of these contact regions, fretting can occur when loads vary. This fretting can lead to fatigue crack initiation and ultimately, to failures.

Verified two-dimensional stresses at the edges of contact have helped in gaining an appreciation of the physics leading to fatigue in dovetail attachments. This physics is described in some detail in Ref. [1]; here, we summarize the aspects pertinent to the present study.

The key contributor to fatigue in dovetail attachments identified in Ref. [1] is a *pinching mechanism* occurring during unloading when friction is present. During loading up, the attachment can be shown to slip. Under these circumstances, stresses can be expected to behave as in a classical Hertzian contact. That is with peak values obeying

$$\sigma_c \propto \sigma_0, \quad \tau_c = \mu\sigma_c, \quad \sigma_h = \pm 2\tau_c \tag{1}$$

where σ_c and τ_c are the normal and shear contact stresses (positive as in (Fig. 1(*b*)), σ_h is the hoop stress, σ_0 is the applied stress acting at the top of the blade section (Fig. 1(*a*)), and μ is the coefficient of friction ($0 \leq \mu \leq 0.4$ in typical attachments). During unloading, stresses completely reverse themselves if $\mu=0$. However, when $\mu \neq 0$, the blade can stick to the disk. The angular periodic arrangement of the blades can then produce pinching because the sides of a representative geometry are not parallel (i.e., the outer near-vertical boundaries of the disk in Fig. 1(*a*) are not parallel). Under these circumstances, we have the following, somewhat unexpected behavior:

$$\sigma_0\downarrow \sigma_c\uparrow \tag{2}$$

that is, the normal contact stress actually increases with unloading. As a consequence, we further have

$$\tau_c\downarrow \sigma_h\downarrow \tag{3}$$

that is, now the shear stress drops dramatically for two reasons: First, because there is less load to oppose ($\sigma_0\downarrow$), and second, because the normal contact stress is now doing more to oppose it ($\sigma_c\uparrow$). As a result, because the hoop stress is largely produced by the shear stress, it too drops dramatically. Thus, minor oscillations in applied loading/rpm (σ_0) can lead to relatively major oscillations in tensile hoop stresses at the edges of contact. These significantly fluctuating hoop stresses are then the harbinger of fatigue failures in dovetail attachments.

One potential means of alleviating these fluctuations is via *precision crowning* [2]. We summarize the pertinent elements of this approach here. Basically, precision crowning seeks to reduce the peak hoop stress $\sigma_h^{\max}$ during loading up when friction is present. This is because if $\sigma_h^{\max}$ is less at maximum load, there is less hoop stress to fluctuate. Further, because during loading up

$$\sigma_c\downarrow \Rightarrow \tau_c\downarrow \Rightarrow \sigma_h\downarrow \tag{4}$$

(see Eq. (1)), this objective is tantamount to reducing the peak contact stress $\sigma_c^{\max}$ during loading up. This latter reduction can be achieved with a small crown of height δ (Fig. 1(*c*)). This produces Hertzian-like contact stresses instead of edge-of-contact peaks in stresses (Fig. 2). This removal of peak contact stresses reduces fluctuations in the hoop stress by 70%, as in Ref. [2].

The analysis in Ref. [2] shows the potential of crowning to alleviate fatigue failures in attachments. However, this analysis is limited to two dimensions, when in fact, dovetail attachments are inherently three-dimensional, and crowning must be entertained both in the plane of Fig. 1, as well as out of the plane of this figure, if it is to be effective. Hence, in Ref. [3], a three-dimensional analysis of an attachment with and without crowning is undertaken. This analysis finds that reductions with crowning of peak contact stresses and attendant hoop stresses still occur, but are less marked because the reduction in contact extent with crowning (see, e.g., Fig. 2) now occurs in two directions. Nonetheless, peak contact and hoop stresses are reduced by 37% on average.

The intent of this note, then, is to investigate an alternative crowning profile that still promotes Hertzian-like contact stresses, but that also increases the area of contact, and therefore reduces contact stresses further. In what follows, we first describe the two crowning profiles considered, then their analysis with finite elements. Thereafter, we check the convergence of the finite element analysis for the two profiles, and compare contact areas and stresses.

2 Crowning Profiles and Finite Element Analysis

The global configuration considered is the same test arrangement, as analyzed in Ref. [3], and described in some detail therein. This test configuration is used in the gas turbine industry to simulate dovetail attachments. It has an applied stress σ_a that acts in a similar manner to σ_0 of Fig. 1, but has a smaller magni-

---

Manuscript received April 14, 2009; final manuscript received May 7, 2009; published online March 30, 2010. Editor: Dilip R. Ballal.

Copyright © 2010 by ASME

Downloaded 02 Jun 2010 to 171.66.16.96. Redistribution subject to ASME license or copyright; see http://www.asme.org/terms/Terms_Use.cfm

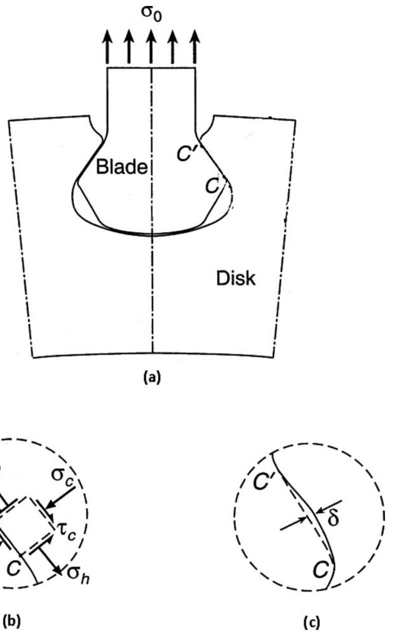

Fig. 1 Dovetail attachment configuration: (*a*) section of attachment, (*b*) close up of disk near lower contact point with stresses acting, and (*c*) in-plane crown on blade flat

tude because it is applied over a larger area. On the contact flats in the test piece that correspond to those on a blade, a crowning profile of height z is introduced, where

$$z = \delta\left(1 - \frac{x^2}{a^2} - \frac{y^2}{b^2}\right) \tag{5}$$

In Eq. (5), δ is the maximum crown height (at $x=y=0$), x and y are rectangular coordinates in the plane of the contact flat, and a and b are the extents of the profile in the x and y directions. These extents are taken to be 7/8 of the total extents available on the original contact flat to enable the profile to be smoothly blended into the flat along its edges.

The profile in Eq. (5) promotes Hertzian contact over a portion of an ellipsoid. This enables the height δ to be initially estimated using an analytical expression for the elastic approach when an ellipsoid indents a half space. This initial height is then varied and checked with finite element analysis to try and ensure that contact spreads throughout most of the profile without extending past the ends of the profile. For the present configuration, this process leads to a height of 0.12 mm, ±20%, as a suitable range of crown heights.

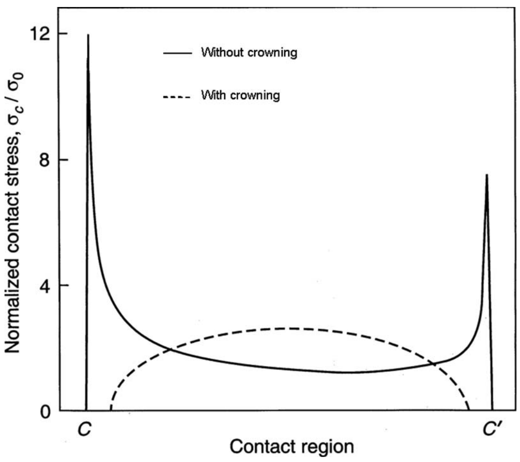

Fig. 2 Contact stress distribution (two-dimensional analysis of Ref. [2])

Table 1 Finite element grids and contact stresses

Grid	No. of spacial elements	No. of contact elements	$\sigma_c^{\max}/\sigma_a$ with Eq. (5)	$\sigma_c^{\max}/\sigma_a$ with Eq. (6)
c	2,127	487	23.2	23.2
m	14,990	1943	25.7	23.9
f	108,870	7765	27.0	24.3

While effective in promoting Hertzian-like contact stresses, and facilitating the determination of appropriate crown heights, the profile of Eq. (5) tends to lead to contact over an elliptical region with an area no greater than πab. Here, instead then, we also consider a crowning profile with height z, given by

$$z = \delta\left(1 - \frac{x^2}{a^2}\right)\left(1 - \frac{y^2}{b^2}\right) \tag{6}$$

In Eq. (6), δ remains, as for Eq. (5). With Eq. (6), Hertzian-like contact stresses may still result because it is effectively the product of two, two-dimensional Hertzian indentor profiles. If this proves to be the case, contact can now spread over an approximately rectangular region with an area of $4ab$, thus realizing a greater contact area than with Eq. (5) with lower contact stresses. We investigate this possibility with a pair of finite element analyses; one applied to the profile of Eq. (5), the other applied to the profile of Eq. (6). Otherwise, the finite element analyses are identical.

For the finite element analysis, eight node hexahedral elements are used to discretize the test piece (SOLID45, ANSYS [4]). We use these low-order elements so as to interface with low-order contact elements that have been found to be effective in the analysis of like configurations. We place a boundary layer of elements in the vicinity of the contact region on both the portion of the test piece simulating the blade and the portion of the test piece simulating the disk. The boundary layer has a depth of 3/8 of the smallest radius of curvature of the blade, a depth that is somewhat more conservative than the value previously tested in the numerical analysis of conforming contact problems. Inside this boundary layer, we create uniform grids of elements, and systematically refine these grids by halving element sides. Outside this boundary layer, we approximately systematically refine the global grids. We do this by specifying the number of elements along the edges of the blade and disk away from the region of interest. We then use the VMESH command in ANSYS [4] to automatically mesh the rest of the region. The resulting global coarse grid (*c*) is shown in Ref. [3]. The numbers of spatial elements for this coarse grid (*c*), and the successive medium (*m*) and fine (*f*) grids are set out in Table 1. While the systematic halving of element sides would see successive three-dimensional grids increase these numbers of elements by factors of 8, here, the approximately systematic scheme used away from the contact region leads to factors of 7.0 and 7.3.

To police contact constraints, we used surface-to-surface contact elements (TARGE170 and CONTA173, ANSYS [4]). These surface elements overlay the spatial elements within the boundary layer on the contact surfaces. An important input parameter for these contact elements in ANSYS is the normal contact stiffness factor (FKN). This factor controls the stiffness of the contacting surfaces, which limits the amount of penetration of the contact surface into the target surface. We override the default value of 1 with a value of 10, in order to help limit penetration while still maintaining good convergence of the contact algorithm. Otherwise, we use the default nonlinear convergence criteria in ANSYS. The numbers of contact elements for the *c*, *m*, and *f* grids are included in Table 1; these increase by nearly a factor of 4 between

Downloaded 02 Jun 2010 to 171.66.16.96. Redistribution subject to ASME license or copyright; see http://www.asme.org/terms/Terms_Use.cfm

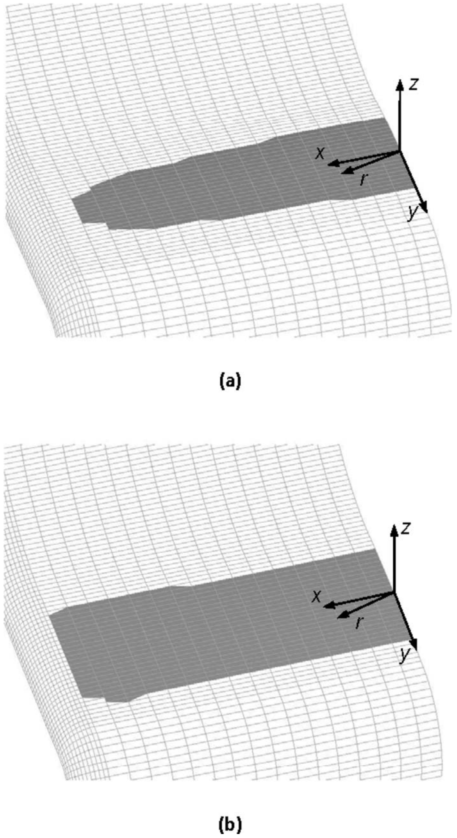

Fig. 3 Contact regions (*a*) with the original crowning profile of Eq. (5), and (*b*) with the alternative crowning profile of Eq. (6)

grids, consistent with systematic halving of element sides in two dimensions.

With these finite element grids, we judge any stress component sought, say σ, to be *converging* if

$$|\sigma^{c}-\sigma^{m}| > |\sigma^{m}-\sigma^{f}| \tag{7}$$

where superscripts denote the grid used in the computation. This particular convergence check was demonstrated to be effective in determining whether or not stress fields are converging in contact problems, in contrast to just a two-grid check [5]. Further, σ is judged to have *converged* if an estimated discretization error e_d is less than the error level sought e_s. Thus

$$e_d = \frac{\sigma^{f}-\sigma^{m}}{\sigma^{f}} \quad |e_d| < e_s \tag{8}$$

for converged σ. Here, we adopt $e_s=0.05$, or a 5% level as satisfactory.

3 Results and Discussion

Table 1 includes finite element values of the maximum normalized contact stresses $\sigma_c^{\max}$ at $x=y=0$, divided by the applied stress σ_a for the two profiles in Eqs. (5) and (6), and for $\mu=0.4$. With grid refinement, increments in these contact stresses are decreasing in accordance with Eq. (7) for both profiles, and accordingly, contact stresses for both profiles are judged to be converging. In fact, stress increments are approximately halving, corresponding to a linear rate of convergence, which is the usual rate found for these contact elements in test problems [6] (ANSYS higher-order contact elements converge slightly slower on average, as in Ref. [6]).

Using the error estimate of Eq. (8), discretization errors for the fine grid stresses with Eqs. (5) and (6) are calculated to be 4.8% and 1.6%, respectively. Because these estimated errors are both less than 5%, we judge the finite element analyses for both profiles to have converged satisfactorily.

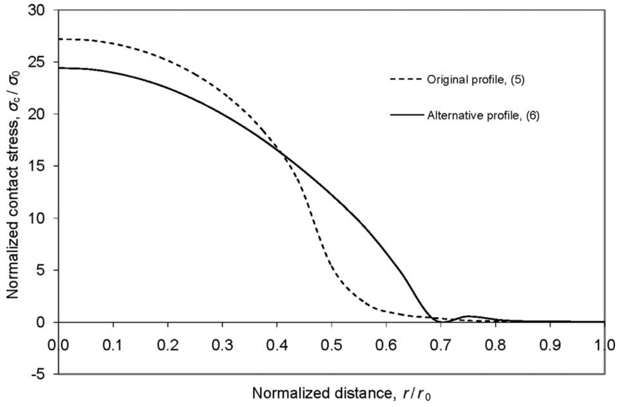

Fig. 4 Contact stress distributions with different crowning profiles

Figure 3 shows the finite element approximations for the contact regions for the two profiles with shaded elements on the blade portion of the test piece. Only halves of such areas are shown; the remaining halves can be obtained by reflection about the y-axis because the yz plane is a plane of symmetry in the test piece configuration. As expected, the contact area attending the profile in Eq. (5) is elliptical in nature, while the contact area attending the profile in Eq. (6) is approximately rectangular, and is larger.

This larger contact region with profile (6) does lead to lower contact stresses. The maximum contact stress in Table 1 is reduced by 10.0% with profile (6). Moreover, Hertzian-like contact stresses are produced throughout the contact region with profile (6). This is illustrated in Fig. 4, along the radial direction $r=(x^2+y^2)^{1/2}$ (in Fig. 4, $r_0=8(a^2+b^2)^{1/2}/7$ is the total available extent in the radial direction). Apparent in Fig. 4 is the reduction in peak Hertzian contact stresses, as well as an increased contact extent. Similar Hertzian-like contact stress distributions occur in the x and y directions with profile (6).

While 10% is certainly not a large further reduction in contact stresses, in fatigue situations, reductions of this magnitude can nonetheless be quite helpful. Given that the alternative profile offered here in Eq. (6) can be as readily implemented analytically as the original profile of Eq. (5), it would seem reasonable to prefer profiles like Eq. (6) in implementing crowning of dovetail attachments.

Acknowledgment

We are most grateful to General Electric Aircraft Engines of Cincinnati for providing the funding for this research. We also appreciate being furnished specifications for the dovetail test piece by Pratt & Whitney. In addition, we are grateful to ANSYS for providing access to their software, which is used exclusively throughout.

Nomenclature

a, b = contact length extents (3D)
C, C' = contact length and points (2D)
e_d = discretization error estimate
e_s = discretization error level sought
r = radial coordinate
x, y = rectangular coordinates
z = crowning profile height
δ = peak crowning height
μ = coefficient of friction
σ_a = applied stress in 3D configuration

Downloaded 02 Jun 2010 to 171.66.16.96. Redistribution subject to ASME license or copyright; see http://www.asme.org/terms/Terms_Use.cfm

σ_0 = applied stress in 2D configuration
$\sigma_c, \sigma_c^{\max}$ = contact stress, maximum contact stress
σ_h = hoop stress
$\sigma^c, \sigma^m, \sigma^f$ = stress found with finite elements on coarse, medium, and fine grids
τ_c = contact shear stress

References

[1] Sinclair, G. B., and Cormier, N. G., 2002, “Contact Stresses in Dovetail Attachments: Physical Modeling,” ASME J. Eng. Gas Turbines Power, **124**, pp. 325–331.

[2] Sinclair, G. B., and Cormier, N. G., 2003, “Contact Stresses in Dovetail Attachments: Alleviation Via Precision Crowning,” ASME J. Eng. Gas Turbines Power, **125**, pp. 1033–1041.

[3] Beisheim, J. R., and Sinclair, G. B., 2008, “Three-Dimensional Finite Element Analysis of Dovetail Attachments With and Without Crowning,” ASME J. Turbomach., **130**, p. 021012.

[4] ANSYS, 2006, *ANSYS Advanced Analysis Techniques, Revision 10.0*, ANSYS Inc., Canonsburg, PA.

[5] Sinclair, G. B., Cormier, N. G., Griffin, J. H., and Meda, G., 2002, “Contact Stresses in Dovetail Attachments: Finite Element Modeling,” ASME J. Eng. Gas Turbines Power, **124**, pp. 182–189.

[6] Sezer, S., and Sinclair, G. B., 2006, “An Assessment of ANSYS Contact Elements,” Proceedings of the 2006 International ANSYS Conference.

Downloaded 02 Jun 2010 to 171.66.16.96. Redistribution subject to ASME license or copyright; see http://www.asme.org/terms/Terms_Use.cfm